Ground Penetrating Radar in Sediments
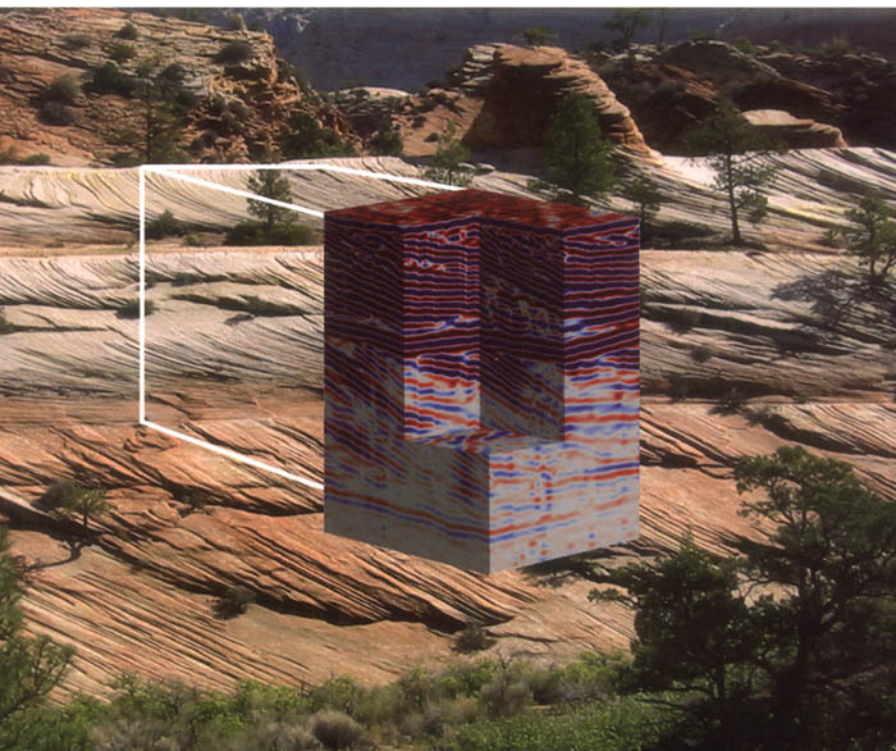
Edited by
C. S. Bristow and H. M. Jol

Ground Penetrating Radar in Sediments

Special Publication reviewing procedures

The Society makes every effort to ensure that the scientific and production quality of its books matches that of its journals. Since 1997, all book proposals have been refereed by specialist reviewers as well as by the Society's Books Editorial Committee. If the referees identify weaknesses in the proposal, these must be addressed before the proposal is accepted.

Once the book is accepted, the Society has a team of Book Editors (listed above) who ensure that the volume editors follow strict guidelines on refereeing and quality control. We insist that individual papers can only be accepted after satisfactory review by two independent referees. The questions on the review forms are similar to those for *Journal of the Geological Society*. The referees' forms and comments must be available to the Society's Book Editors on request.

Although many of the books result from meetings, the editors are expected to commission papers that were not presented at the meeting to ensure that the book provides a balanced coverage of the subject. Being accepted for presentation at the meeting does not guarantee inclusion in the book.

Geological Society Special Publications are included in the ISI Index of Scientific Book Contents, but they do not have an impact factor, the latter being applicable only to journals.

More information about submitting a proposal and producing a Special Publication can be found on the Society's web site: www.geolsoc.org.uk.

Ground Penetrating Radar in Sediments

EDITED BY

C. S. BRISTOW
Birkbeck, University of London, UK

H. M. JOL
University of Wisconsin, USA

THE GEOLOGICAL SOCIETY

The Geological Society of London (GSL) was founded in 1807. It is the oldest national geological society in the world and the largest in Europe. It was incorporated under Royal Charter in 1825 and is Registered Charity 210161.

The Society is the UK national learned and professional society for geology with a worldwide Fellowship (FGS) of 9000. The Society has the power to confer Chartered status on suitably qualified Fellows, and about 2000 of the Fellowship carry the title (CGeol). Chartered Geologists may also obtain the equivalent European title, European Geologist (EurGeol). One fifth of the Society's fellowship resides outside the UK. To find out more about the Society, log on to www.geolsoc.org.uk.

The Geological Society Publishing House (Bath, UK) produces the Society's international journals and books, and acts as European distributor for selected publications of the American Association of Petroleum Geologists (AAPG), the American Geological Institute (AGI), the Indonesian Petroleum Association (IPA), the Geological Society of America (GSA), the Society for Sedimentary Geology (SEPM) and the Geologists' Association (GA). Joint marketing agreements ensure that GSL Fellows may purchase these societies' publications at a discount. The Society's online bookshop (accessible from www.geolsoc.org.uk) offers secure book purchasing with your credit or debit card.

To find out about joining the Society and benefiting from substantial discounts on publications of GSL and other societies worldwide, consult www.geolsoc.org.uk, or contact the Fellowship Department at: The Geological Society, Burlington House, Piccadilly, London W1J 0BG: Tel. +44 (0)20 7434 9944; Fax +44 (0)20 7439 8975; E-mail: enquiries@geolsoc.org.uk.

For information about the Society's meetings, consult *Events* on www.geolsoc.org.uk. To find out more about the Society's Corporate Affiliates Scheme, write to enquiries@geolsoc.org.uk.

Contents

Part IV Engineering and environmental applications

Part V Ancient sediments and tectonics

Part VI Methods

Preface

In recent years, the use of ground penetrating radar (GPR) to investigate the shallow subsurface has transformed the study of sediments. GPR is now an accepted and widely applied tool for the earth scientist, enabling a non-destructive investigation of both modern and ancient sediments. Based on the rapid growth of this field, we organised an international research meeting entitled *Ground Penetrating Radar (GPR) in Sediments: Applications and Interpretation* that was held at the Geological Society of London and the University College of London in August 2001. The objectives of the meeting were: (1) to bring together sedimentary geologists, geomorphologists, engineers and geophysicists; (2) to exchange ideas between GPR users; (3) to promote collaboration; and (4) to extend best practice. The meeting was a great success, with over 80 delegates from around the world. This publication represents the outcome of the conference, and it was notable that almost all of the participants wanted the proceedings in a book so that the papers stayed together in one volume, reflecting a common interest and a bond between researchers. We were particularly pleased by the comments from participants, some of whom had felt isolated in the past but now found camaraderie and an international community to share ideas and experience. We hope that this book will consolidate recent progress and inspire others to use GPR in their research.

The editors wish to acknowledge reviews by the following colleagues: P. Annan, A. Bichler, M. Bakker, D. Belknap, G. A. Botha, N. Cassidy, L. Clemmensen, R. Ll. Collier, D. J. Daniels, J. Degenhardt, C. Ekes, T. Elliott, R. J. Ferguson, D. M. Fitzgerald, A. Gardiner, J. Heinz, J. Hendrickx, K. Holliger, P. Huggenberger. L. Hunter, P. R. Jakobsen, S. Kruse, J. W. Lane, M. Leopold, I. Lunt, G. McMechan, S. McGeary, I. Møller, M. Mulligan, A. Neal, M. L. O'Neal, M. Pedley, K. Pedersen, B. R. Pratt, J. Pringle, D. Redman, K. R. Reicherter, S. Reiss, G. Roberts, M. C. Roberts, G. L. Running IV, G. Sambrook Smith, D. G. Smith, D. Stow, R. van Dam, B. Whiting, P. Wilson and J. Woodward.

The conference and this volume have been supported by the following organizations:

- British Sedimentological Research Group (BSRG)
- Geomatrix Earth Science Ltd
- Geophysical Survey Systems, Inc. (GSSI)
- International Association of Sedimentologists (IAS)
- Sensors and Software, Inc.

We are grateful for their financial support, which has helped bring this meeting together and provided funding for graduate students to attend.

Finally, we wish to thank our respective institutions for their support throughout this endeavour: Research School of Geological and Geophysical Sciences, Birkbeck/University College London, and the University of Wisconsin-Eau Claire.

Charlie Bristow and Harry Jol

This page intentionally left blank

An introduction to ground penetrating radar (GPR) in sediments

CHARLIE S. BRISTOW[1] & HARRY M. JOL[2]

[1]School of Earth Sciences, Birkbeck University of London, Malet Street, London, WC1E 7HXZ, UK (e-mail: c.bristow@ucl.ac.uk)

[2]Department of Geography and Anthropology, University of Wisconsin-Eau Claire, 105 Garfield Avenue, Eau Claire, WI 54702–4004, USA (e-mail: jolhm@uwec.edu)

Introduction

In sedimentary geology, ground penetrating radar (GPR) is used primarily for stratigraphic studies where near-continuous, high-resolution profiles aid in determining: (1) stratigraphic architecture, (2) sand-body geometry, and (3) correlation and quantification of sedimentary structures. In the past, to investigate lateral continuity and variability of sediments, we had to infer the correlation between boreholes, outcrops or shallow trenches. Nowadays, with suitable ground conditions (sediment with high resistivity, e.g. sands and gravels), we can collect GPR profiles that show the subsurface stratigraphy. In addition, 3-D GPR can provide much greater appreciation of sand-body geometry and architecture. GPR is, however, not a universal panacea; in some cases, ground truth is still required because lithological determination is by no means unequivocal, therefore borehole or outcrop data may be required to corroborate the results of a GPR survey. Indeed, the latest GPR survey data, including 3-D depth migration, required both boreholes and outcrop data to generate a 3-D velocity model (e.g. Corbeanu et al. 2001). In addition, fine-grained sediments (low resistivity) and areas with saline groundwaters cause rapid attenuation of the radar signal, leading to poor signal penetration.

This book begins with an introductory paper (Jol & Bristow 2003) aimed at those with little or no experience of GPR and including the basics of data collection, processing and interpretation. The book is then divided into sections on sedimentary environments, including aeolian and coastal, fluvial and alluvial fan, glacial, and lakes; ancient sediments (reservoir analogues); tectonics; and engineering and environmental applications. The final section looks at various aspects of GPR methodology. The chapters all provide case studies from a range of sedimentary environments in Europe, North America and South Africa. This introductory paper attempts to place the papers in this volume in context with the literature and to highlight some areas for further investigation in the future; it is not intended to be an exhaustive literature review.

In compiling the volume we asked authors to follow a few conventions, including the use of: (1) GPR profiles or GPR images instead of radargrams; (2) the term 'reflection(s)' when describing GPR profiles (reflectors are the subsurface interfaces where reflections are generated); and (3) objective stratigraphic terminology to describe the reflection patterns (oblique, continuous) when initially interpreting a GPR profile – once completed, more interpretative terminology can be used, keeping the interpretation separate from the description.

GPR in sediments

In the late 1980s and early 1990s a series of papers showed the potential of GPR as a tool for imaging the shallow subsurface. Papers by Jol and Smith (1991, 1992a, b) and Smith and Jol (1992a, b), clearly demonstrated the potential of GPR, with outstanding profiles within lacustrine deltaic environments. Around the same time, important papers by Davis and Annan (1989), Beres and Haeni (1991) and Gawthorpe et al. (1993) laid down the procedures for GPR surveys and interpretation. These were followed by tests of the penetration and resolution of GPR in sediments (Jol 1995; Smith & Jol 1995a). Early GPR surveys were often tied to outcrop observations or trenched sections in order to verify the results of the geophysics (e.g. Smith & Jol 1992a; Huggenberger 1993; Bristow 1994; Bristow et al. 1996). While early comparisons between GPR profiles and outcrop sections were largely qualitative, more recent outcrop analysis has been more quantitative, aiming to determine the causes of GPR reflections (van Dam & Schlager 2000) and constrain velocity pro-

files for 3-D depth migration and improved interpretation (Corbeanu et al. 2001).

Aeolian and coastal environments

The high resistivity of aeolian sands gives good GPR penetration (>10 m), and the large sedimentary structures within dune sands can be clearly imaged on GPR profiles (Harari 1996; Bristow et al. 1996, 2000a, b; Jol et al. 1998), making them suitable targets for GPR surveys. GPR profiles image cross-stratification and bounding surfaces in dunes, revealing their internal structure and relative chronology. In this volume, two papers, Botha et al. (2003) and Havholm et al. (2003), describe parabolic dunes. In comparison with other GPR surveys of aeolian sediments, the depth of penetration in the Lauder Sandhills described by Havholm et al. (2003) is rather limited: less than 5 m. This is attributed to signal attenuation by pedogenic silts, clays, and carbonate and iron oxides. Botha et al. (2003) use a combination of GPR and optical dating methods to investigate dune activity on the Maputaland coastal dunes in South Africa. Establishing the chronology of dune development is an important step toward understanding the forcing mechanisms (Bailey et al. 2001; Clemmensen et al. 2001) and this area of study is likely to expand.

Despite the proximity of the sea, and large volumes of conductive, saline water, GPR can work extremely well in coastal sediments if there is a freshwater aquifer. Leatherman (1987) reviewed potential applications for GPR in coastal sediments, while Neal and Roberts (2000) provide a good review of subsequent progress. GPR studies of spits and barrier beaches (Jol et al. 1996a; Van Heteren et al. 1996, 1998; Smith et al. 1999) and a prograding foreland (Neal & Roberts 2000) show good resolution of large-scale sedimentary structures from prograding shorefaces. Møller and Anthony (2003) use a combination of radar stratigraphy and radar facies to investigate the structure and stratigraphy of a Holocene barrier beach in Denmark. O'Neal and Dunn (2003) take a sequence-stratigraphic approach to the interpretation of GPR profiles. They use GPR to delineate three unconformity- bounded highstand units within the Quaternary Cape May Formation. The GPR profiles were also used to locate boreholes and pick sample locations for optically stimulated luminescence (OSL) dating. The structure and stratigraphy of coarse-gravel barrier-spit deposits from Lake Bonneville are described in Smith et al. (2003). They demonstrate the effectiveness of GPR in interpreting depositional sequences in coastal sediments, although associated fine-grained sediments, such as salt-marsh deposits, lead to high attenuation.

The use of GPR to define stratigraphy in coastal sediments, to identify stratigraphic horizons such as the transgressive ravinement surfaces identified by O'Neal and Dunn (2003), to develop a relative chronology, and to aid in picking sampling points for geochronological dating is predicted to increase in the future.

Fluvial and alluvial fan environments

There have probably been more GPR studies of river deposits than any other sedimentary environment because of the widespread distribution of river deposits, their ease of access and their importance as shallow aquifers. The variable style of fluvial systems, the heterolithic character of fluvial sediments, their large-scale depositional forms, such as point bars, combined with fresh water, make river deposits particularly suitable for investigation by GPR. The resulting studies have led to significant GPR papers, including those by Beres and Haeni (1991), Gawthorpe et al. (1993), Huggenberger (1993) and Beres et al. (1995). Woodward et al. (2003) use examples of GPR profiles from the South Saskatchewan, a sand-bed braided river in Canada, to illustrate data collection and processing. The ability of GPR to image and characterize the geometry and facies of fluvial sediments in both 2-D and 3-D has proved important for hydrogeologists (Beres & Haeni 1991; Huggenberger et al. 1994; Beres et al. 1995). The characterization of alluvial aquifers for hydrogeological studies using GPR will continue, as will GPR investigations of fluvial sediments to provide information on fluvial stratigraphy and sedimentary architecture (Heinz & Aigner 2003). Heinz and Aigner (2003) use 3-D GPR surveys to identify the geometry and stacking patterns of three architectural styles in outwash gravels.

In this volume, there are two papers that use GPR profiles to describe and interpret alluvial fan deposits. Ekes and Friel (2003) suggest that GPR can be used to assess the evolution of an alluvial fan sequence and, in conjunction with geochronological data, the return frequency of the formative processes, in their case debris flows and floods. This information is useful in understanding alluvial fan evolution and hazard assessment, although they report some difficulty in distinguishing between debris flow and sheetflood facies on the GPR profiles. Roberts et al. (2003) describe radar facies within Holocene fan-delta deposits in Canada and use radar facies to identify beach deposits within the fan delta. They suggest that the preservation of beach deposits within the delta sequence is indicative of a macrotidal setting, while accommodation

space, water depth and sediment supply are important in determining fan-delta architecture.

Glacial environments

GPR has been used to investigate coarser-grained glacial and glaciofluvial deposits in Europe, Canada and the USA (Ulriksen 1982; Sutinen 1992; Beres *et al.* 1995; Fisher *et al.* 1995; Jol *et al.* 1996*c*). In this volume, fluvioglacial outwash of the 1996 Jokulhlaup deposits at Skeiðarársandur in Iceland are described by Cassidy *et al.* 2003). They combine GPR profiles with outcrop observations and published descriptions to interpret the depositional chronology. They recognize three distinct areas of deposition (icewall canyon, proximal outwash fan, distal outwash fan) and four stages of deposition (early rising stage, rising/peak stage, waning stage and post-flood stage). They suggest future applications of their model in bedrock fluvial systems and alluvial-fan feeder systems. Degenhardt *et al.* (2003) use GPR to investigate the structure of a rock glacier; layers within the glacier are interpreted as flow lobes, indicating that the glacier is a composite feature.

Bakker and van der Meer (2003) show GPR profiles through a glaciotectonic push moraine in the Netherlands. The profiles show imbricate thrusts in the proximal area passing into a fold-and-thrust belt, with the fold wavelength increasing in the distal area. They use this as evidence for deformation during one glaciotectonic event. The good penetration (up to 45 m) and continuity of reflections is attributed to the nature of the deformed sediments, which are largely fluvioglacial outwash gravels. Tills with a high clay matrix content are likely to have a much higher attenuation, reducing the depth of penetration. Leopold and Völkel (2003) use GPR to help resolve a stratigraphic problem in Late Pleistocene to Early Holocene slope deposits that are locally covered by peat. Their GPR profiles show a variety of reflection patterns within the peat and good examples of onlapping relationships at the base of the peat.

Lakes

Freshwater lakes are resistive and can therefore be penetrated by GPR where radar can be used for sub-bottom profiling and to investigate water depth and the thickness and extent of sediments (Haeni 1996; Moorman & Michel 1997). Hunter *et al.* (2003*b*) made a GPR survey of a reservoir when it was frozen over in winter, which improved access and the speed of data collection. They use GPR to assess recent sediment deposition in the reservoir and the thickness of sediment above bedrock. Sediment accumulation rates are calculated

from comparison with earlier bathymetric surveys. The sediment thickness data are used to constrain potential dredging depths while the sediment accumulation rates are used to evaluate sediment trap design.

Lake deltas have been studied by Jol and Smith (1991) and by Smith and Jol (1992*a*, *b*, 1997), where large-scale foresets in coarse-grained sediments provide exceptionally good sites for GPR. In this volume, Smith *et al.* (2003) describe the internal structure of coarse-grained barrier and spit deposits that formed in Lake Bonneville, while large-scale foresets from a Lake Bonneville delta provide the test site for an evaluation of reflection characteristics from repetitive layers (Kruse & Jol 2003).

Ancient sediments: reservoir analogues

GPR datasets (2-D and 3-D) collected from outcrops are used as analogues for hydrocarbon reservoirs. This data can also be used to provide both qualitative and quantitative data for petroleum and hydrogeology reservoir modelling (Thompson *et al.* 1995; Jol *et al.* 1996*b*; Corbeanu *et al.* 2001). In Pringle *et al.* (2003*a*), outcrop sedimentary and topographic data are combined with GPR to produce a 3-D model of turbidite channel deposits. The aims of the study are to complement conventional outcrop data and improve the data available for hydrocarbon-reservoir modelling and the results include a quantitative 3-D volumetric model suitable for hydrocarbon-reservoir modelling. Pringle *et al.* (2003*b*) use vertical radar profiles (VRP) to provide time-depth calibration for radar profiles, which improves correlation of reflection events with observed lithological horizons in sedimentary rocks. They include examples from Ordovician and Carboniferous turbidite sequences and Tertiary fluvial sandstones, with impressive resolution at 65 m depth in the Carboniferous rocks.

The literature on GPR in carbonates appears to be rather sparse, with carbonate sedimentologists lagging behind their clastic colleagues in applying GPR to limestones or carbonate sediments. There is clearly a practical problem with operating GPR in many modern carbonate environments because of the attenuation caused by saline waters. However, limestone is highly resistive and should have good potential based on several studies that have been undertaken (Pratt & Miall 1993; Liner & Liner 1995; Sigurdsson & Overgaard 1998; Dagallier *et al.* 2000). Pedley *et al.* (2000) and Pedley and Hill (2003) show that GPR can be used to investigate tufas with different lithologies, giving distinct radar reflections. Pedley and Hill (2003) use this information to investigate paludal tufas, and discriminate between line-sourced tufas and

point-sourced mound tufa deposits. In addition to characterizing carbonate deposits, GPR should be used for void detection in limestones and could be used to investigate caverns and sink holes in karst terrain.

Tectonics

GPR has been used for imaging faults in the subsurface with varying degrees of success (Bilham & Seeber 1995; Smith & Jol 1995b). Reiss et al. (2003) describe faulted alluvial and colluvial sediments in northeastern Spain, southern Spain and Sicily. They show that normal faults can be mapped using GPR and suggest that GPR should be used as a pretrenching tool in palaeoseismic investigations. In addition, they suggest that quantitative evaluation of high-resolution GPR profiles could be used to trace fault segments along strike, assess changes in displacement along faults and possibly to balance sections. It is clear that, given appropriate lithologies, GPR surveys in both 2-D and 3-D should see increased applications in fault analysis and the reconstruction of faulting history, including the manner and size of fault displacements and their relative chronology.

Engineering and environmental applications

GPR is probably most widely used in environmental and engineering field applications, ranging from the detection of reinforcing rods in concrete to water leaks and contamination (see Reynolds 1997 and references therein). In this volume, Hendrickx et al. (2003) present a study with a different application in landmine detection. They test GPR performance in wet and dry conditions and illustrate some of the problems associated with using GPR to detect non-metallic landmines. Hunter et al. (2003a) test the ability of GPR to detect hydrocarbon contamination in permafrost areas. They show that bulk electrical properties (velocity and attenuation) vary systematically between frozen and unfrozen materials. They also show that, where petroleum contamination is pervasive, there is a decrease in attenuation.

GPR methodology

As the use of GPR in the sediments field matures, more technical studies in GPR methodology are being pursued. For example, van Dam et al. (2003) make a detailed assessment of the factors that produce reflections in sediments, in particular the thin layers of cross-stratification which are beneath the normally expected scale of resolution ($\lambda/4$). Using synthetic radar traces and impedance models of thin layers, van Dam et al. (2003) show that reflections from subcentimetre-scale structures are composites of interfering signals and that there are 'tuning effects' which can occur, giving reflections that vary with radar frequency. This paper follows earlier investigations of the influence of iron oxides (van Dam et al. 2002a), organics (van Dam et al. 2002b) and sediment character (van Dam & Schlager, 2000). They conclude that changes in water content associated with small-scale textural changes in sediments are responsible for the changes in dielectric properties that produce radar reflections. Kruse and Jol (2003) use observed relative amplitudes of GPR reflections from dipping delta foreset beds to constrain the permittivity contrasts associated with layers of sediments. They also investigate the difference between thick and thin beds. They show that finite-difference time-domain (FDTD) modelling of GPR data can help to constrain the variability and scaling of electromagnetic properties. Lutz et al. (2003) show that GPR data collected with the antennae parallel and perpendicular can be combined to improve the quality of a GPR profile. They advocate the use of a quadripole survey with two transmitters and two receivers. Further field and laboratory studies of GPR in sediments and the effects of changes in material properties are likely to follow. The use of synthetic GPR profiles to model the signal response is likely to increase and help constrain GPR profile interpretation in the future.

Conclusions

The application of GPR in sediments is expanding rapidly because GPR provides high-resolution images of the shallow subsurface that cannot be derived by any other non-destructive method. The use of GPR has gone beyond characterizing environments by reflection patterns and radar facies and is moving into a more quantitative assessment of sand-body geometry and architecture. GPR has great potential in the selection of borehole locations and picking sample points for geotechnical, stratigraphic and geochronological studies. The use of GPR in imaging shallow stratigraphy should lead to significant advances in Quaternary stratigraphy, geohazards research, the hydrogeology of shallow aquifers and contamination. This volume includes some innovative applications of GPR in sediments, including vertical radar profiles, borehole radar and imaging sedimentary fill beneath a frozen lake. The use of GPR to tackle specific and sometimes longstanding stratigraphic problems is likely to increase, as is the use of true 3-D GPR surveys. Further work is required to con-

strain the identification of buried objects and sub-surface lithology.

References

BAILEY, S. D., WINTLE, A. G., DULLER, G. A. T. & BRISTOW, C. S. 2001. Sand deposition during the last millennium at Aberffraw, Anglesey, North Wales as determined by OSL dating of quartz. *Quaternary Science Reviews*, **20**, 701–704.

BAKKER, M. A. J. & VAN DER MEER, J. J. M. 2003. Structure of a Pleistocene push moraine revealed by GPR: the eastern Veluwe Ridge, The Netherlands. *In*: BRISTOW, C. S. & JOL, H. M. (eds) *Ground Penetrating Radar in Sediments*. Geological Society, London, Special Publications, **211**, 143–151.

BERES, M. & HAENI, F. P. 1991. Application of ground-penetrating-radar methods in hydrogeologic studies. *Ground Water*, **29**, 375–386.

BERES, M., GREEN, A., HUGGENBERGER, P. & HORSTMEYER, H. 1995. Mapping the architecture of glaciofluvial sediments with three-dimensional georadar. *Geology*, **23**, 1087–1090.

BILHAM, R. & SEEBER, L. 1985. *Subsurface Radar Imagery of Near-Surface Fractures Associated with the Borah Peak Earthquake*. United States Geological Survey, Open File Report, 85-290-A.

BOTHA, G. A., BRISTOW, C. S. *ET AL.* 2003. Evidence for dune reactivation from GPR profiles on the Maputaland coastal plain, South Africa. *In*: BRISTOW, C. S. & JOL, H. M. (eds) *Ground Penetrating Radar in Sediments*. Geological Society, London, Special Publications, **211**, 29–46.

BRISTOW, C. S. 1994. A new look at the Lower Greensand using ground-penetrating radar. *Geology Today*, **10**, 24–27.

BRISTOW, C. S., BAILEY, S. D. & LANCASTER, N. 2000*a*. The sedimentary structure of linear sand dunes. *Nature*, **406**, 56–59.

BRISTOW, C. S., CHROSTON, P. N. & BAILEY, S. D. 2000*b*. The structure and development of foredunes on a locally prograding coast: Insights from ground penetrating radar surveys, Norfolk, England. *Sedimentology*, **47**, 923–944.

BRISTOW, C. S., PUGH, J. & GOODALL, T. 1996. Internal structure of aeolian dunes in Abu Dhabi revealed using ground penetrating radar. *Sedimentology*, **43**, 995–1003.

CASSIDY, N. J., RUSSELL, A. J., MARREN, P. M., FAY, H., KNUDSEN, Ó., RUSHMER, E. L. & VAN DIJK, T. A. G. P. 2003. GPR derived architecture of November 1996 jökulhlaup deposits, Skeiðarársandur, Iceland. *In*: BRISTOW, C. S. & JOL, H. M. (eds) *Ground Penetrating Radar in Sediments*. Geological Society, London, Special Publications, **211**, 153–166.

CLEMMENSEN, L. B., PYE, K., MURRAY, A. & HEINEMEIR, J. 2001. Sedimentology, stratigraphy and landscape evolution of a Holocene dune system, Lodbjerg, NW Jutland, Denmark. *Sedimentology*, **48**, 3–27.

CORBEANU, R. M., SOEGAARD, K. *ET AL.* 2001. Detailed internal architecture of a fluvial channel sandstone determined from outcrop cores, and 3-D ground-penetrating radar: Examples form the Middle Cretaceous Ferron Sandstone, east-central Utah. *American Association of Petroleum Geologists Bulletin*, **85**, 1583–1608.

DAGALLIER, G., LAITINEN, A. I., MALARTRE, F., VAN CAMPENHOUT, I. P. A. M. & VEEKEN, P. C. H. 2000. Ground penetrating radar application in a shallow marine Oxfordian limestone sequence located on the eastern flank of the Paris Basin, NE France. *Sedimentary Geology*, **130**, 149–165.

DAVIS, J. L. & ANNAN, A. P. 1989. Ground penetrating radar for high resolution mapping of soil and rock stratigraphy. *Geophysical Prospecting*, **37** 531–551.

DEGENHARDT, J. J., GIARDINO, J. R. & JUNCK, M. B. 2003. GPR survey of a lobate rock glacier in Yankee Boy Basin, Colorado, USA. *In*: BRISTOW, C. S. & JOL, H. M. (eds) *Ground Penetrating Radar in Sediments*. Geological Society, London, Special Publications, **211**, 167–179.

ÉKES, C. & FRIELE, P. 2003. Sedimentary architecture and post-glacial evolution of Cheekye Fan, southwestern British Columbia, Canada. *In*: BRISTOW, C. S. & JOL, H. M. (eds) *Ground Penetrating Radar in Sediments*. Geological Society, London, Special Publications, **211**, 87–98.

FISHER, T. G., JOL, H. M. & SMITH, D. G. 1995. Ground penetrating radar used to assess aggregate in catastrophic flood deposits northeast Alberta, Canada. *Canadian Geotechnical Journal*, **32**, 871–879.

GAWTHORPE, R. L., COLLIER, R. E. LL., ALEXANDER, J., LEEDER, M. & BRIDGE, J. S. 1993. Ground penetrating radar: application to sandbody geometry and heterogeneity studies. *In*: NORTH, C. P. & PROSSER, D. J. (eds) *Characterisation of Fluvial and Aeolian Reservoirs*. Geological Society, London, Special Publications, **73**, 421–432.

HAENI, F. P. 1996. Use of ground-penetrating radar and continuous seismic reflection profiling on surface water bodies in environmental and engineering studies. *Journal of Environmental and Engineering Geophysics*, **1**, 27–35.

HARARI, Z. 1996. Ground-penetrating radar (GPR) for imaging stratigraphic features and groundwater in sand dunes. *Journal of Applied Geophysics*, **36**, 43–52.

HAVHOLM, K. G., BERGSTROM, N. D., JOL, H. M. & RUNNING, G. L., IV. 2003. GPR survey of a Holocene aeolian/fluvial/lacustrine succession, Lauder Sandhills, Manitoba, Canada. *In*: BRISTOW, C. S. & JOL, H. M. (eds) *Ground Penetrating Radar in Sediments*. Geological Society, London, Special Publications, **211**, 47–54.

HEINZ, J. & AIGNER, T. 2003. Three-dimensional GPR analysis of various Quaternary gravel-bed braided river deposits (southwestern Germany). *In*: BRISTOW, C. S. & JOL, H. M. (eds) *Ground Penetrating Radar in Sediments*. Geological Society, London, Special Publications, **211**, 99–110.

HENDRICKX, J. M. H., HONG, S.-H., MILLER, T., BORCHERS, B. & RHEBERGEN, J. B. 2003. Soil effects on GPR detection of buried non-metallic mines. *In*: BRISTOW, C. S. & JOL, H. M. (eds) *Ground Penetrating Radar in Sediments*. Geological Society, London, Special Publications, **211**, 191–198.

HUGGENBERGER, P. 1993. Radar facies: recognition of facies patterns and heterogeneities within Pleistocene Rhine gravels, NE Switzerland. *In*: BEST, J. L. & BRIS-

TOW, C. S. (eds) *Braided Rivers*. Geological Society, London, Special Publications, **75**, 163–176.

HUGGENBERGER, P., MEIER, E. & PUGIN, A. 1994. Ground-probing radar as a tool for heterogeneity estimation in gravel deposits: Advances in data-processing and facies analysis. *Journal of Applied Geophysics*, **31**, 171–184.

HUNTER, L. E., DELANEY, A. J., LAWSON, D. E. & DAVIS, L. 2003a. Downhole GPR for high-resolution analysis of material properties near Fairbanks, Alaska. *In*: BRISTOW, C. S. & JOL, H. M. (eds) *Ground Penetrating Radar in Sediments*. Geological Society, London, Special Publications, **211**, 275–285.

HUNTER, L. E., FERRICK, M. G. & COLLINS, C. M. 2003b. Monitoring sediment infilling at the Ship Creek Reservoir, Fort Richardson, Alaska using GPR. *In*: BRISTOW, C. S. & JOL, H. M. (eds) *Ground Penetrating Radar in Sediments*. Geological Society, London, Special Publications, **211**, 199–206.

JOL, H. M. 1995. Ground penetrating radar antennae frequencies and transmitter powers compared for penetration depth, resolution and reflection continuity. *Geophysical Prospecting*, **43**, 693–709.

JOL, H. M. & BRISTOW, C. S. 2003. GPR in sediments: advice on data collection, basic processing and interpretation, a good practice guide. *In*: BRISTOW, C. S. & JOL, H. M. (eds) *Ground Penetrating Radar in Sediments*. Geological Society, London, Special Publications, **211**, 9–27.

JOL, H. M. & SMITH, D. G. 1991. Ground penetrating radar of northern lacustrine deltas. *Canadian Journal of Earth Science*, **28**, 1939–1947.

JOL, H. M. & SMITH, D. G. 1992a. Geometry and structure of deltas in large lakes: a ground penetrating radar overview. *In*: HANNINEN, P. & AUTIO, S. (eds) *Fourth International Conference on Ground Penetrating Radar, June 8–13, Rovaniemi*. Geological Survey of Finland Special Papers, **16**, 159–168.

JOL, H. M. & SMITH, D. G. 1992b. Ground penetrating radar: recent results. *Canadian Society of Exploration Geophysicists Recorder*, **17**, 15–20.

JOL, H. M., SMITH, D. G. & MEYERS, R. A. 1996a. Digital ground penetrating radar (GPR): An improved and very effective geophysical tool for studying modern coastal barriers (examples for the Atlantic, Gulf and Pacific coasts, U.S.A.). *Journal of Coastal Research*, **12**, 960–968.

JOL, H. M., SMITH, D. G., MEYERS, R. A. & LAWTON, D. C. 1996b. Ground penetrating radar: high resolution stratigraphic analysis of coastal and fluvial environments. *In*: PACHT, J. A., SHERIFF, R. E. & PERKINS, B. F. (eds) *Stratigraphic Analysis Using Advanced Geophysical, Wireline and Borehole Technology for Petroleum Exploration and Production*. Gulf Coast Section Society of Economic Paleontologists and Mineralogists Foundation, 17th Annual Research Conference, 153–163.

JOL, H. M., VANDERBURGH, S. & HAVHOLM K. G. 1998. GPR studies of coastal aeolian (foredune and crescentic) environments: examples from Oregon and North Carolina, U.S.A. *Proceedings of the Seventh International Conference on Ground Penetrating Radar (GPR '98), Lawrence, Kansas, USA, May 27–30*, **2**, 681–686.

JOL, H. M., YOUNG, R., FISHER, T. G., SMITH, D. G. & MEYERS, R. A. 1996c. Ground penetrating radar of eskers, kame terraces, and moraines: Alberta and Saskatchewan, Canada. *Proceedings of the Sixth International Conference on Ground Penetrating Radar (GPR '96), Sendai, Japan, September 30–October 3*, 439–443.

KRUSE, S. E. & JOL, H. M. 2003. Amplitude analysis of repetitive GPR reflections on a Lake Bonneville delta, Utah. *In*: BRISTOW, C. S. & JOL, H. M. (eds) *Ground Penetrating Radar in Sediments*. Geological Society, London, Special Publications, **211**, 287–298.

LEATHERMAN, S. P. 1987. Coastal geomorphological applications of ground-penetrating radar. *Journal of Coastal Research*, **3**, 397–399.

LEOPOLD, M. & VÖLKEL, J. 2003. GPR images of periglacial slope deposits beneath peat bogs in the Central European Highlands, Germany. *In*: BRISTOW, C. S. & JOL, H. M. (eds) *Ground Penetrating Radar in Sediments*. Geological Society, London, Special Publications, **211**, 181–189.

LINER, C. L. & LINER, J. L. 1995. Ground penetrating radar: a near-face experience from Washington County, Arkansas. *Leading Edge*, **14**. 17–21.

LUTZ, P., GARAMBOIS, S. & PERROUD, H. 2003. Influence of antenna configurations for GPR survey: information from polarization and amplitude versus offset measurements. *In*: BRISTOW, C. S. & JOL, H. M. (eds) *Ground Penetrating Radar in Sediments*. Geological Society, London, Special Publications, **211**, 299–313.

MØLLER, I. & ANTHONY, D. 2003. A GPR study of sedimentary structures within a transgressive coastal barrier along the Danish North Sea coast. *In*: BRISTOW, C. S. & JOL, H. M. (eds) *Ground Penetrating Radar in Sediments*. Geological Society, London, Special Publications, **211**, 55–65.

MOORMAN, J. B. & MICHEL, F. A. 1997. Bathymetric mapping and sub-bottom profiling through lake ice with ground penetrating radar. *Journal of Palaeolimnology*, **18**, 61–73.

NEAL, A. & ROBERTS, C. L. 2000. Applications of ground-penetrating radar (GPR) to sedimentological, geomorphological and geoarchaeological studies in coastal environments. *In*: PYE, K. & ALLEN, J. R. L. (eds) *Coastal and Estuarine Environments: Sedimentology, Geomorphology and Geoarchaeology*. Geological Society, London, Special Publications, **175**, 139–171.

O'NEAL, M. L. & DUNN, R. K. 2003. GPR investigation of multiple stage-5 sea-level fluctuations on a siliciclastic estuarine shoreline, Delaware Bay, southern New Jersey, USA. *In*: BRISTOW, C. S. & JOL, H. M. (eds) *Ground Penetrating Radar in Sediments*. Geological Society, London, Special Publications, **211**, 67–77.

PEDLEY, H. M. & HILL, I. 2003. The recognition of barrage and paludal tufa systems by GPR: case studies in the geometry and correlation of Quaternary freshwater carbonates. *In*: BRISTOW, C. S. & JOL, H. M. (eds) *Ground Penetrating Radar in Sediments*. Geological Society, London, Special Publications, **211**, 207–223.

PEDLEY, H. M., HILL, I. & DENTON, P. 2000. Three dimensional modelling of a Holocene tufa system in the Lathkill valley, north Derbyshire, using ground penetrating radar. *Sedimentology*, **47**, 721–735.

PRATT, B. R. & MIALL, A. D. 1993. Anatomy of a bioclastic grainstone megashoal (Middle Silurian, southern Ontario) revealed by ground-penetrating radar. *Geology*, **21**, 223–226.

PRINGLE, J. K., CLARK, J. D., WESTERMAN, A. R. & GARDINER, A. R. 2003*a*. The use of GPR to image three-dimensional (3-D) turbidite channel architecture in the Carboniferous Ross Formation, County Clare, western Ireland. *In*: BRISTOW, C. S. & JOL, H. M. (eds) *Ground Penetrating Radar in Sediments*. Geological Society, London, Special Publications, **211**, 315–326.

PRINGLE, J. K., WESTERMAN, A. R., CLARK, J. D., GUEST, J. A., FERGUSON, R. J. & GARDINER, A. R. 2003*b*. The use of vertical radar profiling (VRP) in GPR surveys of ancient sedimentary strata. *In*: BRISTOW, C. S. & JOL, H. M. (eds) *Ground Penetrating Radar in Sediments*. Geological Society, London, Special Publications, **211**, 225–246.

REISS, S., REICHERTER, K. R. & REUTHER, C.-D. 2003. Visualization and characterization of active normal faults and associated sediments by high-resolution GPR. *In*: BRISTOW, C. S. & JOL, H. M. (eds) *Ground Penetrating Radar in Sediments*. Geological Society, London, Special Publications, **211**, 247–255

REYNOLDS, J. M. 1997. *An Introduction to Applied and Environmental Geophysics*. John Wiley and Sons, Chichester, England.

ROBERTS, M. C., NILLER, H.-P. & HELMSTETTER, N. 2003. Sedimentary architecture and radar facies of a fan delta, Cypress Creek, West Vancouver, British Columbia. *In*: BRISTOW, C. S. & JOL, H. M. (eds) *Ground Penetrating Radar in Sediments*. Geological Society, London, Special Publications, **211**, 111–126.

SIGURDSSON, T. & OVERGAARD, T. 1998. Application of GPR for 3-D visualisation of geological and structural variation in a limestone formation. *Journal of Applied Geophysics*, **40**, 29–36.

SMITH, D. G. & JOL, H. M. 1992*a*. Ground penetrating radar investigation of Lake Bonneville Delta, Provo Level, Brigham City, Utah. *Geology*, **20**, 1083–1086.

SMITH, D. G. & JOL, H. M. 1992*b*. GPR results used to infer depositional processes of coastal spits in large lakes. *In*: HANNINEN, P. & AUTIO, S. (eds) *Fourth International Conference on Ground Penetrating Radar, June 8–13, Rovaniemi*. Geological Survey of Finland Special Papers, **16**, 169–177.

SMITH, D. G. & JOL, H. M. 1995*a*. Ground penetrating radar: antennae frequencies and maximum probable depths of penetration in Quaternary sediments. *Journal of Applied Geophysics*, **33**, 93–100.

SMITH, D. G. & JOL, H. M. 1995*b*. Wasatch Fault (Utah) detected and displacement characterized by ground penetrating radar. *Environmental and Engineering Geoscience*, **1**, 489–496.

SMITH, D. G. & JOL, H. M. 1997. Radar structure of a Gilbert-type delta, Peyto Lake, Banff National Park, Canada. *Sedimentary Geology*, **113**, 195–209.

SMITH, D. G., MEYERS, R. A. & JOL, H. M. 1999. Sedimentology of an upper-mesotidal (3.7 m) Holocene barrier, Willapa Bay, SW Washington, USA. *Journal of Sedimentary Research*, **69**, 1290–1296.

SMITH, D. G., SIMPSON, C. J., JOL, H. M., MEYERS, R. A. & CURREY, D. R. 2003. GPR stratigraphy used to infer transgressive deposition of spits and a barrier, Lake Bonneville, Stockton, Utah, USA. *In*: BRISTOW, C. S. & JOL, H. M. (eds) *Ground Penetrating Radar in Sediments*. Geological Society, London, Special Publications, **211**, 79–86.

SUTINEN, R. 1992. Glacial deposits, their electrical properties and surveying by image interpretation and ground penetrating radar. *Geological Survey of Finland Bulletin*, **359**, 123.

THOMPSON, C., MCMECHAN, G., SZERBIAK, R. AND GAYNOR, N. 1995. Three-dimensional GPR imaging of complex stratigraphy within the Ferron sandstone, Castle Valley, Utah. *Symposium on the Application of Geophysics to Engineering and Environmental Problems, Proceedings*, 435–443.

ULRIKSEN, C. P. F. 1982. *Application of Impulse Radar to Civil Engineering*. Ph.D. thesis, Lund University of Technology, Lund, Sweden.

VAN DAM, R. L. & SCHLAGER, W. 2000. Identifying causes of ground-penetrating radar reflections using time-domain reflectometry and sedimentological analyses. *Sedimentology*, **47**, 435–449.

VAN DAM, R. L., SCHLAGER, W., DEKKERS, M. J. & HUISMAN, J. A. 2002*a*. Iron oxides as a cause of GPR reflections. *Geophysics*, **67**, 536–545.

VAN DAM, R. L., VAN DEN BERG, E. H., SCHAAP, M. G., BROEKMA, L. H., & SCHLAGER, W. 2003. Radar reflections from sedimentary structures in the vadose zone. *In*: BRISTOW, C. S. & JOL, H. M. (eds) *Ground Penetrating Radar in Sediments*. Geological Society, London, Special Publications, **211**, 257–273.

VAN DAM, R. L., VAN DEN BERG, E. H., VAN HETEREN, S., KASSE, C., KENTER, J. A. M. & GROEN, K. 2002*b*. Influence of organic matter in soils on radar-wave reflection: sedimentological implications. *Journal of Sedimentary Research*, **72**, 341–352.

VAN HETEREN, S., FITZGERALD, D. M., BARBER, D. C., KELLEY, J. T. & BELKNAP, D. F. 1996. Volumetric analysis of a New England barrier system using ground-penetrating–radar and coring techniques. *Journal of Geology*, **104**, 471–483.

VAN HETEREN, S., FITZGERALD, D. M., MCKINLAY, P. A. & BUYNEVICH, I. V. 1998. Radar facies of paraglacial barrier systems: coastal New England, USA. *Sedimentology*, **45**, 181–200.

WOODWARD, J., ASHWORTH, P. J., BEST, J. L., SAMBROOK SMITH, G. H. & SIMPSON, C. J. 2003. The use and application of GPR in sandy fluvial environments: methodological considerations. *In*: BRISTOW, C. S. & JOL, H. M. (eds) *Ground Penetrating Radar in Sediments*. Geological Society, London, Special Publications, **211**, 127–142.

This page intentionally left blank

GPR in sediments: advice on data collection, basic processing and interpretation, a good practice guide

HARRY M. JOL[1] & CHARLIE S. BRISTOW[2]

[1]Department of Geography and Anthropology, University of Wisconsin-Eau Claire, 105 Garfield Avenue, Eau Claire, WI 54702–4004 USA (e-mail: jolhm@uwec.edu)

[2]School of Earth Sciences, Birkbeck University of London, Malet Street, London WC1E7HX UK (e-mail: c.bristow@ucl.ac.uk)

Abstract: Within sedimentological studies, ground penetrating radar (GPR) is being used with increasing frequency because it yields images of the shallow subsurface that cannot be achieved by any other non-destructive method. The purpose of this paper is to provide an introduction to the collection, processing and interpretation of GPR data so that future sedimentary studies can be improved. With GPR equipment now being lightweight, robust and portable, proper data collection and survey design methods need to be followed in order to acquire high resolution, subsurface digital data. Various factors are discussed including: reflection profiling, velocity soundings, test surveys, topography, logistics, data quality and extreme environments. Basic data processing and visualization are then reviewed, followed by a discussion on GPR interpretation strategies including a background to radar stratigraphy. For the sedimentary geologist or geomorphologist, GPR offers unique data of the shallow subsurface including stratigraphy, geometry, architecture and structure.

Introduction

The purpose of this paper is to offer guidelines to aid others in collecting optimal ground penetrating radar (GPR) data. The paper is primarily aimed at geologists, sedimentologists and geomorphologists who want to know more background information on conducting a GPR survey and accurately interpreting the results. We have based some of this paper on material that is commonly found in GPR manuals and course notes. However, this literature is rarely focussed on sedimentological or stratigraphic investigations, which are the subject of this volume. Data collection, survey design and target selection are important components of a successful survey and this paper includes some suggestions for optimising these components to achieve good results. We also outline procedures for basic data processing and interpretation. Some aspects of GPR such as equipment specifications and the physics of electromagnetic radiation are beyond the scope of this paper and readers are referred elsewhere for these details (Morey 1974; Annan & Davis 1976; Ulriksen 1982; Daniels et al. 1988; Davis & Annan 1989, Daniels 1996). Advanced processing options are only briefly mentioned as the scope of this paper is intended primarily for inexperienced GPR users. We aim to provide some guidelines of good practice acquired from extensive field experience and identify ways to avoid some common pitfalls.

Data collection and survey design

Background

Before undertaking a GPR study it is important to consider the scientific objectives and practical issues in undertaking the survey. From a scientific view it is essential to establish what data are required to test a hypothesis. This will have implications for the areal size of the survey (consequently the time involved), depth of investigation and resolution required. For practical reasons, it is important to assess the size of the sedimentary target, the nature of the target, and the ground conditions because these will influence the survey logistics and success.

GPR has become an increasingly popular tool in sedimentological studies. Advantages of recently developed GPR systems are that they are lightweight, portable, robust and digital. In addition,

GPR data can be viewed in real time, allowing both quality and results to be assessed in the field. These advances result in rapid acquisition of continuous, shallow subsurface profiles that are ideally suited for the investigation of sediments, shallow stratigraphy and sedimentary architecture from both a 2-D and 3-D perspective.

In radar profiling, a high frequency electromagnetic (EM) pulse is radiated into the ground from an antenna at the surface. The radiated radio-frequency EM energy is reflected back to the surface from interfaces of materials having different dielectric properties (Davis & Annan 1989). These differences are often due to changes in water content associated with various sediment types, grain size, porosity and compaction. The returned energy is collected by a second, matched receiving antenna and is recorded as a function of time. This energy is proportional to the relative permittivity contrasts in the shallow subsurface. To a large degree the velocity of the radar signal within sediments is controlled by water content. For example in saturated conditions, water content (which indicates porosity) can be estimated from the radar velocity using the Topp equation (Topp *et al.* 1980). Different combinations of antennae frequencies and transmitter voltages also influence data collection results in regards to depth of penetration, continuity of reflections, and resolution of the data set. These effects enable the subsurface stratigraphy to be inferred from the character of the reflected signals. In our field experiments, at over 800 sites worldwide, GPR was found to be most effective in electrically resistive materials such as sand, gravel, peat, and limestone (see Doolittle 2002 for aid in locating USA sites). High-quality data were also obtained in similar sediments saturated by freshwater, including marine coastlines. A decrease in data quality was often due to high amounts of silt, clay, caliche (calcrete), and/or saline water in sediments. These deposits, due to their high conductivity, attenuated the EM signal which resulted in limited penetration (Olhoeft 1984; Duke 1990). Surveys can be run in these conductive settings if the targets are relatively shallow and/or have a 'high contrast' to the surrounding material.

GPR systems can be deployed in three basic modes which are referred to as *reflection profiling*, *velocity sounding* and *transillumination*. Reflection profiling and velocity sounding, the two most common forms of GPR surveying in sedimentary environments, will be discussed in the following sections (followed by related aspects of data collection and survey design). Multifold reflection surveys (Fisher *et al.* 1992), a merger of reflection profiling and velocity sounding, and transillumination gathers which form the basis of GPR tomography (Olsson *et al.* 1987), are rarely used in sedimentary studies and therefore will not be discussed in this paper.

Reflection profiling

The most common mode of GPR data collection is single-fold, fixed-offset reflection (bistatic) profiling. The step-like procedure involves repetitive (or continuous) moves of a fixed antennae geometry which gives rise to a cross-sectional image of variations in subsurface dielectric properties (reflections) as a function of two-way travel time. Step mode is preferred for most scientific GPR surveys where high resolution and high quality data are required (Fig. 1). Continuous data collection is not advised for detailed sedimentary studies due to poor coupling between the ground and the antennae (ground contact), potential changes in antennae orientation, and 'smearing of data' because antennae are moved during data collection. Continuous data collection (e.g., deploying antennae behind a moving vehicle) is more suited to reconnaissance surveys such as locating large buried channels.

There are several parameters one must be concerned about during GPR reflection profiling. These include: i) operating frequency and transmitter power, ii) step size, iii) length of time window, iv) time sampling interval, v) antennae separation, vi) line location and spacing, vii) antennae orientation, viii) trace stacking.

i) Operating frequency and transmitter power For each study site, the advantages of depth of penetration versus resolution should be considered before the antennae frequency and transmitter power are selected. The concept from Davis & Annan (1989) known as the 'range – resolution trade-off' involves an increase in resolution and a decrease in range (depth) as the centre frequency of the antennae increases. Lower frequencies increase depth of penetration while higher frequencies improve discrimination ability (Hänninen 1992). Most sedimentary studies use antennae with frequencies between 50 and 500 megahertz (MHz), with the majority of research reported in this volume using 100 MHz antennae. Higher frequency antennae (400 to 1000 MHz) have shorter wavelengths which can yield high resolution but little depth of penetration. Lower frequency antennae (10 to 50 MHz) have longer wavelengths that can yield greater depth of penetration but lower resolution.

In sedimentary environments, stratigraphy occurs at a variety of scales ranging from mm to 10's m in both the horizontal and vertical dimension. To effectively image the subsurface with GPR, various antennae frequencies need to be
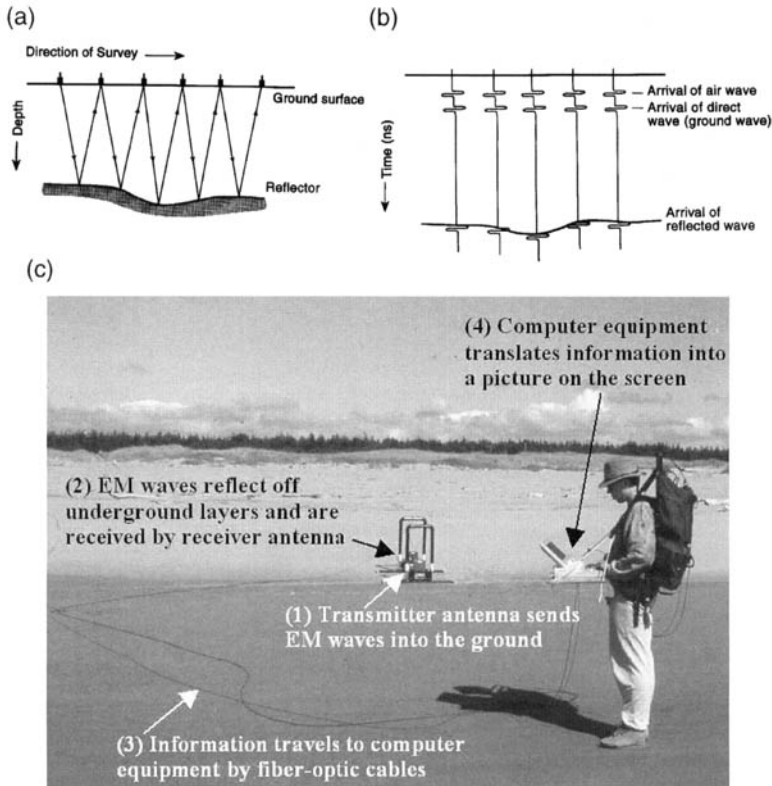
Fig. 1. GPR profiling procedure. (**a**) The step-like procedure involves repetitive moves of both transmitter and receiver at a constant antennae spacing. (**b**) Five schematic GPR traces showing the arrival of air wave and ground wave pulses, and a lower reflected wave from a subsurface reflector (after Jol & Smith 1991). (**c**) GPR field set-up. The system includes operator with backpack (console, portable computer and 12 V battery). Two 100 MHz antennae (closest one is the transmitter, further one is the receiver). The antennae are connected via fibre optic cables (visible as black cables on the sand). Carrying handles attached to the antennae allow for easier transport and are used to secure the fibre optic cables with a loop to absorb accidental fibre optic pulls. In this relatively flat area, a 2 person crew can collect GPR data quickly and efficiently.

employed. Wave theory suggests that the greatest vertical resolution that can be expected is one quarter ($\frac{1}{4}$) of the wavelength (Nyquist sampling interval; Sheriff & Geldart 1982). The higher the frequency the higher the resolution of the GPR image. In other words, to be able to resolve fine scale structures, high frequency antennae are desirable. Table 1 provides theoretical resolution for typical sedimentary environments. Other studies have shown the resolving limits of GPR antennae at certain velocities (Davis & Annan 1989; Jol 1995; Smith & Jol 1995). The actual resolution, however, for deeper reflections is slightly less as the higher frequency energy in the radiated pulse is preferentially attenuated. Changing the centre frequency of a GPR system permits selective enhancement of subsurface responses. In particular, gradational boundaries, such as a 'water table', become better reflectors when frequency is reduced to the point

where the wavelength is long compared to the transition thickness. Continual developments in GPR systems have allowed for a range of antennae frequency to be exploited for use in field studies.

At present, GPR units can be used with a variety of output powers on the transmitter (however, some countries have limited this output). The increase in transmitter power can significantly aid in greater depth of penetration and/or increased continuity of reflections of sedimentary environments (Jol 1995).

ii) Step size Spatial resolution also places a lower bound on the survey design and selection of antennae centre frequency. Step size (the distance between each data collection point, also known as station spacing) is extremely important and should be included in the survey design process. In order to assure the ground response is not spatially ali-

Table 1. *Theoretical values for resolution of GPR in typical sedimentary environments for different antennae frequencies*

| Antenna frequency	Lithology		
	Saturated sand 0.06 m/ns	Damp sand 0.1 m/ns	Dry sand 0.15 m/ns
50 MHz	0.3–0.6 m	0.5–1.0 m	0.75–1.5 m
100 MHz	0.15–0.3 m	0.25–0.50 m	0.375–0.75 m
200 MHz	0.075–0.15 m	0.125–0.25 m	0.1875–0.375 m

Note: The theoretical resolving limit is $\frac{1}{4}$ to $\frac{1}{2}$ of the wavelength (Sheriff and Geldart 1982). The wavelength was calculated using the following equation: $\lambda = v/f$, where λ – wavelength, v – velocity (which is given based on the environment), f – frequency (centre frequency of antennae was used). In reality the peak return frequency is usually less than nominal antennae frequency which leads to reduced resolution, although resolution is related to bandwidth not just peak frequency.

ased, the Nyquist sampling intervals should not be exceeded (Keary & Brooks 1991). The Nyquist sampling interval is $\frac{1}{4}$ to $\frac{1}{2}$ of the wavelength in the host material. In sedimentary studies, a maximum step size of one metre (often less 0.1–0.5 m depending on the antennae frequency) should be used to provide detailed horizontal resolution of sedimentary structures, yet allow profiles to be completed in a timely manner (depending on site conditions). A typical survey with 100 MHz antennae should have a step size of 0.25 m, however, larger step sizes can be used where the sub-surface stratigraphy is composed of continuous horizontal layers. If the step size is too large, the data will not adequately define steeply dipping reflectors or diffraction tails. To image horizontal surfaces, such as the water table, this criterion can be compromised and a greater step size can be used. From a practical viewpoint, increasing the station interval reduces data volume and survey time, yet from a data interpretation standpoint, adhering to the Nyquist sampling interval is very important.

Imaging sedimentary structures in the shallow sub-surface is often a primary aim of GPR surveys in sediments. The data from these environments are collected at various step sizes which influence the horizontal resolution. The decision to increase or decrease the step should be based on a variety of factors including: size of the sedimentary feature being investigated, dip angle, and areal extent of the survey. Large scale sedimentary structures such as sets of cross-stratification in aeolian sands and sandstones, river deposits, deltas and coastal sediments have been successfully imaged using GPR. Some studies of river deposits have been unsuccessful and we suspect that this is primarily due to poor survey design resulting in a lack of resolution of the subsurface. The vertical resolution of GPR is covered in the previous section but the horizontal

resolution is equally important and impacts strongly on the survey design. The radar signal is not directed vertically down into the ground but spreads out from the transmitter, thus it is possible for reflections to come back from reflectors out of the plane of the radar profile. However, most of the reflected energy comes from an elliptical area beneath the transmitter known as the first Fresnel zone which has a radius that is determined by the radar wavelength, velocity and depth to the reflector. To image sets of cross-stratification in the sub-surface the step size relative to the width of a set of trough cross-stratification has to be less than $\frac{1}{4}$ (Fig. 2). At least five measurements (preferably many more) are required to be able to identify the geometry of a trough shaped reflector, any less results in spatial aliasing (Fig. 2). Thus, sets of trough cross-stratification 1 m wide require a step size of 0.2 m or less to be correctly identified. Large troughs >5 m wide could be identified with 1 m step size but a step size of 0.5 m would be much better. A 1 m step size is frequently used with 100 MHz antennae and with this survey configuration sets of trough cross-stratification less than 2.5 m wide are unlikely to be correctly resolved. The resulting reflection pattern is likely to include discontinuous concave and convex reflection patterns that have been seen in GPR profiles of braided river deposits.

A hypothetical survey designed to resolve the top and base of a 1 m thick bed requires a wavelength of between $\frac{1}{4}$ to $\frac{1}{2}$ of the bed thickness (e.g. a wavelength of 0.5 m to 0.25 m to resolve a bed with a thickness of 1 m). A set of cross-stratification, with sufficient contrast in dielectric properties to produce a reflection, dipping at 30° will extend for around 1.75 m (Fig. 3). In order to resolve this feature the horizontal step size needs to be 0.4 m. However, for a bed of 0.2 m thickness the wavelength required to resolve the top and base

(a)

Inferred radar reflections

(b)

(c)

(d)
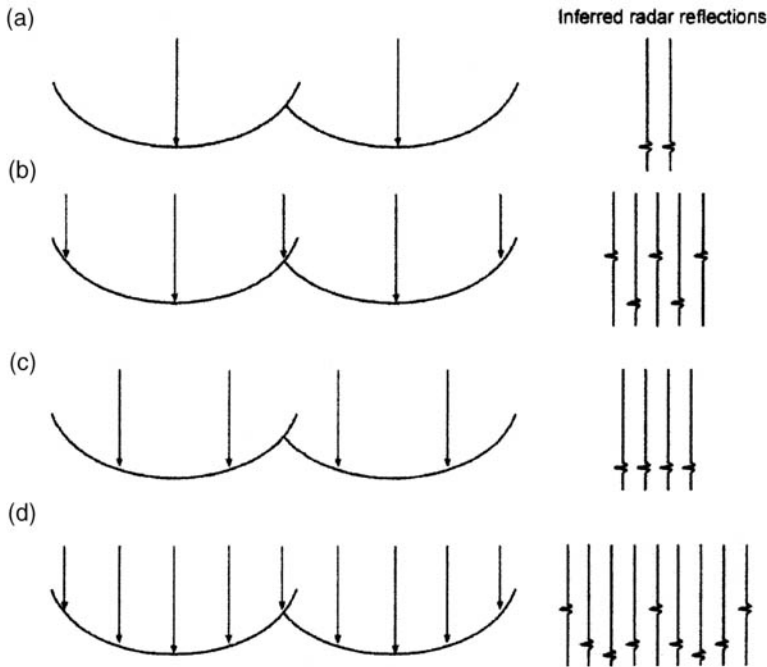
Fig. 2. Spatial aliasing of sedimentary structures due to insufficient horizontal sampling; (**a**) step size equal to trough width fails to image troughs; (**b**) step size $\frac{1}{2}$ of trough width leads to spatial aliasing because troughs are under-resolved; (**c**) step size $\frac{1}{2}$ trough width but different sampling locations could be completely misrepresented; (**d**) step size $\frac{1}{4}$ trough width, the reflections start to resemble trough shapes. A step-size of a minimum of $\frac{1}{4}$ trough width is required to resolve trough cross-stratification and step size should preferably be even less.

of the bed is only 0.1 m to 0.05 m and the step size required to resolve sets of cross-stratification is less than 0.1 m. Very few surveys of sedimentary environments have used step-sizes of less than 0.1 m. Small scale sets of cross-stratification are, therefore, not being imaged because surveys are conducted with too low a resolution (see Woodward *et al.* 2003).

iii) Length of time window When selecting the length of time window for a survey, the window should exceed target depth by around one third (Annan 2002). This will often require prior testing at the site. For deeper penetration, a time window increase will result in larger amounts of data being recorded and processed, and a longer survey time.

iv) Time sampling interval The time sampling interval (sampling rate), is the rate at which the received signal is sampled and is based on the wavelength/frequency of the transmitted signal. As the antennae frequency is increased, a higher sampling rate is needed (based on Nyquist principle – see step size). However, as the time sampling rate is increased (keeping length of time window constant), survey time will also increase.

v) Antennae separation Some antennae have a fixed separation while others can be varied. Antennae separation varies for each antennae frequency but should be as small as possible based on initial testing and survey needs (e.g. 1 m for 100 MHz). A close separation can cause a small amount of signal saturation in the top portion of the trace. However, this is usually compensated by the decrease in geometric distortion of the near surface and the near vertical incidence of reflections (Annan 2002). Depth resolution of targets decreases as antennae separation increases, although this effect is small until antennae separation approaches $\frac{1}{2}$ of the target depth. If little is known about the survey area, a safe rule-of-thumb is to set antennae separation equal to 20% of target depth (A.P. Annan, pers. comm.). In practice, a small antennae spacing is often used because operational logistics usually demand simplicity.

vi) Line location and spacing Where possible, GPR survey line orientation should be laid out to include a grid with lines running parallel and perpendicular to the expected sedimentary dip direction. The collection of lines in grids is usually required to create 2-D visualisations and to make
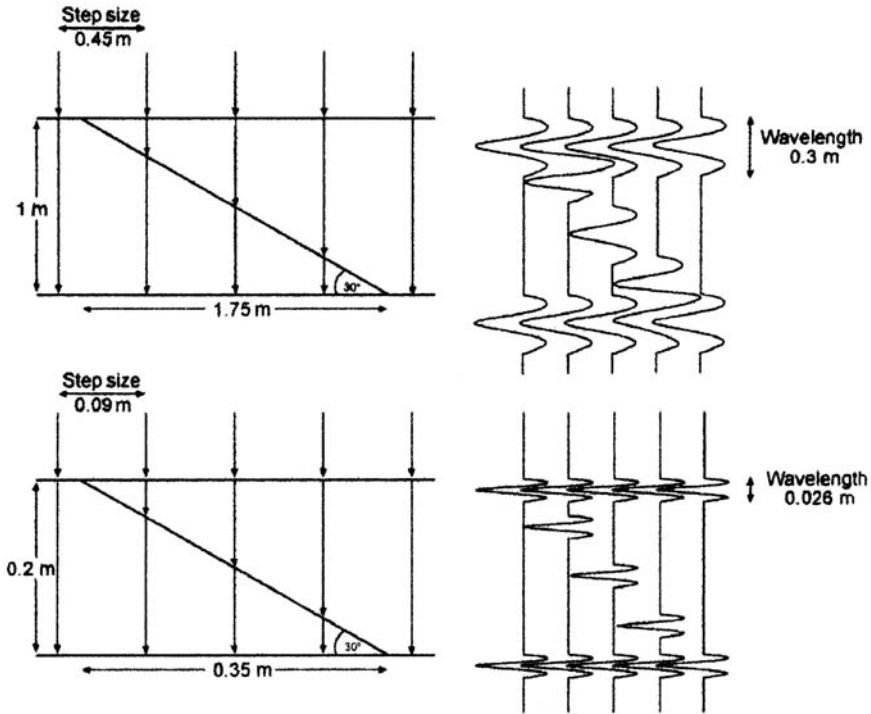
Fig. 3. Imaging sets of cross-stratification in a 1 m thick bed are possible with a step size of less than 0.5 m and wavelength less than 0.5 m. Imaging sets of cross-stratification in a 0.2 m thick bed requires a step size of less than 0.1 m and a wavelength of less than 0.1 m, which is rarely used in field surveys.

tie lines for correlation. Fence diagrams are an effective means to tie 2D lines together and provide an overall perspective of a sedimentary body (Bristow 1995a; Bristow *et al.* 1996, 1999; Roberts *et al.* 1997). Line spacing is usually a compromise between the time taken to conduct a survey and the data density required to image the target. At many sites ground conditions (vegetation, topography, buildings, roads) sometimes prohibit the collection of data in well-defined grids. In such cases, following tracks and trails may be the only way data can be collected.

There is increasing use of 3-D surveys, where closely spaced lines give sufficiently dense data coverage for the construction of 3-D block models (Beres *et al.* 1995). The data can then be processed and exported into a 3-D visualization software package. The 3-D cube enables the depositional framework of the stratigraphic unit of interest to be interpreted in more detail than was possible based on widely spaced 2-D profiles (Figure 4). The sedimentary unit can now be visualised from any viewing angle and sliced so that the internal stratigraphy can be mapped, including bed thickness and volume calculations. We feel that the collection of detailed grid data will lead to a better

understanding of stratigraphic architecture and will result in improved depositional models of sedimentary environments. However, there is a significant increase in the time involved in both the acquisition and processing of 3-D data.

vii) Antennae orientation Selecting antennae orientation does affect the quality of collected data (Jol *et al.* 1995; Lutz *et al.* 2003). Figure 5 illustrates the various modes for antennae deployment. One must remember that antennae are dipolar and radiate with a preferred polarity. The most common orientation that provides the widest angular coverage of a subsurface reflector is the perpendicular broadside to direction of survey approach (PR-BD). This orientation is also the easiest for surveying in sedimentary environments. In some cases, the parallel broadside (PL-BD) better identifies features such as the water table in the subsurface (Van Overmeeren 1994). In addition, close coupling of the antennae to the ground should be maintained in order to maximize reflection energy (Annan 2002). Maintaining a consistent antennae configuration and electronic connections throughout a survey is important because this will allow changes in polarity, due to increases or decreases
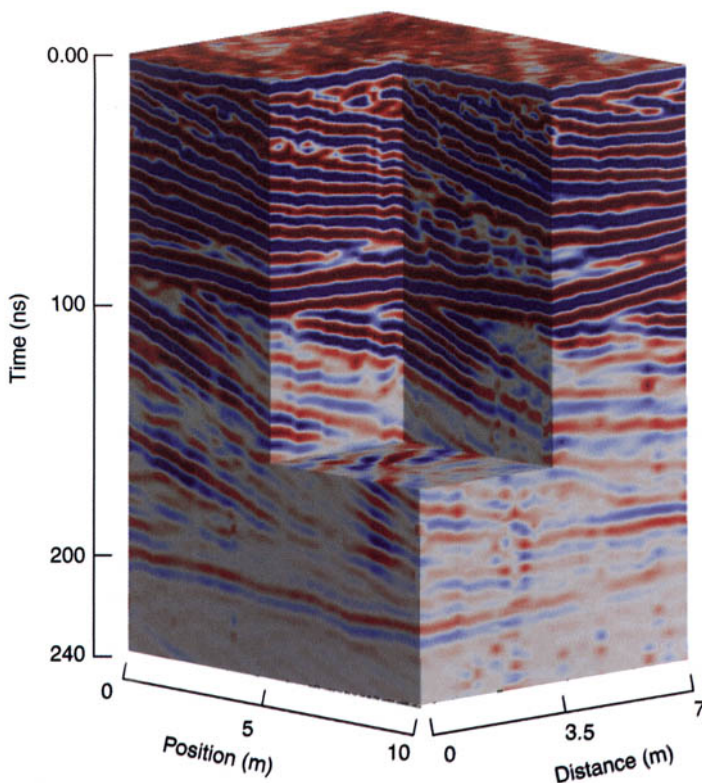
Fig. 4. A 3-D GPR image of an ancient dune complex viewed from the southwest in Zion National Park, Utah, USA (Junck & Jol 2000; there is a colour version of this image on the front cover of this book). The 200 MHz data was collected in a 7 m × 10 m grid with a 0.10 m step size. The image shows 3 sets of dipping reflections interpreted as cross-stratification with 2 horizontal reflections which are interpreted as bounding surfaces. The block model can be used to determine the true dip direction of sets of cross-stratification to reconstruct dune migration and palaeowind direction.
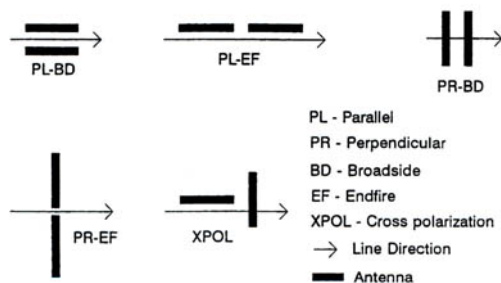
Fig. 5. Illustration of the various modes for antennae deployment/orientation (electric field is assumed to be aligned along the antennae axis; from Annan 2002)

in permittivity (impedance) with depth, to be determined.

viii) Trace stacking Each trace in a GPR profile should be vertically stacked (e.g. 32 or 64 times)

to enhance the return signals by taking the running average for a number of subsequent radar transmissions. In this way, random signals (noise) are minimized while persistent signals (reflections) are emphasized (Ulriksen 1982). An increase in trace stacking will increase the time taken to collect data.

Velocity sounding

In order to transform the two way travel time from reflection profiling into depth, the propagation velocity of EM energy of the profiled sediment must be determined. This can be accomplished by the straightforward process of drilling, digging, vibracoring holes or logging outcrop in order to determine depth, and from the measured reflection time, calculate the velocity. However, more sophisticated and less destructive ways to determine the velocity are available. Common mid point (CMP), Wide-Angle Reflection and Refraction (WARR), and borehole to surface soundings are commonly

used in reflection seismic and can be applied in GPR. CMP and WARR techniques involve conducting a survey in which the spacing between the transmitter and the receiver is successively increased with each step. CMP soundings are generally considered more precise as the antennae are always centred on the same point (Fig. 6). Optimal CMP soundings are obtained when the electric fields of the antennae are parallel and the antennae are moved apart along a line which is perpendicular to the electric field polarization (antennae configuration – perpendicular broadside; see Fig. 5) above a horizontal reflector. Results are used to obtain an estimate of the radar signal velocity versus depth in the ground by measuring the change of the two-way travel time to the reflections.

CMP surveys should be one of the first surveys undertaken upon arrival at the site and if possible, several CMPs should be collected in the study area prior to major surveys being conducted. When collecting a CMP, one should start with the antennae at a minimum separation and move each antenna out every 5 or 10 cm (total antennae separation increases 10 or 20 cm) until there is no signal return, the incidence angle to the deepest reflection is 45–60°, or one reaches the end of the cables. Results from CMP soundings are a plot of antennae

Fig. 6. CMP procedure. (**a**) The separating step-like technique used to determine EM propagation velocity of the near surface sediments. (**b**) An example of a CMP profile used to calculate near surface velocity (Jol & Smith 1991).

separation (distance) versus time (Fig. 6). The dominant wave fronts, which are normally observed, are the direct airwave and then the direct ground wave, followed by any reflected and refracted radar waves. In many cases, the ground wave can be used to calculate the velocity of the sediment being investigated. When using CMP surveys to determine the velocity to a reflecting horizon at depth it is important that the surface is horizontal. Interpretation of the CMP datasets will allow one to calculate velocity (slope of the dipping lines is inversely proportional to the velocity) of the sediment being surveyed which will determine time window depth (depth of penetration). Note that the depth scale is not a linear scale since GPR is a time domain technique. CMPs provide a good estimate of velocity and in most cases, using this procedure, depth to target can be often found within 10–20 cm – accurate enough for most sedimentary studies. More detailed velocity analysis procedures are also available but will not be reviewed here (Fisher et al. 1992).

Additionally, CMP soundings provide other pieces of information about the study site including an estimate of signal attenuation (amplitude fall off with distance), which will aid in designing survey parameters such as antennae separation and an appropriate time window. In areas of surface clutter, CMP surveys can separate above and below ground reflections. Further velocity analysis will be necessary at sites where sediments or water content vary significantly (in depth or horizontally).

Pringle et al. (2003) describe the use of vertical radar profiles (VRP) taken down the face of a rock for site-specific time-depth calibration. In VRP surveys the transmitting antenna is positioned on top of an exposed section, a few meters back from the cliff face, and the receiving antenna is moved down the exposed cliff face. VRP reflection events can be correlated with stratigraphic horizons exposed in the cliff face improving correlation with fixed offset reflection profiles.

Test survey

Before arriving at a study site, background information and permission to enter the site should have been acquired. To employ an effective survey strategy, the orientation of the geomorphic feature under investigation, and potential sedimentary structures (dip and strike), should be known (or predicted) based on aerial photograph or topographic map interpretation. Seeking permission to conduct a GPR survey on an individual's or organization's land can take a few moments from a brief phone call or visit to the respective landowner, to a long application process completed months before. One item to emphasize when requesting permission
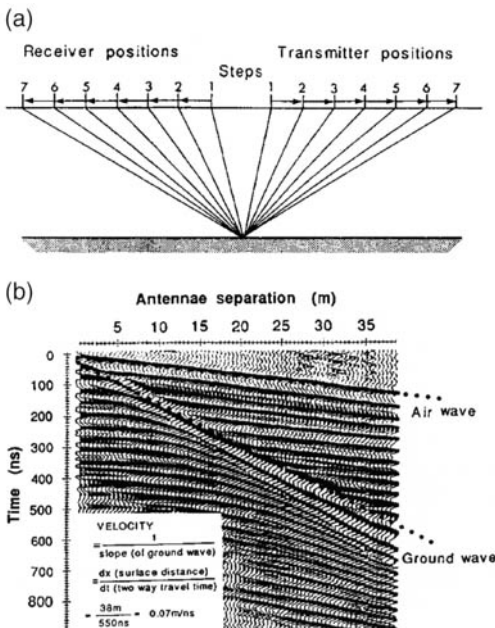
to conduct a GPR survey is that GPR is a non-invasive technology.

Upon arrival at a new site, and with the needs of the research question in mind, it is advisable that a series of trial reflection and CMP surveys be undertaken. These surveys should include trial lines over a short distance (20–30 m) with the full range of all available antennae and transmitter voltages. CMP surveys should then be carried out (preferably over a horizontal reflection if one can be identified). Following the trial surveys the data should be analysed prior to extensive surveys being carried out. This initial testing should provide optimum system configuration and data collection parameters, and tends to minimize the time spent on site while optimising data quality. For each project adequate time needs to be allocated to run through these preliminary procedures which may take up to several hours to complete.

Topography

The collection of topographic data is an essential component of a GPR survey. The measurements should be made along each GPR profile at 5 m intervals (or less) and at breaks of slope. A variety of instruments can be used including optical levels, total station, laser levels, and GPS. In areas with subdued topography (less than 5 m change in elevation), laser levels provide a fast and accurate method for collecting topographic data. In more complex terrain, a total station provides greater flexibility and higher accuracy. Optical levels are perfectly adequate but increase survey time. To gain sufficient accuracy with GPS receivers RTK units are required (note that GPS receivers have difficulty working under trees and require post processing). Essentially, depending on site conditions, we prefer either the laser level and/or total station approach for its ease of operation, accuracy and versatility. When incorporating topographic data into the GPR lines, proper velocities need to be used; incorrect application of velocities and topography can be seen in profiles where normally horizontal reflections such as the water table dip.

Logistics and survey arrangements

Site conditions vary between sedimentary environments which requires equipment set-up to be flexible and practical. We have found that standardizing the GPR system configuration and set-up allows one to compare datasets from one site to another with more accuracy and ease. What follows are some suggestions to aid in effectively carrying out GPR surveys in sedimentary environments:

• GPR equipment (console, laptop and battery)

should be carried in either a 'wheelbarrow' type configuration or, in more rugged environments, a backpack mode (Fig. 1c).

• Along a survey line, we suggest leading with the antennae followed by the console and computer (Fig. 1 and 7). If you are using bistatic antennae the transmitter should follow the receiver. The distance between the antennae and the console/computer should be the full extent of the cables. This set-up will reduce EM energy generated by the computer, console and battery from being picked up by the receiver during surveying (Baker & Cull 1992). Keeping the cables running straight back from the antennae to the console also reduces the risk of cable snagging.

• Selection of equipment to be used, and the number of persons required to operate the GPR system, is dependent on the site conditions and survey parameters. We often collect GPR data with a 2–3 person crew. This allows one to move the antennae, one to operate the computer and assess data quality, and one to move cables, tapes, and antennae if separation is
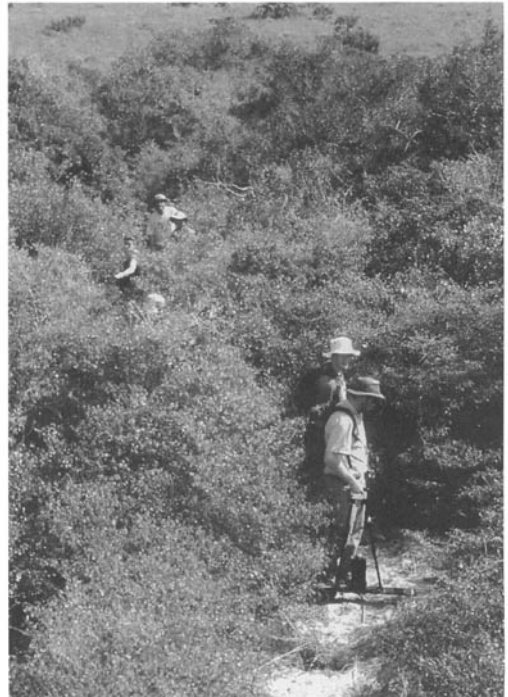
Fig. 7. Effective use of manpower to conduct a GPR survey along a game trail through thick bush in South Africa with 4 people looking after the fibre optic cables, 1 holding the antennae and another looking after the computer and console. Results can be seen in the paper by Botha *et al.* (2003).

greater than 1 m (in rugged environments; Fig. 1 and 7), in addition to performing any other miscellaneous tasks. If one has a well-trained crew, data from a 100 MHz antennae survey at a 1.0 m step (64 stack) in a relatively flat area can be acquired at a rate of 500 m/hour. However, many sedimentary environments are not flat and offer a variety of obstacles (vegetation, steep slopes) which will dramatically slow survey rates by a factor of ten. As GPR data collection can become tedious, achievable goals should be set so that the survey crew does not become discouraged. Changing roles frequently helps to reduce mental and physical fatigue; in addition all crew members are making a full contribution to data collection which aids in team building.

• While collecting GPR data, detailed field notes should be taken of survey layouts, equipment parameters, problems (such as trigger sticking, bad traces, cable problems) and all field observations (including surface features and sources of external noise such as trees, motor vehicles, buildings, overhead power lines, telephone poles, cb/FM transmitters). The appearance of trees or other surface features on the GPR profiles varies depending on the ground contact and resistivity of the sediment. If there is good coupling with the ground then air waves are less of a problem. While in the field one can quickly confirm if surface features such as a tree or wall are being imaged or not. Running a short line up to the tree or wall does this. The profile should show a diagonal reflection that comes to the surface as one approaches the feature in question.

• Metallic cables (power and communication) should be in a constant configuration with respect to the antennae as they can produce EM radiation (noise). Cables lying across the ground can produce confusing or erroneous signals on GPR profiles. They should be secured so that connections do not become stressed or disconnected during surveys. It is good practice to have the cable leave the antennae vertically and move perpendicular back to the console possibly using the operator's shoulder as a pivot point.

• Fibre optic cables are flexible but fragile, however they have the advantage of not producing EM radiation and this reduces one source of noise from the equipment. Careful handling of the fibre optic cables will increase their working life and maintain data quality. Fibre optic cables can be damaged during surveys by being snagged, tugged or trodden on. When this occurs GPR data show time zero drops as well as noise spikes. To avoid this problem,

make sure the fibre optic cable is securely attached with slack at both the antennae and the console (provision of a loop at both ends helps to reduce shock from sharp tugs; Fig. 1c). In addition, keeping the cable out in full length reduces the chance of the cable getting snagged on vegetation or rough terrain. If you have extra personnel they can be deployed to look after the fibre optic cables (Fig. 7). When packing up fibre optic cables carefully roll them up to prevent twists and secure the loop with tape or velcro. To reduce field downtime when a cable breaks – always carry a spare set of fibre optic cables and connections. Like batteries, fibre optic cables will need to be replaced after a certain amount of wear and tear.

• Tasks to be organized prior to data collection: (a) before major field surveys purchase new batteries and keep them fully charged to extend life; (b) always carry spare charged batteries with you in the field; (c) repair kit of tools should be assembled so that one can make repairs while in the field (e.g. screw drivers, pliers, soldering iron, digital voltmeter (multimeter), insulating tape, etc); (d) fibre optic cable ends should be examined regularly, preferably with a small magnifier, for chips, scratches, sunken or projecting ends. These problems can lead to data degradation or receiver error; (e) due to the variety of conditions in which surveys are conducted, a backup portable computer and a spare transmitter should be considered in remote locations; (f) for data collection in the step mode, doublesided metric fibreglass survey tapes (forestry chains) with 0.1 m divisions are essential. Several tapes laid out in advance and during data collection will allow surveys to be conducted without stopping.

• While in the field, the use of a hotel or cabins with electricity is desirable to recharge batteries. In addition, data can be backed-up, processed and plotted. In remote locations with no electricity or accommodations, an extra tent for GPR processing and printing is recommended. A working generator will be needed to recharge the batteries on a nightly basis.

• Upon returning from the field, the following items should be completed on a daily basis: (a) data should be backed-up onto a separate storage media (e.g. disc, zip). Since field surveys are a costly endeavour and computers and/or hard drives do fail, multiple backups are advised. While surveying in the field, data files should be regularly saved to avoid large file sizes; (b) datasheets should be filled out for all lines collected (includes field notes and parameters; see Table 2 for an example); (c) data

Table 2. *Example data sheet that can be used to collate data from daily GPR surveys*

Ground Penetrating Radar Data Sheet
Department of Geography, University of Wisconsin-Eau Claire

Project: _____

Date: _____

File name	Start position	End position	Ant. freq.	Direction	Step size	Ant. spacing	Time scale	Topo	Location & comments

should undergo basic processing and be printed out, if possible. Preliminary interpretation of the plotted lines can check data quality and direct future (or the next days) survey work. Some projects assess problems in real time, with processing and printing undertaken in the field.

- Even though GPR systems are robust, they still contain many sensitive electronic components and delicate connections, therefore, when transporting GPR equipment, there is a need for rugged, waterproof, foam lined cases (e.g. Pelican). When transporting the equipment across borders, a Carnet can provide a relatively easy and cost effective method to avoid delays with customs.

Extreme environments

GPR can operate in extreme environments from deserts to ice caps (Fig. 8), but suitable modifications are required for operating in these conditions; most notably, preventing water from entering electronic equipment and portable computers. Other issues that constantly plague surveys in these extreme environments, are that computer screens fail in very hot conditions, field readability of computer screens in bright sunlight is often poor (this is more severe with active matrix color screens), and battery performance declines in cold (snow and ice) conditions. Providing protection from rain, sun and extreme temperatures is a sensible precaution for most field surveys especially when operating in remote areas (Fig. 8). One simple modification is to place the portable computer, battery and/or console inside a box (insulated if

necessary); this provides some protection from the elements and also gives shade to the screen improving readability. The provision of fully charged spare batteries is always desirable in the field. In arid and sandy environments, windblown sediments can cause serious problems to the computer keyboards, ports, disc drives, electrical and fibre optic connections. It is important these items are suitably protected; wrapping a keyboard in cling film (saran wrap) or similar product, taping the ports shut and being extremely careful with fibre optic ends when making connections helps to reduce the problem of sand and fine dust in all those cracks. The effect of working in extreme environments on the surveying schedule (e.g. breakdowns, maintenance) must also be taken into consideration when establishing a timetable.

Processing and display

Much of the GPR data collected in sedimentological environments requires only minimal processing to enable interpretation. One can often make preliminary interpretations while the data is being collected – a significant benefit of the GPR method. The processing of GPR data is an immense subject. From a signal processing standpoint, there is a wide similarity between impulse radar measurements and reflection seismic; thus there is a whole array of seismic processing techniques and software available to apply to GPR data. Seismic processing packages are available and have been successfully adapted for enhancing radar data (Ulriksen 1982; Fisher *et al.* 1992, 1996). However, when considering the low cost of radar surveys compared with the cost of reflection
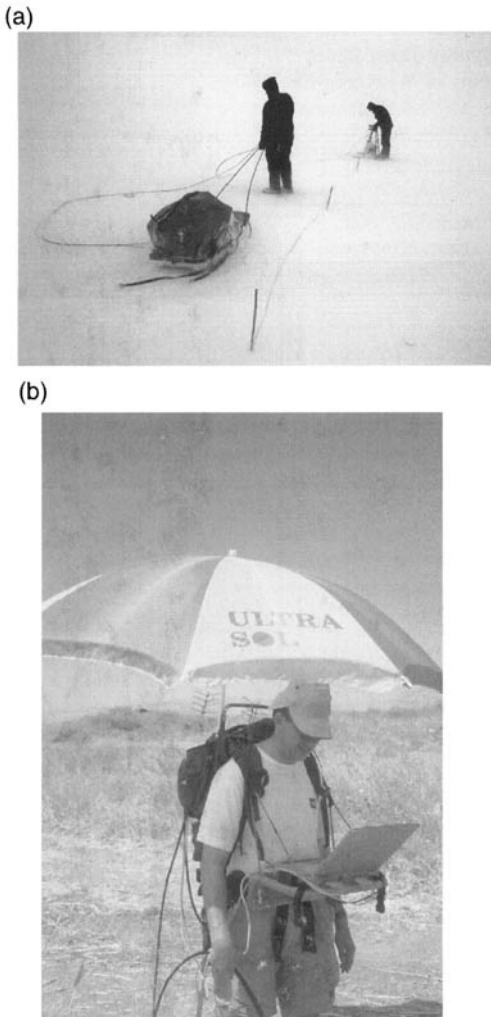
Fig. 8. (a) GPR field set-up in extreme wintry conditions, Iceland. The GPR console, battery and computer are insulated and covered in the sled (foreground) to provide warmth to the equipment as well protect the equipment from the elements. The antennae (background) are wrapped in plastic to prevent any water from entering. (b) Data collection on a hot (>50°C) sunny day in desert conditions, Israel. The sunshade allows the operator to read the computer screen and the equipment to stay within operating temperatures while surveying. The figure demonstrates and attests to the portability and ruggedness of GPR equipment to survey in rough terrain and under varying temperature conditions.

seismic, it is not economical to process radar data to the same extent. If one has not been able to collect good quality data in the field, extensive processing will not change this fact. In this section a brief overview of several basic GPR processing possibilities are addressed.

According to Annan (2002), an important aspect of GPR processing is understanding the need for time gain. A major problem with GPR data is that attenuation of the radar signal in the ground can be highly variable. One can have a low attenuation environment where exploration depths of tens of metres can be readily achieved. In other situations, attenuation can be quite high and depths of only 1 or 2 metres can be penetrated. Another way of viewing the amplitude of signals versus time is shown by a spherical EM wave spreading into the ground; it will fall off inversely with distance into the ground, attenuating exponentially due to the conductivity losses in the sediment. Signals from great depth are very small and may be invisible or indiscernible in the presence of signals from a shallow depth. Therefore, there is a need to equalize amplitudes or apply some sort of time gain function that compensates for the rapid fall off in radar signals from deeper depths. The concept of time varying gain is one that applies a gain to the data which increases with time after the pulse is transmitted. The rise of the gain function is tailored to accommodate the signal fall-off and signal amplitude versus time.

Two of the more popular types of gain function that can be applied to compensate for the rapid signal fall-off are: (1) automatic gain control (AGC), and (2) spherical and exponential gain compensation (SEC).

With an AGC function, the objective is to equalize the amplitudes all the way down each trace. Gains are adjusted by estimating the average signal level at every point on the trace, then computing the gain, which is inversely proportion to the signal level. In areas of weak signal, a gain is large and in areas of strong signal, the gain is small. AGC is ideal for monitoring continuity of reflections, but obliterates all amplitude information. Hence, once data has been processed with AGC, one can no longer make reliable deductions concerning the strength of any particular reflection relative to other reflections (Sensors and Software 1999). When interpreting GPR data in sedimentary environments, it is important to note that in order to identify high amplitude reflections a constant gain is required; it is also worth noting that gain amplifies noise and reflections alike.

The concept of SEC is to apply a linearly increasing time gain combined with an exponential increase. The velocity and attenuation of EM signals through the ground are estimated in order to most effectively compensate for spherical spreading losses and exponential dissipation of energy (Sensors and Software 1999).

In the course of processing, simple filters can also be applied to the data. Temporal filtering is basic, but one of the most powerful for GPR analy-

sis. Down-the-trace-averaging (running average) of the signal replaces the data at a given point by the average over a window centred about that point. This type of averaging acts as a low pass filter by reducing random noise.

Spatial filtering can be applied to remove or emphasize different types of spatial variations. The simplest type is either a high or a low pass filtering of the data. The trace-to-trace averaging (mix) process option adds two or more traces together to produce an average trace. The number of traces to be added together is determined by the user. The primary purpose of this spatial, low pass filtering is to emphasize flat lying or low-angle, gently dipping reflections while suppressing rapidly changing ones (e.g. diffraction tails) or random noise. An alternate approach, trace-to-trace differencing, replaces a trace with the difference between itself and the previous trace. This high pass filter has the effect of enhancing localized, rapidly changing features in the profile (e.g. diffraction tails, point reflectors) and suppressing flat lying and constant features. In practice, high and low pass filters should be considered mutually exclusive because they produce opposite effects on the data (Sensors and Software 1999).

Depending on the proximity of the transmitter and receiver, as well as the electrical properties of the ground, the transmit signal may induce a slowly decaying low frequency wow (wave) on the trace which is superimposed on the high frequency reflections (Moorman 1990). The wow should be corrected before the data is plotted, and before exporting data to seismic processing packages.

A wide variety of other processing techniques can be applied to GPR data and are addressed in the literature (Ulriksen 1982; LaFleche *et al.* 1991; Fisher *et al.* 1992, 1996). Generally speaking, the more sophisticated the processing, the more care that must be taken in field acquisition of the data. For most sedimentary geologists, detailed data processing is out of scope due to time and budget constraints. There is, however, an ongoing discussion about migrating GPR data (e.g. Fisher *et al.* 1996; Neal and Roberts 2001). It is an avenue that GPR is advancing in but, due to field conditions and the need to interpret data while in the field, there has been limited use of migration. All stated dip angles should, however, be corrected to include migration effects because during the process of data collection, dipping reflections on the profile are not in their true position (Ulriksen 1982; Sheriff 2002; Fig. 9). When the antennae are moved over a material containing a sloping reflector, the resulting profile tends to underestimate the depth to the reflector at every point (Fig. 9). If the measured angle in the radar profile is β, then the actual angle (α) can be computed with the mathematical expression $\alpha = \sin^{-1}(\tan \beta)$ (Ulriksen 1982). The maximum recordable slope is identical to the radiation angle of the antennae. This is not a fixed measure, but rather a function of the receiver antenna properties; as a rule, slopes greater then 36° are difficult to record (Ulriksen 1982). If one works through the equation with realistic values for sedimentary environments (1–25°), angles taken from GPR profiles and those that are migrated are likely to be within a degree or two. For most environments, this range is acceptable and overall reflection patterns do not change significantly. However, higher angle features such as faults and fractures can be observed because of offsets in reflections, and scatter from the fault plane.

Display methods are a diverse subject for GPR. The majority of the data in this publication is presented as wiggle trace plots, that is, the amplitude of the trace is plotted left and right along a vertical line which depicts the amplitude of the sig-
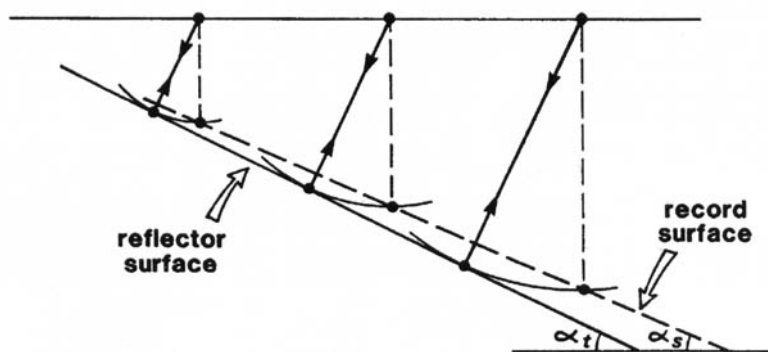
Fig. 9. Schematic diagram demonstrating the effect of collecting data across a dipping reflector. The signal returns perpendicular to the reflector, not directly below the antennae (source-detector). This results in the reflection being higher and shallower (up dip direction) within the GPR image than the actual reflector (from Keary & Brooks 1984).

nal versus time. Aligning these traces adjacent to one another generates a wiggle trace plot which depicts the variation in subsurface features (stratigraphy) versus position. This type of display resembles seismic reflection profiles and allows similar interpretation methodologies. Other techniques include single trace plots (e.g. as on an oscilloscope), and grey scale or colour coding the amplitudes while generating a profile.

In summary, most GPR profiles require little post-processing to enable the interpretation of sedimentological features. It is good practice to first edit data based on any field notes concerning bad traces or other issues. Following data editing, the data should be time zeroed by conducting a first pick and then shifting the dataset based on the first pick. Time zeroing is often an automated procedure in software packages but in some situations (e.g. fibre optic pulls), individual traces will have to be corrected manually. In most cases, the data is now ready to be plotted with procedures that include the application of filters and gains to the data so that stratigraphy can be highlighted. To reduce some of the noise present in datasets, down trace and trace-to-trace filters should be applied using minimum values. It is important to spend time processing and reprocessing datasets to see the effects of using different parameters. Many of the profiles published in the sedimentary literature have applied AGC to stratigraphic data and used a wiggle trace format for display. Further processing of the GPR data may not be time and cost effective for everyday operational surveys, some advanced processing can introduce user bias into interpretation. There is no processing that can compensate for poor data, therefore, good survey design and quality control in the field are most important.

Interpretation methodology

Interpretation of radar profiles is the most subjective part of the GPR methodology. It is important that the person responsible for the interpretation is aware of the aim of the investigation, and the level and accuracy of interpretation required. The factors that contribute to the electrical properties of the sediments also have to be known. To better understand the relations between the radar profile, the field conditions, and medium being measured, it would be advantageous for the interpreter to be present during fieldwork. The profiles should be subjected to preliminary interpretation immediately upon completion, so that one can decide on possible resurveying or, if needed, adjusting the survey plan or data collection parameters.

Before interpreting GPR data, there are several concepts that should be considered. The two direct waves (air and ground) observed at the top of the profile are often the strongest return signals. As a result of the high velocity and low attenuation of radar energy in air, the direct air wave is the first to arrive, travelling at the speed of light. The direct ground wave usually follows the air wave with an arrival time that is a function of the ground surface propagation velocity. Changes in surface conditions can be identified by fluctuations in the arrival time of the direct ground wave.

Following the processing of GPR profiles, an objective interpretation should be undertaken that is independent of other datasets (e.g. cores) and sedimentary models. Many projects that we see are model driven interpretations that miss key components visible in the GPR profiles. Initially, all the data should be printed and laid out on a table. Major reflections should be picked-out, traced around and between profiles, and where possible made into closed loop correlations (Bristow 1994). For this procedure, the coloured crayon still provides a valuable interpretation tool. Many principles used in radar stratigraphic interpretation are derived from basic seismic interpretation methodologies (see next section). Following seismic stratigraphic principles, the next step is to identify reflection terminations and then characterise these as downlap, onlap, offlap, etc. This is the basis for constructing a relative chronology of sedimentary deposits.

During the analysis of the radar profile it is important to identify the origin of the reflections; that is, whether the interfaces indicated represent actual changes in the subsurface or interference. The latter may consist either of entirely random noise or of regularly repeating reflections which are independent of changes in the properties of the medium. A common interference is 'side swipe' responses which give rise to hyperbolic features on GPR records. These are the classic signature of localized features such as pipes, cables or other objects that are spatially limited. Features that run parallel to the profile may produce horizontal or sub-horizontal reflections. A common misconception when interpreting GPR data is that the profile is a vertical section perpendicular to strike. In reality profiles are often oblique to the sedimentary structures. In addition, sedimentary structures are three dimensional and reflections can come from structures outside the plane of the profile.

Core data, outcrop sections, quarry faces and excavated trenches have been widely used to provide ground truth for GPR interpretations (e.g. Smith and Jol 1992; Huggenberger 1993; Bristow 1995a, 1995b; Bristow *et al.* 1996; Woodward *et al.* 2003). Detailed field and lab studies of radar reflections in sediments have also been carried out for this purpose (Topp *et al.* 1980; Knoll 1996; Van Dam and Schlager, 2000; Van Dam *et al.* 2002a,

2002b). In addition, Van Dam *et al.* (2003) conclude that variations in water content associated with small scale textural changes in sediments are responsible for the changes in permittivity that cause reflection of radar signals.

To interpret stratigraphy and facies from radar data, characteristic features of radar reflection records must be identified and then related to sedimentary structures responsible for the reflections. The interpretation methodology that is followed depends on the desired outcome. There are three possible approaches:

1) Buried object – looking for a distinctive signature or radar facies
2) Stratigraphic study – looking for relative chronology – use radar (sequences) stratigraphy to identify bounding surfaces and reflection terminations or truncations
3) Sedimentary study – looking for bounding surfaces to define sandbody architecture and the fill, or radar facies

Examples

1) In the search for buried objects, such as dead bodies or buried treasure, the objective is to locate a specific object, and the method is to identify a reflection signature that is associated with the target. In the case of a buried soil horizon or the water table the objective is to locate a continuous reflection that is caused by the horizon. A buried body or treasure chest should give a characteristic anomaly or hyperbolic reflection pattern.
2) In the search for the relative chronology of sand dune deposits or fluvial sediments the objective is to identify reflections that represent sets of cross-stratification and bounding surfaces so that a relative chronology can be established from cross-cutting relationships. This includes the identification of reflection terminations and truncations indicating onlap, downlap or erosional truncation at stratigraphic horizons.
3) In sedimentary studies for reservoir analogues the sandbody geometry, bounding surfaces and internal fill all need to be identified. In this case a combination of radar facies interpretation and radar stratigraphic analysis is required.

Radar stratigraphy – overview

Radar stratigraphy originates from the principles of seismic stratigraphy which, in turn, are developed from the concepts of physical stratigraphy and the idea that seismic (radar) reflections result from stratal (bedding) surfaces and unconformities. As the material above stratal surfaces and unconformities is younger, a relative record of the chronostratigraphy, as well as depositional and structural patterns, is produced (Mitchum 1977). Sangree & Widmier (1979) noted 'depositional environments can be predicted through an orderly approach to the interpretation of seismic reflections'. Since GPR reflections are analogous to seismic reflections, it follows that depositional environments can also be interpreted from GPR records. Therefore, *radar stratigraphy* can be defined as the study of stratigraphy and depositional facies as interpreted from radar data using seismic stratigraphic principles (definition modified from Mitchum *et al.* 1977a).

Radar stratigraphy is an approach that provides a high resolution perspective of units by putting them in a continuous areal context. A stratigraphic framework is one that divides the radar profile into units which represent periods of essentially continuous sedimentation. The ability to recognize major radar reflection patterns allows bedding planes, bedsets, and sets of cross-stratification to be imaged (Bristow 1995b). These units are composed of relatively conformable and genetically related strata. The depositional units may therefore be interpreted in terms of naturally occurring episodes of sedimentation. The episodes contain primary reflections that parallel bedding and palaeodepositional surfaces.

The gross physiography of the environment in which sediments were deposited is displayed as reflections on the radar section and can be used both to predict facies and reconstruct paleoenvironments. A *radar facies* can be defined as a mappable, three dimensional sedimentary unit composed of reflections whose parameters differ from adjacent units (definition modified from Mitchum 1977). The concept of radar facies is now widely applied in GPR interpretation (Beres and Haeni 1991; Jol and Smith 1991; Huggenberger 1993; Jol 1993; Bristow 1995b; Van Overmeeren 1998; Van Heteren *et al.* 1998) and, while radar facies can be used to discriminate sedimentary environments (Van Overmeeren 1998), it is also worth noting that similar reflection patterns (radar facies) can be produced in a range of different sedimentary environments and, therefore, radar facies should be considered as non-unique. For example, hummocky discontinuous reflections are interpreted as accretionary spit-beach sand and gravel by Van Heteren *et al.* (1998), hummocky vegetated sand dunes by Bristow *et al.* (2000), poorly resolved sets of trough cross-stratification by Bristow *et al.* (1999), and beach ridge deposits by Neal & Roberts (2000). Radar facies provide a means, to classify reflection character and subdivide GPR profiles into units that can be related to sedimentary struc-

tures and depositional environments; they are not a direct indicator of any specific environment. It is worth noting that water content within sediments will have an influence on the strength of the radar reflection returns; for example the reflection from a water table can cut across reflections from sedimentary features (Van Overmeeren 1994).

The basis for the interpretation of radar facies is derived from seismic reflection facies analysis (seismic stratigraphy; Sangree & Widmier 1977; Roksandic 1978; Sangree & Widmier 1979; Brown & Fisher 1980). The process of describing and interpreting the radar reflection parameters within a depositional sequence is known as *radar facies analysis* (radar stratigraphy; Mitchum and Vail 1977). In general, the use of seismic stratigraphy enables the interpretation of depositional facies from seismic data (Mitchum *et al.* 1977b), while radar stratigraphy is particularly useful for investigating the geometry and the relationships between facies (Moorman 1990; Beres & Haeni 1991; Gawthorpe *et al.* 1993).

A discussion of seismic stratigraphic principles for interpretation would be too lengthy for this paper. The original work on seismic stratigraphy can be found in the American Association of Petroleum Geologists Memoir No. 26 edited by Payton (1977), while summaries and case studies are provided by Roksandic (1978), Ramsayer (1979), Anstey (1982), Sheriff (1980, 1982), Bally (1983), Berg & Woolverton (1985), and Hardage (1987). Additions and alternative perspectives in the field include publications by Wilgus *et al.* (1988), Galloway (1989a, 1989b), and Van Wagoner *et al.* (1990, 1991).

Due to the coarse resolution of seismic data, the schematic examples of sequence patterns developed for seismic stratigraphy are large features such as deltaic packages and palaeovalleys. However, when interpreting GPR data it should be noted that there is at least one and sometimes two orders of magnitude between the resolution of reflection seismic data and GPR profiles. GPR provides high resolution data and thus enables the study of smaller depositional units, such as the internal architecture of deltaic environments, river channel fills and sand dunes. These smaller scale features must also be incorporated into the interpretation methodology. Moorman (1990), Beres & Haeni (1991), Jol & Smith (1991), Fitzgerald *et al.* (1992) and Gawthorpe *et al.* (1993) were some of the first to successfully attempt to apply seismic stratigraphic principles to smaller features in radar profiles. They related reflection signatures (patterns) from radar profiles to lithologic and stratigraphic characteristics of sediments.

Summary

In this paper, we have briefly outlined many of our experiences related to the collection, processing, interpreting and publishing of GPR data. We hope that the article will help novice users to quickly adopt the GPR methodology to investigate more sedimentary environments. In conclusion, when considering portability, resolution, cost effectiveness and time efficiency of a research tool for assessing the shallow subsurface stratigraphy (0 to 50 m) in sand, gravel and organic deposits, GPR is unmatched by any other methodology in the earth sciences.

References

ANNAN, A. P. 2002. *Ground Penetrating Radar Workshop Notes.* Sensors and Software, Incorporated, Mississauga, Ontario.

ANNAN, A. P. & DAVIS, J. L. 1976. Impulse radar sounding in permafrost. *Radio Science,* **11**, 383–394.

ANSTEY, N. A. 1982. *Simple Seismics.* International Human Resources Development Corporation, Boston, Massachusetts.

BAKER, P. L. & CULL, J. P. 1992. Acquisition and signal processing of ground-penetrating radar for shallow exploration and open-pit mining. *Exploration Geophysics,* **23**, 17–22.

BALLY, A. W. 1983. *Seismic Expression of Structural Styles a Picture and Work Atlas.* American Association of Petroleum Geologists, Tulsa, Oklahoma, Studies In Geology Series No. 15, Volume 1.

BERES, M., JR. & HAENI, F. P. 1991. Application of ground-penetrating-radar methods in hydrogeologic studies. *Groundwater,* **29**, 375–386.

BERES, M., GREEN, A., HUGGENBERGER, P. & HORSTMEYER, H. 1995. Mapping the architecture of glaciofluvial sediments with three-dimensional georadar. *Geology,* **23**, 1087–1090.

BERG, O. R. & WOOLVERTON, D. G. 1985. *Seismic Stratigraphy II: An Integrated Approach to Hydrocarbon Exploration.* American Association of Petroleum Geologists, Tulsa, Oklahoma, Memoir 39.

BOTHA, G. A., BRISTOW, C. S. ET AL. 2003. Evidence for dune reactivation from GPR profiles on the Maputaland coastal plain, South Africa. *In*: BRISTOW, C. S. & JOL, H. M. (eds) *Ground Penetrating Radar in Sediments.* Geological Society, London, Special Publications, **211**, 29–46.

BRISTOW, C. S. 1994. A new look at the Lower Greensand using ground-penetrating radar. *Geology Today,* **10**, 24–27.

BRISTOW, C. 1995a. Internal geometry of ancient tidal bedforms revealed using ground penetrating radar. *In*:

FLEMMING, B. W. & BARTHOLOMA, A. (eds) *Tidal Signatures in Modern and Ancient Sediments*. International Association of Sedimentologists, Special Publication, **24**, 313–328.

BRISTOW, C. 1995*b*. Facies analysis in the Lower Greensand using ground-penetrating radar. *Journal of the Geological Society, London*, **152**, 591–598.

BRISTOW, C., PUGH, J. & GOODALL, T. 1996. Internal structure of aeolian dunes in Abu Dhabi determined using ground-penetrating radar. *Sedimentology*, **43**, 995–1003.

BRISTOW, C. S., CHROSTON, P. N. & BAILEY, S. D. 2000. The structure and development of foredunes on a locally prograding coast: insights from ground-penetrating radar surveys, Norfolk, UK. *Sedimentology*, **47**, 923–944.

BRISTOW, C. S., SKELLY, R. L. & ETHRIDGE, F. G. 1999. Crevasse splays from the rapidly aggrading, sand-bed, braided Niobrara River, Nebraska: effect of base-level rise. *Sedimentology*, **46**, 1029–1047.

BROWN, L. F., JR. & FISHER, W. L. 1980. *Seismic stratigraphic interpretation and petroleum exploration/ geology and geometry of depositional systems*. American Association of Petroleum Geologists, Tulsa, Oklahoma, Continuing Education Course Note Series Number 16.

DANIELS, D. J. 1996. *Surface-Penetrating Radar*. Institute of Electrical Engineers, London, UK.

DANIELS, D. J., GUNTON, D. J. & SCOTT, H. F. 1988. Introduction to subsurface radar. *IEE Proceedings*, **135**(Part F, No. 4), 277–320.

DAVIS, J. L. & ANNAN, A. P. 1989. Ground-penetrating radar for high-resolution mapping of soil and rock stratigraphy. *Geophysical Prospecting*, **37**, 531–551.

DOOLITTLE, J. A. 2002. *Ground-Penetrating Radar Soil Suitability Map of the Conterminous United States*. World Wide Web Address: http://soils.usda.gov/research/results/posters.htm#soil physics

DUKE, S. R. 1990. *Calibration of Ground Penetrating Radar and Calculation of Attenuation and Dielectric Permittivity Versus Depth*. Master of Science Thesis, Colorado School of Mines, Boulder, Colorado.

FISHER, E., MCMECHAN, G. A. & ANNAN, A. P. 1992. Acquisition and processing of wide-aperture ground-penetrating radar data. *Geophysics*, **57**, 495–504.

FISHER, S. C., STEWART, R. R. & JOL, H. M. 1996. Ground penetrating radar (GPR) data enhancement using seismic techniques. *Journal of Environmental and Engineering Geophysics*, **1**, 89–96.

FITZGERALD, D. M., BALDWIN, C. T., IBRAHIM, N. A. & HUMPHRIES, S. M. 1992. Sedimentologic and morphologic evolution of a beach-ridge barrier along an indented coast: Buzzards Bay, Massachusetts. *In*: FLETCHER, C. H., III & WEHMILLER, J. F. (eds) *Quaternary Coasts of the United States: Marine and Lacustrine Systems*. SEPM-IGCP Special Publications, **48**, 65–75.

GALLOWAY, W. E. 1989*a*. Genetic stratigraphic sequences in basin analysis I: architecture and genesis of flooding-surface bounded depositional units. *American Association of Petroleum Geologists Bulletin*, **73**, 125–142.

GALLOWAY, W. E. 1989*b*. Genetic stratigraphic sequences in basin analysis II: application to northwest Gulf of Mexico Cenozoic basin. *American Association of Petroleum Geologists Bulletin*, **73**, 143–154.

GAWTHORPE, R. L., COLLIER, R. E. LL., ALEXANDER, J., LEEDEER, M. & BRIDGE, J. S. 1993. Ground penetrating radar: application to sandbody geometry and heterogeneity studies. *In*: NORTH, C. P. & PROSSER, D. J. (eds) *Characterisation of Fluvial and Aeolian Reservoirs*. Geological Society, London, Special Publications, **73**, 421–432.

HÄNNINEN, P. 1992. *Application of Ground Penetrating Radar and Radio Wave Moisture Probe Technique to Peatland Investigations*. Geological Survey of Finland, Espoo, Finland, Bulletin **361**.

HARDAGE, B. A. 1987. *Seismic Stratigraphy*. Geophysical Press, London, England, Seismic Exploration Series, Volume 9.

HUGGENBERGER, P. 1993. Radar facies: recognition of characteristic braided river structures of the Pleistocene Rhine gravel (NE part of Switzerland). *In*: BEST, J. & BRISTOW, C. S. (eds) *Braided Rivers*. Geological Society, London, Special Publications, **75**, 163–176.

JOL, H. M. 1993. *Ground Penetrating Radar (GPR): A New Geophysical Methodology Used to Investigate the Internal Structure of Sedimentary Deposits (Field Experiments on Lacustrine Deltas)*. Ph.D. Dissertation, University of Calgary, Calgary, Alberta, Canada.

JOL, H. M. 1995. Ground penetrating radar antennae frequencies and transmitter powers compared for penetration depth, resolution and reflection continuity. *Geophysical Prospecting*, **43**, 693–709.

JOL, H. M., MEYERS, R. A., LAWTON, D. C. & SMITH, D. G. 1994. A detailed ground penetrating radar investigation of a coastal barrier spit, Long Beach, Washington, U.S.A. *In*: BELL, R. S. & LEPPER, C. M. (eds) *Proceedings of the Symposium on the Application of Geophysics to Engineering and Environmental Problems (SAGEEP)*. Boston, Massachusetts, March 27–31, **1**, 107–127.

JOL, H. M. & SMITH, D. G. 1991. Ground penetrating radar of northern lacustrine deltas. *Canadian Journal of Earth Sciences*, **28**, 1939–1947.

JUNCK, M. B. & JOL, H. M. 2000. 3-Dimensional investigation of geomorphic environments using ground penetrating radar. *In*: NOON, D. A., STICKLEY, G. F. & LONGSTAFF, D. (eds) *Proceedings of the Eighth International Conference on Ground Penetrating Radar (GPR 2000)*. Gold Coast, Australia, May 23–26, SPIE (The International Society for Optical Engineering), **4084**, 314–318.

KEARY, P. & BROOKS, M. 1991. *An Introduction to Geophysical Exploration*. Blackwell Scientific Publications, Boston, Massachusetts, (2nd Ed.).

KNOLL, M. D. 1996. *A Petrophysical Basis for Ground Penetrating Radar and Very Early Time Electromagnetics: Electrical Properties of Sand-Clay Mixtures*. Ph.D. Dissertation, University of British Columbia, Vancouver, British Columbia, Canada.

LAFLECHE, P. T., TODOESCHUCK, J.P., JENSEN, O.G. & JUDGE, A. S. 1991. Analysis of ground-probing radar data: predictive deconvolution. *Canadian Geotechnical Journal*, **28**, 134–139.

LUTZ, P., GARAMBOIS, S. & PERROUD, H. 2003. Influence of antenna configurations for GPR survey: information from polarization and amplitude versus offset measure-

ments. *In*: BRISTOW, C. S. & JOL, H. M. (eds) *Ground Penetrating Radar in Sediments*. Geological Society, London, Special Publications, **211**, 299–313.

MITCHUM, R. M., JR. 1977. Part eleven: glossary of terms used in seismic stratigraphy. *In*: PAYTON, C. E. (eds) *Seismic Stratigraphy – Applications to Hydrocarbon Exploration*. American Association of Petroleum Geologists, Tulsa, Oklahoma, Memoir **26**, 205–212.

MITCHUM, R. M., JR. & VAIL, P. R. 1977. Part seven: seismic stratigraphic interpretation procedure. *In*: PAYTON, C. E. (ed.) *Seismic Stratigraphy – Applications to Hydrocarbon Exploration*. American Association of Petroleum Geologists, Tulsa, Oklahoma, Memoirs, **26**, 135–143.

MITCHUM, R. M., JR., VAIL, P. R. & SANGREE, J. B. 1977*a*. Part six: stratigraphic interpretation of seismic reflection patterns in depositional sequences. *In*: PAYTON, C. E. (ed.) *Seismic Stratigraphy – Applications to Hydrocarbon Exploration*. American Association of Petroleum Geologists, Tulsa, Oklahoma, Memoirs, **26**, 117–133.

MITCHUM, R. M., JR., VAIL, P. R. & THOMPSON, S., III. 1977*b*. Part two: the depositional sequence as a basic unit for stratigraphic analysis. *In*: PAYTON, C. E. (ed.) *Seismic Stratigraphy – Applications to Hydrocarbon Exploration. American Association of Petroleum Geologists, Tulsa, Oklahoma, Memoirs*, **26**, 53–62.

MOORMAN, B. J. 1990. *Assessing the Ability of Ground Penetrating Radar to Delineate Subsurface Fluvial Lithofacies*. Master of Science Thesis, University of Calgary, Calgary, Alberta, Canada.

MOREY, R. M. 1974. Detection of subsurface cavities by ground penetrating radar. *Proceedings of the Highway Geological Symposium*, **27**, 28–30.

NEAL. A. & ROBERTS, C. L. 2000. Applications of ground penetrating radar (GPR) to sedimentological, geomorphological and geoarchaeological studies in coastal environments. *In*: PYE, K. & Allen, J. R. L. (eds) *Coastal and Estuarine Environments: Sedimentology, Geomorphology and Geoarchaeology*. Geological Society, London, Special Publications, **175**, 139–171.

NEAL. A. & ROBERTS, C. L. 2001. Internal structure of a trough blowout, determined from migrated ground-penetrating radar profiles. *Sedimentology*, **48**, 291–810.

OLHOEFT, G. R. 1984. Applications and limitations of ground penetrating radar. *54th Annual International Meeting and Exposition of the Society of Exploration Geophysicists, December 2–6, Atlanta, Georgia, Expanded Abstracts with Biographies*, 147–148.

OLSSON, O., FALK, L., FORSLUND, L. & SANDBERG, E. 1987. *Crosshole Investigations – Results From Borehole Radar Investigations*. Stripa Project TR 87–11. SKB, Stockholm, Sweden.

PAYTON, C. E. 1977. *Seismic Stratigraphy – Applications to Hydrocarbon Exploration*. American Association of Petroleum Geologists, Tulsa, Oklahoma, Memoirs, **26**.

PRINGLE, J. K., WESTERMAN, A. R., CLARK, J. D., GUEST, J. A., FERGUSON, R. J. & GARDINER, A. R. 2003. The use of vertical radar profiles (VRPs) in GPR surveys of ancient sedimentary strata. *In*: BRISTOW, C. S. & JOL, H. M. (eds) *Ground Penetrating Radar in Sediments*. Geological Society, London, Special Publications, **211**, 225–246.

RAMSAYER, G. R. 1979. Seismic stratigraphy – a funda-

mental exploration tool. *Offshore Technology Conference Proceedings, Paper 3568*, 1859–1867.

ROBERTS, M. C., BRAVARD, J-P. & JOL, H. M. 1997. Radar signatures and structure of an avulsed channel: Rhone River, Aoste, France. *Journal of Quaternary Science*, **12**, 35–42.

ROKSANDIC, M. M. 1978. Seismic facies analysis concepts. *Geophysical Prospecting*, **26**, 383–398.

SANGREE, J. B. & WIDMIER, J. M. 1977. Part nine: seismic interpretation of clastic depositional facies. *In*: PAYTON, C. E. (ed.) *Seismic Stratigraphy – Applications to Hydrocarbon Exploration*. American Association of Petroleum Geologists, Tulsa, Oklahoma, Memoirs, **26**, 165–184.

SANGREE, J. B. & WIDMIER, J. M. 1979. Interpretation of depositional facies from seismic data. *Geophysics*, **44**, 131–160.

SENSORS & SOFTWARE, INC. 1999. *PulseEKKO 100 User's Guide*. Sensors & Software, Incorporated, Technical Manual 25, Mississauga, Ontario.

SHERIFF, R. E. 1980. *Seismic Stratigraphy*. International Human Resources Development Corporation, Boston, Massachusetts.

SHERIFF, R. E. 1982. *Structural Interpretation of Seismic Data*. American Association of Petroleum Geologists, Tulsa, Oklahoma, Education Course Note Series #23.

SHERIFF, R. E. 2002. *Encyclopedic Dictionary of Exploration Geophysics*. Society of Exploration Geophysicists, Tulsa, Oklahoma, Geophysical References Series, **13**.

SHERIFF, R. E. & GELDART, L. P. 1982. *Exploration Seismology Volume 1: History, Theory and Data Acquisition*. Cambridge University Press, New York, New York.

SMITH D. J. & JOL, H. M. 1992. Ground -penetrating radar investigation of a Lake Bonneville delta, Provo level, Brigham City, Utah. *Geology*, **20**, 1083–1086.

SMITH, D. G. & JOL, H. M. 1995. Ground penetrating radar: antennae frequencies and maximum probable depths of penetration in Quaternary sediments. *Journal of Applied Geophysics*, **33**, 93–100.

TOPP, G. C., DAVIS, J. L. & ANNAN, A. P. 1980. Electromagnetic determination of soil water content: Measurements in coaxial transmission lines. *Water Resources Research*, **16**, 574–582.

Ulriksen, C. P. F. 1982. *Application of Impulse Radar to Civil Engineering*. Ph.D. Thesis, Lund, Sweden: Lund University of Technology, (republished by Geophysical Survey Systems Inc., Hudson, Hew Hampshire).

VAN DAM, R. L. & SCHLAGER, W. 2000. Identifying causes of ground-penetrating radar reflections using time-domain reflectometry and sedimentological analyses. *Sedimentology*, **47**, 435–449.

VAN DAM, R. L., SCHLAGER, W., DEKKERS, M.J. & HUISMAN, J. A. 2002*a*. Iron oxides as a cause of GPR reflections. *Geophysics*, **67**, 536–545.

VAN DAM, R. L., VAN DEN BERG, E. H., VAN HETEREN, S., KASSE, C., KENTER, J. A. M. & GROEN, K. 2002*b*. Influence of organic matter in soils on radar-wave reflection: Sedimentological implications. *Journal of Sedimentary Research*, **72**, 341–352.

VAN DAM, R. L., VAN DEN BERG, E. H., SCHAAP, M. G., BROEKMA, L. H. & SCHLAGER, W. 2003. Radar Reflections from Sedimentary Structures in the Vadose

Zone. *In*: BRISTOW, C. S. & JOL, H. M. (eds) *Ground Penetrating Radar in Sediments*. Geological Society, London, Special Publications, **211**, 257–273.

VAN HETEREN, S., FITZGERALD, McKINALY, P. A. & BUYNEVICH, I. V. 1998. Radar facies of paraglacial barrier systems: coastal New England, USA. *Sedimenology*, **45**, 181–200.

VAN OVERMEEREN, R. A. 1994. High speed georadar data acquisition for groundwater exploration in the The Netherlands. *Proceedings of the Fifth International Conference on Ground Penetrating Radar, June 12–16, Kitchener, Ontario*, **3**, 1057–1073.

VAN OVERMEEREN, R. A. 1998. Radar facies of unconsolidated sediments in The Netherlands – a radar stratigraphy interpretation method of hydrogeology. *Journal of Applied Geophysics*, **40**, 1–18.

VAN WAGONER, J. C., JONES, C. R., TAYLOR, D. R., NUMMEDAL, D., JENNETTE, D. C. & RILEY, G. W. 1991. Sequence stratigraphy applications to shelf sandstone reservoirs, outcrop to subsurface examples. *American Association of Petroleum Geologists, Tulsa, Oklahoma, Field Conference, September*, 21–28.

VAN WAGONER, J. C., MITCHUM, R. M., CAMPION, K. M. & RAHMANIAN, V. D. 1990. *Siliciclastic Sequence Stratigraphy in Well Logs, Cores, and Outcrops: Concepts for High-Resolution Correlation of Time and Facies*. American Association of Petroleum Geologists, Tulsa, Oklahoma, Methods in Exploration Series, **7**.

WILGUS, C. K., HASTINGS, B. S., POSAMENTIER, H., VAN WAGONER, J., ROSS, C. A. & KENDALL, C. G. S. C. 1988. *Sea-Level Changes: An Integrated Approach*. Society of Economic Paleontologists and Mineralogists, Special Publications, **42**.

WOODWARD, J., ASHWORTH, P. J., BEST, J. L., SAMBROOK SMITH, G. & SIMPSON, C. J. 2003. The use and application of GPR in sandy fluvial environments: methodological considerations. *In*: BRISTOW, C. S. & JOL, H. M. (eds) *Ground Penetrating Radar in Sediments*. Geological Society, London, Special Publications, **211**, 127–142.

This page intentionally left blank

Evidence for dune reactivation from GPR profiles on the Maputaland coastal plain, South Africa

GREG A. BOTHA[1], CHARLIE S. BRISTOW[2], NAOMI PORAT[3], GEOFF DULLER[4], SIMON J. ARMITAGE[4], HELEN M. ROBERTS[4], BRENDAN M. CLARKE[1], MXOLISI W. KOTA[1] & PHILO SCHOEMAN[1]

[1]Council for Geoscience, KwaZulu-Natal Unit, P.O. Box 900, Pietermaritzburg, 3200, South Africa (e-mail: gabotha@mweb.co.za)

[2]School of Earth Science, Birkbeck, University of London, Malet Street, London, WC1E 7HX, UK

[3]Geological Survey of Israel, 30 Malkhe Israel Street, Jerusalem, Israel

[4]Institute of Geography and Earth Sciences, University of Wales, Aberystwyth, Ceredigion, SY23 3DB, Wales, UK

Abstract: The Maputaland area of northeastern South Africa is characterized by extensive dune-fields which developed during polyphase reworking of regional aeolian cover sand from the Mid-Pleistocene to the Holocene. Extended parabolic dunes, many preserved only as wind-rift trailing limbs, as well as areas of sinuous crested dunes, hummocky dune systems and the high, composite, accretionary coastal barrier dune cordon are the dominant dune forms. There are few natural sections exposing the stratigraphic succession and unequivocal relative age relationships between dune systems are uncommon. A ground penetrating radar (GPR) survey of dunes and representative aeolian sand stratigraphic units was undertaken in order to investigate the internal structure of the different dune forms and identify stratigraphic relationships between buried sedimentary units. The GPR profiles revealed that the trailing limbs of almost all the parabolic dunes that were surveyed comprise stacked sand units, separated by low-angle reflections inter-preted as bounding surfaces, which accumulated through polyphase vertical accretion. Most extended parabolic dunes are aligned north–south and the upper parts of the dunes are charac-terized by inclined reflections in GPR profile interpreted as large-scale sets of cross-stratification with apparent dips toward the west. A hummocky dune revealed cross-stratified aeolian sand superimposed on a truncated dune form and probably formed through deflation of pre-existing dunes. Using 100 MHz and 200 MHz antennae, it is clear that GPR is capable of imaging very fine sedimentary structures and buried erosional surfaces in the homogeneous aeolian sand of Maputaland. At some of the sites investigated, the buried sand units identified were sampled by hand-augering for infrared-stimulated luminescence dating. The age determinations on these samples suggest that vertical accretion of up to 7 m of sand occurred intermittently over variable time scales up to 25 000 years on some parabolic dune limbs during the Late Pleistocene. In some complex dunefields, adjacent dunes were mobilized at different times, suggesting that remobilization was localized. The implications of the complex internal structure and vertical accretion of extended parabolic dunes are discussed in the context of changes in vegetation cover and water table due to seasonal and short-term cyclical climate variations as well as long-term climate change patterns during the last glacial cycle and the Holocene.

The Maputaland region of northern KwaZulu-Natal Province, South Africa, and Maputo Province of southern Mozambique includes the coastal plain lying east of the Lebombo Mountain escarpment between St Lucia Estuary in the south and Maputo Bay in the north (Fig. 1). Despite almost one cen-tury of geological mapping since the initial reports of Anderson (1901, 1904), and geological mapping of the region (Geological Survey 1985a, b), the stratigraphic relationships between the subsurface succession of weathered aeolian sand units and the surficial dune topography are poorly understood.
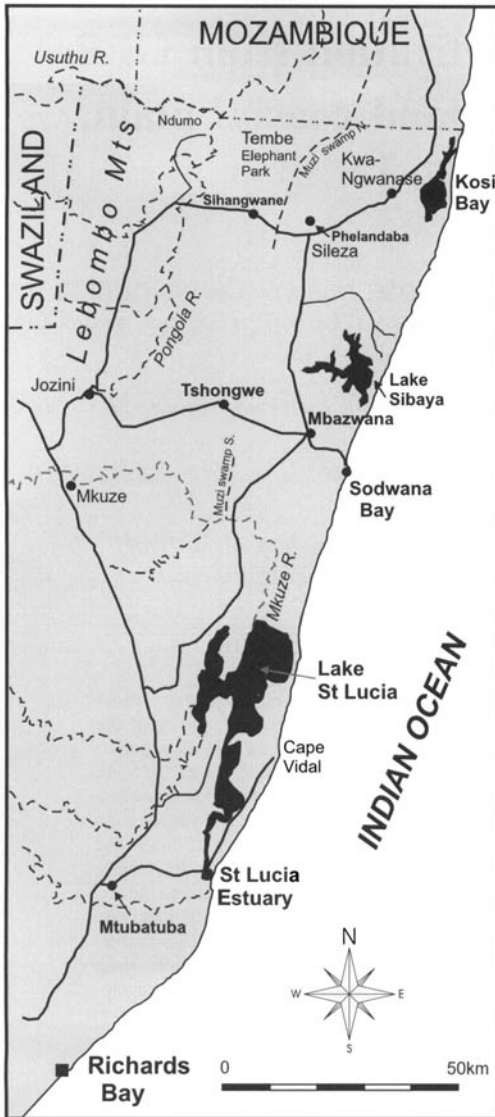
Fig. 1. Locality map showing the towns, main roads and rivers of the southern Maputaland region in northern KwaZulu-Natal province, South Africa. Coastal lakes and estuaries are shaded black.

There are few naturally exposed sections through the stratigraphic succession and the internal structure of compound dunes or relative age relationships between dune systems is poorly constrained. A recent re-evaluation of the regional stratigraphic framework and initial description of the Late Cenozoic Maputaland Group (Botha 1997*a*), updated by the same author in the synthesis by Maud and Botha (2000), has provided a simplified stratigraphic system which recognizes the composite

nature of many aeolian sand bodies or dune forms (Fig. 2).

The critical need to identify buried sand units or dune topography beneath the surface of composite dunes was highlighted by the initial near-surface luminescence dating programme conducted by Botha and Porat (2000), which showed that dunes of widely disparate ages occur within the same dune system. Most samples for luminescence dating were obtained by hand-augering to a depth of 3 m in order to avoid the effects of near-surface bioturbation and shallow reworking. The sand appeared homogenous at the majority of sites and it was not possible to discern possible bounding surfaces or reactivation surfaces between buried sand units. Blind sampling, unconstrained by a knowledge of subsurface stratigraphy, could result in a biased geochronological or palaeoenvironmental interpretation. Identification of buried sand units could facilitate future sequential dating through the dune that would provide a more reliable assessment of the accretion of aeolian sand on composite dunes.

Geophysical techniques, including detailed bathymetry and shallow seismic profiling, have provided significant stratigraphic detail of the aeolian sand succession beneath the coastal lake basins of Lake Sibaya (Miller 1996, 2001) and the Kosi lake system (Wright 1997). These investigations have revealed truncated aeolian sand units and buried palaeotopography which corroborated the marine transgression/regression events of the Late Pleistocene to Holocene sea-level curve derived from the Sodwana Bay continental shelf and littoral zone (Ramsay 1995, 1996). Early unpublished attempts to elucidate the internal structure of coastal plain dunes close to Lake Sibaya using GPR showed that depositional stratification could be discerned in the electrically resistive sands (Craill *et al.* 1993; Du Plessis 1993).

In order to assess the depositional history of dune formation in the relatively homogenous, pedogenically altered dune sands, the use of GPR profiling was identified as the most suitable non-destructive method with resolution capable of determining the fine internal structures of sand dunes. Application of this technique elsewhere has successfully identified the internal structures of complex dunes (Bristow *et al.* 2000*a, b*). The use of high-resolution GPR profiling of representative parabolic, hummocky and sinuous crested dunes across the broad Maputaland coastal plain aimed to determine whether these dune forms are simple or composite features. Future luminescence dating of buried aeolian sand bodies or truncated dunes could then facilitate a more detailed palaeoenvironmental reconstruction of the region.
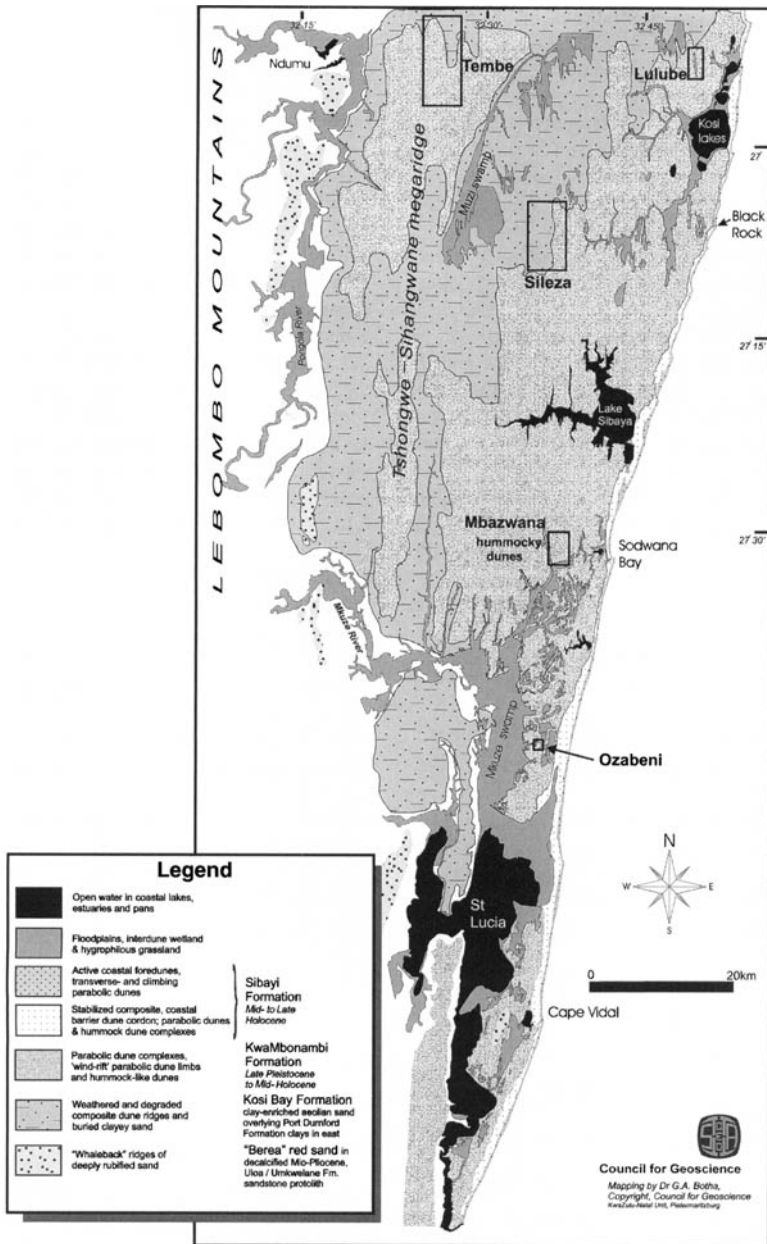
Fig. 2. Geological map showing the distribution of aeolian sand stratigraphic units relative to incised drainage lines linked to coastal water bodies. The positions of sites investigated with GPR transects are shown by blocks. (Dune forms characteristic of the younger aeolian sand stratigraphic units are shown in Fig. 3.)

Geological evolution of the Maputaland coastal plain

The stratigraphy of the Maputaland coastal plain region reflects the onlapping lateral arrangement of littoral and marine regressive facies of different ages, due to the dominant influences of periodic epeirogenic uplift in the Neogene and superimposed sea-level fluctuations throughout the Late Mesozoic and Cenozoic, as reconstructed from the fragmented research summarized by Hobday (1975), Davies (1976), Dingle *et al.* (1983), Par-

tridge and Maud (1987), Watkeys *et al.* (1993), Botha (1997*a*), Maud and Botha (2000) and Wright *et al.* (2000) and depicted here in Fig. 2. Late Jurassic volcanic rocks and a succession of Mid- to Late Cretaceous marine sediments are unconformably overlain by a thin remnant layer of littoral marine and aeolian sediments deposited during the Late Neogene marine regression. These deeply weathered sands are now rubified to form 'Berea' red sand, which forms broad 'whaleback' dunes along the western side of the Pongola and Mkuze River valleys and Lake St Lucia (Fig. 2). Coastal outcrops of Mid- to Late Pleistocene Isipingo Formation calcified dunes and beach deposits and the more widespread, clay-enriched Port Durnford/ Kosi Bay Formations, comprising coastal lake and aeolian sediments, represent events during the penultimate glacial cycle (oxygen isotope stages [OIS] 7 to 5e) and underlie the younger dune cover inland (Botha 1997*a*; Maud & Botha 2000). The last glacial cycle is recorded by widespread aeolian cover sands of the KwaMbonambi Formation dune systems across the coastal plain. The composite, high coastal barrier dune cordon comprising the Sibayi Formation forms a narrow, forested ridge defining the seaward margin of the coastal plain (Figs 2 & 3).

The north–south orientation of inland dunes is oblique to the present coastal wind regime of northerly to northeasterly summer winds and winter system of strengthened southwesterly winds and offshore westerly 'land breezes' (Fig. 3). The orientation and topography of the high coastal barrier dune cordon, the long fetch of coastal lakes and the irregular, vegetated interior dunes influence the wind patterns inland.

Morphology of Maputaland coastal plain and dune systems

Aeolian sand of the Late Neogene to Holocene covers different parts of the coastal plain and is responsible for the distinctive terrain morphological regions of Maputaland (Figs 2 & 3). Many dunes are either 'compound dunes', where the dunes are two or more of the same type, or 'complex dunes', which comprise two or more different dune forms (Tinley 1985; Pye & Tsoar 1990). The inland areas of the Maputaland coastal plain are characterized by a very prominent north–south alignment of highly elongated parabolic dune forms whereas the coastal barrier cordon exhibits shorter parabolic dunes aligned toward the northwest or southwest off the beach and foredunes (Fig. 3). Understanding the long-term evolution of this ancient coastal plain largely depends on a knowledge of the chronological and palaeoenvironmental context of complex dune forms and their morpho-

logical development in response to remobilization or sand accretion.

East of the Pongola River valley a variable layer of reddish brown 'Berea' sand underlies Kosi Bay Formation sand, forming the core of the Tshongwe–Sihangwane composite sand megaridge, which is up to 16 km wide and rises to elevations of up to 143 m a.m.s.l. (above mean sea level) (Figs 2 & 3). The catena of clay-enriched, distinctly mottled soils developed within Kosi Bay Formation dune sands has been truncated and buried over much of the crest of the Tshongwe–Sihangwane megaridge and coastal plain toward the east by KwaMbonambi Formation dunes. On the lower-lying eastern coastal plain, these closely spaced, composite parabolic dune plumes, wind-rift parabolic limbs and hummocky dune systems are separated by expanses of hygrophilous grassland or seasonal wetlands. Interdune slacks and complex dune/wetland systems separated by extended parabolic dunes occur in the headwaters of the Kosi and Sibaya lake catchments. The 'gegenwalle' patterns of low sinuous ridges within seasonal wetlands (Paul 1944) occur at Nkwankwane near Phelandaba in the north, the northern Muzi swamp catchment and the Ozabeni wetlands (Figs 2 & 3).

The complexity of the dune systems in areas close to the drainage catchments of the coastal lakes, including the Kosi system, Sibaya, Mgobezeleni, Bhangazi and St Lucia (Figs 2 & 3), has been enhanced by the combined effects of marine transgression/regression cycles, which influenced the regional groundwater table and fluvial channel incision, and the periodic reworking of the dunes. The KwaMbonambi Formation dunes span the last glacial cycle in this area. The north–south-aligned parabolic dune remnants surrounding estuaries and marine embayments inundated during the Last Interglacial were etched by fluvial incision during the regression preceding the Last Glacial Maximum (LGM) low sea level. The luminescence dating framework described by Botha and Porat (2000) shows that aeolian deflation during the LGM to Mid-Holocene redistributed sand in dune plumes northward from the former lake basins onto the surrounding dune systems. A zone of complex hummocky dunes, degraded parabolic dunes and sinuous to linear dune limb remnants up to 5 km wide occurs immediately inland of the coastal dune cordon between the coastal lakes (Fig. 3). Localized hummocky dune complexes developed inland during the Mid- to Late Holocene when accretion was widespread against the coastal barrier dunes. The high, composite coastal barrier dune cordon comprises at least four generations of dunes comprising the Sibayi Formation, and some of the ascending parabolic dunes reach heights of over 172 m a.m.s.l. in this area. The beach and
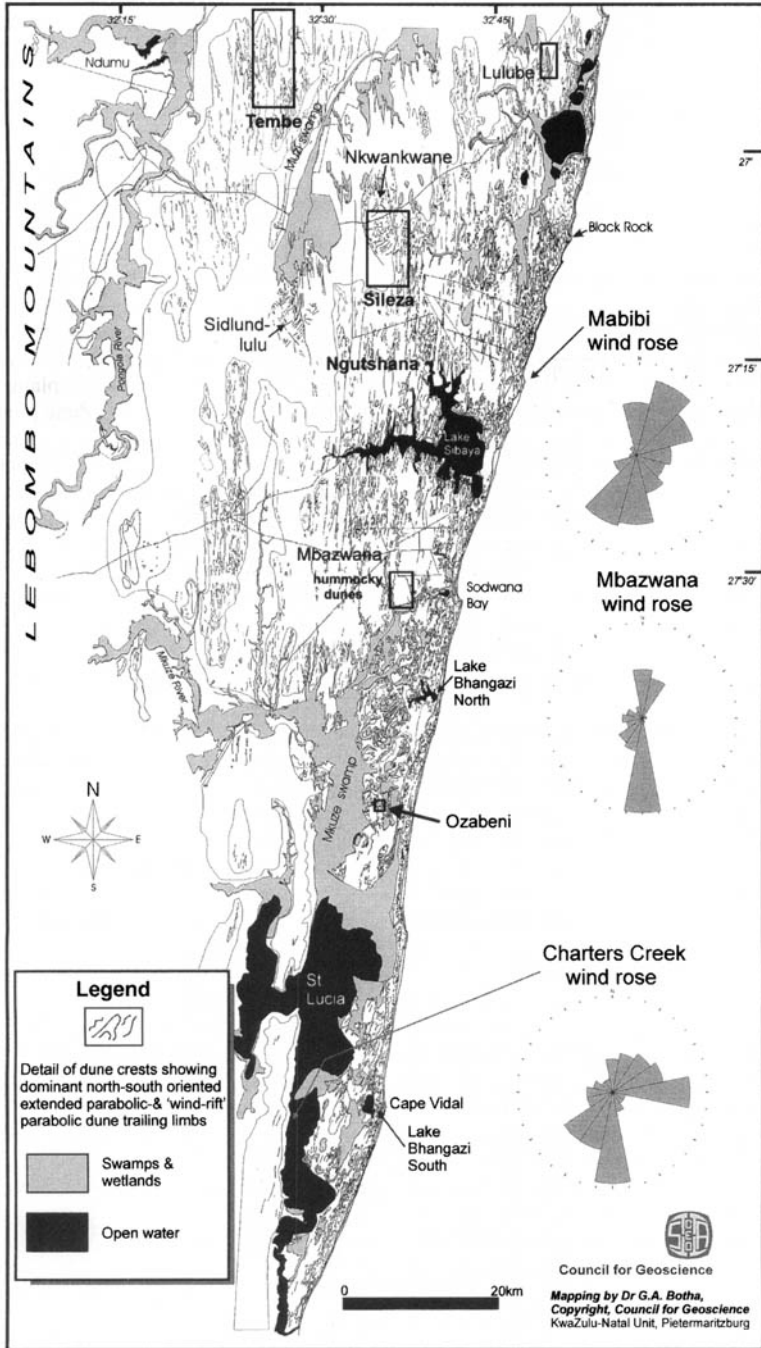
Fig. 3. Dune systems associated with the various aeolian sand stratigraphic units shown using dune crest form lines. Wetlands are shaded grey and open water is shown in black. Many of the dunes are extended or elongated parabolic dunes or remnant 'wind-rift' limbs as well as polygenetic hummocky dune complexes. Note the reduced dune density of degraded dune forms on the older stratigraphic units. GPR study sites described in the text are shown by blocks on map.

foredune complex is remarkably linear, broken only by shallow, low-spiral curve embayments.

The GPR transects were positioned to provide insight into the internal structure of a range of representative dune types forming part of the complex terrain underlain by the diachronous KwaMbonambi Formation aeolian sands. The most widely represented dune form on the inland dune plain or high coastal barrier are vegetated parabolic dunes or the 'wind-rift' degraded remnants of the trailing limbs or arms of elongate or extended, parabolic dunes (Pye 1983, 1993; Pye & Tsoar 1990; Tinley 1985). The extended parabolic dunes are characterized by a range of terminal morphologies and prominent asymmetrical trailing arms or limbs having steep external slopes and gentler internal slopes, which migrate outward at a slower rate (Thompson 1983; Pye & Tsoar 1990; Pye 1993). The concave interdune depression or deflation corridor between the stabilized trailing limbs is commonly a poorly drained flat surface with very low, vermiform sand ridges in this region. The GPR traverse in the northern part of Tembe Elephant Park was over a typical large parabolic dune limb and the site was selected because the framework of luminescence dating in this area suggested long-term sand accretion in the complex parabolic dune-field (Botha & Porat 2000). The Lulube dune is a striking example of an isolated extended dune (Figs 2 & 3). Composite parabolic dunes or degraded dune limbs in the Sileza area can be traced for up to 8 km and many linear dune limb remnants are 2.5–4.5 km in length.

The broad definition of 'hummock dunes' by Pye and Tsoar (1990) is convenient in the context of Maputaland, where it encompasses the complexes of irregular, vegetated sand hills, commonly less than 10 m high and varying from 30 m to 200 m across. Hummock dune forms or hummocky dune topography is most extensive inland of the high coastal barrier dune and, in many areas, these apparently over-steepened dunes, with intervening semicircular interdune hollows, frequently flooded to form perennial wetlands, seem to have formed from localized wind scour and 'blowout' development in stabilized parabolic dune systems. There is a particularly well-developed hummock dune complex southeast of Mbazwana which covers an area of about 8 km², surrounded by complex, irregular parabolic dune limbs (Fig. 3).

GPR traverses across representative dune forms

The internal structures of typical parabolic and hummocky dune forms were characterized using GPR profiling. This non-destructive technique is capable of imaging sedimentary stratification, truncated and buried topography and changes in sediment texture in the low-conductivity sands that dominate the dune systems. The GPR equipment and techniques utilized in this study were based on those employed by Bristow *et al.* (2000*a*, *b*) to profile coastal dunes in England and linear dunes in Namibia. The Sensors & Software Inc.'s pulseEKKO 100 GPR system utilized is designed for deep-sounding geological surveys and the 100 MHz and 200 MHz antennae frequencies were employed during the surveying. Theoretically, the best overall penetration is achieved in dry, sandy sediment with the higher conductivity of moist, saline or clayey substrates and heavy mineral concentrations absorbing or scattering the propagated waves (Bristow *et al.* 2000*b*).

Sites within the complex polyphase dune systems on the Maputaland coastal plain were selected on the basis of the previous aerial photograph interpretation, field investigations and the stratigraphic framework for the Cenozoic deposits in the region defined by Botha (1997*a*, *b*). The field investigations also benefited from an existing framework of provisional luminescence dates which have been summarized by Botha and Porat (2000). The GPR study assisted with the selection of additional luminescence dating sites, but the main focus was to profile good examples of representative dune forms, those with interesting stratigraphic relationships, or to investigate areas where a range of luminescence ages from surficial sands suggested localized reworking/accretion and stratigraphic complexity.

The pulseEKKO 100 GPR control unit and 12 V battery were housed in a modified golf cart for mobility. A laptop computer was attached to the control unit to process the reflection signals. In order to attain an acceptable balance between depth of penetration and detail of reflection signals most traverses were undertaken using the 100 MHz antennae with 1 m spacing and 0.5 m step interval on transects measured along a fibreglass tape. Sites with low relief and potentially fine stratigraphy were surveyed using the 200 MHz antennae, 0.5 m spacing and 0.25 m step size. Common mid-point surveys determined that the velocity of the propagated wave through the dry ground was 0.12 m ns^{-1} and this value was used to convert two-way travel time values to depth. A velocity of 0.06 m ns^{-1} was assumed for saturated sands. The Sensors & Software Inc. software package was used to process the traverse data, adjust parameters for optimum detail, merge adjacent traverses and correct for the topography. Minimal processing was used to retain the integrity of the raw data. Initial processing parameters included automatic gain control (AGC) with gain maximum value 200, trace-to-trace filter 1, down-the-trace filter 1 and

dewowing. A Sokkia Total Station was utilized to survey elevation along the traverse line at 5 m spacing. The profile data was migrated in order to remove possible interference patterns but made little difference to any of the profiles presented here.

Results

Over 4300 m of GPR profile data were collected from 14 sites across the Maputaland coastal plain. The selection of GPR profiles presented here demonstrate the composite internal structure and stratigraphic complexity of polyphase sand accretion on distinctive, representative parabolic and hummocky dunes of the KwaMbonambi Formation across the coastal plain (Figs 2 & 3). The sites described below include a large extended parabolic dune at Lulube near Kosi Bay and the narrow limb of an extended parabolic dune from a closely spaced system in the Sileza Nature Reserve. A linear segment of a degraded dune limb was traversed in the northern part of Tembe Elephant Park. A high hummock dune was traversed within the hummocky dune topography near Mbazwana and a sinuous crested dune, which lies isolated by surrounding wetlands, was profiled at Mosquito Hill, Ozabeni wilderness area, Greater St Lucia Wetland Park.

Lulube extended parabolic dune

The terrain morphology around the Kosi Bay lake system provides useful relative dating evidence that can be used to estimate the age of the dune system (Fig. 4a). On the western margin of the lake system, truncated, Middle to Late Pleistocene Kosi Bay Formation dune sand and wetland deposits underlie the regional KwaMbonambi Formation sands forming north–south-aligned parabolic dunes that are truncated by incised stream valleys, probably in response to lowered base level during the marine regression preceding the LGM. Bathymetric and seismic profiling surveys of the lake floor show that the incised estuary was cut off from the sea by beach-barrier washover fan sediments and subsequently by accretion of ascending parabolic dunes on the high coastal barrier dune cordon during the Early to Mid-Holocene (Wright 1997; Wright et al. 2000). Luminescence dates on dunes south of the Kosi lakes reveal sand mobility toward this area from the south during the latter part of OIS 3 and around the LGM (Botha & Porat 2000).
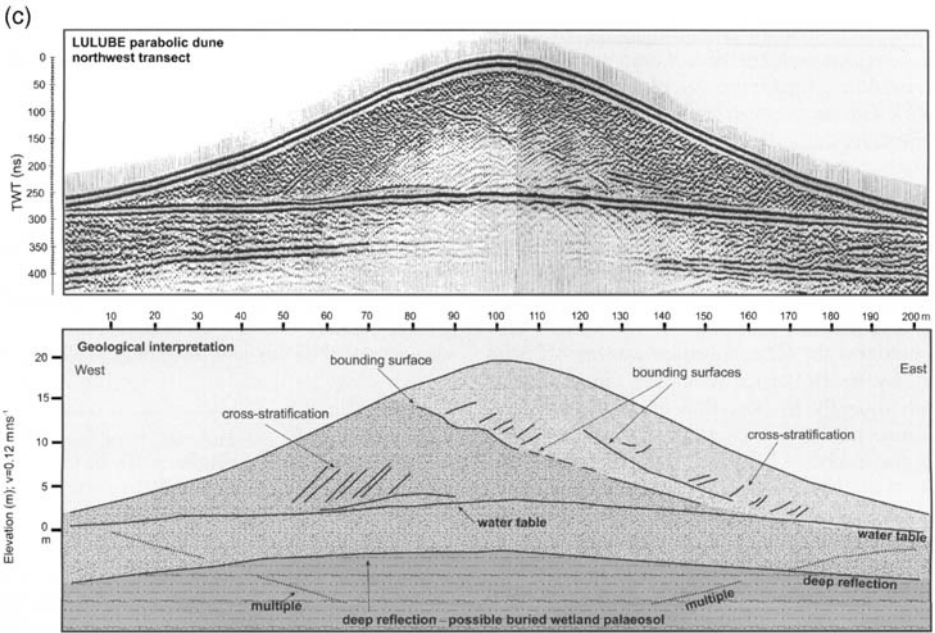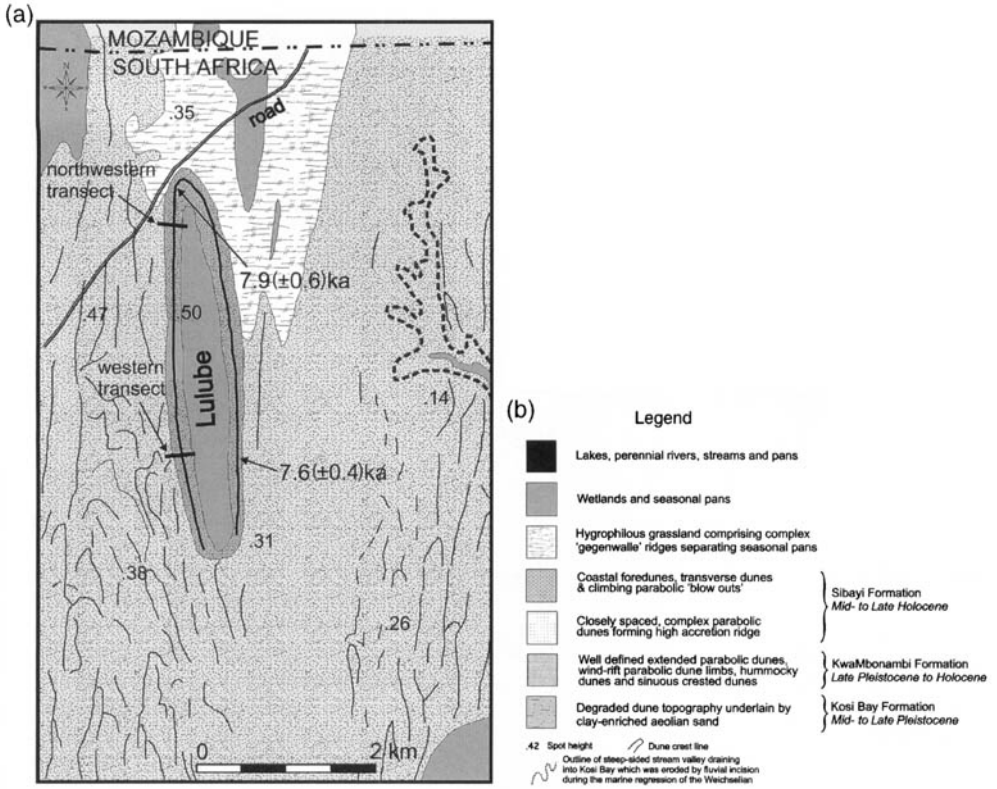
The Lulube extended parabolic dune is situated on an almost flat plain underlain by aeolian sand at 32 m a.m.s.l. in the Mahlungulu area about 5 km north of the Kosi Bay Nature Reserve camp site (Figs 3 & 4a). This extended parabolic dune, aligned on 355° is 4.3 × 0.9 km and rises 18 m
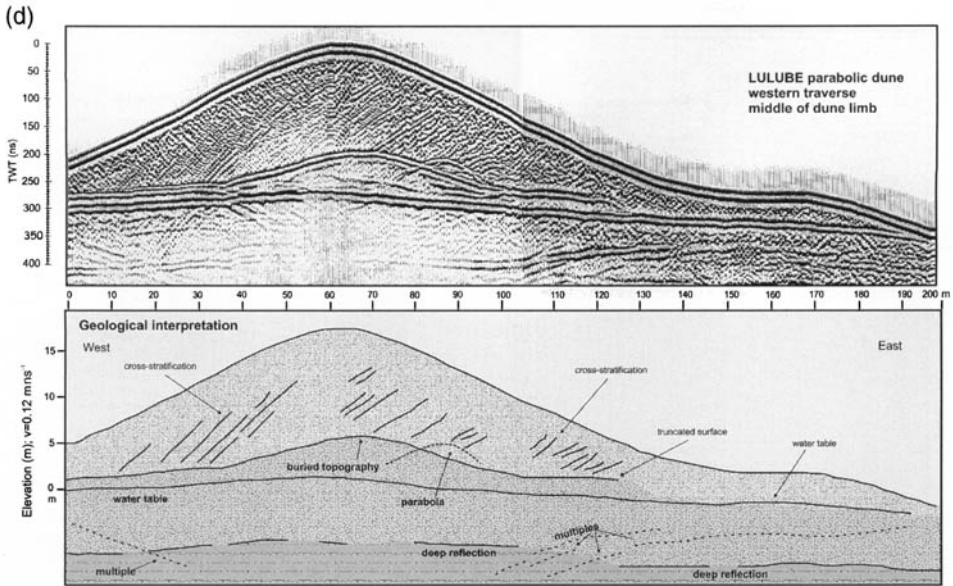
above the surrounding plain at its highest point along its western limb. The surrounding, closely spaced, discontinuous linear dune segments, 300 m to 600 m in length, with a few well-preserved parabolic dunes up to 1.5 km in length, aligned from 340° to 005°, is apparently older than the single large-scale Lulube feature. Preliminary infrared-stimulated luminescence dates show that the nose of the parabolic dune reached its current position in the Early Holocene. A low dune positioned within the apex of the dune nose may be the result of secondary reworking of sand from the seasonal wetland that floods the interlimb trough during wet periods.

A series of four GPR profiles were run across the dune nose and limbs, and the results of 100 MHz traverses over the northwestern and western profiles are presented here (Fig. 4a–d). The water table forms a strong continuous, subhorizontal reflection beneath the dune and dipping reflections beneath the water table are probably multiples of the water table because they mirror the dune topography (Fig. 4c). The northwestern profile (Fig. 4c) shows NW-dipping reflections interpreted as cross-bed foresets and two irregular reflections dipping toward the southeast, which could be bounding surfaces separating accreted sand units. The traverse across the western limb using 100 MHz antennae achieved good signal penetration to 20 m depth and the 200 m-long GPR profile shows that the dune top comprises westward-dipping reflections interpreted as cross-bed sets up to 10 m thick (Fig. 4d). These structures overlie and downlap onto a strong reflection with low relief that has a form roughly symmetrical with that of the dune surface. This surface is sharply truncated at 125 m along the transect, suggesting that the surface could represent buried topography, possibly with a well-developed soil profile.

A shorter traverse (not shown) across the lower eastern limb did not reveal any structures in the ~5 m above the water-table reflection. However, a greater depth of penetration beneath the water table was achieved at this site, revealing stacked sets of

---

Fig. 4. (a) Geology and dune crest form lines in the area surrounding the large extended parabolic dune Lulube near Kosi Bay. The positions of the northwestern and western GPR traverses are shown. The positions of the luminescence dates from 3 m depth on the nose and eastern limb are shown (Porat, pers. comm.). (b) Legend showing the regional stratigraphic units represented on the geological maps in Figs 4a, 5a, 6a, 7a and 8a. (c) GPR profile from a traverse using 100 MHz antennae across the northwestern part of the nose of the prominent extended parabolic dune at Lulube. The geological interpretation shows vertical accretion of stacked, cross-stratified sand units.

(a)

(b) Legend

Lakes, perennial rivers, streams and pans

Wetlands and seasonal pans

Hygrophilous grassland comprising complex 'gegenwalle' ridges separating seasonal pans

Coastal foredunes, transverse dunes & climbing parabolic 'blow outs' } Sibayi Formation *Mid- to Late Holocene*

Closely spaced, complex parabolic dunes forming high accretion ridge

Well defined extended parabolic dunes, wind-rift parabolic dune limbs, hummocky dunes and sinuous crested dunes } KwaMbonambi Formation *Late Pleistocene to Holocene*

Degraded dune topography underlain by clay-enriched aeolian sand } Kosi Bay Formation *Mid- to Late Pleistocene*

.42 Spot height   Dune crest line

Outline of steep-sided stream valley draining into Kosi Bay which was eroded by fluvial incision during the marine regression of the Weichselian

(c)

LULUBE parabolic dune northwest transect

Geological interpretation

West   East

bounding surface   bounding surfaces

cross-stratification   cross-stratification

water table   water table

multiple   deep reflection – possible buried wetland palaeosol   multiple

Fig. 4. (d) GPR profile from the transect across the middle section of the western limb of Lulube parabolic dune. The cross-stratified upper part of the dune buries a reflection which is interpreted as buried topography. TWT, two-way time.

small-scale reflectors dipping toward the east and discontinuous concave reflections interpreted as sets of trough cross-stratification. The strong reflection deep beneath the water table imaged in the other profiles was not present at this site.

The GPR profiles provide evidence of an apparent westerly movement of the western dune limb through accretion of sand on the slipfaces of an active dune, forming large-scale planar sets of cross-stratification in the dune (Fig. 4a, c & d). The arrangement of bounding surfaces indicates upwind stacking of accreting sets of cross-stratification, which is unusual in parabolic dunes. The surface over which the dune advanced displayed low relief. The long extension of the dune points to a southerly prevailing wind that was strong enough to cause vortices capable of transporting sand over the western limb.

Sileza extended parabolic dunefield and gegenwalle wetland

The Sileza Nature Reserve lies southwest of KwaNgwanase town and Lulube dune, close to the settlement of Phelandaba (Fig. 1) and the southern margin of the Nkwankwane 'gegenwalle'/wetland complex (Figs 3 & 5a). The wetland is bounded by a narrow sand ridge with the form of a very broad parabolic dune (Fig. 5a). The striking, closely spaced pattern of low, extended parabolic dune limbs in this area is the northern end of a

wide plume of discontinuous, compound parabolic dunes that extend for over 20 km northward of Lake Sibaya (Fig. 3). The area offered an opportunity to obtain a GPR profile from a typical parabolic dune (Fig. 5a).

The GPR profile shown in Fig. 5b is from the western side of the western limb of the extended parabolic dune investigated at Sileza. Dense sand forest and thicket on the eastern side of the dune limb precluded GPR survey and it was only a cleared pathway through the bush that enabled the 100 MHz GPR traverse of the western side. Despite the 1 m spacing between readings and surrounding trees, the profile is remarkably clear. Three westerly dipping reflections are interpreted as bounding surfaces separating vertically accreted sand units. The upper sand unit at a depth of 3 m was dated at 10.5 ka and, at 6 m depth, beneath a bounding surface, the sand accumulated at 11.5 ka (Porat, pers. comm.).

The undulating land surface to the west of the parabolic dune investigated is characterized by short linear dune limb segments and the eastern margin of the wetland complex is marked by a low linear dune (Figs 5a & c). A GPR traverse was undertaken across the transition from the low dune into the wetland. It ended on a very slight topographic rise that marks the start of the complex array of very low, sinuous gegenwalle ridges that occur within the wetland (Figs 3 & 5a). The dominance of discontinuous subhorizontal reflections
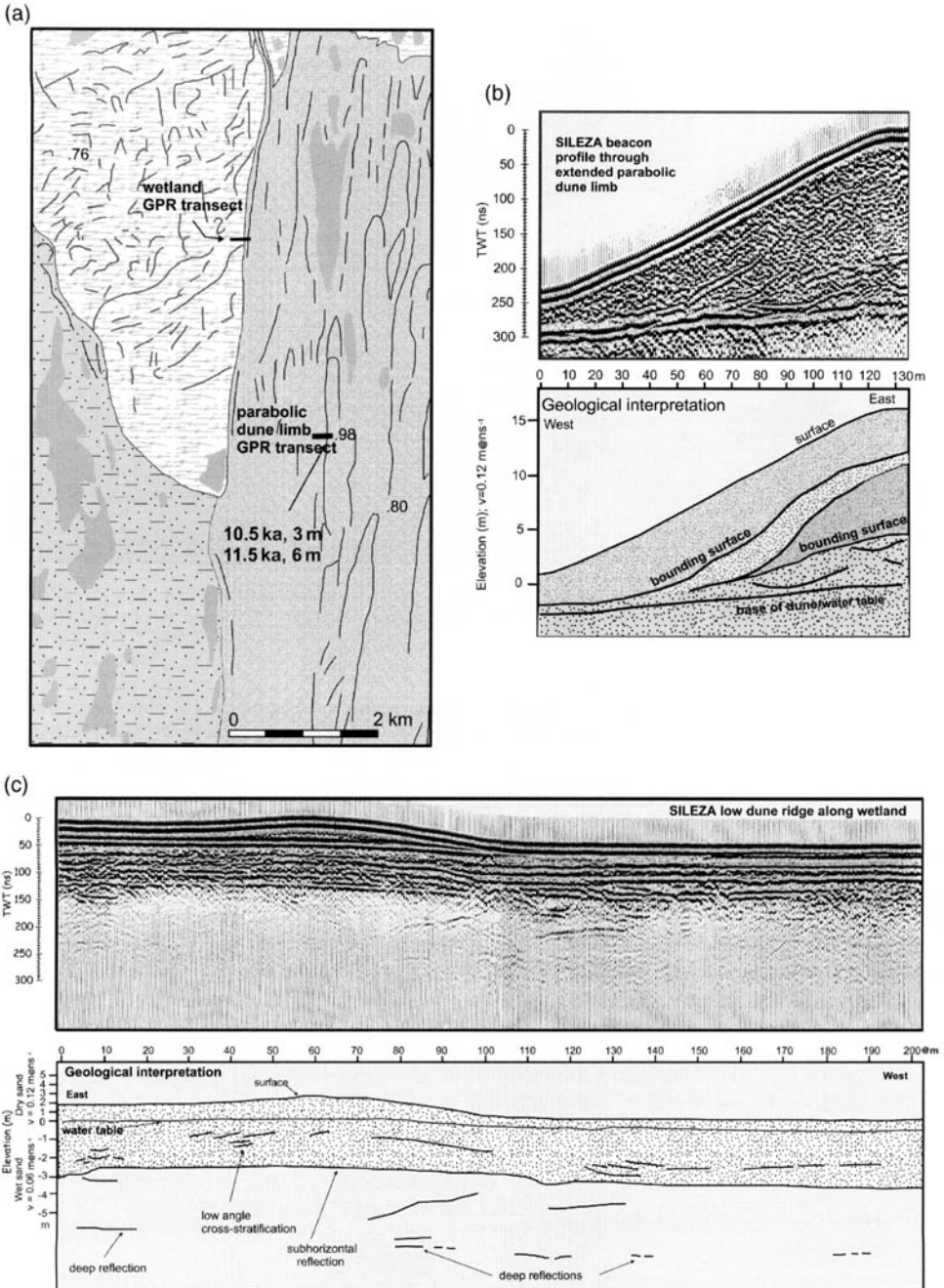
Fig. 5. (a) Geological map of the parabolic dune system in Sileza Nature Reserve close to the southeastern margin of Nkwankwane seasonal wetland. The positions of GPR traverses carried out along the marginal dune defining the edge of the wetland and across the western flank of a high parabolic dune limb are shown. (See Fig. 4*b* for legend.) (b) Profile from a GPR transect using 100 MHz antennae across the western side of the high parabolic dune investigated at Sileza. The geological interpretation indicates vertically accreted sand units separated by bounding surfaces. (c) GPR transect across the margin of the seasonal wetland and low boundary dune. The profile shows discontinuous subhorizontal reflections that represent shallow troughs and thin beds of sand.

with localized low-angle or curved reflectors suggests vertical accretion of thin beds of aeolian sand with localized sets of cross-stratification or irregular reflections which could be deflation hollows (Fig. 5c). No distinct structures can be detected in the low eastern sand ridge. The sand ridge unit is continuous with the surficial strata in the wetland, suggesting that this dune could have been deflated from the wetland or possibly represents a marginal sand deposit related to high water levels.

Tshongwe–Sihangwane megaridge, Tembe Elephant Park

A prominent terrain feature of central Maputaland is the broad Tshongwe–Sihangwane sand megaridge forming the interfluve between the Pongola River valley and the north- and south-draining linear Muzi wetlands (Figs 1, 2 & 3). The ridge extends for about 80 km and is up to 15 km wide, reaching an elevation of 143 m in the north of Tembe Elephant Park near Sihangwane and 134 m a.m.s.l. north of Tshongwe settlement in the south (Figs 3 & 6a). The sand ridge has a composite megaridge form, possibly enhanced by incision of the Pongola River. It was created by weathered Late Neogene to Pleistocene dune sands which were buried beneath a complex pattern of KwaMbonambi Formation discontinuous, extended parabolic dunes, up to 8 km long; wind-rift parabolic dune limbs and hummocky dunes create the surficial topography. The antiquity of the core of the megaridge is exhibited by the advanced pedogenic profile development in clay-enriched and ferruginous soil profiles within Kosi Bay Formation sands exposed on the ridge flanks and hardpan calcrete in the Muzi floodplain, which contrast with the young, quartzose aeolian surficial sands.

GPR profiling of a representative parabolic dune limb using 100 MHz antennae aimed to ascertain whether the pedogenically modified Kosi Bay Formation aeolian sands could be imaged beneath the surficial sand cover. The preliminary framework of luminescence dates from dunes near Sihangwane, and the northern part of Tembe Elephant Park had also revealed a long period of sand accretion within a dune limb and disparate ages from near-surface layers in adjacent dunes. The 10 m vertical profile through an exposed dune west of Sihangwane (Figs 1 & 3) showed that accumulation occurred from 14.6 ka to 8.8 ka (Porat, pers. comm.). At the surveyed transect 14.8 km to the north (Fig. 6a), two adjacent dune ridges, sampled 1.3 km apart, produced ages of 10.8 ka and 23.2 ka respectively. The dune with the younger upper layer was chosen for the GPR survey in order to ascertain whether older sand units occur at depth.

A traverse 180 m long was surveyed from west
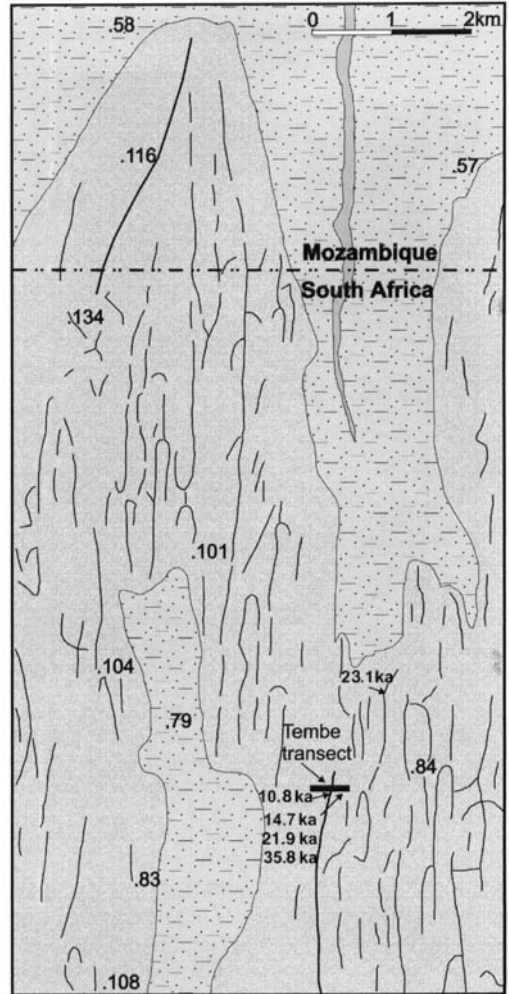
Fig. 6. (a) Geological map showing the dune crest form of parabolic dunes in the northern part of the Tshongwe–Sihangwane megaridge in Tembe Elephant Park. The dunes appear to have over-ridden older clay-enriched strata. The transect was positioned close to the site of a luminescence-dated dune crest to investigate whether older sand units occur buried beneath the young surface layer. The vertical sequence of luminescence-dated sand units identified by the 100 MHz GPR profile are shown in Fig. 6b. (See Fig. 4b for legend.)

to east over the 8 m-high sand ridge (Fig. 6b). A series of three low-angle reflections within the dune, interpreted as bounding surfaces between aeolian sand units, divide the sand into four stratigraphic packages. The lowest surface (1) has a subhorizontal attitude, the subsequent surface (2) dips toward the west and the overlying bounding surface (3) dips to the east at a low angle. The youngest layer contains reflections with an apparent west-
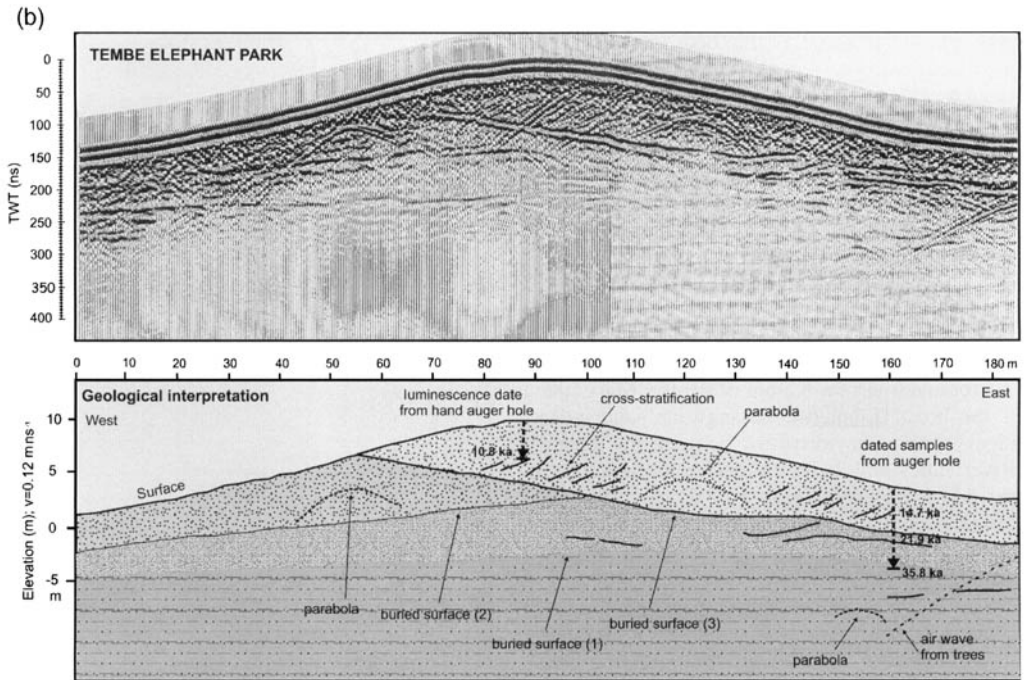
Fig. 6. (b) GPR profile from a 100 MHz transect across a wind-rift parabolic dune limb in the northern part of Tembe Elephant Park. The profile shows a series of deep reflections interpreted as bounding surfaces separating stacked aeolian sand units. The uppermost cross-stratified unit is terminal Pleistocene in age and the older units at depth accumulated over a period of 25 ka (luminescence dates after Porat, pers. comm.).

ward dip, which are interpreted as sets of cross-stratification indicating dune migration in a general westerly direction. The GPR profile indicates that the previously dated sand layer was the youngest stratigraphic unit at a depth of 3 m below the dune crest (100 m position) and represents a period of active dune migration also represented by the Sihangwane road-cutting site to the south (Figs 1 & 2). Further sampling of the eastern side of the dune (160 m mark) to a depth of 6.3 m enabled penetration to a depth representative of the oldest sand unit (1) at the base of the dune. Luminescence dates of 35.8 ka, 21.9 ka and 14.7 ka were obtained (Porat, pers. comm.). The combination of GPR profiling and high-resolution luminescence dating has shown that sand accreted toward the west on the surveyed dune whereas the adjacent dune with older sand near the surface (Fig. 6a) was either stable or accreted a thinner layer of sand during these events.

Mbazwana hummocky dunefield

The settlement of Mbazwana lies southwest of Lake Sibaya about 9 km from the coast at an elev-ation of about 64 m a.m.s.l. (Figs 1, 3 & 7a). This area lies within the dunefield, comprising closely spaced, extended parabolic dunes and wind-rift trailing limbs that are characteristic of the landscape around the incised Sibaya catchment tributary streams. Luminescence dating of isolated parabolic dune complexes on this surface confirmed that some areas were mobile during OIS 2 (Botha & Porat 2000).

The distinctive, complex hummocky dunefield that lies north of the Mbazwana stream headwaters, close to the interfluve between this system and the eastward-draining Mgobezeleni lake catchment, is bounded by a semicontinuous dune ridge that defines a very broad parabolic form (Fig. 7a). The dunefield width tapers from 2.5 km to 1.5 km in the north and extends for 3.8 km north of a broad wetland that lies at about 30 m a.m.s.l. The individual dunes are 5–10 m high and are characterized by short limbs of less than a few hundred metres and many dune forms have branching or coalescing limbs. There is a general NNW–SSE trend of limb orientations. Hummocky dune forms and parabolic blowouts are characteristic of the coastal plain strip immediately inland of the high coastal barrier cor-
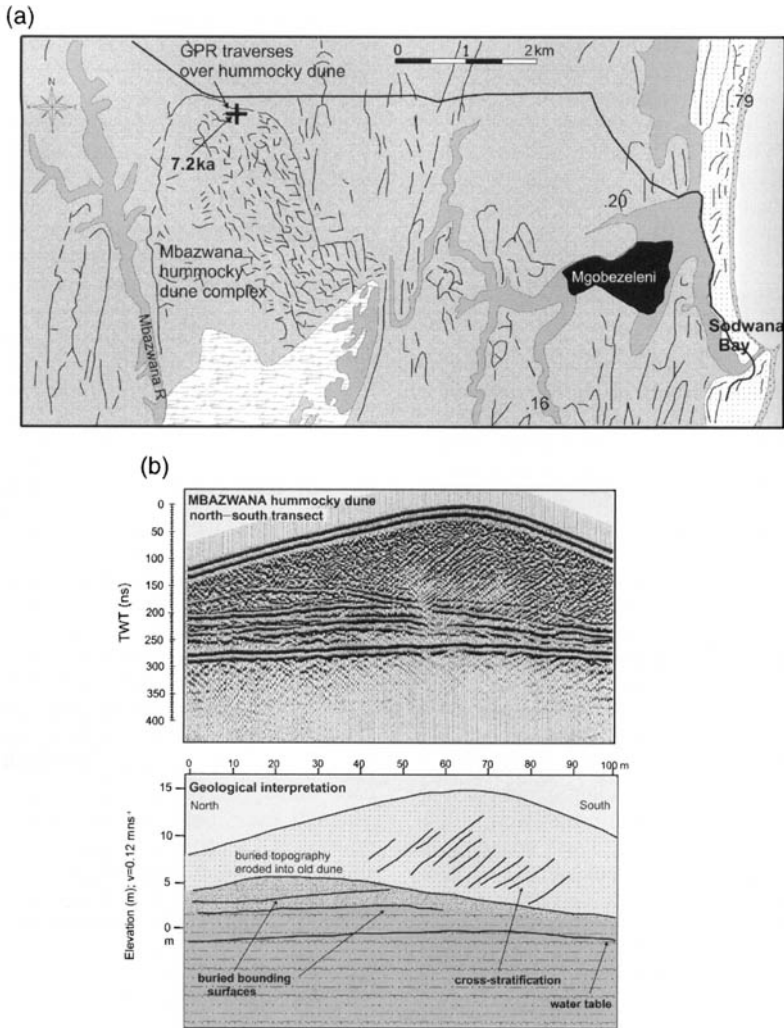
Fig. 7. (a) Geology of the area southeast of Mbazwana showing the hummocky dune complex relative to the incised Mbazwana stream and Lake Mgobezeleni. The position of the luminescence-dated dune in the north where the GPR traverses were carried out are indicated. (See Fig. 4b for legend.) **(b)** North–south-oriented GPR profile through a large hummocky dune form in the hummocky dune complex located southeast of Mbazwana. The direction of sand movement, confirmed by another perpendicular GPR transect, shows the upper cross-stratified sand unit accreted toward the northwest, burying truncated dune topography.

don and, in many areas, it appears as if the dunes are the result of polyphase reworking and disruption of the wind-rift limbs of stabilized parabolic dunes. Luminescence dating of a high dune crest in the north of the dunefield indicated that this dune was stabilized at 7.2 ka (Porat, pers. comm.). The aim of the GPR survey across this particular dune was to determine the internal structure of this typical hummock form and, if possible, to interpret the mode of formation of these enigmatic dune forms.

Two 100 Mhz GPR profiles oriented north–south and west–east (not shown) were collected across a

hummocky dune about 13 m high (Fig. 7b). The north–south profile presented here shows subhorizontal basal reflections truncated by an undulating reflection that defines a low, domed surface which is out of phase with the present dune crest (Fig. 7b). The dune crest is formed of a cross-stratified sand unit defined by reflections with an apparent northerly dip. The profile perpendicular to this traverse (not shown) exhibits reflections dipping toward the west, indicating that the true direction of sand migration was toward the northwestern quadrant, which is consistent with the elongation

of many dune crests in the complex. Both the modern dune surface and the buried hummocky topographies are interpreted as deflationary landscapes formed by erosional modification of pre-existing dunes. Future work is required to elucidate the relationship between the hummocky dunes and the peripheral parabolic dune in order to define whether the dune hummocks represent a later phase of remobilization.

Sinuous crested transverse dune, Ozabeni wilderness area

The dune traversed by GPR lies in the Greater St Lucia Wetland Park, south of the Mbazwana area (Figs 1 & 3). An extensive area of seasonal wetlands lies between the southward-draining Mbazwana stream and the Mkuze River swamps and the composite coastal barrier cordon in the east (Figs 2 & 3). The flat wetlands, sinuous dune forms and pristine grassland of the Ozabeni wilderness area are drained to the east by the incised catchment tributaries of Lake Mgobezeleni and Lake Bhangazi North (Figs 3 & 7a). The distinctive gegenwalle ridge/wetland complexes are surrounded by low, curvilinear dune ridges or sinuous crested transverse dunes on a relatively flat surface (Fig. 8a). Larger sinuous crested transverse dunes, separating wetlands and seasonally inundated hygrophilous grasslands or surrounding ovoid pans, are often broadly convex toward the west. Luminescence dates from the low dunes bounding the wetlands toward the north indicate dune activity during the Early to Mid-Holocene (Botha & Porat 2000). The Mosquito Hill site presented an opportunity to run a GPR profile using the 100 MHz antennae across a prominent dune ridge between an expansive wetland and a flat land surface, which might confirm whether the flat surface continues beneath the dune or whether the core of the dune preserves older dune topography (Fig. 8a).

The GPR profile shows an exceptionally clear image of the internal dune structure with sets of cross-stratification dipping toward the west in the sand above a basal reflection, which is probably the regional water table (Fig. 8b). A low-angle surface dipping to the west within the cross-stratified unit is interpreted as a reactivation surface. The large sets of cross-strata with an apparent westerly dip downlap onto a low-angle reflection dipping gently to the west, which appears to correlate with the low gradient of the land surface that slopes toward the Mkuze swamps in the west. The western footslope of the dune is underlain by a wedge of sand with internal stratification approximating the present dune slope and is interpreted as sheetwash colluvium derived off the former avalanche face. This probably reflects the erosive effects of high rainfall

of this area. Shallow trough-shaped reflections under the surface on the eastern dune slope could indicate some localized aeolian reworking.

On the basis of the GPR profile, two auger holes were drilled (Fig. 8b). A sample was taken from the upper, cross-stratified layer of the dune and a hand-augered hole to a depth of 6 m on the base of the western footslope penetrated strata correlated with the low-gradient land surface to the west. Infrared-stimulated luminescence dates confirm that the buried, flat land surface was stabilized around 17.3 ka, whereas the crest of the overlying dune migrated westward to this position around 6.6 ka (Porat, pers. comm).

Discussion

Development of Maputaland dunefields

Maputaland is characterized by complex dune patterns formed by intact and wind-rift parabolic dune limbs, coalesced parabolic dune limbs, compound 'welded' parabolic dunes or multiple phases of parabolic dune accretion to form large megaridge complexes. The internal structures of typical Maputaland dune forms identified during the GPR survey indicate that many parabolic dune limbs are probably composite features comprising vertically stacked, accreted sand units. Despite a pronounced north–south pattern defined by the alignment of parabolic dune limbs (Fig. 3), the parabolic dunes profiled at Lulube and Tembe exhibited internal structures interpreted as indicating a general westerly sand transport direction over the dune limbs. The Ozabeni sinuous crested transverse dune also migrated toward the west. The typical hummock dune profiles showed buried truncated dune topography and a northwesterly direction of sand movement.

Sand accretion and dune remobilization can be interpreted in the context of the long-term evolution of the dune systems constrained by the preliminary framework of luminescence dates (Botha & Porat 2000) and the dates obtained from the buried sand layers identified during the GPR survey of the sites described. Although palaeoenvironmental evidence from this region is limited to palynological records from dated Holocene peat deposits (Mazus 1997; Grundling *et al.* 1998) and buried wetland diatomite sediments (Maud *et al.* 1997), the longer term development of the dune systems can be assessed relative to the regional terrain morphological and palaeoenvironmental changes during the Mid- to Late Pleistocene and Holocene in response to climatic and base level changes influenced by glacio-eustatic sea-level fluctuations.

The last glacial cycle included the stepwise coo-
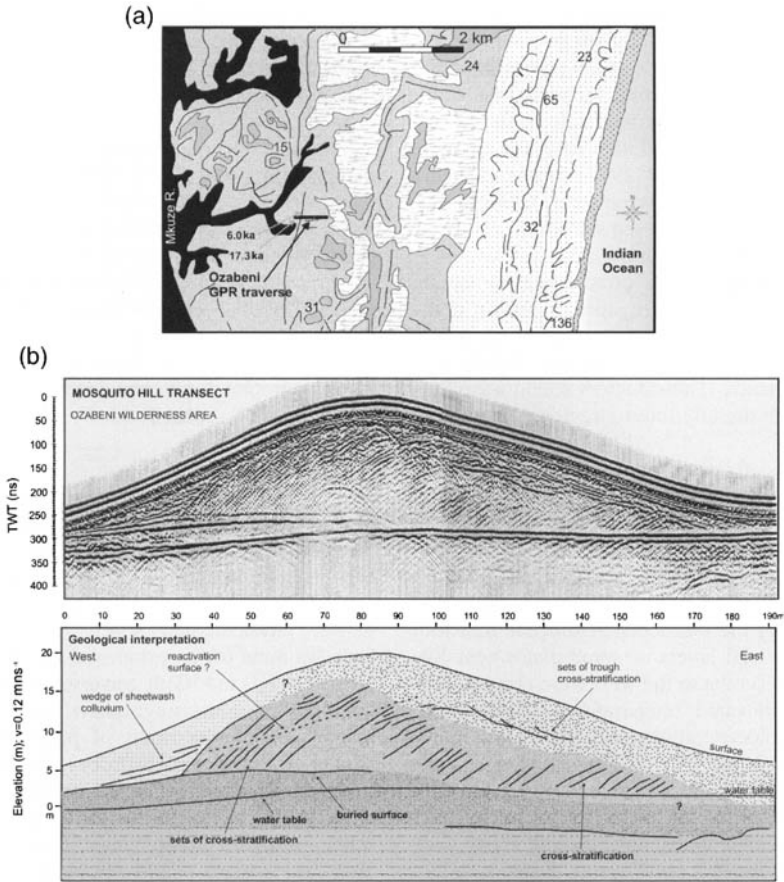
Fig. 8. (a) Geological map showing the position of the GPR transect over the sinuous crested dune at Mosquito Hill, Ozabeni wilderness area, relative to the high coastal barrier dune cordon and the incised tributary of the Mkuze River wetlands. The positions of luminescence dates in the dune crest and the older sand unit beneath the base of the dune are indicated (Porat, pers. comm.). (See Fig. 4*b* for legend.) **(b)** GPR profile and geological interpretation of the sinuous crested transverse dune forming Mosquito Hill, northern St Lucia wetlands. The profile shows vertical accretion of sand units and a strong westward transport component shown by cross-stratification. A wedge of sheetwash redistributed sand buries the base of the dune slipface.

ling and environmental desiccation of the eastern parts of southern Africa during OIS 3 and 2 preceding the LGM (Botha *et al.* 1992; Partridge *et al.* 1992). Around 18 ka BP the marine regression exposed the sandy continental shelf off Maputaland to a depth of about −125 m (Ramsay 1995, 1996; Ramsay & Cooper 2002), resulting in drainage incision to the lowered base level and emergence of the aeolian sand substrate in the catchment basins of coastal water bodies (Wright *et al.* 2000). This incision of drainage networks in the unconsolidated aeolian sand aquifer and long-term drawdown of groundwater tables was probably rapid during the marine regression. The geological and palaeoenvironmental evidence from Maputaland during the Late Pleistocene and Holocene concurs

broadly with the statement by Kocurek *et al.* (2001) that it is 'Widely recognized that the continental aquifer immediately adjacent to the marine body adjusts to sea level'. Kocurek *et al.* (2001) noted that the water table in some aeolian systems is a control on the type and rate of accumulation and defines the depth to which deflation will occur in the formation of regional bounding surfaces. In such 'wet' aeolian systems, water table-controlled deflationary surfaces are created as wind deflation of sand proceeds to the water table or its capillary fringe and is represented by a diagnostic planar surface. The regional behaviour of the water table over time can affect aeolian systems at the basinal scale when vegetation cover in sandy substrate is controlled by falling water-table conditions, with

resultant change from hygrophilous grassland to drier grassland with a woody shrub component or forest during longer periods of lowered water table.

The cessation of diatomite accumulation within Mbazwana area interdune wetlands in the Mkuze River and Mseleni River/Lake Sibaya catchments during OIS 2 (Maud *et al.* 1997) can be attributed to drawdown of the groundwater table due to stream incision to the lowered sea base level. However, the present Lake Sibaya basin is elevated at ~20 m a.m.s.l. behind the coastal barrier and the expansive swamps in the Siyadla catchment draining into the Kosi lakes system are perched, at least locally, above the clay-enriched Kosi Bay Formation aeolian sands. These factors sound a cautionary note when directly linking regional water table to sea level.

The dunes forming the surface of the dry Tshongwe–Sihangwane megaridge accreted sand layers, albeit locally and episodically, during OIS 3 and 2 in the terminal stages of the Pleistocene (~36 ka to 10.8 ka). Sand accreted on parabolic dune limbs at Sileza (11.5–10.5 ka) and Lulube (7.9 ka) during the Pleistocene/Holocene transition when the surficial layers of some dunes near Sihangwane and Tembe to the west were also accumulating. The elevated temperatures and humidity during the Holocene altithermal and a rapid rise in sea level continued into the Mid-Holocene, when sea levels reached elevations close to those of the Eemian high sea-level stands (Ramsay 1995, 1996). It is evident that stabilization of active parabolic dune plumes occurred during the Mid- to Late Holocene, when sustained peat accumulation in interdune wetlands and deflation hollows after ~7 ka (Grundling *et al.* 1998) reflected a rise in regional groundwater-table level. The distinctive dune/wetland complexes, where vegetation-stabilized gegenwalle sand ridges occur within seasonally inundated wetlands (Paul 1944; Pye & Tsoar 1990; Pye 1993), suggest that sand mobilization from interdune troughs or intradune deflation corridors of the common parabolic dune forms on the Maputaland coastal plain was controlled not only by changes in vegetation cover but jointly by seasonally or longer term, cyclically high groundwater levels.

The Ozabeni wilderness area is characterized by very extensive wetlands between the coastal barrier and the Mkuze swamps in the west and is also bounded by the northeastern shallows of St Lucia and the Mgobezeleni catchment, which limit the sand supply area. The westward sand migration of the sinuous crested dune at the Mosquito Hill transect could be interpreted as inland migration of a transgressive coastal barrier parabolic dune complex. However, in this part of the coastal barrier, the cordon is composed of rubified and locally

calcified Mid- to Late Pleistocene sands, which implies that this high terrain form was stable and in existence at the time of the Holocene sand remobilization that resulted from the marine transgression.

The concept of seasonally or cyclically, climatically controlled sand deflation from interdune wetlands or intradune limb depressions and episodic accretion onto existing dune structures is supported by the unusual stacking of sand units on the asymmetrical western limbs of parabolic dunes surveyed. The long-term evolution of the Maputaland coastal plain shows a broad correspondence between the youngest-dated phases of sand mobilization, around 6 ka, and the incidence of peat deposits in interdune wetlands.

Conclusions

The interpretation of the geomorphic evolution of Maputaland during the Late Pleistocene and Holocene is inhibited by the lack of natural sections through the dunes and compounded by poorly preserved physical and stratigraphic relationships between dune forms comprised of variably weathered aeolian sand. GPR traverses were undertaken over dunes comprising quartz sand in order to reveal whether the limbs of parabolic dunes are simple or compound features. The GPR profiles revealed the complex internal structure of representative dune forms and elucidated the stratigraphic relationships in some areas. Large-scale planar cross-bed foresets, shallow troughs, stacked aeolian sand units separated by bounding surfaces and buried dune topography were identified. Several GPR transects across the limbs of the northward-extended parabolic dunes at Lulube and a traverse over a Sileza parabolic dune limb revealed stacked sand units, suggesting polyphase vertical accretion on the western dune limb. The hummock dune form within the hummocky dune complex at Mbazwana displayed a northwesterly sand migration direction from the apparent dips of inclined reflections recorded in perpendicular traverses. Sand transport toward the westerly quadrant was confirmed by foresets preserved within a sinuous crested transverse dune at Ozabeni just inland from the coastal barrier.

The detail provided by the GPR traverses facilitated hand-augering to sample buried sand units at specific depths and the resultant luminescence dates provide valuable chronological control on the periodicity of dune remobilization. Vertical accretion rates on parabolic dune limbs were probably variable but sand movement occurred, probably episodically, over long periods of time, i.e. 25 ka at the Tembe site, as opposed to ~6 ka at the nearby Sihangwane dune and less than 1 ka on the

Sileza dune limb. It is clear that, without luminescence dating, the periodicity of dune remobilization cannot be assessed accurately and that the identification of the internal stratigraphy of dunes using GPR profiles is necessary for precise sampling of the sequence of accreted sand units.

The situation of many parabolic dune systems adjacent to seasonal wetlands or development of temporary lakes within the interlimb corridor suggests that seasonal groundwater fluctuations could have influenced the polyphase reworking of dunes or deflation from ephemeral wetlands with localized accretion on adjacent parabolic dune limbs. The dominant parabolic and hummocky dune forms and vertical accretion of sand units suggest that vegetation stabilization of dune limbs, possibly related to seasonal or longer term, quasi-cyclical fluctuations in precipitation, was one of the dominant controls on dune remobilization. Regional sand movement had ceased by the Mid-Holocene, when peat swamps occupied many interdune wetlands.

The findings of the GPR survey provide critical detail of the internal structure of diverse, complex dune forms which reinforces the interpretation of the polycyclic evolution of the regional dune systems based on dune-form mapping supported by geochronological studies.

References

ANDERSON, W. 1901. *First Report on the Geological Survey of Natal and Zululand.* Surveyor General's Department, P. Davis and Sons, Pietermaritzburg, 138 pp.

ANDERSON, W. 1904. *Second Report on the Geological Survey of Natal and Zululand.* Surveyor General's Department, West, Newman and Co., London, 146 pp.

BOTHA, G. A. 1997a. The Maputaland group: A provisional lithostratigraphy for coastal KwaZulu-Natal. *In:* BOTHA, G. A. (ed.) *Maputaland: Focus on the Quaternary Evolution of the South-East African Coastal Plain, Field Guide and Abstracts.* INQUA Commission on Quaternary Shorelines, Africa Subcommission, 21–26.

BOTHA, G. A. 1997b. Soil development index (SDI): a method for characterising and distinguishing weathered dune sand. *In:* BOTHA, G.A. (ed.) *Maputaland: Focus on the Quaternary Evolution of the South-East African Coastal Plain, Field Guide and Abstracts.* INQUA Commission on Quaternary Shorelines, Africa Subcommission, 88–89.

BOTHA, G. A. & PORAT, N. 2000. Dune system remobilisation on the Maputaland coastal plain, South Africa during the Late Pleistocene and Holocene. *Quaternary International,* **63/64,** 29–30.

BOTHA, G. A., SCOTT, L., VOGEL, J. C. & VON BRUNN, V. 1992. Palaeosols and palaeo-environments during the Late Pleistocene Hypothermal in northern Natal. *South African Journal of Science,* **88,** 508–512.

BRISTOW, C. S., BAILEY, S. D. & LANCASTER, N. 2000a. The sedimentary structure of linear sand dunes. *Nature,* **406,** 56–59.

BRISTOW, C. S., CHROSTON, P. N. & BAILEY, S. D. 2000b. The structure and development of foredunes on a locally prograding coast: insights from ground-penetrating radar surveys, Norfolk, UK. *Sedimentology,* **47,** 923–944.

CRAILL, C., FOURIE, C. J. S. & HAUGER, M. E. 1993. *Lake Sibaya: An Integrated Survey to Evaluate the Penetration and Resolution of the pulseEKKO IV Radar Over a Dune Situated Next to the Lake.* Council for Geoscience, Pretoria, Unpublished Reports, **1993-0126,** 15 pp.

DAVIES, O. 1976. The older coastal dunes in Natal and Zululand and their relation to former shorelines. *Annals of the South African Museum,* **71,** pp. 19–32.

DINGLE, R. V., SIESSER, W. G. & NEWTON, A. R. 1983. *Mesozoic and Tertiary Geology of Southern Africa.* A. A. Balkema, Rotterdam, 375 pp.

DU PLESSIS, A. 1993. *A Ground Penetrating Radar Profile over a Dune at Lake Sibaya,* Natal. Council for Geoscience, Pretoria, Unpublished Reports, **1993-0059,** 5 pp.

GEOLOGICAL SURVEY. 1985a. *2632 Kosibaai, 1:250 000 Geological Series.* Department of Mineral and Energy Affairs, Pretoria.

GEOLOGICAL SURVEY. 1985b. *27½32 St Lucia, 1:250 000 Geological Series.* Department of Mineral and Energy Affairs, Pretoria.

GRUNDLING, P. -L., MAZUS, H. & BAARTMAN, L. 1998. *Peat Resources in the Northern KwaZulu-Natal Wetlands: Maputaland.* Department of Environmental Affairs and Tourism, Pretoria, 102 pp.

HOBDAY, D. K. 1975. Quaternary sedimentation and development of the lagoonal complex, Lake St Lucia, Zululand. *Annals of the South African Museum,* **71,** 93–113.

KOCUREK, G., ROBINSON, N. I. & SHARP, J. M., JR. 2001. The response of the water table in coastal aeolian systems to changes in sea level. *Sedimentary Geology,* **139,** 1–13.

MAUD, R. R. & BOTHA, G. A. 2000. Deposits of the south eastern and southern coasts. *In:* PARTRIDGE, T. C. & MAUD, R. R. (eds) *The Cenozoic of Southern Africa.* Oxford Monographs on Geology and Geophysics, **10,** 19–32.

MAUD, R. R., PARTRIDGE, T. C., ALHONEN, P., DONNER, J. & VOGEL, J. C. 1997. A preliminary assessment of

the environmental conditions represented by the Mbaz-
wana diatomite (Zululand coast). *In*: BOTHA, G. A.
(ed.) *Maputaland: Focus on the Quaternary Evolution
of the South-East African Coastal Plain, Field Guide
and Abstracts.* INQUA Commission on Quaternary
Shorelines, Africa Subcommission, 73–74.

MAZUS, H. 1997. *Pollen Analysis of Some Late Holocene
Peat Deposits from Natal Mire Complex,* Maputaland.
Council for Geoscience, Pretoria, Unpublished Reports,
1997-0087, 8 pp.

MILLER, W. R. 1996. *Sequence Stratigraphy of the Latest
Mesozoic and Cenozoic Sediments Below Lake Sibaya,
Northern KwaZulu-Natal.* Council for Geoscience, Pre-
toria, Unpublished Reports, **1996-0318**, 38 pp.

MILLER, W. R. 2001. *The Bathymetry, Sedimentology and
Seismic Stratigraphy of Lake Sibaya, Northern Kwa-
Zulu-Natal.* Council for Geoscience, Pretoria, Bull-
etins, **131**, 94 pp.

PARTRIDGE, T. C. & MAUD, R. R. 1987. Geomorphic
evolution of southern Africa since the Mesozoic. *South
African Journal of Geology*, **90**, 179–208.

PARTRIDGE, T. C., AVERY, D. M. *ET AL.*. 1992. Late Pleis-
tocene and Holocene climatic change in Southern
Africa. *South African Journal of Science*, **86**, 302–306.

PAUL, K. H. 1944. *Morphologie und Vegetation der Kur-
ischen Nehrung.* Nova Acta Leopoldina, **13/6**, 378 pp.

PYE, K. 1983. Formation and history of Queensland coas-
tal dunes. *Zeitschrift fr Geomorphologie N.F. Suppl.-
Bd.*, **45**, 175–204.

PYE, K. 1993. *Late Quaternary Development of Coastal
Parabolic Megadune Complexes in Northeastern Aus-
tralia.* International Association of Sedimentologists
Special Publications, **16**, 23–44.

PYE, K. & TSOAR, H. 1990. *Aeolian Sand and Sand
Dunes.* Unwin Hyman, London, 396 pp.

RAMSAY, P. J. 1995. 9000 years of sea-level change along
the southern African coastline. *Quaternary Inter-
national*, **31**, 71–75.

RAMSAY, P. J. 1996. *Quaternary Marine Geology of the
Sodwana Bay Continental Shelf, Northern Kwazulu-
Natal.* Council for Geoscience, Pretoria, Bulletins, **117**,
86 pp.

RAMSAY, P. J. & COOPER, J. A. G. (2002) LATE QUAT-
ERNARY SEA-LEVEL CHANGE IN SOUTH AFRICA. *Quat-
ernary Research*, **57**, 82–90.

THOMPSON, C. H. 1983. Development and weathering of
large parabolic dune systems along the subtropical
coast of eastern Australia. *Zeitschrift für Geomorpholo-
gie N.F. Suppl.-Bd.*, **45**, 205–225.

TINLEY, K. L. 1985. *Coastal Dunes of South Africa.*
South African National Scientific Programmes Reports,
CSIR, Pretoria, **109**, 297 pp.

WATKEYS, M. K., MASON, T. R. & GOODMAN, P. S. 1993.
The rôle of geology in the development of Maputaland,
South Africa. *Journal of African Earth Sciences*, **16**,
205–221.

WRIGHT, C. I. 1997. *3.5 kHz Seismic Investigations from
the Kosi Estuary/Lake System, Northern KwaZulu-
Natal.* Council for Geoscience, Pretoria, Unpublished
Reports, **1997-0110**, 17 pp.

WRIGHT, C. I., MILLER, W. R. & COOPER, J. A. G. 2000.
The Late Cenozoic evolution of coastal water bodies
in Northern KwaZulu-Natal, South Africa. *Marine
Geology*, **167**, 207–229.

GPR survey of a Holocene aeolian/fluvial/lacustrine succession, Lauder Sandhills, Manitoba, Canada

K. G. HAVHOLM[1], N. D. BERGSTROM[1], H. M. JOL[2] & G. L. RUNNING IV[2]

[1]Department of Geology/[2]Department of Geography and Anthropology, University of Wisconsin-Eau Claire, Eau Claire, WI 54702–4004, USA (e-mail: havholkg@uwec.edu)

Abstract: A stream cut-bank at Flintstone Hill, Lauder Sandhills, Glacial Lake Hind Basin, southwestern Manitoba, exposes an extensive Holocene sedimentary sequence. Ground penetrating radar (GPR) is used to determine lateral continuity of four major stratigraphic units (wetland complex, Mid-Holocene aeolian dune, sandsheet/fluvial, Late Holocene aeolian dune) and to image primary sedimentary features within the dune strata. Depth of GPR signal penetration is only about 5 m. Signal attenuation is attributed to the presence of primarily pedogenic silts/clays and carbonate- and iron sesquioxide-rich horizons within the sandier units. Nevertheless, the stratigraphic units are shown by GPR, and confirmed by core data, to be laterally continuous within the survey area. Finer-scale dune strata are not well displayed in the aeolian units. Signal attenuation above the Mid-Holocene unit and relatively high iron sesquioxide concentrations within the unit limit imaging of well-preserved dune foreset strata. In the Late Holocene unit, depositional strata are poorly preserved and GPR primarily images soil A-horizons formed on surfaces of temporary stabilization within the dune sediment.

A Holocene sedimentary succession comprising four major units is displayed along several cut-bank exposures of the Souris River in the Lauder Sandhills (Figs 1 & 2). A basal lacustrine/wetland mud and peat unit (unit A) is overlain by an aeolian dune sand unit (unit B). This, in turn, is overlain by a sand and silt fluvial/sand sheet unit (unit C), and the sequence is capped by another aeolian dune sand unit (unit D, Fig. 2a). Pedogenic features include multiple soil A-horizons within unit D and well-developed clay lamellae in units C2 and D. Unit C1 has elevated carbonate content. Locally, unit B has prominent iron and manganese mottles, especially at the top, and is leached of iron or gleyed at the base. Figure 2b illustrates this sedimentary sequence and includes dates on some features within it; sedimentological analysis and radiocarbon and luminescence dating of these units is ongoing (Boyd 2000; Bergstrom et al. 2001, 2002; Running et al. 2001 & unpublished data).

For this study, a ground penetrating radar (GPR) survey was performed at Flintstone Hill, adjacent to one of the cut-bank exposures, in order to determine (1) whether the units exposed in cut-bank profiles can be traced laterally in radar profiles and (2) whether sedimentary structures, particularly dune internal stratigraphy, can be further eluci-

dated. This research is part of a much larger project to determine landscape evolution in, and human interaction with, ecologically diverse localities within the Canadian Plains region (Running et al. 2001; see also website of SCAPE project at http://scape.brandonu.ca).

GPR signals reflect prominently from boundaries between materials with contrasting electrical impedance (Brewster & Annan 1994). In sediments, water content exerts a major control on electrical permittivity, a primary property affecting impedance. Water content is in turn controlled by sediment characteristics such as grain size, organic content and presence of iron oxides, which all affect the amount of pore water retained in a sediment (e.g. van Dam & Schlager 2002; van Dam et al. 2002). Because the four major units of the study sequence alternate between sandy aeolian sediments and units of fluvial and lacustrine origin with elevated silt/clay content, contacts between the contrasting lithologies are expected to generate GPR reflections.

GPR has been used with great success in a number of Holocene aeolian dunes since the early 1990s, when Schenk et al. (1993) published radar images of the internal stratigraphy of an area of the Great Sand Dunes in Colorado, USA. Some more
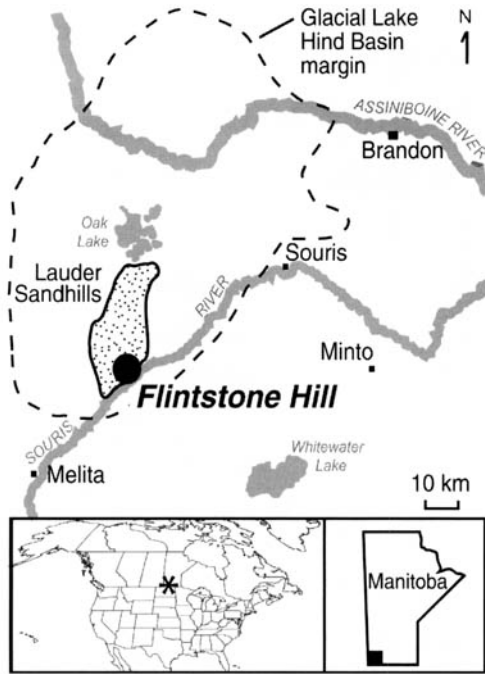
Fig. 1. Location of study site at Flintstone Hill, in the Lauder Sandhills, southwestern Manitoba, Canada.

recent examples include radar images of the internal stratigraphy of Namibian desert linear dunes (Bristow *et al.* 2000) and studies of coastal dune history that show phases of dune activity and dune stabilization in Denmark (Clemmenson *et al.* 1996) and the mid-Atlantic coast of the USA (Jol *et al.* 1998). Clear internal dune stratigraphy is also imaged in densely wooded parabolic dunes in North Carolina and Virginia coastal dunes (Jol & Havholm, unpublished data). Therefore, GPR is expected to delineate dune strata within the aeolian component of the sedimentary succession in the study area.

Setting

Flintstone Hill is in the Lauder Sandhills, a group of dunefields in the southwestern quadrant of the Glacial Lake Hind Basin, approximately 80 km southwest of Brandon, southwestern Manitoba (Fig. 1). The basin was deglaciated between 12 ka and 11 ka BP as Glacial Lake Hind formed and evolved through a series of phases as described by Sun and Teller (1997). Early on, Glacial Lake Hind experienced through-flowing drainage at various times from the north, west and south, and drained eastward to Lake Agassiz via the Pembina, and later also the Assiniboine, spillways (phases 2–4 of Sun and Teller 1997). Glacio-fluvial, -deltaic and -
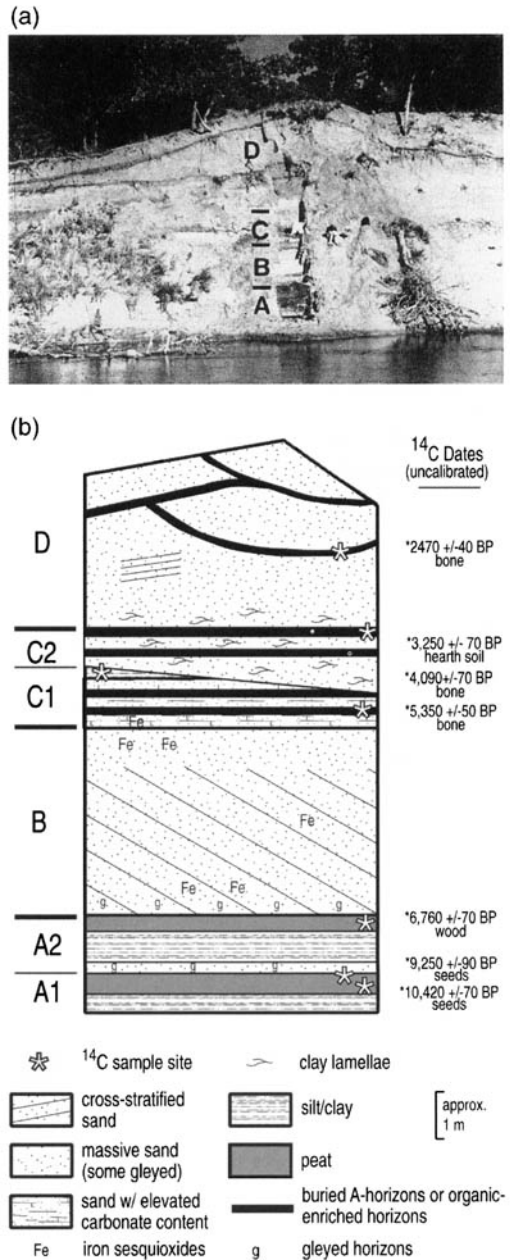
Fig. 2. (a) Profile 2000-3 in the Souris River cut-bank, showing units A–D; height of dune crest above river is about 8 m (see Fig. 3 for location). **(b)** Schematic representation of sedimentary units exposed at Flintstone Hill. Asterisks mark positions of radiocarbon ages listed at right (dates from Boyd 2000 and unpublished data). The explanation also applies to cores and profiles shown in Figure 4.

lacustrine sediments filled the basin. As the spill-way outlets incised, lake level lowered until the basin was drained. Oak Lake and adjacent wetlands are the last remnants of the ancestral glacial meltwater lake.

The sand component of the glaciogenic deposits is reworked by wind into at least 18 small dune-fields that are scattered throughout the basin, cover-ing over 70 km^2 (Oak Lake Dunes, see David 1977). The dunes, like most in the Canadian plains, are parabolic dunes that are currently stabilized and vegetated (David 1977; Pfeiffer & Wolfe 2002). Dune arms in the Lauder Sandhills are oriented WNW–ESE (average orientations for 18 dune clus-ters range from 96° to 134°, Ollendick et al. 2000), with arms nearly parallel to the modern average wind direction (resultant drift direction, Brandon, 126°, Wolfe 2001). Dunes in the small dunefield that includes Flintstone Hill have dune arms 500–2000 m long and up to 10 m high.

Methods

The GPR acquisition system used in the study is a pulseEKKO 100 with a 400 V transmitter and 100 MHz antennae. Step separation is 0.5 m and antennae separation is 1 m. Basic processing used to produce the digital profiles (GPR traverses) includes automatic gain control (AGC), signal satu-ration correction, trace stacking (horizontal averag-ing of 3) and point stacking (running average of 7). A near-surface radar velocity measurement of 0.12 m ns^{-1} is calculated from a common mid-point (CMP) survey at the site and is used to deter-mine signal depth penetration. Topographic map-ping using a laser level allows correction for terrain variability and is tied in to a site survey using a Topcon Total Station and a Trimble ProXRS global positioning system (GPS), calibrated using a local base station for increased precision. Ground truth is provided by both cut-bank exposures and by 4.5 cm diameter cores collected with a Geoprobe system.

Data

Transects imaged run along the crests of parabolic dune arms (transects 1r1 and 1r2) and perpendicu-lar to these (transects 1c1–1c3) in order to provide both information in three dimensions (Fig. 3) and the fullest imaging possible of the uppermost dune unit. Of 500 m of transect length collected, 400 m of representative transect are presented here. The GPR signal penetrated to approximately 5 m depth (Fig. 4a–e), which is shallower than expected given the quartz-rich sand-dominated sedimentary sequence observed at the site. Nevertheless, radar-stratigraphic units correlate to stratigraphic units
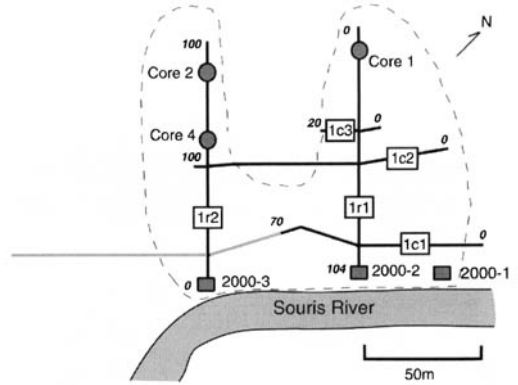

Fig. 3. Details of GPR transect grid at Flintstone Hill. Dashed line indicates approximate shape of component of dune imaged; squares indicate locations of cut-bank profiles; circles indicate geoprobe cores. GPR transects denoted with the letter 'r' run parallel to the dune arms. Transects with the letter 'c' cross the dune arms. Italic-ized numbers indicate positions (in metres) on each tran-sect. Only the black portion of transect 1c1 is shown in this paper.

exposed in outcrop. They can be traced laterally away from the cut-bank exposure and are con-firmed by core data.

A distinctive subhorizontal reflection separates two radar-stratigraphic units, an upper and lower unit, where the lower unit is close enough to the surface to be imaged (e.g. transect 1r2 position 60–100 [Fig. 4b]). The lower unit displays some appar-ent NW-dipping reflections (e.g. transect 1r2 pos-ition 64–70 [Fig. 4b]) and some apparent SE-dipping reflections (e.g. transect 1r2 position 85–94 [Fig. 4b]) that may represent the upper portions of a trough-shaped feature. Dipping strata are also suggested in the unit on transect 1c2 (position 47–90 [Fig. 4e]), where they are interrupted by an irregular subhorizontal reflection (transect 1c2 pos-ition 49–85 [Fig. 4e]). A small part of another prominent reflection at the base of the lower unit is imaged at a depth of 250 ns (transect 1c1 pos-ition 0–4 [Fig. 4c]). However, on a substantial por-tion of the transects, the signal did not penetrate to the base of the lower GPR unit.

The upper unit contains examples of concave-upward reflections up to 20 m wide and 3.5 m deep (e.g. transect 1r2 position 6–26 [Fig. 4b]), as well as concave-downward reflections (e.g. transect 1c2 position 20–37 [Fig. 4e]. Apparent SE-dipping reflections are also present locally, approximately 1.5 m thick (e.g. transect 1r1 position 36–50 [Fig. 4a]).

Transect intersections provide a three-dimensional view locally. The SE-dipping reflec-tions on transect 1r1 downlap onto a bowl-shaped
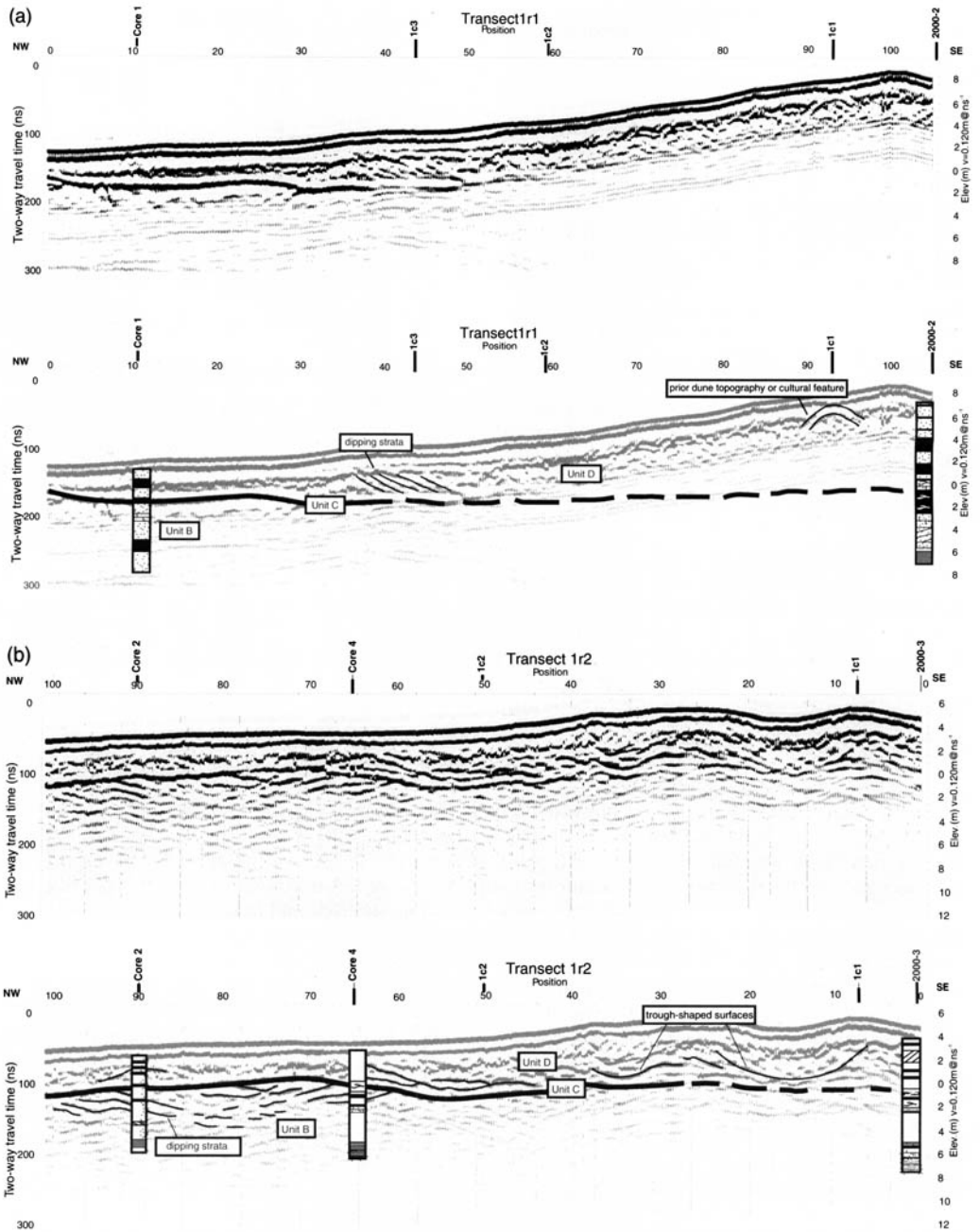
Fig. 4. GPR transects and profile and core data: (**a**) transect 1r1, (**b**) transect 1r2, (**c**) transect 1c1, (**d**) transect 1c3, (**e**) transect 1c2 (see Fig. 3 for locations and Fig. 2 for explanation of symbols for profiles and cores). Positions of intersecting transect lines, profiles and cores are shown across the top of each transect. The upper profile in each is uninterpreted; the lower profile is interpreted. Bold line highlights reflections interpreted as unit C, dashed where projected. Thinner lines indicate reflections interpreted as dune strata, buried relict dune surfaces or iron mineral concentrations. The bold line at about 250 ns on transect 1c1 in (c) marks a reflection inferred to be the top of unit A.
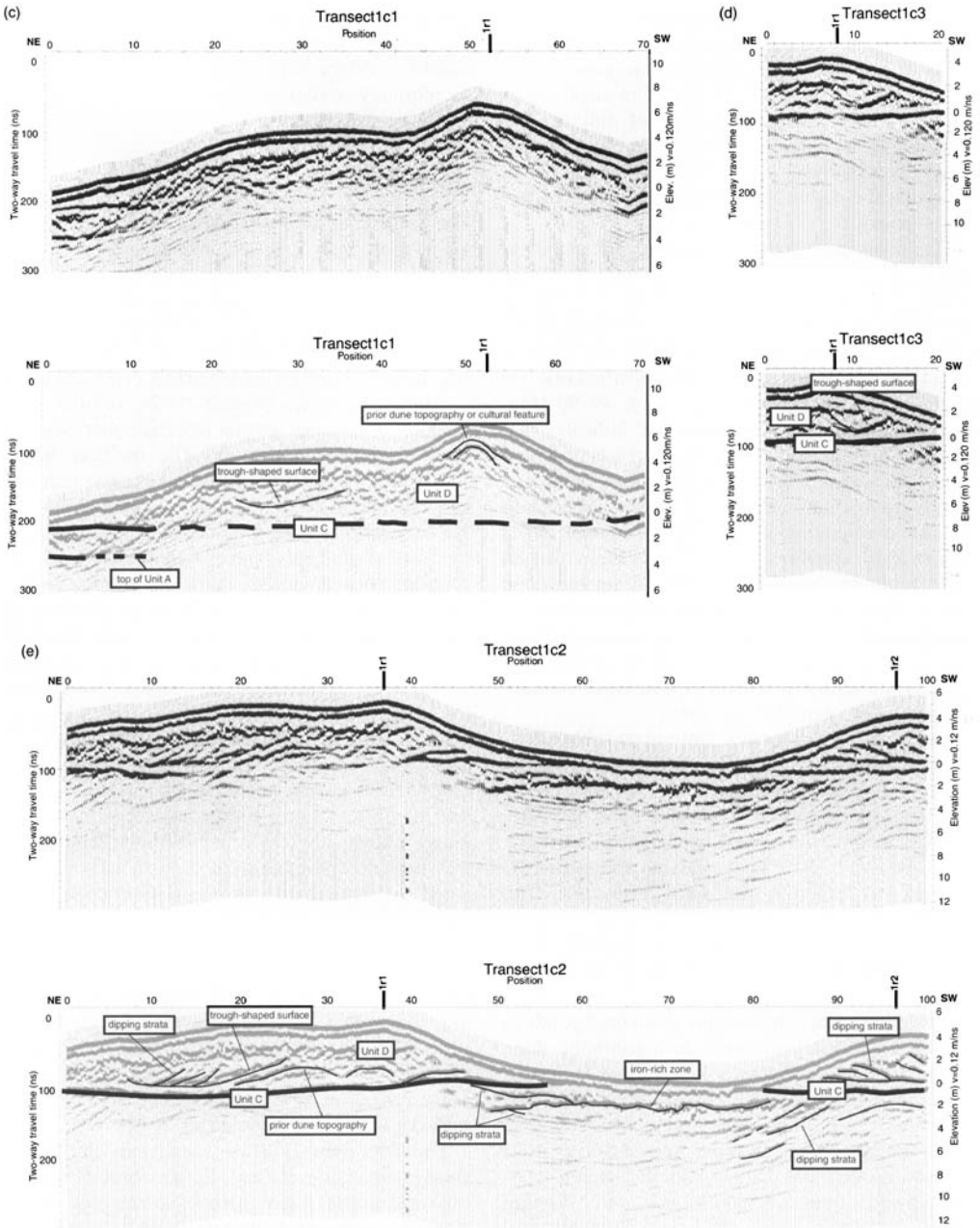
Fig. 4. (c–e) Continued.

feature approximately 5 m wide and 2 m deep at the intersection of transects 1r1 and 1c3. A dome-shaped feature approximately 7 m wide and 3 m deep is imaged at the intersection of transects 1c1 and 1r1.

Interpretation

A comparison of the radar transects to the cut-bank profiles and geoprobe cores indicates that the radar-stratigraphic units correspond to the stratigraphic

units, although radar signal penetration is rarely deep enough to reach the wetland complex strata (unit A). The prominent reflection on transect 1c1, position 0–5, at about 250 ns (3.5 m depth [Fig. 4c]), probably represents the top of unit A. The reflection is not extensive enough nor close enough to any ground-truth points to confirm this interpretation, but the depth and prominence of the reflection supports it.

The lower radar-stratigraphic unit corresponds to unit B, which represents a phase of Mid-Holocene (6760–5350 uncalibrated radiocarbon years before present/RCYBP) dune migration. Although limited radar data are available from the unit, dipping reflections imaged on transect 1r2 (position 60–100 [Fig. 4b]) and transect 1c2 (position 49–90 [Fig. 4e]) suggest troughs. The geometry indicates that eastward-dipping angle-of-repose foresets observed in two dimensions in the cut-bank may belong to trough cross-strata in three dimensions. This would indicate a migrating dune with a sinuous, rather than straight, crestline. Alternatively, these troughs could represent blowout features within the dune strata. The irregular reflection on transect 1c2 (position 49–85 [Fig. 4e]) may represent an irregular bounding surface between sets of dune cross-strata or, more likely, a band of iron oxide staining that cross-cuts dune foreset strata.

The prominent, laterally continuous subhorizontal reflection at 0 m elevation on the depth scale in Figure 4 corresponds to unit C, a sandsheet/fluvial unit deposited between 5350 and 3250 RCYBP. Unit C contains silty and organic-rich horizons that retain moisture and thereby elevate electrical permittivity to generate the GPR reflection. The reflection is imaged in every GPR transect that penetrates to sufficient depth and is confirmed in cores, suggesting that unit C is continuous in the subsurface.

The upper radar-stratigraphic unit corresponds to unit D, a deposit interpreted as a parabolic dune that migrated into the area in the Late Holocene (3250–2470 RCYBP). In most transects, this unit has a thin (~1 m-thick) upper zone with a chaotic reflection pattern that, in some areas, resolves itself downward into more distinct patterns, such as concave-upward, concave-downward and dipping reflections. Bowl-shaped reflections probably represent deflation-scour features with soil A-horizon development, as observed in the cut-bank exposure (Fig. 2). GPR images suggest that, locally, steeply dipping foresets are preserved where sand blew into one of these blowouts, although such strata were not observed in the exposure (see intersection of transects 1r1 and 1c3 [Fig. 4a & d] and transect 1c2 position 10–26 [Fig. 4e]). Concave-down and low-angle dipping reflections may represent other past surfaces of stabilization within the dune unit.

The dome-shaped reflection at the intersection of transects 1r1 and 1c1 (Fig. 4a & c), although steep-sided for a dune surface, appears to indicate dune accretionary stratigraphy; alternatively, it may indicate a buried cultural feature.

Discussion

The limited depth of penetration of the GPR signal, rarely more than 5 m, was unexpected in the dune sand-dominated sedimentary succession at Flintstone Hill. Quartz-rich sand dunes elsewhere have been successfully imaged to depths of 15–20 m (e.g. Jol *et al.* 1998; Bristow *et al.* 2000). Signal attenuation increases as electrical conductivity of a material increases (Annan 1992), and the study succession contains several materials that typically have elevated conductivity. The multiple buried soil A-horizons in unit D and the organic-rich horizons in unit C have a silt/clay content as high as 9% (e.g. Hopkins & Running 2000). Clay lamellae in units C2 and D also have a slightly elevated clay content. Silt/clay-sized particles within coarser sediments have been shown to cause signal attenuation (Jol & Smith 1991; Jol *et al.* 1996). Elevated carbonate content, such as that in unit C1 (up to 5%), also contributes to signal attenuation (Smith & Jol 1992).

GPR imaging of dune internal stratigraphy is only partly successful in this study. In outcrop, the Late Holocene dune sediment (unit D) shows very limited preservation of primary depositional features; a few low-angle wind-ripple laminations were observed in one profile. Stratigraphy is dominated by surfaces of various shapes (concave-up, concave-down, sloping) associated with soil A-horizons. The surfaces represent temporary stabilization during parabolic dune evolution. Reflections of similar shape and scale are observed in the radar images. Elevated levels of organics and silt/clay-sized particles at the surfaces, which provide greater water-retention capacity, probably cause reflection of electromagnetic energy at the surfaces (van Dam & Schlager 2002).

The older (Mid-Holocene) dune unit (unit B) has good preservation of dune slipface foresets in some cut-bank profiles and in parts of some cores. Unfortunately, signal attenuation in overlying sediments provides limited imaging of unit B. Radar transects display only a few dipping strata. A large-scale trough may represent a trough-shaped bounding surface similar to those imaged elsewhere (e.g. Schenk *et al.* 1993; Bristow *et al.* 2000) or possibly a deflation scour. A prominent, irregular subhorizontal reflection near the top of this unit is probably caused by iron/manganese sesquioxides, emplaced post-depositionally, which are typically concentrated near the top and bottom of unit B and

which cross-cut depositional features more commonly than they parallel them. Horizons with elevated iron oxide content have been shown to generate radar reflections because of increased pore-water retention relative to smoother quartz grains (van Dam et al. 2002). Significant attenuation of GPR signal at this reflection suggests that the moist iron-stained sediment has a high conductivity.

Conclusions

A GPR survey of the predominantly aeolian Holocene sedimentary succession at Flintstone Hill allows subsurface imaging of the major stratigraphic units observed in cut-bank exposures. The units are traced laterally away from the exposed sections and further confirmed by core data. Limited depth of signal penetration (~5 m) is attributed primarily to pedogenic silt/clay, carbonate and sesquioxide-rich horizons within the sandy sediment. Despite the limited depth of penetration, GPR provides useful data on the stratigraphy of the area around Flintstone Hill. In areas of low dune relief, unit C and parts of unit B, and even the top of unit A, are imaged. With the collection of more GPR data in dune hollows and areas adjacent to the dunefield, these units may be traced outward from Flintstone Hill further to determine their lateral extent.

Fine-scale depositional features of the dune strata are not as well imaged in this sedimentary sequence as in some other dune studies. In the upper dune unit (unit D), dune strata are poorly preserved in the sediment. In unit D, GPR primarily images the surfaces of temporary stability that developed soil A-horizons before they were buried or eroded. In the lower dune unit (unit B), although dune slipface foresets are well preserved, a combination of signal attenuation and interference by iron-rich horizons that cross-cut stratification limit imaging of primary dune strata. Successful imaging of some dipping and trough-shaped strata suggests that more could be learned about the nature of the dunes that generated this sediment package with further radar imaging in topographically low areas.

References

ANNAN, A. P. 1992. *Ground Penetrating Radar Workshop Notes.* Sensors and Software, Inc., Mississauga, Ontario, 150 pp.

BERGSTROM, N. D., HAVHOLM, K. G. & RUNNING, G. L., IV. 2002. Mid-Holocene dune and sand-sheet environment, Lauder Sandhills, Glacial Lake Hind Basin, southwestern Manitoba, Canada. *Abstracts of the Geological Association of Canada Annual Meeting, 27–29 May, Saskatoon, Saskatchewan,* p. 9.

BERGSTROM, N. D., HAVHOLM, K. G., RUNNING, G. L., IV & JOL, H. M. 2001. Ground penetrating radar investigations of post-glacial stratigraphy, Flintstone Hill Site, southwest Manitoba. *Abstracts of GPR in Sediments Conference, 20–21 August 2001, London,* p. 9.

BOYD, M. 2000. Changing physical and ecological landscapes in southwestern Manitoba in relation to Folsom (11,000–10,000 BP) and McKean (4000–3000 BP) site distributions. *In:* RADENBAUGH, T. A. & DOUAUD, P. (eds) *Changing Prairie Landscapes.* Canadian Plains Research Center, Regina, Saskatchewan, 21–38.

BREWSTER, M. L. & ANNAN, A. P. 1994. Ground penetrating radar monitoring of a controlled DNAPL release: 200 MHz radar. *Geophysics,* **59,** 1211–1221.

BRISTOW, C. S., BAILEY, S. D. & LANCASTER, N. 2000. The sedimentary structure of linear sand dunes. *Nature,* **406,** 56–59.

CLEMMENSEN, L. B., ANDREASEN, F., NIELSEN, S. T. & STEN, E. 1996. The Late Holocene coastal dunefield at Vejers, Denmark: characteristics, sand budget and depositional dynamics. *Geomorphology,* **17,** 79–98.

DAVID, P. P. 1977. *Sand Dune Occurrences of Canada.* Department of Indian and Northern Affairs, National Parks Branch, Ottawa, Contract No. 74–230.

HOPKINS, D. G. & RUNNING, G. L., IV. 2000. Soils, dunes and prairie vegetation: lessons from the Sandhills of North Dakota. *In:* RADENBAUGH, T. A. & DOUAUD, P. (eds) *Changing Prairie Landscapes.* Canadian Plains Research Center, Regina, Saskatchewan, 31–57.

JOL, H. M. & SMITH, D. G. 1991. Ground penetrating radar of northern lacustrine deltas. *Canadian Journal of Earth Sciences,* **28,** 1939–1947.

JOL, H. M., VANDERBURGH, S. & HAVHOLM, K. G. 1998. GPR studies of coastal aeolian (foredune and crescentic) environments: examples from Oregon and North Carolina, USA. *Proceedings of the Seventh International Conference on Ground Penetrating Radar, 27–30 May, University of Kansas, Lawrence, Kansas,* **2,** 681–686.

JOL, H. M., SMITH, D. G., MEYERS, R. A. & LAWTON, D. C. 1996. Ground penetrating radar: high resolution stratigraphic analysis of coastal and fluvial environments. *In:* PACT, J. A., SHERIFF, R. E. & PERKINS, B.

F. (eds) *Stratigraphic Analysis Using Advanced Geophysical, Wireline and Borehole Technology for Petroleum Exploration and Production*. Gulf Coast Section Society of Economic Paleontologists and Mineralogists Foundation 17th Annual Research Conference, 153–163.

OLLENDICK, C. M., LONG, K. A., LAHNER, J. T. & RUNNING, G. L., IV. 2001. Parabolic dunes and agricultural land use: Glacial Lake Hind Basin, southwestern Manitoba. *Association of American Geographers Abstracts Volume, 97th Annual Meeting*, 711–712.

PFEIFFER, Z. K. & WOLFE, S. A. 2002. *Sand Dune Orientations in the Prairie Provinces of Canada*. Geological Survey of Canada Open Files, **4117**. [CD-ROM]

RUNNING, G. L., IV, HAVHOLM, K. G. ET AL. 2001. Postglacial geomorphology, stratigraphy, and paleoenvironmental history at Flint Stone Hill, Oak Lake Sandhills, southwestern Manitoba. *Association of American Geographers Abstracts Volume, 97th Annual Meeting*, 819–820.

SCHENK, C. J., GAUTIER, D. L., OLHOEFT, G. R & LUCIUS, J. E. 1993. Internal structure of an aeolian dune using ground penetrating radar. *In*: PYE, K. & LANCASTER, N. (eds) *Aeolian Sediments, Ancient and Modern*. International Association of Sedimentologists Special Publications, **16**, 61–69.

SMITH, D. G. & JOL, H. M. 1992. Ground penetrating radar investigation of a Lake Bonneville delta, Provo level, Brigham City, Utah. *Geology*, 20, 1083–1086.

SUN, C. S. & TELLER, J. T. 1997. Reconstruction of Glacial Lake Hind in southwestern Manitoba, Canada. *Journal of Paleolimnology*, **17**, 9–21.

VAN DAM, R. L. & SCHLAGER, W. 2002. Identifying causes of ground penetrating radar reflections using time-domain reflectometry and sedimentological analyses. *Sedimentology*, **47**, 435–449.

VAN DAM, R. L., SCHLAGER, W., DEKKERS, M. J. & HUISMAN, J. A. 2002. Iron oxides as a cause of GPR reflections. *Geophysics*, **67**. [In press]

WOLFE, S. A. 2001. *Potential Sediment Transport by Wind in the Prairie Provinces. Natural Resources Canada*. World Wide Web Address: http://sts.gsc.nrcan.gc.ca/clf/

A GPR study of sedimentary structures within a transgressive coastal barrier along the Danish North Sea coast

INGELISE MØLLER[1] & DENNIS ANTHONY[1,2]

[1]*Geological Survey of Denmark and Greenland, Øster Voldgade 10, DK-1350 Copenhagen K, Denmark (e-mail: ilm@geus.dk)*
[2]*Present address: Royal Danish Administration of Navigation and Hydrography, Overgaden over Vandet 62B, DK–1023 Copenhagen K, Denmark (e-mail: dea@fomfrv.dk)*

Abstract: The Danish North Sea coast is characterized by the presence of coastal barrier systems. One of these systems, the Holmsland Barrier, is a transgressive wave-dominated barrier. For the purpose of studying large-scale architecture in a transgressive barrier, as well as small-scale sedimentary structures, a ground penetrating radar (GPR) field experiment has been carried out. The study focuses on the identification of high-amplitude reflections of the large-scale architecture of the barrier and the recognition of small-scale structures for interpretation of coastal processes. The observed radar facies fall into two groups, both interpreted as storm washover deposits. One group, dominated by parallel to subparallel reflection, is related to the seaward horizontal stratification in the washover fans. The other group, dominated by sigmoid and oblique clinoforms, is related to delta foreset stratification, indicating that the washover fans are terminated in standing water. The observations derived from the GPR study of the Holmsland Barrier suggest that this transgressive barrier is composed almost entirely of washover deposits with local small amounts of aeolian deposits. This study has shown that the GPR method is outstanding in mapping both large-scale architecture and small-scale internal structures in a coastal barrier.

Coastal barriers are typical morphological features of dynamic coasts. Many different types exist and the types of individual barriers at different locations are primarily related to the interplay between sea-level change, wave energy, tidal range, sediment flux, geology and 'initial' morphology. The most common type of coastal barrier, however, is the transgressive barrier, characterized by a general landward retreat (e.g. Davis, 1994).

Different barrier types are generally assumed to contain sedimentary structures that reflect their origin. Internal structures of present transgressive barrier coasts have traditionally been studied from vibrocores and open transects in the unsaturated zone. In recent years, ground penetrating radar (GPR) has proved to be a successful tool for studying sedimentary structures in a variety of depositional environments, such as fluvial environments (e.g. Beres *et al.* 1999; Vandenberghe & Overmeeren 1999), aeolian environments (e.g. Bristow *et al.* 2000) and in barriers (Smith & Jol 1992; Jol *et al.* 1996). The GPR method has the advantage of producing continuous high-resolution images of internal sedimentary structures in a non-destructive, time- and cost-effective way.

The objective of the present study was to describe and analyse the internal sedimentary structures in a transgressive barrier coast and, from these, to obtain an understanding of the processes forming the barrier. A GPR study was therefore carried out on the Holmsland Barrier, a highly dynamic, wave-dominated, transgressive coastal barrier along the central part of the Danish North Sea coast (Fig. 1).

Geomorphological and geological settings

The study area is on the northern part of the 30 km-long and 2 km-wide Holmsland Barrier along the Danish North Sea coast (Fig. 1). The barrier is wave-dominated and the tidal range is between 0.5 m and 0.8 m, but wind stress during severe storms can add more than 2 m of set-up to the sea level; this normally occurs several times each winter. The inlet between the North Sea and the lagoon
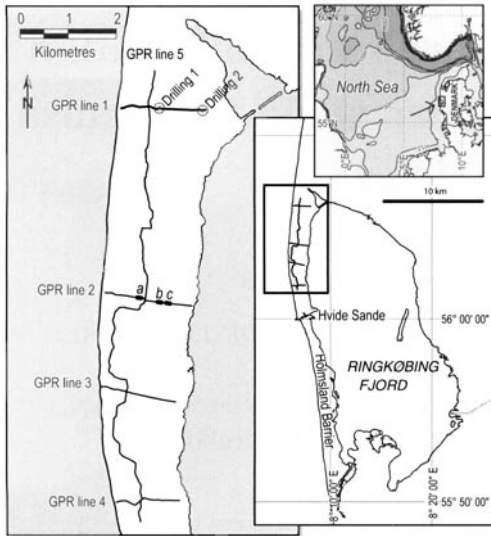
Fig. 1. Location map of the Holmsland Barrier along the Danish North Sea coast, showing GPR lines 1–5. (For GPR line 1 see Fig. 2; for sections of GPR line 2, located at 'a', 'b' and 'c', see Figs 3, 4 & 5 respectively.)

(Ringkøbing Fjord) is situated at Hvide Sande (Fig. 1) and is controlled by a sluice lock.

The study area was glaciated several times during the Quaternary. The last glaciation did not reach the area and its terminal moraine is located approximately 50 km north and 80 km east of the study area. The geomorphology of the area, however, is strongly influenced by sediments from earlier glaciations. It was assumed that the area has not experienced Holocene sea levels higher than those at present (Krog 1979), although a number of sea-level fluctuations close to the present level have probably occurred (Mörner 1976).

Along the major part of the North Sea coast, including the study area, the coast is replenished by the Danish Coastal Authorities in order to prevent an otherwise natural coastal retreat of the barrier (Kystinspektoratet 1998). Prior to the coastal replenishment programme, old back-barrier marsh deposits were locally observed on the North Sea foreshore as a consequence of the landward migration of the barrier (Andersen 1963). The present net longshore littoral transport is southward (Laustrup *et al.* 2000).

GRP experiment

The GPR method images sedimentary structures in the ground that are related to changes in dielectric properties. The GPR method operates by transmitting a very short electromagnetic pulse into the ground using an antenna. Abrupt changes in dielec-

tric properties cause some of the electromagnetic energy to be reflected back to the ground surface, where it is recorded and amplified by a receiving antenna. The recorded signal is registered as amplitude and polarity versus two-way travel time. The signal is processed and displayed as a GPR profile, in which the vertical axis is expressed as two-way travel time in nanoseconds (ns) and the horizontal axis is a distance axis along the measured survey line in the field. The vertical axis can be converted to depth or elevation if the radar-wave velocity in the penetrated material is determined. A detailed description of the GPR method can be found in, e.g., Davis and Annan (1989).

Survey details

GPR data were collected along four east–west-oriented 1.4–1.9 km lines and a 10 km mainly north–south-oriented line. The east–west-oriented GPR lines 1–4 run across the Holmsland Barrier from the beach at the North Sea coast over the fore-dunes toward the lagoon behind the barrier (Fig. 1). The north–south-oriented GPR line 5 crosses the east–west-oriented GPR lines (Fig. 1). The GPR lines are partly located on footpaths in the vegetated dunefield and back-barrier area as well as on gravel roads in an area with summer residences.

The GPR data were collected in step moode with a Sensors and Software Inc. pulseEKKO 100 system equipped with a 400 V transmitter and 100 MHz antennae. The data were sampled with a step size of 0.5 m and a 1 m antenna spacing.

Data processing

Standard processing included dewowing and a three-point time filtering, as well as scaling using automatic gain control (AGC). An AGC time window of one or four pulse-widths was used. AGC with a time window of four pulse-widths enhances relatively strong reflections, whereas an AGC with a time window of one pulse-width amplifies all reflections equally. The latter gain is used when low-amplitude reflections from internal structures need to be studied.

Topographic correction based on cartographic information was applied to all profiles.

Velocity determination by borehole log correlation

Two auger drillings with liner are located on the GPR profile 1 at Drilling 1 (at station 833 m) and Drilling 2 (at station 1696 m) (Figs 1 & 2). Drilling 1 goes through well-sorted, medium-grained sand to a depth of 5.5 m, where it hits a clay-rich layer
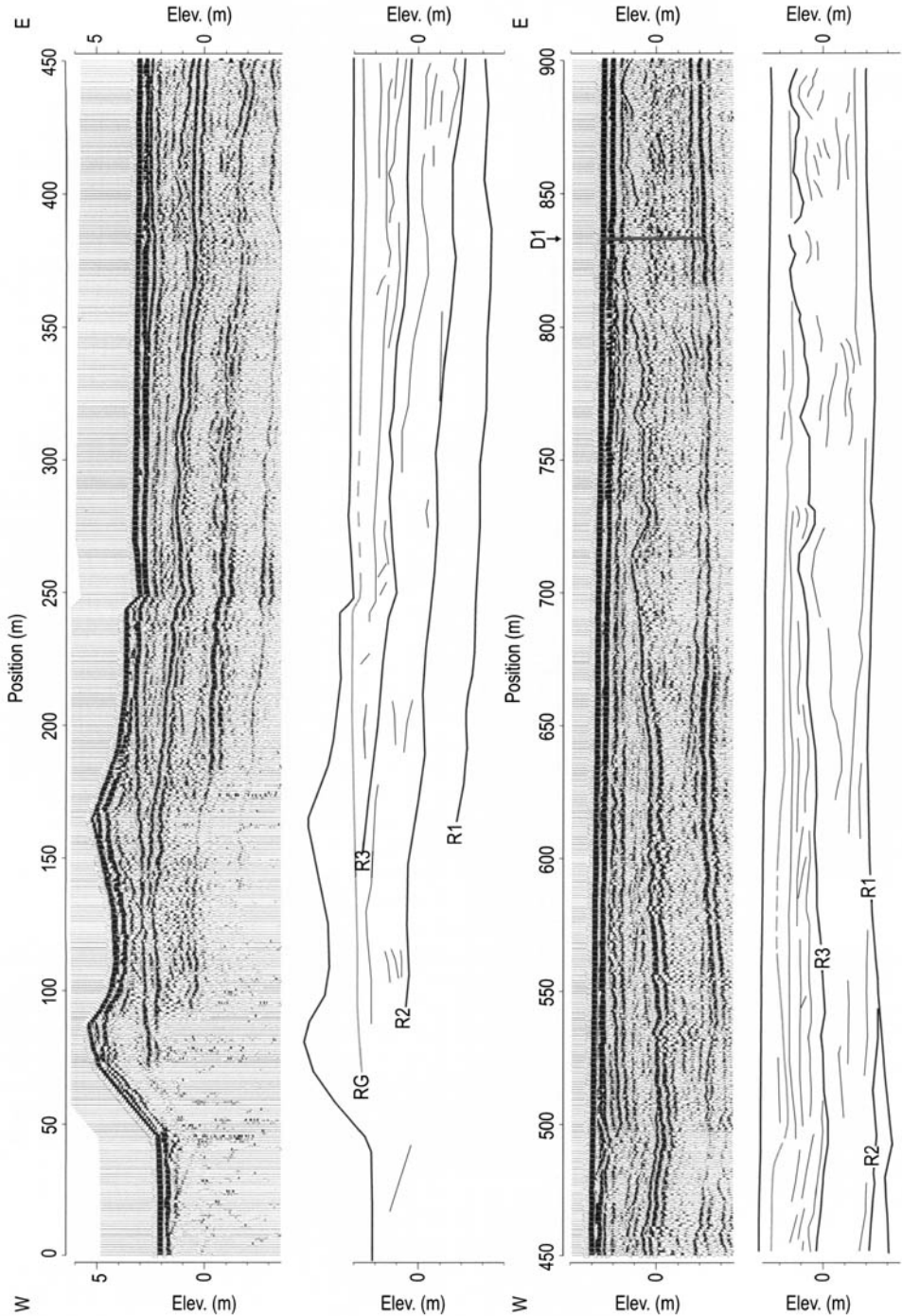
Fig. 2. GPR line 1 and line drawings (in full length, separated into four sections) showing major sedimentary structures. R1–R3 (heavy lines), continuous high-amplitude reflections; RG (grey line), interpreted as the groundwater table. The depth conversion is based on a velocity of 0.06 m ns^{-1}.
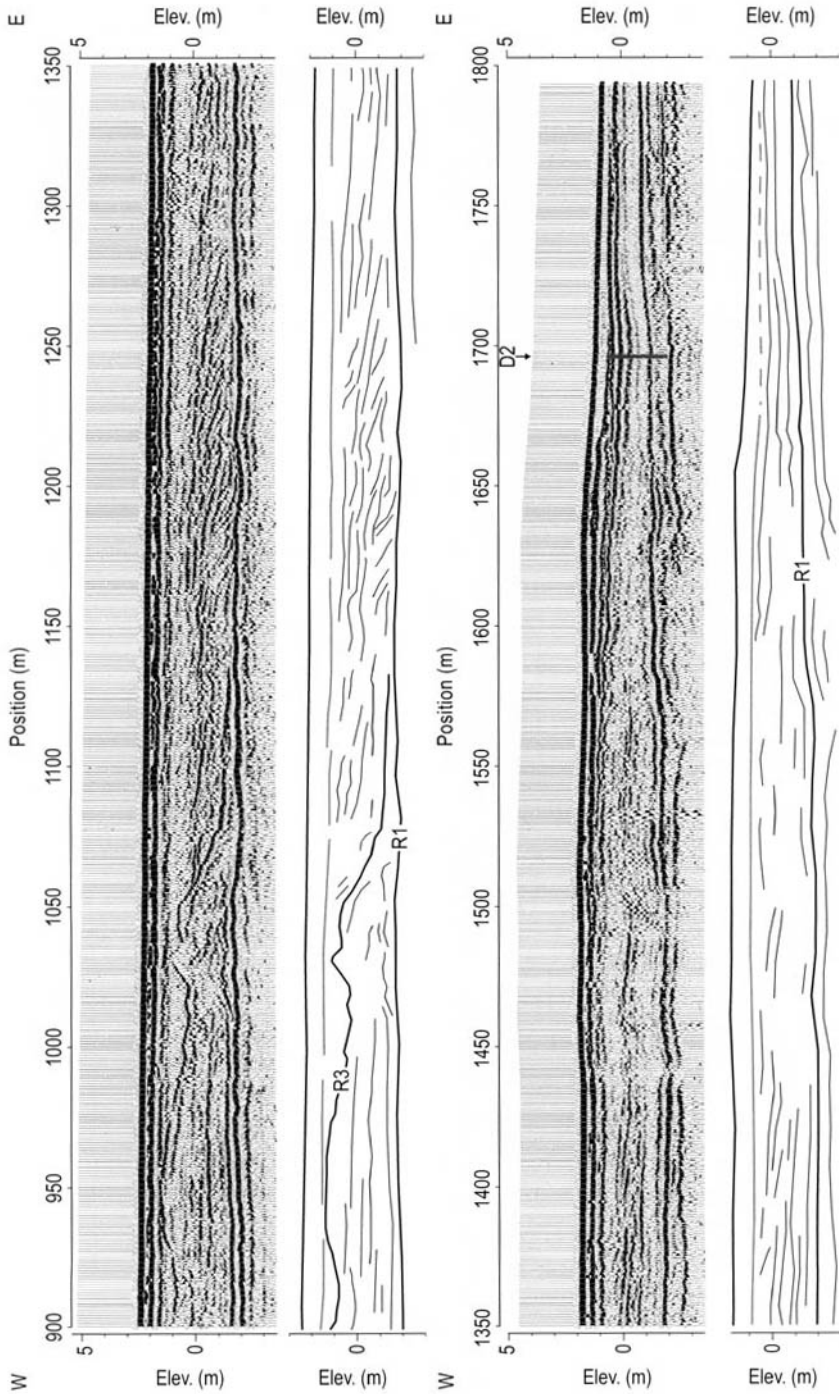
Fig. 2. Continued.

and is terminated. The groundwater table is detected at a depth of 1.9 m. A reflector at 30 ns is interpreted as a reflection from the groundwater table, resulting in a velocity of 0.13 m ns^{-1} for the unsaturated sand. The top of the clay-rich layer at 5.5 m correlates with a high-amplitude reflection at 137 ns, resulting in an interval velocity of 0.06 m ns^{-1} for the saturated sand. At Drilling 2, the lithology is sand with thin layers of peat and marine clay above 3.7 m and till below. The groundwater table was detected at a depth of 1 m. It has only been possible to correlate the top of the till layer to a reflection in the GPR profile. This resulted in an average velocity of 0.07 m ns^{-1}. The velocities found from correlation with the drill logs are consistent with velocities for equivalent materials reported in the literature (e.g. Davis and Annan 1989).

Because of topographic variations and a dipping groundwater table, it was not practical to use an elevation scale, which takes into account velocity change at the groundwater table. Therefore, the elevation scale is based on a velocity of 0.06 m ns^{-1}, found to be valid for saturated sand in this area.

Observations and interpretations

The description and characterization of the GPR profiles fall into two parts. The first part characterizes the continuous, high-amplitude reflections that separate the GPR sections into main units. In the second part, focus is on radar-facies analysis of low- to medium-amplitude reflections. The descriptions follow the terminology of radar sequence and radar-facies analyses (e.g. Beres & Haeni 1991; Gawthorpe *et al.* 1993).

Continuous high-amplitude reflections

Descriptions of the high-amplitude reflections are exemplified in GPR line 1 (Fig. 2). For practical reasons GRP lines 2–4 are not displayed. The pattern of high-amplitude reflections is similar in all four east–west profiles (lines 1–4); thus the description of line 1 covers all GRP profiles.

Line 1 is presented as a GPR profile as well as a line drawing in Figure 2. The GPR profile is scaled with AGC with a time window of four pulse-widths, such that the amplitude ratio is preserved. Thereby, a few continuous, relatively high-amplitude reflections appear clearly.

The stratigraphically lowest-lying high-amplitude reflection (R1) is nearly continuous across the barrier from the back of the foredunes at a depth of about 7 m to the end of the GPR line, 600 m from the lagoon shore (Fig. 2). R1 is continuous, almost straight, partly paired and has a

slight seaward (westward) dip, except in the westernmost part. The apparent eastward dip in the westernmost part may be due to errors in the topographic correction. The signal is strongly attenuated below this reflector.

In the western part of the profile, a continuous, almost straight reflection (R2) dips slightly eastward and apparently downlaps onto the lower high-amplitude reflection (R1) at about position 550 m (Fig. 2).

An uppermost-lying, continuous high-amplitude reflection (R3) is found in the western part, straight and slightly eastward-dipping until it reaches a position of 700 m, where it becomes hummocky and closer to the surface (Fig. 2). At about 1050 m, R3 starts to dip eastward and at 1140 m it downlaps onto reflection R1 at a depth of about 4 m. Below the foredunes in the western part (see Fig. 2), reflection R3 lies below another high-amplitude reflection (RG). In the rest of the profile, RG becomes a medium- to low-amplitude and partly discontinuous to continuous reflection.

### Internal structures from low- and medium-amplitude reflections

Low- to medium-amplitude reflections display internal structures of the barrier. Several types of radar facies have been identified. One radar facies, which consists mainly of subhorizontal parallel reflections, appears in all GPR lines, although it is most prominent at the westernmost part and at the very eastern end of the profiles close to the lagoon shore.

Another prominent radar facies in the western part of the GPR lines consists of parallel, slightly eastward-dipping reflections, which are continuous at distances of 50–200 m. This radar facies is illustrated in an 80 m-long section from the western part of GPR line 2 (Fig. 3). Some reflections downlap onto a basal, continuous high-amplitude reflection (at about 120 ns).

Further eastward, radar facies are characterized by short, eastward, steeper-dipping reflections. These radar facies are displayed in Figures 4 and 5. In Figure 4, the two steeply dipping sequences are separated by a straight, continuous, slightly eastward-dipping reflection between 90 ns and 130 ns. The lower sequence of inclined reflections consists of sigmoid clinoforms downlapping onto a lower, continuous high-amplitude reflection. To the east, between 1200 m and 1240 m (Fig. 4), the reflections gradually become more divergent. The upper sequence of steeply inclined reflections consists of a mixture of oblique and sigmoid clinoforms that downlap onto the straight, slightly dipping reflection separating the two inclined sequences. The reflections in the sequence are
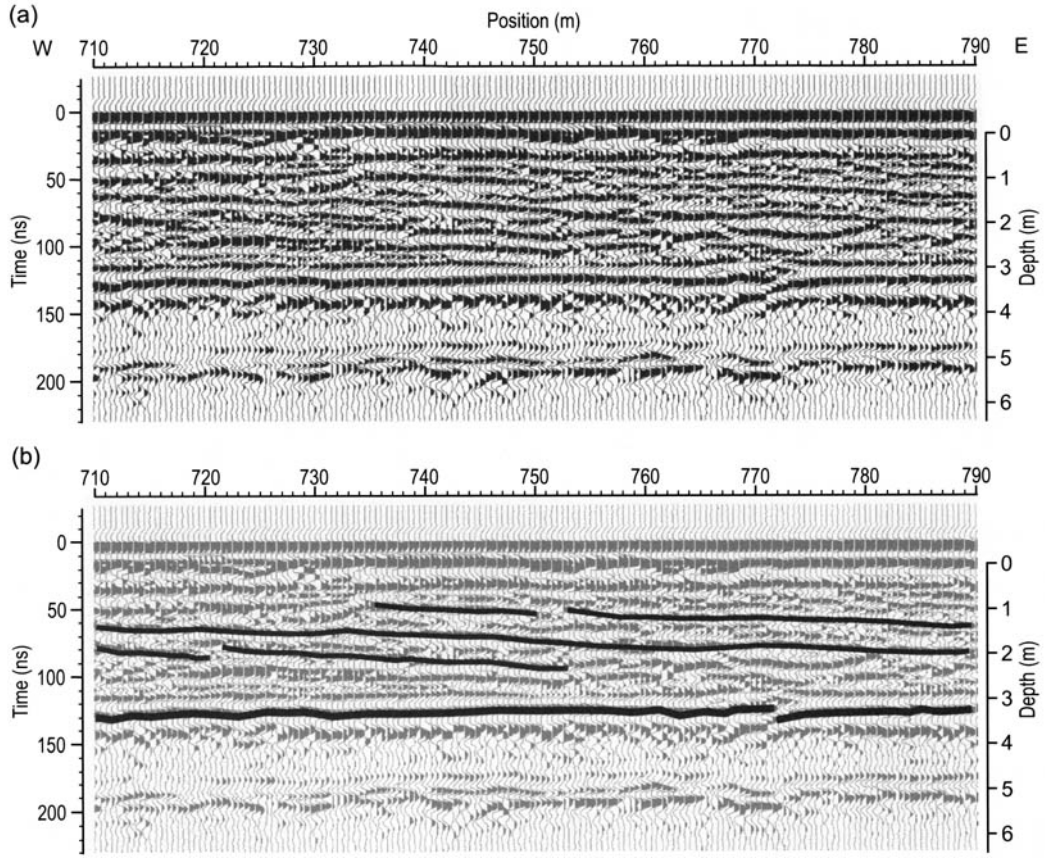
Fig. 3. Section of GPR line 2 (located at 'a' in Fig. 1) showing: (a) prominent continuous low-angle dipping reflections from the seaward barrier, and (b) these reflections highlighted. The reflections are interpreted as horizontal stratified deposits in the proximal part of a washover fan. The depth conversion is based on a velocity of 0.06 m ns^{-1}.
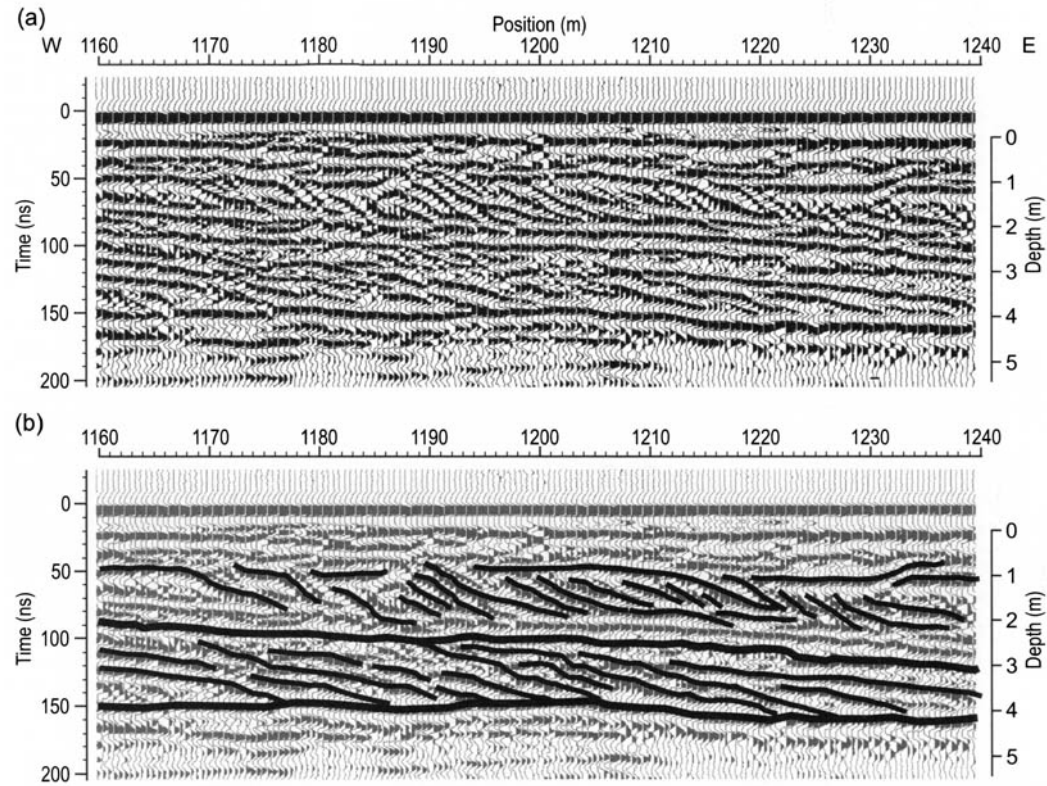
Fig. 4. Section of GPR line 2 (located at 'b' in Fig. 1) showing (**a**) two sets of prominent, steeply dipping reflections and (**b**) these reflections highlighted. The reflections are interpreted as two sets of delta foresets deposited in the distal part of a washover fan. The depth conversion is based on a velocity of 0.06 m ns^{-1}.
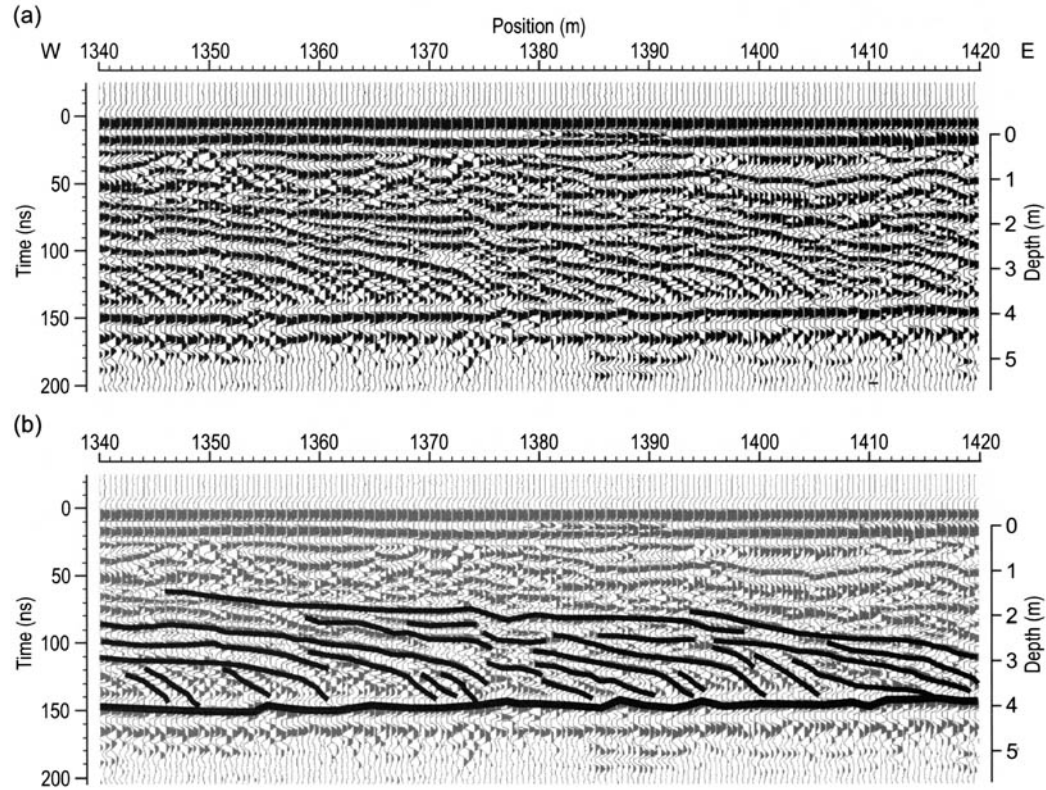
Fig. 5. Section of GPR line 2 (located at 'c' in Fig. 1) showing (**a**) prominent steeply dipping reflections and (**b**) these reflections highlighted. The reflections are interpreted as delta foresets deposited in the distal part of the washover fan. The depth conversion is based on a velocity of $0.06 \, \text{m ns}^{-1}$.

bounded above by discontinuous parallel reflections. The reflections in the upper sequence have a steeper dip than those in the lower sequence. At 100 m (Fig. 5) further east, a sequence with even more steeply dipping reflections is found. In this sequence, the radar facies is characterized by sets of small, parallel oblique clinoforms that toplap onto larger sigmoidal clinoforms. All clinoforms downlap on a continuous high-amplitude reflection at about 150 ns.

Interpretations and discussions

The observed pattern, with internal structures dominated by parallel, subparallel and low-angle dipping reflections in the seaward half of the GPR lines (Fig. 3), and with sequences of steeper-dipping sigmoidal and oblique prograding clinoforms in the other half of the profile (Figs 4 & 5), corresponds to internal sedimentary structures discussed as storm washover fans (Schwartz 1975, 1982). According to Schwartz (1975, 1982), the seaward part of a washover fan has a horizontal stratification and, where the washover fan terminates in a pond or a lagoon, delta foreset stratification will develop. The parallel, subparallel and low-angle dipping reflections are therefore interpreted as the horizontal stratified part of a washover fan. The steeper-dipping sigmoidal and oblique clinoforms indicate that the washover fans terminated in shallow standing water and are therefore interpreted as delta foresets (Figs 4 & 5).

The continuous, high-amplitude reflections (R1, R2 and R3 in Fig. 2) are interpreted as boundaries between individual sequences of washover deposits. Information from boreholes in the barrier indicates that some high-amplitude reflections can be caused by a thin layer of peat or clay at the boundaries. Drilling 1 on GPR line 1 (Fig. 2) penetrated through reflection R3 without giving a clear indication of the cause of this reflection. Only a slight increase in organic material in an otherwise homogeneous sand is observed. The hummocky part of reflection R3 in the central part of the barrier (Fig. 2) is interpreted as a buried dunefield. At Drilling 2 on GPR line 1(Fig. 2), in the northernmost part of the barrier, the lower-lying high-amplitude reflection R1, which can be followed across the entire barrier, is correlated with the boundary between the glaciogenic sediments and the overlying barrier sediments. Other borehole logs in the northern part of the barrier also report glaciogenic sediments found at a depth of 5–10 m. The topmost high-amplitude reflection, RG, beginning at the foredunes, is interpreted as the groundwater table (Fig. 2). The reflection of the groundwater table can be followed as a medium-

to low-amplitude reflection across the rest of the profile (Fig. 2).

Figure 6a displays line drawings of GPR lines 1–4 and thus the internal structures of the northern Holmsland Barrier (see Fig. 1 for location of profiles). In Fig. 6b, the corresponding interpretations of sedimentary structures of the profiles are shown for each individual line. All four profiles have comparable patterns and the individual major units, separated by the high-amplitude reflections, are correlated using the crossing GPR line 5. Therefore, the profiles are divided into major units, valid for all four profiles, and subdivided into structural units according to the radar facies, following the interpretations described above. The present aeolian dunes are the top unit (TU). The TU is confined to the active foredune area. Small shallow dunes also exist eastward, but are included in the stratigraphically upper unit (UU). The UU is the unit above reflection R3. The topmost part (UU-1) consists of low-angle washover deposits and the lower part (UU-2) is the terminal high-angle continuation of UU-1, with abundant delta foresets. In line 2, a part of the UU is interpreted as aeolian deposits (UU-3). The middle unit (MU), below the UU, is divided into a washover subunit and an aeolian subunit. The GPR signal is generally attenuated below reflection R3, and internal structures are therefore less pronounced. There are, however, both low- and high-angle washover deposits locally in MU-1. The MU-1 forms a landward-sloping wedge and the aeolian part of the middle unit (MU-2) is draped onto the terminal part of MU-1, where it continues landward for a short distance. It has not been possible to deduce any clear internal structures from the lower unit (LU), because of the attenuation of the GPR signal below reflection R2. It is likely that this unit also comprises washover deposits, but this has not been verified.

Summary and conclusions

The Holmsland Barrier, a transgressive barrier along a wave-dominated part of the Danish North Sea coast was studied using GPR. Four GPR lines were shot across the barrier and a fifth profile was surveyed parallel with the barrier to enable stratigraphical correlation between the four GPR cross-sections.

A few continuous high-amplitude reflections occurring across the barrier were used to divide the stratigraphy into several radar facies and individual sedimentary sequences. The various radar facies observed can be divided into three main groups. One group, consisting of parallel, subparallel and low-angle dipping reflections, is interpreted as horizontal stratified washover deposit, whereas the
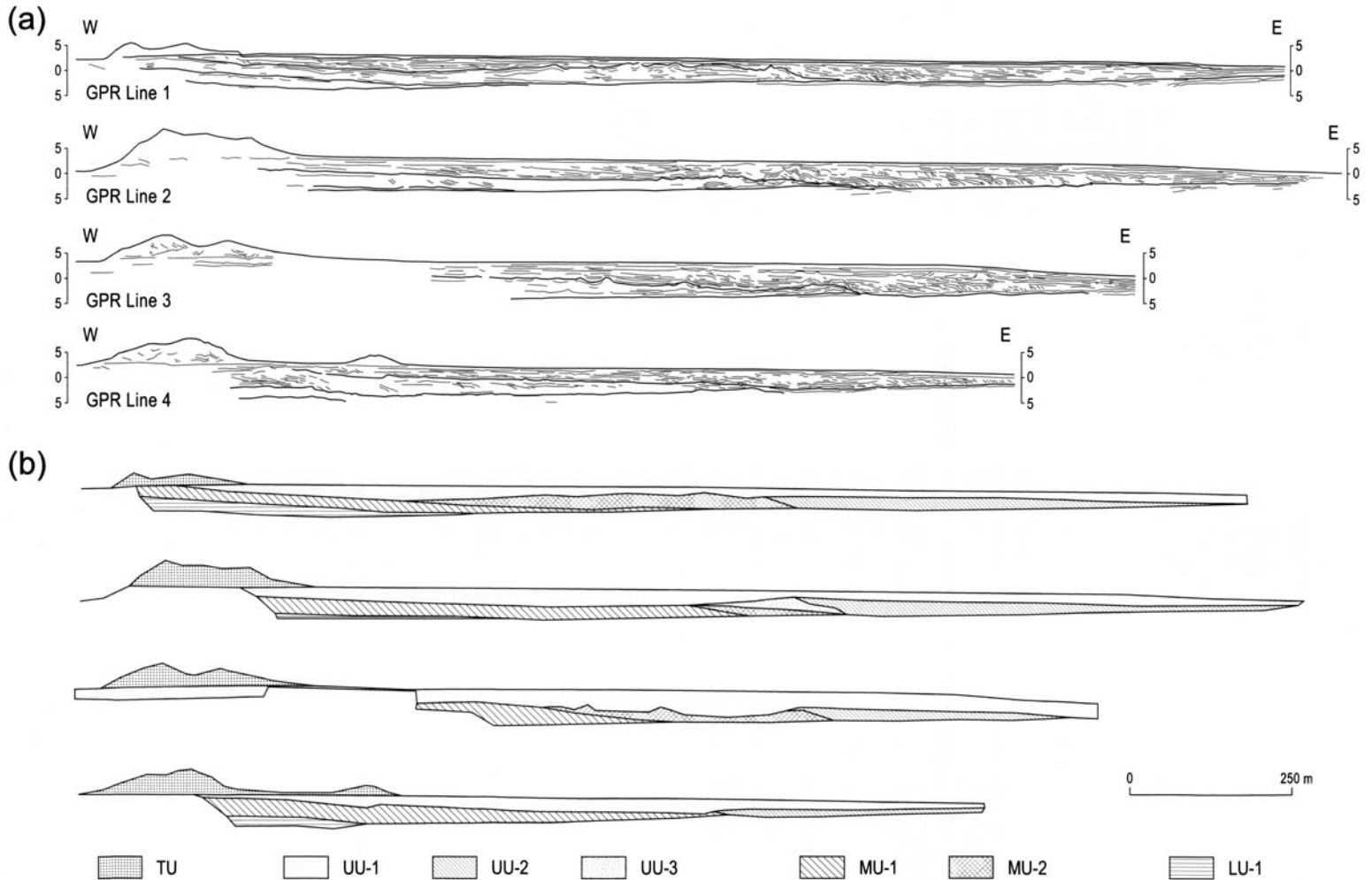
Fig. 6. Cross-sections of the Holmsland Barrier. (a) GPR lines 1–4 displayed as line drawings. (b) Geomorphological and stratigraphical interpretation. TU (top unit), active aeolian dunes. UU (upper units): UU-1, most recent washover deposits divided into parallel stratification; UU-2, delta foresets; UU-3, aeolian deposits. MU (middle units): MU-1, older washover deposits; MU-2, aeolian deposits. LU (lower units): LU-1, oldest unit, presumably washover deposits.

second group, dominated by sigmoidal and oblique clinoforms is interpreted as delta foresets related to washover deposits terminating in standing water. The third group represents aeolian deposits, with a chaotic appearance.

Observations of internal structures in the Holmsland Barrier, derived from four GPR crosssections, all suggest that the coastal barrier is composed almost entirely of washover deposits, with aeolian deposits locally.

The several sequences of washover deposits, as well as the presence of buried dunefields, suggest that general dynamic conditions have shifted during the development of the barrier, going from high-dynamic periods, with frequent storm washover, to calm periods with surface stabilization. The shifts are presumably linked to climate fluctuations. However, datings are required to document the frequency of both the long-term depositional cycles and the short-term individual washover events, and to link these shifts to climate fluctuations.

References

ANDERSEN, S. A. 1963. *Geologisk fører over Holmsland og dens Klit.* Populærvidenskabeligt Forlag — Copenhagen.

BERES, M., JR & HAENI, F. P. 1991. Application of ground-penetrating-radar methods in hydrogeologic studies. *Ground Water*, **29**, 375–386.

BERES, M., HUGGENBERGER, P., GREEN, A. G. & HORSTMEYER, H. 1999. Using two- and three-dimensional georadar methods to characterize glaciofluvial architecture. *Sedimentary Geology*, **129**, 1–24.

BRISTOW, C. S., CHROSTON, P. N. & BAILEY, S. D. 2000. The structure and development of foredunes on a locally prograding coast: insights from ground-penetrating radar surveys, Norfolk, UK. *Sedimentology*, **47**, 923–944.

DAVIS, L. J. & ANNAN, A. P. 1989. Ground-penetrating radar for high-resolution mapping of soil and rock stratigraphy. *Geophysical Prospecting*, **37**, 531–551.

DAVIS, R. A. 1994. Barrier island systems – a geological overview. *In*: DAVIS, R. A. (ed.) *Geology of Holocene Barrier Island Systems.* Springer-Verlag, Berlin, 1–46.

GAWTHORPE, R. L., COLLIER, R. E. LL, ALEXANDER, J., BRIDGE, J. S. & LEEDER, M. R. 1993. Ground penetrating radar: application to sandbody geometry and heterogeneity studies. *In*: NORTH, C. P. & PROSSER, D. J. (eds) *Characterization of Fluvial and Aeolian Reservoirs.* Geological Society, London, Special Publications, **73**, 421–432.

JOL, H. M., SMITH, D. G. & MEYERS, R. A. 1996. Digital ground penetrating radar (GPR): a new geophysical tool for coastal barrier research (Examples from Atlantic, Gulf and Pacific coasts, U.S.A.). *Journal of Coastal Research*, **12**, 960–968.

KROG, H. 1979. Late Pleistocene and Holocene shorelines in western Denmark. *In*: OELE, E., SCHÜTTENHELM, R. T. E. & WIGGERS, A. J. (eds) *The Quaternary History of the North Sea.* Symposia Universitatis Upsaliensis Annum Quengentesimum Celebrantis, Acta Universitatis Upsaliensis, **2**, 75–83.

KYSTINSPEKTORATET. 1998. *Menneske, Hav, Kyst og Sand.* Kystinspektoratet (Danish Coastal Authorities). [English summary]

LAUSTRUP, C., MADSEN, H. T., KNUDSEN, S. B. & SØRENSEN, P. 2000. Coastal steepening in Denmark. *Coastal Engineering 2000 – Conference Proceedings,* Sydney, Australia, July 16–21, 2000, 2428–2438.

MÖRNER, M. A. 1976. Eustatic changes during the last 8000 years in view of radiocarbon calibration and new information from the Kattegat region and other northwestern European coastal areas. *Palaeogeography, Palaeoclimatology, Palaeoecology*, **19**, 63–85.

SCHWARTZ, R. K. 1975. *Nature and Genesis of Some Storm Washover Deposits.* US Army Corps of Engineers, Coastal Engineering Research Center, Technical Memoranda, **61**, p. 69.

SCHWARTZ, R. K. 1982. Bedform and stratification characteristics of some modern small-scale washover sand bodies. *Sedimentology*, **29**, 835–849.

SMITH, D. G. & JOL, H. M. 1992. GPR results used to infer depositional processes of coastal spits in large lakes. *In*: HÄNNINEN, P. & AUTIO S. (eds) *Fourth International Conference on Ground Penetrating Radar, 8–13 June 1992, Rovaniemi, Finland.* Geological Survey of Finland, Special Papers, **16**, 169–177.

VANDENBERGHE, J. & VAN OVERMEREEN R. A. 1999. Ground penetrating radar images of selected fluvial deposits in the Netherlands. *Sedimentary Geology*, **128**, 245–270.

This page intentionally left blank

GPR investigation of multiple stage-5 sea-level fluctuations on a siliciclastic estuarine shoreline, Delaware Bay, southern New Jersey, USA

MICHAEL L. O'NEAL[1] & RICHARD K. DUNN[2]

[1]Education Department, Loyola College in Maryland, Baltimore, Maryland, 21210, USA
(e-mail: moneal@loyola.edu)
[2]Department of Geology, Norwich University, Northfield, Vermont, 05663, USA

Abstract: Ground penetrating radar (GPR) surveys were used to identify three distinct sea-level highstands within the oxygen isotope stage (OIS) 5-equivalent sediments of the Quaternary Cape May Formation in southern New Jersey. The three units, QCM1a, QCM1b, and QCM1c, are designated as submembers of the Cape May 1 member. The transgressive ravinement surfaces (TRS) forming the bounding unconformities of these units are recognized as laterally extensive reflections on the radar records and have been corroborated as gravel lag deposits and associated lithological discontinuities in continuous vibracores and hand-augered boreholes. GPR and litho-logical data have been used to interpret these highstand deposits in a sequence-stratigraphic framework. These units are thin (3 m or less), lithologically similar and present limited geo-morphic expression of their individual existence beneath a low terrace (+6 m to mean sea level/MSL) on the northern margin of Delaware Bay. In the upper two units, QCM1b and QCM1a, radar surveys across subtle, bay-margin parallel, sublinear topographic highs of 3 m relief or less in the Jones Island area reveal internal structures consistent with geomorphic interpretation as stranded estuarine shorelines. The newly identified shoreline complexes are located well bayward of, and lower in elevation than, the commonly accepted +5 m to +6 m MSL OIS 5e shoreline. This older shoreline abuts the Cedarville Scarp and is attributed to the sea-level highstand associated with QCM1a. GPR was also used to accurately place vibracores for gathering samples of the three units for optically stimulated luminescence dating. Together, these three highstand deposits record sea-level fluctuations within OIS 5, at time scales shorter than those commonly recognized in the mid-Atlantic region.

A complex record of Cenozoic sea-level change is preserved in the siliciclastic sediments of the mid-Atlantic coastal plain of North America. During the past few decades, third- and fourth-order sea-level cycles (10^6–10^5 yr) (Ma–100 Ka) have been identified in the region in lithological cores and sand and gravel quarries (Owens & Denny 1979; Owens & Minard 1979; Mixon 1985; Sugarman et al. 1993; Ramsey 1997; Newell et al. 2000), and seismic surveys obtained on the adjacent continental shelf (Colman & Mixon 1988; Toscano et al. 1989; Colman et al. 1990; Sheridan et al. 2000). The delineation of less extensive sedimentary successions recording fifth-order cycles (10^5–10^4 yr) (100 Ka–10 Ka) has proven problematic due to the spatial constraints of coring and the low (comparatively) resolution of the seismic method. In recent studies, however, ground penetrating radar (GPR) has been successfully used in stratigraphic studies on the coastal lowlands adjacent to

the Delaware Bay estuary (Fig. 1). In this area, O'Neal (1997) and O'Neal and McGeary (2002) identified six emergent sediment units deposited during climate-induced fifth-order sea-level highstands of Mid- to Late Pleistocene age within the Cape May Formation.

In global climate and sea-level change studies, the last warm-climate, interglacial period (Sangamonian) is often used as a model for understanding the potential for future change within the current interglacial episode. This time period corresponds in part with marine oxygen isotope stage (OIS) 5, with the peak warmth and highest sea levels attributed to a narrow time range of a few ka during substage 5e, centred at 125 ka (Fig. 2). Uncertainties exist, however, regarding short-term fluctuations (10^4–10^3 yr) (10 Ka–Ka) in temperatures and sea levels during OIS 5, making comparisons with the present difficult. Recent efforts in the mid-Atlantic region to identify higher than present
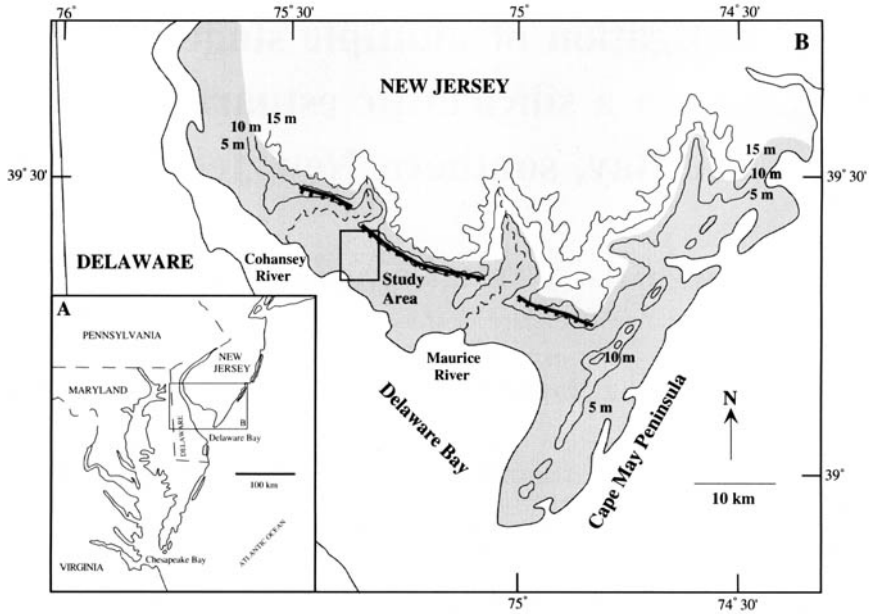
Fig. 1. (a) Inset map of mid-Atlantic region of North America, showing location of Delaware Bay. (b) Map of southern New Jersey showing study area, shaded outcrop pattern of Quaternary Cape May Formation (modern salt marsh omitted), Cedarville Scarp, Delaware Bay and the Cape May Peninsula. Generalized topography adapted from USGS 1 : 100 000 metric series maps (modified from O'Neal & McGeary 2002).
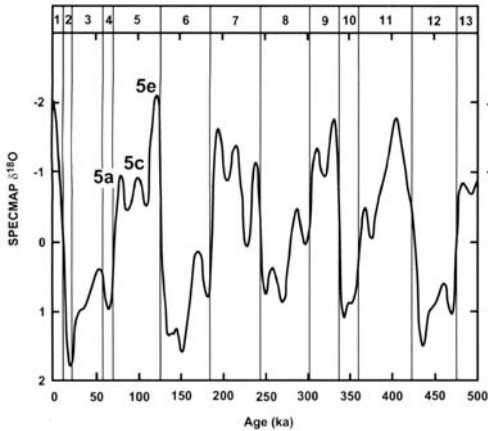
Fig. 2. Stacked, smoothed SPECMAP marine oxygen isotope curve plotted versus age. Odd-numbered substages 5a, 5c and 5e are labelled (modified from Imbrie *et al.* 1984).

OIS 5 highstand deposits (and hence warm-climate deviations) younger than substage 5e have suffered from difficult stratigraphic (Szabo 1985; Wehmiller *et al.* 1992; Wehmiller & Miller 2000) or geochronological (Ramsey 1993, 1997) control. On a global scale, the debate continues as to whether

substage 5e is the only OIS 5 time period to record sea levels higher than present (Toscano 1992; Ludwig *et al.* 1996; Toscano & Lundberg 1999; Hearty & Kaufman 2000). The need for refinement of the OIS 5 highstand record with good stratigraphic and geochronological control is clear.

Study area and goals

The Quaternary sediments of the Cape May Formation occupy two broad, gently sloping terraces, separated by the Cedarville Scarp (Fig. 1), along the northern margin of Delaware Bay in southern New Jersey, and are subdivided into three members, Cape May 1, 2 and 3, in increasing age order (Newell *et al.* 2000). These estuarine-marine deposits were emplaced during Mid- to Late Pleistocene sea-level highstands and stratigraphically overlie the fluvial Miocene–Pliocene Bridgeton Formation and the marine Miocene Cohansey Formation. The Cenozoic geologic history of the region is summarized in Newell *et al.* (2000) and O'Neal and McGeary (2002).
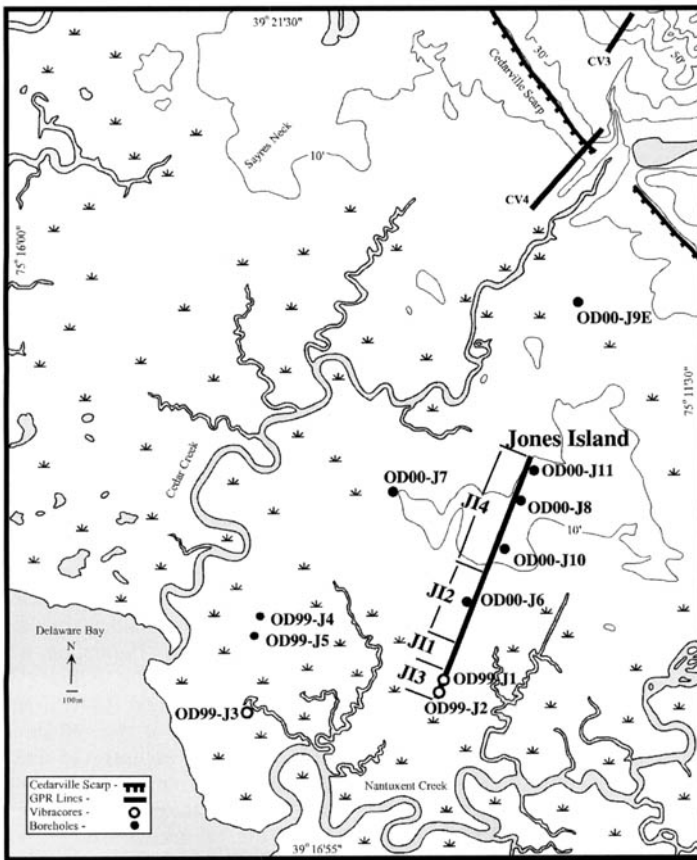
O'Neal and McGeary (2002) used 50 MHz GPR, vibracores and hand-augered boreholes to delineate four submembers of Cape May 3 beneath the older, upper terrace that slopes gently from +18 m to +9 m mean sea level (MSL). In this same study,

Cape May 1 and 2, and the modern salt marsh, were found to underlie the younger lower terrace that slopes from +6 m to MSL. The two terraces are separated by the Cedarville Scarp, formed by erosion during the sea-level cycles that deposited the sediments of Cape May 1 and 2. Two of the radar lines used in that study, CV3 and CV4, are shown crossing the Cedarville Scarp from the upper to lower terrace in Figure 3.

O'Neal et al. (2000) used amino acid racemization dating to place age estimates equivalent to OIS 9 and/or OIS 11 on the submembers of Cape May 3. These estimates fit well with other local and global coastal records (Belknap 1979; Riggs & Belknap 1988; Wehmiller et al. 1992; Hearty et al. 1999a, b; El-Asmar & Wood 2000; Hearty & Kaufman 2000; Rostami et al. 2000) and suggest, by stratigraphic position, that Cape May members 2 and 1 correlate with highstands during OIS 7 or 9, and 5, respectively.

Figure 3 shows the study location on the lower terrace in the Jones Island area of southern New Jersey (see inset in Fig. 1 for regional location). This broad, nearly flat terrace is bordered by Delaware Bay and the Cedarville Scarp. It is separated into a wide, fringing salt marsh in the lowland section and a gently undulating plain in the upland. The interfluves of the upland contain low-relief (3 m or less) sublinear topographic highs that roughly parallel the modern bay margin. A network of small rivers and creeks drains both terraces, forming meandering tidal channels across the salt marsh. Tilled agriculture is the predominant land use in the upland areas.

The primary goals of this investigation were to delineate and date unconformity-bounded highstand deposits, presumably stemming from separate sea-level cycles, within the OIS 5-equivalent sediments of the Cape May Formation as defined by Newell et al. (2000) and O'Neal and McGeary (2002). An additional goal was to use GPR to accu-

Fig. 3. Location map of GPR profiles JI1-4 in the Jones Island area. Also shown are hand-augered boreholes and vibracores obtained during this study. 50 MHz GPR profiles of O'Neal and McGeary (2002) are shown relative to the Cedarville Scarp. Elevation contours adapted from the Cedarville USGS 7.5' topographic quadrangle map.

rately locate optimal areas for vibracoring super-posed highstand units, providing good stratigraphic control for optically stimulated luminescence (OSL) dating. Based on the geomorphology of the lower terrace, the linear feature of Jones Island was chosen for GPR investigation as a possible stranded shoreline of an OIS 5 sea-level event younger than substage 5e. The shoreline of this 5e event is seen well inland and is represented by the Cedarville Scarp (Figs 1 & 3).

Methods

GPR use in coastal areas has proved successful in delineating sedimentary structures (Leatherman 1987; Jol & Smith 1991, 1992a, b; Meyers et al. 1994; Bridge et al. 1995; Jol et al. 1996), locating buried palaeochannels (Wyatt & Temples 1996; O'Neal & McGeary 2002) and interpreting Holocene coastal geomorphic development (FitzGerald et al. 1992; Hill & FitzGerald 1992; van Heteren et al. 1994). Recent coastal stratigraphic GPR studies in the Delaware Bay region include O'Neal (1997) and O'Neal and McGeary (2002).

The GPR used in this study was a 250 MHz, broadband Noggin system, manufactured by Sensors and Software, Inc. This fixed-separation, bistatic system is a tow-behind model that produces a non-alterable graphic output from initial user-specified wave velocity/depth profile (initial wave velocity selection of $0.1 \, m \, ns^{-1}$ was verified by corroboration of major reflections with lithology in boreholes), stacking and collection interval values. Though topographic correction was not possible with the final output, this unit was chosen for its speed of operation and small size. Manual correction for the subtle topography encountered in the field area was considered a reasonable trade-off for the constraints imposed by long profiles collected in the width of one row in an agricultural field.

Sediments from superposed highstand units identified in this study were collected in situ via vibracore and processed for OSL dating at the University of Illinois in Chicago. A multiple aliquot additive dose method was applied to quartz grains in the $100-150 \, \mu m$ size fraction. Green light (540 nm) stimulation was used to excite natural and laboratory-induced luminescence, and the resulting emission was isolated with Corning 7-59 and 5-58 filters and measured by a standard photomultiplier tube. The total bleach method was used to calculate equivalent doses. An exponential fit was used to model the additive β dose response with interpolation to the solar reset level at <20% of the highest applied β dose. The equivalent dose was calculated as a mean value for integrals between 3 and 90 seconds after initial exposure to green excitation. The dose rate was determined from Uran-

ium and Thorium content, measured by α-counting, and from $^{40}K\%$ measured by inductively coupled plasma-mass spectrometry (ICP-MS). The OSL dating methods used in this study are fully described in Forman et al. (2000).

Results

Stratigraphic framework

During the course of this investigation, approximately 2.3 km of GPR data were collected in four continuous profiles in the Jones Island area (Fig. 3). Profiles JI4, JI2, JI1 and JI3, in landward to bayward order (Figs 4, 5 & 6) were acquired to resolve the sea-level highstand stratigraphy of the OIS 5 deposits across and bayward of this topographic high.

In the interpretive Figures 4, 5 and 6, only major reflections exhibiting characteristics of the unconformities that bound sea-level highstand deposits are labelled. Though none of the major reflections was truncated by another, smaller internal reflections, indicative of sedimentary deposition, are seen to be truncated from above, or to downlap onto, these major reflections throughout the profiles. Each major reflection is designated an alphabetical label that is consistent throughout the profiles.

Because the lithology throughout the area is predominantly sand on sand, deposited in intertidal to shallow subtidal zones, coarse sands and gravelly sands encountered in cores and boreholes are considered possible evidence of a bounding unconformity along a transgressive ravinement surface (TRS). The coarse sediments of a TRS in a siliciclastic setting are deposited in a nearly continuous, bayward-sloping sheet in the high-energy environment of an active shoreline cutting into and riding over underlying deposits during a rise in sea level (Nummedal & Swift 1987). The combination of a laterally continuous major reflection that coincides with substantial coarse sand and gravelly sand deposits was considered evidence of such an unconformity in this study. Coarse sand, granules and pebbles are abundant in the adjacent, fluvial Miocene Bridgeton Formation, which serves as the source of much of the sediment in the Quaternary Cape May Formation (O'Neal & McGeary 2002).

The geometry of the reflections shown in the GPR profiles in Figures 4, 5 and 6 was combined with lithology from boreholes, and with vibracores and topographic data from transit surveys, to produce the sequence-stratigraphic cross-section shown in Figure 7. A vertical exaggeration of 75× was used to enhance the subtle topography.

Reflection A appears at an elevation slightly above MSL on the northeastern (landward) end of
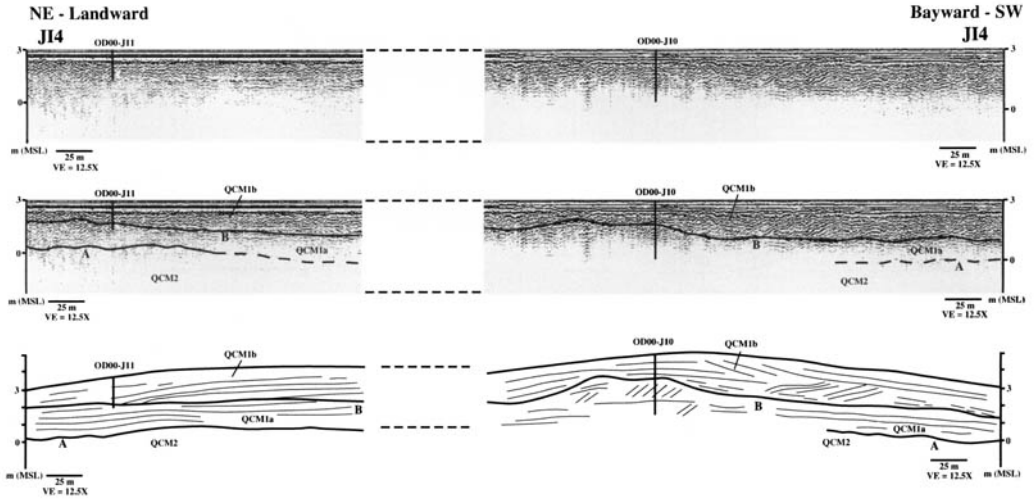
Fig. 4. 250 MHz GPR profile JI4 and interpretations collected in the Jones Island area of southern New Jersey. Prominent reflections A and B represent transgressive ravinement surfaces (TRS) forming the bounding unconformities of the OIS 5-age highstand units QCM1a and QCM1b, as identified in this study. The central section of profile JI4 is redundant and has been omitted here due to space constraints.
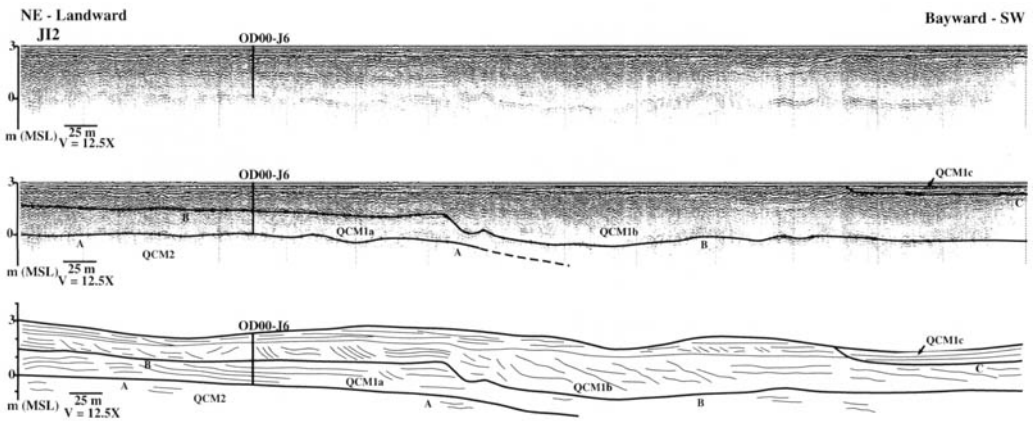
Fig. 5. 250 MHz GPR profile JI2 and interpretations collected in the Jones Island area of southern New Jersey. Prominent reflections A, B and C represent transgressive ravinement surfaces (TRS) forming the bounding unconformities of the OIS 5-age highstand units QCM1a, QCM1b and QCM1c, as identified in this study.

GPR line JI4 (Fig. 4) and correlates well with the base of the OIS 5-equivalent Cape May 1 deposits identified by O'Neal and McGeary (2002) near the Cedarville Scarp (Figs 1 & 3). The reflection may be traced discontinuously southwest (bayward) at this elevation until it begins to slope more steeply, midway along GPR line JI2 (Fig. 5). Coarse, gravelly sands were found at the same elevation as reflection A in boreholes OD00-J10 and J6 (Fig. 7). A projection of the sloping reflection from JI2 bayward correlates well with the gravel unit encountered at the base of vibracore OD99-J3 (Fig.

7). These lines of evidence suggest that reflection A is a TRS, forming the lower bounding unconformity of the lowermost unit in Cape May 1, herein designated QCM1a. This unit cuts into and overlies Cape May 2 (QCM2) (Fig. 7).

Reflection B appears at an elevation of +2 m MSL on the northeastern (landward) end of GPR line JI4 (Fig. 4), dipping gently to an elevation of ~+1.5 m MSL on the southwestern end of the profile. Allowing for topographic correction (Fig. 4), this reflection slopes gently landward to the northeast and bayward to the southwest, peaking beneath
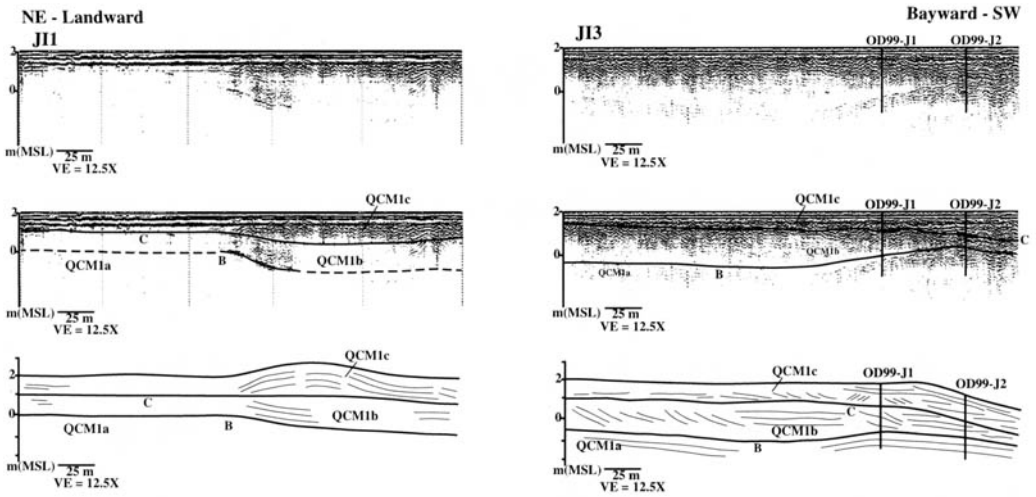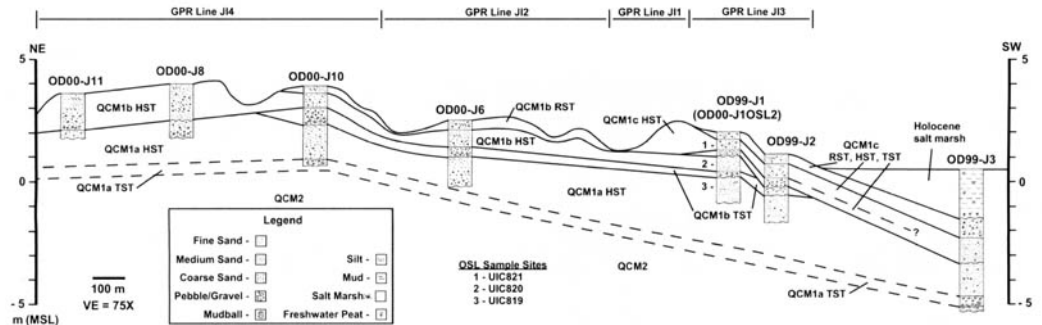
Fig. 6. 250 MHz GPR profiles JI3 and JI1 and their interpretations collected in the Jones Island area of southern New Jersey. Prominent reflections B and C represent transgressive ravinement surfaces (TRS) forming the bounding unconformities of the OIS 5-age highstand units QCM1a, QCM1b and QCM1c, as identified in this study.

Fig. 7. Sequence-stratigraphic cross section of the Jones Island area, southern New Jersey, showing the interpretation of OIS 5-age highstand units QCM1a, QCM1b and QCM1c, as identified in this study. Lithology from boreholes and vibracores, ground penetrating radar profile locations and OSL dating sites are also shown. HST, highstand systems tract; RST, regressive systems tract; TST, transgressive systems tract.

the crest of the topographic high near borehole OD00-J10. Reflection B maintains this elevation (~+1.5 m) midway through GPR line JI2 (Fig. 5), where it dips to approximately MSL. With minor deviations, this reflection maintains this orientation across GPR profiles JI1 and JI3 (Fig. 6) before dipping more steeply bayward. From the northeast (landward), boreholes OD00-J11 and J8 (Fig. 7) reveal coarse sand at the elevation of reflection B, while boreholes OD00-J10 and J6, and vibracores OD99-J1 and J2, encountered a gravelly coarse sand deposit (Fig. 7). Together, this evidence suggests that reflection B is a TRS, forming the lower bounding unconformity of an intermediate unit in Cape May 1, herein designated QCM1b. The difference in lithology along the TRS of reflection B,

most pronounced beneath the topographic high in profile JI4 (Fig. 4), suggests a decrease in energy as sea level reached its maximum elevation during the highstand of this time (Fig. 7).

The third major reflection encountered in this radar investigation, reflection C, appears abruptly from just below land surface on the southwestern (bayward) end of GPR line JI2 (Fig. 5). This reflection truncates smaller, internal reflections of unit QCM1b below and may be traced at an elevation of ~+1 m MSL across GPR lines JI1 and JI3 (Fig. 6). Near the southwest (bayward) end of profile JI3, reflection C dips bayward to an elevation of ~−1 m MSL. Gravelly coarse sands were found at the elevation of reflection C in vibracores OD99-J1 and J2 (Fig. 7). Projection of this sloping reflec-

tion bayward correlates well with the gravelly coarse sand deposit found at the base of the middle unit (below the salt-marsh deposits) in vibracore OD99-J3 (Fig. 7). This projection, and the absence of a third highstand unit in vibracore OD99-J3, indicates that unit QCM1b has been truncated by the TRS coincident with reflection C. These lines of evidence suggest that this TRS forms the lower bounding unconformity of the uppermost Cape May 1 unit identified in this study. This unit is herein designated QCM1c.

Radar stratigraphy

Reflections A and B respectively form the lower and upper bounding unconformities of unit QCM1a. Internal reflections in this unit, throughout the radar profiles shown in Figures 4, 5 and 6, are generally flat-lying to gently bayward-dipping. Borehole OD00-J6 and vibracores OD99-J1, J2 and J3 (Fig. 7) reveal the lithology of this unit to be predominantly medium, pebbly sand, with occasional silt and fine sand (above the basal gravel). Together, this evidence suggests deposition in a sandy offshore/bay-bottom environment. In contrast, the lithology of QCM1a coarsens landward of borehole OD00-J6, shown in the coarse sands and gravels of boreholes OD00-J10, J8 and J11 (Fig. 7). Together with the landward-dipping internal reflections in profile JI4 (Fig. 4) beneath borehole OD00-J10, these data suggest higher energy deposition, possibly as sand and gravel bars in a shallow, offshore or bay-bottom environment.

Unit QCM1b is bounded by reflection B and the modern land surface across most of GPR profiles JI4 (Fig. 4) and JI2 (Fig. 5). Bayward of borehole OD00-J10 in Figure 4, the internal reflections vary between dipping landward and bayward. Above the basal gravel (TRS) in this borehole is a medium to coarse sand deposit (Fig. 7). The lithology and internal reflections at this location suggest deposition in a shallow nearshore to shoreface environment, possibly as foreshore bars welding onto a shoreface. The landward-dipping internal reflections landward of borehole OD00-J10, composed of medium, pebbly and silty sands as shown in boreholes OD00-J8 and 11 (Fig. 7), suggest deposition as overwash in a backshore environment. These data suggest that this section of the Jones Island area represents the shoreline during the sea-level high of QCM1b time.

The internal reflections of unit QCM1b in profile JI2 (Fig. 5) are more variable. In the landward end of the profile, these reflections range from flat-lying to bayward- and landward-dipping. The medium, pebbly sands of this unit, shown in borehole OD00-J6 (Fig. 7), suggest deposition in a shallow nearshore environment. In contrast, the internal reflections bayward of the dip in reflection B in profile JI2 (Fig. 5) reveal a bayward progression from steeply dipping clinoforms to nearly flat-lying horizons. This suggests deposition toward the offshore as sediments prograded into deeper water. The fine to medium sands of the upper section of this unit (above the basal gravel) in vibracore OD99-J1 (Fig. 7) support this interpretation. A thin (1 m or less) set of nearly flat-lying internal reflectors at the top of unit QCM1b is shown on the bayward end of profile JI4 (Fig. 4) and across profile JI2 (Fig. 5) until they are truncated by reflection C. The coarse, pebbly and silty sand of these upper sediments suggests deposition during regression as sea level fell in QCM1b time.

Reflection C forms the basal unconformity (the TRS) of unit QCM1c. Above the coarse sands and gravels associated with this TRS in vibracores OD99-J1 and J2 (Fig. 7) is a succession of medium, pebbly to silty sand, capped by a coarser unit of sands and gravels. As with unit QCM1b, this sequence suggests an overall highstand cycle of transgression and regression. The internal reflections of unit QCM1c support this interpretation. The topographic high in profile JI1 (Fig. 6) contains internal reflections indicative of bayward deposition on its bayward side and overwash on its landward side, suggesting the location of the QCM1c shoreline. This is further supported by the variable internal reflections in profile JI3 (Fig. 6), landward of the bayward break in slope. These reflections, combined with the vibracore-derived lithology, suggest deposition in a shallow nearshore environment. At the slope break, the lower internal reflections flatten and dip bayward, suggesting deposition in deeper water. The upper internal reflections near the vibracores in Figure 6 flatten and mimic the modern land surface. The gravelly, silty, coarse sand of these upper sediments was probably deposited in a regressive setting during the sea-level fall of QCM1c time.

OSL dating

GPR was used to locate optimal sites for obtaining sediment samples for OSL dating that could be retrieved in superposition, within the depth range of the land-based vibracoring method. Following the placement of test vibracores OD99-J1 and J2 near the bayward end of profile JI3 (Fig. 6), a second vibracore, OD00-J1OSL2, was obtained immediately adjacent to OD99-J1. This core was sectioned under darkened laboratory conditions, and representative samples of each of the three Cape May 1 highstand units were taken for OSL dating.

The results of the OSL laboratory analyses

yielded minimum age control only and are shown in Table 1. The sample from the oldest unit, QCM1a, was saturated respective to equivalent dose, preventing calculation of a numerical age. The QCM1b sample was near saturation, yielding a minimum age of 101 (±15) ka. The youngest sample, QCM1c, showed poor precision in determining the additive dose, yielding an imprecise minimum age of 37 (±6) ka.

Discussion

Highstand stratigraphy

In the Jones Island area of southern New Jersey, the oldest subunit of the Cape May 1 member, QCM1a, exists entirely in the subsurface. The lithology of this unit, revealed in boreholes and vibracores, suggests a sandy offshore/bay-bottom environment of deposition. The shoreline during QCM1a time was located further inland, along the Cedarville Scarp (Fig. 3). A gravelly sand bar is present within the unit at the northeastern (landward) end of the study area. The basal gravels and coarse sands coincident with major radar reflection A (Figs 4, 5 & 7) are representative of a thin, transgressive systems tract (TST) deposited during the sea-level rise of QCM1a time. The overlying coarse sands in the landward section and the medium sands in the bayward section of the unit (Fig. 7) represent deposition in shallow and moderate depth waters during the QCM1a highstand, in a highstand systems tract (HST). The upper limit of unit QCM1a is unknown in this location because it has been removed during the transgressions associated with the overlying QCM1b and QCM1c units, along the TRS associated with major reflections B and C, respectively.

The overlying highstand units QCM1b and QCM1c mantle the surface of the lower terrace (Fig. 7). The lithology of QCM1b suggests deposition in a sandy nearshore environment to the southwest (bayward). To the northeast (landward), below the topographic high of Jones Island, the coarse sands in borehole OD00-J10 (above the basal gravel), contrasted with the medium sands in OD00-J8 and J11, suggest shoreface and backshore, respectively, depositional environments.

This evidence is consistent with the geomorphic interpretation that Jones Island represents a stranded estuarine shoreline. Figure 7 shows the sequence-stratigraphic interpretation of the basal gravels and overlying sands of QCM1b as a thin TST and a continuous backshore to nearshore HST, respectively. The uppermost silty, pebbly sands of this unit are interpreted as a thin regressive systems tract (RST), deposited during the sea-level fall of QCM1b time. This unit has been incised along major reflection C by the transgressive event associated with unit QCM1c and has been removed completely bayward of GPR profile JI3 (Fig. 7).

While not delineated on topographic maps as an area of relief, topographic data collected herein, combined with GPR profiles JI1 and JI3 (Fig. 6) and the lithology seen in vibracores OD99-J1 and J2 (Fig. 7), suggest that unit QCM1c contains a low, stranded estuarine shoreline complex. Above the gravelly coarse sands of a thin TST at the base of this unit in vibracore OD99-J1 is a medium to coarse, pebbly sand deposit, indicating a shoreface to shallow nearshore environment (Fig. 7). This same interval in vibracore OD99-J2, further bayward (Fig. 7), contains a medium, silty to pebbly sand deposit, suggesting slightly deeper water in a moderate-depth nearshore or bay bottom environment. These bayward-fining sediments, combined with the landward-sloping internal reflections seen in QCM1c, landward of the topographic high in GPR profile JI1 (Fig. 6), support the interpretation of the middle section of this unit as a continuous backshore to nearshore HST. The uppermost silty, pebbly sands seen in vibracores OD99-J1 and J2 represent a thin RST, deposited as sea level fell in QCM1c time. The subtlety of these geomorphic features has been enhanced by the 75× vertical exaggeration used in the cross-section of Figure 7.

Age estimates

The OSL dates obtained in this study are not conclusive enough to assign the highstand units QCM1a, QCM1b and QCM1c to specific time periods within OIS 5. They do, however, suggest that multiple, higher than present highstands occurred within OIS 5. The sediments of QCM1a are saturated with respect to additive dose and so could be

Table 1. *Results of OSL analyses of highstand sediments of Cape May 1 submembers*

Unit	Lab #	Equivalent dose (Gy)	U (ppm)	Th (ppm)	K%	Moisture (%)	Dose rate (Gy/ka)	GSL age (ka)
QCM1c	UIC821	>39 ± 6	1.71 ± 0.22	3.93 ± 0.59	0.43 ± 0.01	14 ± 2	1.06 ± 0.06	>37 ± 6
QCM1b	UIC820	>80 ± 13	0.89 ± 0.11	2.02 ± 0.29	0.38 ± 0.01	14 ± 2	0.79 ± 0.05	>101 ± 15
QCM1a	UIC819	Saturated	4.42 ± 0.67	1.72 ± 0.25	0.18 ± 0.01	14 ± 2	N/A	N/A

of OIS 5 age or older. A ~125 ka, OIS 5e age of this unit is likely, nonetheless, because it correlates well with a highstand unit identified by O'Neal and McGeary (2002) at the globally recognized OIS 5e sea-level elevation of +5–6 m MSL along the Cedarville Scarp (Figs 1 & 3), adjacent to the study area. This interpretation is supported by the near-saturated state of the sediments of QCM1b, at 101 (±15) ka. With a possible range (albeit a minimum age) of 86–116 ka, unit QCM1b could possibly have been deposited in any of the warm-climate peaks indicated by the marine OIS record, though it lies closer to OIS 5a and 5c (Fig. 2). The poor-precision date of 37 (±6) ka for QCM1a is unlikely because such a highstand would have occurred during a globally recognized time of climate-induced lowered sea level. This unit was probably deposited during a highstand in late OIS 5, though an OIS 5e or a Holocene age cannot be completely discounted at this time.

Conclusions

GPR has successfully been used to delineate three, thin (3 m or less), unconformity-bounded highstand units within the Cape May 1 member of the Quaternary Cape May Formation on the northern margin of Delaware Bay, in southern New Jersey. Two newly identified younger submembers, designated QCM1b and QCM1c, were deposited during separate sea-level cycles within OIS 5. Their stranded shorelines are found well bayward of that of the lower, older submember, QCM1a, and exhibit subtle geomorphic expression as bay margin-parallel, sublinear topographic highs of 3 m relief or less. The shoreline of submember QCM1a (OIS 5e) is found along the Cedarville Scarp and was previously attributed to the whole of QCM1.

Radar was also successfully employed to accurately locate continuous vibracore and hand-auger sites, to correlate radar- and sediment-derived stratigraphy and to collect sediments for OSL dating. The geochronological analyses are suggestive, but inconclusive at this time. Whether units QCM1a, QCM1b and QCM1c are attributable to multiple sea-level events within OIS 5e alone, or to some combination of OIS 5e and 5c or 5a, their identification as highstand units deposited during distinct sea-level cycles within OIS 5 provides an improved record of higher than present sea-level fluctuation, at time scales shorter than commonly recognized in the mid-Atlantic region.

References

BELKNAP, D. F. 1979. *Application of Amino Acid Geochronology to Stratigraphy of Late Cenozoic Emerged Marine Units of the Atlantic Coastal Plain.* Ph.D. thesis, University of Delaware.

BRIDGE, J. S., ALEXANDER, J., COLLIER, R. E. LL. & GAWTHORPE, R. L. 1995. Ground-penetrating radar and coring used to study the large-scale structure of point-bar deposits in three dimensions. *Sedimentology*, **42**, 839–852.

COLMAN, S. M. & MIXON, R. B. 1988. The record of major Quaternary sea-level changes in a large coastal plain estuary, Chesapeake Bay, eastern United States. *Palaeogeography, Palaeoclimatology, Palaeoecology*, **68**, 99–116.

COLMAN, S. M., HALKA, J. P., HOBBS, C. H., MIXON, R. B. & FOSTER, D. S. 1990. Ancient channels of the Susquehanna River beneath Chesapeake Bay and the Delmarva Peninsula. *Bulletin of the Geological Society of America*, **102**, 1268–1279.

EL-ASMAR, H. M. & WOOD, P. 2000. Quaternary shoreline development: the northwest coast of Egypt. *Quaternary Science Reviews*, **19**, 1137–1149.

FITZGERALD, D. M., BALDWIN, C. T., IBRAHIM, N. A. & HUMPHRIES, S. M. 1992. Sedimentologic and morphologic evolution of a beach-ridge barrier along an indented coast; Buzzards Bay, Massachusetts. *In*: FLETCHER, C. H., III, & WEHMILLER, J. F. (eds) *Quaternary Coasts of the United States: Marine and Lacustrine Systems*. Society of Economic Paleontologists and Mineralogists Special Publications, **48.**, 65–75.

FORMAN, S. L., PIERSON, J. & LEPPER, K. 2000. Luminescence geochronology. *In*: NOLLER, J. S., SOWERS, J. M. & LETTIS, W. R. (eds), *Quaternary Geochronology, Methods and Applications.* American Geophysical Union, Reference Shelf, **4**, 157–176.

HEARTY, P. J. & KAUFMAN, D. 2000. Whole-rock amino-stratigraphy and Quaternary sea-level history of the Bahamas. *Quaternary Research*, **54**, 163–173.

HEARTY, P. J., KINDLER, P., CHENG, H. & EDWARDS, R. 1999a. A +20 m Middle Pleistocene sea-level highstand (Bermuda and the Bahamas) due to partial collapse of Antarctica ice. *Geology*, **27**, 375–378.

HEARTY, P. J., KINDLER, P., CHENG, H. & EDWARDS, R. 1999b. The Kaena highstand on O'ahu, Hawai'I: Further support for partial Antarctic ice collapse during marine isotope stage 11. *American Geophysical Union, Fall Meeting, December 13–17, San Francisco, Programs with Abstracts.*

HILL, M. C. & FITZGERALD, D. M. 1992. Evolution and Holocene stratigraphy of Plymouth, Kingston, and Duxbury Bays, Massachusetts. *In*: FLETCHER, C. H., III & WEHMILLER, J. F. (eds) *Quaternary Coasts of the United States: Marine and Lacustrine Systems*). Society of Economic Paleontologists and Mineralogists Special Publications, **48**, 45–56.

IMBRIE, J., HAYS, J. D. ET AL. 1984. The orbital theory of Pleistocene climate: support from a revised chronology of the marine $\delta^{18}O$ record. *In*: BERGER, A. L., IMBRIE, J., HAYS, J. D., KUKLA, G. & SALTZMAN, B. (eds) *Milankovitch and Climate, Part I.* Dordrecht, Kluwer, 269–305.

JOL H. M. & SMITH, D. G. 1991. Ground penetrating

radar of northern lacustrine deltas. *Canadian Journal of Earth Science*, **28**, 1939–1947.

JOL, H. M. & SMITH, D. G. 1992*a*. Geometry and structure of deltas in large lakes: a ground penetrating radar overview. *Special Papers, Geological Survey of Finland*, **16**, 159–168.

JOL, H. M. & SMITH, D. G. 1992*b*. Ground penetrating radar: recent results. *Canadian Society of Exploration Geophysics Recorder*, **27**, 15–20.

JOL, H. M., SMITH, D. G. & MEYERS, R. A. 1996. Digital ground penetrating radar (GPR): a new geophysical tool for coastal barrier research (examples from the Atlantic, Gulf and Pacific coasts). *Journal of Coastal Research*, **12**, 960–968.

LEATHERMAN, S. P. 1987. Coastal geomorphological applications of ground-penetrating radar. *Journal of Coastal Research*, **3**, 397–399.

LUDWIG, K. R., MUHS, D. R., SIMMONS, K. R., HALLEY, R. B. & SHINN, E. A. 1996. Sea-level records at ~80 ka from tectonically stable platforms: Florida and Bermuda. *Geology*, **24**, 211–214.

MEYERS, R. A., SMITH, D. G., JOL, H. M. & HAY, M. B. 1994. Internal structure of Pacific Coast barrier spits using ground penetrating radar. *Proceedings of the 5th International Conference on GPR, Waterloo Center for Groundwater Research, June 12–16, Kitchener, Ontario, Canada, 843–854.*

MIXON, R. B. 1985. *Stratigraphic and Geomorphic Framework of Uppermost Cenozoic Deposits in the Southern Delmarva Peninsula, Virginia and Maryland.* United States Geological Survey Professional Papers, **1067–G**.

NEWELL, W. L., POWARS, D. S., OWENS, J. P., STANFORD, S. D. & STONE, B. D. 2000. *Surficial Geological Map of Central and Southern New Jersey.* United States Geological Survey Miscellaneous Investigations Series Maps, **I-2540-D**.

NUMMEDAL, D. & SWIFT, D. J. P. 1987. Transgressive stratigraphy at sequence-bounding unconformities; Some principles derived from Holocene and Cretaceous examples. *In*: NUMMEDAL, D., PILKEY, O. & HOWARD, J. (eds) *Sea-Level Fluctuations and Coastal Evolution.* Society of Economic Paleontologists and Mineralogists Special Publications, **41**, 241–259.

O'NEAL, M. L. 1997. *Ground Penetrating Radar Analysis of Composite Quaternary Coastal Terraces on the Northern Margin of the Delaware Bay.* Ph.D. thesis. University of Delaware.

O'NEAL, M. L. & MCGEARY, S. 2002. Late Quaternary stratigraphy and sea-level history of the northern Delaware Bay margin, southern New Jersey, USA: a ground penetrating radar analysis of composite Quaternary coastal terraces. *Quaternary Science Reviews*, **21**, 929–946.

O'NEAL, M. L., WEHMILLER, J. F. & NEWELL, W. L. 2000. Amino acid geochronology of Quaternary coastal terraces on the northern margin of Delaware Bay, southern New Jersey, USA. *In*: GOODFRIEND, G. A., GOODFRIEND, G. A., COLLINS, M. J., FOGEL, M. L., MACKO, S. A. & WEHMILLER, J. F. (eds) *Perspectives in Amino Acid and Protein Geochemistry.* Oxford University Press, New York, 301–319.

OWENS, J. P. & DENNY, C. S. 1979. *Upper Cenozoic Deposits of the Central Delmarva Peninsula, Maryland*

and Delaware. United States Geological Survey Professional Papers, **1067–A**.

OWENS, J. P. & MINARD, J. P. 1979. *Upper Cenozoic Sediments of the Lower Delaware Valley and the Northern Delmarva Peninsula, New Jersey, Pennsylvania, Delaware and Maryland.* United States Geological Survey Professional Papers, **1067–D**.

RAMSEY, K. W. 1993. Geologic Map of the Milford and Mispillion River Quadrangles. Delaware Geological Survey Geologic Map Series, **8**, scale 1 : 24,000.

RAMSEY, K. W. 1997. Geology of the Milford and Mispillion River Quadrangles. Delaware Geological Survey Reports of Investigations, **55**.

RIGGS, S. R. & BELKNAP, D. F. 1988. Upper Cenozoic processes an environments of margin sedimentation. *In*: GROW, J. A. & SHERIDAN R. E. (eds) *U.S. Atlantic Continental Margin.* Geological Society of America, Boulder, Colorado, The Geology of North America, **1–2**, 131–176.

ROSTAMI, K., PELTIER, W. R. & MANGINI, A. 2000. Quaternary marine terraces, sea-level changes and uplift history of Patagonia, Argentina: comparisons with predictions of the ICE-4G (VM2) model of the global process of glacial isostatic adjustment. *Quaternary Science Reviews*, **19**, 1495–1525.

SHERIDAN, R. E., ASHLEY, G. M., MILLER, K. G., WALDNER, J. S., HALL, D. W. & UPTEGROVE, J. 2000. Offshore-onshore correlation of Upper Pleistocene strata, New Jersey coastal plain to continental shelf and slope. *Sedimentary Geology*, **143**, 197–207.

SUGARMAN, P. J., MILLER, K. G., OWENS, J. P. & FEIGENSON, M. D. 1993. Strontium-isotope and sequence stratigraphy of the Miocene Kirkwood Formation, southern New Jersey. *Bulletin of the Geological Society of America*, **105**, 423–436.

SZABO, B. J. 1985. Uranium-series dating of fossil corals from marine sediments of the United States coastal plain. *Bulletin of the Geological Society of America*, **96**, 398–406.

TOSCANO, M. A. 1992. Record of oxygen isotope stage 5 on the Maryland Inner Shelf and Atlantic Coastal Plain - a post-transgressive-highstand regime. *In*: FLETCHER C. H., III & WEHMILLER, J. F. (eds) *Quaternary Coasts of the United States, Marine and Lacustrine Systems.* Society of Economic Paleontologists and Mineralogists, Special Publications, **48**, 89–99.

TOSCANO, M. A. & LUNDBERG, J. 1999. Submerged Late Pleistocene reefs on the tectonically-stable S.E. Florida margin: high-precision geochronology, stratigraphy, resolution of substage 5a sea-level elevation, and orbital forcing. *Quaternary Science Reviews*, **18**, 753–767.

TOSCANO, M. A., KERHIN, R. T., YORK, L. L., CRONIN, T. M. & WILLIAMS, S. J. 1989. *Quaternary Stratigraphy of the Inner Continental Shelf of Maryland.* Maryland Geological Survey Reports of Investigations, **50**.

VAN HETEREN, S., FITZGERALD, D. M. & MCKINLAY, P. A. 1994. Application of ground-penetrating radar in coastal stratigraphic studies. *Proceedings of the 5th International Conference on GPR, June 12–16,* Waterloo Center for Groundwater Research, Kitchener, Ontario, Canada, 869–881.

WEHMILLER, J. F. & MILLER, G. H. 2000. Aminostratigraphic dating methods in Quaternary geology. *In*:

NOLLER, J. S., SOWERS, J. M. & LETTIS, W. R. (eds) *Quaternary Geochronology, Methods and Applications.* American Geophysical Union, Reference Shelf, **4**, 187–222.

WEHMILLER, J. F., YORK L. L., BELKNAP, D. F., & SNYDER, S. W. 1992. Theoretical correlations and lateral discontinuities in the Quaternary aminostrati-graphic record of the U.S. Atlantic coastal plain. *Quaternary Research*, **38**, 275–291.

WYATT, D. E. & TEMPLES, T. J. 1996. Ground-penetrating radar detection of small-scale channels, joints and faults in the unconsolidated sediments of the Atlantic coastal plain. *Environmental Geology and Water Sciences*, **27**, 219–225.

This page intentionally left blank

GPR stratigraphy used to infer transgressive deposition of spits and a barrier, Lake Bonneville, Stockton, Utah, USA

DERALD G. SMITH[1], CHRIS J. SIMPSON[1,2], HARRY M. JOL[3], RICHARD A. MEYERS[1] & DONALD R. CURREY[4]

[1]*Department of Geography, University of Calgary, Calgary, Alberta, T2N 1N4, Canada (e-mail: dgsmit@ucalgary.ca)*

[2]*Present address: Department of Geography, Simon Fraser University, Burnaby, British Columbia, V5A 1S6, Canada*

[3]*Department of Geography, University of Wisconsin-Eau Claire, Eau Claire, WI 54702-4004, USA*

[4]*Department of Geography, University of Utah, Salt Lake City, Utah, 84112-1183, USA*

Abstract: Ground penetrating radar (GPR) stratigraphic profiles of the classic cross-valley barrier and associated spits of Late Pleistocene Lake Bonneville, near Stockton, Utah, are used to infer transgressive depositional style and internal sedimentary structures. From onlapping patterns of radar reflections, which mimic subsurface stratigraphy, we reconstruct the following depositional sequence and style: (1) at the north end of the Rush Valley, the barrier formed by vertical accretion while keeping pace with hydro-isostatic-forced basin subsidence and/or slow lake-level rise; (2) a reorientation of the longshore transport pathway, induced by continued basin subsidence and/or a lake-level rise, produced a spit that prograded 2.5 km southwestward into Rush Valley. The NW-dipping radar reflections from the spit onlap SE-dipping reflections from the back-barrier, indicating that this spit was deposited after the barrier; (3) a final rise in lake level and/or basin subsidence again reoriented longshore transport and deposited the smaller upper spit. Radar reflections from the upper spit onlap the proximal eastern margin of the Stockton spit. This upper spit is the final landform deposited during the Bonneville highstand. The depositional sequence inferred from radar stratigraphy agrees with the transgressive hypothesis formulated in 1890 by G. K. Gilbert.

Located in northwestern Utah State, Late Pleistocene Lake Bonneville at its highstand inundated 51 000 km² of interconnected fault-block basins up to an elevation of 1552 m, with a maximum depth of 300 m (Gilbert 1890; Currey 1990). Beginning sometime after 28 ka, Lake Bonneville began rising from levels comparable to those of modern-day Great Salt Lake and culminated at the Bonneville highstand shoreline for approximately 500 a at 15 ka (Oviatt 1997). Near the village of Stockton, coastal processes of the Bonneville highstand deposited a cross-valley barrier and two spits. At approximately 14.5 ka, sediments in Red Rock Pass catastrophically failed and lake discharge eroded an outlet spillway channel, drawing lake levels down 108 m (Malde 1968; Currey *et al.* 1983; Jarret & Malde 1987; O'Connor 1993). Following the outlet failure, water levels in Bonneville never again achieved the elevation of the former highstand (Currey *et al.* 1983).

Located between Tooele and Rush Valleys, 53 km southwest of Salt Lake City, Utah, the Stockton barrier and spit complex was first described and illustrated by Gilbert (1885, 1890; Figs 1 & 2). Threshold control at the Bonneville shoreline provided the stability necessary for construction of the landform assemblage. Within the assemblage, a 1.2 km-long upper-level spit occupies the highest position (1594 m), followed by the 2.5 km-long Stockton spit at 1585 m, and thirdly the 3.0 km cross-valley barrier (Stockton Bar, 1576 m). Burr and Currey (1988) hypothesize that the entire complex was deposited in 500 a, while Lake Bonneville was near its highstand limit.

While the eastern margin of Lake Bonneville received the largest influx of clastic sediment from

Fig. 1. Overview of the Stockton complex looking east (from Gilbert 1890). Location of view is on the left side of Figure 2. In the left distance is the Bonneville erosional shoreline and sediment transport corridor from Tooele Valley. The Stockton barrier extends diagonally across the diagram, while the southwest-trending Stockton spit is in the right-middle. The upper spit is barely detectable behind the Stockton spit. On either side of the barrier arcuate shorelines formed at lower lake levels are visible.
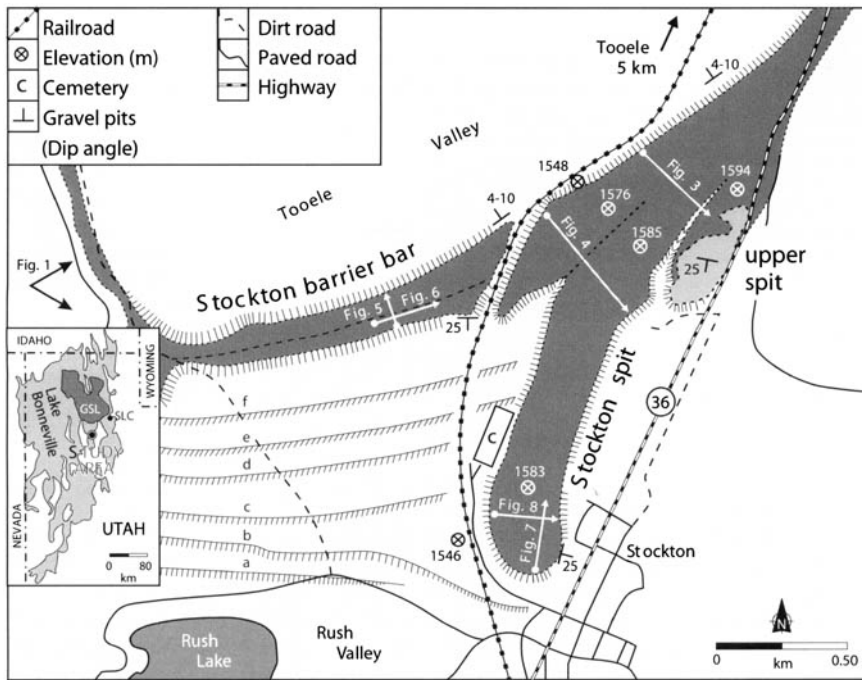
Fig. 2. Location of the barrier bar and spits near Stockton, Utah. Radar cross-sectional profiles are mapped on the barrier and spit surfaces. Letters a–f indicate the sequence and position of the prebarrier concave northward shorelines formed by waves from the north of prebarrier Lake Bonneville (Gilbert 1890).

rivers draining the Uinta and Wasatch mountains (Lemons *et al.* 1996), the rest of the sub-basins' coastal deposits were derived from alluvial fans and weathered bedrock. In the study area, waves and longshore currents, and possibly moving blocks of shore ice, eroded gravel and boulders from nearby alluvial fans in the Tooele Valley and deposited the barrier-and-spit complex (Fig. 1; Gilbert 1890; Burr & Currey 1988).

Four gravel-pit exposures are present within the

complex (Fig. 2). The largest is a 26 m-deep rail-road-cut through the barrier. Though largely concealed by colluvium, the uppermost *in situ* deposits exhibit gently inclined (4–10°) strata dipping northward and steeper-dipping (25°) strata to the south. Eastward-inclined strata at 25° are visible in the upper portion of an exposure near the distal end of the Stockton spit. At the distal end of the upper spit, a third exposure shows gravel beds dipping up to 25° SW. The fourth exposure, in the most proximal part of the spit-and-barrier complex, shows gravel beds dipping 4–10° NW, similar to the north side of the railroad-cut.

Grain size of the sediment (foundation) beneath the barrier and spit is uncertain. Gilbert (1890) suggested that a series of northward concave (plan view), stepped, palaeobeach strandlines located up to 2 km south of the back-barrier were deposited in a sequence of steps as shore positions moved progressively northward (see a [lowest] to f [highest] in Fig. 2). Since the present barrier consists of gravel, it therefore seems reasonable that the sub-barrier foundation also consists of beach gravel. Presently, strandlines (shorelines a–f, Fig. 2) located south of the barrier are mantled with a silt-rich fine-grained sediment, probably deposited in quiescent water following formation of the barrier. Gilbert (1890) also suggested that beneath the northward-accreted beach sequence (a–f, Fig. 2) a lower but reversed sequence may have been deposited earlier. If beach gravel underlies the barrier, it is probable that compaction of sub-barrier sediment is insignificant and cannot account for the elevation differences between the barrier and upper spit.

Gilbert (1890) determined that the shoreline of the Bonneville phase was not horizontal on a regional scale. The Bonneville shoreline, for example, is 74 m higher along the Lakeside Mountains (near the basin centre) than those near the Red Rock Pass. Similarly, the lower Provo shoreline (equivalent to Red Rock Pass) at mid-basin was bowed upward to a maximum of 59 m. Gilbert (1890) attributed these strandline deformations to hydro-isostatic rebound following removal of the Lake Bonneville water load. Without the aid of internal stratigraphic exposures, Gilbert (1890) hypothesized, on the basis of hydro-isostatic lake water influence on the crust, that the cross-valley barrier and spits near the village of Stockton were deposited in a transgressive sequence (from north to southeast) during the Bonneville highstand.

The objectives of our research were two-fold. The first was to test whether ground penetrating radar (GPR) could detect onlapping structures of younger landforms over older features, thus providing a useful geophysical approach to determine the depositional sequence (transgressive or regressive)

of other coastal landforms . The second objective was to explore the internal sedimentary structure of the barrier and spits with GPR and, from the reflection patterns of sedimentary structures, to interpret palaeodepositional processes.

GPR methodology

GPR can provide high-resolution lithostratigraphic profiles to depths of 70 m in sand and gravel under ideal conditions (Smith & Jol 1995). A pulse of high-frequency electromagnetic energy (EM), usually in the 10–1000 MHz range, is transmitted into the ground and is partially reflected back to the surface because of changes in bulk electrical properties. This permits identification of contacts, including changes in sediment grain size (facies change), mineralogy, density, bedrock contact and water content (Davis & Annan 1989). Quartz-rich clastic sediments free of silt, clay, caliche and brackish–saline groundwater produce the best results (Jol & Smith 1991). Sediments in the barrier and spits in this study are, for the most part, dry except for the upper metre of soil, which, on a seasonal basis, is occasionally snow-covered (0–30 cm), saturated and frozen. Where minor amounts of tufa and caliche are present in the barrier, radar penetration with 50 MHz antennae is limited to depths of 14 m, whereas 27 m depths are attainable in the 'cleaner' spit sediment. GPR theory and methodology are discussed at length elsewhere (Ulriksen 1982; Davis & Annan 1989).

GPR profiles presented here were acquired using a pulseEKKO IV system in reflection survey mode with a 1000 V transmitter (pulser voltage) and 50 MHz antennae. Antennae separation of 2 m (oriented perpendicularly to the direction of movement) and 1 m step intervals (equal to one vertical wiggle trace) were used in order to maximize penetration while maintaining high stratigraphic resolution (0.5–1.0 m, assuming a two-way velocity of $0.1 \, m \, ns^{-1}$). Each trace was vertically stacked 64 times with a sampling rate of 800 ps. Profiles were processed and plotted using pulseEKKO IV (version 4.2) software with automatic gain control. Depth scales are determined using an average near-surface velocity determined from common mid-point surveys (CMP) conducted at each site (Davis & Annan 1989). For the Stockton study area, two-way travel velocities of $0.12 \, m \, ns^{-1}$ and $0.14 \, m \, ns^{-1}$ for the barrier and spits, respectively, were calculated and consistent. Each profile was topographically corrected using laser-levelled data. The two uppermost continuous reflections in all profiles represent air- and ground-wave arrivals, respectively, and are not part of the stratigraphic data. The ground wave is the datum from which depth measurements are made. Reflec-

tions below the ground wave are interpreted to represent stratigraphy and, when continuous, represent time lines of sedimentation.

A total of 7000 m of radar profiles along 33 different tracks were shot on the barrier and two spits at frequencies of 100, 50, 25 and 12.5 MHz; due to space limitations in this paper and repetitive stratigraphy, we will present 1457 m of the 50 MHz data in six profiles (Fig. 2). Two nearly parallel profiles, 400 m apart, shot across the northern section of the spits and barrier determined the sequence of landform deposition. Two other profiles shot along the mid-barrier, cross-wise and lengthwise, helped determine the barrier style of deposition. Two final profiles shot cross-wise and lengthwise at the distal end of the Stockton spit determined its depositional style.

Radar stratigraphy results

Across the spits and barrier, a 400 m-long radar profile (oriented 132° relative to geographic north, as are all subsequent measurements) from mid-barrier to the crest of the upper spit reveals radar stratigraphy and sequence of deposition (Figs 3 & 4). NW-dipping reflections along the northwestern margin of the upper spit onlap SE-dipping reflections on the southeastern side of the Stockton spit. Between the Stockton spit and barrier, NW-dipping reflections along the northwestern margin of the spit onlap SE-dipping reflections in the back-barrier. A second radar profile (450 m), located 400 m southeastward of Figure 3 and oriented 140° was shot across only the barrier and Stockton spit (Fig. 4). This profile shows a similar radar stratigraphic relationship to that in Figure 3; NW-dipping reflections from the northwestern margin of the spit onlap SE-dipping reflections of the back-barrier.

Two GPR profiles were shot on the barrier 700 m west of the railroad track (Fig. 2). The south–north 110 m profile shot across the width of the barrier shows stacked convex stratigraphy (Fig. 5). The southern portion of the barrier is dominated

by steeply SW-inclined (25°) reflections which rest against the convex reflections. The northern side of the barrier shows less steep reflections inclined 4–10°. A 50 m long GPR profile shot from west to east, parallel to the trend of the barrier, shows horizontal reflections to a depth of 14 m (Fig. 6).

At the distal end of the Stockton spit two GPR profiles were shot (Fig. 2), one 215 m-long, oriented longitudinally along the spit axis (Fig. 7), the other 245 m-long, oriented across the spit (Fig. 8). The longitudinal profile has an azimuth of 10° and begins at the upper break in slope at a United States Geological Survey monument. Station 200 m intersects the cross-spit profile in Figure 8 at station 175 m. The cross-spit profile (Fig. 8) was oriented 100° from west to east, beginning and ending at the upper break in slope. Figure 7, between stations 70 m and 190 m, shows two packages of inclined strata, both dipping 25° southward, separated by a prominent horizontal reflection. The cross-spit profile exhibits convex-shaped reflections between stations 165 m and 245 m (Fig. 8). Steeply inclined (25°) westerly reflections between stations 0 m and 165 m constitute the majority of the spit volume.

Transgressive sequence and internal structures

Radar stratigraphy from the two spits and barrier (Figs 3 & 4) reveals a southeastward transgression,
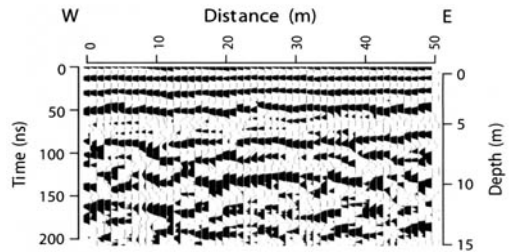
Fig. 6. GPR profile showing horizontal reflections shot from west to east along the barrier axis.
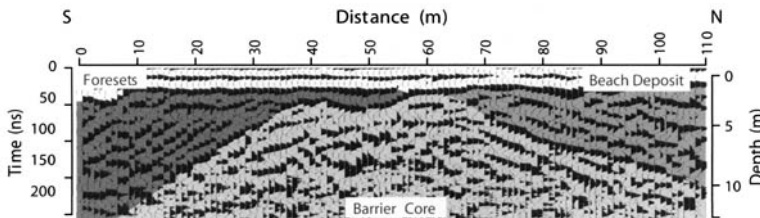

Fig. 5. South–north GPR profile across the barrier shows stacked convex reflections as part of the core. Width of foreset beds on the south margin increases towards the east and accounts for the remainder of the barrier. This westward-thinning wedge of foreset facies indicates that duration of deposition was limited relative to other facies. Poor quality of data is due to tufa and/or caliche matrix in the near-surface gravel.
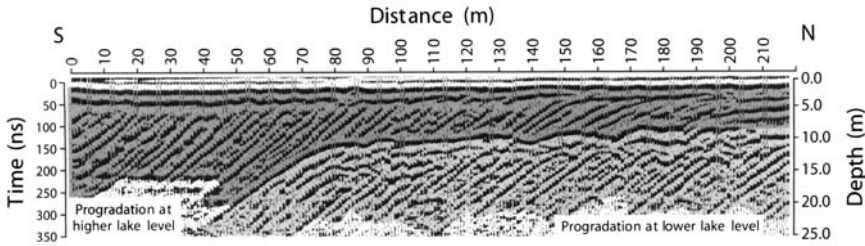
Fig. 7. At the distal end of the Stockton spit, a longitudinal radar profile shows two sequences of steeply inclined (25°) foreset strata separated by a prominent continuous horizontal reflection.
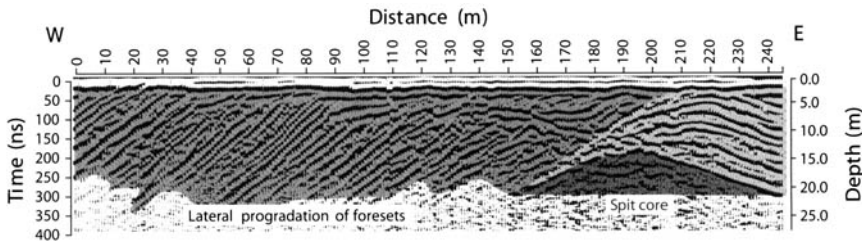
Fig. 8. Cross-sectional radar profile of the distal Stockton spit, showing one set of convex-shaped reflections buried by another. Extensive steeply-inclined westward-dipping foresets make up the majority of the Stockton spit.

influenced by a basin subsidence and/or lake level rise and shifting longshore transport routes (Fig. 9a). Onlapping patterns of radar reflections demonstrate that barrier strata underlie sediment of the Stockton spit, which in turn underlies sediment of the upper spit. Both profiles shot 400 m apart show the same pattern to depths of about 20 m.

The first feature to form at Stockton was the barrier, which received at least 26 m of gravel, mostly by vertical accretion, probably keeping pace with basin subsidence, as proposed by Burr and Currey (1988). This is apparent in the cross-barrier profile shown in Figure 5, which reveals a stacked sequence of convex-shaped reflections constituting the barrier core. Horizontal reflections shown in a GPR profile, shot from west to east along the barrier axis, are indicative of vertical aggradation (Fig. 6). This pattern precludes the possibility of westward progradation of spit foresets in building the barrier, as might be expected, and is typical in most stable large lakes (Smith & Jol 1992).

Continued basin subsidence initiated a second phase of barrier deposition. For a short period of time, gravel washed over the barrier, widening it, as it prograded southward into the Rush Valley, as indicated in Figures 3, 4 and 5, by steeply dipping foreset beds (~25°). These foresets (underwater angle of repose) extend from the top of the barrier core, suggesting that their formation began after it vertically accreted to its final thickness. The steeply inclined foresets on the back-barrier (between sta-

tions 80 m and 160 m in Fig. 3, and stations 110 m and 280 m in Fig. 4) rest directly on a prominent basal reflection.

Gently inclined reflections (4–10°) on the northern side of the barrier and spits are associated with the palaeobeach, which we believe was severely impacted by large storm waves. These reflection angles contrast with the steeper reflections imaged in the foreset beds. Foresets with 25° slopes represent the steepest underwater angle of repose for gravel and sand that can be maintained before failure.

As barrier deposition progressed, storm waves overtopped the barrier, transporting silt and clay into the comparatively quiescent waters in the back-barrier area (Rush Valley). Along with fine-grained material from sources within the Rush Valley, this material settled and formed a silt-dominated mud bed. This mud facies, exposed on the ground surface south of the barrier, causes a probable perched water table or saturated sand and silt, imaged as a prominent basal reflection between stations 80 m and 340 m (Fig. 3), below which there is a notable loss of signal return. All antennae frequencies (100, 50, 25 and 12.5 MHz) shot along this profile exhibited the same basal reflection, followed by a loss of signal return, suggesting that the reflector is saturated silt and clay, which would explain the prominent reflection.

Further subsidence and/or lake-level rise reoriented the longshore transport corridor to bypass the

barrier and begin deposition of the Stockton spit. The convex-shaped core of the Stockton spit is located between stations 270 m and 365 m (Fig. 3), and stations 320 m and 440 m (Fig. 4). Between stations 160 m and 190 m (Fig. 3), and 260 m and 300 m (Fig. 4), steeply inclined radar reflections of the northwestern spit margin onlap opposite dipping back-barrier sediments.

Radar stratigraphy in Figure 7 shows a southward-prograding two-storied foreset at the distal end of the Stockton spit. The two packages of steeply inclined (25°) foreset beds, one above the other, are separated by a prominent horizontal reflection (Fig. 7). The lower foreset package is interpreted as the initial spit core deposited at a lower lake level. The prominent horizontal reflection may represent a beach deposit or a sand bottomset layer deposited in advance of the upper foreset package. Because this layer is probably finer-grained and retains moisture, it will provide a different radar-resistive characteristic than adjacent gravel facies. Given that progradation rather than vertical accretion of spits is most common in stable water bodies (Smith & Jol 1992), the second foreset package may have been a response to a sudden lake-level rise. A rapid increase in lake level allowed the upper package of foresets to overtop and prograde beyond foresets in the initial spit core. The cross-spit reflection patterns shown in Figure 8 confirm the presence of two separate spit cores. The initial spit core is represented by the lowermost set of convex-shaped radar stratigraphy, which is overlain by convex reflectors of the second spit core deposited at a higher lake level. At station 200 m on Figure 8 (intersection with Fig. 7), the difference in elevation between the two spit cores is approximately 7.5 m. The core of the upper level foreset package is, however, offset to the east and is at a maximum thickness near station 220 m (Fig. 8). Thus, we hypothesize a rise in lake level of 8–10 m in the Stockton area. A significant portion (70%) of the Stockton spit, between stations 0 m and 180 m (Fig. 8), was deposited by westward accretion of foresets . The irregular stepping-up nature from east to west of the nearly flat reflections at the top of the foresets (Fig. 8) suggests minor increases in lake level during westward progradation.

Further subsidence and/or lake-level rise reoriented the longshore transport pathway 400 m further east to deposit the upper spit. Radar stratigraphy shows inclined strata from the upper spit lapping onto the southeastern side of the Stockton spit (between stations 340 m and 375 m in Fig. 3). An additional, yet smaller, uppermost spit was described by Gilbert (1890); its relationship to the present upper spit would most probably have followed the same depositional onlapping pattern as the other two spits described in this study.

Discussion

Our results from GPR-imaged stratigraphy of the Stockton barrier and spits clearly demonstrate the sequence of deposition as being landward or transgressive (Fig. 9a). This depositional sequence is opposite (regressive, Fig. 9b) to the lakeward progradational sequences that one might interpret without previous knowledge of the isostatic subsidence that accompanied lake-level rise. From either near-stable or falling water-level situations, such as those in the Great Lakes (Law 1989; Kesik *et al.* 1990; Chrzastowski & Thompson 1994; Thompson & Baedke 1995) or northern Alberta (Smith & Jol 1992), barriers and spits generally follow a regressive sequence.

In gravel, high-resolution GPR can show palaeodepositional patterns of subsurface stratigraphy, from which depositional style can be interpreted. Most barriers in the Great Lakes and northern Alberta (Lake Athabasca) formed initially as prograding spits across a bay (our unpublished GPR data from Hamilton, Ontario, Lake Ontario and Duluth, Minnesota, Lake Superior). For the Stockton barrier south–north- and west–east-oriented
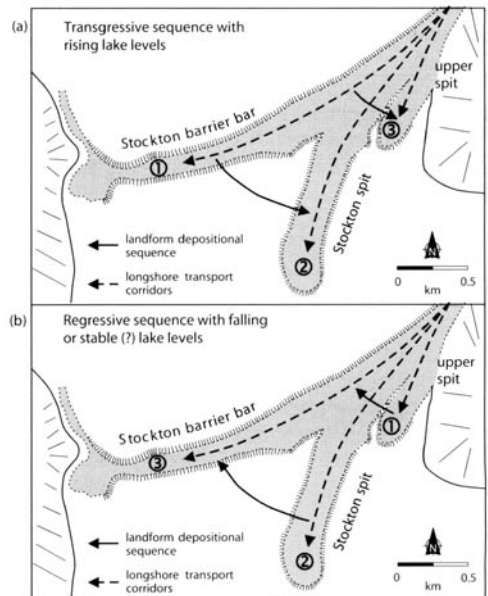

Fig. 9. (**a**) Transgressive sequence as proposed by Gilbert (1890) and Burr and Currey (1988) in response to basin subsidence and/or rising lake level. (**b**) Regressive sequence expected if features had formed during a period of stable or falling lake levels.

radar profiles show stacked convex and horizontal reflections, respectively, which can only be interpreted as slow vertical accretion, not progradation. To our knowledge, depositional style of the Stockton barrier is different from existing models (Law 1989; Kesik *et al.* 1990; Chrzastowski & Thompson 1994; Thompson & Baedke 1995).

Internal stratigraphy and depositional style of the Stockton spit, though complex, is similar to others of Holocene age (Nielsen *et al.* 1984; Nielsen 1988; Smith & Jol 1992). In spite of the large volume of sediment stored in nearby alluvial fans, it is incredible that so much large-calibre sediment was transported in a short period of time, perhaps 400–600 a, while threshold control existed (Burr & Currey 1988; Oviatt *et al.* 1992). Perhaps storms of that period (15.0–14.5 ka) were of such high magnitude, frequency and duration that nothing comparable exists today. The influence of longshore transport aided by shore ice is unknown. Transport of boulders frozen into large sheets of moving shore ice could be an effective process and help explain the large number of boulder-sized clasts (30–40 cm b-axis) in the Stockton spit relative to the cobble-sized clasts in the barrier.

Our results confirm observations by Gilbert (1890) and Burr and Currey (1988) that, once coast gravel is emplaced, it is relatively resistant to wave erosion during subsequent rising and falling stages of lake level. This is expressed by the absence of truncated reflections that would represent planed-off parts of the barrier or Stockton spit. This might be explained by the minimal rounding that would have occurred given the short transport distances from the Tooele Valley alluvial fans. The angular to subangular fragments would interlock and become very resistant to entrainment. In spite of high-energy waves and vigorous longshore processes, our results suggest that coast gravel landforms in the foreshore zone of Lake Bonneville were scarcely modified. This opinion is supported by the relative inability of waves to modify either the proximal Stockton spit or barrier following basin subsidence and/or lake-level rise.

This study demonstrates the effectiveness of radar stratigraphy for interpretating depositional sequences of different coastal landforms. In addition, complex radar stratigraphy can be used to interpret depositional style and patterns of coastal features. Our GPR results verify the landward (southward) transgressive depositional sequence proposed by Gilbert (1890) and elaborated by Burr and Currey (1988). Their hypothesis was interpreted from coastal morphology and knowledge of Lake Bonneville water-level fluctuations and basin subsidence. Without prior extensive knowledge of a coastal suite of landforms, GPR is the quickest

and most cost-effective means of understanding depositional history.

It took over a hundred years and the advent of new technology (GPR) before Gilbert's (1890) hypothesis for the depositional sequence of the Stockton barrier and spit complex could be conclusively tested. The results confirm the work of Gilbert (1890) and show that no amount of technology can replace careful analysis and critical reasoning.

References

BURR, T. N. & CURREY, D. R. 1988. The Stockton bar. *In:* MACHETTE, M. N. (ed.) *In the Footsteps of G.K. Gilbert — Lake Bonneville and Neotectonics of the Eastern Basin and Range Province.* Utah Geological and Mineral Survey, 66–73.

CHRZASTOWSKI, M. J. & THOMPSON, T. A. 1994. Late Wisconsinan and Holocene geologic history of the Illinois–Indiana coast of Lake Michigan. *Journal of Great Lakes Research*, **20**, 9–26.

CURREY, D. R. 1990. Quaternary palaeolakes in the evolution of semidesert basins, with special emphasis on Lake Bonneville and the Great Basin, USA. *Palaeogeography, Palaeoclimatology, Palaeoecology*, **76**, 189–214.

CURREY, D. R., OVIATT, C. G. & PLYLER, G. B. 1983. Lake Bonneville stratigraphy, geomorphology, and isostatic deformation in west-central Utah. *In:* GURGEL, K. D. (ed.) *Geologic Excursions in Neotectonics and Engineering Geology in Utah: Guidebook Part IV.* Utah Geological and Mineral Survey Special Studies, **62**, 63–82,

DAVIS, J. L. & ANNAN, A. P. 1989. Ground penetrating radar for high-resolution mapping of soil and rock stratigraphy. *Geophysical Prospecting*, **37**, 531–551.

GILBERT, G. K. 1885. The topographic features of lake shores. *US Geological Survey Fifth Annual Report*: 1883–1884, 69–123.

GILBERT, G. K. 1890. Lake Bonneville. *US Geological Survey Monograph*, **1**.

JARRETT, R. D. & MALDE, H. E. 1987. Paleodischarge of the Late Pleistocene Bonneville Flood, Snake River, Idaho, computed from new evidence. *Bulletin of the Geological Society of America*, **99**, 127–134.

JOL, H. M. & SMITH, D. G. 1991. Ground penetrating radar of northern lacustrine deltas. *Canadian Journal of Earth Sciences*, **28**, 1939–1947.

KESIK, A. B., LAW, J. & McFALL, G. 1990. Geomorphology and geology of Lake Ontario; north shore. *In:*

McKENZIE, D. I. (ed) *Quaternary Environs of Lakes Erie and Ontario, Waterloo, ON*, Escart Press, 163–265.

LAW, J. 1989. *The Sandbanks Dune/Bay Barrier Complex, Prince Edward County, Ontario, Morphology and Change over the Past 1200 years*. Ph.D. thesis, University of Waterloo, Waterloo, Ontario.

LEMONS, D. R., MILLIGAN, M. R. & CHAN, M. A. 1996. Paleoclimatic implications of Late Pleistocene sediment yield rates for the Bonneville Basin, northern Utah. *Palaeogeography, Palaeoclimatology, Palaeoecology*, **123**, 145–159.

MALDE, H. E. 1968. The Catastrophic Late Pleistocene Bonneville Flood in the Snake River Plain, Idaho. US Geological Survey, Professional Papers, **596**, 52 pp.

NIELSEN, E. 1988. *Surficial Geology of the Swan River Area, Winnipeg, MB*. Manitoba Department of Energy and Mines, Mineral Resources Division.

NIELSEN, E., GRYBA, E. M. & WILSON, M. C. 1984. Bison remains from a Lake Agassiz spit complex in the Swan River Valley, Manitoba; depositional environment and paleoecological implications. *Canadian Journal of Earth Sciences*, **21**, 829–842.

O'CONNOR, J. E. 1993. *Hydrology, Hydraulics, and Geo-morphology of the Bonneville Flood*. Geological Society of America, Boulder, Colorado, Special Papers, **274**.

OVIATT, C. G. 1997. Lake Bonneville fluctuations and global climate change. *Geology*, **25**, 155–158.

OVIATT, C. G., CURREY, D. R. & SACK, D. 1992. Radiocarbon chronology of Lake Bonneville, eastern Great Basin, U.S.A. *Palaeogeography, Palaeoclimatology, Palaeoecology*, **99**, 225–241.

SMITH, D. G. & JOL, H. M. 1992. GPR results used to infer depositional processes of coastal spits in large lakes. *Geological Survey of Finland Special Paper*, **16**, 169–177.

SMITH, D. G. & JOL, H. M. 1995. Ground penetrating radar: antenna frequencies and maximum probable depths of penetration in Quaternary sediments. *Journal of Applied Geophysics*, **33**, 93–100.

THOMPSON, T. A. & BAEDKE, S. J. 1995. Beach-ridge development in Lake Michigan; shoreline behavior in response to quasi-periodic lake-level events. *Marine Geology*, **129**, 163–174.

ULRIKSEN, C. P. F. 1982. *Application of Impulse Radar to Civil Engineering*. Ph.D. thesis, Lund University of Technology, Lund, Sweden.

Sedimentary architecture and post-glacial evolution of Cheekye fan, southwestern British Columbia, Canada

CSABA ÉKES[1, 2] & PIERRE FRIELE[3]

[1]*Department of Geography, Simon Fraser University, Burnaby, B.C., Canada, V5A 1S6 (e-mail: ekes@sfu.ca)*

[2]*Present address: Terraprobe Geoscience Corp., 5210 Sunningdale Road, Burnaby, B.C., Canada, V5B 1M5*

[3]*Box 612, Squamish, B.C., Canada, V0N 3G0*

Abstract: The purpose of this paper is to examine the internal architecture and post-glacial evolution of Cheekye fan, British Columbia, Canada. Analysis of a large database of ground penetrating radar (GPR) profiles has allowed the identification of ten reflection configurations that characterize this high-energy environment. GPR profiles augmented with test-pit, well-log and radiocarbon data provided detailed subsurface information and revealed the large-scale internal architecture and Holocene sedimentation history of Cheekye fan. Based on a shift in reflection configuration with depth, GPR data appears to record a change in the mode of deposition through time. This data suggests that Cheekye fan is a paraglacial fan, largely a product of the geological past. This fact should be taken into consideration when making future hazard estimates.

This study was initiated to test the utility of ground penetrating radar (GPR) in imaging alluvial fans, a landform that has had little attention by GPR practitioners. Despite a growing body of alluvial fan literature, there remains a lack of understanding of the processes and controls influencing alluvial fan sedimentation (for discussion see Blair & McPherson 1992, 1994a; Hooke 1993; Blikra & Nemec 1998; Blair 1999). This is partly due to the lack of detailed stratigraphic information (Blair & McPherson 1994a). The paucity of data on the three-dimensional internal architecture of alluvial fans reflects the difficulty of drilling in these landforms and of finding appropriate sections for study. Recognizing the recent success of GPR to image the subsurface, it was felt that GPR could provide a means of reducing this sampling problem on alluvial fans. The production of long, continuous two-dimensional profiles with relatively deep penetration would allow major architectural elements and their interrelationships to be determined. This in turn would facilitate the interpretation of long-term fan evolution.

Of special interest on alluvial fans is the return frequency of the formative processes (e.g. flooding, debris flow, avulsion). Since the architectural elements delineated by GPR can be attributed to dominant sedimentary processes, a reliable model may help to determine the dominant process active on a fan, or whether a shift in the dominant process has occurred over time. However, a detailed hazard analysis is not possible without chronological control. Thus, GPR must be applied in conjunction with other investigative approaches.

Cheekye fan was selected for this investigation. It is located at the mouth of the Cheekye River, on the western flank of Mount Garibaldi within the southern Coast Mountains of British Columbia, about 70 km north of Vancouver (Fig. 1). Cheekye fan is a complex landform composed of Late Pleistocene, terraced, colluvial–glacial kame deposits (Friele & Clague 2002) and a Holocene alluvial fan, known as the lower Cheekye fan (Friele *et al.* 1999).

The community of Brackendale, within the Municipality of Squamish, is located on the distal portion of the southern sector of the lower fan. Development pressures have pointed to the need for a more thorough understanding of fan processes. In order to understand the magnitude and frequency of natural hazards and to provide recommendations for future development, an exten-
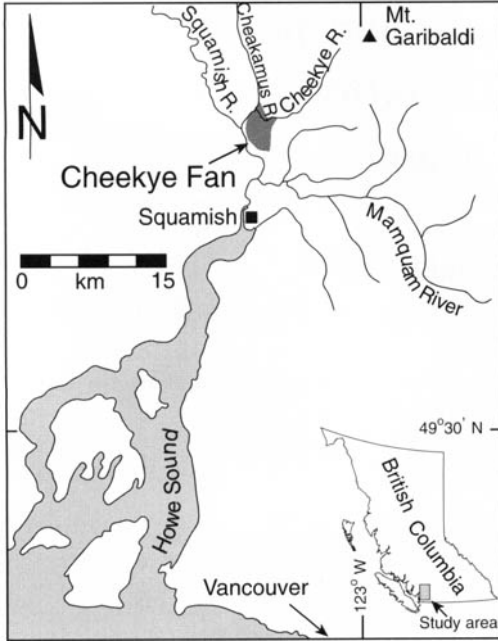
Fig. 1. Location of Cheekye fan in southwestern British Columbia, Canada.

Fig. 2. Location and extent of Cheekye fan and its catchment basin showing stream orders.

sive geotechnical review was undertaken by Thurber Engineering Ltd and Golder Associates Ltd (1993). Their 1993 report provides radiocarbon-dated stratigraphy from numerous shallow test pits, yielding a geochronological framework for the last 6 ka of fan development. This study builds on the Thurber and Golder (1993) dataset by extending their shallow test-pit data to a greater depth, allowing a better understanding of the processes that have affected the fan throughout the entire Holocene. This contributes to hazard analyses in a qualitative way by placing the reconstructed Late Holocene geochronology in the context of the entire post-glacial record.

Environmental setting

This is an area of complex geology. Late Cenozoic magma, generated as a product of subduction of the Juan de Fuca plate beneath the North American plate margin, produced the Garibaldi Volcanic Belt (Keen & Hyndman 1979; Green *et al.* 1988). Volcanism was active in the region during deglaciation when peléean-style eruptions built up the dacitic tuff breccia cone that surrounds Mount Garibaldi (Mathews 1952) (Fig. 2). Part of this tuff breccia cone was deposited on and against the valley glacier, about 10.6 ka BP (Friele & Clague 2002), and collapsed as the glacier melted, depositing an esti-

mated 2.9 km^3 of material in the Squamish River valley (Mathews 1952).

Prior to progradation of the Squamish River delta to its present position, the proto lower fan extended into the Howe Sound fjord as a fan-delta. The fan-delta was built during a period of higher sea level 10.2–9.8 ka BP and later developed into an alluvial fan as sea levels fell in response to isostatic rebound (Friele *et al.* 1999). Cheekye River had incised the ice-contact materials of the upper and middle fan by 10 ka BP (Clague *et al.* in press), providing abundant sediment for redeposition to the lower fan during this early period. The vertically structured lavas and pyroclastics underlying the western flank of Mount Garibaldi provided the predominant source of sediment available for delivery to the lower Cheekye fan in the Late Holocene. Ninety percent of the sediment delivered to the lower fan arrived in the first 4 ka of fan development (Friele *et al.* 1999).

Present climate is characterized by a mean annual rainfall of about 2200 mm, with wet winters and moist summers. Extreme rainfall produces floods in fall (rainfall) and winter (rain on snow). This modern climate has existed with minor variation for about 4.5 ka BP; however, during the early Holocene, mean annual precipitation was up to 40% less (Mathewes & Heusser 1981). Thus, the decline in sediment supply through the Holocene was accompanied by an increase in runoff (Fig. 3).

In summary, lower Cheekye fan is a paraglacial (*sensu* Church & Ryder 1972) alluvial fan, developed in a wet, west-coast climate. Fan growth was affected by dramatic changes in sediment supply, base level and climate throughout the Holocene. These shifts in controlling parameters probably conditioned shifts in the dominant processes, affecting the fan throughout the Holocene. Poten-
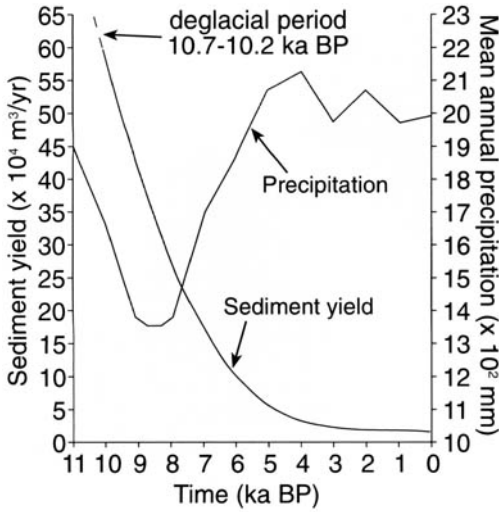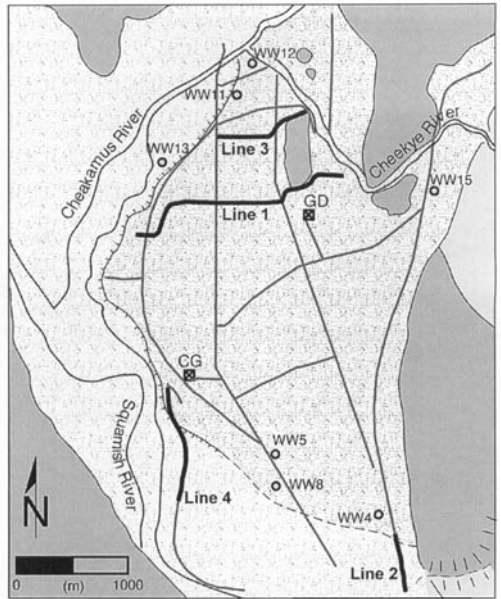
Fig. 3. Precipitation and best-fit curve showing declining sediment yield for Cheekye fan from onset of paraglacial period to present.

Fig. 4. Surficial geology map of Cheekye fan showing layout of GPR survey lines. Thick black lines show location of profiles shown in Figures 10–13. CG, Cheekye gravel pit exposure; GD, garbage dump exposure; WW, water well.

tial changes in sedimentation style are the subject of this paper.

Cheekye fan

Lower Cheekye fan (hereafter referred to as Cheekye fan) is bounded by the Cheakamus and Squamish Rivers to the west and by bedrock outcrops to the north and east, and grades into the Squamish floodplain to the south (Figs 2 & 4). The fan has a radius of 3–4 km, an average slope of 4.5% and covers an area of about 8.3 km² (Thurber & Golder 1993). The western edge of the fan is truncated by the Cheakamus and Squamish Rivers, producing a scarp about 15 m high in places (Fig. 5). The southern edge of the fan is graded to the Squamish River floodplain at about 10 m above sea level (a.s.l.). A number of bedrock outcrops exist in the northern portion of the fan, at the mouth of Cheakamus River, and an outcrop of ice-contact fan deposits exists near the apex. Debris flow materials cover about 50% of the fan outward from the apex (Thurber & Golder 1993).

Cheekye River flows in a westerly direction from the apex to the central part of the fan at 120 m a.s.l. (Figs 2 & 4). Along this proximal part of the fan, the channel is entrenched with a minimum of 5 m freeboard and is partly confined by bedrock outcrops. At 120 m a.s.l., the channel turns 90° to the north, discharging into Cheakamus River. No abandoned channels are evident on the surface. Downfan from the 120 m a.s.l. elevation, the fan is incised less than 5 m.

The stratigraphy of parts of the fan is exposed in a number of pits and cut-banks (Thurber & Golder 1993). The upper 10–15 m of fan sediment is a complex consisting of matrix-supported debris-flow diamicton and clast-supported, weakly planar bedded to massive sheetflood deposits (Figs 5 & 6).

Debris flow units vary in thickness from about 5 m in the proximal locations in the fan to 0.5–2 m in distal locations. Dates from about 15 m depth near the western edge of the fan indicate that this material has accumulated in the last 6600 years.

A 10 m-deep by 40 m-long pit at the Squamish municipal garbage dump exposed four distinct debris flow units, ranging from 0.5 m to 5.5 m in thickness, which overlie weakly stratified sheetflood gravels (Fig. 7). The surface unit is up to 5.5 m thick, massive, dark brown-grey, gravelly–bouldery, poorly sorted matrix-supported diamicton. The clasts are angular to subrounded and maximum clast size is 1 m in diameter. The larger clasts are composed of grey and purple porphyritic, dacitic to andesitic volcanic rock. Logs up to 80 cm in diameter are common at the base of this unit and provide an average age of 1315 (±83) yr BP (Fig.

Fig. 5. Western edge of Cheekye fan truncated by Squamish River. Cut face is *c*.15 m high and exposes predominantly horizontally bedded sheetflood gravels.

Fig. 6. Photograph of exposure at Cheekye Gravel pit showing crudely bedded sheetflood gravel. Outcrop is oriented perpendicular to flow direction. (Person lower left indicates scale.)

7). A date from beneath the lowest debris-flow unit yielded an age of 4810 (±80) yr BP (Ékes 2000).

Sheetflood gravel is exposed at the operating Cheekye Gravel gravel pit near the southwestern edge of the fan (Fig. 6). Two units of crudely bedded sheetflood gravel separated by a 0.8 m-thick moderately sorted debris-flow diamicton are exposed in a more than 100 m long, and in places 8 m high, NW–SE wall. The upper, 6 m-thick, grey, clast-supported gravel unit rests on a sharp, erosional contact. Mean clast size is 10–15 cm; maximum clast size is 80 cm. Clasts are sub-rounded–rounded and composed mostly of grey, green and purple rhyolite and green phyllite. Horizontally layered or tabular cross-bedded lenses of medium to coarse sand are visible within the gravel unit; these layers are 10–80 cm thick and can be followed over 10 m laterally. The large pebbles and

cobbles commonly exhibit imbrication. No grading is apparent; the largest clasts are found 3 m from the top of the unit. This unit appears massive, but poorly developed horizontal bedding is discernible locally (Fig. 6). Vertical and horizontal log casts are common.

Methods

GPR is a high-resolution geophysical tool based on propagation and reflection of electromagnetic waves (EM) in the frequency range 10–1000 MHz. Subsurface reflections are caused by changes in dielectric properties, controlled in unconsolidated materials primarily by pore filling, sediment type, stratification and grain size. Particularly in electrically low-conductive sediments, the GPR method has proved to be a powerful tool in environmental,

S   N
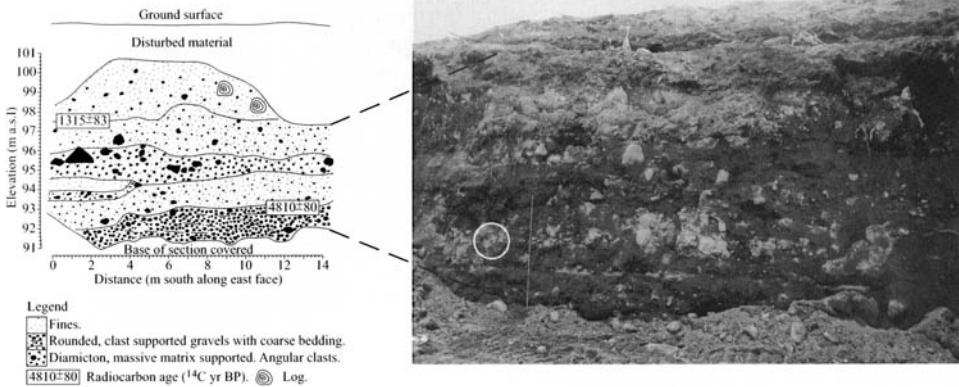
Fig. 7. Photograph and stratigraphy of debris flow diamicton at the Squamish municipal garbage dump exposure. Survey rod on photo is 3 m long. Hammer (circled) marks location of sample that yielded 4810 ($\pm$80) ^{14}C age.

hydrogeological, glaciological, permafrost, geotechnical and sedimentological studies (e.g. Beres & Haeni 1991; Bridge *et al.* 1995; Bristow 1995; Arcone 1996; Bristow *et al.* 1996; van Heteren *et al.* 1998; Moorman *et al.* 1988; Moorman & Michel 2000; Russel *et al.* 2001; Arcone & Delaney 2002; Olhoeft & Selig 2002).

Profiling by GPR is similar to sonar and seismic reflection profiling; the radar produces a short pulse of high-frequency electromagnetic energy that is transmitted into the ground. Some of the energy is reflected back to the surface due to a change in bulk electrical properties of different subsurface lithologies and the character of the interface (Davis & Annan 1989). At the surface, a receiver monitors reflected energy versus delay time. The pulse delay time from the energy transmitted into the ground and reflected back to the receiver is a function of the strength of energy transmitted into the ground, the EM propagation velocity through the sediment, the depth of subsurface reflectors and the character of the interface (Davis & Annan 1989; Jol 1993).

Contrasts in the dielectric constants of the different sediment types usually cause strong reflections from lithological boundaries in the subsurface (Jol & Smith 1991). The strength of the reflected signal is approximately proportional to the difference in dielectric constants of the sediment interface (Davis & Annan 1989). Changes in the dielectric constant also affect the rate of attenuation of energy passing through the ground. These effects enable the subsurface stratigraphy and ground-moisture conditions to be inferred from the character of the radar return signals (Jol & Smith 1992*a*).

GPR surveys on Cheekye fan were conducted along existing trails, roads and dykes (Fig. 4). A pulseEKKO IV system was used with a 400 V transmitter. The system consists of two unshielded antennae, a console unit and a display and data-storage unit (laptop). The GPR was powered by a 12 V battery and, for most surveys, was assembled on a golf cart to increase mobility and ease of operation (Fig. 8). All surveys presented here were carried out with the 50 MHz antenna for two reasons: (1) it provided the depth penetration required (10–30 m), and (2) it offered the resolution (1–2 m) that allowed the identification of the major alluvial fan facies and architectural elements. GPR data were collected in a step-recording mode, providing the best ground coupling and best data quality. Antenna separation was 1 m and 2 m; step size was 0.5 m and 1 m. The sections presented here are corrected for topography.

Common mid-point (CMP) gathers were measured in order to derive sediment velocities. CMP survey mode involves systematically increasing the antenna separation over a CMP. For horizontal reflectors, the layer velocity was then calculated from the recorded two-way travel times. The average near-surface velocity based on CMPs was 0.10 m ns^{-1}.

Data were processed using the pulseEKKO software package (V 4.2). Automatic gain control was applied for presentation. The number of stacks was 64 per trace. Low-pass temporal filtering (averaging seven traces) was applied to reduce random noise. The horizontal scale of all profiles is distance in metres and the vertical scale is shown as both two-way travel time in nanoseconds and

Fig. 8. PulseEKKO IV GPR field system outfitted with 50 MHz antennae set up for profiling: console and display unit attached to golf cart (1); transmitter antenna (2); receiver antenna (3); fibre-optic cable (4); survey line (5).

depth in metres based on near-surface velocity derived from CMP measurements. The profiles presented show a 4 : 1 vertical exaggeration unless stated otherwise.

GPR calibration

The reliability of GPR data interpretation is dependent on the experience of the interpreter and their familiarity with the Quaternary history of the area. On Cheekye fan, interpretation of GPR profiles was verified by stratigraphic information from outcrop data, well logs, test-pit descriptions and air photographic and topographical cross-section analysis. In addition, interpretation of radar facies was greatly aided by an extensive calibration exercise carried out on alluvial fans and related sediment bodies throughout southwestern British Columbia (Ékes 2000). As part of this project, over 95 km of GPR data from various sites in southern British Columbia were collected and analysed. These sites include various types of mass-movement deposits, fluvial environments and alluvial fans. Wherever possible GPR was calibrated against exposed outcrops (Ékes & Hickin 2001). The experience gained from conducting this regional calibration greatly enhanced our ability to understand GPR response and aided interpretation where other subsurface information was limited.

GPR facies

Radar facies are described in terms of reflection continuity, shape, amplitude, internal reflection configuration and external form using the approach applied by Jol & Smith (1991), Beres & Haeni

(1991), van Heteren *et al.* (1998) and Beres *et al.* (1999). Ten macro-scale radar facies distinguished by reflection patterns were identified on Cheekye fan profiles (Fig. 9). Macro-scale radar facies are defined here as a radar facies exceeding *c.* 2 m thickness and *c.* 40 m in horizontal distance on a two-dimensional GPR profile. The full lengths of all GPR profiles (Fig. 4) were analysed and inter-

Fig. 9. Summary of GPR facies and their interpretation for Cheekye fan.
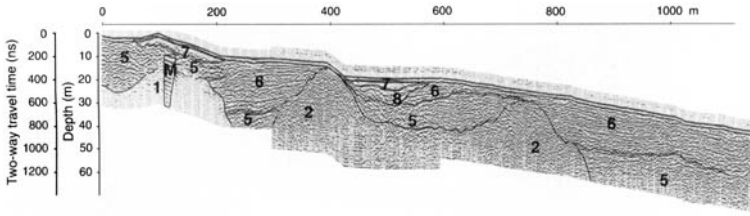
Fig. 10. Line 1 GPR profile (for interpretation of facies codes see Fig. 9). M, Multiples.

preted but only selected profiles are presented in this paper. A summary description of radar facies is given below. (For a more detailed facies description and analysis see Ékes & Hickin 2001).

1. Reflection-free facies

A reflection-free configuration may signify: (1) massive homogenous lithological units; (2) the presence of highly conductive dissolved minerals in groundwater, or (3) the presence of sediments containing high clay content that attenuates all of the EM signal (e.g. van Heteren *et al.* 1998). Attenuation of the EM signal is exhibited in some very prominent ways in units characterized by high conductivity losses. Examples are shown in Figures 10 and 11.

Till is a common deposit on the study area with high clay content. Boreholes WW11 and WW12 (Fig. 4), drilled on the northern section of the fan, encountered a 20 m-thick till unit below 12 m of fan gravel (Thurber & Golder 1993). The poorly defined reflection pattern and lack of penetration on profiles from the northern part of Cheekye fan are interpreted as till.

2. Bedrock

A macro-scale hyperbolic reflection pattern is identified on many radar profiles, most of which were collected in areas with nearby bedrock outcrops. Sections with hyperbolic facies are characterized by prominent irregular reflections that mark

the top of the bedrock unit. Their internal pattern is often one of stacked hyperbolas or diffractions taking the inverted chevron shape (Figs 10 & 12). Penetration within this facies is good, often greater than 800 ns (40 m). Examples of bedrock facies are given on Line 1 between 310 m and 855 m (Fig. 10), and on Line 3 between 0 m and 190 m (Fig. 12) sections.

3. Alluvial fan facies 1

Chaotic reflection pattern with wide-crown mesoscale diffractions occurs at 300 ns (15 m) or greater and is characterized by reflection discontinuity with hyperbolas of meso-scale. No stacking is apparent nor is the inverted chevron pattern present (Fig. 11). This reflection configuration is found on medial to distal parts of the fan in basal stratigraphic horizons.

This signal pattern is interpreted as having originated from bouldery debris-flow sediments. Diffractions point to the presence of boulders and the chaotic pattern indicates the lack of internal structure. The fact that this facies is found at the base and margin of the fan suggests that bouldery debris flows were the predominant processes in early fan formation and these events commonly reached the distal fan. These bouldery deposits may represent debris reworked from ice-contact materials of the upper and middle fan.

The pattern on Line 2 between 240 m and 555 m at 375 ns (18 m) depth (Fig. 11) is also interpreted as bouldery fan facies. Here, due to the closeness
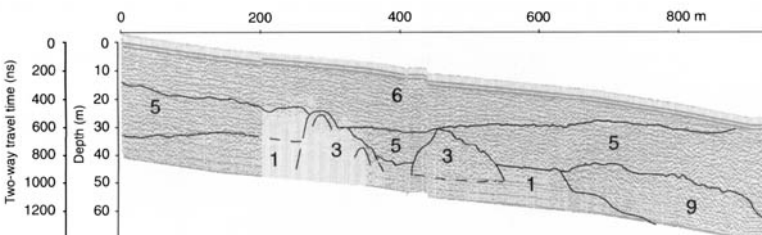
Fig. 11. Line 2 GPR profile (for interpretation of facies codes see Fig. 9).
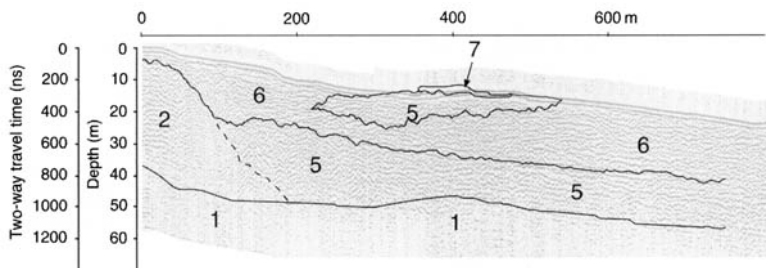
Fig. 12. Line 3 GPR profile and its interpretation. (for interpretation of facies codes see Fig. 9).

of a steep bedrock cliff (Fig. 4), this reflection pattern is interpreted as imaging rockfall sediments. There is field evidence of recent and past rockfalls and slides at this location (Ékes 2000).

4. Alluvial fan facies with utility cables and pipes

A chaotic reflection pattern is prevalent on GPR profiles which were collected along paved roads. These lines run through the community of Brackendale, where the survey was conducted partly on the asphalt road surface. Individual reflections are mostly discontinuous and often chaotic with prominent micro-scale hyperbolas. This facies is characterized by shallow penetration and by many multiples, indicating an environment generally not favourable for GPR surveys.

The high-frequency chaotic radar facies exclusively occurs on GPR lines from areas where the upper part of the natural stratigraphy has been disturbed (Fig. 13). Diffraction patterns caused by overhead power lines, trees and other large objects on or above the surface are common. Some of the individual hyperbolic reflections were caused by fire hydrants along the survey line. Multiples are caused by antenna ringing, probably due to the vicinity of metal objects such as fence posts or vehicles.

5. Alluvial fan facies 2

This facies is characterized by short, discontinuous, irregular or wavy reflection patterns and is prevalent in most transects (Figs 10–13). Closer to the apex of the fan this facies is generally present on the surface. With increasing distance from the apex this pattern is found at greater depth.

This facies is interpreted as having resulted from massive and weakly stratified debris flow and/or sheetflood deposits. The lack of stratification and lobate character of the massive, matrix-supported debris-flow units explain the discontinuous and chaotic nature of the radar reflections. The fact that this facies is more prevalent closer to the apex and at greater depth in distal areas suggests that there has been a decrease in the average runout distance of matrix-supported debris flows through the Holocene.

6. Alluvial fan facies 3

This facies is characterized by strong, surface-parallel, horizontally continuous reflections, which can be followed over several hundred metres (Figs 10–13). This pattern is prevalent on the majority of the transects. Generally it is found at younger stratigraphic positions on the fan and is more common with increasing distance from the apex.
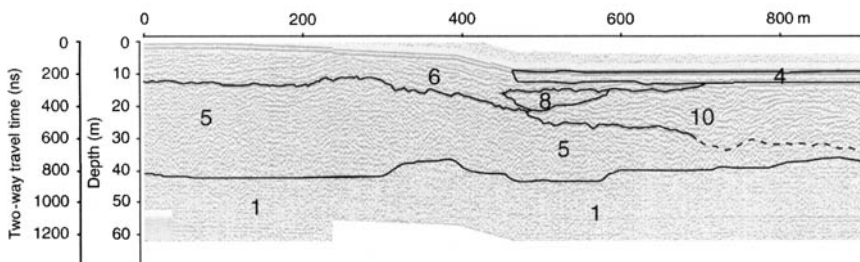
Fig. 13. Line 4 GPR profile (for interpretation of facies codes see Fig. 9).

This facies is interpreted on the basis of well logs, shallow test pits and exposures, as well as GPR reflection pattern, as horizontally bedded sheetflood sand and gravel and clast-rich, debris-flow diamicton.

7. Alluvial fan facies 4

This facies is characterized by a chaotic reflection pattern and poor signal penetration. The best examples are found on profiles collected in the vicinity of Squamish municipal garbage dump. Elsewhere, this pattern is found in a near-surface position; e.g. on Line 1 (60–210 m) (Fig. 10).

This pattern is interpreted as clay-rich, matrix-supported diamicton. The debris-flow unit observed at the garbage dump exceeds 5 m thickness at these locations and in places overlies a series of similar diamicts (Fig. 7). The high clay content explains the lack of penetration and poor data quality. Elsewhere, the younger debris-flow deposit is thinner (<3 m); therefore, its effect on signal penetration is not as dramatic.

8. Channel fill

Trough-shaped reflectors were found on some of the strike-oriented profiles. Most examples of this pattern occur near the fan surface, e.g. Line 1 between 440 m and 570 m (Fig. 10). Their lateral extent is from 30 m to 280 m and depth rarely exceeds 5 m.

Width and depth of these features corresponds well with the size of the existing channel on Cheekye fan (50–100 m). Interpretation is based on this fact and the classic trough shape (Fig. 10). The fact that these features are not found at depth may support the proposition that debris flows declined in frequency and runout through time, allowing channels to develop as sediment supply decreased (Fig. 3).

9. Delta foresets

Steeply inclined, high-amplitude clinoforms were observed on three profiles: e.g. Line 2 between 630 m and 920 m (Fig. 11). This reflection pattern is 10–20 m thick and is only found below GPR facies interpreted as alluvial-fan sediments. Similar reflection patterns from Late Pleistocene and Holocene river deltas were interpreted as delta foresets by Jol & Smith (1992a, b).

The elevation of the top of the foreset package is about 45 m in the centre of the fan (Fig. 11) near the garbage dump and declines downfan. At the distal edge of the fan, the top of the foresets sits at −10 m. These elevations are consistent with relative sea-level fall from the local marine limit to the Early Holocene lowstand, spanning the period 10.2–9 ka BP (Friele et al. 1999; Friele & Clague 2002).

10. Fluvial facies

Sigmoidal oblique reflection patterns are characterized by high-amplitude, continuous reflections and good signal penetration. A complex sigmoidal reflection pattern corresponds with a variety of internal structures, such as epsilon cross-beds and longitudinal bar foresets, which in turn are interpreted as evidence of channel and bar migration and point bar deposition. These features together are the basis for interpreting this radar facies as fluvial sediments. This pattern is found exclusively on the margin of Cheekye fan on Line 4 (520–900 m) (Fig. 13). Line 4 was surveyed on an artificial dyke built on the Squamish floodplain in the vicinity of the active channel (Fig. 4). At this locality fluvial sediments onlap distal fan sediments due to the combined factors of floodplain aggradation and Late Holocene sea-level rise (Clague et al. 1982).

Internal architecture of Cheekye fan

Analysis of over 27 km of continuous GPR data provided detailed subsurface information well beyond the reach of test pits and drill holes. Identification of floodplain, bedrock, fan-delta foresets, till, channels and four alluvial fan facies in conjunction with knowledge of local Quaternary sea-level change and test-pit data enabled the construction of a *generalized* model of internal fan architecture (Fig. 14).

Fan deposits overlie till and hummocky bedrock near the apex in the proximal fan sector and at the mouth of Cheakamus River in the northern fan sector (Fig. 14). It is also likely that bouldery sediments reworked from ice-contact rock-avalanche debris underlie a portion of the fan near the apex. The topography of this complex underlying surface is not fully known. A well log near the apex (WW15; Fig. 4) indicates bedrock at 30 m depth, as do a number of recent cores sunk at the garbage dump (Ékes 2000). GPR penetration increased downfan to 40 m and did not encounter bedrock, suggesting a greater thickness of alluvial fan deposits in that direction. Two well logs (WW11 and WW12; Fig. 4) in conjunction with GPR data at the mouth of Cheakamus River, indicate 10–20 m depth to till at that locality.

Two basic architectural components were defined within fan sediments: subaqueous sediments, represented by foresets, and subaerial alluvial fan sediments. Foreset beds, prominent on Line 1 (Fig. 11), indicate a fan-deltaic setting for lower
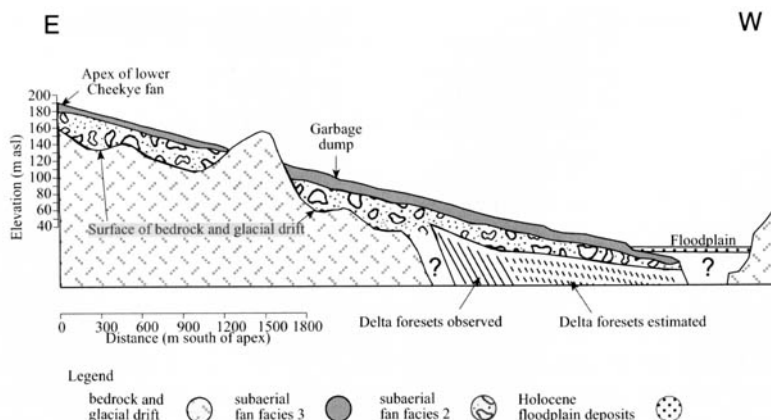
Fig. 14. Schematic cross-section of Cheekye fan showing its internal architecture.

Cheekye fan and suggest that the lower fan continued to prograde during the period of sea-level fall 10.2–9 ka BP (Friele *et al.* 1999).

Alluvial fan sediments can be further divided into four GPR facies (Fig. 9). Fan facies 1, the deepest of the fan facies, is interpreted as being bouldery, representing reworked ice-contact materials deposited during early fan development. Fan facies 2, interpreted as predominantly matrix-rich, debris-flow diamicton, is predominant at lower stratigraphic horizons and at the apex of the fan. Alluvial fan facies 3, interpreted as chiefly parallel-bedded sheetflood sand and gravel and clast-rich debris-flow diamicton, becomes the dominant facies in the upper 20–25 m of the fan stratigraphic column in the western, central and southern fan sections, indicating that sheetflood activity and fluvial reworking were more dominant processes in the later development of the fan. Channel-fill patterns seen at shallow depth (e.g. Fig. 10) suggest a tendency toward channel incision through time as sediment supply decreased. Parallel bedding may, in part, represent a decline in sediment deposition rate allowing surface winnowing to take place, giving more apparent stratification.

Discussion

GPR distinguished reliably between alluvial fan and non-alluvial fan sediments. There is a clear separation between delta foresets and overlying fan sediments as well as bedrock and overlying fan sediments (Figs 10–13). The top of the underlying till could only be tentatively delineated with GPR; well-log data was used to verify this interpretation.

Although initial GPR calibration surveys showed some promise in distinguishing debris flow from sheetflood, the results are not consistent (cf.

Ékes & Hickin 2001). Debris-flow sediments produce distinctive radar signals if their conductivity is sufficiently different from those of adjacent units and if the thickness and depth of a sediment body in question is within the range of the transmitter antenna frequency. This was the case with alluvial fan facies 4, which is characterized by chaotic or poorly defined reflection configuration and found locally in a near-surface position. This facies is interpreted as matrix-rich, debris-flow diamicton with high clay content and exceeding 3 m thickness.

Clast-rich debris-flow sediments and sheetflood gravels can have a very similar appearance in outcrops or in test pits and a similar conductivity. Therefore, these units may produce very similar radar signals. Moreover, the thickness of individual units is often below the resolution of the 50 MHz antennae. Therefore, fan facies 2 and 3 could not be conclusively interpreted as being of either debris flow or sheetflood origin, only as matrix-rich diamicton *or* poorly bedded sheetflood sand (facies 2) and as horizontally bedded sheetflood sand and gravel *or* clast-rich debris flow diamicton (facies 3). The distinction between fan facies 2 and 3 is based on the presence or absence of horizontally continuous and layered elements. The ultimate interpretation was based on detailed knowledge of the Quaternary history of the area and on an understanding of the development of paraglacial alluvial fans reflecting the likely predominance of sediments within that facies.

Based on GPR data, a model for fan development extending back to the deglacial period (10.2 ka BP) is proposed. High sedimentation rates contributed to rapid growth in the Early Holocene, despite relative sea-level fall and low precipitation rates. These high sedimentation rates probably resulted in a very active fan surface with frequent

channel changes driven by aggradation. A high sediment supply and relatively low runoff regime probably led to the dominance of debris-flow activity (GPR alluvial fan facies 2). After about 6 ka BP sediment supplies declined and runoff gradually increased. This may have conditioned a shift to sheetflood dominance (GPR alluvial fan facies 3), at least at distal portions of the fan. At some point the Squamish and Cheakamus Rivers coalesced with the Cheekye fan, eroding the fan toe and producing the steep scarp along the fan's northern and western edge. Distal truncation indicates the decreasing activity in the Late Holocene. Reduction in sediment supply may have contributed to a tendency toward channel stability and incision, leading to the development of channel-fill features. The depth and distribution of radiocarbon dates gives some indication of Holocene fan evolution. Ages of near-surface deposits indicate that the southern sector of the fan has probably been largely inactive for about 7 ka BP. During the Mid-Holocene, fan activity was concentrated in the central sector and eventually shifted to the northern sector, where the channel is located today. GPR data suggest that debris flows were predominant and commonly reached the distal fan early in the Holocene, but that later unconfined debris flows halted near the apex. This is supported by surface deposits and historical records (Thurber & Golder 1993), indicating that unconfined debris flows have affected the apex, while only channelized debris flows have reached the fan toe.

Blair & McPherson (1994a, b) presented a model for fan formation whereby a strong relationship exists between the primary sedimentary processes active on fans and the evolutionary stage of the fan drainage basins. Sediment gravity flows triggered by collapse of bedrock cliffs are important in alluvial fan construction during their early stages of development, as is the case here with the collapse of the western face of Mount Garibaldi onto the waning ice sheet. As the basin becomes more dissected, and as the fan builds out, there is a shift from sediment-gravity to fluid-gravity dominated deposition. Blair & McPherson (1994a) and Blair (1999) argue, however, that at a given stage of development alluvial fans are dominated by either debris flow or sheetflood processes and that geologic and weathering conditions in the drainage basin usually promote one of these processes to the near exclusion of the other. In the case of the Death Valley fans studied by Blair (1999), the period of fan evolution covers many millions of years; whereas with the Cheekye fan the period of evolution spans the Holocene Epoch. Thus, the paraglacial fan model (Church & Ryder 1972) represents a dramatically telescoped version of the Blair & McPherson (1994a, b) fan evolution model.

References

ARCONE, S. A. 1996. High resolution of glacial ice stratigraphy: a ground penetrating radar study of Pegasus Runway, McMurdo Station, Antarctica., *Geophysics*, **61**, 1653–1663.

ARCONE, S. A. & DELANEY, A. J. 2002. A field study of GPR attenuation rates in natural and contaminated silt. *In*: KOPPENJAN, S. K. & LEE, H. (eds) *Ninth International Conference on Ground Penetrating Radar*. Proceedings of the Society of Photo-Optical Instrumentation Engineers, **4758**, 302–307.

BERES, M., JR. & HAENI, F. P. 1991. Application of ground-penetrating radar methods in hydrogeologic studies. *Groundwater*, **29/3**, 375–386.

BERES, M., HUGGENBERGER, P., GREEN, A. G. & HORSTMEYER, H. 1999. Using two- and three-dimensional georadar methods to characterize glaciofluvial architecture. *Sedimentary Geology*, **129**, 1–24.

BLAIR, T. C. 1999. Cause of dominance by sheetflood vs. debris-flow processes on two adjoining alluvial fans, Death Valley, California. *Sedimentology*, **46**, 1015–1028.

BLAIR, T .C. & MCPHERSON, J. G. 1992. The Trollheim alluvial fan and facies model revisited. *Bulletin of the Geological Society of America*, **104**, 762–769.

BLAIR, T. C. & MCPHERSON, J. G. 1994a. Alluvial fans and their natural distinction from rivers based on morphology, hydraulic processes, sedimentary processes and facies assemblages. *Journal of Sedimentary Research*, **64/3**, 450–489.

BLAIR, T. C. & MCPHERSON, J. G. 1994b. Alluvial fan processes and forms. *In*: ABRAHAMS, A. D. & PARSONS, A. J. (eds) *Geomorphology of Desert Environments*. Chapman & Hall, London, 355–402.

BLIKRA, L. H. & NEMEC, W. 1998. Postglacial colluvium in western Norway: depositional processes, facies and palaeoclimatic record. *Sedimentology*, **45**, 909–959.

BRIDGE, J., ALEXANDER, J., COLLIER, R. E. LL., GAWTHORPE, R. L. & JARVIS, J. 1995. Ground-penetrating radar and coring used to study the large-scale of point-bar deposits in three dimensions. *Sedimentology*, **42**, 839–852

BRISTOW, C. S. 1995. Facies analysis in the Lower Greensand using ground penetrating radar. *Journal of the Geological Society, London*, **152**, 591–598.

BRISTOW, C., PUGH, J. & GOODALL, T. 1996. Internal structure of aeolian dunes in Abu Dhabi determined using ground penetrating radar. *Sedimentology*, **43**, 995–1003.

CHURCH, M. & RYDER, J. M. 1972. Paraglacial sedimen-

tation: a consideration of fluvial processes conditioned by glaciation. *Bulletin of the Geological Society of America*, **83**, 3059–3072.

CLAGUE, J. J., HARPER, J. R., HEBDA, R. & HOWES, D. E. 1982. Late Quaternary sea-levels and crustal movements, coastal British Columbia. *Canadian Journal of Earth Sciences*, **19**, 597–618.

CLAGUE, J. J., FRIELE, P. A. & HUTCHINSON, I. [IN PRESS] DEBRIS FLOWS IN THE CHEEKYE RIVER BASIN, BRITISH COLUMBIA. *Environmental and Engineering Geoscience*.

DAVIS, J. L. & ANNAN, A. P. 1989. Ground penetrating radar for high resolution mapping of soil and rock stratigraphy. *Geophysical Prospecting*, **37**, 531–551.

ÉKES, C. 2000. *Radar Facies and Architecture of Alluvial Fans and Related Sediments in High-Energy Alpine Environments, British Columbia*. Ph.D. thesis, Simon Fraser University, Burnaby, British Columbia, Canada.

ÉKES, C. & HICKIN, E. J. 2001. Ground penetrating radar facies of the paraglacial Cheekye Fan, southwestern British Columbia, Canada. *Sedimentary Geology*, **143**, 199–217.

FRIELE, P. A & CLAGUE, J. J. 2002. Readvance of glaciers in the British Columbia Coast Mountains at the end of the last glaciation. *Quaternary International*, **87**, 45–58.

FRIELE, P. A, ÉKES, C. & HICKIN, E. J. 1999. Evolution of Cheekye fan, Squamish, British Columbia: Holocene sedimentation and implications for hazard assessment. *Canadian Journal of Earth Sciences*, **36**, 2023–2031.

GREEN, N. L., ARMSTRONG, R. L., HARAKAL, J. E., SOUTHER, J. C. & READ, P. B. 1988. Eruptive history and K-Ar geochronology of the Late Cenozoic Garibaldi Volcanic Belt, southern British Columbia. *Bulletin of the Geological Society of America*, **100**, 563–579.

HOOKE, R. L. 1993. The Trollheim alluvial fan and facies model revisited: Discussion and reply. *Bulletin of the Geological Society of America*, **105**, 563–567.

JOL, H. M. & SMITH, D. G. 1991. Ground penetrating radar of northern lacustrine deltas. *Canadian Journal of Earth Sciences*, **28**, 1939–1947.

JOL, H. M. & SMITH, D. G. 1992a. Ground penetrating radar: recent results. *Canadian Society of Exploration Geophysicists*, **17/10**, 15–20.

JOL, H. M. & SMITH, D. G. 1992b. GPR results to infer depositional processes of coastal spits in large lakes. *In*: HANNINEN, P. & AUTIO, S. (eds) *Fourth Inter-national Conference on Ground Penetrating Radar*. Geological Survey, Finland, Special Papers, **16**, 169–177.

JOL, H. M. 1993. *Ground Penetrating Radar (GPR): a New Geophysical Method Used to Investigate the Internal Structure of Sedimentary Deposits (Field Experiments on Lacustrine Deltas)*. Ph.D. thesis, University of Calgary, Calgary, Alberta.

KEEN, C. E. & HYNDMAN, R. D. 1979. Geophysical review of the continental margins of eastern and western Canada. *Canadian Journal of Earth Sciences*, **16**, 712–747.

MATHEWS, W. H. 1952. Mount Garibaldi, a supraglacial Pleistocene volcano in southwestern British Columbia. *American Journal of Science*, **250**, 553–565.

MATHEWES, R. W. & HEUSSER, L. E. 1981. A 12000 year palynological record of temperature and precipitation trends in southwestern British Columbia. *Canadian Journal of Botany*, **59**, 707–710.

MOORMAN, B. J. & MICHEL, F. A. 2000. Glacial hydrological system characterization using ground-penetrating radar. *Hydrological Processes*, **14**, 2645–2667.

MOORMAN, B. J., JUDGE, A. S. & LAFLECHE, P. T. 1988. The use of ground penetrating radar in permafrost regions. 2nd National Student Conference on Northern Studies, Ottawa, Ontario, Abstract of Papers, 101–102.

OLHOEFT, G. R. & SELIG, E. T. 2002. Ground-penetration radar evaluation of railway track substructure conditions. *In*: KOPPENJAN, S. K. & LEE, H. (eds) *Ninth International Conference on Ground Penetrating Radar*. Proceedings of the Society of Photo-Optical Instrumentation Engineers, **4758**, 48–53.

RUSSELL, A. J., KNUDSEN, Ó, FAY, H., MARREN, P. M, HEINZ, J. & TRONICKE, J. 2001. Morphology and sedimentology of a giant supraglacial, ice-walled, jökulhlaup channel, Skeiotarárjökull, Iceland: implications for esker genesis. *Global and Planetary Change*, **28**, 193–216.

THURBER ENGINEERING LTD & GOLDER ASSOCIATES LTD. 1993. *Cheekye River Terrain Hazard and Land Use Study, Final Report*. Ministry of Environment, Lands and Parks. Burnaby, British Columbia.

VAN HETEREN, S., FITZGERALD, D. M., MCKINLAY, P. A. & BUYNEVICH, I. V. 1998. Radar facies of paraglacial barrier systems: coastal New England, USA. *Sedimentology*, **45**, 181–200.

Three-dimensional GPR analysis of various Quaternary gravel-bed braided river deposits (southwestern Germany)

J. HEINZ & T. AIGNER

Geological Institute, University of Tübingen, Sigwartstrasse 10, 72076 Tübingen, Germany
(e-mail: T.Aigner@uni-tuebingen.de)

Abstract: Closely spaced (1 m) ground penetrating radar (GPR) profiles were used for a three-dimensional characterization and comparison of glaciofluvial gravel-bed deposits in palaeodischarge zones of the Würmian Rhine glacier (southwestern Germany). Previous sedimentological outcrop investigations revealed three regionally reoccurring architectural styles of gravel bodies. For each of these styles a three-dimensional GPR dataset has been acquired in active gravel pits in order to calibrate the radar profiles with outcrop walls and to analyse, in three dimensions, the depositional elements and their stacking pattern in the subsurface.

The GPR data were interpreted by mapping reflection terminations in order to delineate genetically related units. In particular, radar facies types and radar sequence boundaries were used to define and map depositional elements. Both accretionary and cut-and-fill depositional elements could be identified. Accretionary elements are characterized by horizontally to low-angle inclined (1–3°) and moderately continuous reflections (5–30 m) terminating on flat sequence boundaries; they represent the deposits of gravel sheets and traction carpets. In contrast, cut-and-fill elements are characterized by low to steeply inclined (3–25°), often discontinuous reflections terminating on concave to trough-shaped lower truncation boundaries; these are interpreted as scour-pool fills and small dissection elements (e.g. chutes and lobes).

The three basic architectural styles of gravel bodies can be distinguished on the basis of the size and proportion of cut-and-fill elements mapped within the radar images. One type of gravel body is composed of an amalgamation of large cut-and-fill elements whereas the other two types are dominated by accretionary elements and differ by the proportion of smaller cut-and-fill elements.

The results show that GPR is an adequate technique to illuminate the sedimentary architecture of the various types of gravel bodies. GPR data allow detailed three-dimensional reconstruction of depositional elements and their stacking pattern in the subsurface.

Most glaciofluvial gravel-bed deposits of braided rivers have a highly heterogeneous sedimentary architecture. Centimetre to metre-scale lithofacies units with lateral extensions of decimetres to tens of metres are organized into genetically related units (depositional elements). These elements represent former geomorphologic units of an ancient river system. Thus, in order to understand the palaeofluvial environment as well as to enable adequate quantitative analysis of these deposits, information on their three-dimensional architecture is required (Brierley 1996).

Starting with the work of Ulriksen (1982), the ground penetrating radar (GPR) technique has been applied in an increasing number of case studies to image sedimentary structures and architectures in the shallow subsurface (about 2–40 m depth). This technique works well in low-conductive sediments, such as sand and gravel deposits, and many studies have documented that the geophysical (dielectric) properties are closely related to primary sedimentary structures (e.g. Van Dam 2001). Hence, two-dimensional GPR profiles have been used, among others, for delta deposits (e.g. Jol & Smith 1991; Smith & Jol 1992, 1997), fluvial deposits (e.g. Bridge *et al.* 1998; van Overmeeren 1998; Vandenberghe & Overmeeren 1999) and proximal glaciofluvial deposits (e.g. Huggenberger 1993; Beres *et al.* 1995; Olsen & Andreasen 1995). Additionally, a large-scale (>5m) arrangement of parallel profiles or profiles arranged in a large-scale grid enabled the geometrical reconstruction of prominent fluvial sedimentary units (e.g. Stephens 1994; Bridge *et al.* 1995; Asprion & Aigner 1997; Bristow *et al.* 1999). However, these measurements are often inadequate to resolve the three-dimensional character of metre-scale fluvial architectural elements. Recently, closely (<1 m) spaced GPR

profiles have been measured (e.g. Beres *et al.* 1995; McMechan *et al.* 1997; Asprion & Aigner 1999), leading to a highly detailed cube of continuous GPR information. Beres *et al.* (1999) illuminated the three-dimensional architecture of highly heterogeneous braided river deposits in the Swiss part of the Rhine Valley by using three-dimensional GPR data.

Based on comparative outcrop investigations of 25 sites within palaeodischarge zones of the whole Rhine glacier area, three basic recurrent architectural styles of braided river deposits (including the type presented by Beres 1995) can be distinguished. The detailed sedimentological analysis of these different architectural styles is documented in a separate publication (Heinz *et al.* in press). The major objectives in the present paper are:

1. To document and discuss the possibilities of the GPR technique in order to characterize these different architectural styles. Therefore GPR profiles were calibrated with corresponding outcrop walls.
2. To map depositional elements in the subsurface using three-dimensional GPR surveys and to quantify their dimension and proportion within the different gravel-body types.

The overall aim is to contribute to a sedimentological database of lithofacies and preserved depositional elements with three-dimensional GPR characterization and make it applicable to subsurface studies (e.g. prediction of aquifer heterogeneity).

Sedimentology

This paper focuses on the principal architectural patterns of various gravel bodies as detected by the GPR technique. For details concerning the processes, formation and interpretation of fluvial gravel-bed deposits we refer to previous studies (e.g. Best & Bristow 1993, Siegenthaler & Huggenberger 1993; Heinz *et al.* in press) and only a brief summary is given here.

The fluvial environment can be reconstructed by recognition of the record and preservation of depositional elements (Miall 1985; Siegenthaler & Huggenberger 1993), which are characterized by specific external shapes and internal structures. Two groups of depositional elements can be classified here (cf. Heinz & Aigner 1999).

1. 'Cut-and-fill elements' are characterized by an erosive concave lower bounding surface with a sedimentary fill deposited almost immediately after the erosional phase, preserving the depression. Examples are scour-pool fills which are formed at channel bends and chan-

nel confluences (Ashmore 1993) of a braided river system and small dissection elements occurring on, e. g., bar-complexes.
2. 'Accretionary elements' show an aggradational and/or progradational stratification style built up on a flat lower bounding surface. These deposits are interpreted as in-channel accumulations (i.e. gravel bars). Their dominant appearance in outcrops are gravel sheets (stacking of many horizontal to subhorizontal, about 0.1–0.2 m-thick sheet-like units with lateral extension of tens of metres), traction carpets (massive, 0.5–2.0 m-thick units with lateral extension of hundreds of metres) and gravel dunes (cross-stratified units with a thickness of 0.3–1.5 m and a lateral extension of tens of metres).

Depositional elements are made up of different lithofacies types. In glaciofluvial gravel deposits of the Rhine glacier area the major lithofacies types are: (1) poorly sorted gravel, (2) alternating gravel, (3) well-sorted sand and gravel, and (4) cobble- and boulder-rich gravel. The most frequent lithofacies is 'poorly sorted gravel' (mixture of sand and gravel with a sand proportion of 30%), which occurs in cut-and-fill elements as well as in accretionary elements. Lithofacies type 'alternating gravel' (composed of a lower zone of bimodal to polymodal gravel and an upper zone of graded, well-sorted openwork gravel) appears dominantly in cross-stratified elements (scour pools, gravel dunes). Lithofacies type 'well-sorted sand and gravel' is mostly found in areas of diminished flow (e.g. in marginal parts of scour-pool fills and the lee side of channel accumulations). In contrast, lithofacies type 'cobble- and boulder- rich gravel' (cobble-and-boulder proportion of 30–40%) indicates high-magnitude events and appears exclusively in accretionary elements (particularly traction carpets).

Comparative analysis of 25 gravel pits in palaeodrainage zones of the Würmian Rhine glacier area (see Fig. 1) revealed three regionally reoccurring sedimentary architectures of gravel bodies, classified here as types A, B and C. For each type an outcrop wall photograph is shown in Figure 2.

Type A is abundant in the Rhine Valley. Gravel bodies are characterized by an amalgamation of large cut-and-fill elements with a thickness of 1–3 m and lateral extensions of 10–>30 m (Fig. 2a; note that the cut face is directed perpendicularly to the overall palaeoflow direction from east to the west). The cut-and-fill elements are constructed of cross-stratified sets consisting chiefly of the lithofacies types poorly sorted gravel and alternating gravel. In this example, thick units of stratified sands are also preserved within the cut-and-fill
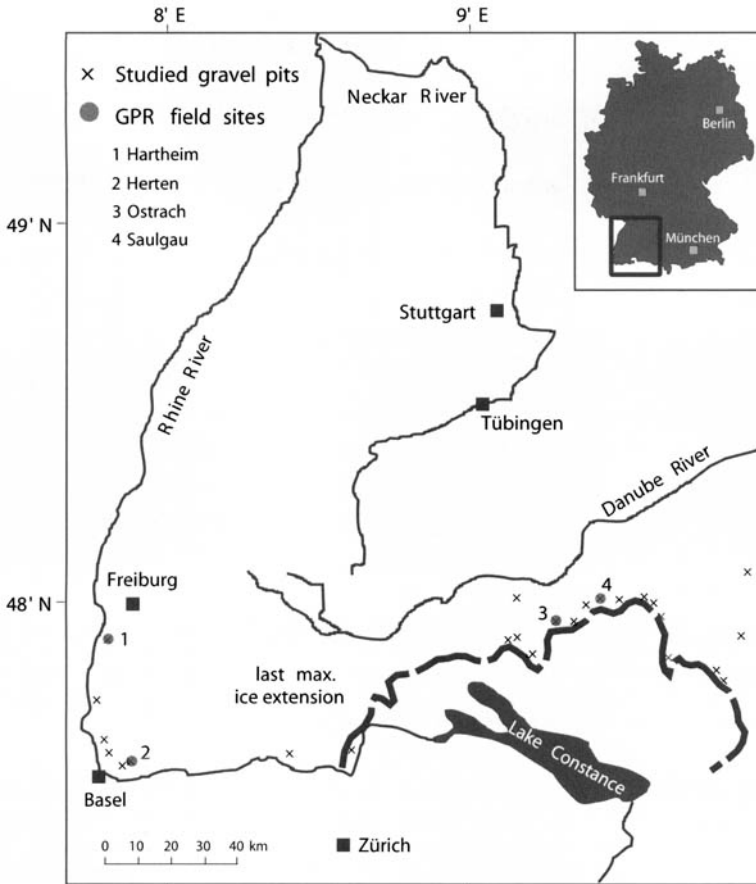
Fig. 1. Location of the studied sites in southwestern Germany related to the last maximum ice-extension of the Würmian Rhine glacier lobe.

elements. Accretionary elements occur only as relicts. They are represented by horizontal to subhorizontal units of gravel sheet deposits (poorly sorted gravel).

In contrast, types B and C gravel bodies are dominated by accretionary elements (stacking of horizontally to subhorizontally stratified gravel sheets) and the cut-and-fill elements are generally much smaller in dimension. Type B gravel bodies show a proportion of cut-and-fill elements of 30–35% on average. Their lateral extensions vary from 7 m to 30 m with a mean thickness of 0.7–0.8 m (Heinz *et al.* in press). Within type C gravel bodies, the proportion and dimension of cut-and-fill elements is even more reduced (proportion <20%, thickness 0.3–0.6 m, lateral extension 2–18 m). Particularly in this kind of gravel deposits, it is very difficult to recognize the small-scale structures because they mainly consist of poorly sorted gravel with little contrasts visible at the outcrop

walls. Both type B and type C gravel bodies occur in palaeodischarge zones which drained the Rhine glacier north of the river Danube (see Fig. 1).

GPR reflections, acquisition and processing

GPR reflections appear to be associated with changes in the residual water content of different lithofacies types (Huggenberger 1993), which is primarily controlled by their grain size and sorting. Strong reflections are expected between poorly sorted lithofacies types (poorly sorted gravels, cobble- and boulder-rich gravels), matrix-free openwork gravel (upper zone of lithofacies 'alternating gravel') and sand-dominated lithofacies types (e.g. well-sorted sand, bimodal gravel).

Resolution is controlled vertically by the frequency of the antennae used (high frequency = high resolution and lower penetration depth),
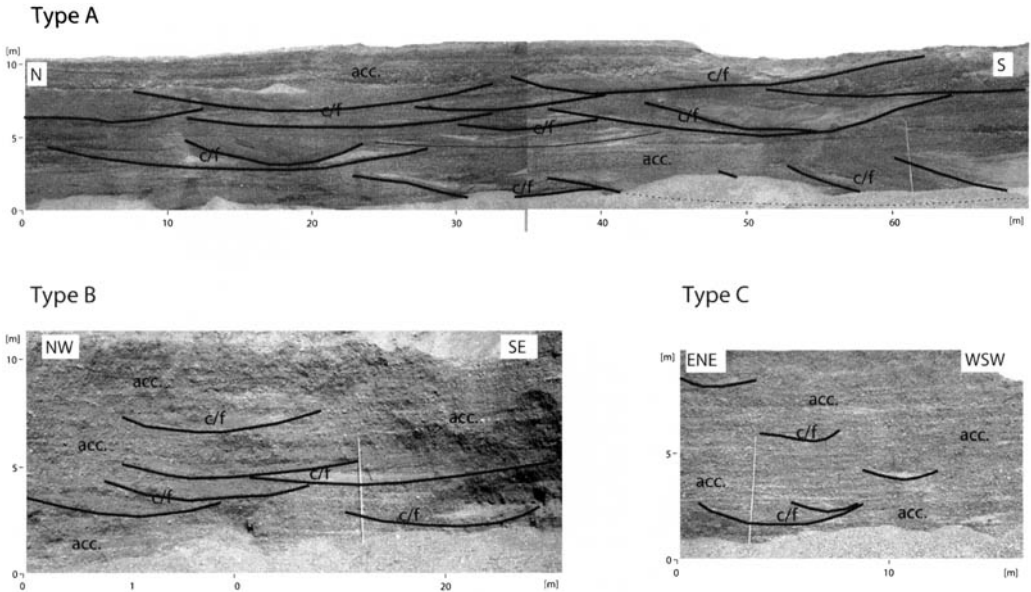
Fig. 2. Outcrop-wall photographs showing the three different architectural types of gravel bodies recognized in palaeo-discharge zones of the Rhine glacier. Type A occurs in the Rhine valley and is composed of an amalgamation of large cut-and-fill elements (c/f) with relics of accretionary elements (acc.). Types B and C occur in the northern discharge areas of the former Rhine glacier. In general, the deposits are dominated by accretionary elements. In gravel-body type B, cut-and-fill elements are more frequent and larger in size than in type C.

whereas the lateral resolution is conditioned by the Fresnel zone (mean volume of the reflected wavefront), which is controlled by the wavelength and the depth of the object (lateral resolution diminishes with depth) and the distance between measurements.

The GPR data presented here were measured with a GSSI (Geophysical Survey Systems Inc.) system (model SIR-10A) and a pair of 300 MHz antennae (separation of transmitter and receiver was fixed at 1.4 m). For this study, this frequency represented the best compromise between high resolution and adequate penetration depth. Useful information was obtained to a depth of 5–10 m below the surface. Common mid-point (CMP) and radar-tomography measurements (e.g. Beres *et al.* 1999; Tronicke *et al.* 1999) give an average near-surface wave velocity of 0.1 m ns^{-1}, resulting in an effective vertical resolution in the order of a few decimetres.

Data acquisition was carried out in those parts of the selected gravel pits where soil and weathered material had already been removed and uniform surface conditions predominated. The three-dimensional grids were arranged by parallel GPR profiles with a spacing of 1 m in one direction and 1–5 m in the orthogonal direction, covering areas of 600–1750 m² for the individual surveys. Whereas 1 m spacing (in one direction) was

important in order to obtain a continuous three-dimensional cube of radar data, the spacing of the orthogonal lines was determined by the size of the subsurface structures. Orthogonal lines were used to control the interpretation of the mapped depositional elements. Thus, a spacing of 5 m was applied for gravel-body type A, 2 m for type B and 1 m for type C (compare to the size of depositional elements in Fig. 2).

The data were collected in a continuous mode; the antennae were pulled along a tape with 'step-velocity', so that a trace was received every 0.1 m (maximum value). To determine the location of the traces a marker was set at every metre. No stacking of traces has been carried out in the field. Each three-dimensional grid was measured in one day.

Raw data were processed with band-pass filter, automatic gain control and Kirchhof migration using the PC-based system Reflex (K. J. Sandmeier, Karlsruhe, Germany). Creation and presentation of the three-dimensional cube of radar data was carried out with the software Slicer Dicer. Processed radar profiles of one direction were compiled and horizontally interpolated. We found that, with a spacing of 1 m, all vertical details of a radar profile were correctly interpolated and imaged within the three-dimensional cube (in the case of 300 MHz antennae).

Interpretation and mapping of depositional

elements was carried out with the three-dimensional software Gocad. From profile to profile, the respective elements were outlined and several surfaces could be modelled. The erosional lower bounding surface of cut-and-fill elements was much easier to recognize in the radar images than individual units of horizontally to subhorizontally stacked accretionary elements (gravel sheets). Therefore mainly the lower borders of cut-and-fill elements are highlighted in the figures.

Results

1. Calibration of GPR profiles

Calibrating GPR data is important in order to appraise the reliability of the radar method in different depositional environments. In former studies, calibration has been carried out with core data (e.g. Bridge *et al.* 1995, 1998) or nearby outcrop faces (e.g. Huggenberger 1993; Asprion 1997; Rea & Knight 1998). In this study the data were verified by nearby outcrop faces and (where possible) by direct comparison of GPR profiles with the (later) excavated outcrop wall. In the Herten gravel pit several GPR profiles were measured and marked at the surface. During excavation of the gravel pit the successive vertical outcrop sections could be matched exactly with the sites of the previously measured GPR profiles, resulting in a direct comparison of outcrop walls and corresponding radar image.

One such example of a photographed outcrop wall, GPR image and interpretation according to depositional units (units A–F) is shown in Figure 3.

Unit A is characterized in the radar image by continuous and high-amplitude, subhorizontal reflections. This simple pattern corresponds well with the horizontally stratified gravel sheets in the uppermost 1.8 m of the outcrop.

Within unit B, inclined, low- to moderate-amplitude reflections downlap and onlap onto relatively continuous high-amplitude reflections that truncate lower strata. Both the depth and geometry of unit B correspond well with the outcrop photograph. The base of this unit consists of a matrix-rich (silty) gravel layer, which is responsible for the strong (double wavelet) reflection. Upper parts of unit B comprise trough cross-stratified 'alternating gravel' with a large proportion of openwork gravel. The radar image shows inclined reflections with dips slightly less than the dip angle of the cross-stratification in the photograph, particularly towards the south. Additionally, the number of alternating gravel cross-strata is higher than the number of reflections, indicating that not every single layer could be resolved.

The wedge shape of unit C is clearly shown in
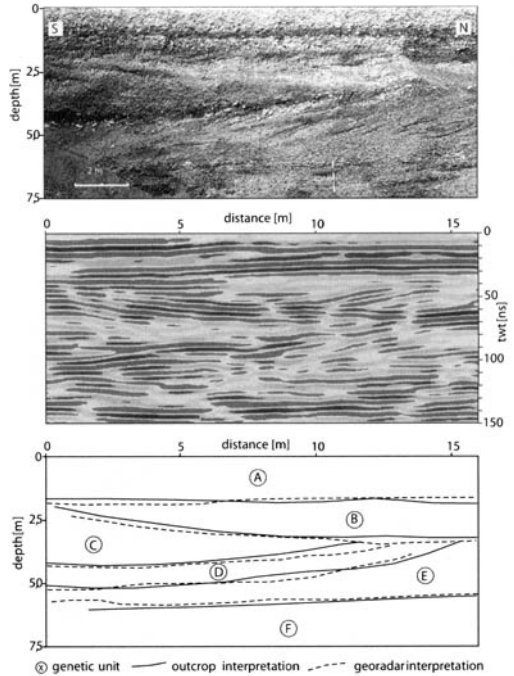
Fig. 3. Comparison of outcrop-wall photograph and radar image at the Herten gravel pit. Position and external shape of the depositional units (A–F) correspond well with the radar image. Internal structures are indicated in the upper units (A, B and C) whereas within the lower units (D, E and F) the stratification is not resolved adequately. Varying amplitudes correspond to changes in lithofacies types but identification of individual strata is ambiguous without outcrop information.

the radar image. The low- to moderate-amplitude, discontinuous internal reflection pattern shows that this unit is comparatively homogeneous (mainly sand-rich, poorly sorted gravel).

Unit D is composed of cross-stratified alternating gravel (southern part) and (sand-rich) 'poorly sorted gravel' (northern part of unit D). In the radar image, high-amplitude reflections appear in the southern and central parts of unit D, where alternating gravel is situated below the 'poorly sorted gravel' of unit C. In the northern part of unit D, low to moderate amplitudes are present, indicating only slight contrasts in lithofacies. The internal cross-stratification could not be recognized without outcrop information.

In outcrop, unit E is composed mostly of cross-stratified, poorly sorted gravel with intercalated thin (5–10 cm) and discontinuous layers of openwork gravel. While the position and geometry of unit E can be identified in the radar profile, the internal cross-stratification is not revealed, but appears as subhorizontal reflections with low to moderate amplitudes.

The lowermost unit F consists of sand-rich, poorly sorted gravel intercalated with subhorizontally stratified, discontinuous beds of openwork gravels (10–20 cm in thickness). Units F and E show no clear boundary and are difficult to separate in the radar image. The reflection pattern of unit F can be described as subhorizontal, moderate to highly continuous, with moderate to high amplitudes. However, the length of reflections does not correspond to the discontinuous openwork beds as seen in the outcrop section.

The detailed comparison of radar image and out-

crop wall showed that the depth position (velocity = 0.1 m ns^{-1}) and external shape of the depositional units are well reproduced in the GPR profile. They can be defined by reflection terminations, distinct reflection patterns and, in some cases, by the occurrence of high-amplitude radar boundaries. In general, the amplitudes of reflections are controlled by the permittivity contrasts between the single lithofacies types constructing the depositional units. Thus the contrasts in these gravel-bed deposits are often more dominant within a depositional unit than between them. This means
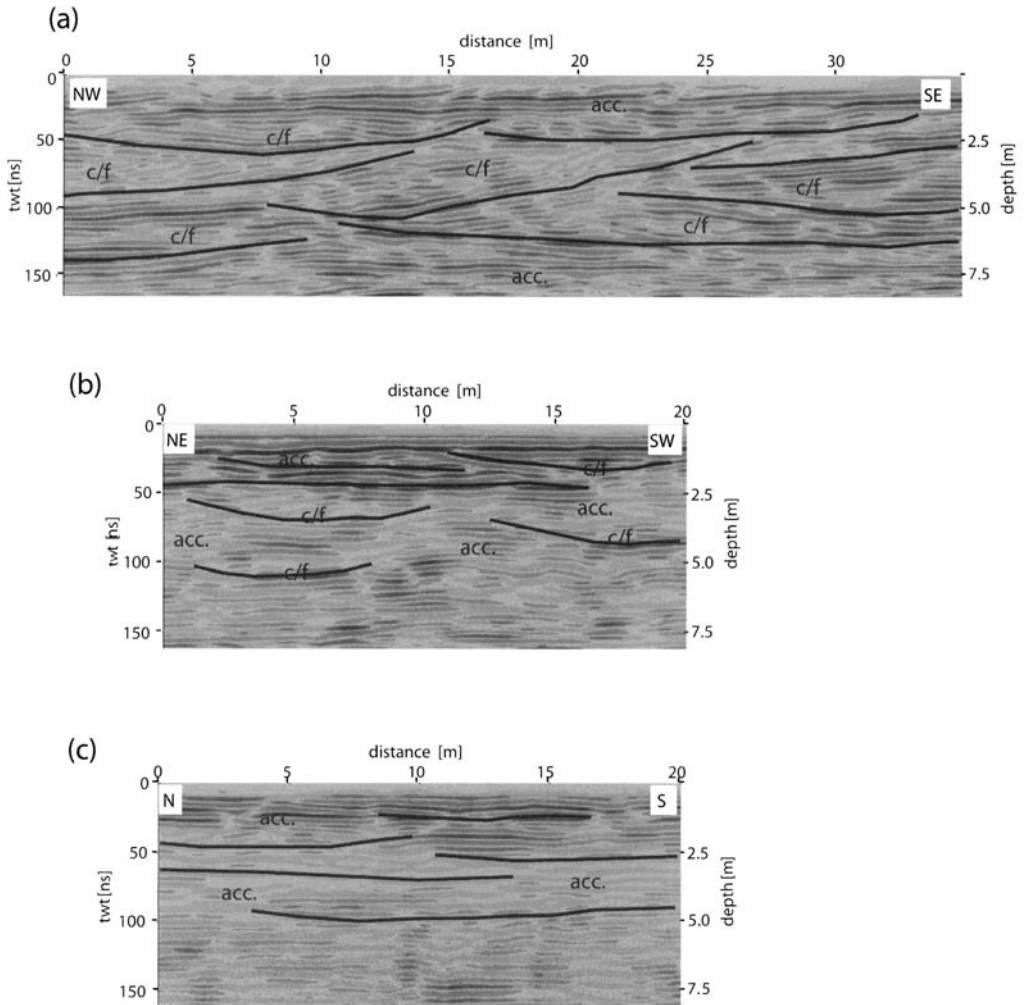
Fig. 4. Comparison of two-dimensional radar profiles reflecting different types of gravel-body architecture. Data are processed (band-pass filter, Kirchhof migration) and depositional elements are outlined within the images. (**a**) Amalgamation of mainly large-scale cut-and-fill (c/f) elements indicated by units of inclined reflections terminating on lower boundaries. (**b**) Dominance of accretionary (acc.) elements (subhorizontal to horizontal reflector pattern) with local cut-and-fill elements (small truncation zones). (**c**) Stacking of accretionary elements indicated by mainly subhorizontal reflector pattern.

that, for the delineation of the units, a sedimentological interpretation is required. In the upper and middle part (units A, B and C), the internal structure of depositional units is well depicted in the radar image. However, this is not possible in the deeper parts (units D and E). Within unit D, the internal is marked by a high-amplitude reflection resulting from the high contrast between the interface of elements C and D (especially in the southern part). Within unit E, it is assumed that the transmitted wavelength (of the electromagnetic wave) was too long to resolve the small-scale beds (5 cm thick openwork gravels). In unit F, the reduction of resolution is probably responsible for the relatively continuous reflections, even though the openwork gravel layers are more discontinuous. Obviously, when comparing outcrop and GPR sections, it must be considered that the radar profile is affected by off-axis reflections from the subsurface.

Small-scale (vertical, <0.1 m; lateral, 1–3 m) lithofacies changes cannot be recognized in the radar images. This is probably due to signal interference, diffractions, differences in velocity and resolution. High-amplitude reflections indicate high contrasts in relative permittivity but it is often difficult to predict the changes in lithofacies from this data alone.

2. Case studies

(a) Hartheim/Herten gravel pit. The two study sites are situated in the Rhine Valley (see Fig. 1). Both sites show a very similar sedimentary architecture of gravel-body type A. Data acquisition in the Hartheim gravel pit was carried out on the top floor

of the outcrop. Soil and weathered material were removed and GPR lines could be measured on a dry and flat area of 1750 m². The grid had a length of 50 m in the NE–SW direction and a width of 35 m in the NW–SE direction. Parallel, continuous GPR lines were measured at 1 m spacing (NW–SE lines) and at 5 m spacing (NE–SW lines). An electrical powerline about 20 m away from the grid produced noise signals (hyperbolas) in the deeper parts of some radar images.

Figure 4a shows a typical GPR profile of this site. In the middle part of the section (from 30 ns to 140 ns) the reflections are mostly inclined (3–15°), dipping in different directions. Due to truncations, these reflections are discontinuous (1–10 m). With respect to the dips of reflections and reflection terminations (downlap and onlap), several genetically related units with trough-shaped lower boundaries were recognized. They are interpreted as cut-and-fill elements.

In some parts (e.g. in the uppermost part) of the radar image, horizontal to subhorizontal, more continuous reflections (10–30 m in lateral extent) are interpreted as accretionary elements. A nearby outcrop face revealed a record of complex scour-pool fills and relics of gravel sheets (see also Fig. 2a).

The data cube and its interpretation (Fig. 5) shows a three-dimensional stacking of cut-and-fill elements and relics of accretionary elements. Units 02–05 and 08 represent the lower bounding surface of scour-pool fills. Cut-and-fill elements are often amalgamated and some are elongated in palaeoflow direction (south–north). Dimensions of the detected cut-and-fill elements are given in Figure 7. Because the depositional elements are sometimes far larger
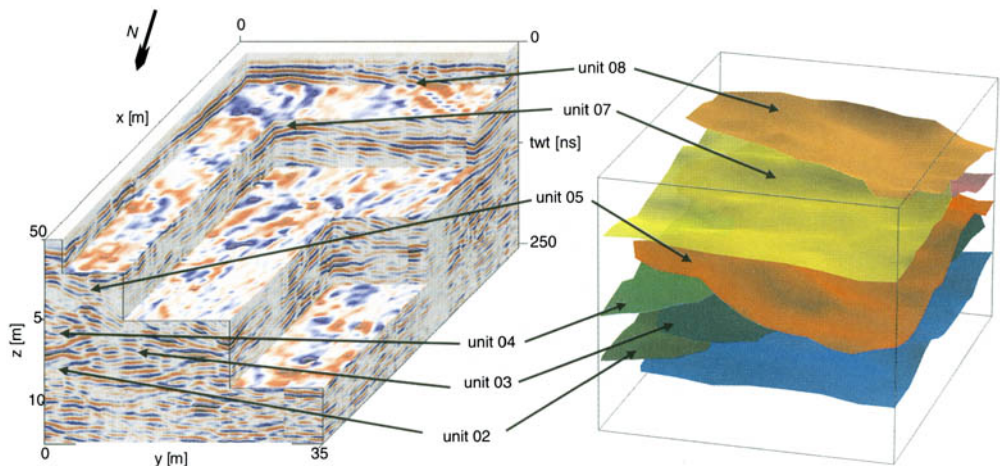
Fig. 5. Three-dimensional GPR data and spatial position of depositional elements as interpreted at the Hartheim site (gravel-body type A). Surfaces represent the lower boundaries of depositional elements. Deposits of units 02–05 build up complex scour-pool fills (cut-and-fill elements).

than the extent of the radar grid, these values represent minimum dimensions.

In order to obtain more data about dimensions of cut-and-fill elements in this type of gravel body (type A), a second site (Herten) with an area of 28 × 44 m was investigated with three-dimensional GPR surveys. A similar architectural pattern is revealed in the GPR profiles, showing a dominant preservation of large cut-and-fill elements and a smaller proportion of accretionary elements (see also Fig. 2). The dimensions of cut-and-fill elements are included in Fig. 7. In both sites radar images could be interpreted to a depth of 8–10 m.

(b) Ostrach gravel pit. This site is situated in Upper Swabia close to the last maximum ice-extension of the Würmian Rhine glacier (see Fig. 1). GPR lines were measured on a middle terrace of the Ostrach gravel pit, positioned about 6 m below the original surface. Acquisition was carried out in winter and a thin (5 cm) layer of snow covered the flat gravel surface. The size of the grid was 20 × 30 m. Parallel GPR lines of the longer profiles were directed NW–SE and spaced 1 m apart while the orthogonal profiles (NE–SW direction) were separated by a distance of 2 m.

A characteristic two-dimensional radar image of
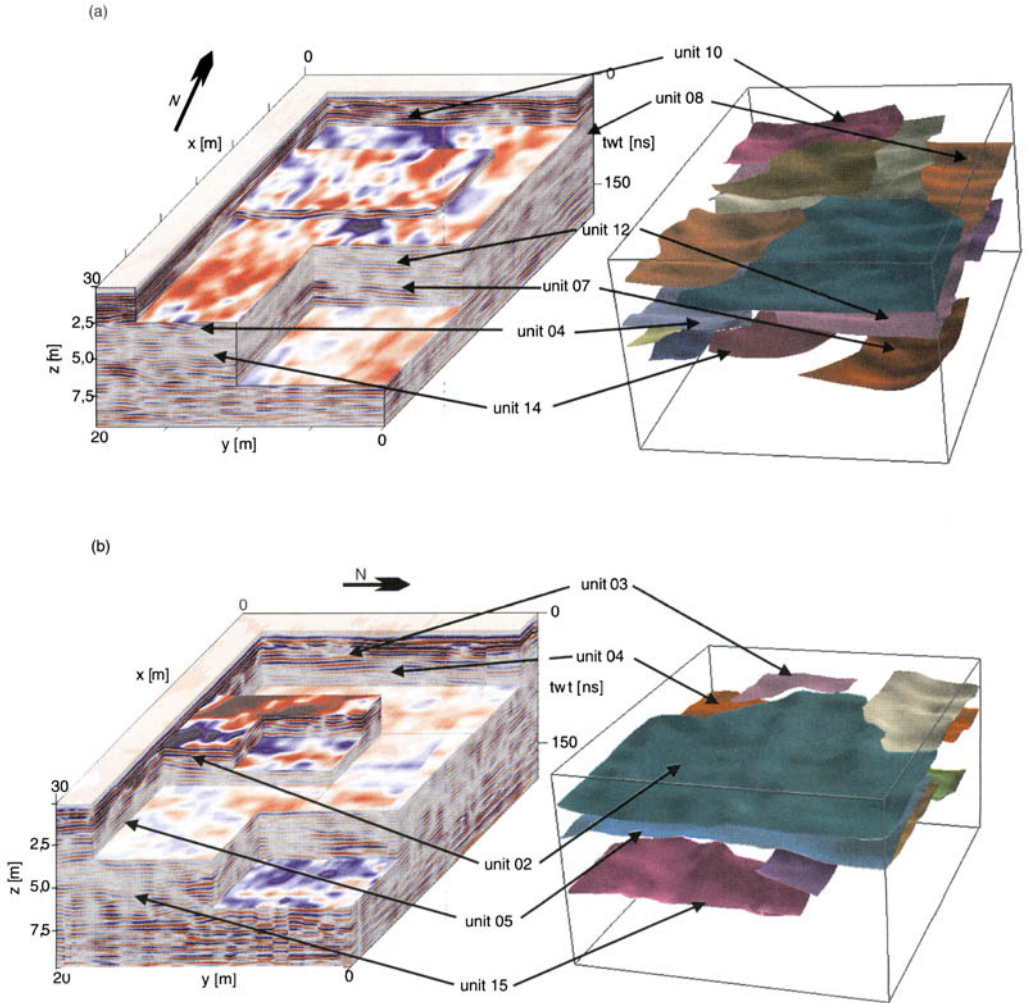
Fig. 6. (a) Three-dimensional GPR data and interpretation of depositional elements obtained at the Ostrach site (gravel-body type B). Flat and relatively extensive surfaces (e.g. units 12 and 08) represent accretionary elements (gravel sheet deposits) while small and slightly concave surfaces show the position of local cut-and-fill elements (e.g. units 07, 10 and 14). (b) Three-dimensional GPR data of the Saulgau site (gravel-body type C). The GPR images are characterized by subhorizontal reflections indicating stacked accretionary elements (e.g. units 02, 04, 05 and 15). Rarely, small-scale cut-and-fill elements are present (e.g. unit 03).

this site is shown in Figure 4*b*. Large parts of the image are characterized by horizontal to subhorizontal reflections with low to moderate continuity (5–15 m). This reflection pattern is disrupted by local truncations. Low-angle inclined (1–5°), discontinuous (1–3 m), low- to moderate-amplitude reflections occur within these units. A nearby outcrop face (see Fig. 2*b*) revealed a dominance of accretionary elements (gravel-sheet deposits) and local, smaller-scale cut-and-fill elements (scourpool fills).

The three-dimensional GPR survey is shown in Figure 6*a*. The lower truncation zone of cut-and-fill elements is relatively easy to delineate whereas it is difficult to pick the (sub) horizontal reflection pattern of stacked accretionary elements (i.e. gravel sheets). Therefore, apart from the cut-and-fill elements (e.g. units 04, 07, 10 and 14), only a few prominent horizontal reflections of accretionary elements were mapped in the subsurface data cube (e.g. unit 12). In the uppermost 4 m it was possible to detect small-scale cut-and-fill elements (e.g. units 04, 08 and 10) while below this, only larger and more prominent units could be recognized. Below 7 m, no sedimentological interpretation according to depositional elements could be carried out. It is clear that not every depositional unit that would be noticed at the outcrop wall is represented in the radar image. This can be explained by low contrasts, thin beds and a relatively large mean reflection volume in comparison to the size of the units. The GPR data volume revealed 11 local, partly amalgamated cut-and-fill elements which are slightly elongated in palaeoflow direction (SE–NW). Their dimensions are shown in Figure 7.

(c) Saulgau gravel pit. The Saulgau site is situated close to the terminal moraine complex of the last maximum ice-extension (Upper Swabia). GPR lines were measured on the surface of the gravel pit where soil and weathered material had already been removed. Data was acquired on a 30 × 20 m grid on a flat and slightly damp gravel surface. The longer lines were oriented east–west and the orthogonal lines oriented north–south; both sets of lines were spaced 1 m apart.

A typical GPR profile of the site is shown in Figure 4*c*. The whole radar image is characterized by a subhorizontal, low to moderately continuous (3–15 m) reflection pattern. In this case the sedimentological interpretation with regard to depositional elements was very difficult. As already documented in Figure 2*c*, the gravel body is mainly composed of numerous stacked gravel-sheet deposits with very rare, small-scale cut-and-fill elements. Hence, the interpreted surfaces shown in Figure 6*b* do not necessarily represent boundaries of single depositional elements but show relatively

prominent and traceable, probably composite, reflections, which reproduce the diffuse architectural style of the gravel body. Within the uppermost 3 m, it was possible to detect four small cut-and-fill elements. Their dimensions (see Fig. 7) are similar to those of the Ostrach site but no directional elongation could be recognized. Interpretation of the reflections was carried out to a depth of 5 m. Below 5 m, the signal could no longer be interpreted.

Discussion

The GPR to outcrop wall calibration demonstrated the possibilities of, and limits to, the detection of depositional elements in the subsurface. The broad classes of the accretionary- and cut-and-fill-elements in particular were almost always recognizable in the radar images. Due to reflection terminations, the lower boundary of cut-and-fill elements can be detected in the radar profiles. In contrast, it is difficult to define the boundaries of accretionary elements, which are usually constructed by stacks of thin gravel sheets.

For each sedimentary type of gravel body, a characteristic radar pattern was apparent. In gravel-body type A, inclined reflections terminate on lower truncation boundaries (complex stacking of large cut-and-fill elements). Gravel-body type B showed horizontal to subhorizontal reflection patterns with more scattered small-scale truncations. Individual depositional elements can be detected in the upper 7 m of the gravel body. By comparison, discrete depositional elements are very difficult to recognize in the radar images of gravel-body type C. Only a few small-scale truncation zones are visible in the radar image. The radar pattern is dominated by subhorizontal reflections, which reflect the stacking of diffuse gravel sheets in these deposits.

Three-dimensional GPR data clearly improve the reliability of subsurface interpretations and allow the detection in detail of the geometry of cut-and-fill elements in the subsurface. In Figure 7, their dimensions are quantified for each site investigated. Type A gravel bodies can clearly be differentiated from types B and C gravel bodies due to the larger dimension of these elements. Types B and C can be distinguished by the total number of cut-and-fill elements detected.

The overall dimensions of cut-and-fill elements derived from the three-dimensional GPR data correspond well with those measured directly at the outcrop wall (Table 1). However, very small-scale elements (<0.5 m in thickness and <3 m in length), which appear particularly in gravel-body type C, cannot be resolved with the 300 MHz antennae used in this study (particularly those in the deeper parts of the deposits). Due to the restric-
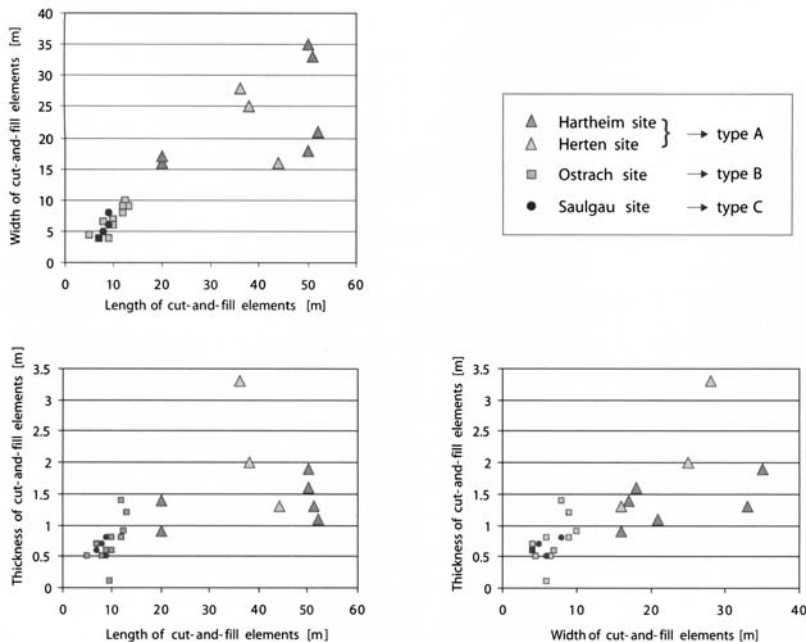
Fig. 7. Cross-plots of the dimensions of cut-and-fill elements as mapped with three-dimensional GPR surveys at the different sites. Within the Herten and Hartheim sites (type A), cut-and-fill elements are characterized by large dimensions within a broad range. The Ostrach site (type B) can be distinguished from the Saulgau site (type C) by the total number of cut-and-fill elements and slightly larger dimensions.

Table 1. *Comparison of the proportion and dimension of cut-and-fill elements within the three types of gravel deposits*

| | Gravel-body type | | |
	A	B	C
Study site	Hartheim Herten	Ostrach	Saulgau
Percentage of	80 85	35	15
c/f elements	>80 >80	30–40	<10
Size of c/f elements (m):			
Median	1.7 1.9	0.8	0.6
thickness	*1.4* *2.2*	*0.7*	*0.6*
Max. thickness	4.0 3.5	1.5	1.0
	1.9 *3.3*	*1.4*	*0.8*
Median width	21 30	9	4.3
	23 *23*	*7*	*5.7*
Max. width	40 38	15	12
	35 *28*	*10*	*8*
Median length	45 39	13	4.3
	40 *39*	*9.5*	*8*
Max. length	70 >60	20	12
	52 *44*	*12.5*	*9*

Values derived from outcrop analysis
Values derived from three-dimensional GPR data

ted radar grid size, dimensions of cut-and-fill elements of gravel-body type A have smaller maximum values than those measured directly at the more extensive outcrop faces.

The total proportion of cut-and-fill elements was not calculated exactly for this study. However, a rough visual estimate clearly reflects the orders of proportion. Within gravel-body type A, the proportion of cut-and-fill elements is >70–80%; for gravel-body type B a range of 30–40% is estimated and, for type C, less than 10% (compare with data of Table 1).

Conclusions

This three-dimensional GPR study recognized distinct sedimentary architectures in highly heterogeneous glaciofluvial gravel deposits in the palaeo-discharge areas of the Würmian Rhine glacier lobe. GPR profiles were calibrated with nearby outcrop faces or by exact comparison of radar images with the corresponding outcrop sections.

Depositional elements were interpreted according to their reflection pattern and external shape. Reflection amplitudes are related to contrasts between different lithofacies types constructing depositional elements. However, it is not possible

unambiguously to predict the petrophysical properties of single strata from these reflections.

Three types of gravel body architecture were differentiated using three-dimensional GPR surveys. They were classified according to the proportion and size of cut-and-fill elements. Thus, three-dimensional GPR surveys provide a means for both qualitative and quantitative three-dimensional characterization of these deposits.

As gravel deposits contain important groundwater resources in this region, the GPR technique is an appropriate, non-destructive tool for characterizing aquifer heterogeneity.

References

ASHMORE, P. E. 1993. Anabranch confluence kinetics and sedimentation processes in gravel-braided streams. *In*: BEST, J. & BRISTOW, C. (eds) *Braided Rivers*. Geological Society, London, Special Publications, **75**, 130–146.

ASPRION, U. & AIGNER, T. 1997. Aquifer architecture analysis using ground-penetrating radar: Triassic and Quaternary examples (S. Germany). *Environmental Geology*, **31**, 66–75.

ASPRION, U. & AIGNER, T. 1999. Towards realistic aquifer models: a three-dimensional georadar case study of Quaternary Gravel Deltas (Singen Basin, SW Germany). *Sedimentary Geology*, **129**, 281–297.

BERES, M., GREEN, A. G., HORSTMEYER, H. & HUGGENBERGER, P. 1995. Mapping the architecture of glaciofluvial sediments with three-dimensional georadar. *Geology*, **23**, 1087–1090.

BERES, M., HUGGENBERGER, P., GREEN, A. G. & HORSTMEYER, H. 1999. Using two- and three-dimensional georadar methods to characterize glaciofluvial architecture. *Sedimentary Geology*, **129**, 1–24.

BEST, J. & BRISTOW, C. (eds) 1993. *Braided Rivers*. Geological Society, London, Special Publications, **75**, 413 pp.

BRIDGE, J., COLLIER, R. & ALEXANDER, J. 1998. Large-scale structure of Calamus River deposits (Nebraska, USA) revealed using ground-penetrating radar. *Sedimentology*, **45**, 977–986.

BRIDGE, S. J., ALEXANDER, J., COLLIER, R. E. LL., GAWTHORPES, R. L. & JARVIS, J. 1995. Ground-penetrating radar and coring to study the large-scale structure of point-bar deposits in three dimensions. *Sedimentology*, **42**, 839–852.

BRIERLEY, G. J. 1996. Channel morphology and element assemblages: a constructivist approach to facies modelling. *In*: CARLING P. A. & DAWSON, M. R. (eds) *Advances in Fluvial Dynamics and Stratigraphy, West Sussex, England*. John Wiley & Sons, Chichester, 263–298.

BRISTOW, C. S., SKELLY, R. L & ETHRIDGE, F. G. 1999. Crevasse splays from the rapidly aggrading, sand-bed braided Niobrara River, Nebraska. Effects of base-level rise. *Sedimentology*, **46**, 1029–1047.

HEINZ, J. & AIGNER, T. 1999. Faziesanalyse und Dynamik würmzeitlicher Sanderablagerungen (Raum Ostrach, Oberschwaben, SW-Deutschland). *Zentralblatt für Geologie und Paläontologie*, **1**, 319–336.

HEINZ, J., KLEINEIDAM, S., TEUTSCH, G. & AIGNER, T. (in press) Heterogeneity patterns of Quaternary glaciofluvial gravel bodies (SW-Germany): Application to hydrogeology. *Sedimentary Geology*.

HUGGENBERGER, P. 1993. Radar facies: recognition of patterns and heterogeneities within Pleistocene Rhine gravels, NE Switzerland. *In*: BEST, J. & BRISTOW, C. (eds) *Braided Rivers*. Geological Society, London, Special Publications, **75**, 163–176.

JOL, H. M. & SMITH, D. G. 1991. Ground penetrating radar of northern lacustrine deltas. *Canadian Journal of Earth Sciences*, **28**, 1939–1947.

MCMECHAN, G. A., GAYNOR, G. C. & SZERBIAK, R. B. 1997. Use of ground-penetrating radar for 3-D sedimentological characterization of clastic reservoir analogs. *Geophysics*, **62**, 786–796.

MIALL, A. D. 1985. Architectural-element analysis: A new method of facies analysis applied to fluvial deposits. *Earth Sciences Review*, **22**, 261–308.

OLSEN, H. & ANDREASEN, F. 1995. Sedimentology and ground-penetrating radar characteristics of a Pleistocene sandur deposit. *Sedimentary Geology*, **99**, 1–15.

REA, J. & KNIGHT, R. 1998. Geostatistical analysis of ground-penetrating radar data: A means of describing spatial variation in the subsurface. *Water Resources Research*, **34**, 329–339.

SIEGENTHALER, C. & HUGGENBERGER, P. 1993. Pleistocene Rhine gravel: deposits of a braided river system with dominant pool preservation. *In*: BEST, J. & BRISTOW, C. (eds) *Braided Rivers*. Geological Society, London, Special Publications, **75**, 147–162.

SMITH, D. G. & JOL, H. M. 1992. Ground-penetrating radar investigation of a Lake Bonneville delta, Provo level, Brigham City, Utah. *Geology*, **20**, 1083–1086.

SMITH, D. G. & JOL, H. M. 1997. Radar structure of a Gilbert-type delta, Peyto Lake, Banff National Park, Canada. *Sedimentary Geology*, **113**, 195–209.

STEPHENS, M. 1994. Architectural element analysis within the Kayenta Formation (Lower Jurassic) using ground-probing radar and sedimentological profiling, southwestern Colorado. *Sedimentary Geology*, **90**, 179–211.

TRONICKE, J., HEINZ, J. & APPEL, E. 1999. Geophysical radar techniques for the characterization of heterogeneous Quaternary gravel deposits. *Proceedings of the 5th Meeting of the Environmental and Engineering Geophysical Society – European Section, Budapest, Hungary, 1999*, 83–84.

ULRIKSEN, C. P. F. 1982. *Application of Impulse Radar*

to Civil Engineering. Ph.D. thesis, Lund University of Technology, Lund.

VAN DAM, R. L. 2001. *Causes of Ground-Penetrating Radar Reflections in Sediments.* Ph.D. thesis, University Amsterdam, Amsterdam.

VAN OVERMEEREN, R. A. 1998. Radar facies of unconsolidated sediments in The Netherlands: a radar stratigraphy interpretation method for hydrogeology. *Journal of Applied Geophysics,* **40,** 1–18.

VANDENBERGHE, J. & VAN OVERMEEREN, R. A. 1999. Ground penetrating radar images of selected fluvial deposits in the Netherlands. *Sedimentary Geology,* **128,** 245–270.

Sedimentary architecture and radar facies of a fan delta, Cypress Creek, West Vancouver, British Columbia

M. C. ROBERTS[1], H. -P. NILLER[2] & N. HELMSTETTER[2]

[1]Departments of Geography and Earth Sciences, Simon Fraser University, Burnaby, British Columbia V5A 1S6, Canada (e-mail: mroberts@sfu.ca)
[2]Universität Regensburg, Institut für Geographie, Universitätsstrasse 31, 93040 Regensburg, Germany

Abstract: Fan deltas are common depositional features along the macro-tidal, fjorded coast of southern British Columbia. To determine the sedimentary architecture of the Cypress Creek fan delta, West Vancouver, British Columbia, a combined ground penetrating radar and geomorphological study was carried out. Five radar facies were identified and their associated geomorphic environments were established: oblique clinoform radar facies (delta front); mounded radar facies (debris-flow deposits); undulating subhorizontal radar facies (beach zone); concave radar facies (river channels) and horizontal radar facies (salt-water intrusion). The delta plain was formed primarily by debris flows, some of which reached the delta front to form prograding foreset beds. Radar facies analysis established the occurrence of arcuate scars and masses of slumped material, signifying mass movement on the delta front. Wave action, working over a 4.9 m tidal range, has reworked the distal delta-plain debris-flow sediments into an armoured gravel beach. A depositional model is proposed for a fan delta in a macro-tidal fjord setting.

Fan deltas are isolated but distinctive depositional features scattered along the fjord coast of southwestern British Columbia. With pocket beaches, submarine fans and braid deltas they represent one of the few active depositional environments occurring on this dominantly bedrock coast. In this region, a fan delta is typically deposited at the mouth of a high-relief drainage basin having a sufficiently thick veneer of surficial deposits to provide a source for repeated debris-flow events. The surficial material is usually composed of varying combinations of till, fluvioglacial, weathering and colluvial deposits plastered on the bedrock flanks of a fjord. Where rivers are eroded into bedrock drainage basins and lack a veneer of surficial deposits, the fan deltas are either absent or very small. The dominant depositional processes forming the fan deltas are debris flows, and river floods that typically occur after rain-on-snow or high-intensity but low-periodicity precipitation events.

Prior to the emergence of a fan delta, a subaqueous fan accumulates below sea level on the fjord sidewall. With continued aggradation, the top of the expanding subaqueous fan reaches sea level, where it forms a fan-delta plain. With continued progradation of the fan, the delta plain becomes more extensive and the beach, on its outer edge, becomes wider and more geomorphically distinctive. Where a stream crosses the beach zone, some of its load bypasses the beach and is deposited on the delta front, though a certain volume is retained in the tidal zone as a channel-mouth bar or is added to the beach sediments. The outer edge of the delta plain is at the place where the subaqueous delta plain meets the delta front and is demarcated by a well-defined break in slope. The delta fronts of fjord fan deltas can have slopes reaching 20° in places. The subaerial fan-delta plain reflects the overall morphology of an alluvial fan with a marked convexity in cross-profile that diminishes with distance from the apex of the fan.

The similarities, links and differences between the sedimentary prisms that form fan deltas and braid deltas have been the subject of a rapidly growing literature ever since the introduction of the term 'fan delta' into the literature by Holmes in 1965. Discussions of the terminology, processes and architecture of fan deltas are to be found in pa, braid deltas occur primarily at the head of fjords, where they are fed by gravel-bed rivers that form a wide delta plain with Gilbert-type deltaic large-

scale foresets. The nature of submarine sedimentation and morphology of coarse-grained fan deltas along this coast has been described by Prior and Bornhold (1988, 1990). In this paper, we focus on the geomorphology and sedimentary structure of a fan delta. The lack of outcrop, combined with the difficulty of drilling into the cobble–boulder gravel that forms most fan deltas in southwestern British Columbia, severely limits the analysis of the depositional architecture of a fan delta. One way of overcoming these difficulties is the use of ground penetrating radar (GPR) to provide images of the subsurface. Analysis of GPR data yields reflection patterns that can be grouped into radar facies that, in turn, can be linked to specific fan-depositional environments (Jol & Smith 1990; Van Heteren *et al.* 1998).

In this study, GPR is used to define the depositional architecture and geomorphology of a high-energy, coarse-gravel fan delta deposited at the mouth of Cypress Creek in the municipality of West Vancouver, British Columbia (Fig. 1). The specific objectives of the study are: (1) to establish the components forming the depositional architecture of a debris-flow-dominated fan delta using radar facies analysis; (2) to integrate surface sections, surface debris-flow evidence, shore sedimentation and well logs with the radar-defined facies of the fan delta; and (3) to propose a depositional model for a coarse-grained fan delta on a macro-tidal coast.

Physical setting

The drainage basin of Cypress Creek is located on the southern edge of the Coast Mountains of British Columbia. The bedrock geology of the drainage basin consists largely of granodiorite with lesser amounts of gneiss (Roddick 1965). A thin veneer of till, fluvioglacial deposits and colluvium (Clague 1994) covers the bedrock of the basin. The geomorphic evolution of the Cypress Creek drainage basin has been strongly influenced by the glaciers flowing across the Coast Mountains and down the Fraser Lowland during the Late Wisconsinan glaciation (Armstrong 1990).

The drainage-basin area of Cypress Creek is 13.4 km², with the subaerial part of the fan delta having an area of 0.26 km² (Fig. 2). The fan delta has a maximum width, from east to west, of c.800 m and a maximum axial length, from the fan apex to the mouth at sea level, of c.400 m. The receiving basin for the fan delta is the Burrard Inlet, a macro-tidal estuary (maximum tidal range of 4.9 m), located on the eastern side of the Strait of Georgia, a major water body separating Vancouver Island from the mainland of the province. Although it had been occupied by glaciers, Burrard
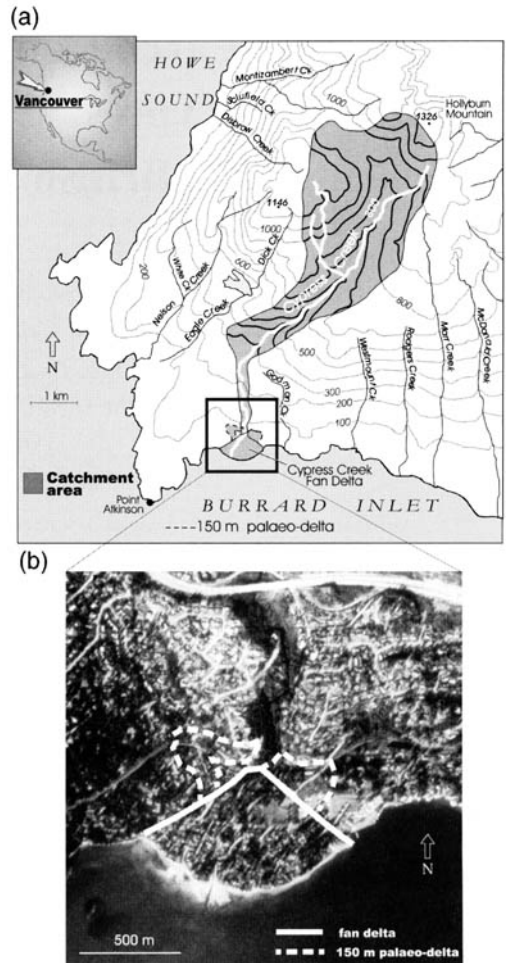
Fig. 1. (a) Location map of the drainage basin and fan delta of Cypress Creek. (b) Aerial view of Cypress Creek fan delta clearly showing (white tones) the beach zone and deposition at the mouth of the creek. The location of the 150 m highstand delta is shown. (Photo source: A. Roberts, Simon Fraser University.)

Inlet does not have a sill and it is shallower (10–110 m depth) than the adjacent fjord of Howe Sound, where water depths reach 280 m. The basin floor onto which the fan is prograding has depths of 30 m seaward of the fan.

The drainage basin extends from sea level to an altitude of 1326 m (Fig. 1), with an accompanying marked climatic gradient. At sea level (Point Atkinson), annual precipitation averages 1250 mm, but increases to 2950 mm at Hollyburn Ridge, at an elevation of 950 m. The upper part of the basin extends into a subalpine zone, receiving several metres of snow per annum as part of a total annual precipitation averaging 3500 mm. The forest cover

Fig. 2. A topographic map of the fan delta showing the location of the GPR lines, drill core sites and fan cross-sections.

of the basin reflects the climatic and topographic gradients, with western hemlock (*Tsuga heterophylla*), cedar (*Thuja plicata*) and Douglas fir (*Pseudotsuga menziesii*) dominant in the lower elevations and increasing amounts of mountain hemlock (*Tsuga mertiana*) and spruce (*Picea*) at higher altitudes. The very highest elevations of the basin are classified as alpine with a cover of shrubs and dwarfed trees.

Sea-level history

A controlling factor in the geomorphic evolution and sedimentary architecture of fan deltas along the British Columbian coast is sea-level change resulting from the post-glacial isostatic rebound that took place after the retreat of the Cordilleran Ice Sheet (Late Wisconsinan) and the interaction of the accompanying eustatic sea-level rise. After the ice had retreated, around 12 ka, the sea invaded the isostatically depressed Burrard Inlet and rela-

tive sea level was established close to the present 150 m elevation level. With the onset of isostatic rebound, sea level fell rapidly to about 40 m by 11.5 ka (Clague 1983). Between 9 ka and 8 ka, sea level stabilized at 12 m below present-day sea level, after which it rose until a short-lived still-stand occurred between 6.2 ka and 5.8 ka (Williams and Roberts 1989). Once the stillstand came to an end, sea level resumed its rise until present sea level was reached around 2.3 ka.

Fan deltas started to aggrade immediately after Burrard Inlet became ice-free and continued to form intermittently during falling sea levels. In the case of the largest fan delta on the northern side of Burrard Inlet, the Capilano River (about 10 km east of Cypress Creek), there is evidence of at least three palaeofan-deltas graded to former sea levels at 150 m, 90 m and 55 m. For Cypress Creek, there is only evidence of one palaeofan-delta at 150–155 m, below which the present active fan delta has graded to modern sea level.

Deposition of the modern Cypress Creek fan delta was probably initiated after sea level started to rise from its lowest level of −12 m. With increasing accommodation space being provided by rising sea level, the creek probably continued to replenish its subaqueous fan upslope from the fan developed at the −12 m level. Once sea-level rise stabilized at around 2.3 ka, accommodation space growth was halted, progradation became the dominant depositional style, and the modern delta plain was established.

Methods

GPR surveys were conducted to establish the sedimentary architecture of the Cypress Creek fan delta. GPR has proved to be an effective technique for reconstructing the sedimentary structure of coarse sediments and coarse clastic Quaternary depositional environments (Jol & Smith 1991; Huggenberger 1993; Roberts *et al.* 1997). For a more theoretically based discussion about GPR, see Davis & Annan 1989; Jol 1995; Annan & Cosway 1996; Conyers & Goodman 1997. In this study, we used a pulseEKKO IV radar system (400 V transmitter) to obtain strike and dip profiles of the fan delta. Antennae with a centre frequency of 100 MHz were used with a separation of 1 m and steps of 0.5 m. Traces were collected using a sampling interval of 800 ps (picoseconds) over a time window of 500 ns (nanoseconds) and were stacked vertically 64 times. For the purpose of display, automatic gain control (AGC), dewow, and topographical and reverse corrections were applied to the datasets. A common mid-point (CMP) gather was acquired to obtain velocities for depth conversions: an average velocity of 0.10 m ns^{-1} was calculated and penetration depths of up to 15 m were achieved. The study area was completely urbanized, so location of GPR lines was not always optimal. However, the fortuitous location of a soccer-field of an elementary school on the central part of the fan allowed us to lay out a grid of 10 m-spaced dip and strike lines in order to obtain a three-dimensional view of the subsurface (Fig. 2). Other lines were collected along roads, ditches and the fan delta's beach.

A fan delta generally has few stratigraphic sections because its delta plain is roughly graded to sea level and it usually lacks road-cuts or channel-bank exposures. In the case of the urbanized Cypress Creek, property-accessibility issues reduce the number of potential sections even more. Fortunately, well logs were available from water wells that had been drilled for a federal research laboratory on the edge of the fan delta (Pacific Hydrology Consultants Ltd 1995); these logs provided some degree of lithological control for the GPR profiles

(shown later in Fig. 8). The beach facies consist primarily of coarse debris-flow and fluvial sediments reworked and redistributed by tidal and wave processes. The beach facies were mapped at a scale of approximately 1 : 5000. Aerial photographs, topographical maps and hydrographical charts were examined to determine the exact form and size of the fan delta and to construct a longitudinal profile from different parts of the study area.

Radar facies of fan delta
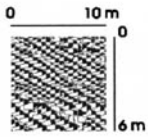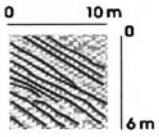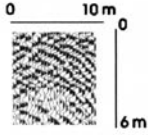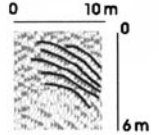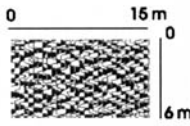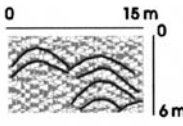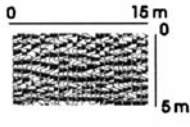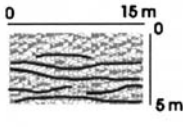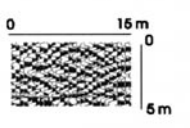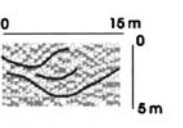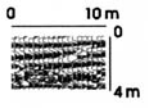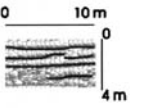
A radar facies is defined as a mappable, three-dimensional sedimentary unit composed of radar reflections having characteristic properties that can be used to differentiate it from other facies in a given profile (Jol & Smith 1991). Analysis of some 3000 m of GPR lines shot across the fan delta resulted in the identification of five major radar facies, which are discussed below (Table 1).

Radar facies I: oblique clinoform radar facies

Description This facies is characterized by prominent oblique reflections with amplitudes that tend to decline down dip but can be quite variable, with strong and weak amplitudes alternating along a single reflection (Fig. 3). Although the reflections are usually parallel to one another, they show, in some profiles, a tendency for convergence (Table 1; Fig. 4). In several GPR profiles, there are groupings of oblique reflections separated by slight changes in dip (Fig. 4) or by a bounding disconformity, implying that the reflections were formed by a process that changed position or intensity on the fan delta. Dips of the reflectors vary between 10° and 20°. When the reflections are viewed along the depositional strike they are either horizontal or have very low dips. The oblique reflectors of this facies have, on some lines, abrupt upper terminations. There are rare examples of sigmoidal patterns (Table 1) and the best example is on the lower boundary of the facies in line Stn 135/137 (Fig. 3). When GPR lines are taken along both the dip and strike of the fan delta (Fig. 5), a three-dimensional view emerges of the tie-in between the steeply dipping progradational reflections and their horizontal equivalents in the strike orientation.

Interpretation This radar facies is interpreted as representing the foreset beds of the fan delta. The fluctuations in dips of these beds recorded in radar lines is a result of the shifting of Cypress Creek across the delta plain. Debris flows that followed the course of the creek would, in time, clog the

Table 1. *Signatures of the radar facies forming the fan delta*

Radar facies	Description	Original pattern	Interpreted pattern
I	Progradational radar facies a) oblique subfacies b) sigmoidal subfacies		
II	Mounded radar facies		
III	Low relief transgressive radar facies		
IV	Concave radar facies		
V	Horizontal radar facies		

channel, causing the stream to avulse to a new position on the delta plain. A result of this channel-shifting is a displacement of the location of the supply of fresh sediment to the delta front, leading to a change in delta foreset geometry.

Radar facies II: mounded radar facies

Description Characterizing this facies are reflection patterns forming a series of hummocks or mounds (Table 1). In places, the convex reflections forming the mounds are individual features quite segregated from adjoining reflections (see Fig. 3, northern end of facies II) but, in other locations, the reflections forming a mound will interfinger with reflections

from adjacent mounds. The internal reflection patterns within a mound vary from being stacked (an irregularly layered signature) to fragmented (where it is inferred that an erosional process has removed part of the pattern).

Interpretation These mounded features are interpreted as the radar image of the outer surface and, to a lesser degree, the internal bedding of debris-flow lobes that flowed over the subaerial surface of the fan delta. The facies occurs above or landward of the inferred foreset beds (facies I) and is the main component of the delta's topset beds. Modern debris-flow deposits are often deposited side by side with, or onlap adjacent to, previously
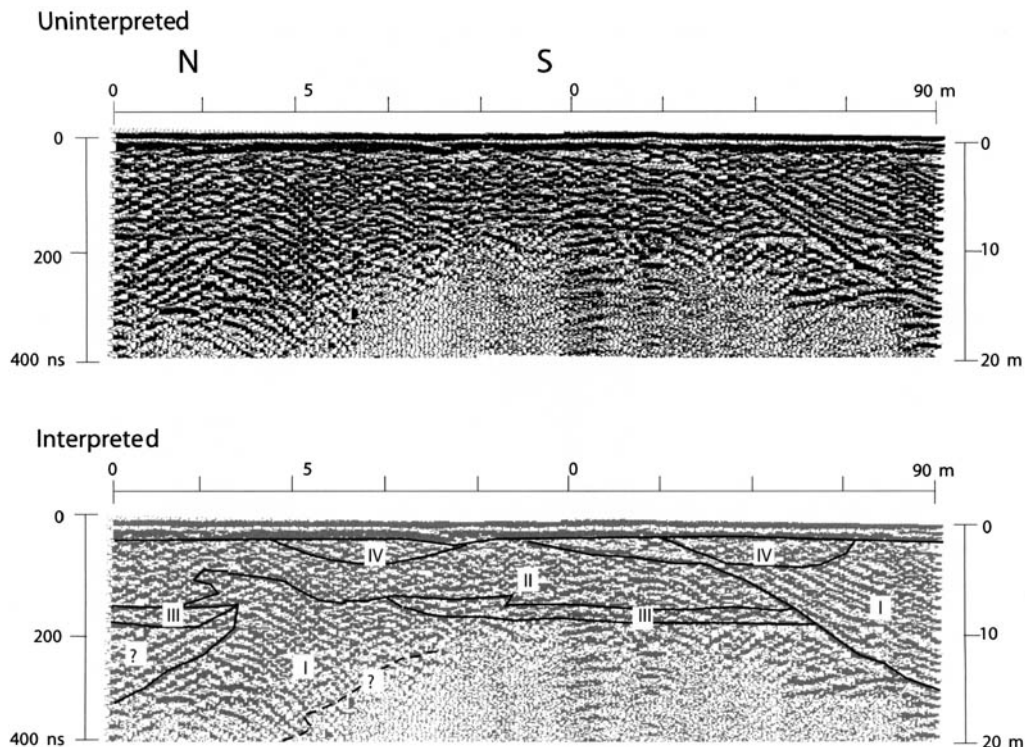
Fig. 3. The radar facies of GPR lines Stn 135/137. Roman numerals refer to the facies discussed in the text. (See Fig. 2 for location of GPR lines.)

deposited lobes, resulting in a regular to irregular convex surface morphology. These onlapping and roughly layered flows form a convex, stacked radar signature. Active debris flows can, on occasions, erode previously deposited flows or reactivate them and deposit them further down slope, all resulting in the fragmentation of the continuity of the radar reflections imaging a debris flow. The rugose texture of debris-flow terrain can produce radar-reflection signatures that can be similar to hyperbolic diffractions. Therefore, a challenge in the interpretation of the reflection patterns of this facies involves differentiating between the mounded signal, representing debris flows, and hyperbolic events (diffractions) emanating from individual, large boulders occasionally rafted by the debris flows. Applying air-velocity and ground-velocity grids to the tails of suspected hyperbolic events showed that, for the most part, the mounds were real reflection patterns and not hyperbolic events. There is a clear hyperbolic event in line Stn 100 and it is centred on the 83 m-distance mark (Fig. 5); its tails can be seen extending outwards from a central point.

Radar facies III: undulating subhorizontal radar facies

Description This facies is distinguished by high-amplitude, horizontal to very gently undulating single or double reflections that truncate the underlying reflections and form a 'platform' for overlying reflections (Table 1). The reflections form a low-angle ramp dipping seaward, where it may merge with the sigmoidal upper part of the clinoforms of facies I or simply truncate the clinoforms. Of the five facies characterizing the fan delta, it is the thinnest, with a thickness varying between 1 m and 2 m (Fig. 3).

Interpretation This facies is interpreted as the beach zone of the fan delta. The reworking of the seaward edge of debris-flow lobes and fluvial deposits on the delta plain forms a wide (up to 100 m) beach truncating the underlying sediments. This truncation is captured by the horizontal radar reflections of this facies.

Uninterpreted

Interpreted
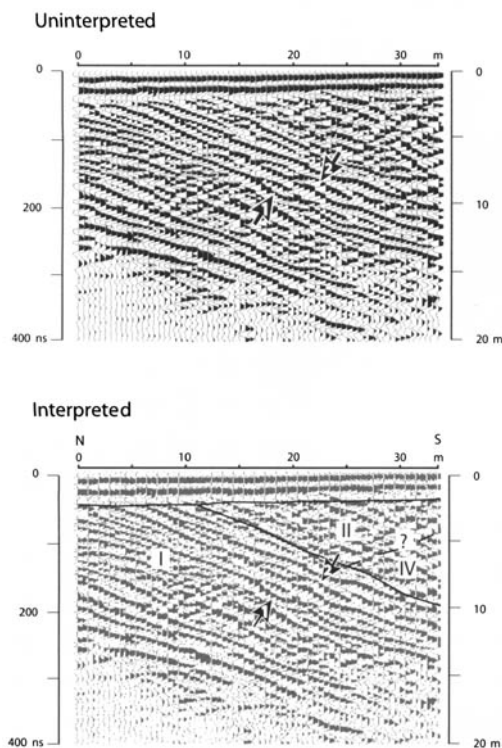
Fig. 4. GPR line 123: a dip line across the foreset beds of the fan delta. This line illustrates the slight changes in the dip of the foreset reflections and the radar signatures of slope failures. Numbered arrows: 1, concave scar of a delta-front failure site; 2, site of slumped mass that has shifted down slope. (See Fig. 2 for location of GPR lines.)

Radar facies IV: concave radar facies

Description This facies is characterized by reflections having concave geometries and moderate to strong continuity; the base of the facies is defined by moderate- to high-amplitude reflections (Table 1; Fig. 3). Above the reflection defining the basal, concave bounding discontinuity of the facies, there can be other concave reflectors or short, dipping reflectors which may, or may not, be aligned. In rare situations, there is a horizontal reflection capping the concave package. Facies IV is often difficult to distinguish because of its limited extent and its potential confusion with the infill areas between the mounded reflections of facies II.

Interpretation These concave reflections are interpreted as the radar images of the fan delta's distributary channels. The channel boundary is usually a well-defined concave reflection, because it is abruptly eroded into the underlying delta-plain deposits. At present, there are two active creeks

crossing the delta: the larger one (Cypress Creek), at its mouth is 20 m wide and 2 m deep, while the smaller one is 2.3 m wide and 1 m deep. This size differentiation is reflected in the radar images of the channel cross-sections found in the fan delta (Fig. 3).

Radar facies V: horizontal radar facies

Description This minor and spatially limited facies is typified by high-amplitude reflections continuous for short distances and then broken by transparent zones that completely lack any radar signal (Table 1).

Interpretation This reflection pattern is typically generated in one of two ways: either by salt-water intrusion beneath the delta plain, or where a GPR line has been run on the active beach and the signal is lost completely because of salt water present in the beach sediments.

Depositional and geomorphical environments

The depositional environments of a fan delta are established by combining the mapping of the modern geomorphology with subsurface images provided by the GPR. Four major depositional environments are identified: delta plain, channel zone, beach zone and delta font.

Delta plain

The delta plain of a fan delta can be subdivided into two zones: (1) the subaerial delta plain extending from the bedrock boundary at the back of the fan to the low tideline; and (2) the subaqueous delta plain which is the morphological continuation of the subaerial plain extending from the low tideline to the break in slope at the top edge of the delta front.

Subaerial delta plain This geomorphic unit has a 2–4° slope from the fan's apex — where the stream emerges from its bedrock valley — to the low tideline (Fig. 2). In cross-section from east to west, the fan has a convex profile with the high point roughly coinciding with the channel of Cypress Creek. The surface of the delta plain is formed primarily by bouldery hummocks (Fig. 6b) interspersed, in places, with gravelly aprons. In its natural state, prior to the residential land use of today, this hummocky landscape was covered by an old-growth forest (Douglas fir, western hemlock and red cedar; Fig. 6b). Repeated deposition of debris flows formed this landscape and, by extension, the
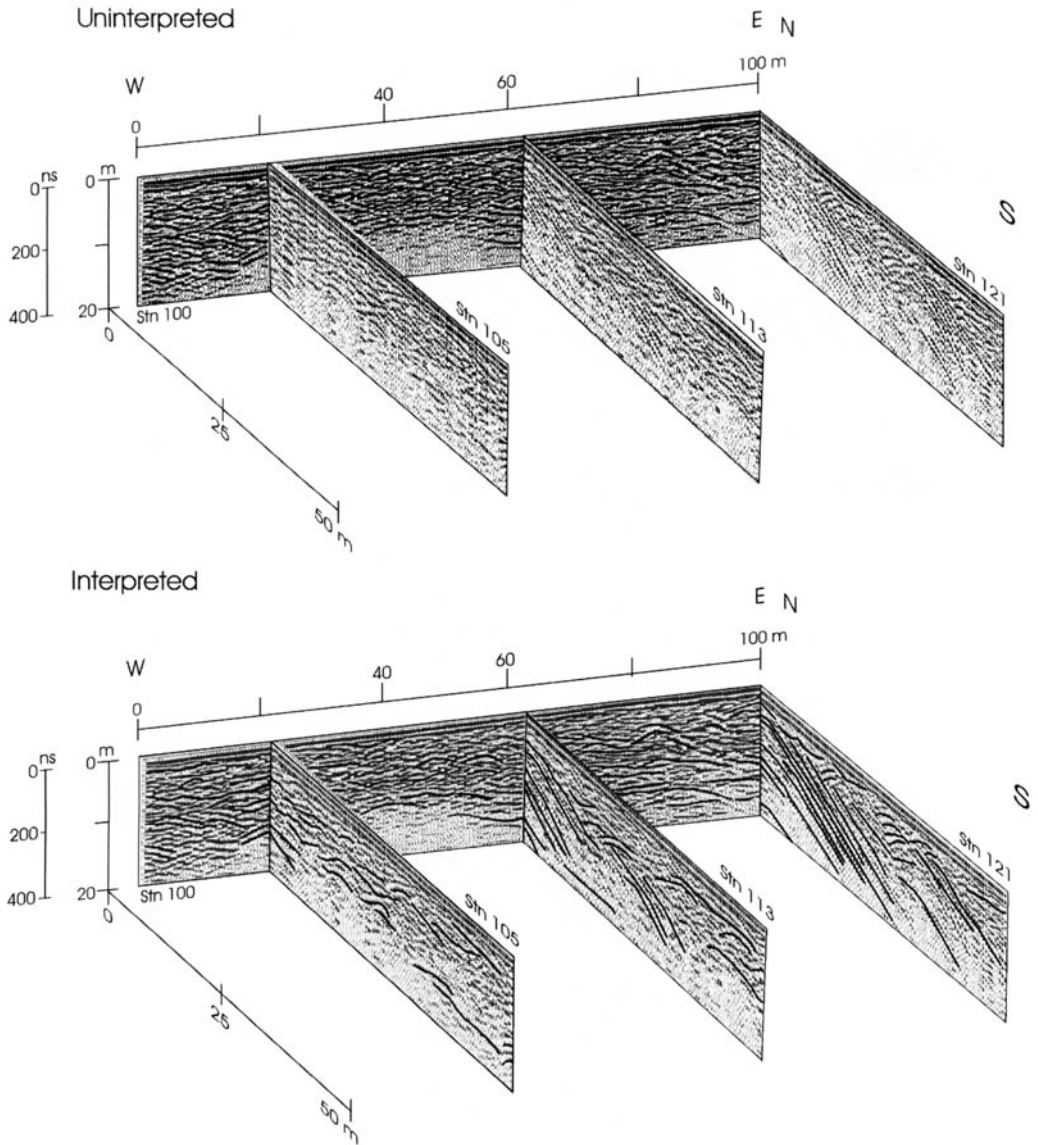
Fig. 5. A fence diagram of the relationship between the steeply dipping delta-front reflections and the horizontality of the same reflections in the strike direction. (See Fig. 2 for location of the GPR lines.)

topset beds of the fan delta. The largest trees would have slowed, or even blocked, the debris flows and prevented them from spreading out over the delta plain. The debris-flow lobes were deposited when a surge of sediment, leaving the confines of the bedrock gorge of the creek, decelerated and then halted on the low slopes of the delta plain. The lobes are produced by a frontal concentration of cobbles and boulders, some rolling and others suspended, in a slurry of pebbles, granules and sand

that precedes the finer tail of the complete debris-lobe event. The radar reflections of radar facies II reproduce the convex geometry of these lobes. The debris-flow deposits are characterized by poorly sorted, sandy matrix-supported gravels (Gms) and clast-supported gravels (Gm) with localized areas of open-framework cobble gravels (Fig. 6d). Very large boulders, up to 1 m in diameter, are partly embedded in the surface areas of many lobes. In core, the topset bed of the delta can attain a thick-
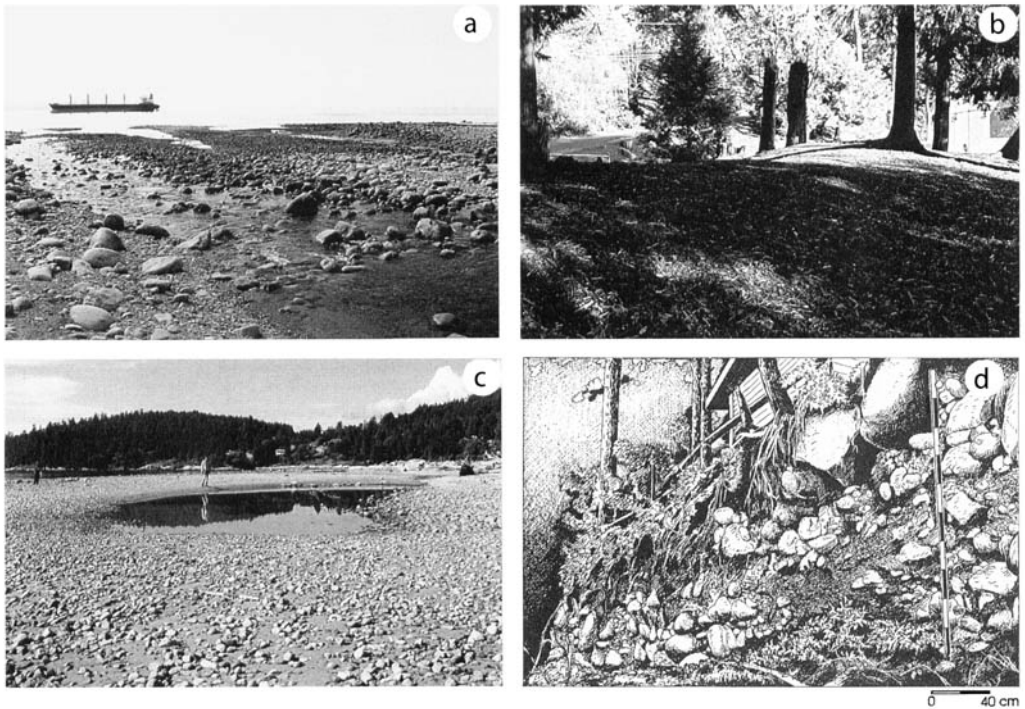
Fig. 6. (a) Channel-mouth bars of Cypress Creek at low tide (see also Figure 7). (b) The hummocky surface of a debris-flow lobe. (c) View across the beach. (d) A drawing from a photograph of a section through debris-flow deposits showing rudimentary stratification.

ness of 12 m (well 4–94 in Fig. 7). From the few exposures available (Fig. 6d), individual gravel beds have limited continuity, a finding that fits with radar facies II, which shows mounded reflections having limited spatial extent, typically 5–8 m across, often interfingering with reflections from adjacent mounds (see facies II in the upper part of Fig. 3).

In places along the banks of Cypress Creek, where it crosses the upper subaerial delta plain, there are gravel aprons that splay out from the channel. The aprons are typically 5–10 m wide and up to 50 m long and are composed of normally graded beds between 10 cm and 35 cm thick. Insights into the formation of an apron occurred in 1985, when the coarse frontal lobe of a debris flow that had flowed down the channel of Cypress Creek halted and blocked the passage of a slurry of finer particles (mainly sand and pebbles with a few cobbles) trailing the frontal lobe. This slurry flowed out of the channel and was deposited on the uneven surface of the delta plain, draping the hummocky surface or infilling depressions. A separate GPR signature for the apron has not been identified; a not unexpected outcome given the thinness of the unit.

The seaward edge of the subaerial delta plain is sharply trimmed by wave action where a beach has formed (see Beach zone below). Morphologically, the beach is distinguished by a smooth to undulating surface, in marked contrast to the hummocky surface of the rest of the subaerial delta plain.

Subaqueous delta plain This part of the delta plain extends from the low tideline to the break in slope at the top edge of the delta front; the break in slope occurs in a water depth of about 1.5 m (at mean low tide). The width of this geomorphic unit varies from 10 m to 80 m. The gravels within the unit are finer, compared to the beach zone, and are mainly pebbles with lesser amounts of cobbles. The flattened, upper part of a sigmoidal radar reflection in line Stn 135/137 (Fig. 3) may represent the subaqueous part of the delta plain with the inclined part of the reflection being the delta front.

Channel zone

Crossing the delta plain are two creeks. The major one, Cypress Creek, drains the complete basin while a smaller tributary stream to the west drains a small basin on the hillslope above the western

side of the fan (Figs 2 & 7). Where Cypress Creek emerges from a narrow bedrock gorge onto the fan, it has a width of 12.5 m and a depth of 2.1 m; downstream, the channel narrows to 10 m where residential development encroaches the banks (which have been rip-rapped). At the high tidemark along the edge of the delta plain, where the channel enters the tidal zone, it widens to 25 m.

The channel sediments consist of poorly sorted, cobble gravels, with lesser amounts of sand. Boulders (up to 1.5 m in diameter) are scattered up and down the channel, though with a greater concentration near the fan's apex. The sand component of the bedload is found either as the matrix of the gravel in the channel lag or as isolated lee accumulations behind boulders or bars, or in indentations in the channel banks. In places, the channel gravels are clearly remnants of debris-flow lobes that have been modified by subsequent fluvial events. Where the stream enters the tidal zone, channel-mouth bars are formed (Figs 6*a* & 8). Some of the channel gravel in the tidal zone is moved by wave action from the channel onto the adjacent beach, though most of the gravel is moved through the tidally influenced reach of the channel and deposited on the delta front. Volumetrically, these deposits are a minor component (about 15%) of the delta-plain sediments.

Beach zone

The beach zone is the seaward edge of the subaerial delta plain where debris-flow and river sediments are reworked by wave action. The beach zone extends from the upper beach, the highest part of which is above normal high tides, to the lower beach that extends to the lowest tideline (Fig. 8). The surface morphology of the beach varies from a smooth, sandy uniform surface at the western edge of the fan delta to the low-relief, gently convex lobate gravels of the central part of the beach (Fig. 6*c*). This lobate geometry is partly captured by the map of the gravel facies (Fig. 8), which shows systematic variations in the surface concentrations of different gravel sizes. These lobate patterns, it is suggested, are linked to the wave erosion of debris flows in the beach zone, whereby the upper part of a debris-flow lobe is eroded leaving a basal lobate remnant. Wave action tightly packs sand between the gravel clasts and forms a lag resistant to erosion, thereby preserving, albeit faintly, the lobate forms of eroded debris flows; these forms are not to be confused with beach cusps that form on some beaches. The low relief and gentle dips of the beach are represented by the gently undulating reflections of radar facies III (Fig. 3).

Upper beach The upper beach is the inland fringe of the beach zone rising between 1.0 m and 1.5 m above the level of the more extensive lower beach. Although the surface of the upper beach is covered largely by sand with occasional pebbles, a section through the beach revealed the following sequence: from 1.5 m to 1.0 m — pebble–cobble gravel with a sand matrix; from 1.0 m to 0.5 m — sand with scattered pebbles; and from 0.5 m to the surface — coarse sand. The GPR image of the upper beach sediments can be seen in facies III of line Stn 135/137 (Fig. 3), between 35 m and 49 m (horizontal distance) and around 6 m to 7.5 m in depth, where it is imaged by a set of parallel reflections in an en echelon pattern with regard to the reflections of the lower beach, which are slightly lower in elevation. This configuration of the radar reflections, the landward set being slightly higher than those of the seaward set, is a direct image of the geomorphological relationship between the upper and the lower beach discussed above.

Lower beach For the most part, the lower beach is armoured by gravel. The winnowing of the sand and granules from the surface gravel produces a stable lag, or armour, resistant to further erosion. The armour displays lobate patterns in grain size (Fig. 8). In areas where boulder gravel or boulder–cobble gravel facies are dominant, the individual boulders are commonly randomly dispersed. This is a reflection of the manner in which the largest boulders are often randomly distributed in a debris-flow front as it surges across the delta plain. That wave action has not removed these localized variations in gravel texture is partly a function of the sheltering effect of Point Atkinson (Fig. 1) blocking waves with a westerly component — the direction of winter winds having the potentially largest fetch. The waves from shorter fetch directions have not been able to entrain the gravel to the degree where reworking would have removed the lobate texture patterns. The laterally extensive beach armour is formed by a single or, more rarely, double clast layer, below which is gravel with a matrix of coarse sand or sand and pebbles. Scattered within the beach gravels are whole and broken tests of mussels (*Mytilus* spp., *Clinocardium* spp.), cockles (*Nucella* spp.) and barnacles (*Balanus* spp.): an assemblage typical of rocky and coarse gravel shorelines (Bourgeois & Leithold 1984) and which formed once the beach was cut into the pre-existing sediments.

The lowest part of the lower beach extends from the low tideline to the break of slope at the top edge of the delta front; this part of the beach is coincident with the subaqueous delta plain. The gravel occurring in this zone is usually finer
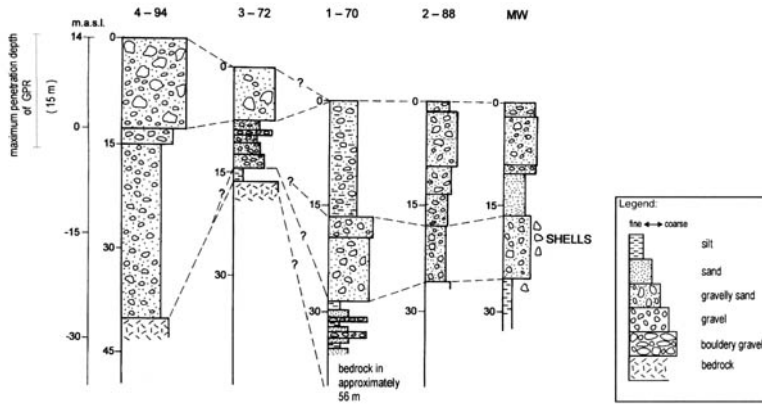
Fig. 7. Correlation of core logs drilled into the Cypress Creek fan delta (Pacific Hydrology Consultants). (See Fig. 2 for core locations.) m a.s.l., metres above sea level; MSL, mean sea level.

(pebble to pebble–cobble gravel) than that in the rest of the lower beach. Evidence for the stability of the gravel in this beach zone is shown by the growth of seaweed (kelp) covering most of the subaqueous beach material, with mussels growing in clusters across many clasts.

Delta front

The radiating delta front of Cypress Creek has a gradient varying from 16° to 22° (see profiles in Fig. 2) and flattens out in the prodelta to 2°. The submarine cone (delta front plus prodelta) extends out into Burrard Inlet for a distance of 500 m and to a depth of about 50 m. The morphology of the delta front is modified by the presence of small sedimentary lobes representing different locations of Cypress Creek as it shifted across the delta plain.

Only limited direct observations on delta-front sediments were collected as part of this project. Measurements were carried out using a lead weight with a waxed base that either adhered to or carried imprints of the sampled sediments. Underwater sampling revealed zones of coarse gravel near where the present Cypress Creek enters the ocean, as well as zones of sand. Silt was found covering sand and gravel, as fine drape. Soundings down the delta front and onto the prodelta revealed a fining from sand, to sand and silt, to silt. During times of flooding in the main channel, the floodwaters carry a suspended load with a high fine sand and silt content, forming a plume that can extend up to 100 m into Burrard Inlet. The gravel bedload is transported across the delta plain and into the beach zone, where it is either added to the beach material by wave action or deposited on the delta front. The overall coarsening-up sequence of the delta front is documented in core 3–72 (−16 m to 1 m) and core MW (−30 m to −10 m) (Fig. 7).

Prior and Bornhold (1988, 1990) have carried out detailed investigations of delta-front processes and sedimentation in British Columbian fjord environments and have demonstrated that, once floodwaters reach the delta front, some combination of normal sedimentation (sediment settling out of suspension and being moved by the tides) and subaqueous gravity processes, including slumping, debris flows and turbidity currents, occurs. On the delta front of the Britannia Beach fan delta, 60 km north of the present study area, Prior and Bornhold (1988) identified shallow channels (chutes) eroded by rapid sediment flows.

During periods of rapid sediment accumulation on the delta front, unstable lobes of material can slump downslope leaving small scarps. Where the scarps are high enough (≥ 1 m) and the slumped material is deposited immediately downslope, it is sometimes possible to identify a radar signature for such a slope failure. A detailed examination of the oblique dipping reflections of facies I, in the centre of line Stn 123, reveals slight indentations in the normally straight reflection patterns that are interpreted as slump scars (Fig. 4). In other places, there is evidence of the slumped material where short convex reflections are either downslope of a scar or are found as isolated hummocks without a slump scar that can be directly related to it (Fig. 4).

Discussion

Sea-level change and fan-delta evolution

Any examination of post-glacial fan deltas in the coastal regions of British Columbia must incorporate, in some way or other, sea-level changes induced by glacio-isostatic movements and, to a lesser degree, by eustatic changes (Clague 1983).

When the late Wisconsinan glaciers melted and left the fjords, and the Coast Mountains became ice-free, the sea invaded the isostatically depressed lowlands and established a shoreline at about 150 m above present sea level. Cypress Creek deposited a highstand fan delta aggraded to this sea level (Fig. 1). With the onset of falling sea level, this earliest delta was left stranded on the hillside above the modern fan delta. A continued fall in sea level and the accompanying decline in accommodation space resulted in the sediments being eroded from the Cypress Creek drainage basin being transported down the channel directly to a subaqueous cone. The evidence for a subaqueous cone is the occurrence of facies I at the northern end of line Stn 135/137 (Fig. 3) at a depth between 12 m and 20 m; deposition at such a depth probably implies emplacement prior to sea-level rise after 9–8 ka because, at that time, sea level was around −12 m. There is no evidence of intermediate-level deltas between the 150 m palaeodelta and the modern one. After a lowstand was reached sometime between 9 ka and 8 ka (Williams & Roberts 1989), sea level started to rise, leading to increased accommodation space which, in turn, led to sediment accumulating on the subaqueous cone, such that the cone accreted vertically and the top of the cone gradually reached sea level. With the stabilization of sea level (around 2.3 ka), there followed a widening of the cone's top to form a delta plain, because the lack of accommodation space forced the delta to prograde. One outcome of the increase in delta-plain width was that fewer and fewer debris flows had sufficient kinetic energy to cross the low slope (<5°) of the plain and deposition took place prior to reaching the delta front; nevertheless, the finer tails of the debris flows, containing sand, granules and silt, often continued to flow across the delta plain. As a consequence, smaller and smaller amounts of coarse debris reached the delta front and, over time, the average grain size of the prograding delta front declined.

Macro-tidal fan deltas: a diagnostic facies

Fan deltas, deposited along the coastal fringes of the glaciated mountains of southwestern British Columbia, are often flanked by wide beaches which, in the subsurface, generate a distinctive radar signature — undulating subhorizontal radar facies (III). This facies, it is argued here, is diagnostic of macro-tidal fan deltas because it differentiates this style of delta from fans deposited in large lakes, or along micro-tidal coasts, where beach development is limited because of the limited vertical range over which waves can act. Gravel beaches are rarely mentioned in the research literature of modern fan deltas, although they have

been preserved and recognized in ancient rocks (Collela 1988). In the macro-tidal regime of the British Columbian coast, wave action takes place over a 4.9 m tidal range and, given the low slope of the subaerial delta plain, can deposit a beach up to 100 m in width. The radar characterization of the beach is expressed by two or three parallel radar reflections (Figs 3 & 9) that cut across and truncate the reflections of underlying facies or, in a few places, makes a lateral transition into the sigmoid architecture of the upper foreset beds. Lithologically, the beach is represented by a matrixsupported gravel overlain by a one-clast pebble or cobble (very rarely boulder) layer (Fig. 8). This vertically limited, but spatially extensive facies is a distinctive element in the three-dimensional architecture of the Cypress Creek fan delta (Fig. 9).

Proposed depositional model for Cypress Creek

In proposing a depositional model for a fan delta, it is necessary to place it within a climatic, physiographical and oceanographical context, because it is these regional factors that influence the depositional processes which construct the architecture of the fan system. Although adjacent fan deltas may be distinguished from one another by such variables as drainage-basin size, shape, degree of forest cover and length of channel banks formed by surficial material (a measure used to estimate the potential of debris-flow generation), these variables are not, for the most part, the main determinants of fan-delta architecture. They control the amount of sediment being delivered to the fan, not its depositional form.

Coastal British Columbia has a mild, wet, west-coast climate (Barry & Chorley 1968), with precipitation maximums enhanced by topographical effects of the mountainous terrain. Water floods can be produced within a normal precipitation regime but, for geomorphologically significant water floods and debris flows to occur, some form of meteorological triggering is usually required. Such triggering events include (1) localized cells of intense rainfall having return periods of 2–5 years (Hungr *et al.* 1984); and (2) rain-on-snow events occurring when warm temperatures and rain ripen a snowpack to temperature levels that cause rapid melting of the snow, producing high runoff followed by the initiation of debris flows. Whatever the trigger, the intense generation of runoff combined with rapidly increasing pore pressures in the surficial sediments leads to slope failure that translates into a debris flow. It is repeated debris-flow activity that largely constructs the delta plain and provides the sediment source for the progradation
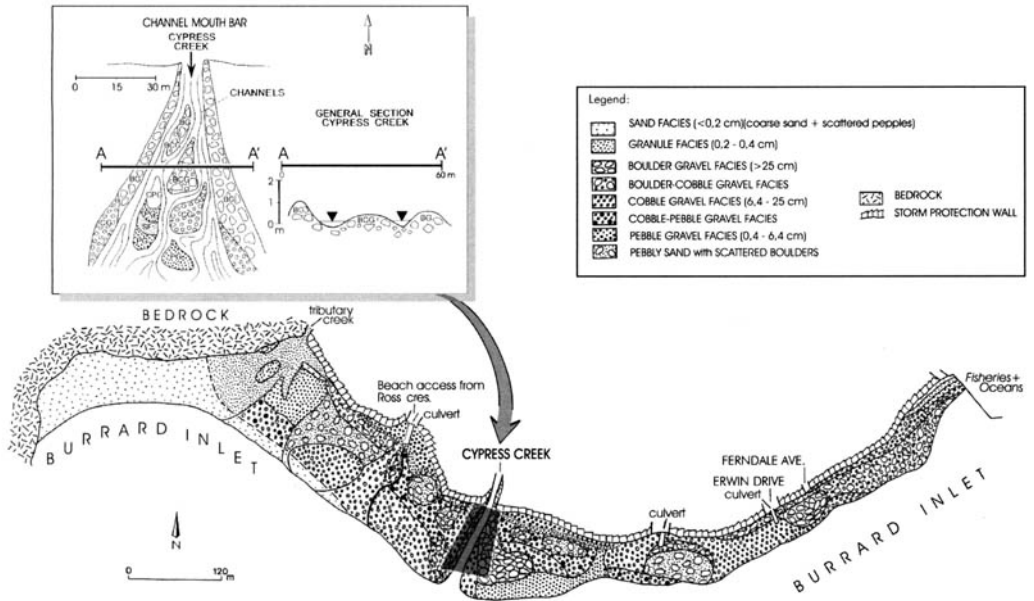
Fig. 8. The sedimentary facies of the beach zone and the channel-mouth bars of the Cypress Creek fan delta. The beach zone is the modern analogue of radar facies III.

of the delta front. In short, debris flows are an important element of this proposed depositional model.

The glaciated physiographical setting is broadly characterized by steep slopes and adjacent deep ocean water into which the fan deltas can prograde. Given an equal supply of debris, water depth is often a determining factor in whether a fully developed fan delta or a partially modified alluvial fan will be formed. In deep fjords, where water depths can reach 100 m along their flanks, alluvial fans rarely develop a delta plain because the accommodation space is so large that the subaqueous cone will not accumulate a sufficient volume to reach sea level. However, if the receiving basin is relatively shallow (as is the case with Burrard Inlet in the vicinity of Cypress Creek, where water depths only reach 40 m), a fan delta will construct a sedimentary prism large enough to reach sea level and form a delta plain.

Oceanographical influences on the model can be resolved into two major components: tidal regime and wave climate. The tidal regime of Burrard Inlet is mixed semidiurnal with the two high waters separated by, alternately, a very low tide and a second low tide that is only about a metre or less than the high tides. Under such conditions, waves, although rarely reaching heights of 60 cm, can rework a wide gravel beach. The Cypress Creek fan is in a sheltered location, being east of Point Atkinson and

within Burrard Inlet (Fig. 1), so fetch is limited and maximum wave heights greater than 60 cm only occur 10% of the time (Thomson 1981).

The depositional model, based on the Cypress Creek fan delta (Fig. 9), contains the following components: a delta plain dominated by debris-flow deposition and crossed by a river channel; a wide beach zone truncating delta-plain deposits, and a prograding delta front. The internal architecture of the model was established by radar facies analysis (Fig. 9b).

Conclusions

The Cypress Creek fan delta evolved during a period of complex sea-level change. Initially, after the retreat of the ice and the subsequent marine inundation of the isostatically depressed Coast Mountains and lowlands, a palaeodelta was aggraded to a shoreline established at 150 m above present sea level. Sea level fell from the immediate postglacial highstand and present-day sea level was reached by 2.3 ka. The fan delta has five major radar facies: I, oblique clinoform radar facies representing the foreset beds of the delta front; II, mounded radar facies providing images of debris-flow lobes forming the delta's topset beds; III, undulating subhorizontal radar facies representing the beach zone; IV, concave radar facies, the GPR characterization of distributary channels, and V, horizontal radar

(a)

(b)
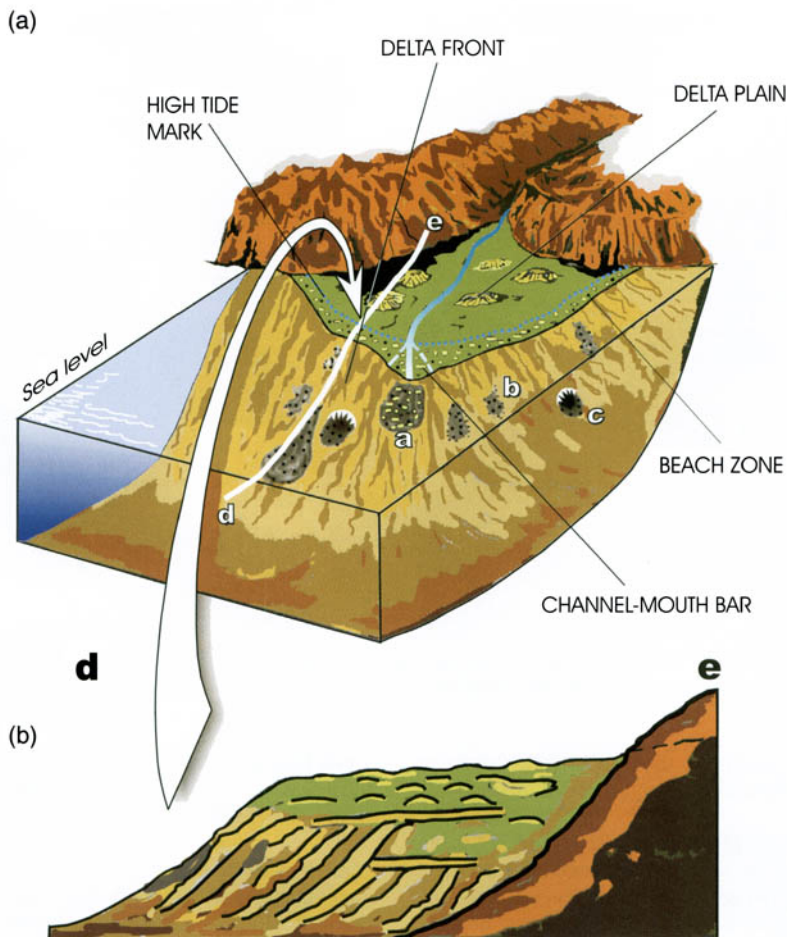
Fig. 9. A proposed depositional model for a fan delta on a macro-tidal coast prograding into a relatively shallow (=40 m) receiving basin. (**a**) Depositional model directly linked to the geomorphic features of the fan delta: a, gravel lobe deposited by the distributary channel on the delta front; b, slumped mass from a slope failure; c, slope-failure scar with slumped material. (**b**) The internal architecture of the fan delta, based on radar reflection signatures.

facies, a minor reflection pattern representing saltwater intrusion. It was concluded that radar facies — radar facies III — was diagnostic of macro-tidal fan deltas, because the wide beach and its associated deposits combine to provide a distinct, and discriminating element in the fan's architecture.

The shallow waters of the receiving basin are a constraint on accommodation space and high sediment flux from the Cypress Creek basin, and results in the vertical aggradation of the subaqueous cone to sea level, thus providing a foundation for the development of a wide delta plain. The seaward edge of the delta plain was reworked by waves operating over a 4.9 m tidal range and pro-

ducing a wide beach — a distinguishing property of a macro-tidal fan delta.

A depositional model of a fan delta was constructed to integrate the geomorphical, sedimentological and radar datasets.

Fan deltas are not only of geoscientific interest but also of public-policy interest, because they are frequently the sites of urban settlement, despite risks from such natural hazards as debris flows, river floods and spring-tide inundation. Extensive property damage and even loss of life have all occurred on fan deltas in southwestern British Columbia (Hartley 1996) and the hazard management of fans is becoming a very important policy issue (Hungr *et al.* 1984).

Hence, it is essential that land-management decision-making is based on a thorough understanding of the geomorphology and sedimentology of fans in order that policy has a geoscientific rationale to enable effective planning.

References

ANNAN, A. P. & COSWAY, S. 1996. Ground penetrating radar. Survey design. Paper prepared for the Annual Meeting of the Symposium on the Application of Physics to Environmental and Engineering Problems, 26–29 April 1992, Chicago. [pulseEKKO IV Run User's Guide, Version 4.2]

ARMSTRONG, J. E. 1990. *Vancouver Geology*. Geological Association of Canada, Vancouver, 128 pp.

BARRY, R. G. & CHORLEY, R. J. 1968. *Atmosphere, Weather and Climate*. Methuen, London, 319 pp.

BOURGEOIS, J. & LEITHOLD, E. L. 1984. Wave-worked conglomerates — depositional processes and criteria for recognition. *In*: KOSTER, E. H. & STEEL, R. J. (eds) *Sedimentology of Gravels and Conglomerates*. Canadian Society of Petroleum Geologists Memoirs, **10**, 331–343.

CLAGUE, J. J. 1983. Glacio-isostatic effects of the Cordilleran ice sheet, British Columbia, Canada. *In*: SMITH, D. E. & DAWSON, A. (eds) *Shorelines and Isostacy*. Academic Press, London, 321–343.

CLAGUE, J. J. 1994. Quaternary stratigraphy and history of south-coastal British Columbia. *Bulletin of the Geological Survey of Canada*, **481**, 181–192.

COLLELA, A. 1988. Pliocene–Holocene fan deltas and braid deltas in the Crati Basin, southern Italy: a consequence of varying tectonic conditions. *In*: NEMEC, W. & STEEL, R. (eds) *Fan Deltas: Sedimentology and Tectonic Settings*. Blackie & Son, Glasgow, 50–65.

CONYERS, L. B. & GOODMAN, D. 1997. *Ground Penetrating Radar: An Introduction for Archaeologists*. Walnut Creek, London, New Delhi, 232 pp.

DAVIS, J. L. & ANNAN, A. P. 1989. Ground penetrating radar for high resolution mapping of soil and rock stratigraphy. *Geophysical Prospecting*, **37**, 531–551.

HARTLEY, B. 1996. *Alluvial Fan Hazard Management in British Columbia*. Master of Natural Resource Management thesis, Simon Fraser University, Burnaby, B.C., 143 pp.

HOLMES, A. 1965. *Principles of Physical Geology* (2nd edition). The Roland Press Co., New York, 1288 pp.

HUGGENBERGER, P. 1993. Radar facies: recognition of facies patterns and heterogenities within Pleistocene Rhine gravels, NE Switzerland. *In*: BEST, J. & BRISTOW, C. (eds) *Braided Rivers*. Geological Society, London, Special Publications, **75**, 163–176.

HUNGR, O., MORGAN, G., & KELLERHALS, R. 1984. Quantitative analysis of debris torrent hazards for design of remedial measures. Canadian Geotechnical Journal, **21**, 663–677.

JOL, H. 1995. Ground penetrating radar antennae frequencies and transmitter powers compared for penetration depth, resolution and reflection continuity. *Geophysical Prospecting*, **43**, 693–709.

JOL, H. & SMITH, D. 1991. Ground penetrating radar of northern lacustrine deltas. *Canadian Journal of Earth Sciences*, **28**, 1939–1947.

MCPHERSON, J., SHANGMUGAN, G. & MOIOLA, R. 1987. Fan deltas and braid deltas: Varieties of coarse-grained deltas. *Bulletin of the Geological Society of America*, **99**, 331–340.

NEMEC, W. 1990. Deltas — remarks on terminology and classification. *In*: COLELLA A. E. & PRIOR, D. B. (eds) *Coarse-Grained Deltas*. International Association of Sedimentologists Special Publications, **10**, 3–12.

POSTMA, G. 1990. Depositional architecture and facies of river and fan deltas: a synthesis. *In*: COLELLA, A. E. & PRIOR, D. B. (eds) Coarse-Grained Deltas. International Association of Sedimentologists Special Publications, **10**, 13–27.

PRIOR, D. B. & BORNHOLD, B. D. 1988. Submarine morphology and processes of fjord fan deltas and related high-gradient systems: modern examples from British Columbia. *In*: NEMEC, W. & STEEL, R. (eds) *Fan Deltas: Sedimentology and Tectonic Settings.* Blackie & Son, Glasgow, 125–143.

PRIOR, D. B. & BORNHOLD, B. D. 1990. The underwater development of Holocene fan deltas. *In*: COLELLA A. E. & PRIOR, D. B. (eds) *Coarse-Grained Deltas*. International Association of Sedimentologists Special Publications, **10**, 75–90.

PACIFIC HYDROLOGY CONSULTANTS LTD. 1995. *Completion Report. Construction and Capacity Testing of Production Well 4-94, Capacity Testing of Well 3-72 and Installation of a Water Level Monitoring Well at West Vancouver Laboratory of Fisheries and Oceans Canada at 4160 Marine Drive in West Vancouver, British Columbia.* Prepared for Public Works Canada.

ROBERTS, M., BRAVARD, J. -P. & JOL, H. 1997. Radar signatures and structure of an avulsed channel: Rhine River, Aoste, France. *Journal of Quaternary Science*, **12**, 35–42.

RODDICK, J. A. 1965. *Vancouver North, Coquitlam, and Pitt Lake Map-Areas, British Columbia with Special Emphasis on the Evolution of the Plutonic Rocks*. Geological Survey of Canada Memoirs, **335**, 276 pp.

THOMSON, R. E. 1981. *Oceanography of the British Columbia Coast. Fisheries and Aquatic Sciences*, Department of Fisheries and Oceans, Ottawa, Special Publications, **56**, 291 pp.

VAN HETEREN, S., FITZGERALD, D. M., MCKINLAY, P.
    A. & BUYNEVICH, I. V. 1998. Radar facies of paragla-
    cial barrier systems: coastal New England, USA. *Sedi-
    mentology*, **25**, 181–200.

WILLIAMS, H. F. L. & ROBERTS, M. C. 1989. Holocene
    sea-level change and delta growth: Fraser River delta,
    British Columbia. *Canadian Journal of Earth Sciences*,
    26, 1657–1666.

The use and application of GPR in sandy fluvial environments: methodological considerations

JOHN WOODWARD[1,*], PHILIP J. ASHWORTH[2], JAMES L. BEST[1],
GREGORY H. SAMBROOK SMITH[3] & CHRISTOPHER J. SIMPSON[4]

[1]*School of Earth Sciences, University of Leeds, West Yorkshire, LS2 9JT, UK*
[2]*Division of Geography, School of the Environment, University of Brighton, Lewes Road, Sussex, BN2 4GJ, UK*
[3]*School of Geography, Earth and Environmental Science, University of Birmingham, Birmingham, B15 2TT, UK*
[4]*Department of Geography, Simon Fraser University, 8888 University Drive, Burnaby, British Columbia, V5A 1S6, Canada*
[*]*Now at Physical Sciences Division, British Antarctic Survey, High Cross, Madingley Road, Cambridge, CB3 0ET, UK (e-mail: jwoo@bas.ac.uk)*

Abstract: Ground penetrating radar (GPR) is a popular technique for imaging and interpreting sedimentary architecture. However, current literature shows a wide range in the quality of information provided on the GPR methodology and processing technique. It is therefore difficult to judge the validity of the GPR interpretations and this produces inherent difficulties for comparison between surveys. This paper describes the key steps required to collect, process and interpret GPR surveys in sandy fluvial sediments. GPR data from the South Saskatchewan River, Canada, are used to illustrate each stage of data collection and processing. Particular attention is given to the appropriate set-up conditions for the GPR software and hardware, the selection of data-processing techniques and velocity analysis. Methods for the interpretation of GPR reflectors are also investigated using ground-truth control provided by a cut-face exposure. This paper presents recommendations for a systematic and rigorous methodology for the collection, processing and interpretation of GPR data in sandy fluvial environments. The paper suggests that all data-collection parameters and processing steps should be recorded or tabulated in any GPR publication to facilitate comparisons between surveys.

Traditionally, study of the sedimentology of modern rivers has been based upon analysis of cut-faces, cores and shallow trenches above the water table (e.g. Smith 1974; Cant & Walker 1978; Crowley 1983; Bridge et al. 1986; Bristow 1993) and has enabled much progress in our understanding of these complex deposits. Data provided by such techniques are, however, often only one- or two-dimensional, are patchy in terms of spatial coverage, and involve surveys that are time-consuming to implement (cf. Bridge 1993). Due to these limitations, fluvial sedimentologists are now applying a variety of different approaches to improve the spatial resolution of data and imaging of the subsurface. One such approach is the use of ground penetrating radar (GPR), which can provide a much improved record of subsurface stratigraphy and can be successfully utilized in both sandy

deposits (e.g. Bridge et al. 1998; Ferguson & Brierley 1999; Fielding et al. 1999; Vandenberghe & van Overmeeren 1999; van Dam & Schlager 2000) and gravels (e.g. Huggenberger 1993; Beres et al. 1995). Since GPR holds enormous potential for such studies, it is appropriate to assess critically the different set-up configurations and data-processing steps that can influence data output and interpretation. Key considerations for the collection of comparable, high-quality GPR data sets include: (1) the methodology applied in the field for data collection, (2) the processing steps of the raw data to enhance data display, (3) velocity analysis to enable an estimate of depth, and (4) sedimentological interpretation of the GPR data.

This paper will address these issues using GPR data obtained from the sand-bed, braided South Saskatchewan River, Canada, and provide a metho-

dological framework for GPR investigations of fluvial sediments that builds upon past research (e.g. Daniels *et al.* 1988; Davis & Annan 1989; Peters *et al.* 1994; Jol 1995; Tillard & Dubois 1995; Young & Sun 1999). By drawing attention to these methodological issues, it is anticipated that the quality of future GPR studies can be improved in order to aid both interpretation and comparison between datasets.

Field site

The South Saskatchewan River is the largest river in the southern Canadian Prairies, originating in the Rocky Mountains and flowing into Hudson Bay.

The study area near the town of Outlook (Fig. 1*b*), is located in a semi-arid grassland zone in the south-central part of Saskatchewan (Fig. 1*a* & *b*), where the river is incised by approximately 30 m into Cretaceous shales and sandstones and into more recent Quaternary surface deposits. The river valley is between 0.5 km and 1 km wide and the river channel has a braided platform, with the active channel width being between 50 and 300 m. Bars range in size from 50 m long and 30 m wide up to 700 m long and 350 m wide (Fig. 1*c* & *d*). All bars in the active channel are inundated at diurnal high flow (the river is dammed upstream of the study reach) and during flood events. The generally flat bartops are exposed at summer low flow, but
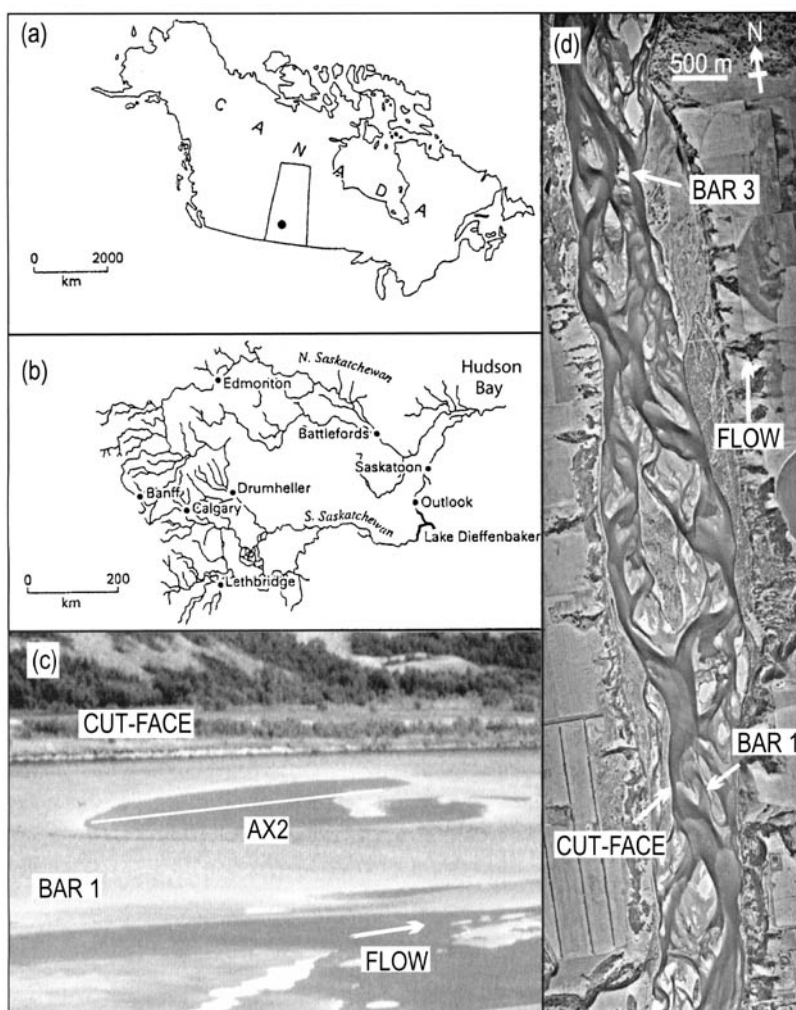
Fig. 1. (**a**) and (**b**) Location of the South Saskatchewan River, Canada. (**c**) Photograph of BAR 1, showing the location of GPR line AX2 and the cut-face profiles (flow left to right). (**d**) Aerial photograph showing location of study bars within the active channel at low flow (flow bottom to top).

the water table remains close to the bar surface. Bars in the South Saskatchewan appear to develop from the amalgamation and stacking of dunes, to the order of 0.5 m high, which are ubiquitous in all active channels. Also present are lobate bars that migrate downstream at 50–300 m per annum and possess distinct avalanche faces up to 0.5 m high. More details on the geomorphology and sedimentology of the South Saskatchewan are given by Cant and Walker (1976, 1978).

Field methodology

Perhaps the most important methodological issue in collecting usable GPR data is a robust field programme that provides a sound foundation for subsequent processing and interpretation. The field methodology applied when collecting data in the South Saskatchewan is given in Table 1. When designing a survey programme, consideration of several factors is essential:

Choice of GPR system There are now a number of commercially available GPR systems that can be used for data collection. Some of these, such as the pulseEKKO 100 and 1000 (Sensors and Software,

Inc.; Fig. 2*a* & *b*) and RAMAC/GPR (Malå Geoscience) systems allow both common midpoint (CMP) and common-offset (CO) modes of data collection. CO data collection involves taking data profiles by moving the antennae along the survey line. In CMP surveys the antennae are moved progressively further apart at an equal offset from the central survey point. CMP data allows inferences to be made about the velocity of electromagnetic (EM) wave propagation in the subsurface. Other systems, such as the Noggin (Sensors and Software, Inc.) and SPRscan (ERA Technology) do not allow CMP data collection and are used primarily for commercial applications in urban environments, e.g. surveys that aim to locate near-surface pipes and cables, and where velocity determination is less important.

Mode of data collection Data can be collected in either continuous or step mode. In continuous mode, the antennae are dragged over the surface (cf. Davis & Annan 1989). This mode of operation degrades data quality in subsequent data-stacking and makes some processing steps, such as migration and topographic correction, less reliable. Such degradation is prevalent in rough terrain, e.g.

Table 1. *Details of collection parameters and processing steps for all GPR profiles shown in this paper*

Data collection						
Line	AX2	AX2	AX2	CMPX1	CF900a	CY6
Figure	3, 4, 6, 10	4	4	8	9	11
Location	BAR1	BAR1	BAR1	BAR1	CUT-FACE	BAR3
GPR unit	PE 100	PE 1000	PE 1000	PE 1000	PE 1000	PE 1000
Survey	CO	CO	CO	CMP	CO	CO
Antennae frequency (MHz)	200	450	900	450	900	450
Antennae separation (m)	0.75	0.25	0.25		0.25	0.25
Station spacing (m)	0.10	0.05	0.02	0.05	0.02	0.05
Mode of data collection	SAC	SAC	SAC	SAC	SAC	SAC
Stacks	64	64	64	64	64	64

Processing						
Dewow	8.71	22.5	47.8	22.5	47.8	22.5
Drift removal	✓	✓	✓		✓	✓
Set time-zero	✓	✓	✓		✓	✓
Band-pass filter	50–100–220–440	150–300–500–1000	250–500–1000–2000		250–500–1000–2000	150–300–500–1000
Background removal	200	100	100		100	100
Depth conversion velocity (m ns^{-1})	0.05	0.05	0.05	0.05	0.05	0.05
Elevation statics	✓	✓	✓		✓	✓
Gain (AGC, ns)	25	20	15	20	15	20

Ground-truthing
Cut-face experiments used for interpretation
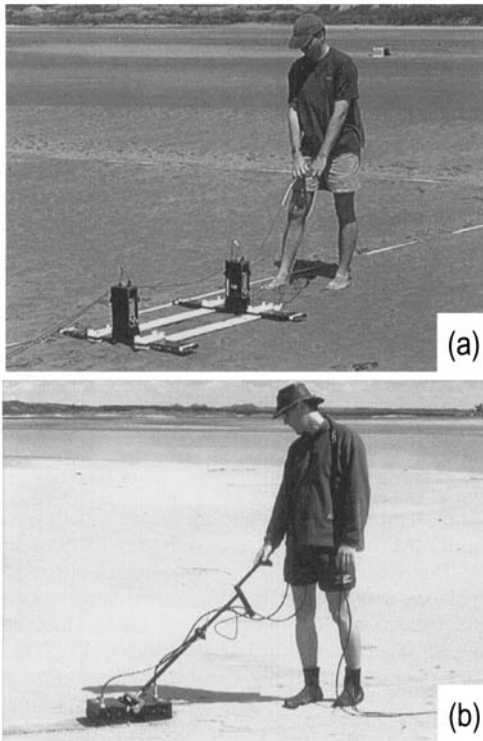
Fig. 2. (a) 200 MHz antennae with the pulseEKKO 100 GPR unit. (b) 900 MHz antennae in use with the pulseEKKO 1000 GPR unit.

on vegetated barforms, where radio-frequency interference is affected by changes in ground-coupling, as the height of the antennae above the ground will change through the survey (Peters *et al.* 1994). Areas where elevation changes rapidly, e.g. on bar slipfaces or channel margins, will also suffer from degradation of data quality for the same reason (Lehmann & Green 2000; Lehmann *et al.* 2000). In step mode, the antennae are held a constant distance apart and moved progressively along the profile. A reading is taken at predetermined intervals along a tape placed beside the survey line, and hence the exact position of every trace taken on the profile is known. This process is made simpler and more accurate if the antennae are mounted on a purpose-built sledge which ensures that the antennae are a constant distance apart (Fig. 2). For the South Saskatchewan study detailed herein, GPR data were collected in step mode, which is recommended for two-dimensional surveys in fluvial environments. For three-dimensional GPR surveys, the increased acquisition time in step mode may be prohibitive (e.g. Beres *et al.* 1995; Beres, *et al.* 1999; Lehmann & Green 1999).

Stacking tests Stacking is an averaging process undertaken during data collection in step mode. At each survey station (i.e. at every location on the survey line) a number of traces are collected and the mean value at each location on the survey line is saved as the record for the trace. This averaging suppresses spurious traces, such as atmospheric EM radiation that can often degrade a single trace in a dataset. The number of traces averaged in a data file is a trade-off between a constructive averaging procedure (where the more traces that are averaged, the better the station trace) and the time taken to collect a station trace. Multiple trace collection and averaging is time-consuming and may add little to the quality of the dataset. After field-testing of different stacks, from 16 to 256, a stack of 64 was selected for data collection in the South Saskatchewan as little change in the trace output was observed with increased averaging, yet the time for collection is sufficiently small (<10 s) to allow rapid data collection. In fluvial environments where EM noise pollution is more severe, e.g. in urban areas and near to airports, building sites or radio masts, a higher stacking may be more appropriate, such as 128 or 256 stacks.

Station spacing If the distance between survey points on a CO profile is too great, steeply dipping and small features cannot be imaged (March & Bailey 1983; Sheriff & Geldart 1995). This spatial aliasing results in waveforms being incorrectly correlated between adjacent traces (Fig. 3, Smith 1984; Daniels *et al.* 1988; Arcone 1995; Bernabini *et al.* 1995: Reynolds 1997). The size of the river, the scale of sedimentary features present and the features of interest to the survey must all be considered. To illustrate this point, in the Jamuna River, Bangladesh, a step size of 0.5 m was used for GPR surveys (Best *et al.*, in press). However, if such a step size were used for the smaller South Saskatchewan River, where internal structures are <2 m in length, very few survey traces would be collected above them, making many structures unresolvable (Fig. 3). With a trace spacing of 0.1 m, the steeply dipping structures (DS) are visible, but the image loses definition with a 0.2 m, 0.5 m or 1.0 m trace-spacing. Indeed, for a feature to be resolvable with any degree of accuracy, it is desirable that more than ten traces be collected directly above it.

Choice of frequency A wide range of antennae frequencies, from 12.5 MHz to 1200 MHz, is available with commercial GPR systems. A trade-off exists between penetration (the depth to which there is enough power output by the antennae to produce a detectable reflection and therefore image the subsurface structure) and data resolution (the

Distance along profile (m)
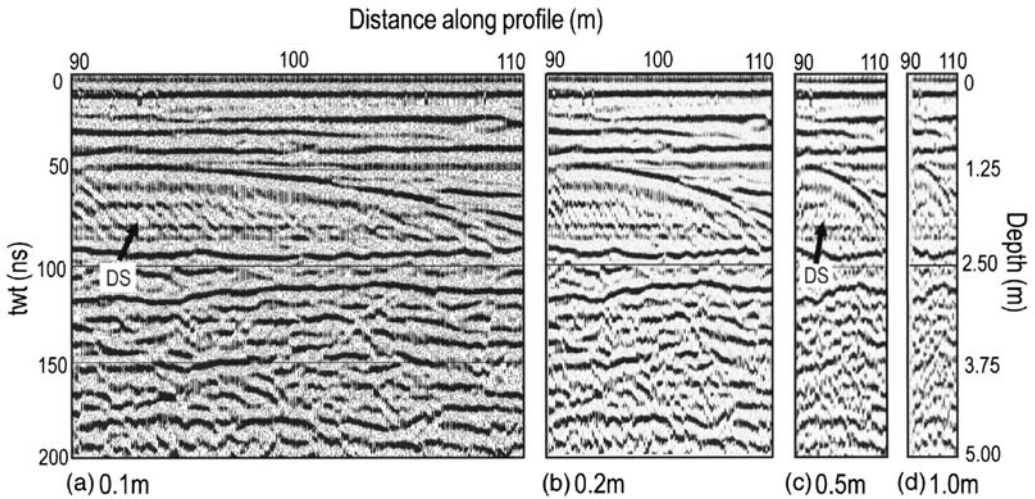
Fig. 3. The results of changing station spacing are plotted with the same number of traces per cm of plot: (**a**) with a spacing of 0.10 m, the near-horizontal and dipping structures (DS) are visible; (**b**) with a spacing of 0.20 m, the near-horizontal feature is visible but the steeply DS are becoming difficult to image; (**c**) with a spacing of 0.50 m, only the near-horizontal structure is imaged clearly; and (**d**) with a spacing of 1.0 m, the DS features appear to dip in the wrong direction due to spatial aliasing.

size of feature resolvable using the radar). The lower the frequency of the antennae, the poorer the resolution but the greater the depth of penetration (e.g. Davis & Annan 1989; Jol 1995). This is illustrated in Figure 4, which shows a section of a line from the South Saskatchewan that was resurveyed at three different frequencies (200, 450 and 900 MHz). The use of different frequency antennae can often aid data interpretation by allowing a range in the scale of features to be imaged. Again, as with station spacing, the choice of frequency requires consideration of the scale of the river and the size of the feature under investigation. With 100 MHz antennae in the Jamuna River, Best *et al.* (in press) calculated their theoretical resolution to be 0.3 m in wet sand, assuming a resolution of one quarter of the GPR wavelength (Reynolds 1997). This resolution proved acceptable for profiling the large-scale bedforms present in the Jamuna. However, in the saturated sands of the South Saskatchewan, where the velocity of propagation of EM waves is 0.05 m ns^{-1} (see below), use of 200 MHz antennae provided a theoretical vertical resolution of 0.06 m, while 450 MHz antennae provided a resolution of less than 0.03 m. The majority of surveys in the South Saskatchewan study were collected using 200 MHz antennae and a pulseEKKO 100 radar system. Key profiles were then rerun with 450 MHz antennae using a pulseEKKO 1000 radar system to examine smaller-scale sedimentary structures.

Mapping of surface structures During GPR data collection, careful records must be taken of all surface structures on and near the profile lines. This must include: (1) the location of surface water; (2) the angle, location and dip of any visible structure that crosses the GPR line; (3) change in soil type; (4) nearby trees, posts, buildings, metal objects; and (5) the presence of any overhead electrical or telephone wires. Careful recording of such features may significantly aid data interpretation, since spurious reflections can often be discounted by considering the effects of above-surface reflectors. The locations of GPR profiles must be known to allow repeat surveying; the elevation along the profile lines must be recorded accurately using a Total Station or level to enable topographic correction of the radar transects.

Processing methodology

All GPR data require processing, the aim of which is to sharpen the signal waveform by improving the signal-to-noise ratio (Reynolds 1997). The outcome of processing is a cross-section of the subsurface electrical properties, displayed in terms of the two-way travel time (twt), i.e. the time taken for a wave to move from the transmitter to a reflector and return to the receiver. The amount of processing undertaken can range from basic, which allows rapid data output, to the more time-consuming application of algorithms designed for use on
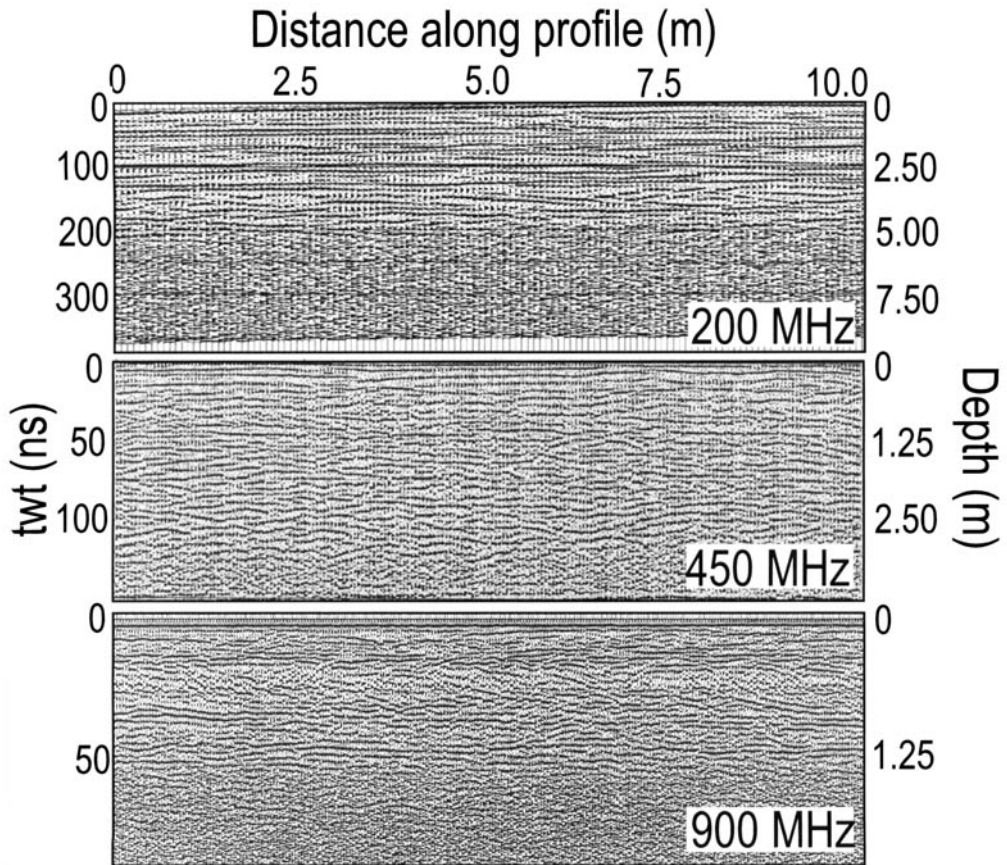
Fig. 4. Data for the first 10 m of GPR line AX2 on BAR 1, showing profiles collected with 200, 450 and 900 MHz antennae. The high-frequency antennae allow the near-surface structure to be interpreted (processing steps for these lines are shown in Table 1) whilst the lower frequencies allow better depth of penetration and imaging of deeper features.

seismic datasets, which produce higher-quality output (e.g. Daniels *et al.* 1988; Jol 1995; Liner & Liner 1995). Some processing packages, such as pulseEKKO software, will significantly improve data output, but are not as sophisticated as seismic-based packages, such as Gradix 1.10 software, which allow the user more control of processing parameters. However, it is evident that post-processing may significantly improve GPR output quality and this demands clear description and listing of all processing stages in GPR studies so that the effects of various parameters can be assessed.

All data profiles for the South Saskatchewan study were processed using Gradix 1.10 software (Interpex Ltd, USA). As there are numerous processing packages available, it is important to state the nature of the processing undertaken and the control parameters employed. This section describes the optimal processing sequence

developed for the 200 MHz CO profile labelled AX2 (see Fig. 1c for location). The processing sequence shown in Figure 5 was applied to all 200 MHz profiles from the South Saskatchewan. The same processing sequence has also been applied to data collected with other frequency antennae, with appropriate filter gates (Table 1). Steps taken to optimize the data series (see Fig. 5) will be explained briefly and exemplified using output from survey lines. Many survey parameters were derived from user experience and iterative improvements.

Time-zero correction During a GPR survey, the first waveform to arrive at the receiver from the transmitter is the air wave. There is a delay in the time of arrival of the first break of the air wave on the graphical output due to the length of the fibre-optic cables connecting the antennae and the con-

SET TIME-ZERO

DEWOW
(8.71 MHz)

BANDPASS FILTER
(50-100-220-440 MHz)

BACKGROUND REMOVAL
(200 point window below air wave)

TRACE WINDOWING

DEPTH CONVERSION
(Using velocity of 0.05 m ns^{-1})

ELEVATION STATICS
(Using elevation data from EDM survey)

AGC
(25 ns window with trace multiple of 5)
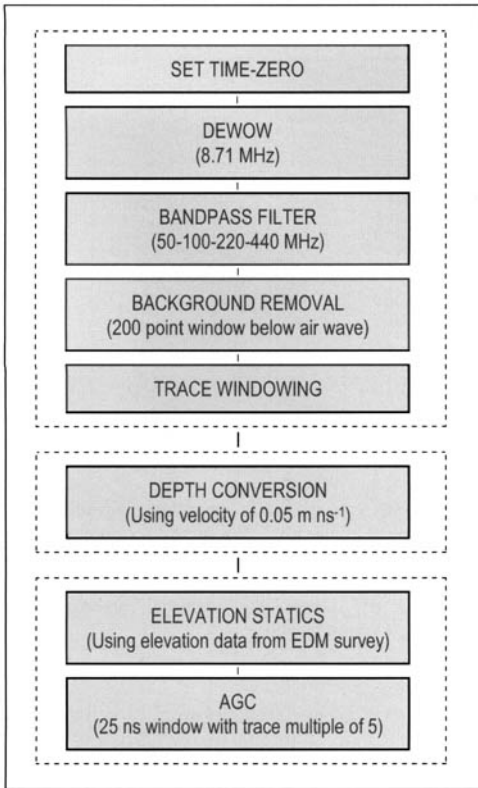
Fig. 5. Processing sequence for GPR line AX2. This processing sequence was applied to all the 200 MHz data collected.

sole electronics. This delay does not remain constant during a survey as the unit must warm-up to its ambient operating temperature, thus creating drift in the arrival time. Drift may also be caused by problems in the fibre-optic cables (nicks or breaks in the cable) and the internal electronics of the GPR Tx (transmitter antenna) and Rx (receiver antenna) units, control unit or trigger switch. In CO surveys, the antennae are held a constant distance apart, enabling any drift to be corrected by aligning the air-wave arrival at zero on the graphical output.

Dewow filtering GPR data often have a low-frequency noise component in the trace (<1 MHz) that obscures real data at higher frequencies due to its high amplitude (Hatton *et al.* 1986). The low-frequency noise is a result of saturation of the electronics from the large amplitude of the air wave and the direct wave that travels along the ground/air interface (Daniels *et al.* 1988). To remove this noise (or wow), each trace is filtered in the time domain, passing frequencies above the specified high-pass frequency. The filter frequency

is decided by repeat filtering of the raw data at different frequencies and selecting the frequency that best removes the wow peak from the amplitude spectra (Fig. 6). It is customary to remove the wow peak before band-pass filtering (see below), even though the wow would be removed by band-pass filtering.

Band-pass filtering Filtering allows the removal of noise at the high and low end of the amplitude spectrum. Some processing packages have only a low-pass filter that would be applied after a dewow (high-pass) filter. For the 200 MHz antennae, the peak central frequency response, around which the filters are centred, is approximately 125 MHz. The peak frequency value is determined from an amplitude spectrum plot of the GPR profile (see Fig. 7). The filter used for the South Saskatchewan data was a trapezoidal band-pass filter (Fig. 6*d*) in which four frequencies are defined as gates. Below F1, the amplitude response of the filter is 0; between F1 and F2 the filter tapers between 0 and 1; between F2 and F3 the response is 1, whilst the filter then tapers from F3 to F4, returning to a zero response after F4. Care must be taken to ensure that the tapered sections are not too steep or multiples will be artificially created around high-amplitude reflectors in the data. For this reason, it is usual to keep the pairs of frequency values for the slopes of the filter at an octave (i.e. 40–80 or 300–600). The frequency gates chosen for the South Saskatchewan data were 50, 100, 220 and 440 MHz. These values were chosen after thorough study of the amplitude spectra and repetitive trials with different filter parameters.

Background removal Background noise is a repetitive signal created by slight ringing in the antennae, which produces a coherent banding effect, parallel to the surface wave, across the section (Shih & Doolittle 1984; Goodman 1994; Stenberg & McGill 1995; Conyers & Goodman 1997). Background removal effectively eliminates this banding without degrading useful information within the trace (Fig. 6). An operator window is specified, e.g. 100, which defines the number of traces used for one calculation. The window must be as narrow as possible, but must not remove short, horizontal reflectors from the profile. The average signal from the traces in the operator window is considered to be noise and is subtracted from the current trace. Care must be taken in this process not to remove real linear events in the profile. The time window where the filter operates must, therefore, be specified so that the filter is not applied until after the surface wave.
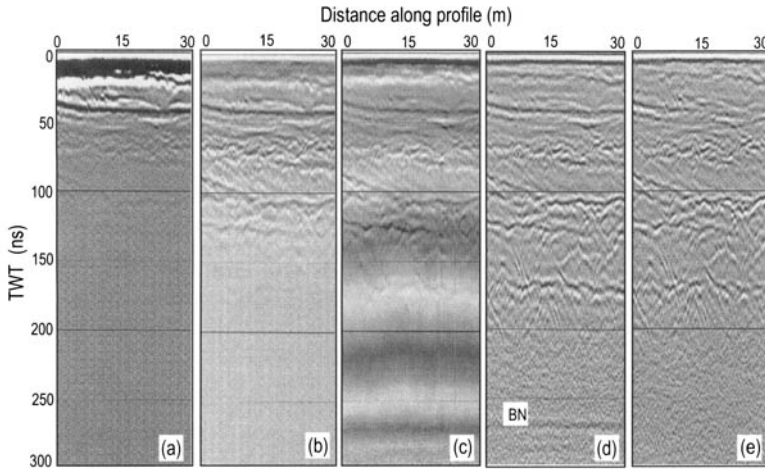
Fig. 6. All processing steps applied to the GPR line AX2 on BAR 1. (**a**) Raw data with a constant gain of 10. (**b**) Raw data with an AGC gain with window width of 25 ns. (Gain is applied as the final step of any processing string to enhance the visual clarity of the data. The effects of gain are demonstrated and are then applied to all output. In Figure 5, gain is shown as the final processing step.) (**c**) Dewowed with a high-pass cut-off of 8.71 MHz. (**d**) Band-pass filtered using a trapezoidal filter with gates 50–100–220–440 MHz, BN showing the horizontal banding still to be removed by the background filter. (**e**) Background removal with a 200-point window.

Migration Migration is applied to collapse diffraction hyperbolae (the reflection patterns created by point reflectors in a GPR profile) back to their original source location and to position dipping features correctly. Migration algorithms assume that all echoes arise from within the vertically orientated two-dimensional plane of the GPR profile (Fountain & Jacobel 1997). Migration algorithms were not found to optimize the radar signal for the South Saskatchewan and therefore were not applied. This might be due to the flat nature of most reflectors, the lack of point reflectors in the profile, the presence of offline reflectors or the migration algorithms present in the processing package.

Elevation statics and depth conversion Surveyed elevation data are used to apply topography to the GPR survey line. Firstly, trace windowing is applied to the data to remove all artefacts in the survey that arrived before the time-zero arrivals. The actual elevations recorded for survey points along the profile are then entered into the data-processing package and the time-zero arrivals are 'hung' from the topographic profile by applying a time shift to each individual trace. Depth conversion is a simple display correction that allows the GPR profile to be displayed as a cross-profile of distance along the profile line plotted against elevation. This requires calculation of a velocity of propagation for the EM energy in the subsurface for the survey area (see below).

Application of gains Gains are used to enhance the signal amplitude with increasing two-way travel time (twt) on a data trace. Gains are required because the amplitude of a reflected signal decreases with time and depth due to attenuation, geometrical spreading, partial reflection and scattering (Davis & Annan 1989; Peters *et al.* 1994; Reynolds 1997). Gains are usually applied at the end of any processing series for display of the traces. While many gain functions exist, e.g. constant, linear and exponential gains, the most commonly applied is an automatic gain control (AGC). AGC is a time-varying gain that runs a window of chosen length along each trace, point-by-point, finding the average amplitude over the length of the window about each point. A gain function is then applied such that the average at each point is made constant along the trace. For line AX2, an AGC with a window of 25 ns was found to be most applicable (Fig. 6*b*). The width of the twt window will depend upon antennae frequency and the amplitude response of the subsurface and is best evaluated by systematic trials.

Velocity analysis

A detailed knowledge of the subsurface velocity field for the propagation of EM energy is critical to any thorough GPR processing. A number of methods exist for calculating the velocity of EM wave propagation in the subsurface, including (1) CMP analysis, (2) calculation from linear and
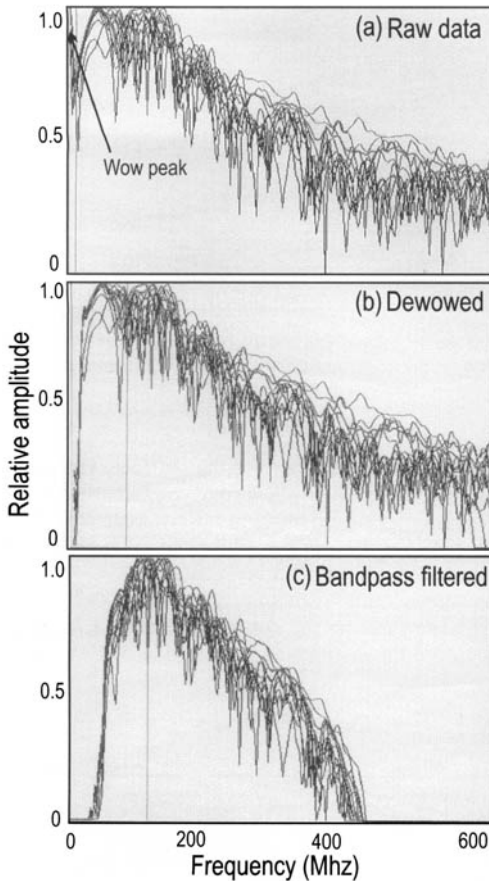
Fig. 7. The amplitude spectra for the 200 MHz GPR line AX2 on BAR1: (**a**) raw data, showing the low-frequency wow peak; (**b**) dewowed with a high-pass filter of 8.71 MHz, resulting in removal of the wow peak; (**c**) after band-pass filtering with a trapezoidal filter with gates 50–100–220–440 MHz. The cut-off after 440 MHz shows the removal of high-frequency noise.

hyperbolic refraction patterns, (3) recognizing reflectors at a known depth in the profile (e.g. by linking reflections to horizons in cores), (4) the use of cut-face experiments, or (5) cross-borehole tomography (e.g. Hatton *et al.* 1986; Tillard & Dubois 1995; Reynolds 1997). CMP analysis is the most common method of velocity calculation.

For CMP surveys, the first arrival is the air wave, which travels directly from the transmitter to the receiver. The air-wave arrival is followed by a ground-coupled wave that propagates through the ground at the surface–air interface (Fig. 8). Below this are non-linear reflections from horizons at depth in the profile. The velocity of EM propagation can be calculated from these reflections by regressing the move-out distance against the twt

values, provided that (1) the layer reflector is horizontal, and (2) the small spread approximation holds, i.e. the move-out distance is much smaller than the depth to the reflector picked for the CMP (Reynolds 1997).

CMP surveys were conducted on two different bars in the South Saskatchewan. In order to minimize errors, only reflectors seen on CO profiles from near-horizontal subsurface planes (dip <1°) were used to calculate CMP velocities. The twt of the main reflections from the CMPs were picked manually for each successive step-out of the antennae (Fig. 8). The square of the antennae separation was then plotted against the square of the twt, and an ordinary least-squares regression undertaken. Calculation of the inverse of the square root of the slope from the regression permits the velocity of propagation of EM waves to be estimated. Twelve CMP surveys were carried out in the South Saskatchewan, with eight 200 MHz CMPs producing 24 reflections from which a velocity could be calculated, and four 450 MHz CMPs producing seven reflections from which a velocity could be calculated. The mean of the velocities, calculated by averaging the speed of propagation before the inverse velocity value was calculated is 0.051 ($\pm$ 0.006) m ns^{-1}, which compares favourably with published velocities for EM propagation in saturated sand of 0.05 m ns^{-1} (Davis & Annan 1989).

Interpretation of GPR data

Accurately identifying and interpreting GPR reflections requires a detailed knowledge of the local environment. Thus, to aid interpretation of the subsurface stratigraphy, a ground-truth control is required, which can be obtained from trenching following the GPR survey (e.g. Taylor and Macklin 1997; van Dam *et al.* see p. 257), coring (e.g. Bridge *et al.* 1998; Vandenberghe & van Overmeeren 1999), cut-face experiments (e.g. Liner & Liner 1995; Asprion & Aigner 1997; Vandenberghe & van Overmeeren 1999; van Dam & Schlager 2000; Kowalsky *et al.* 2001), or comparison with output obtained by other independent geophysical techniques (e.g. Camerlynck *et al.* 1994; Smith *et al.* 2002). The most effective form of ground-truth control is to trench parts of the profile immediately after data collection. However, in many fluvial environments this is not feasible due to the remote nature of many sites, the shallow depth of the water table and the non-cohesive nature of the sediments. Cut-face experiments allow direct control in a similar way to trenching, although cut-faces are often located away from the active in-channel bars and may be above the water table. Coring is also extremely useful for identifying gross structural trends across an area,
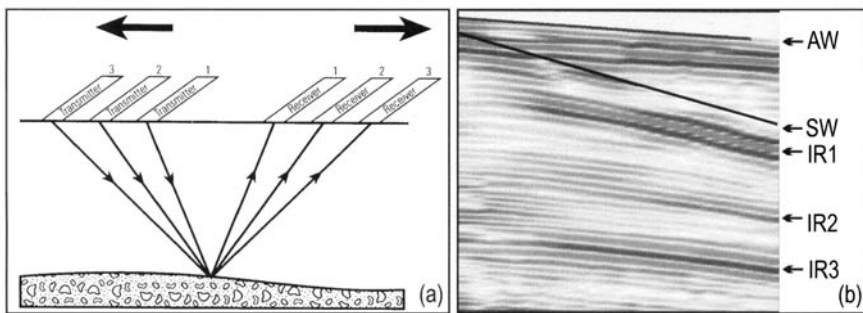
Fig. 8. (a) Method of CMP data collection with the antennae being moved progressively further apart. (b) CMP output showing the linear air-wave (AW) and surface-wave (SW) reflections, and three hyperbolic internal reflections (IR1–IR3).

although a dense coring network is required to link the GPR reflectors in three dimensions (e.g. Bridge *et al.* 1995).

For the present South Saskatchewan River study, GPR ground-truth control was obtained using a 2 m-high, 20 m-long cut-face (Fig. 1c), a section of which is shown in Figure 9. A 900 MHz frequency GPR profile was collected along a 40 m

line, 1 m from the edge of the cut-face. Historical aerial photographs show the cut-face represents recent erosion into an old (>50 a) vegetated mid-channel bar. Before describing the GPR profiles, a number of issues must be considered:

1. The sands in the cut-face were dry and therefore the velocity of propagation of EM waves
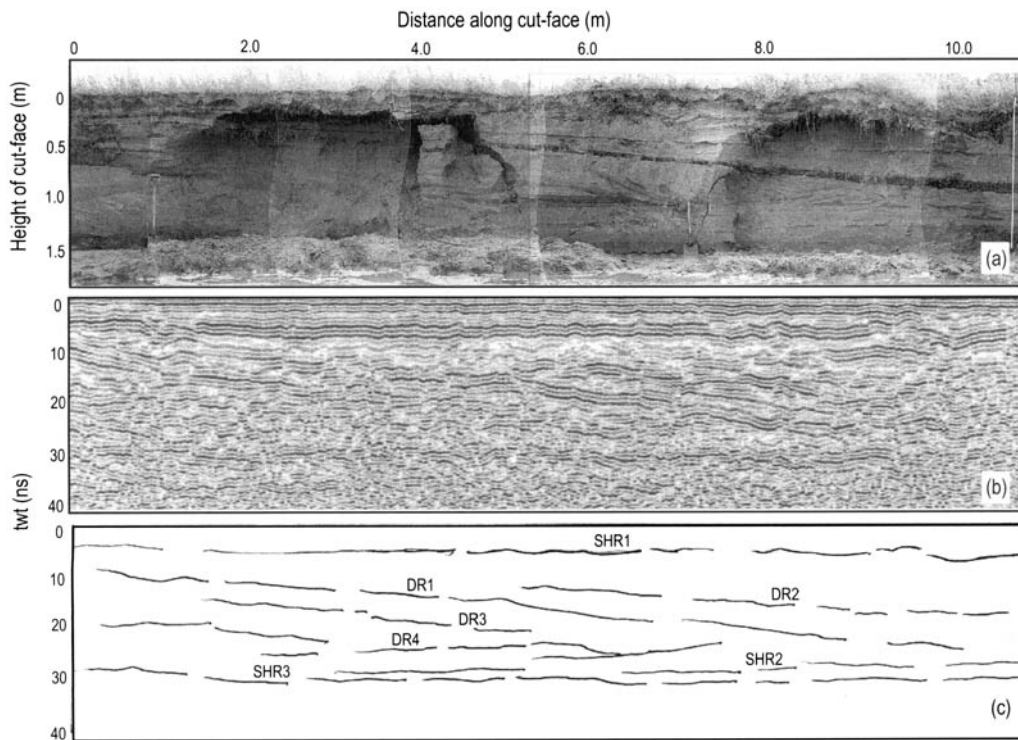
Fig. 9. Ground-truth control experiment. (a) Photographic montage of the cut-face, showing the major reflectors. (b) A 900 MHz GPR profile for the cut-face. (c) Interpretation of GPR profile, allowing comparison with the photographic montage (see text for further details). DR, dipping reflections; SH, subhorizontal reflections.

was three times faster than in the saturated sands of the active channel (velocity of EM propagation in dry sands is 0.15 m ns^{-1}, Davis & Annan 1989). To compensate for this higher velocity, 900 MHz antennae were used to provide comparable resolution to the 200 MHz antennae used in the saturated sands. This produces an approximate comparison since wave behaviour, particularly due to antennae dispersion, is likely to be different between the 200 MHz and 900 MHz antennae pairs.

2. The change from wet to dry sands for the cut-face experiment results in a change from a two-phase system (water and sediment) where porosity, and therefore water content, is the key control on dielectric constants, into a three-phase system (air, water and sediment) where factors other than porosity play a role in determining dielectric properties (van Dam et al. see p. 257). This transition may change the amplitude and polarity characteristics of some reflectors for the cut-face relative to the active channel reflectors.

3. The presence of a decimetre-thick organic soil horizon on top of the profile produces a series of radar multiples. These multiples confuse the profile and obscure low-amplitude radar reflectors at depth in the profile. This feature complicates interpretation of reflectors and could not be removed by processing due to the complex, dipping nature of many reflectors.

4. The GPR profile will not mirror exactly the cut-face, since the sedimentary structures are three-dimensional and may dip into the cut-face or change in their three-dimensional form. This three-dimensionality may thus result in some features being present at different depths in the GPR profile as compared to the cut-face, or some features not being present at all.

5. Little is known about edge-effects produced by running GPR profiles close to a near-vertical cut-face. Similar to the near-face experiment in a road-cut described by Liner and Liner (1995), the present comparison between the GPR profile and logged cut-face, suggests that the near-face effects are small and insignificant in this instance.

GPR reflections and sedimentological interpretation

A number of reflections are marked on the GPR profile and interpretation of the cut-face (Fig. 9). These include: (1) a subhorizontal reflection (SHR1) that runs across the top of the profile, (2) two high-amplitude dipping reflections (DR1 and DR2), (3) two lower-amplitude dipping reflections

(DR3 and DR4) in the middle part of the section, and (4) two further subhorizontal reflections (SHR2 and SHR3) that run across the profile at the base of the section.

These reflections can be compared directly with bounding surfaces between depositional units visible in the cut-face, shown in the photographic panorama and interpretation in Figure 9a and c. The nature of the radar patterns produced by the depositional units aids the interpretation of the section.

- SHR1 is interpreted as the interface between the organic-rich soil horizon and the underlying sediment. This soil horizon had a higher water content than the dry sands beneath it and thus produced a high-amplitude reflection. The velocity of propagation of EM waves in this soil horizon is thought to have been lower than that in the sands, and therefore this surface section of the profile is disproportionately wide on the GPR profile (Figure 9b).
- DR1 is a high-amplitude reflection from a 0.02–0.10 m-wide clay drape that runs across the entire cut-face. The clay was probably deposited during a period of low flow when the river deposited only fine-grained suspended load at this locality, or, given the inclined nature of the reflector, in an area of flow deceleration in the lee of a bar.
- DR2 represents a second clay drape which is <0.02 m thick and bifurcates from the main clay reflection, DR1, at ~5 m along the profile.
- DR3 represents an erosion surface between depositional units. There appears to be little change in particle size between the units above and below the contact, which is defined by an irregular interface between the bedding features within the upper and lower depositional units that represents an episode of soft-sediment deformation.
- DR4 represents a reflection from an interface within the lower depositional unit. The erosional interface is defined by a marked change in sand-grain size (median grain size of 0.30 mm below to 0.23 mm above) and depositional characteristics (low-angle to angle-of-repose cross-stratification).
- SHR2 represents an intermittent reflector from a thin (<0.01 m) gravel lag. This material is probably sourced from the reworking of bank deposits of Quaternary sediments and represents accumulation of fine gravels above an erosion surface, with the gravels probably having overpassed a smooth sand surface.
- SHR3 is a reflection from a thick (>0.10 m) layer of clay at the base of the cut-face sequence. This reflection marks the penetration depth of the GPR, since the clays are thick and

are saturated because they are at the current river level, thus preventing further penetration into the subsurface.

Interpretation of GPR reflections in active channel bars

Results from the ground-truth control interpretation can be applied to the study of the modern, active in-channel bars. The ground-truth control experiment suggests that thin clay drapes of mm–cm scale, which frequently separate depositional units, produce the dominant high-amplitude, continuous reflections in the subsurface. High-amplitude reflections, such as IR shown in Figure 10, are low-angle, laterally extensive features that are similar to the form of the clay drapes documented in the cut-face. It is suggested here that the majority of low-angle, high-amplitude reflections seen in the subsurface are a result of the presence of clay in the profile.

Erosion surfaces between bedforms can also be imaged in the cut-face but these reflections are not as prominent, nor as continuous, as the reflections from clay drapes. In addition, marked grain-size

changes and thin pebble stringers in the cut-face produce GPR reflections within packets of sand. Small features, such as ripple foresets, could not be resolved in the GPR record for the cut-face. However, larger cross-sets in the active channel could be imaged, particularly if the sets are identified by marked changes in the grain-size distribution and are in the order of >0.10 m in thickness. Large cross-stratification produced by an outwardly accreting bar margin (Bar 3, Fig. 1*d*) is shown in Figure 11. These sets were the largest visible structures found in the surface/subsurface structure of the active bars and are visible in the GPR record as a result of grain-size changes produced by waning flow conditions at the end of each successive increment of deposition (Fig. 11*b* & *c*).

At the base of the GPR profiles there is a strong continuous reflector (see BR, Fig. 10), which is present at approximately the same depth along the 10 km stretch of the river where GPR traces were collected. Below this reflection, no further reflections are visible, suggesting that a marked change in reflective characteristics is present below this level. This reflection is interpreted as marking the interface between the active channel-fill and the
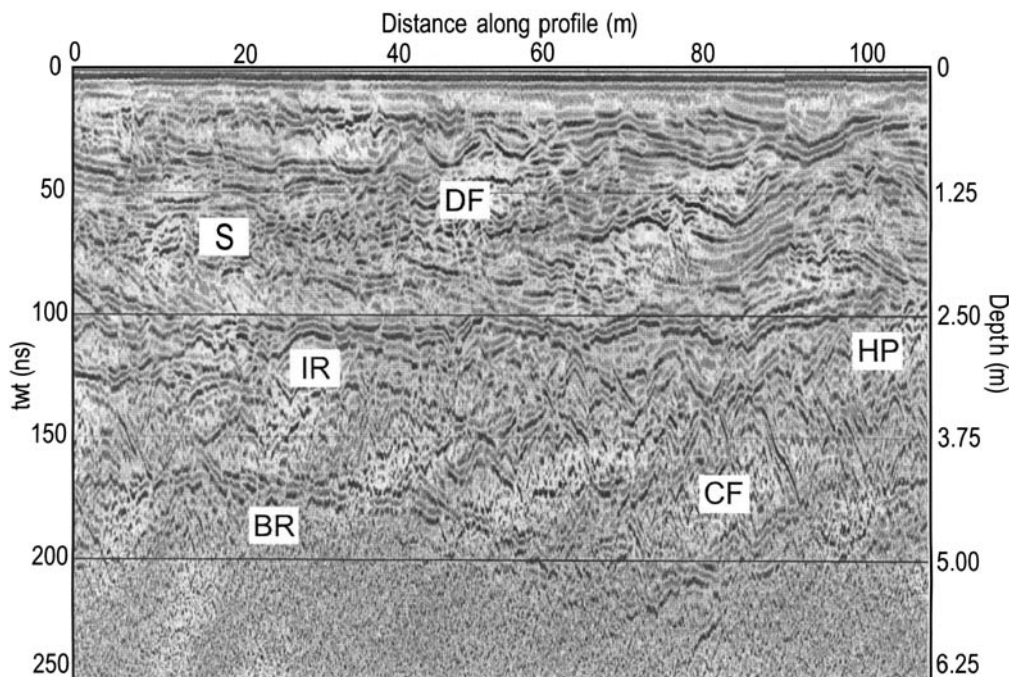
Fig. 10. 200 MHz CO profile of GPR line AX2, BAR 1. DF, dune troughs highlighted by erosional surfaces in the sand-body; S, sets from dunes or small bar fronts; IR, a prominent, continuous reflection, that represents a clay drape; HP, may represent hyperbolic reflections, although they are poorly resolved due to their depth in the profile; CF, a channel-fill; BR, a strong basal reflection thought to represent the interface between channel sands and the underlying Quaternary sediments.
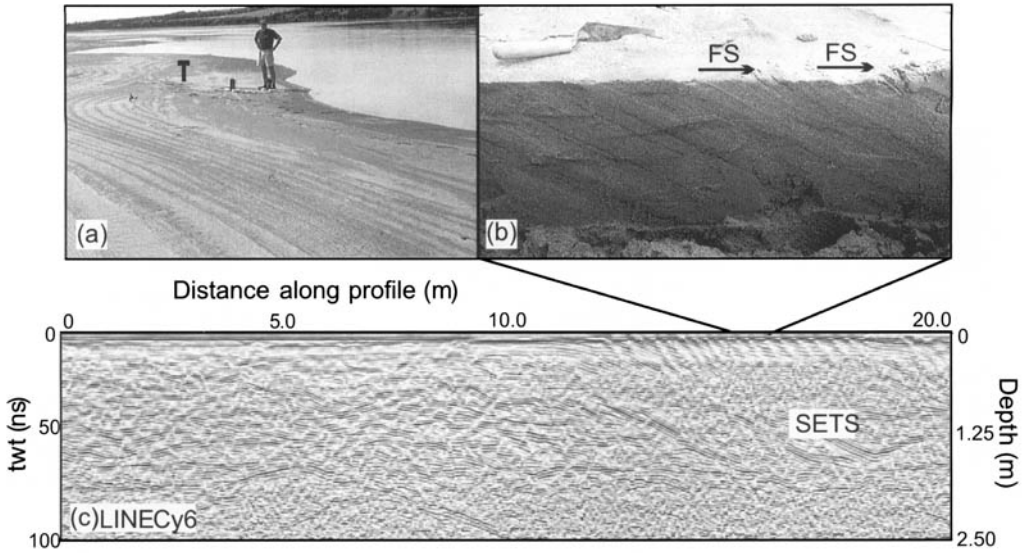
Fig. 11. Large sets produced at the margin of an obliquely accreting bar, in which the sets are picked out by grain-size differences. (**a**) Photograph of the bar margin (flow left to right) showing the surface expression of the sets on the asymmetric limb of BAR 3 and location of the shallow trench (T), illustrated in (**b**) which shows fining sequences (FS), picked out by grain-size differences, within each set. (**c**) Line CY6 on BAR 3, running across the sets shown in (a) and (b). The bar has prograded from left to right, and the large sets grow in size to the right and extend for a large proportion of the flow depth.

underlying Quaternary clay-rich till. This interface would also be expected to produce this high-amplitude reflection, since saturated clay-rich sediments have a very different dielectric constant to saturated sands. Sediments have filled a possible scour feature or channel cut into this interface in an early stage of deposition, marked by CF in Figure 10. Above this feature a number of hyperbolic reflectors (HP) are apparent, but these cannot be migrated and, owing to their depth in the profile, are likely to be poorly resolved or spatially aliased structures.

Conclusions

The quality of the GPR results obtainable in fluvial environments will reflect both the nature of the sediments and local conditions together with the care applied to the methodology for data collection, processing and interpretation. This paper has described the key steps (Fig. 12) required to collect, process and interpret GPR reflectors in a sandy fluvial environment, as exemplified by data collected on the South Saskatchewan River. Particular importance is placed on ground-truth control obtained from a cut-face, which provides the necessary verification for the interpretation of GPR signals in the active-channel environment. This overview outlines an approach suitable for appli-

cation to future GPR surveys in sandy fluvial environments and should lead to an improvement in the quality of GPR studies, which will aid interpretation of, and comparison between, data-sets.

Many of the procedures required to collect, process and interpret GPR data in sandy fluvial environments are also applicable to GPR surveys in other depositional environments. Care must be taken to choose a suitable GPR system with antennae frequency appropriate for the scale of features under investigation. Field data should be collected, where possible, in step mode with a stacking of >32 and a station spacing appropriate to the scale and dip of the underlying sedimentary structures. Processing should entail time-zero correction, high- (wow) and low-pass filtering, background removal, depth and elevation correction and application of gains. In order to correct adequately for depth, the velocity of EM radiation should be calculated in the field. In appropriate circumstances, particularly where hyperbolic reflections are encountered, migration should also be applied. The exact value assigned to any data collection step or processing sequence will be dependent upon the scale, depth and nature of subsurface reflectors and the nature of the GPR equipment used for the survey. Substantial differences could be expected with changes in sediment type, e.g. between a gravel
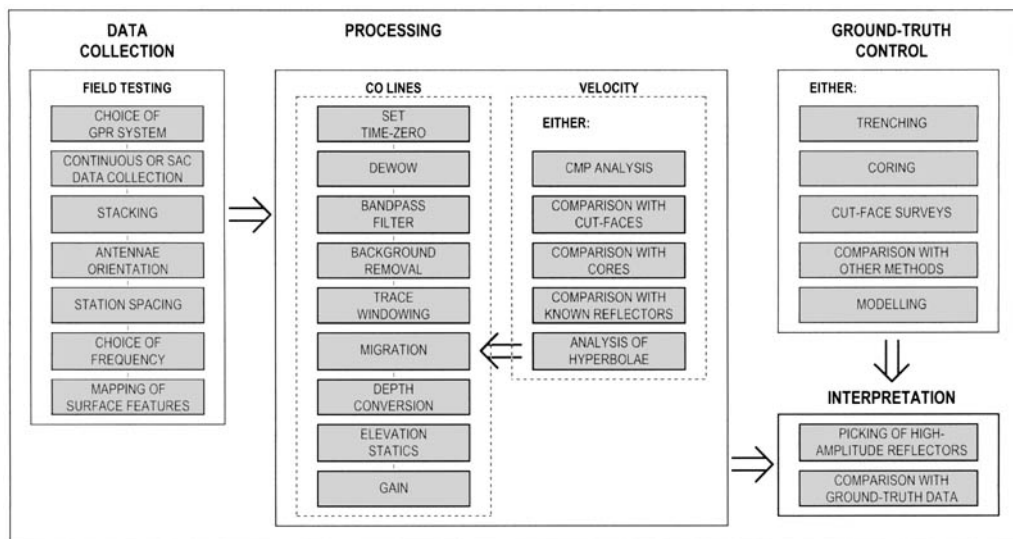
Fig. 12. Summary of all the necessary steps required to collect, process and interpret high-quality GPR data sets. Velocity analysis is fed into the CO processing before processed data sets are analysed with the help of data from ground-truth control surveys.

and sand bed fluvial environment. A series of generic principles of data collection and processing should, however, be applied.

All data collection, parameters and processing steps should be recorded or tabulated in any publication, recording the methods and processing applied to each GPR line used in the paper. The details recorded should include the gates of any filters used, as well as the collecting system and processing package. In order to interpret GPR data with any confidence, it is also highly desirable to provide and describe some form of ground-truth control, preferably from trenching, coring or cut-face surveys.

References

ANNAN, A. P. & COSWAY, S. W. 1993. Ground penetrating radar survey design. *pulseEKKO 100 System Technical Description,* **54,** 1–12.

ARCONE, S. A. 1995. Numerical studies of the radiation patterns of resistively loaded dipoles. *Journal of Applied Geophysics,* **33,** 39–52.

ASPRION, U. & AIGNER, T. 1997. Aquifer architecture analysis using ground-penetrating radar: Triassic and Quaternary examples (S. Germany). *Environmental Geology,* **31,** 66–75.

BERES, M., GREEN, A. G., HUGGENBERGER, P. & HORSTMEYER, H. 1995. Mapping the architecture of glaciofluvial sediments with three-dimensional georadar. *Geology,* **23,** 1087–1090.

BERES, M., HUGGENBERGER, P., GREEN, A. G. & HORSTMEYER, H. 1999. Using two- and three-dimensional georadar methods to characterize glaciofluvial architecture. *Sedimentary Geology,* **129,** 1–24.

BERNABINI, M., PETTINELLI, E., PIERDICCA, N., PIRO, S. & VERSINO, L. 1995. Field experiments for characterization of GPR antennae and pulse propagation. *Journal of Applied Geophysics,* **33,** 63–76.

BEST, J. L, ASHWORTH, P. J, BRISTOW, C. S. & RODEN, J. E. (In press) Three-dimensional sedimentary architecture of a large, mid-channel sand braid bar, Jamuna River, Bangladesh. *Journal of Sedimentary Research.*

BRIDGE, J. S. 1993. The interaction between channel geometry, water flow, sediment transport and deposition in braided rivers, *In*: BEST J. L. & BRISTOW, C. S. (eds) *Braided Rivers.* Geological Society, London, Special Publications, **75,** 13–72.

BRIDGE, J. S., COLLIER, R. E. LL. & ALEXANDER, J. 1998. Large-scale structure of Calamus River deposits (Nebraska, USA) revealed using ground-penetrating radar. *Sedimentology, 45*, 977–986.

BRIDGE, J. S., ALEXANDER, J., COLLIER, R. E. LL., GAWTHORPE, R. L. & JARVIS, J. 1995. Ground-penetrating radar and coring used to study the large-scale structure of point-bar deposits in three dimensions. *Sedimentology, 42*, 839–852.

BRIDGE, J. S., SMITH, N. D., TRENT, F., GABEL, S. L. & BERNSTEIN, P. 1986. Sedimentology and morphology of a low-sinuosity river: Calamus River, Nebraska Sand Hills. *Sedimentology, 33*, 851–870.

BRISTOW, C. S. 1993. Sedimentary structures exposed in bar tops in the Brahmaputra River, Bangladesh. *In*: BEST J. L. & BRISTOW, C. S. (eds) *Braided Rivers*. Geological Society, London, Special Publications, 75, 211–289.

CANT, D. J. & WALKER, R. G. 1976. Development of a braided-fluvial facies model for the Devonian Battery Point Sandstone, Quebec. *Canadian Journal of Earth Sciences, 13*, 102–119.

CANT, D. J. & WALKER, R. G. 1978. Fluvial processes and facies sequences in the sandy braided South Saskatchewan River, Canada. *Sedimentology, 25*, 625–648.

CONYERS, L. B. & GOODMAN, D. 1997. *Ground-Penetrating Radar: An Introduction for Archaeologists*. Altamira Press, Walnut Creek, 232 pp.

CAMERLYNCK, C., DABAS, M. & PANISSOD, C. 1994. Comparison between four electromagnetic methods for stone features characterization: an example. *Archaeological Prospecting, 1*, 5–18.

CROWLEY, K. D. 1983. Large-scale bed configurations (macroforms), Platte River Basin, Colorado and Nebraska: primary structures and formative processes. *Bulletin of the Geological Society of America, 94*, 117–133.

VAN DAM, R. L. & SCHLAGER, W. 2000. Identifying causes of ground-penetrating radar reflections using time-domain reflectometry and sedimentological analyses. *Sedimentology, 47*, 435–450.

DANIELS, D. J., GUNTON, D. J. & SCOTT, H. F. 1988. Introduction to subsurface radar. *Institution of Electrical Engineers, Proceedings, 135(F4)*, 278–320.

DAVIS, J. L. & ANNAN, A. P. 1989. Ground-penetrating radar for high-resolution mapping of soil and rock stratigraphy. *Geophysical Prospecting, 37*, 531–551.

FIELDING, C. R., ALEXANDER, J. & McDONALD, R. 1999. Sedimentary facies from ground-penetrating radar surveys of the modern, upper Burdekin River of north Queensland, Australia: consequences of extreme discharge fluctuations. *In*: SMITH, N. D. & ROGERS, J. (eds) International Association of Sedimentologists Special Publications, 28, 347–362.

FOUNTAIN, A. G. & JACOBEL, R. W. 1997. Advances in ice radar studies of a temperate alpine glacier, South Cascade Glacier, Washington, U.S.A. *Annals of Glaciology, 24*, 303–308.

GOODMAN, D. 1994. Ground penetrating radar simulation in engineering and archaeology. *Geophysics, 59*, 224–232.

HATTON, L., WORTHINGTON, M. H. & MAKIN, J. 1986. *Seismic Data Processing: Theory and Practice*. Blackwell Scientific, Oxford, 177 pp.

HUGGENBERGER, P. 1993. Radar facies: recognition of facies patterns and heterogeneities within Pleistocene Rhine gravels, N.E. Switzerland. *In*: BEST J. L. & BRISTOW, C. S. (eds) *Braided Rivers*. Geological Society, London, Special Publications, 75, 163–176.

JOL, H. M. 1995. Ground penetrating radar antennae frequencies and transmitter powers compared for penetration depth, resolution and reflection continuity. *Geophysical Prospecting, 43*, 693–709.

KOWALSKY, M. B., DIETRICH, P., TEUTSCH, G. & RUBIN, Y. 2001. Forward modelling of ground-penetrating radar data using digitised outcrop images and multiple scenarios of water saturation. *Water Resources Research, 37*, 1615–1625.

LEHMANN, F. & GREEN, A. G. 1999. Semi-automated georadar data acquisition in three dimensions. *Geophysics, 64*, 719–731.

LEHMANN, F. & GREEN, A. G. 2000. Topographic migration of georadar data: Implications for acquisition and processing. *Geophysics, 65*, 836–848.

LEHMANN, F., BOERNER, D. E., HOLLIGER, K. & GREEN, A. G. 2000. Multicomponent georadar data: Some important implications for data acquisition and processing. *Geophysics, 65*, 1542–1552.

LINER, C. L. & LINER, J. L. 1995. Ground-penetrating radar: A near-face experience from Washington County, Arkansas. *The Leading Edge*, January, 17–21.

MARCH, D. W. & BAILEY, A. D. 1983. A review of two-dimensional transform and its use in seismic processing. *First Break, 1*, 9–21.

PETERS, L., DANIELS, J. J. & YOUNG, J. D. 1994. Ground penetrating radar as a subsurface environmental sensing tool. *Proceedings of the Institute of Electrical and Electronics Engineers, 82*, 1802–1822.

REYNOLDS, J. M. 1997. *An Introduction to Applied and Environmental Geophysics*. Wiley, 796 pp.

SHERIFF, R. E. & GELDART, L. P. 1995. *Exploration Seismology* (2nd edition). Cambridge University Press, Cambridge, 592 pp.

SHIH, S. F. & DOOLITTLE, J. A. 1984. Using radar to investigate organic soil thickness in the Florida everglades. *Soil Science of America Journal, 48*, 651–656.

SMITH, A. M., MURRAY, T., DAVIDSON, B. M., CLOUGH, A. F., WOODWARD, J. & JISKOOT, H. 2002. Late-surge glacial conditions on Bakaninbreen, Svalbard and implications for surge termination. *Journal of Geophysical Research, 107(B8)*, 10.1029/2001 JB 000475.

SMITH, G. S. 1984. Directive properties of antennas for transmission into a material half-space. *Institute of Electrical and Electronics Engineers Transactions on Antennas and Propagation, AP-32*, 232–246.

SMITH, N. D. 1974. Sedimentology and bar formation in the upper Kicking Horse River, a braided meltwater system. *Journal of Geology, 82*, 205–223.

STENBERG, B. K. & McGILL, J. W. 1995. Archaeological studies in southern Arizona using ground penetrating radar. *Journal of Applied Geophysics, 33*, 209–225.

TAYLOR, M. P. & MACKLIN, M. G. 1997. Holocene alluvial architecture and valley floor development on the River Swale, Catterick, North Yorkshire, U.K. *Proceedings of the Yorkshire Geological Society, 51*, 317–327.

TILLARD, S. & DUBOIS, J. -C. 1995. Analysis of GPR data: wave propagation velocity determination. *Journal of Applied Geophysics, 33*, 77–91.

VANDENBERGHE, J. & VAN OVERMEEREN, R. A. 1999. Ground-penetrating radar images of selected fluvial deposits in The Netherlands. *Sedimentary Geology,* **128**, 245–270.

YOUNG, R. A. & SUN, J. 1999. Revealing stratigraphy in ground-penetrating radar data using domain filtering. *Geophysics,* **64**, 435–442.

Structure of a Pleistocene push moraine revealed by GPR: the eastern Veluwe Ridge, The Netherlands

MARCEL A. J. BAKKER[1,3] & JAAP J. M. VAN DER MEER[2]

[1]*Institute for Biodiversity and Ecosystem Dynamics (IBED), Physical Geography and Soil Science, University of Amsterdam, The Netherlands (e-mail: m.bakker@nitg.tno.nl)*
[2]*Dept. of Geography, Queen Mary, University of London, Mile End Road, London E1 4NS, UK*
[3]*TNO–NITG, The Netherlands Institute of Applied Geoscience TNO – The National Geological Survey, P.O. Box 80015, 3508 TA Utrecht, The Netherlands*

Abstract: The classic idea on the architecture of the push moraines of The Netherlands is one of imbricated thrusts. This study shows a more complete model of the structural style within a push moraine. We have mapped three glaciotectonic styles using 50 MHz ground penetrating radar (GPR).

The moraines are composed of coarse-grained unconsolidated sediments of fluvial and glacio-fluvial origin. Maximum penetration depth is about 45 m. In a 12 km cross-section over the eastern Veluwe Ridge we have encountered the following glaciotectonic styles. Style I is found near the former ice margin and consists of imbricated thrust sheets, with thrust planes dipping towards the former glacier. Style II, further away from the glacier, is a combination of folds and thrust structures. The folds have a wavelength of up to 200 m and an amplitude of 40 m. Style III is almost entirely composed of large-scale folds with wavelengths of 400 m maximum. Toward the most distal parts of the ridges the folds flatten out.

The study shows that GPR is capable of imaging large-scale glaciotectonic structures, resulting in a factual model of the eastern Veluwe push-moraine architecture and better insight into post-glacial denudation amounts and push-moraine genesis.

The glacial structure of large areas in northwestern Europe is characterized by huge glaciotectonic structures. They were created when Pleistocene ice sheets reworked large accumulations of unconsolidated sediments. During the penultimate glaciation (Saalian) the northern half of The Netherlands was ice-covered. Along the southern rim of the ice sheet a large-scale push-moraine complex was developed, which extends all the way into Germany and Poland (Van der Wateren 1995; Benneth 2001). In The Netherlands the push moraines are also referred to as 'ice-pushed ridges'.

The geometry of the push moraines in The Netherlands was established during the early 1950s, including general strike and an interpretation of the morphostratigraphy (Maarleveld 1953, 1981). Geological investigation was only possible in gravel pits of limited extent, along road cuttings and in drillings (Van den Berg & Beets 1987). At that time it was believed that the push moraines

mainly consisted of non-glacial deposits. More recent studies have pointed at the presence of meltwater deposits at the distal flanks of the ridges and partly on top of the ridges (Ruegg 1983). The full extent of the meltwater deposits remained unclear. Structural and sedimentological analyses of push moraines by Van der Wateren (1985, 1987, 1995) was mainly based upon large-scale exposures in Germany and Spitsbergen. He was able to show that push-moraine formation is the effect of pressure gradients, caused by the weight of the ice mass on the weak sedimentary sequences, rather than mere frontal glacial pushing (bulldozing).

In Boulton *et al.* (1984) an overview was given of the knowledge of the internal structure at the time. It was all based upon shallow exposures of limited extent and depth. Considering the complete lack of exposures after the mid-1980s, it was suggested that a geophysical approach would gain bet-

ter insight of the internal structure of the Dutch push moraines.

Presently, the ridges are part of an extensive nature reserve. They are also one of the largest aquifers in the country. Continuing extraction of drinking water has led to local drops in the water table (several metres), significant enough to effect vegetation. Hence, the need for detailed information on the internal structure has increased among groundwater modellers.

To arrive at a closer understanding of push-moraine architecture, a mapping technique based upon geophysical research techniques, including ground penetrating radar (GPR) and high- resolution seismics (HRS) was developed. This paper deals with results from GPR surveying.

Van Overmeeren (1998) suggested that well-defined glaciotectonic structures in GPR images of push moraines are seldom seen. The goals of this paper are to show the suitability of GPR to study the complex architecture of push moraines, to show that a variety of structural styles exist and to present and discuss examples of each of them.

Research area

The data discussed in this paper were collected at the southern part of the eastern Veluwe push moraine. This moraine is by far the largest is the country, with a length of about 50 km and a width of about 12 km (Fig. 1). The ridge rises about 70–

100 m above the surrounding lowland and is situated west of a deep glacial tongue basin underneath the present River IJssel. The direction of pressure, as exerted by the glacier was from the east, toward the west and southwest. The basin is the source area of much of the sediments now piled up in the ridge. Strike of the pushed strata is usually perpendicular to the direction of pressure and deformation (Maarleveld 1981). The total thickness of the pushed sequences is estimated at about 150–200 m.

Methodology

The technique of GPR has been described elsewhere (Davis & Annan 1989). It has been applied successfully within The Netherlands on a variety of landforms (Van Overmeeren 1994, 1998; Vandenberghe & Van Overmeeren 1999; Goes 2000).

The Dutch push moraines offer favourable conditions for GPR surveying. Generally, the groundwater table is deep (20–50 m below the surface). Furthermore, the ridges are composed of coarse, quartz-rich sands and gravels. Fine-grained layers (clays/silts) take up about 1–5% of the total volume and form good reflectors. A maximum penetration depth of 670 ns (two-way travel time) or approximately 45 m can be achieved using 50 MHz antennae. This is close to the maximum probable penetration depth in Quaternary soft sediments (Smith & Jol 1995). In this study, penetration depth is about 5–10 m deeper than the groundwater table.
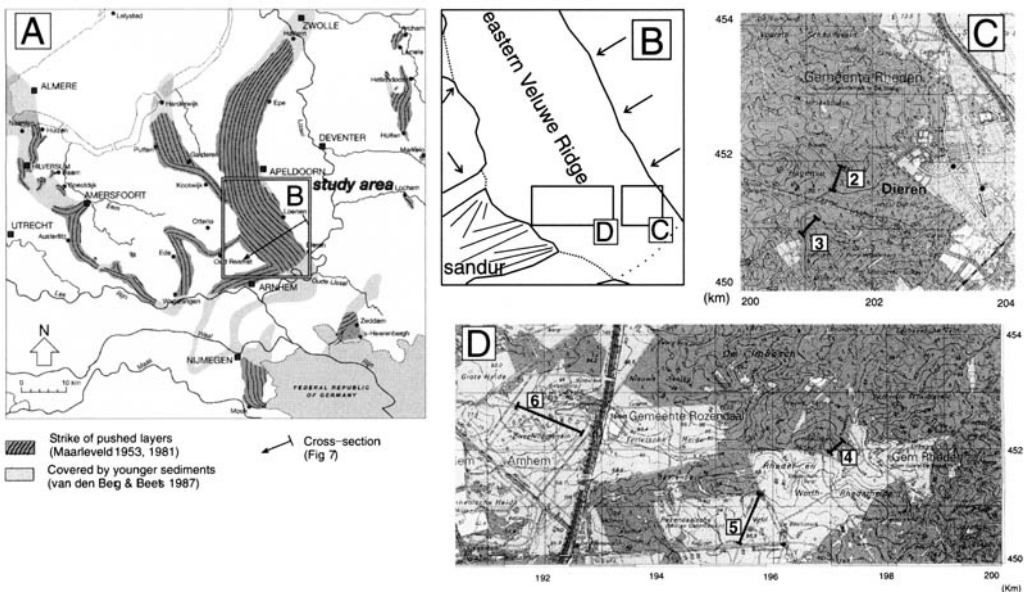
Fig. 1. Location maps. (a) Map showing study area and outline of the push moraines in the central east Netherlands (after Maarleveld 1953, 1981; Van den Berg & Beets, 1987). (b) Simplified map of study area; arrows indicate direction of glaciotectonic pressure. (c) and (d) Details of topographic map showing exact locations of Figures 2–6.

Field surveys were carried out by a high-speed data acquisition system described by Van Overmeeren (1994). It was possible to conduct about 8–10 km of 50 MHz GPR profiles per day using a pulseEKKO 100 system. All the examples discussed in this paper are 50 MHz reflection surveys, using a 1000 V transmitter. Step size was 0.50 m. Each trace was averaged 8 or 16 times. The time window was usually set upon expected penetration depth, which in turn is related to the depth of the groundwater table. The antennae were housed in a polyethylene carrier. The antenna separation was fixed at 2.0 m. An All Terrain Vehicle pulled the carrier and was capable of driving at a constant speed of 1 or 2 km/h. The system was triggered by an electronic odometer. Positioning in the field was by GPS. An average signal velocity of 0.135 m/ns for 50 MHz was determined from common midpoint surveys.

In order to deduce relationships between structural styles, sediment facies and radar facies, high-quality drilling was carried out on selected GPR sections. Complementary data from borehole logging and cone-penetration tests (CPT) served the same purpose and were also used to define the deeper parts of the ridges (Bakker, 2002).

Field conditions and processing

Mixed forests cover about 80% of the surface area of the push moraines. Access into these forests is only possible via unpaved forest tracks. Data acquisition involved grid-surveying over these tracks. Grid density was defined by spacing of forest tracks, generally every 150–500 m. This implies that three-dimensional (3-D) surveying is usually not possible. The remainder of the area consists of heath and grasslands with higher accessibility.

On certain occasions the quality of the GPR runs proved to be poor. The cause for this could not always be established. One of the causes could be the antenna orientation relative to the strike of dipping reflectors (Van Overmeeren 1994). Diffraction hyperbolae are to be expected in situations with complex tectonized sediments, wedging strata and the presence of cobble- and boulder-sized gravels in the subsurface. These are all common phenomena in push-moraine areas. Also unwanted reflections via above-surface objects (fences/trees) can disturb the data. The presence of subsurface cables and wires could easily be established from detailed infrastructure maps. A migration routine can be applied to correct diffraction effects, but it can affect the original reflection patterns. In this paper only unmigrated GPR profiles are shown.

In GPR surveying none of the negative effects mentioned above were necessarily a problem (see also Lønne & Lauritsen 1996). In most situations

it was still possible to trace the large-scale geological pattern.

Processing involved trace-to-trace and down-the-trace filtering, dewowing and automatic gain control (AGC). Particular attention was given to elevation corrections. Elevation data were extracted from detailed contour and spot-height maps (scale 1 : 10,000). The topographic information was integrated with the data file in pulseEKKO 4.2 software.

Sedimentary facies in push moraines

The push moraines in the central Netherlands consist of several architectural elements:

A. Glaciotectonized fluvial deposits. These are preglacial in origin (Mid- to Early Pleistocene) and usually deposited in braiding river systems in which cross-stratified gravelly sands and gravels dominate. Fine-grained sediments have been deposited in sheltered locations and are mostly limited in extent and thickness. More widespread deposition of fine-grained sediments, including local peat formation, was possible during interglacial stages. A variety of sediment structures occur, ranging from cross-stratification to parallel stratification, overprinted by glaciotectonic structures. Over 80% of the push-moraine complex consist of type A.

B. Glaciofluvial deposits. These were deposited during and immediately after push-moraine formation, mostly in alluvial-fan facies. Characteristic are parallel stratified sheetflood deposits. This stratification can be disturbed by synsedimentary deformation. In the study area, these deposits consist almost completely of reworked local material, i.e. they are derived from the gravelly sands and gravels mentioned above, the finest fraction being washed away. The content of glacial material (Scandinavian erratics) is usually very low.

Non-glacial deposits include slope deposits (the result of post-tectonic mass movements in periglacial conditions) and aeolian deposits (dunes and cover sands and Holocene shifting sands).

We will now discuss examples of GPR profiles collected across the eastern Veluwe Ridge. GPR surveying was carried out over the entire southern part of the moraine. Examples of the encountered structural styles will be shown, ordered from proximal (ice-marginal) area towards the undeformed foreland in the distal direction (Fig. 1). All the images are parts of longer GPR profile sections. Orientation of the profiles in Figures 2–5 is NE–SW, i.e. perpendicular to the general strike of the pushed deposits. Figure 6 shows an ESE–WNW-

orientated radar profile. All the GPR surveys are primarily interpreted in terms of macroscale glacio-tectonic deformation styles and bedding-plane reflectors.

Style I: imbricated thrusts

Style I occurs in the ice-proximal parts of the moraine. Facies is dominated by many oblique or dipping reflectors (Fig. 2). The apparent angle of the features is about 20–25°. They dip generally toward the northeast and can be detected down to a depth of 30 m below the surface. The reflectors are thrust planes composed of fine-grained sediments, as verified by numerous borings and CPT data (Bakker, 2002). This style resembles the classic idea of imbricate thrusts.

The continuous, subhorizontal reflector with negative polarity in Figure 2 is interpreted as the groundwater table. This was checked and confirmed at available water-level stations, in borings and from CPT data. The thrust planes act as hydrological barriers, impeding groundwater flow and resulting in steps in the groundwater table (Van Overmeeren 1997; Goes 2000). In Figure 2 steps are visible at the positions 800–850 m and 1025 m along the profile. The steps are about 2–7 m in the area of style I.

Style II: imbricated thrusts and folds

Style II occurs in the middle zone of the push moraine, distal to style I. Figure 3 shows a GPR section of 270 m collected in this part of the moraine. It includes an asymmetric fold structure and thrusts. Fragments of the water table are also visible, including a step of about 4 m. The wavelengths of the folds within style II are in the order of 250 m with an amplitude of about 40 m. The folds generally have an asymmetric form with fold axis mostly dipping northeast. In the example in Figure 3 the anticlinal structure is expressed in the present-day terrain morphology, but this is usually not the case.

This architecture is a reflection of a stress regime, the source of which was from the right (northeast). A relatively moderate pressure led to folding, while subsequent low-angle thrusting occurred, representing enhanced horizontal shortening. However, offset along the thrusts seems to be limited (>2 m) in this figure.

In the distal direction the folds become more prominent and the number of thrusts decreases. The radar profile of Figure 4 is 450 m long and shows asymmetric folds, a low-angle thrust set (station 2500–2600) and a normal fault (station 2800). Application of a strong gain (AGC) yields better information on deeper reflections (not shown). From the image, it is clear that the present-day relief bears no relation to the subsurface structure.

Structural relationships are indicated by dashed lines. In this example reconstruction of truncated folds leads to an estimation of about 17 m of post-glacial denudation.
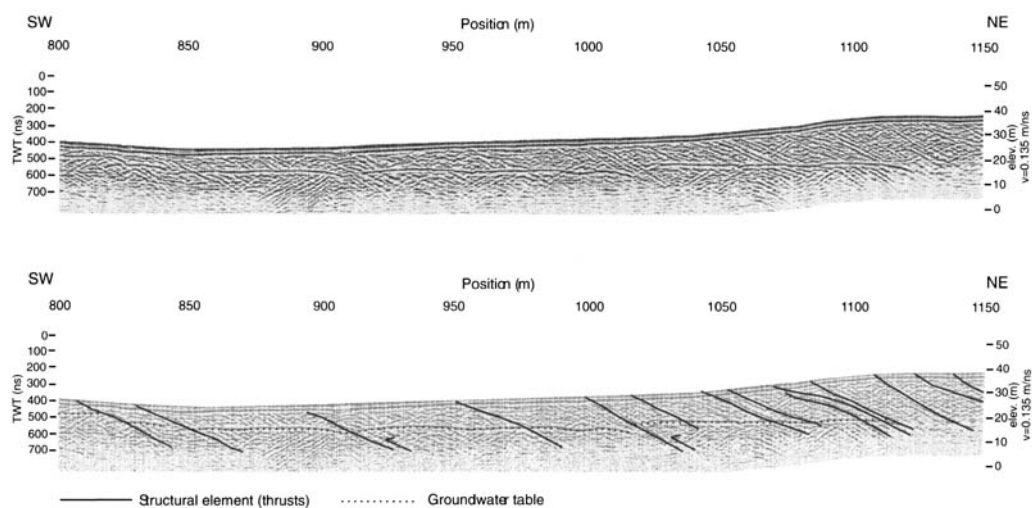
Fig. 2. 50 MHz GPR section showing style I. The structural elements are thrust planes, dipping towards the source of pressure. These imbricate thrusts frequently occur with steps in the groundwater table, which can be observed at 800–850 m and at 1025 m along the profile.
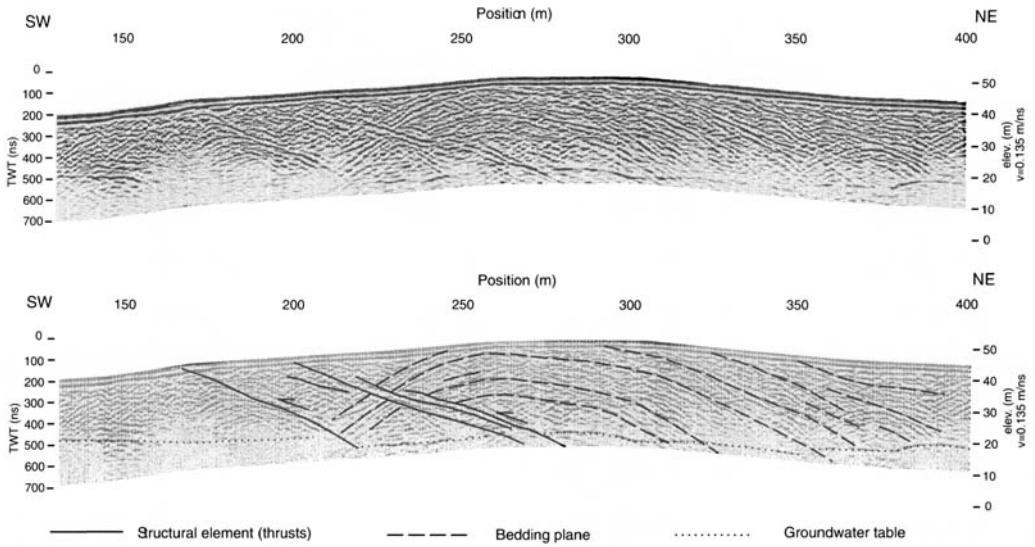
Fig. 3. 50 MHz section showing style II, consisting of folds and thrusts. An asymmetric fold and thrusts are visible in this example. At 220 m and 350 m a step in the groundwater table is visible.
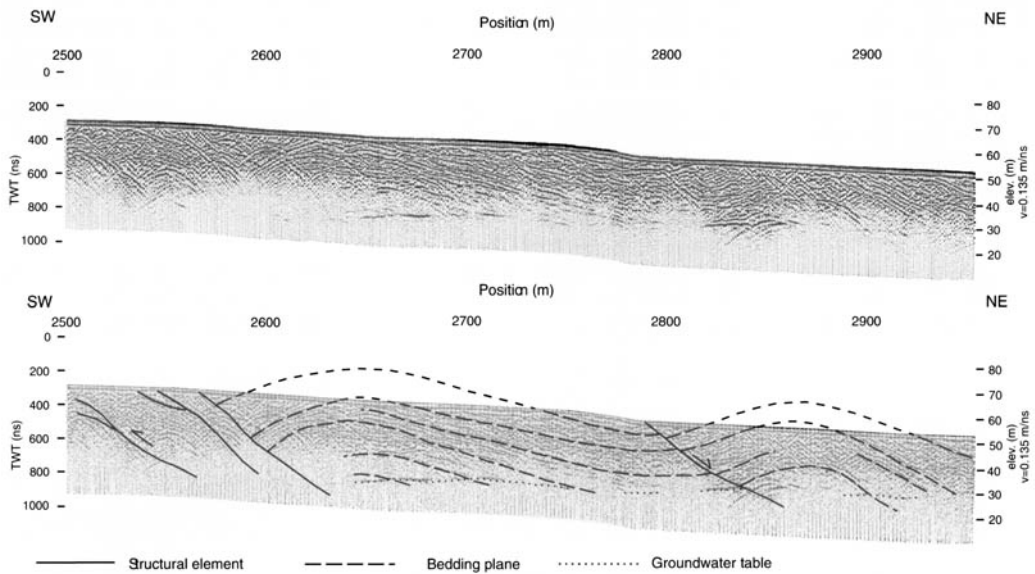
Fig. 4. 50 MHz GPR section showing style II, consisting of asymmetric folds, a thrust set (station 2500–2600) and a normal fault (station 2800). Note slight vertical exaggeration. Post-glacial denudation is about 17 m.

Style III: large-scale folds

In the area of style III the GPR profiles are characterized by strong continuous and parallel reflector sets. Figure 5 is a representation of this style, occurring in the distal parts of the ridge. The section shown is about 1000 m long. The surface is about 90 m above sea level and the maximum sig-

nal penetration is about 40 m. The water table is not visible. The figure depicts three anticlinal structures. Each antiform shows a sedimentological sequence, represented by three major continuous bedding plane reflectors. Thrusts are absent. In this area the largest folds, with wavelengths of 400 m and an amplitude of 30 m have been recorded. Core analysis showed that the reflections are the result
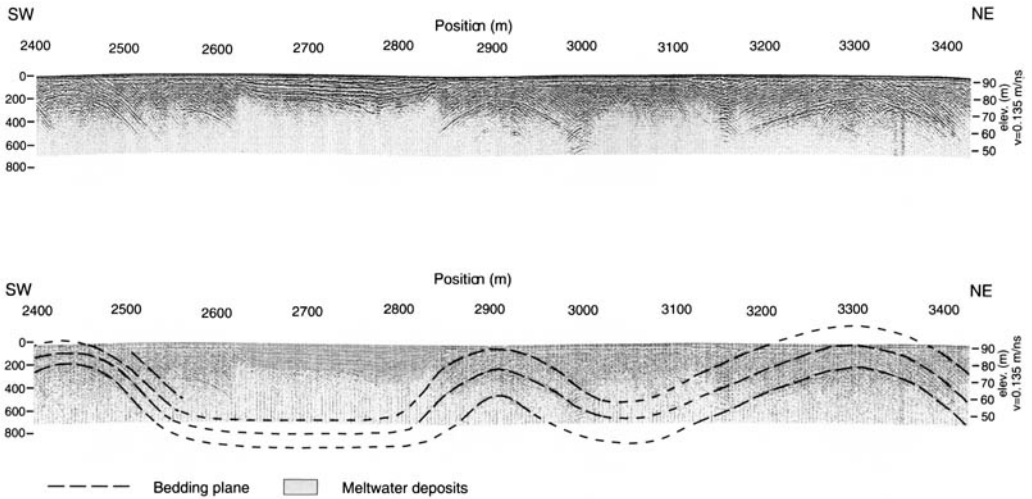
Fig. 5. 50 MHz GPR section showing style III. In this region GPR reflections are typically strong, continuous and often parallel. This profile shows a sequence of folded bedding planes. Note double vertical exaggeration. At 2620–2850 m syntectonic infilling by (melt)water occurred. Post-glacial truncation of folds is about 20 m.

of parallel fining-upward sequences (Bakker 2002). They are possibly locally reworked meltwater deposits, but lack glacial erratics at this location.

Note that a significant part of the anticlinal forms have been truncated. The minimum denudation is at least 20 m for this example. The synforms are filled with fine-grained and coarse-grained meltwater deposits, some of which were synsedimentary deformed (station 2620–2850). There are several subhorizontal reflections visible cross-cutting the folded strata. They are interpreted as wetting fronts, the result of groundwater migration after periods of rainfall.

Figure 6 presents a GPR section from the extreme distal part of the eastern Veluwe push moraine. Once more, continuous bedding-plane reflector sets are visible. In this area folds tend to flatten, ultimately grading into the undeformed outwash plain (sandur) of the foreland. Thrusts have been observed in this area, but they are rare.

Radar facies as presented within Figures 5 and 6 have the same appearance as GPR data from the undeformed sandur. From drill-sample analyses it is clear that some of the sequences contain glacial erratics. It is very likely that parts of the pushed sequences are synsedimentary tectonized glaciofluvial deposits.
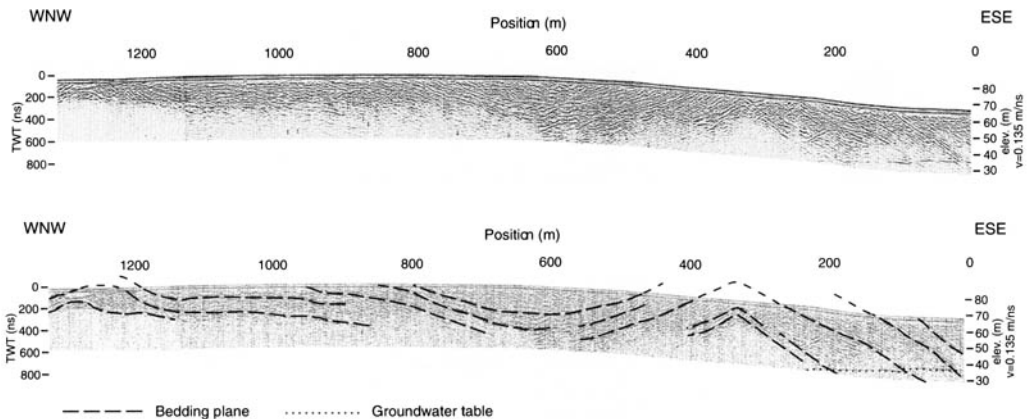
Fig. 6. 50 MHz GPR section showing structural style III by continuous undulating bedding-plane reflectors. Vertical exaggeration >2 ×. This style is indicative of the very distal parts of the moraine and shows large-scale folds, which flatten out toward the southwest.

Post-glacial evolution

As mentioned in the discussion of the figures, structural analyses of the GPR profiles make it possible to reconstruct post-glacial denudation.

Denudation of push moraines is generally the result of prolonged erosion by wind action and mass-wasting (Riezebos *et al.* 1986). Reconstruction of truncated folds leads to estimates of 15–20 m of surface level lowering, as a minimum. The denudation occurred largely during the Weichselian cold phase, but also during Late Saalian deglaciation, as evidenced by valley incision and initial alluvial-fan formation.

The current morphology of the Dutch push moraines is a reflection of denudation and erosion processes and bears no direct relation with the internal structure according to the GPR sections shown.

Synthesis of glaciotectonic architecture

The classic idea on the Dutch push-moraine architecture is one of imbricated thrusts (Maarleveld 1981). Although this model was later differentiated by Van der Wateren (1995), the architecture of the Veluwe push-moraine complex remained unclear to date.

Figure 7 presents a synthetic model of the established glaciotectonic architecture in a cross-section over the eastern Veluwe moraine (Fig. 1*a*). The model is an assembly of about 250 km of conducted GPR surveys. In the study area, the structural styles are arranged in a NE–SW (proximal–distal) sequence. In the extreme northeast, imbricated thrust sheets occur at a moderate angle and are of varying thickness (style I). Thin sheets dominate and horizontal shortening is maximal. Recent HRS on the post-Saalian lowland suggests that the thrust planes are probably rooted in the Early Pleistocene fluvial Waalre Formation. This formation is known for its thick clay layers and acts as the zone of detachment, or décollement, of the moraine. Style II is a combination of medium-scale folds with superimposed thrusts, with intermediate horizontal shortening. Style III consists of large-scale fold structures, locally with thrust features and minimal horizontal shortening. This grades ultimately into the undeformed sandur.

Overall, the amount of horizontal shortening decreases in the distal direction, suggesting form. tion of the structural complex within a single deformation event.

The presented sequence of structural styles has strong analogies with a push-moraine complex in Spitsbergen (Boulton *et al.* 1999). It was shown that most of the Holmstrømbreen sequence was formed in a proglacial setting and that it was never actually overridden by the ice. This could well apply to the situation in The Netherlands, in which case glacial overriding did not extend beyond style I.

A feature debated in the past is the plateau-like tops of many ridges. Some authors have attributed this to glaciplanation during overriding of the
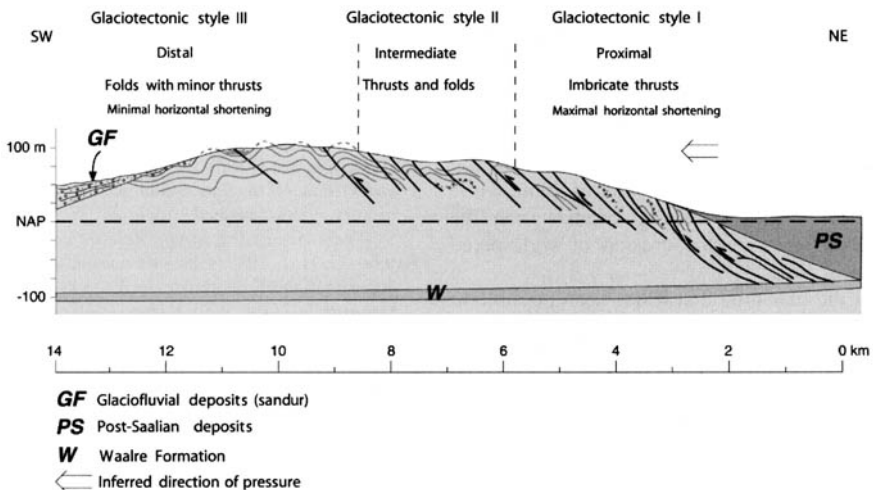
Fig. 7. Synthetic model of the eastern Veluwe push moraine based on all GPR data and from HRS (deeper parts style I). Size of the structural elements is not to scale. Note vertical exaggeration. Bold lines indicate thrusts (with arrows indicating relative movement), grey lines indicate deformed sedimentary strata. Horizontal shortening decreases in distal direction. NAP (Normaal Amsterdams Peil) is current sea level. The Waalre Formation is an Early Pleistocene fluvial system including thick clay layers and forms the décollement for the push moraine.

ridges (see discussion in Teunissen 1961). An important argument for this option has been the distribution of Scandinavian glacial erratics, which have been found on every part of the ridges, with the highest frequencies in proximal settings (De Zanger 1980). Others have explained the plateaux by periglacial denudation in the form of wind action and mass wasting (Van der Wateren 1985).

The distribution of northern erratics in distal settings can easily be explained in terms of glaciofluvial dynamics. We suggest that the deposition of glaciofluvial sediments has been much more widespread than previously established and that it was part of a large-scale system of glacier advance, push-moraine formation and meltwater deposition (see also Kluiving 1994; Boulton *et al.* 1999). A significant amount of the meltwater deposits has subsequently been eroded by weathering, water and wind. The scattered distribution of erratics is therefore not necessarily a relict of glacial overriding.

Conclusions

This paper shows that low-frequency GPR is capable of imaging large-scale structures. The continuity of reflections in push moraines is often remarkable. Although the reflection configuration can be chaotic in places, this does not always hinder structural analysis and mapping of architectural elements in the Dutch push moraines.

Synthesis of the structural styles within the eastern Veluwe push moraine shows a general decrease in glaciotectonic deformation in the ice-distal direction. This suggests that the push moraine was formed during only one glaciotectonic event. Hence, the exceptional large dimensions of the eastern Veluwe Ridge do not have to be explained via complex ice-marginal dynamics (Maarleveld 1981).

We have shown that the post-glacial denudation of the push moraines is in the order of 20 m, while the scattered occurrence of erratics can be explained in terms of the erosion of widespread meltwater deposits.

This is the first time that it has been possible to present a factual model of the internal architecture of part of a push moraine using GPR. The technique makes it possible to establish the position and size of hydrological compartments. Our model enables the mapping and prediction of the presence and orientation of hydrological barriers.

References

BAKKER, M. A. J. 2002. A comparison of ground-penetrating radar facies and sediment characteristics in a Pleistocene push moraine in The Netherlands. *In*: KOPPENJAN S. K. & LEE, H. (eds.) *Ninth International Conference on Ground Penetrating Radar*. Proceedings of the Society of Photo-Optical Instrumentation Engineers, **4758**, 317–322.

BENNETH, M. R. 2001. The morphology, structural evolution and significance of push moraines. *Earth Science Reviews*, **53**, 197–236.

BOULTON, G. S., RUEGG, G. J. H., VAN DER MEER, J. J. M. & BEETS, D. J. 1984. Structure and origin of the ice-pushed ridges of The Netherlands. *KNGMG Newsletter*, **5**, 4–6.

BOULTON, G. S, VAN DER MEER, J. J. M., BEETS, D. J., HART, J. K. & RUEGG, G. H. J. 1999. The sedimentary and structural evolution of a recent push moraine complex: Holmstrømbreen, Spitsbergen. *Quaternary Science Reviews*, **18**, 339–371.

DAVIS, J. L. & ANNAN, A .P. 1989. Ground penetrating radar for high resolution mapping of soil and rock stratigraphy. *Geophysical Prospecting*, **37**, 531–551.

DE ZANGER, F. A. P. 1980. Die Höhenlage des Eises des Gletscherlobus während der Formung des Stauchwalles von Arnheim (Niederlande). *Eiszeitalter und Gegenwart*, **30**, 19–28.

GOES, B. J. M. 2000. *Een Methode voor het Karteren van Laterale Grondwaterstromingsbarrieres en Anisotrope Zones in Gestuwde Gebieden*. TNO-rapport, NITG, 00-330-A, 1–57.

KLUIVING, S. J. 1994. Glaciotectonics of the Itterbeck-Uelsen push moraines, Germany. *Journal of Quaternary Science*, **9**, 235–244.

LØNNE, I. & LAURITSEN, T. 1996. The architecture of a modern push-moraine at Svalbard as inferred from ground-penetrating radar measurements. *Arctic and Alpine Research*, **28**, 488–495.

MAARLEVELD, G. C. 1953. Standen van het landijs in Nederland. *Boor en Spade*, **6**, 95–112.

MAARLEVELD, G. C. 1981. The sequence of ice-pushing in the central Netherlands. *Mededelingen Rijks Geologische Dienst*, **34**, 2–6.

RIEZEBOS, P. A., BOULTON, G. S. ET AL. 1986. Products and effects of modern eolian activity in a nineteenth century glacier-pushed ridge in West Spitsbergen, Svalbard. *Arctic and Alpine Research*, **18**, 389–396.

RUEGG, G. H. J. 1983. Glaciofluvial and glaciolacustrine deposits in the Netherlands. *In*: EHLERS, J. (ed) *Glacial Deposits In North-West Europe*. Balkema, Rotterdam, 379–392.

SMITH, D. G. & JOL, H. M. 1995. Ground penetrating radar: antenna frequencies and maximum probable depths of penetration in Quaternary sediments. *Journal of Applied Geophysics*, **33**, 93–100.

TEUNISSEN, D. 1961. *Het Middennederlandse Heuvelgebied*. Ph.D. thesis, Utrecht University.

VAN DEN BERG, M. W. & BEETS, D. J. 1987. Saalian glacial deposits and morphology in The Netherlands. *In*: VAN DER MEER, J. J. M. (ed.) *Tills and Glaciotectonics*. Balkema, Rotterdam, 235–251.

VANDENBERGHE, J. & VAN OVERMEEREN, R. A. 1999. Ground penetrating radar images of selected fluvial

deposits in Ridgeerlands in the Netherlands. *Sedimentary Geology*, **128**, 245–270.

VAN OVERMEEREN, R. A. 1994. High speed georadar data acquisition for groundwater exploration in The Netherlands. *Proceedings of the Fifth International Conference on Ground Penetrating Radar, Waterloo Center for Groundwater Research, Kitchener, Ontario*, 1057–1073.

VAN OVERMEEREN, R. A. 1997. Imaging groundwater 'steps' in push moraines by georadar. *In*: McCANN, D. M., EDDLESTON, M., FENNING, P. J. & REEVES, G. M. (eds) *Modern Geophysics in Engineering Geology*. Geological Society, Engineering Geology Special Publications, **12**, 63–73.

VAN OVERMEEREN, R. A. 1998. Radar facies of unconsolidated sediments in The Netherlands: A radar stratigraphy interpretation method for hydrogeology. *Journal of Applied Geophysics*, **40**, 1–18.

VAN DER WATEREN, F. M. 1985. A model of glacial tectonics, applied to the ice-pushed ridges in the central Netherlands. *Bulletin of the Geological Society of Denmark*, **34**, 55–74.

VAN DER WATEREN, F. M. 1987. Structural geology and sedimentology of the Dammer Berge push moraine, FRG. *In*: VAN DER MEER, J. J. M. (ed.) *Tills and Glaciotectonics*. Balkema, Rotterdam, 157–182.

VAN DER WATEREN, F. M. 1995. Structural geology and sedimentology of push moraines – processes of soft sediment deformation in a glacial environment and the distribution of glaciotectonic styles. *Mededelingen Rijks Geologische Dienst*, **54**, 1–168.

This page intentionally left blank

GPR derived architecture of November 1996 jökulhlaup deposits, Skeiðarársandur, Iceland

N. J. CASSIDY[1], A. J. RUSSELL[1], P. M. MARREN[1], H. FAY[1], Ó. KNUDSEN[2], E. L. RUSHMER[1] & T. A. G. P. VAN DIJK[1]

[1]*School of Earth Sciences and Geography, Keele University, Staffordshire, ST5 5BG, UK*
(e-mail: n.j.cassidy@esci.keele.ac.uk)
[2]*Klettur Consulting Engineers, Bíldshöfða 12, Box 661, IS 121 Reykjavík, Iceland*

Abstract: Skeiðarársandur in southeastern Iceland, with an area of >1000 km², is the world's largest active proglacial outwash plain. In July–August 2000, a total of over 10 km of ground penetrating radar (GPR) profile data (at 50 MHz and 100 MHz) was collected from a variety of proglacial outwash sediments across the Gígjukvísl channel region of the Skeiðarársandur plain. GPR-profile results and their corresponding facies interpretations are presented for the flood deposits of a single supraglacial outwash fan and its associated source-proximal ice-walled canyon created entirely by the November 1996 jökulhlaup event. By combining the GPR data with ground surveying, photogrammetry and detailed sedimentary outcrop evidence, this study adds a new perspective to the large-scale analysis of single, high-magnitude flood events and the sedimentary record of former, ice-proximal outwash plains. The GPR derived architectures point to a higher degree of sediment reworking than predicted by previous sedimentary models and may provide a useful analogue for the study of sedimentation within similar bedrock fluvial and alluvial fan feeder systems.

Jökulhlaups (glacial outburst floods) are believed to play a dominant role in the evolution of proglacial outwash plains in many parts of the world and appear to have a strong influence on the morphology, dynamics and development of glacier margins. An improved understanding of their sedimentary characteristics is therefore invaluable for the analysis of former ice-sheet dynamics, sedimentary processes, rates of deglaciation and the prediction of future jökulhlaup hazards. With an area of >1,000 km², Skeiðarársandur is the world's largest active proglacial outwash plain and contains a variety of proglacial jökulhlaup and non-jökulhlaup deposits. In late September 1996, a volcanic eruption beneath the Vatnajökull icecap, southwestern Iceland, resulted in the release of approximately 3.8 km³ of meltwater over the Skeiðarársandur outwash plain in early November 1996. The ground penetrating radar (GPR) study presented in this paper concentrates on the large-scale sedimentary analysis of an ice-proximal, supraglacial outwash fan (referred to here as the Gígjukvísl outwash fan) and its associated ice-walled canyon, which were created entirely by a single outburst flood event during the November 1996 jökulhlaup (Fig. 1). The sedimentary and geomorphological characteristics of the deposits have

been described in detail by Russell and Knudsen (1999*a*, *b*), Russell *et al.* (1999, 2001) and Roberts *et al.* (2000*a*, *b*; 2001), using a variety of techniques, including ground surveying, photogrammetry and the detailed sedimentary analysis of exposed channel boundaries and ice-block sections. Unfortunately, these techniques can only provide localized information on the hydraulic and depositional environment and therefore any sedimentary interpretations may not be fully applicable to the larger-scale sandur architecture.

The primary objective of this study is to examine the large-scale sedimentary architecture of the Gígjukvísl outwash fan by the combined use of GPR 'imaging', photogrammetry and sedimentary exposure analysis. A programme of GPR surveying was initiated in July 2000, resulting in the collection of more than 10 km of 50 MHz and 100 MHz GPR data across the full length of the outwash fan. A pulseEKKO 100 GPR system, configured in co-planar, 'broadside' reflection mode, was used for all profile sections, pseudo-three-dimensional (3D) grids and targeted common mid-point (CMP) velocity surveys (collected in the areas associated with the pseudo-3D grids and exposed sections). Photographs taken by Dr M. T. Guðmundsson, along with media footage and airborne videos collected
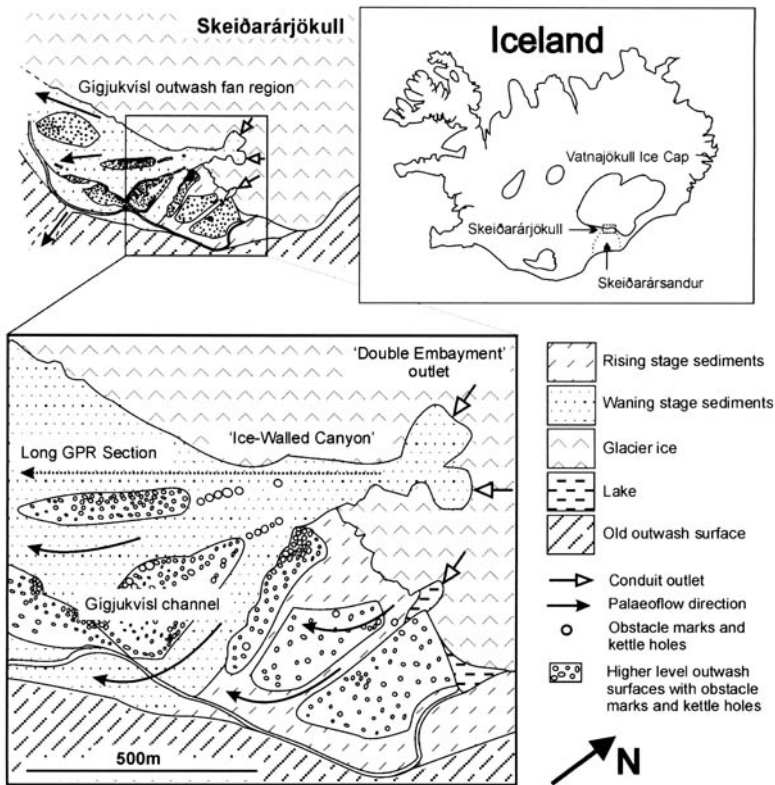
Fig. 1. Location map for the Vatnajökull icecap, Skeiðarársandur outwash plain, ice-proximal, jökulhlaup outwash fan and the long, flow-parallel GPR section.

by Dr A. Russell, have provided vital information on the jökulhlaup flow conditions within the embayment, ice-walled canyon and outwash plain. An inventory of the collected GPR data is provided in Table 1, along with the associated GPR system configurations and survey details. The location of the GPR profiles and exposed sections are provided in Figure 2.

The quality of the collected data was consistently high; therefore only simple processing steps were required in order to interpret the data in detail. Each of the collected sections was edited for noisy/corrupt traces, dewowed, adjusted to time zero, topographically corrected and converted to a standard PCX grey-scale image for interpretation. The CMP analyses revealed approximately linear velocity profiles for each survey location, ranging from ~0.08 m ns^{-1} at the near-surface through to 0.06 m ns^{-1} at depth. This equates to a subsurface relative permittivity range of approximately $\varepsilon_r = 14$–25 and is consistent with the relative permittivity of wet, poorly sorted sands and gravels (Reynolds 1997). Using an average velocity value of 0.07 m ns^{-1} as the uniform value for depth con-

version, the observable signal penetration is approximately 20 m, which is deeper than the calculated total thickness of the outwash deposits (Knudsen *et al.* 2001).

The November 1996 jökulhlaup

The volcanic eruption beneath the Vatnajökull icecap commenced on 30 September 1996 (Guðmundsson *et al.* 1997) and, over the next month, 3.4 km^3 of meltwater travelled subglacially into the Grímsvötn subglacial lake until a critical drainage level was reached on the morning of 5 November (Björnsson 1997). The resulting jökulhlaup began at the most easterly outlet river, the Skeiðará, at 07.20 h (local time) and reached a peak discharge of 45,000 m^3 s^{-1} within 14 hours (Björnsson 1997). In the Gígjukvísl channel, jökulhlaup flows burst from single-conduit outlets and crevasses up to 2 km in length (Snorrason *et al.* 1997; Roberts *et al.* 2000*a, b*; Roberts *et al.* 2001), with the main flow exiting from a fracture complex outlet that migrated retrogressively during the mid- to late-rising, peak and early waning stages of the

Table 1. *Inventory of GPR data*

Location	Survey type	Radar frequency (MHz)	Details
Outwash fan	Co-planar reflection profile	50	Flow-parallel, long-profile section (2044 m) with 2 m antenna separation and 0.5 m spatial interval. Data collected in discrete step mode with 400 V pulse, 16 stacks, 600 ns time window and 1.6 ns temporal interval.
	Co-planar reflection profile	100	Flow-parallel, targeted 100 MHz profile section (150 m) corresponding to the 40–190 m positions of the 50 MHz long-profile section (within ice-walled canyon region). 1 m antenna separation and 0.25 m spatial interval. Data collected in discrete step mode with 400 V pulse, 16 stacks, 400 ns time window and 0.8 ns temporal interval.
	Co-planar reflection pseudo-3D grid	50 & 100	Central area of the outwash fan corresponding to the 1560–1610 m positions of the 50 MHz long-profile section (edge of proximal and distal fan regions). Ten flow-perpendicular sections (90 m) with 5 m section spacing centred on the long-profile section line. GPR system configuration as for the 50 MHz long-profile section and targeted 100 MHz profile section.
	Co-planar reflection pseudo-3D grid	50	Central area of the outwash fan corresponding to the 40–85 m positions of the 50 MHz long-profile section (within ice-walled canyon region). Seven flow-perpendicular sections (50 m) with 7.5 m section spacing centred on the long-profile section line. GPR system configuration as for the long-profile section.
	CMP velocity surveys	50 & 100	Central position of pseudo-3D grids along 50 MHz long-profile section line. Co-planar 'broadside' mode with GPR system configuration as for the 50 MHz long-profile section and targeted 100 MHz profile section.
Control section	Co-planar reflection profile	50 & 100	Near flow-parallel 'control' profile section (90 m) running adjacent to the face of the exposed section at the flanks of the outwash fan (at a maximum of 4 m from the 60°+ dipping exposure face). GPR system configuration as for the 50 MHz long-profile section and targeted 100 MHz profile section.
	CMP velocity surveys	50 & 100	Central position of the 'control' profile section. Co-planar 'broadside' mode with GPR system configuration as for the 50 MHz-long-profile section and targeted 100 MHz profile section.

flow. This resulted in a spectacular double-headed 'embayment' and 'ice-walled canyon' feature that extended over 500 m into the glacier margin (Fig. 1) (Russell & Knudsen 1999*a*, *b*; Russell *et al.* 1999, 2001; Roberts *et al.* 2000*a*, *b*, 2001).

Photographic evidence and media footage taken during the daylight hours of 5 November show that, in the early rising stages of the flood, only minor outflows were present at the ice margin (in the location of the subsequent embayment). However, before the creation of the embayment, early-rising stage floodwaters from the east had been observed exiting the ice margin and flowing in a westerly direction along the Gígjukvísl channel

into the existing proglacial, backwater lake. During the 17 hours of darkness between 16.30 h on 5 November and 09.3 0h on 6 November, the main fracture complex began to develop and the flows were concentrated in the embayment area (i.e., at the point of lowest glacial, hydraulic potential along the ice margin). By the morning of 6 November, however, waning stage flows were observed emerging from the newly formed double embayment and flowing across the outwash fan in a southerly direction. Large-scale flow separation and macro-turbulence was observed, particularly around the angular cliff edges of the ice margin, while rhythmic flow pulses of between 2 s and 4 s
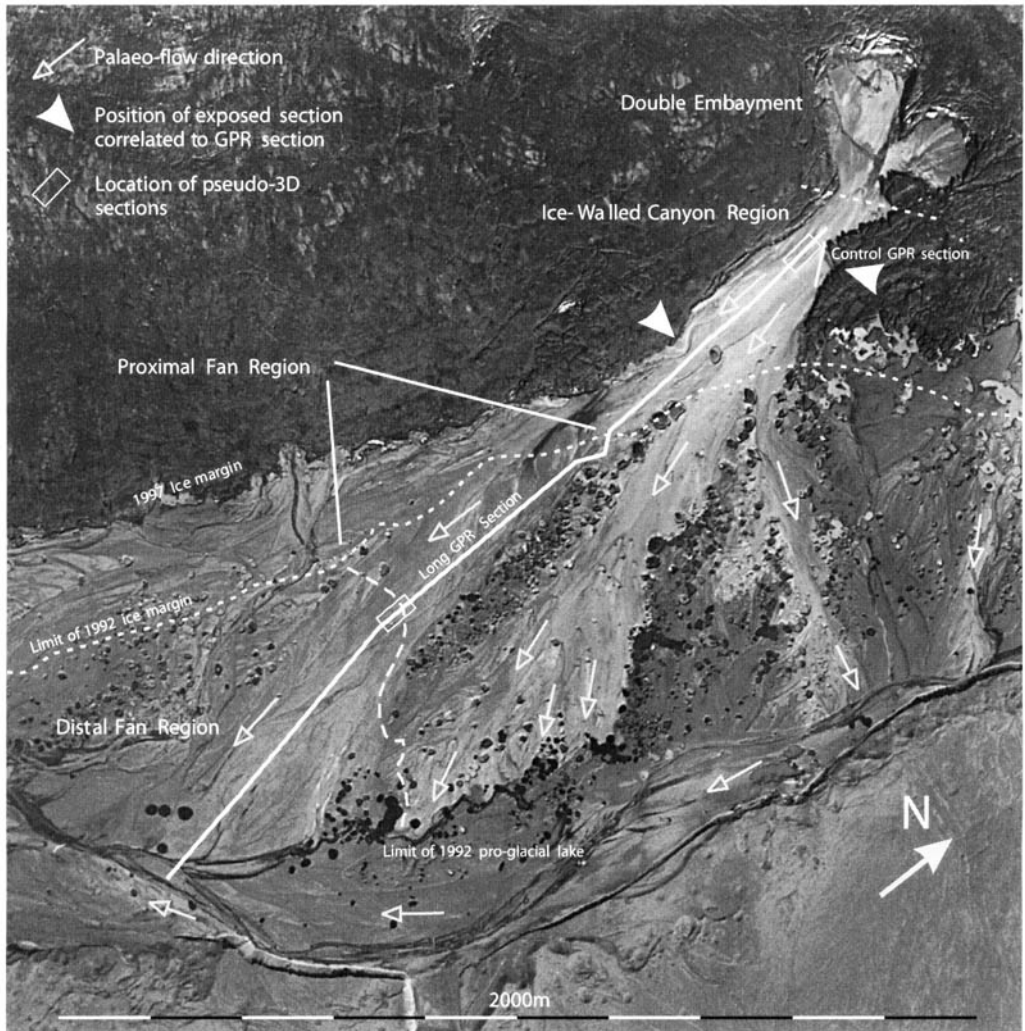
Fig. 2. Location of the ice-walled canyon, proximal and distal fan regions, extended and control GPR sections, palaeo-flow and exposed sections used to correlate the GPR sections with the known sedimentary evidence. (Photo source: Landmaelinger Islands).

duration exited the western embayment conduit, forming discrete flood-surface waves at the apex of the ice-walled canyon. Peak-flow shear stresses and flood powers for the western chamber and ice-walled channel have been calculated by Russell *et al.* (2000) as $5000 \, \mathrm{Nm^{-2}}$ and $40,000 \, \mathrm{Wm^{-2}}$, respectively, and are therefore capable of trans-porting sedimentary material of up to 20 cm diam-eter in suspension.

Depositional environment on the jökulhlaup outwash fan

The sedimentary environment and hydraulic con-ditions across the outwash fan can be subdivided into three distinct regions, summarized as follows.

1. Embayment and ice-walled canyon region

- Geometrically restricted, high-energy, deep flows during the late-rising/peak-flow stages, progressing into shallower supercritical flows during the waning stages.
- Transportation of large ice blocks (up to 45 m in diameter) and boulder-sized materials as suspended loads.
- High sediment concentrations, with the rapid deposition of relatively fine- to coarse-grained material in turbulent, overcapacity flow con-ditions.
- Localized channelling and bedload transport of deposits during the later waning stages.

- An evolving depositional environment during the headward excavation of the ice-walled canyon with the syn-flood creation of proximal accommodation space and the removal of over 5 million m^3 of ice.

2. Proximal outwash fan region

- A zone of rapid-flow expansion, downstream from the ice-walled canyon, with reduced flows of shallower depth.
- Rapid transfer/flux of suspended material to bedload as flow exits the canyon region.
- Prolonged waning-stage flows resulting in the development of an armoured layer of waning-stage deposits with later channelling and bedload transportation.
- Surface deposition of ice blocks in distinct, flow-parallel linear zones, producing areas of localized flow separation and supercritical flow conditions.

3. Distal outwash fan region

- Reduced flows with the progressive widening of the outwash fan and 'ponding' of the outwash waters within the southern region of the Gígjukvísl channel.
- Deposition of finer-grained material during the late-rising, peak and waning stages over the pre-embayment and early-rising stage deposits.
- Far-distal zone affected by the post-flood action of the main Gígjukvísl channel outwash river, with sediment reworking at the confluence of the two flows.

The locations of the 1992 preflood and 1997 post-flood ice margins, proglacial lake and outwash fan can be seen in the aerial photographs of Figures 3a and b. These clearly show the extent of the double embayment and ice-walled canyon, the distribution of the outwash sediments and the zones of stranded ice blocks. The three depositional regions are also illustrated in Figure 2, together with the palaeoflow information, location of the extended flow-parallel GPR fan section, control GPR section and pseudo-3D surveys, plus the exposed sections used to correlate the GPR data to the known sedimentary evidence.

GPR profile sections and facies interpretations

The full, flow-parallel, 50 MHz long-profile section and its associated GPR facies interpretation diagram are subdivided into four 500 m-long sections (Figs 4a–d). Coherent, identifiable reflections are represented with a solid boundary line while a dashed boundary line illustrates less coherent reflections or interpolated features. Note that, in the facies interpretation diagrams, the position and inter-relationship of the reflector truncations and their associated boundary interpretations are based solely on the coherence of the reflections and the continuity of the observed signal. No attempt has been made, systematically, to interpret boundary relationships through GPR facies techniques (i.e. sequence stratigraphy mapping). Although these methods have been used successfully in finer-grained fluvial sediments (e.g. Gawthorpe et al. 1999), the presence of interfering diffraction events from the coarser-grained material makes it difficult to determine the true nature of the reflection terminations. Instead, local onlap, toplap and downlap relationships have been identified for particular units, and only in circumstances where the facies interpretation is of significant relevance to the characterization of the depositional environment.

Significant diffraction events are represented by a small point-source 'box' located at the apex of each diffraction hyperbola and the topographically corrected time-zero ground surface is illustrated by a continuous solid line at the top of each subsection. The continuous strong reflection located at approximately 150 ns (two-way travel time) in the long profile is interpreted as the local water table. It is represented in the facies diagram by a heavy dashed line running consistently through all sections and is estimated to be at a depth of approximately 5 m, based on a uniform average velocity of 0.07 m ns^{-1}. This is consistent with spring-line depths in the exposed sections and the level of the distal outwash river. In the region of the ice-walled canyon, however, this strong reflection may not be an accurate representation of the actual water table because large blocks of locally buried ice, observed in the exposed sections at similar levels, may have a significant yet localized effect on subsurface groundwater conditions. Note that, in each of the illustrated sections, an automatic gain control (AGC) has been applied to the data (to a maximum value of 200 × the recorded signal value) and that the quoted dip angles have been determined directly from the unmigrated GPR sections. As a result, the estimated dip angles will be 10–20% greater than the true dip angle of the feature.

Ice-walled canyon region

The three distinct depositional regions (i.e. the ice-walled canyon, proximal fan and distal fan) can be clearly identified in the GPR sections by their significantly contrasting radar facies. In the ice-walled canyon region the signal penetration is relatively low (in comparison to the far-distal fan region), yet the majority of the reflections and diffractions are
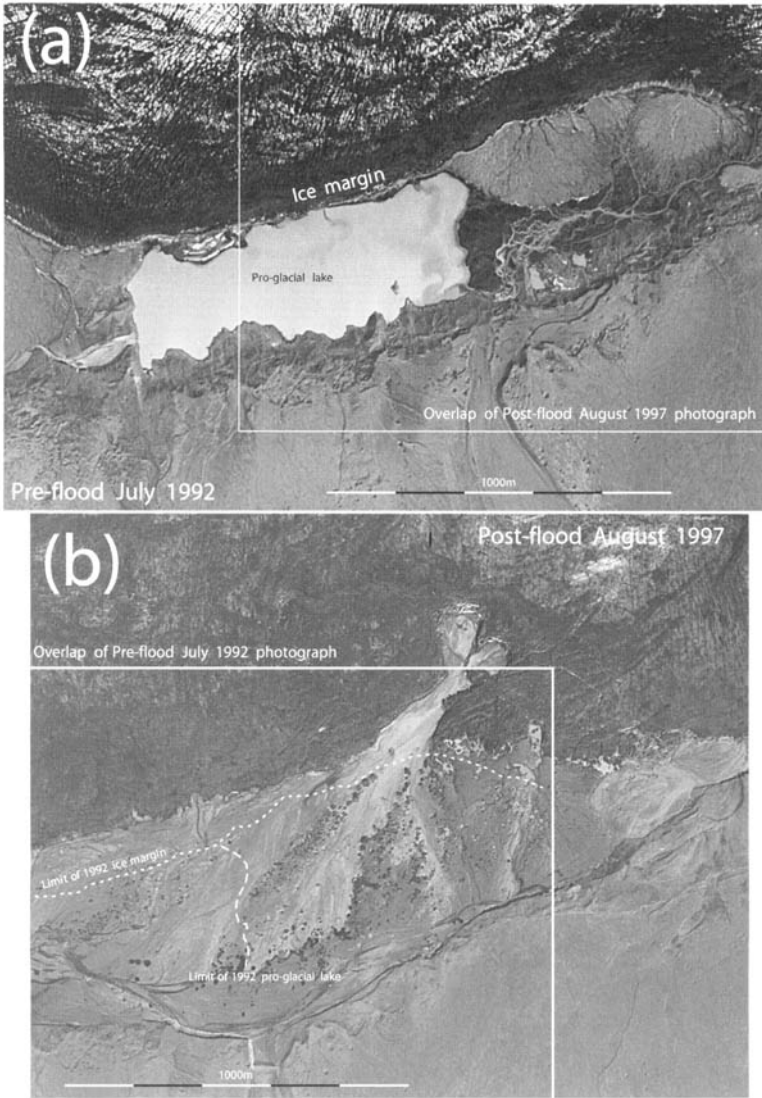
Fig. 3. 1992 preflood and 1997 post-flood aerial photographs of the glacial margin, Gígjukvísl channel and proglacial zone (Photo source: Landmaelinger Islands).

of moderate to high amplitude with high coherence and continuity. Within this region, three separate facies zones can be identified:

- A prominent zone at 0–180 m (Fig. 4*a*) of deeper penetration (~15 m) with distinctive, large-scale, upstream dipping stoss-side reflections of moderate dip angles (~15°) and few diffractions. Overlying these stoss-side reflections are much finer-scaled units of predominately low-angled, upstream dipping reflectors. In this case, a distinct erosional sequence boundary surface can be identified at the base

of the finer-scaled units, with the upper reflections downlapping at the interface and the lower, larger-scale stoss-side reflections toplapping at much lower angles.

- Two zones at 200–400 m and 500–650 m (Figs 4*a* & *b*) of relatively poor penetration, high diffraction density and few deep reflections. In both of these zones, the majority of diffractions are located near the 'water table' boundary (although low-amplitude diffractions can be observed at the base of the section). Coherent downstream and upstream dipping reflections can be identified in the finer-scaled upper units,

(a)

(b)
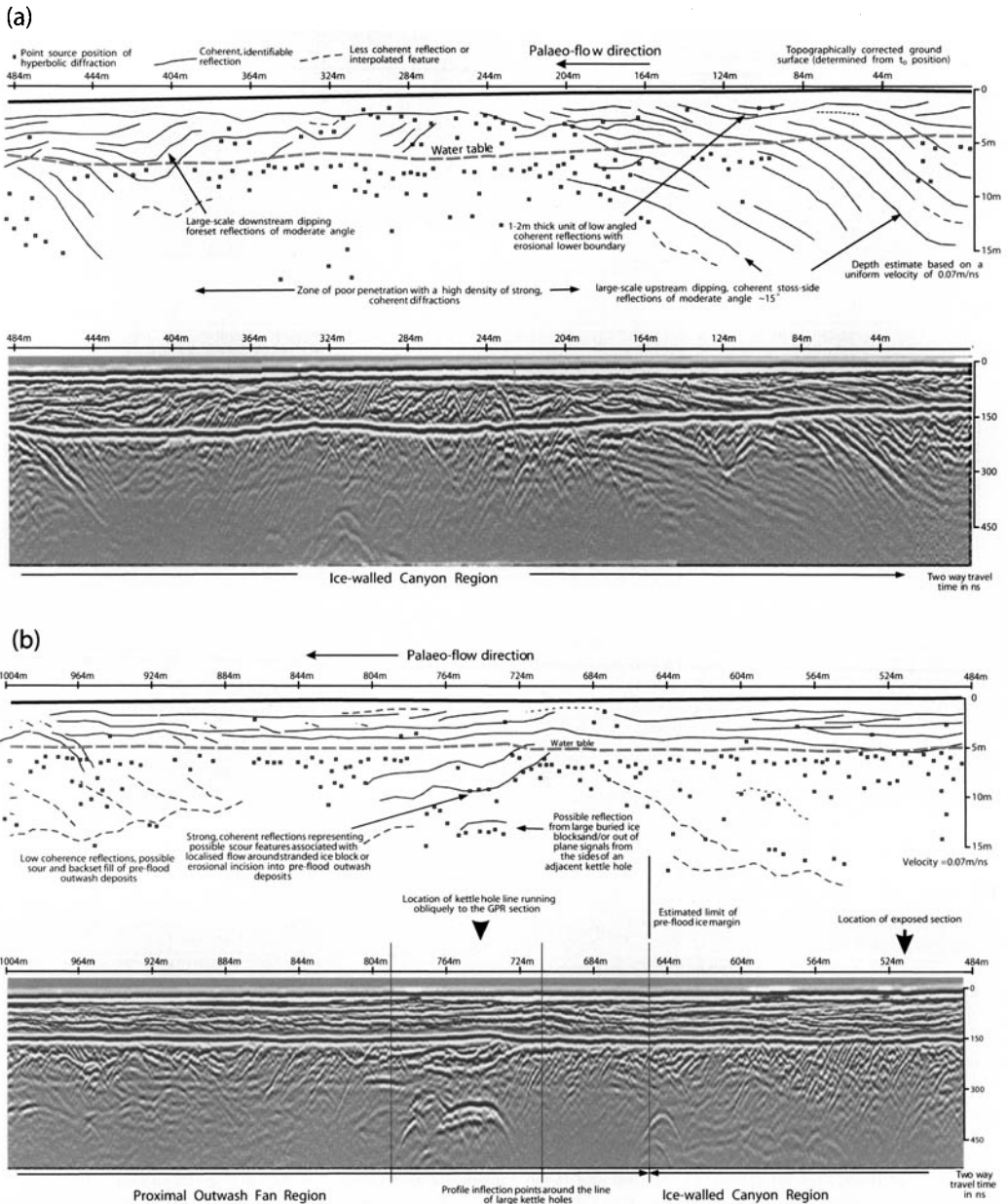
Fig. 4. (a) 50 MHz GPR section and facies interpretation for the ice-walled canyon region of the long, flow-parallel profile. (b) 50 MHz GPR section and facies interpretation for the proximal outwash fan region of the long, flow-parallel profile.

but are less prominent than in the other zones. Boundary relationships are difficult to identify but individual downlapping and onlapping terminations can be seen in the shallow downstream dipping, low-angled foreset reflections located between 500 m and 650 m.

• A narrow zone at 360–480 m (Fig. 4a) contain-

ing large-scale, coherent, downstream dipping, moderate-angled (~15°) foreset reflections of consistent form and identifiable boundary relationships. Distinct upper and lower sequence boundaries can be identified with associated onlap, toplap and downlap relationships. Penetration is good (~15 m) with the

(c)
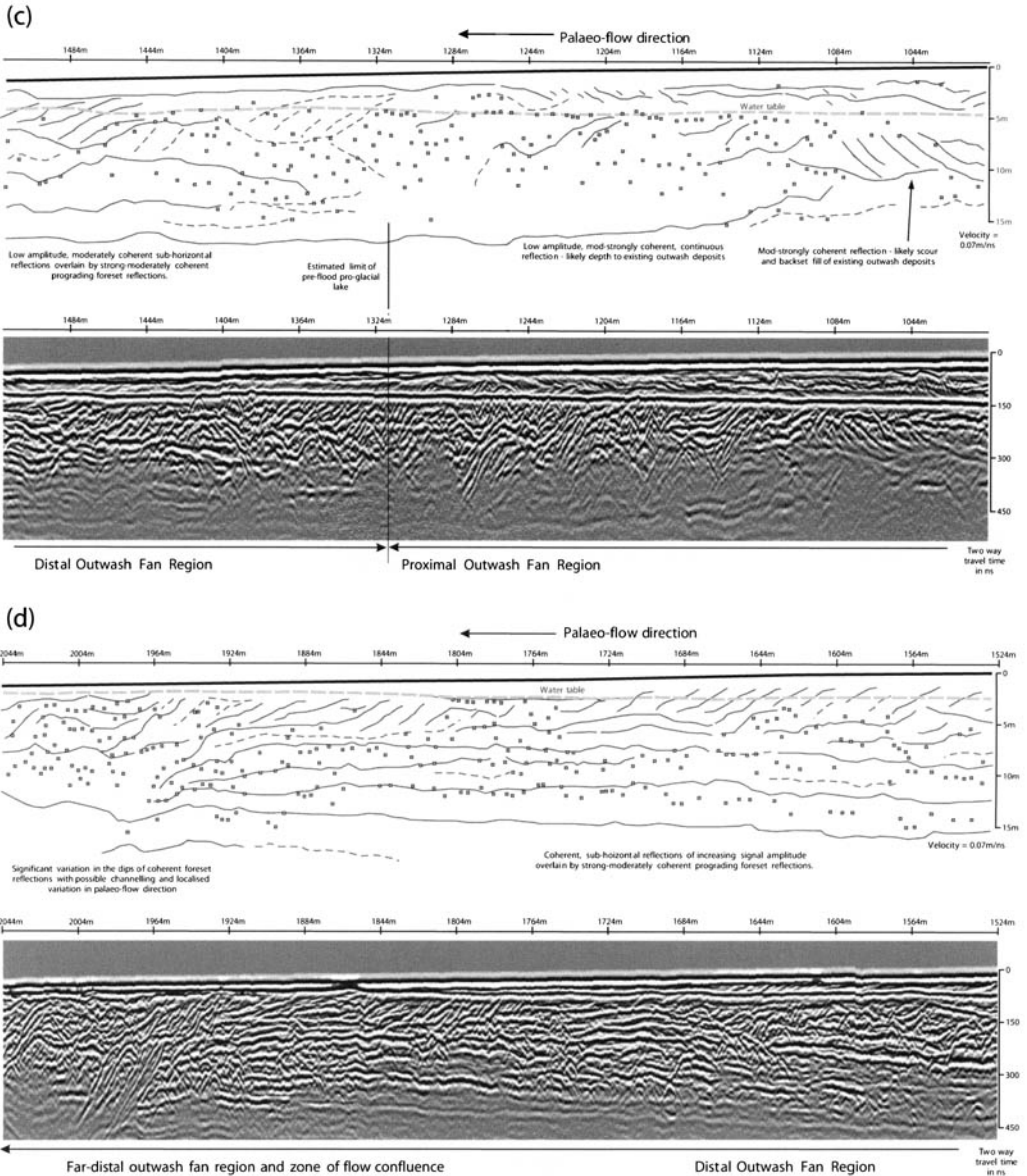
Fig. 4. (continued) (**c**) 50 MHz GPR section and facies interpretation for the proximal and distal outwash fan regions of the long, flow-parallel profile. (**d**) 50 MHz GPR section and facies interpretation for the distal outwash fan region of the long, flow-parallel profile.

presence of deeper, individual, large-scale, upstream dipping stoss-side reflections at the end of the zone (460–480 m).

The most striking features of this ice-walled canyon region are the deep, well-defined, large-scale, upstream dipping stoss-side beds of the first 200 m of the section. Situated in the centre of the ice-walled canyon, these large upstream dipping units

are interpreted as the stoss-sides of flow-transverse channel macro-forms, possibly associated with a hydraulic jump (standing wave), migrating upstream during the late-rising/peak-flow stages of the flood and the headward excavation of the ice-walled canyon. The presence of these rarely preserved, supercritical stoss-side bedforms is considered diagnostic of high sedimentation rates in rapid, shallow flows and suggests the syn-flood

creation of headward-migrating accommodation space. The bedforms are, in general, coarser-grained and thicker than the deposits of the proximal and distal fan regions and represent rapid deposition, almost directly from suspension, of coarse sediment at the base of turbulent, channel-restricted flows. The erosional contact and finer-scaled features of the upper unit represent the later, waning-stage flow deposits and are associated with reduced flow conditions, localized sediment reworking and the passage of a series of smaller-scale antidunes (Alexander *et al.* 2001).

These two distinct sedimentary units can be seen in more detail in the corresponding 100 MHz GPR profile (shown in Fig. 5) collected between the 40 m and 190 m positions of the long 50 MHz traverse line. The 100 MHz profile shows the detailed structure of the upper, finer-scaled units and the relationship of the toplapping large-scale, stoss-side bedforms to the erosional sequence boundary. Orthogonal sections collected as part of the pseudo-3D grids reveal that, in general, the large upstream dipping bedforms are laterally extensive, with profile-parallel dips and similar 3D geometries. The finer, smaller-scaled upper units are not as geometrically uniform, with the shallowest reflections showing more localized forms and significant variations in dip angle away from the profile plane. This evidence suggests that, during the mid-late-rising and peak-flow stages, palaeoflow directions were relatively uniform and consistent with the generalized, profile-parallel orientation. However, in the later or waning stages, the palaeoflow directions changed and the resulting depositional geometry became more dependent on the localized flow conditions, probably as a result of the removal/dissipation of the hydraulic jump. Flows became supercritical, resulting in the development of low-angled migrating antidune structures within the confines of the canyon walls. The sedimentary outcrop evidence found in 'control' sections exposed by the retreating ice walls supports this waning stage interpretation. The exposures reveal similar bedform geometries, scales and, more significantly, clast imbrication evidence of downstream palaeoflows within the upstream dipping antidune beds. They are invaluable for ground-truthing the GPR sections and assessing the physical nature of the reflections. Figure 6 illustrates the 100 MHz control section collected adjacent to the face of an exposure located at the eastern flank of the ice-walled canyon and is orientated sub-parallel to the palaeoflow direction. With the corresponding facies interpretation superimposed onto a panoramic photograph of the section, a high degree of correlation can be established between the identified reflections and observable bedforms in the exposure. The detailed sedimen-

tary logs from this outcrop, and from adjacent outcrops running obliquely to the section, suggest that the strong continuous reflections are related to significant and laterally persistent changes in the clast-matrix ratio rather than to any specific sedimentary horizon (e.g. a narrow cobble band). This is consistent with the assumption that the deposits are in a highly wet state and that the reflections are generated from porosity-dependent permittivity contrasts in the matrix (i.e. variations in volumetric water content due to porosity change) rather than any particular 'lithological' variation.

The absence of deeper, coherent reflection events in the two zones dominated by strong, shallow diffractions suggests a significant change in the geometry of the deeper deposits and/or a much higher degree of signal-scattering in the near-surface deposits. With the majority of the diffractions grouping close to the 'water table' reflector, it is feasible that these zones represent areas of highly irregular broken ice (interspersed with coarse-grained sediment) or horizons of boulder material lying close to the water-table level. Of the two possible alternatives, the sedimentary and outcrop evidence supports the 'broken ice' interpretation. Significant quantities of subsurface ice, and the corresponding absence of any boulder material, can be found in the exposed control section near the lake's surface level. Although this is not truly indicative of the sedimentary conditions along the central section of the ice-walled canyon, it is likely that the two depositional environments are similar. In addition, sedimentary outcrop evidence from the downstream end of the ice-walled channel section confirms the presence of buried ice close to the water-table level (Fig. 7). The photographs also show the detailed structure of the finer, small-scaled waning-stage deposits and the existence of upstream-dipping antidunes and oriented clast imbrication structures. On this basis, we interpret these two zones as areas of syn-flood excavated ice that form an irregular eroded base to the retrograding ice canyon.

Proximal outwash fan region

The margin of this region (660–800 m, Fig. 4b) is characterized by an abrupt change in the GPR facies with the presence of strong, coherent reflectors at depth, an increase in the observable signal penetration and a change in the distribution of diffractions. Located at the edge of the proglacial outwash plain, the GPR profile alters course around a line of large kettle holes (the collapsed remnants of melting, buried ice blocks), therefore deviating from its flow-parallel orientation. Within this zone, a strong, 30 m-long, coherent, continuous reflector is present at a depth of about 15 m. Associated with

100MHz GPR section and facies interpretation

Palaeo-flow direction

Depth estimate based on a
uniform velocity of 0.07m/ns
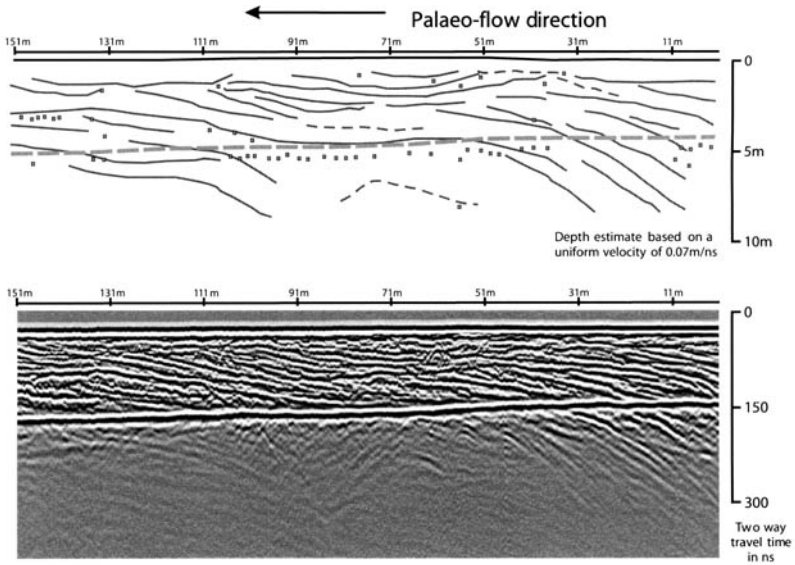
Corresponding 50MHz GPR section and facies interpretation

velocity = 0.07m/ns

Distance (in m) along long
50MHz profile
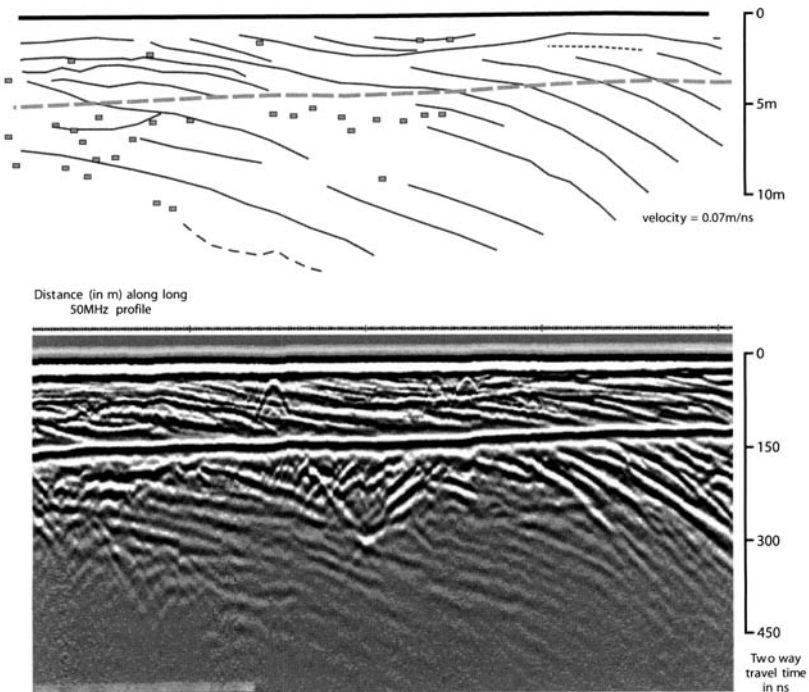
Fig. 5. 50 & 100 MHz GPR section and facies interpretation for the stoss-side accreting bedforms section of the ice-walled canyon region.
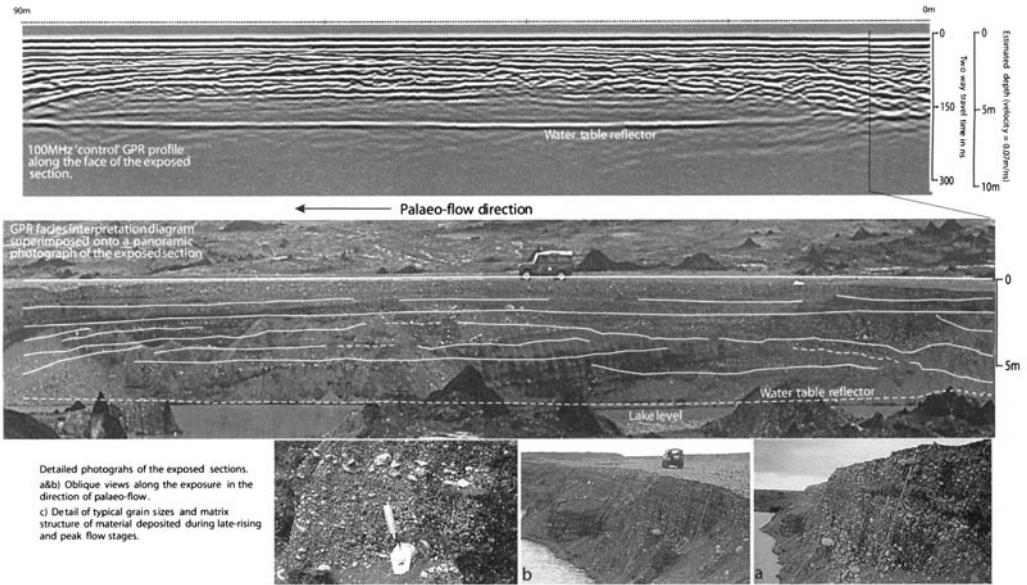
Fig. 6. 100 MHz GPR section, facies interpretation and exposed section photographs for the 'control' section at the flank of the ice-walled canyon.

this feature are a number of strong diffractions and a strong, coherent scour or channel reflection at ~2 m below the water table. The finer-grained upper units, immediately above this scour feature, appear to have no direct relationship to the deeper sediments and show similar facies to the waning-stage deposits of the ice-walled canyon region. There are a number of plausible interpretations for these features:

- Given that this region represents the start of unrestricted, reduced flows at the boundary of the preflood ice margin (in relatively shallow floodwater depths), it is possible for large (+20 m) ice blocks to have been stranded at the apex of the fan during the mid-rising stage and then buried by later, rising-/waning-stage deposits. The deeper reflections/diffractions would represent the remains of buried ice and the scour feature would represent the slumping of the later deposits.
- The deep reflector is an out-of-plane, sideswipe signal from the sides of the kettle hole (approximately 4 m deep and less than 10 m away from the section line) with the scour feature an effect of the localized flow variations around the stranded ice block.
- The scour feature represents an erosional surface incised into the preflood and early-rising stage outwash sediments; the deeper feature represents a buried ice block formed in a similar fashion to the first interpretation.

To date, there is no definitive interpretation for these features. The line of large kettle holes running obliquely to the main profile line points strongly to the presence of melting ice masses at depth, as does the slightly elevated water table associated with the feature. However, the relatively undisturbed sediments in the upper unit suggest that the scour feature is not a product of post-flood slumping. The out-of-plane, sideswipe interpretation cannot be ruled out either, because the relative strength of the reflection signal is contrary to the lower-amplitude nature of the surrounding, deeper features. The presence of scour-and-fill features later in the section supports the third, erosional-surface interpretation and it is feasible that the outburst from the initial fracture zone eroded into the existing deposits. Ultimately, it is likely that these distinctive features are caused by a combination of the three processes and that the presence of extensive, locally buried ice is highly probable.

In the mid-part of the proximal outwash fan region (980–1100 m; Fig. 4*b* & *c*) the GPR facies evolve into a zone of moderate to strongly coherent, upstream dipping backset reflections downlapping onto an erosional boundary surface reflection at a depth of approximately 10 m. These reflections are interpreted as scour-and-fill features created by the mid-rising flow stages eroding into earlier, pre-embayment early-rising stage deposits (generated by the initial jökulhlaup flood at the eastern, or
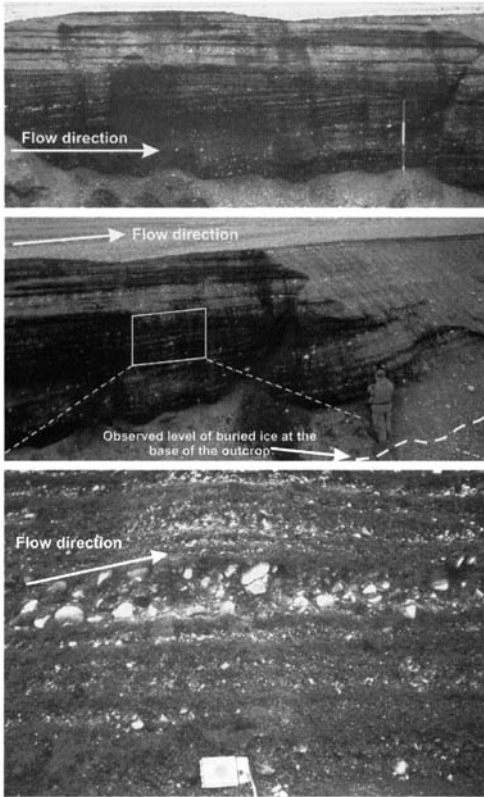
Fig. 7. Exposed section photographs from the downstream region of the ice-walled canyon.

downstream, side of the embayment). As seen in other parts of the section, the finer-scaled units associated with the later, waning-stage flows also overlie these scour-and-fill deposits. Further along the profile (1140–1300 m; Fig. 4c), these scour-and-fill features pass into a zone of low-coherence, discontinuous, downstream dipping reflections that may represent additional scour features or downstream-migrating foresets. Although it is difficult to determine the exact nature of these features, it is possible to identify a deeper, low-amplitude, continuous, coherent reflection at approximately 15–18 m. This feature is likely to represent the base of the jökulhlaup deposits and is consistent with the net aggradation of the outwash deposits determined from pre-and post-flood photogrammetry (Knudsen *et al.* 2001).

Distal outwash fan region

The distal fan region (1300–1800 m; Fig. 4c & d) marks a transition to relatively shallow, unconfined, expanding flows into deeper waters near the southern margin of the main Gígjukvísl channel.

For the majority of the section, the GPR facies are very similar, with deep penetration (up to ~20 m) and continuous, highly coherent, flat-lying reflections below downlapping, coherent foreset reflections of moderate angle (~10°). The deeper reflections are interpreted as vertically accreted deposits that are related to the pre-embayment, early-rising stages. The overlying foreset reflections indicate fan progradation of shallower, rising-to-peak stage deposits into a deeper 'backwater' environment. The corresponding orthogonal GPR sections, collected as part of the second pseudo-3D grid, reveal that both sets of deposits are, in general, laterally extensive, with similar 3D geometries and facies forms.

At the far-distal region of the outwash fan (1800–2044 m; Fig. 4d), the GPR facies change significantly. The deep, flat-lying reflections are truncated abruptly by strong, higher-angled foreset reflections and possible channel scour-and-fill features. This indicates interaction between flows from the outwash fan and from the main Gígjukvísl channel river, resulting in a zone of flow confluence. Video-footage, taken during the late-waning stage of the flood, shows the main Gígjukvísl river flow crossing the far-distal end of the fan at almost 90° to the direction of the outwash fan flow. This is consistent with the observed sedimentary evidence and indicates that the scour features relate to late-waning stage processes within the confluence zone.

Summary

By combining the GPR sections, facies interpretations, sedimentary analysis and documented evidence, a better understanding of the depositional chronology of the November 1996 jökulhlaup can be provided for the fracture outlet area, ice-walled canyon and associated outwash fan. Figure 8 summarizes this chronology in the form of a cross-section model with the preflood, food and post-flood conditions represented as follows.

1. Preflood condition: stable ice margin with preflood, proximal outwash fan and proglacial lake.
2. Flood condition

• Early rising stages (pre-embayment): pre-embayment flows from the east of the embayment area. Deposition into the existing proglacial lake.
• Rising/Peak stages: headward excavation of the ice-walled canyon, transportation of large ice blocks and the erosion of the canyon base. Deposition of large-scale stoss-side, upstream dipping bedforms in the ice-walled canyon, scour-and-fill of preflood and early-rising stage
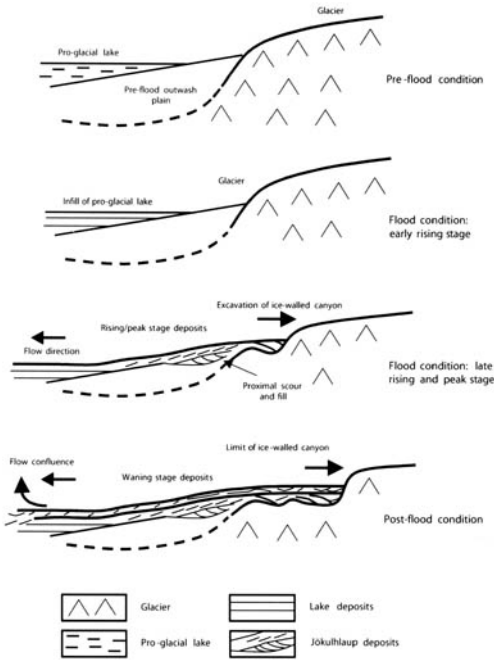
Fig. 8. Preflood, flood and post-flood summary of the main facies units and depositional environments.

deposits and the deposition of prograding fore-sets on the outwash fan. Confluence of flows at the far-distal region of the fan.

- Waning stage: final position of ice-walled canyon, deposition of fine-scaled, upper deposits of varying bedform types. Localized channelling and flow migration. Confluence of flows at the far-distal region of the fan.

3. Post-flood condition: downwasting and retreat of the ice margin, melting of buried ice and reworking of far-distal fan deposits.

Conclusions

The use of GPR data to characterize the architecture of these unique deposits adds a new perspective to the sedimentary record of single, high-magnitude events, pointing to much greater sediment reworking and depositional complexity than previously predicted (Maizels 1997; Russell & Knudsen 1999a, b). There is a clear prevalence for the generation of supercritical channel-scale macro-forms under the confined flow conditions provided by the expanding ice-walled canyon and hydraulic jump. The GPR-derived architectures are invaluable for investigating the larger-scale fluvial process and may provide useful models for the study of sedimentation within similar bedrock flu-

vial and alluvial-fan feeder systems. In this study, we have shown that the coarse-grained jökulhlaup deposits are ideal for investigation by GPR and that the combined use of GPR facies interpretations with sedimentary outcrop evidence can produce detailed models of the depositional environment. This is only the beginning; future GPR work on Skeiðarársandur will concentrate on the large-scale 3D geometry of the ice-walled canyon, proximal deposits and their relationship to the coarse-grained non-jökulhlaup facies of the main Skeiðarársandur outwash plain.

References

ALEXANDER, J., BRIDGE, J. S., CHEEL, R. J. & LECLAIR, S. F. 2001. Bedforms and associated sedimentary structures formed under supercritical water flows over aggrading sand beds. *Sedimentology*, **48**, 133–152.

BJÖRNSSON, H. 1997. Grímsvatnahlaup Fyrr og Nú. *In*: Haraldsson, H. (ed.) *Vatnajökull: Gos og Hlaup*. Vegagerðin, Reykjavik, Iceland, 61–77.

GAWTHORPE, R. L., COLLIER, R. E., ALEXANDER, J., BRIDGE, J. S. & LEEDER, M. R. 1999. Ground penetrating radar: application to sandbody geometry and heterogeneity studies. *In*: NORTH C. P. & PROSSER, D. J. (eds) *Characterisation of Fluvial and Aeolian Reservoirs*. Geological Society, London, Special Publications, **73**, 433–442.

GUÐMUNDSSON, M. T., SIGMUNDSSON F. & BJÖRNSSON H. 1997. Ice-volcano interaction of the 1996 Gjálp subglacial eruption, Vatnajökull, Iceland. *Nature*, **389**, 954–957.

KNUDSEN Ó, JÓHANNESSON, H., RUSSELL, A. J. & HARALDSSON, H. 2001. Changes in the Gígjukvísl river channel during the November 1996 jökulhlaup, Skeiðarársandur Iceland. *Jökull*, **50**, 19–32.

MAIZELS, J. K. 1997. Jökulhlaup deposits in proglacial areas. *Quaternary Science Reviews*, **16**, 793–819.

REYNOLDS, J. M. 1997. *An Introduction to Applied and Environmental Geophysics*. John Wiley & Sons, Chichester, England.

ROBERTS, M. J., RUSSELL, A. J., TWEED, F. S. & KNUDSEN, Ó. 2000*a*. Ice fracturing during jokulhlaups: implications for englacial floodwater routing and outlet development. *Earth Surface Processes and Landforms*, **25**, 1429–1446.

ROBERTS, M. J., RUSSELL, A. J., TWEED, F. S. & KNUDSEN, Ó. 2000*b*. Rapid sediment entrainment and englacial deposition during jökulhlaups. *Journal of Glaciology*, **46**, 349–351.

ROBERTS, M. J., RUSSELL, A. J., TWEED, F. S. & KNUDSEN, Ó. 2001. Controls on englacial sediment deposition during the November 1996 jökulhlaup, Skeiðarárjokull, Iceland. *Earth Surface Processes and Landforms*, **26**, 935–952.

RUSSELL, A. J. & KNUDSEN, Ó. 1999*a*. Controls on the sedimentology of the November 1996 jökulhlaup deposits, Skeiðarárjokull, Iceland. *In*: SMITH, N. D., ROGERS, J. & PLINT, A. G. (eds) *Fluvial Sedimentology*. International Association of Sedimentology Special Publications, **28**, 315–329.

RUSSELL, A. J. & KNUDSEN, Ó. 1999*b*. An ice-contact rhythmite (turbidite) succession deposited during the November 1996 catastrophic outburst flood (jökulhlaup), Skeiðarárjökull, Iceland, expressed. *Sedimentary Geology*, **127**, 1–10.

RUSSELL, A. J., KNUDSEN, Ó., MAIZELS, J. K. & MARREN, P. M. 1999. Channel cross-sectional area changes and peak discharge calculations on the Gígjukvísl during the November 1996 jökulhlaup. Skeiðarársandur Iceland. *Jökull*, **47**, 1–14.

RUSSELL, A. J., KNUDSEN, Ó., FAY, H., MARREN, P. M., HEINZ, J. & TRONICKLE, J. 2001. Morphorphy and sedimentology of a giant supraglacial, ice-walled, jökulhlaup channel, Skeiðarárjökull, Iceland: implications for esker genesis. *Global and Planetary Change*, **28**, 193–216.

SNORRASON, Á., JÓNSSON, P., PÁLSSON, S., ÁRNASON, S., SIGURDSSON, O., VÍKINGSSON, S., SIGURDSSON, Á. & ZÓPHÓNÍASSON, S.. 1997. Hlaupið á Skeiðarársandi haustið 1996: Útbreiðsla, rennsli og aurburður. *In*: HARALDSSON, H. (ed.) *Vatnajökull: Gos og Hlaup*. Vegagerðin, Reykjavik, Iceland, 79–137.

GPR survey of a lobate rock glacier in Yankee Boy Basin, Colorado, USA

JOHN J. DEGENHARDT JR[1], JOHN R. GIARDINO[2] & M. BRIAN JUNCK[3]

[1]High Alpine Research Program (HARP) and Department of Geography, Texas A & M University, College Station, Texas 77843-3147, USA (e-mail: degenjj@tamu.edu)
[2]HARP, Office of Graduate Studies and Department of Geology and Geophysics, Texas A & M University, College Station, Texas 77843-1113, USA (e-mail: rickg@tamu.edu)
[3]Department of Geography, University of Calgary, Calgary, Alberta T2N 1N4, Canada (e-mail: mbjunck@ucalgary.ca)

Abstract: The internal structure of a lobate rock glacier located in the San Juan Mountains of southwest Colorado was investigated using ground penetrating radar (GPR). A 440 m, 25 MHz longitudinal profile oriented along the central axis of the rock glacier shows moderate to strongly coherent reflection horizons or layers that can be recognized clearly to a depth of 30–35 m. The layers are interpreted as representing ice-supersaturated sediments and coarse, blocky rockslide debris that are the result of flow, perhaps generated by seasonal snow pack covered by episodic debris flows or high-magnitude discharges of talus from the cirque headwall. Profiles collected at 50 MHz indicate that, in the upper 20 m thickness of the rock glacier, many of these layers are laterally continuous. The total depth of penetration (~40 m at 25 MHz) was sufficient to detect the rock glacier-cirque-floor contact, which is composed of underlying moraine. Several prominent reflection events that subdivide the profile into broad 10–15 m-thick layers represent contacts between major depositional units. These units are believed to be individual flow lobes that were initiated at various cirque-headwall locations. We interpret this rock glacier to be a composite feature that formed by a process involving the development and subsequent overlap of discrete flow lobes that have over-ridden older glacial moraine and protalus rampart materials. The latter materials have been incorporated into the present flow structure of the rock glacier.

Rock glaciers are lobate or tongue-shaped landforms composed of mixtures of poorly sorted, angular, blocky rock debris and ice (Giardino 1979). Although they are located in cirques and valleys of many mountain ranges throughout the world, rock glaciers remain poorly understood constituents of alpine debris systems. Active (flowing) rock glaciers transport the surplus debris from talus slopes and glaciers downvalley or downslope to other debris systems. Barsch (1977) and Giardino (1979) addressed the role of rock glaciers in terms of debris systems and found that rock glaciers account for approximately 60% of all mass transport in the alpine environments where they occur. As such, they are of great importance to the geomorphic periglacial transport systems in high mountains. For example, 40–60% of the debris being transported in the Sangre de Cristo Mountains of Colorado can currently be described as rock glaciers (Giardino et al. 1987). Barsch et al. (1979) estimated that 15–20% of periglacial mass transport in the Swiss Alps is incorporated in active

rock glaciers. Thus, rock glaciers constitute an important component of a cascading system in which stream water, groundwater and rock materials move from mountain headwalls and talus slopes to environments downvalley (Giardino & Vitek 1988).

Significance and occurrence of rock glaciers

Within the alpine environment, rock glaciers are the visible expression of mountain permafrost, making them principal geo-ecological indicators within alpine geosystems. As stores for ice and permafrost, they are valuable surrogates for information on past atmospheric and water compositions (i.e. dissolved solids, heavy metals, pollutants and oxygen isotope ratios) and are useful for monitoring global change (i.e. predicted global warming, see Steig et al. 1998). Rock glaciers occupy the heads of many of the watersheds that supply communities with water throughout western

North America and other parts of the world. They act as long-term (centuries to millennia) reservoirs for water, releasing a steady flow over the course of a year. Rock glaciers are also being considered from a planetary perspective. Similar morphological features have been discovered on Mars (Squyres 1978; Lucchitta 1993; Degenhardt & Giardino 1999) and Callisto, one of the moons of Jupiter (Chuang *et al.* 1999). Based on their morphological similarity to rock glaciers, these landforms have been postulated to contain significant volumes of frozen water.

Although distinctive and widely distributed, the occurrence and significance of rock glaciers often go unnoticed. They generally occur in dry, continental areas rather than humid regions, perhaps because thin to absent snow cover favours their persistence (Humlum 1997). Ages of rock glaciers range from incipient forms on Pico de Orizaba volcano (Palacios & Vazquezselem 1996) to 500-year-old forms associated with the Little Ice Age (Humlum 1996). Many are several thousand years old (e.g. Kaeaeb *et al.* 1997; Calkin *et al.* 1998) and some relict rock glaciers are believed to have formed at the end of the last Ice Age about 10 ka ago (Sandeman & Ballantyne 1996; Humlum 1998). The occurrence of past or present glaciers is not a necessary prelude to the formation of rock glaciers because these landforms exist in both glacial and non-glacial areas.

Formation of rock glaciers

Rock glaciers are a physical response to three types of geomorphic processes: (1) glacial, (2) periglacial (Johnson 1984), and (3) talus (Shakesby *et al.* 1987). The pioneering work of Wahrhaftig and Cox (1959) suggested that rock glaciers were formed by permafrost processes creating a frozen mixture of rock debris and ice within talus or moraine materials. With the advent of new technology and the global interest in recognizing and studying rock glaciers, these findings have been affirmed and expanded by subsequent studies (see Haeberli 1985; Barsch 1996). A few studies also provide evidence of thick massive ice in the rock glacier interior and suggest that some forms are actually debris-covered glaciers (e.g. Potter 1972; Clark *et al.* 1994).

Rock-glacier formation begins with accumulation of ice in the upper reaches of the rock glacier. The ice flows downslope, where it ablates slowly within or beneath the debris of the rock glacier. General requirements for the formation of rock glaciers have been reviewed by Corte (1987). Rock glaciers are generally situated at the base of massive, homogeneous and fractured cliffs and are rarely found where debris is finely crushed or

where headwall fractures are excessively large (Wahrhaftig & Cox 1959; Evin 1987).

Although the morphology of rock glaciers and other lobate landforms with surficial ridges and furrows is well documented (Giardino *et al.* 1987), it is also necessary to understand the flow dynamics responsible for generating these characteristic features. Information about the internal composition and fabric of a rock glacier is required to understand the flow dynamics (Potter *et al.* 1998), but the difficulty and costs associated with direct observation of the internal characteristics make acquisition of these data problematic. For example, direct rheological measurements (i.e. flow direction, flow velocity and stress fields) are time-dependent and lengthy because the flow of rock glaciers ranges from millimetres to decimetres per annum.

Without detailed internal evidence of stresses and strain rates, temperatures, ice-rock mixtures and bedrock characteristics, discussion of the process or processes that form rock glaciers is premature. On this basis, the study of rock glaciers has evolved toward the development of field methods for characterizing ice/debris ratios and rheological models. Current understanding of the movement of a rock glacier, outlined in the work of Haeberli (1985) and Barsch (1996), is based on models of creep flow adopted from studies of glaciers and limited physical data from rock glaciers around the world (e.g. Burger *et al.* 1999; Konrad & Humphrey 2000).

The movement of rock glaciers has been related to many topographical, lithological and climatic variables. Equations for mass transport in confined valleys, locations where rock glaciers commonly form, suggest that the thickness of a rock glacier should increase downslope. Kinematic wave theory (Gerber & Scheidegger 1979) dictates that the geometry of valley and cirque walls control mass transport resulting from gravity. Ridge-and-furrow structures, therefore, represent 'buckling' of the material to compensate for decreased velocity of flow downvalley with a corresponding increase in force provided by faster-flowing material upvalley (Fink 1980).

Geological setting

Yankee Boy Basin, located in the San Juan Mountains of southwestern Colorado, was chosen as the study site because of the abundance of rock glaciers. The site is in close proximity to a variety of rock-glacier types that include lobate (Fig. 1), valley-side and tongue-shaped morphologies (Wahrhaftig & Cox 1959; Burger *et al.* 1999). Exposed rocks in Yankee Boy Basin (Fig. 2) are almost exclusively comprised of Tertiary vol-
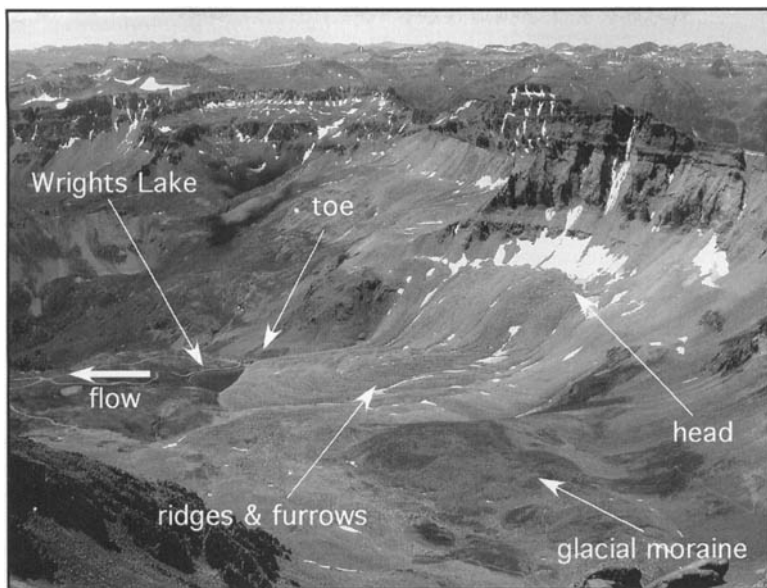
Fig. 1. Yankee Boy Basin rock glacier, located in the San Juan Mountains of southwestern Colorado. Photograph taken from the top of nearby Mt Sneffels, a 4328 m (14 200 ft) peak. The rock glacier is approximately 500 m (1640 ft) long from the snowline to the toe at Wright's Lake, and 300 m (984 ft) wide at the middle. The rock glacier flows down a cirque, which is bounded on the southwestern side by Gilpin Peak ridge (4174 m), seen in the background.
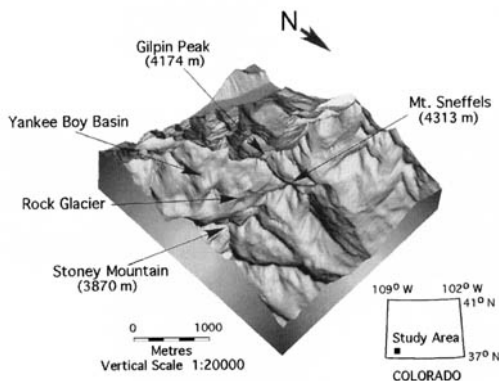
Fig. 2. Geographic location of the Yankee Boy Basin study site with hillslope shaded relief map illustrating the mountainous setting within the San Juan Mountain Range of southwestern Colorado.

canics, which are underlain by a block of Precambrian quartzite (Luedke & Burbank 1976). Mountain peaks that flank the basin are composed of San Juan volcanics, including Gilpin Peak tephra deposits, the Picayune Formation and the San Juan Formation. The Picayune Formation consists of a series of flows, breccias and tephra layers of intermediate composition and the San Juan Formation is mainly bedded tephra deposits of felsic composition. In the area of Mt Sneffels, and along

the northern edge of the basin, the mountains also include cores composed of older granodiorite and gabbro stock containing Precambrian quartzite inclusions. Quaternary deposits, consisting mainly of the San Juan Formation, cover most of the basin floor, with limited exposure of the granodiorite and gabbro stock. The easily eroded bedrock supplies the parent material for deposits such as rock glaciers, alluvium, glacial drift and landslide deposits. Holocene talus deposits cover much of the valley walls, and rock glaciers typically occupy cirques and cirque valleys.

Application of GPR

To fully understand the movement and deformation patterns within the interior of a rock glacier, a fundamental (i.e. generic) description of development is required. In this study, ground penetrating radar (GPR) is being used to 'look' inside a lobate rock glacier to identify its internal structure. GPR offers the sophistication of other geophysical techniques combined with portability and ease of use. It is ideally suited to applications in alpine regions, where logistics and access are generally prohibitive. This study is being conducted in an effort to understand the formation history of a lobate rock glacier (see Fig. 1) by identifying its internal structure and determining the origin of ridges and furrows, a characteristic feature of rock glaciers. To date,

GPR has been used on only three rock glaciers worldwide (Berthling *et al.* 2000; Degenhardt *et al.* 2000; Isaksen *et al.* 2000).

Theoretical background

The generation of digital GPR profiles involves the transmission of high-frequency (10–1000 MHz) electromagnetic (EM) radio (radar) pulses into the ground and measuring the time elapsed between transmission, reflection off a subsurface discontinuity and reception back to a surface radar antenna. The profiles, which are similar in appearance to standard seismic profiles (Annan & Davis 1976), represent that portion of the transmitted EM that is reflected back to the ground surface as a result of changes in the bulk electrical properties of the underlying materials (Smith & Jol 1997). Such changes in electrical properties can be attributed to sedimentological variation (i.e. changing grain size), facies changes, differences in state of materials (i.e. water-rock or water-ice contacts), mineralogy and density. These factors are closely linked to the water content of a material, which plays a crucial role in the generation of GPR reflections.

The Yankee Boy rock glacier contains flowing water beneath the surface and may also contain 'free' water within pore spaces or cavities. In terms of propagating GPR waves, water has a direct effect on the capacity of a transmitting material to store electrical potential energy under the influence of an electric field (permittivity). Because relative permittivity for water is high (81) relative to that for dry rock (<9), even a small amount of water may increase the bulk permittivity of the rock (Reynolds 1997).

Porosity (φ) must also be considered with regard to the proportions of constituents present and their respective dielectric constants. The relationship between bulk relative permittivity (ε_r) and φ for an external field applied perpendicular to bedding is:

$$\varepsilon_r = \varepsilon_m \varepsilon_w / [(1 - \phi)\varepsilon_m + \phi \varepsilon_w] \qquad (1)$$

where ϵ_m and ϵ_w are the permittivities for the rock matrix and pore fluid water, respectively (Reynolds 1997). Thus, the average GPR velocity through a rock glacier medium will be the weighted affect of the contributions from rock, granular materials, ice and water – each having significantly different dielectrical properties. For example, the GPR wave velocity through fresh water is 0.033 m ns^{-1}, whereas it is 0.12 m ns^{-1} through a low-porosity sandstone (McCann *et al.* 1988). Given this range of water-dependent velocity values, accurate analysis and interpretation of the GPR data require that special attention be given to all of the above factors.

Equipment and methodology

GPR data were collected at antenna frequencies of 25 MHz and 50 MHz using a pulseEKKO 100A system from Sensors & Software, Inc. The system was configured in perpendicular broadside reflection mode using constant source-receiver offsets. A step interval of 1 m (4 m antennae spacing) was used for the 25 MHz (centre frequency) configuration, and a step interval of 0.5 m (2 m antennae spacing) was used for the 50 MHz configuration. Each collected section was edited for noisy/corrupt traces and adjusted to time zero. On all profiles, the horizontal scale is distance in metres (m) and the vertical scale is presented as two-way travel time (twt) in nanoseconds (ns) and depth in metres. Data were acquired using a 1000 V transmitter and stacked 64 times with a time sampling rate of 800 ps. The profiles were processed and plotted in standard grey-scale and wiggle-trace formats using pulseEKKO software. The two earliest continuous reflections in all profiles represent air-wave and ground-wave arrivals, respectively.

The locations of the GPR transects were chosen for the purpose of identifying gross internal features and to determine if links can be established between the internal structure and surface morphology. The data were collected over two summers on a section of the rock glacier where ridges and furrows are prominent (Fig. 3). Two 50 MHz
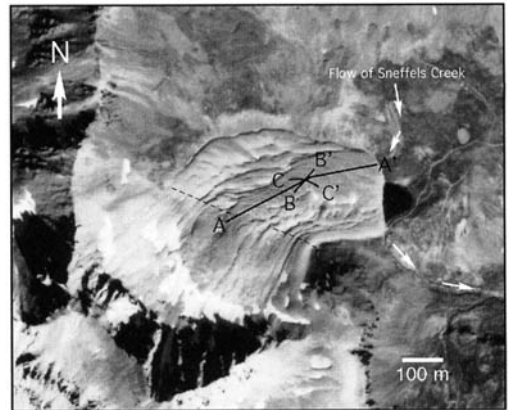
Fig. 3. United States Department of Agriculture (USDA) 1 : 20000-scale vertical aerial photograph of Yankee Boy rock glacier taken in 1979. GPR transects are indicated by solid lines. The common mid-point (CMP) survey was performed along the western end of C–C'. The dashed line indicates the inflection where slope of the rock glacier decreases sharply. Position of the line is based on topographic surveys of the rock glacier. Upslope of the inflection line (headwall side), the direction of rock glacier flow is toward the northeast. Downslope of the inflection line (downvalley side) the flow is to the east.

surveys were made in July 2000, and a single 25 MHz survey was made in July 2001. The 25 MHz survey consists of a 440 m longitudinal transect line (A–A') that begins in the middle of the head area of the rock glacier and terminates at the crest of the toe. It trends in a northeasterly direction and is oriented approximately normal to a series of arcuate transverse ridges and furrows that extend down the central portion of the rock glacier. A bend in the profile transect was made at 255 m to a more easterly direction so that the transect line would remain approximately normal to the ridges and furrows and so that a greater profile length could be attained.

The two 50 MHz surveys were conducted along the same series of ridges and furrows as A–A'. One of these surveys was made along an 86 m linear transect (B–B') that trends to the northeast (~N45°E) and crosses A–A' at a distance of 238 m. Transect B–B' was offset rotationally from A–A' so that its orientation would be perpendicular to the strike axes of ridges and furrows on that part of the rock glacier. The other transect, C–C', follows 75 m along the top of a prominent ridge in the series. It trends in a general east-west direction and curves toward the southeast at its end. C–C' intersects B–B' at 38 m and provides a perspective that is normal to the ridge axis.

Data processing

All processing was completed using Win_EKKO Pro version 1.0, a Windows®-based software package that accompanies the pulseEKKO GPR system. The raw reflection data were first corrected using a time filter for signal saturation (dewow). An automatic gain control (AGC) gain was applied to the dewowed data using a manual gain limit of GMAX = 500 followed by spatial low-pass filtering at 20% cutoff. The low-pass cutoff percentage marks the spatial frequency above which data are removed and below which data are preserved. The cutoff frequency is defined as a percentage of the spatial Nyquist frequency (f_{nyq}) in 10% increments from 10% to 90% (Sensors & Software 1996) as given by the equation:

$$f_{nyq} = \frac{1}{2 \times Step\ size} \tag{2}$$

For example, if the step size is 1 m (e.g. using 50 MHz antennae), $f_{nyq} = 0.5$ cycles m^{-1}. The 25 MHz section was migrated (see Media characteristics below) using synthetic aperture image reconstruction (two-dimensional Kirchhoff method) and the 50 MHz sections were left unmigrated. Finally, topographic corrections were applied to the profiles using laser-surveyed elevation data collected along the GPR transect lines.

Results

Media characteristics

The common mid-point (CMP) method was used to determine an average velocity value for the rock glacier medium. Two CMP surveys were conducted, one during the July 2000 field season ($f = 50$ MHz), and the other during the July 2001 season ($f = 25$ MHz). Both surveys (Fig. 4) were collected along the western portion of transect C–C' under similar weather conditions. This location was chosen because the topography along the ridge crest is relatively flat and because several strong subhorizontal reflectors were detected within 200 ns ($f = 50$ MHz) of the rock-glacier surface.

Two semblance analyses, performed using the Win_EKKO CMP Analysis Program, each yielded a best-fit velocity value of 0.12 m ns^{-1}. The solutions, which centred upon reflections at 15 ns and 70 ns in the 50 MHz and 25 MHz profiles, respectively, were based on CMP velocity values that were wide-ranging. For example, the 25 MHz velocities range from approximately 0.24 m ns^{-1} at the near-surface to 0.09 m ns^{-1} at depth. The high near-surface velocities are the result of surface irregularities encountered as the antennae were moved along the boulders and large blocky clasts that comprise the surface of the rock glacier. In addition to the gaps between the flat antennae and
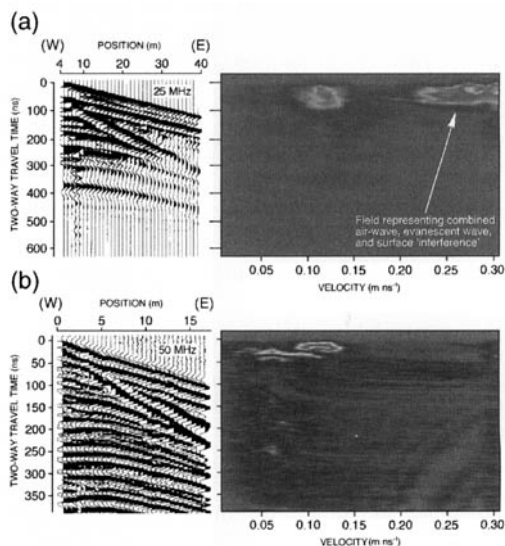
Fig. 4. Common mid-point (CMP) surveys collected at (a) 25 MHz, and (b) 50 MHz. Accompanying semblance-analysis diagrams are shown to the right. A best-fit velocity value of 0.12 m ns^{-1}, obtained in both semblance solutions, was used for the average velocity of the rock glacier medium.

the rock-glacier surface, the active layer (upper 3 m) of the rock glacier also contains a significant amount of air-filled void space (i.e. cavities) which increases GPR wave velocities. This phenomenon is apparent in the 25 MHz semblance diagram (Fig. 4*a*), where values in the high-amplitude field above 50 ns approach 0.33 m ns^{-1} (air-wave velocity). This field probably represents a combination of air, evanescent and 'interference' from the surface. The low velocity value for the reflection located at 40 ns in the 50 MHz CMP profile (0.07 m ns^{-1}) indicates a ε_r value of approximately 18, which is consistent with the relative permittivity of wet to saturated coarse-grained sands and gravels (Reynolds 1997).

The relatively high velocity of 0.12 m ns^{-1} was chosen as the average (representative) value for the rock glacier medium, based on the assumption that the 'deeper' velocities (i.e. 0.07–0.09 m ns^{-1}) represent the lower limit in a range of values. In reality, the velocity of the rock glacier medium probably falls within a range of values between 0.09 m ns^{-1} and 0.14 m ns^{-1}. A velocity of 0.12 m ns^{-1} equates to an approximate relative permittivity (ε_r) of 6, which falls within the range of (ε_r) values for permafrost (Daniels & Roberts 1994; Reynolds 1997). The average velocity is slightly lower than values for rock glaciers located in continuous permafrost regions (e.g. Berthling *et al.* 2000; Isaksen *et al.* 2000), which is consistent for a water-bearing permafrost rock glacier located in a temperate alpine region. It should be noted that a higher velocity value was used for migration of the 25 MHz GPR section (0.15 m ns^{-1}), based upon iterative results over a range of values from 0.09 m ns^{-1} to 0.17 m ns^{-1}. The objective of the migration was to verify the coherence of the strongest reflections without compromising the overall clarity of the profile. A velocity value of 0.15 m ns^{-1} was most effective for improving the clarity of strong reflections while maintaining the interpretability of the less coherent reflections.

Resolution and signal penetration

The theoretical vertical resolution of the GPR signals was determined using the equation (e.g. Reynolds 1997):

$$\lambda/4 = (V/F)/4 \qquad (3)$$

Where λ is the wavelength (m), V is the wave velocity of the medium (m ns^{-1}), and F is the centre frequency of the antenna (MHz). At 25 MHz, the calculated vertical resolution is 1.2 m. Therefore any layers visible on the 25 MHz profiles have a thickness of greater than 1 m. The maximum depth achieved at this frequency was approximately 330 ns (~40 m). The 50 MHz antennae provided a

maximum depth of signal penetration to 500 ns (~26 m) and resolution of at least 0.75 m, given a calculated theoretical vertical resolution of 0.60 m.

The 25 MHz GPR profile section The unmigrated 440 m longitudinal GPR profile (A–A'), shown in the upper part of Figure 5, effectively depicts the topographic characteristics along the centre portion of the rock glacier. The steeply sloping surface at the beginning of the profile marks the accumulation zone at the head of the rock glacier. Ridges and furrows, which begin at the 35 m position, are represented by undulations along the top of the section. Elevations range from 3800 m at the beginning of the profile (rock glacier head) to 3735 m at the end (beginning of the oversteepened toe) and ridge-and-furrow relief ranges from 1 m to 5 m.

Gross structural features are defined by numerous reflections of variable coherence that are recognizable down to ~800 ns (45 m). A strongly coherent reflection along the bottom of the profile
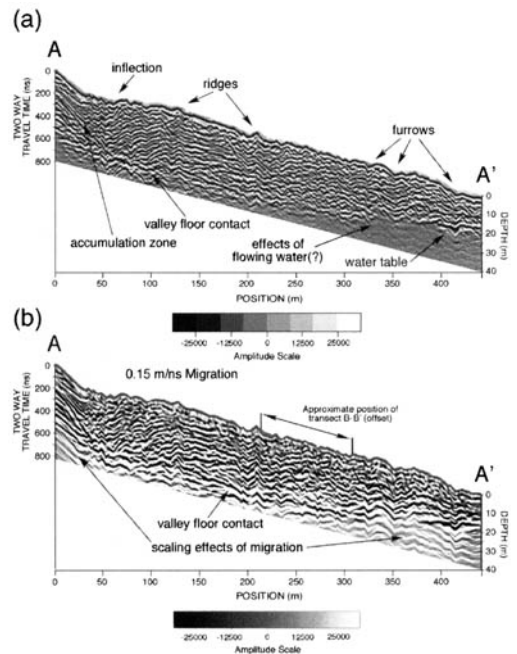
Fig. 5. Topographically corrected longitudinal profile collected at $f = 25$ MHz (velocity $= 0.12$ m ns^{-1}): (**a**) unmigrated section, and (**b**) migrated section; The water table is in hydrological communication with Wright's Lake, which is located at the right of the profile. Topographic corrections were applied using laser-survey data that was collected along the same transect line as the GPR survey. Note that ringing at the bottom of the profile from 90 m to 210 m was not removed because further processing would result in loss of detail. The ringing in the migrated profile is an artefact of the processing software.

(~750 ns) represents the contact between the rock glacier and the cirque floor. It defines the complete cross-sectional shape of the rock glacier. Thickness ranges from ~15 m at the head of the rock glacier to a maximum of ~40 m at the middle and decreases to a thickness of ~18 m at the toe. The shape of this reflector is consistent with the 'scooped' contour of a glacially scoured cirque. Along the profile, and down the flow line of the rock glacier, there is a transition in the dip of the reflection horizons. In the first 50 m, the reflection horizons slant downward, parallel to the surface. Further along the profile, from 50 m to 125 m, the reflection horizons trend upward toward the surface at ~45° and display undulated patterns similar to that exhibited at the top of the profile (e.g. ridge-and-furrow topography). From 125 m to 230 m, the reflections parallel the surface and again trend upward toward the surface further down profile.

Migration revealed six moderately strong coherent reflection horizons throughout the profile, ranging in length from 75 m to 400 m. The horizons are subparallel to the surface and to each other and converge toward the beginning of the profile. In general, the reflections are approximately horizontal beyond 100 m, making them subparallel with the top surface of the profile. The orientations of less coherent reflections parallel these major horizons, and non-coherent reflections and diffraction events occur in the upper 5 m of the profile. Diffraction events are more prevalent throughout the section from 50 m to 125 m. It should be noted that, although migration enhanced the moderately to strongly coherent reflections, the presence of interfering diffraction events generated by the coarse-grained and talus-sized materials of the rock glacier make it difficult to determine the true nature of the reflection terminations in some parts of the profile.

The 50 MHz GPR profile sections (unmigrated)
The two 50 MHz sections, rendered in wiggle-trace format, provide more detail about the subsurface structure in an area of the rock glacier where ridges and furrows are well developed. Profile B–B', shown in Figure 6, represents an 86 m cross-sectional view in a direction normal to the ridges and furrows. Topographic relief varies from 1 m to 2 m as measured from the bottom of the deepest furrow to the top of the highest ridge. The profile is characterized by a series of dipping reflections that downlap onto more continuous subhorizontal reflections. The downlapping reflections, which dip in a general downslope direction, range in length from 5 m to 7 m and terminate against the subhorizontal reflections at angles of 10°–20° from horizontal. The subhorizontal reflections range in length from 10 m to 30 m and generally trend
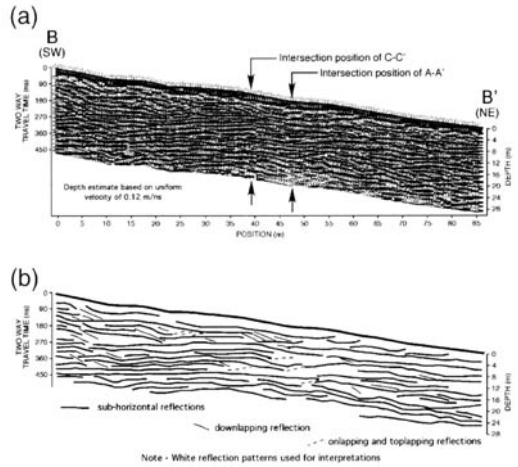
Fig. 6. Topographically corrected 50 MHz GPR profile B–B', oriented normal to prominent ridges and furrows, as shown in Figure 3. (a) Processed data without interpretations. (b) Facies interpretations generated from profile above. The section is characterized by many dipping reflections that terminate against more continuous subhorizontal reflections. Data were processed using Win_EKKO software provided by Sensors and Software, Inc.

toward the top of the profile at shallow angles. A small number of toplapping reflections are also present in the central part of the profile (35–50 m). They are 3–5 m in length and are oriented at 5°–10° to the subhorizontal reflections.

The upward trend of subhorizontal reflections in B–B' is consistent with reflections that are identifiable on the 25 MHz longitudinal profile, A–A' (see Fig. 5 inset). These reflections represent segments of longer subhorizontal reflectors that slant toward the rock-glacier surface at low angles (~5°). Two of these, located at 140 ns and 490 ns, can be correlated to moderately strong coherent reflections (major horizons) from 220 m to 310 m on profile A–A'.

Profile C–C', shown in Figure 7, was made along the crest of a prominent ridge that crosses profile B–B' at 38 m. It represents a view of the reflectors as they appear normal to the ridge axis. Continuous reflections form an undulate structure reminiscent of a gentle synclinal fold over the length of the profile. Reflections are subparallel with the surface from 0 m to 15 m and dip downward at ~10° from 15 m to 55 m. Beyond 60 m, the reflections slant upward at ~10°. Short downlapping and toplapping reflections terminate at angles of 5–10° against the more continuous subhorizontal reflections, as observed in B–B'.

The intersection of profiles in Figures 6 and 7 shows that continuous reflections in B–B' can be
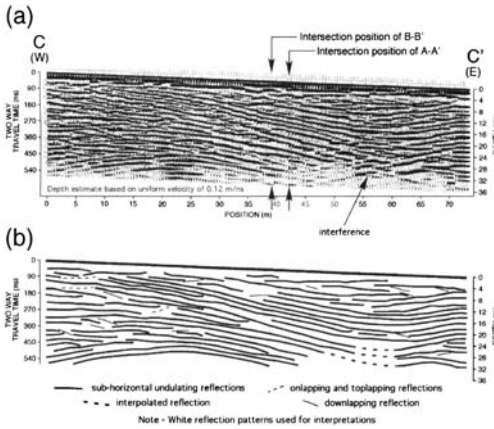
Fig. 7. Topographically corrected 50 MHz GPR profile C–C', oriented along the crest of a prominent ridge in the sequence of ridges and furrows crossed by A–A' (Fig. 3). (a) Processed data without interpretations. (b) Facies interpretations generated from profile above. The section is characterized by many undulating reflections that resemble a synclinal structure. The dip in the layers is interpreted to be a longitudinal furrow that was filled in by over-riding flow-lobe materials.

correlated with those in C–C' (Fig. 8). Reflections at 330 ns and 480 ns are the most continuous in both profiles and can be clearly traced from one profile to the other. Almost all of the less-

continuous reflections can be correlated between the two profiles at the point of intersection. In addition, correlation can be made between many of the reflections at both ends of the two profiles. This indicates that some of the reflectors in this part of the rock glacier are laterally continuous (i.e. represent laterally continuous layers).

Discussion

Composition and inner structure

The 50 MHz profiles indicate a complex stratigraphy for the layers that underlie prominent ridges and furrows. However, it can be seen that many of these layers are laterally continuous (e.g. Figs 7 & 8). The degree of continuity observed in the layers, and the average velocity value of the rock glacier medium, suggest that alternating ice-rich and ice-poor layers make up the bulk of the rock glacier medium to a depth of at least 20 m. The layers are interpreted to be the result of flow, perhaps generated by seasonal snow pack covered by episodic flows or high-magnitude discharges of talus debris. This view is supported by Haeberli and Vonder Mühll (1996), who argue that the ice created in the accumulation zone of the rock glacier derives mainly from snowdrifts or from water in the active layer. Isaksen et al. (2000) also concluded that large mass-movement events are of great impor-
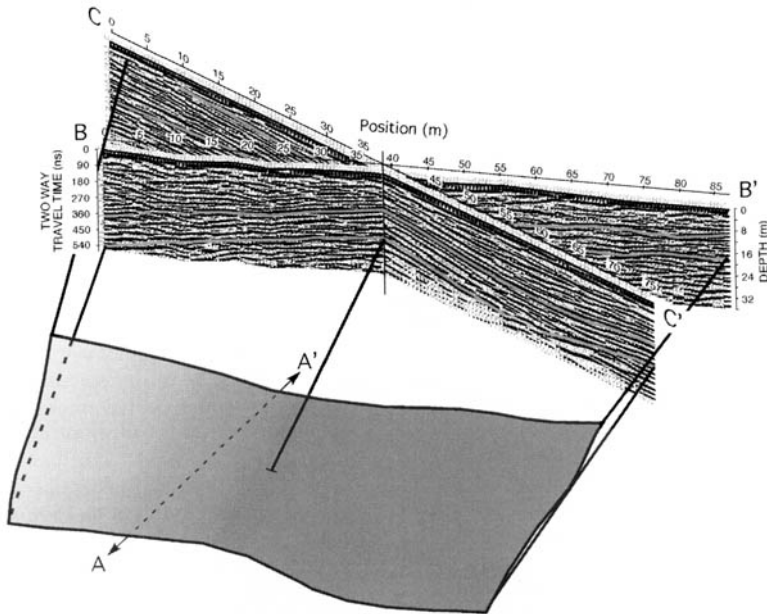
Fig. 8. The intersection of profiles B–B' and C–C' shows the continuity of layers in the upper 20 m of the rock glacier. Lateral continuity is as much as 70 m in all directions. Approximate position of profile A–A' is indicated for clarity.

tance in the process of debris input and preservation of ice in the frozen sediments.

Unpublished descriptions of a 7.6 m length of drill core, recovered by the authors in 1997 from a position approximately 50 m east of profile B–B', confirm the presence of alternating layers of coarse ice-rich and ice-poor layers that range from 0.5 m to 1 m in thickness. The layers are composed mainly of blocks and platy clasts that span less than 0.5 m in the largest dimension. The overall ratio of debris to ice was found to range from 60% to 70%, and some ice layers are comprised of up to 30% silts and fines. Lenses of clean ice were also recovered, ranging in thickness from 0.1 m to 0.5 m. This is generally consistent with findings for drill-core samples from other rock glaciers of permafrost origin (Haeberli 1985; Barsch 1996) and descriptions from an exposed rock glacier near Longyeardalen, Svalbard (Liestøl 1962).

Deformation of the layers involves minor (gentle) folding and small-scale, terminal overlap (as evidenced by downlapping reflections in profile B–B' and C–C', see Figs 6 & 7). An example of larger-scale adjustment is also seen in profile C–C', where continuous layers along a ridge undulate in a style similar to synclinal folding. The structure is believed to have formed when individual layers, or perhaps a unit of layers, flowed over an older deposit. The deposits filled in a longitudinal furrow, which is visible on the aerial photograph. The over-riding flow extended eastward and spread to the southeast.

Gross features

The longitudinal profile and accompanying interpretation (Fig. 9) provide a general picture of the overall structure of the rock glacier. Six continuous horizons, defined by moderately strong coherent reflections, divide the rock glacier into a series of distinct subhorizontal components that are interpreted as layered depositional units. Layers within each unit are 1–3 m thick and generally conform to the orientation and character of the main horizons.

In the head portion of the rock glacier, the layers are flat and closely spaced. This type of layering is consistent with a process in which snow and talus debris, accumulated at the lower reaches of the talus slope, moves in tension down the steep gradient of the head. Below the zone of accumulation, the layers exhibit a more undulating structure and upward slant. Here, materials leaving the accumulation zone encounter a decrease in the slope of the cirque floor. The highly undulated character of the layers marks the onset of compressive stresses, which are likely to be at a maximum (Barsch 1996). This is consistent with
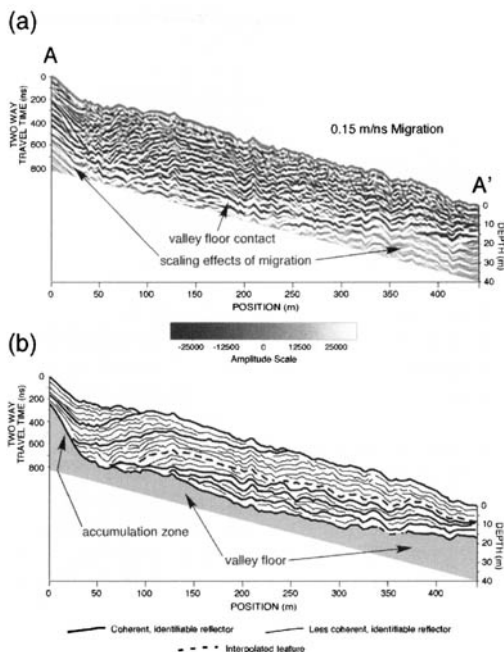
Fig. 9. (a) Migrated longitudinal profile from Figure 5, with (b) accompanying interpretation. Seven main depositional units can be identified and each unit is comprised of layers that are subparallel to the major reflection horizons.

observations made by Giardino (1979) and Haeberli (1985), who report that ridge-and-furrow development is most pronounced at sites of increased compression (i.e. slope decline). It is suggested here that ridges and furrows originate as small surface irregularities just beyond the slope inflection and develop into large ridges and furrows at lower sections of the rock glacier, where slope decline results in increased compressive stresses.

The upward slant of the layers is similar to results for steady-state flow-modelling of debris-covered glaciers (rock glaciers) by Konrad and Humphrey (2000). They showed that flow paths in the ablation area initially curve up toward the surface (where ablation rates are relatively high) but turn back to parallel the surface further downvalley (where ablation rates are lower). The structure observed in Figure 9 is generally consistent with this type of behaviour, which reinforces the idea that layers comprising permafrost rock glaciers deform by creep. In this regard, Barsch (1992) states definitively that the creep of supersaturated mountain permafrost is the important and decisive process in rock glacier formation.

The difference in orientation and character of layers in the upper 10–12 m of the rock glacier compared to layers in underlying units suggests

that a process of material over-ride is governing the gross structural character of the rock-glacier interior. Beyond 125 m, the layers in the bottom half of the rock glacier do not deviate significantly from the horizontal, in contrast to the upper layers, which assume a variety of orientations with respect to horizontal. Such a difference in character can be attributed to changes in flow direction that result when supply of talus shifts from one location on the headwall to another. This effect can also be achieved through variable rates of talus supply along different parts of the headwall. The controlling factor for direction of flow is, therefore, the maximum gradient encountered by the flow, given its location within the cirque. The result over time is the generation of multiple-source flows leading to discrete depositional units (i.e. flow lobes).

The upward slant of reflectors from 210 m to 320 m (along A–A') can be explained by examining the profile line shown on the aerial photograph in Figure 3. The flow of materials along the centre-most portion of the rock glacier appears to have

been diverted by an underlying (older) depositional unit (flow lobe). The exposed portion of the underlying flow lobe stands in higher relief than the lobe that immediately overlies it, thus providing a gradient that forces flow of the over-riding lobe to a more easterly direction.

Model for rock glacier formation

As the aerial view in Figure 3 suggests, the rock glacier can be considered in terms of a series of discrete flow lobes. Such a model is supported by the gross internal structure as interpreted from the 25 MHz longitudinal survey. Figure 10 shows one interpretation for how the major depositional units of the rock glacier may be correlated with individual flow lobes as mapped on the aerial photograph. The terminations of the major horizons in the interpreted profile match closely with the exposed and inferred boundaries of the flow lobes in plan view. Using this method, a sequence of seven discrete flow lobes is identifiable. It appears that the lobes
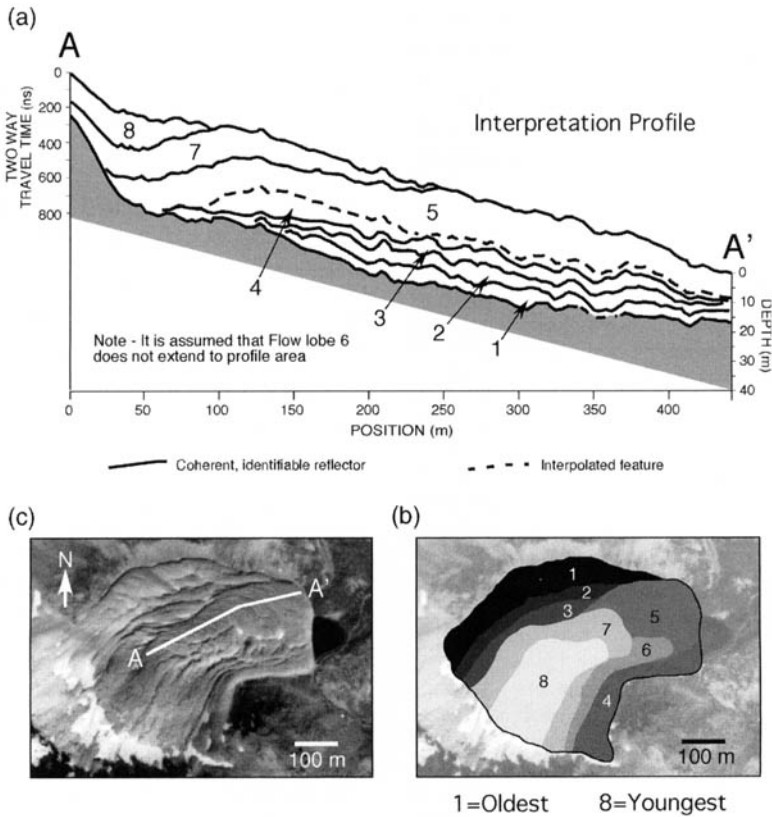
Fig. 10. (a) Correlation between the main depositional units (interpreted from the GPR profile in Fig. 9) and (b) the flow-lobe boundaries as mapped on the 1 : 20 000-scale vertical aerial photograph. (c) Location of the 440 m longitudinal transect is included for reference. The rock glacier is made up of multiple over-riding lobes.

flow down the cirque valley together as a composite geomorphological unit.

From this exercise, a model for rock-glacier development can be formulated. Figure 11 illustrates in plan view the proposed sequence of events involved in the formation of the Yankee Boy rock glacier. Using a fundamental system of superposition, it appears that the lower half of the rock glacier was formed by a series of five flow lobes that flowed over each other in a prograding fashion from north to south. Two younger flow lobes followed this sequence, one of which (labelled '8' on Fig. 11) remains active today. As indicated in the profile, layers in the lower part of the rock glacier appear truncated and are not continuous to the head area. This implies 'pinch-out' of the earliest layers by subsequent (overriding) layered units. In terms of flow-lobe development, this means that the first

lobes to form flowed along different avenues of the valley floor. Thus, the rate and position of talus production along the headwall controls the avenue and direction of the flow lobes.

Conclusions

The results of this radar investigation show that the Yankee Boy rock glacier consists of horizontal to subhorizontal layers of ice-rich and ice-poor strata. These layers, some of which are laterally continuous up to 70 m in all directions, are interpreted to be ice-supersaturated sediments and coarse, blocky rockslide debris. The layers are considered to be the result of flow, perhaps generated by seasonal snow pack covered by episodic debris flows or high-magnitude discharges of talus.

Major depositional units, identifiable by prominent reflection events in the GPR profiles, are believed to be individual flow lobes that formed at different positions along the cirque headwall. On this basis, it is concluded that the formation history of the rock glacier involves incorporation of ice within talus debris to form supersaturated permafrost and subsequent creep of this material downvalley. We interpret this rock glacier to be a composite feature formed by a process involving the development and overlap of discrete flow lobes. Of the eight lobes indicated by aerial photography, a sequence of seven discrete lobes is identifiable in the GPR profile. It appears that the lobes flow down the cirque valley as a composite geomorphological unit.

Fig. 11. Model for rock-glacier formation based on GPR interpretations made from the 440 m, 25 MHz longitudinal profile and the layering sequence (1–8) also depicted in Figure 10. The location and rate of talus supply along the headwall controls the avenue (i.e. slope) and direction of flow for each lobe.

References

ANNAN, A. P. & DAVIS, J. L. 1976. Impulse radar sounding in permafrost. *Radio Science*, **11**, 383–394.

BARSCH, D. 1977. Nature and importance of mass-wasting by rock glaciers in alpine permafrost environments. *Earth Surface Processes*, **2**, 231–245.

BARSCH, D. 1992. Permafrost creep and rock glaciers. *Permafrost and Periglacial Processes*, **2**, 175–188.

BARSCH, D. 1996. *Rock Glaciers – Indicators for the Present and Former Geoecology in High Mountain Environments*. Springer-Verlag, Berlin, 331 pp.

BARSCH, D., FIERZ, H. & HAEBERLI, W. 1979. Shallow core drilling and bore-hole measurements in permafrost of an active rock glacier near the Grubengletscher, Wallis, Swiss Alps. *Arctic and Alpine Research,* 11, 215–228.

BERTHLING, I., ELZELMULLER, B., ISAKSEN, K. & SOLLID, J. L. 2000. Rock glaciers on Prins Karls Forland II: GPR soundings and the development of internal structures. *Permafrost and Periglacial Processes,* 11, 357–369.

BURGER, K. C., DEGENHARDT, J. J., JR. & GIARDINO, J. R. 1999. Engineering geomorphology of rock glaciers. *In:* Giardino, J. R., Marston, R. A. & MORISAWA, M. (eds) *Engineering Geology – Changing the Face of Earth.* 28th Binghamton Symposium Special Volume, Elsevier Science B. V., The Netherlands, 93–132.

CALKIN, P. E., KAUFMAN, D. S., PRZYBYL, B. J., WHITFORD, W. B. & PECK, B. J. 1998. Glacier regimes, periglacial landforms, and Holocene climate change in the Kigluaik Mountains, Seward Peninsula, Alaska, USA. *Arctic and Alpine Research,* 30, 154–165.

CHUANG, F. C., GREELEY, R., MOORE, J. M. & THE GALILEO SSI TEAM. 1999. Large-scale mass movements observed from the Galileo Nominal Mission. Abstracts of papers Submitted to the 30th Lunar and Planetary Science Conference, 15–19 March, Houston, Texas, USA, 85, abstract no. 1292.

CLARK, D. H., CLARK, M. M. & GILLESPIE, A. R. 1994. Debris-covered glaciers in the Sierra Nevada, California, and their implications for snowline reconstructions. *Quaternary Research,* 41, 139–153.

CORTE, A. E. 1987. Rock glacier taxonomy. *In:* GIARDINO, J. R., SHRODER, J. F., JR & VITEK, J. D. (eds) *Rock Glaciers.* Allen & Unwin, London, 27–39.

DANIELS, J. J. & ROBERTS, R. L. 1994. Ground penetrating radar for geotechnical applications. *In: Geophysical Investigation of Sites.* Balkema, Rotterdam, 1–13.

DEGENHARDT, J. J., JR. & GIARDINO, J. R. 1999. Kinematic wave models for Martian landforms based on rock glacier analogs. *Meteoritics and Planetary Science,* 34 (4) Supplement, A31.

DEGENHARDT, J. J., JR., GIARDINO, J. R., JUNCK, M. B., QUINTANA, M. P. & MARSTON, R. A. 2000. Evaluating the internal structure of a rock glacier using ground penetrating radar (GPR): Yankee Boy Basin, CO, USA. *Geological Survey of America, Abstracts with Programs,* 32 (7), A516.

EVIN, M. 1987. Lithology and fracturing control of rock glaciers in southwestern Alps of France and Italy. *In:* GIARDINO, J. R., SHRODER, J. F., JR. & VITEK, J. D. (eds) *Rock Glaciers,* Allen & Unwin, London, 83–106.

FINK, J. 1980. Surface folding and viscosity of rhyolite flows. *Geology,* 8, 250–254.

GERBER, E. K. & SCHEIDEGGER, A. E. 1979. Systematics of geomorphic surfaces and kinematics of movements thereon. *Zeitschrift für Geomorphologie. N. F.,* 23, 1–12.

GIARDINO, J. R. 1979. *Rock Glacier Mechanics and Chronologies: Mt. Mestas, Colorado.* Ph.D. thesis, University of Nebraska, 244 pp.

GIARDINO, J. R. & VITEK, J. D. 1988. The significance of rock glaciers in the glacial-periglacial landscape continuum. *Journal of Quaternary Science,* 3, 97–103.

GIARDINO, J. R., SHRODER, J. F., JR. & VITEK, J. D. (eds). 1987. *Rock Glaciers.* Allen & Unwin, Boston, 355 pp.

HAEBERLI, W. 1985. *Creep of Mountain Permafrost: Internal Structure and Flow of Alpine Rock Glaciers.* Mitteilungen der Versuchsanstalt für Wasserbau, Hydrologie und Glaziologie, Zurich, 77, 183 pp.

HAEBERLI, W. & VONDER MÜHLL, D. 1996. On the characteristics and possible origins of ice in rock glacier permafrost. *Zeitschrift für Geomorphologie, Supplementband,* 104, 43–57.

HUMLUM, O. 1996. Origin of rock glaciers from Mellemfjord, Disko Island, central west Greenland. *Permafrost and Periglacial Processes,* 7, 361–380.

HUMLUM, O. 1997. Active layer thermal regime at three rock glaciers in Greenland. *Permafrost and Periglacial Processes,* 8, 383–408.

HUMLUM, O. 1998. Rock glaciers on the Faeroe Islands, the North Atlantic. *Journal of Quaternary Science,* 13, 293–307.

ISAKSEN, K., ODEGARD, R. S., EIKEN, T. & SOLLID J. L. 2000. Composition, flow and development of two tongue-shaped rock glaciers in the permafrost of Svalbard. *Permafrost and Periglacial Processes,* 11, 241–257.

JOHNSON, P. G. 1984. Rock glacier formation by high-magnitude low-frequency slope processes in the southwest Yukon. *Annals of the Association of American Geographers,* 74, 408–419.

KAEAEB, A., HAEBERLI W. & GUNDMUNDSSON, G. H. 1997. Analysing the creep of mountain permafrost using high precision aerial photogrammetry: 25 years of monitoring Gruben rock glacier, Swiss Alps. *Permafrost and Periglacial Processes,* 8, 408–426.

KONRAD, S. K. & HUMPHREY, N. F. 2000. Steady-state flow model of debris-covered glaciers (rock glaciers). *Institute for Hydrospheric-Atmospheric Sciences Publications,* 264, 255–263.

LIESTØL, O. 1962. Talus terraces in Arctic regions. *Norsk Polarinstitutts Årbok,* 1961, 102–105.

LUCCHITTA, B. K. 1986. Mars: periglacial and glacial forms of relief. *In:* KARTASHOV I. P. & NIKIFOROVA K. V. (eds) *Studies of the Quaternary Period.* Selected Papers from the XI INQUA Congress, 1–9 August 1982, Moscow, USSR. Nauka: Quaternary Research, Moscow, 183–193.

LUEDKE, R. G. & BURBANK, W. S. 1976. *Map Showing Types of Bedrock and Surficial Deposits in the Telluride Quadrangle, San Miguel, Ouray, and San Juan Counties, Colorado.* US Geological Survey, Reston, Virginia, USA, Miscellaneous Investigations Series.

McCANN, D. M., JACKSON, P. D. & FENNING, P. J. 1988. Comparison of the seismic and ground-probing radar methods in geological surveying. *Institution of Electrical Engineers Proceedings,* 135 (F4), 380–390.

PALACIOS, D. & VAZQUEZSELEM L. 1996. Geomorphic effects of the retreat of Jamapa glacier, Pico de Orizaba volcano (Mexico). *Geografiska Annaler,* 78A, 19–34.

POTTER, N., JR. 1972. Ice-cored rock glacier, Galena Creek, northern Absaroka Mountains, Wyoming. *Bulletin of the Geological Society of America,* 83, 3025–3057.

POTTER, N., JR., STEIG, E. J., CLARK, D. H., SPEECE, M. A., CLARK, G. M. & UPDIKE, A. B. 1998. Galena Creek

rock glacier revisited-new observations on an old controversy. *Geografiska Annaler,* **80A**, 251–265.

REYNOLDS, J. M. 1997. *An Introduction to Applied and Environmental Geophysics.* Wiley, Chichester, 796 pp.

SANDEMAN A. F. & BALLANTYNE C. K. 1996. Talus rock glaciers in Scotland – characteristics and controls on formation. *Scottish Geographical Magazine,* **112**, 138–146.

SHAKESBY, R. A., DAWSON, A. G. & MATTHEWS, J. A. 1987. Rock glaciers, protalus ramparts and related phenomena, Rondane, Norway: a continuum of large-scale talus-derived landforms. *Boreas,* **16**, 305–317.

SMITH, D. G. & JOL, H. M. 1997. Radar structure of a Gilbert-type delta, Peyto Lake, Banff National Park, Canada. *Sedimentary Geology,* **113**, 195–209.

SQUYRES, S. W. 1978. Martian fretted terrain: flow of erosional debris. *Icarus,* **34**, 600–613.

STEIG, E. J., FITZPATRICK, J. J., POTTER, N., JR & CLARK, D. H. 1998. The geochemical record in rock glaciers. *Geografiska Annaler,* **80A**, 277–286.

WAHRHAFTIG, C. & COX, A. 1959. Rock glaciers in the Alaska Range. *Bulletin of the Geological Society of America,* **70**, 383–436.

This page intentionally left blank

GPR images of periglacial slope deposits beneath peat bogs in the Central European Highlands, Germany

MATTHIAS LEOPOLD* & JÖRG VÖLKEL*

*Present address: Department of Landscape Ecology & Soil Science, Institute of Geography, University of Regensburg, 93040 Regensburg, Germany
(matthias.leopold@geographie.uni-regensburg.de)

Abstract: This research investigates the use of ground penetrating radar (GPR) to determine the continuity of periglacial slope deposits under peat bogs. In the Central European Highlands, periglacial slope deposits are a common parent material for soils and play a critical role in determining the nature of chemical and physical processes in soil development. There is a common agreement on the general distribution of these slope deposits, but there is an ongoing debate in German literature concerning the actual age of these deposits. In particular, the youngest head can usually be found under peat bogs of Late Glacial age (^{14}C and pollen stratigraphy) and has lead to a minimum age determination of pre-Alleröd. Stratigraphic investigations were made using drill cores, and GPR was used to define the continuity of the head under the bog. Several examples from southeastern Bavaria are given.

Periglacial slope deposits are widely spread over the geomorphical landscapes of the Central European Highlands (Fig. 1). They occur at nearly all elevations within the Highlands and, under normal circumstances, have been formed under a cold periglacial morphodynamic regime. These deposits differ considerably from the younger colluvial sediments of Holocene age that are also found in the Highlands.

Nowadays, periglacial slope deposits are divided into several stratigraphic units forming periglacial layers (AG Boden 1994; Völkel 1995). The British term 'head' was used for the translation of the German names of these layers. 'Head' describes a sheet of poorly sorted, angular rock debris with changing percentages of fine material mantling a hillslope which was formed and deposited by gelifluction and cryoturbation. The youngest, at the top, is the Upper Head, underlain by the Middle Head, which occurs only seldom, and, on the bottom, the multilayered Lower Head (Fig. 2). These units vary extremely in their physico-chemical properties. Therefore, they play a critical role in all pedogenic and hydrologic processes.

The Upper and Middle Heads have an aeolian component as documented by a high percentage of fine sediment (silt and clay). Late Glacial and Holocene pedogenic processes always have an effect on the youngest periglacial slope deposits (Upper Head), but only a partially effect in the Middle Head, but no effect on the Lower Head. For this reason, the Upper and Middle Heads form an ecosystem. They control all physico-chemical and pedogenic processes, such as weathering and mineral creation and transformation, as well as the storage of nutrients or pollutants. Furthermore, they function as the exclusive living space of the edaphon and represent possible space for root development. For all these processes and interactions the contact with the Lower Head is a major barrier, isolating and segregating the ecological importance of the upper units in a very impressive way. However, it is the Lower Head which controls hydrological processes. Because of its high permeability, resulting from the high coarse-sediment content (stones), nearly all of the hillslope interflow runs through the Lower Head. Since the periglacial slope deposits play such an important role in the Highlands' ecosystems, the question of determining the time of their formation is an essential part of understanding the ecosystem's evolution.

A widespread assumption exists that the Upper Head was formed during the Younger *Dryas* stage. Based on the results of the Greenland Icecore Project (GRIP) drill cores (Johnsen *et al.* 1992) or the dendrochronological results of Becker *et al.* (1991) and Friedrich *et al.* (1999,) the Younger *Dryas*
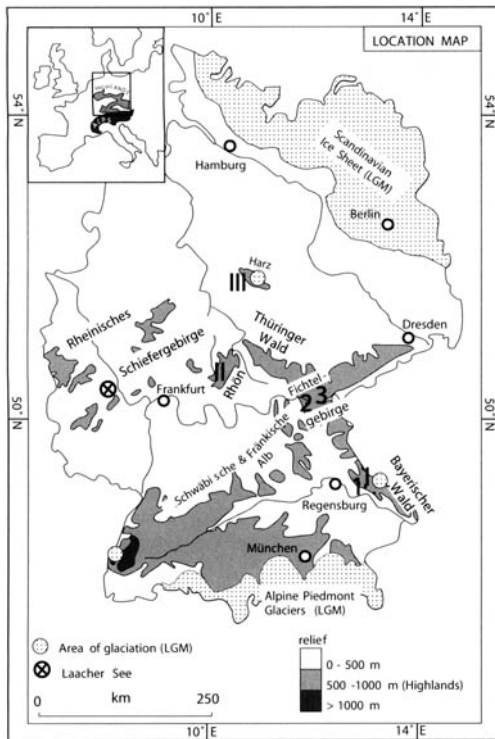
Fig. 1. Location map of the study sites. 1, Kugelstadt Moos (Bayerischer Wald); 2, Seelohe (Fichtelgebirge); 3, Häusellohe (Fichtelgebirge). Other bog sites referred to in this paper: I, Totenau (Bayerischer Wald; e.g. Völkel *et al.* 2001); II, Schwarzes Moor (Rhön; e.g. Völkel *et al.* 2001); III, Radauer Born, Schwarzer Sumpf (Harz; e.g. Völkel & Leopold 2001). The inset map shows the location of the study area within western Europe.

ends around 11,570 Cal BP. The varve-chronology investigations by Merkt & Müller (1999) have resulted in comparable dates (11,590 and 11,560 Cal BP). The diffuse mixing in the head of heavy minerals of the tephra, produced by the plinian eruption of the Laacher See volcano (Laacher See Tephra, or LST) (12,900 Cal BP according to Bogaard 1995; 12,880 years BP according to Brauer *et al.* 1999; 13,010–13,200 Cal BP according to Friedrich *et al.* 1999), has been used as evidence for a precise age determination of a formation during the Younger *Dryas* (AG Boden 1994, p. 363; Benda 1995). Based on chronostratigraphical principals, a tephra can only be used as a marker if it is found as an *in situ* band. Otherwise pedo-bioturbation during the Younger *Dryas*, and, indeed, the entire Holocene, could have lead to the diffuse mixture of LST minerals into the Upper Head and would not indicate the age of formation. The tephra of the Laacher See eruption did not reach large parts of Central Europe (Juvigné 1980;

Bogaard & Schmincke 1985). In southeastern and northeastern Bavaria, e.g. the Fichtelgebirge and the Bayerischer Wald, a mixing of LST minerals cannot be documented (Völkel 1995). Earlier studies had to use different methods for an age determination of the Upper Head (Völkel & Mahr 1997; Mahr 1998; Raab 1999). For that reason peat bogs were chosen. If the Upper Head is older than Late Glacial bogs, the Head must be below the peat but, if the Head is younger, then it will be found within the peat as a mineral layer. Earlier work (Völkel & Mahr 1997; Völkel & Leopold 2000, 2001, Völkel *et al.* 2001) has already demonstrated a pre-Younger *Dryas* age for the Upper Head in certain areas, because the peat overlying the Upper Head is older than Younger *Dryas* and, on the other hand, no mixed mineral layer could be identified (Table 1; for additional details and radiocarbon data see Völkel & Leopold 2001, p. 278).

Subsurface data establishing the depth and extent of peat bogs has been traditionally based on point-sampling using soil pits and drill-core information. By using ground penetrating radar (GPR) the subsurface understanding of the bog can be enhanced by providing a two-dimensional image that both links and extends the drill-core data to specific GPR reflections. A GPR profile with lithological control (drill core) is, essentially, a geological cross-section. Initial work carried out by Völkel & Leopold (2001) and Völkel *et al.* (2001) has shown the potential of GPR in stratigraphic studies of periglacial slope deposits. In this study, GPR is used to establish whether the periglacial slope deposits are interbedded with, or underlie, the peat bogs; this stratigraphic information is critical in establishing whether the periglacial deposits pre-date the bog or were deposited coevally with the peat.

Study areas

Figure 1 shows the study areas where GPR was used for detecting periglacial slope deposits under Late Glacial bogs. All study areas are located between the northern Scandinavian ice sheet and the southern Alpine glaciers. Except for a few local glaciers in the Highlands, this area fell under the influence of periglacial conditions during the last glaciation. The investigation sites range in altitude between 800 m and 1000 m a.s.l. (above sea level) and, as such, are situated in the higher parts of the Highlands: the Bayerischer Wald, the Fichtelgebirge and the Rhön. This makes them highly sensitive to possible climatic changes with reactivation of periglacial processes, such as the formation of periglacial slope deposits during Late Glacial times.

Schematic stratigraphy of periglacial slope deposits in Central European Highlands

Ideal Section	Photograph	Periglacial Head	Genetic Processes	Clast Fabrics	Fines Distribution
(cm) 0 20 40 60 80	(cm) 0 20 40 60 80	Upper Head	Aeolian Input Cryoturbation	Random orientation	Sand/Silt / Clay (%) 30/50/20
		Middle Head	Aeolian Input, Cryoturbation, Solifluction	Orientated fabrics	40/40/20 or 30/50/20
		Lower Head	Solifluction (multi-bedded)	Orientated fabrics	60/25/15

Fig. 2. Stratigraphic overview of the periglacial slope deposits in the Central Europe Highlands. Nomenclature according to Völkel *et al.* (2001) following AG Boden (1994).

Table 1. *Pollen stratigraphy and ages of peat bogs in Central European Highlands*

Locality Region	Name of bog	Pollen stratigraphy	Author
Bayerischer Wald	Totenauer Moor	Ia/Bölling	Stalling 1987
	Kugelstatt Moos	III/Younger *Dryas*	O. Nelle, Regensburg, pers. comm. 2001
Fichtelgebirge	Seelohe	II/Alleröd	Hahne 1992
	Häusellohe	I/Bölling	H.J. Beug, Göttingen, pers. comm. 2001
Rhön	Schwarzes Moor	Ib/Bölling	Grosse-Brauckmann *et al.* 1987
Harz	Radauer Born	III/Younger *Dryas*	Beug *et al.* 1999
	Schwarzer Sumpf	III/Younger *Dryas*	Beug *et al.* 1999

Methods

The radar lines were collected using a RAMAC CU II GPR system. A detailed horizontal profile was obtained using 100 MHz antennae with a 1.0 m separation and steps of 0.5 m. The 100 MHz antennae were chosen to achieve the necessary penetration depth down to 6 m because 200 MHz and higher antennae were found not to penetrate the peat body down to the mineral base. Each trace was vertically stacked 16 times. Automatic gain control (AGC) was used in processing the signal. A common mid-point survey (CMP) with 0.25 m steps was used to obtain an estimate of velocity (0.042 m ns^{-1} for peat and 0.06 m ns^{-1} to 0.085 m ns^{-1} for slope deposits), which was used to determine the depth scale of the profile. Direct correlation with drill-core logs helped calibrate the velocities with the subsurface stratigraphic units.

Radar images were processed using the REFLEX software WIN 1.4 from Sandmeier Software. Raw data were filtered using background removal and averaging.

Results

After a short description of the main radar facies the results of the GPR lines of all the three study areas introduced here are presented with the raw data on top with travel time. The second image gives the interpretation linked with a depth scale. As CMP surveys showed, peat (0.042 m ns^{-1}), loamy Upper Head (0.06–0.08 m ns^{-1}), and sandy Lower Head and saprolite (0.08–0.085 m ns^{-1}) all had slightly different velocities. Thus the actual thickness of the periglacial slope deposits differ slightly from that in the radar profile, whereas the depth of the peat bog is accurate.

The radar facies

Despite the high variance in geology and accompanying sediments, and in the elevation and varying ages and development histories of the peat bogs in the different study areas, the reflections can be classified into characteristic radar facies. Four main radar facies can be documented in the several radar images for which we give some basic information.

- Radar facies 1 is represented by subhorizontal, partly wavy reflections which are often continuous for several decametres. This reflection pattern is characteristic for the upper part of the peat and can often be found throughout the whole peat body.
- Radar facies 2 has a slightly concave trough-shaped pattern, often truncating or onlapping the horizontal reflections of radar facies 1. It occurs within the peat and therefore its distribution is restricted to that of the bog. It is either closely linked to the underlying relief or can be found separated within the horizontal reflection pattern of radar facies 1.
- Radar facies 3 is characterized by continuous clinoform reflections with different dips. These oblique reflections are typical for the slope deposits or the saprolite. As periglacial slope deposits cover the relief with all kinds of different steepness, there is no characteristic dipping angle. Dipping reflections sometimes also occur within the lower part of peat complexes.
- Radar facies 4 are small hyperbola. They occur either within radar facies 1, indicating tree logs within the peat, or in radar facies 3, indicating isolated unweathered blocks in the slope deposits or sometimes even in the saprolite.

The Kugelstatt Moos (Bayerischer Wald)

In the Kugelstadt Moos (Fig. 3), periglacial slope deposits occur both outside the confines of the bog and underneath it. The bog is divided into two parts, the smaller western and the larger and deeper eastern part, which are separated by an outcrop at 80 m on the radar line. Pollen stratigraphy has placed the bog's basal age into the Younger *Dryas* period (O. Nelle 2001, pers. comm., radiocarbon dating in progress).

Bedrock Over the whole area, outcrops of solid bedrock (granite or gneiss) are only found at the mountain summits. On the valley slopes and the lowlands, a thick layer of sandy saprolite (up to several tens of metres) is found. The saprolite is marked by reflections of radar facies 3 below the Upper Head, between 110 m and 130 m (Fig. 3). Between 0 m and 30 m, next to profile 7034–2, the

saprolite can be distinguished from the Lower Head by its slightly higher dip. This reflection gets lost at around 60 m. It may appear again at the end of the radar lines, but there is no clear evidence without drill-core correlation. Between 150 m and 170 m at 120 ns and 220 ns (2 m and 4.5 m depth), there is a weak, but still visible reflection. We found that this does not correlate with any geologic feature.

Periglacial slope deposits Periglacial slope deposits can be detected with GPR in the entire line. Next to pit 7034–2, between 0 m and 20 m, the oblique, continuous reflections of radar facies 3 is well documented. Typical reflections of this facies are found between 90 m and 180 m, at the transition of the organic peat towards the mineral Upper Head. The great difference between the dielectric constants for these two materials is responsible for the reflection. Around 90 m some hyperbole reflections may indicate bigger blocks of granite. At 110 m a truncated reflection may indicate slope deposits running over horizontally bedded saprolite (Völkel *et al.* 2001).

Peat The upper part of the peat is characterized by continuous subhorizontal and wavy reflections of radar facies 1 (e.g. Halleux 1990; Roberts *et al.* 2000). At 110 m to 150 m, between 100 ns and 200 ns, the peat reflections change towards a more concave trough-shaped form (radar facies 2), which is sometimes cut by weak subhorizontal reflections. Dipping reflections (radar facies 3) often merge into the concave reflections of radar facies 2. The reflections within the peat probably indicate layers with a different water content, linked with a changing density due to different stages of humification of the peat. In the Kugelstatt Moos we did not encounter any tree logs while drilling but, based on experiences from other peat bogs, buried trees must be taken into consideration for hyperbole reflections in the peat (e.g. at 142 m at ~50 ns). The peat has a clear onlap relationship with the underlying Upper Head, indicative of growth from the bottom of the bog to the top. However, several breaks and cuts, which can be linked to different radar facies, probably indicate an occasional interruption of an overall continuous peat growth. More importantly, there is no indication of an intermixed mineral layer in the peat reflection, which correlates well with the drill-core data.

The Seelohe (Fichtelgebirge)

The morphology of the bog's base (Fig. 4) shows a step (exaggerated scale ratio of 1 : 20) on the eastern side between 240 m and 260 m. On this step, near core 5937–6, the oldest parts of the bog (pollen stratigraphy and ^{14}C dates give an Alleröd age, Hahne 1992) are found.
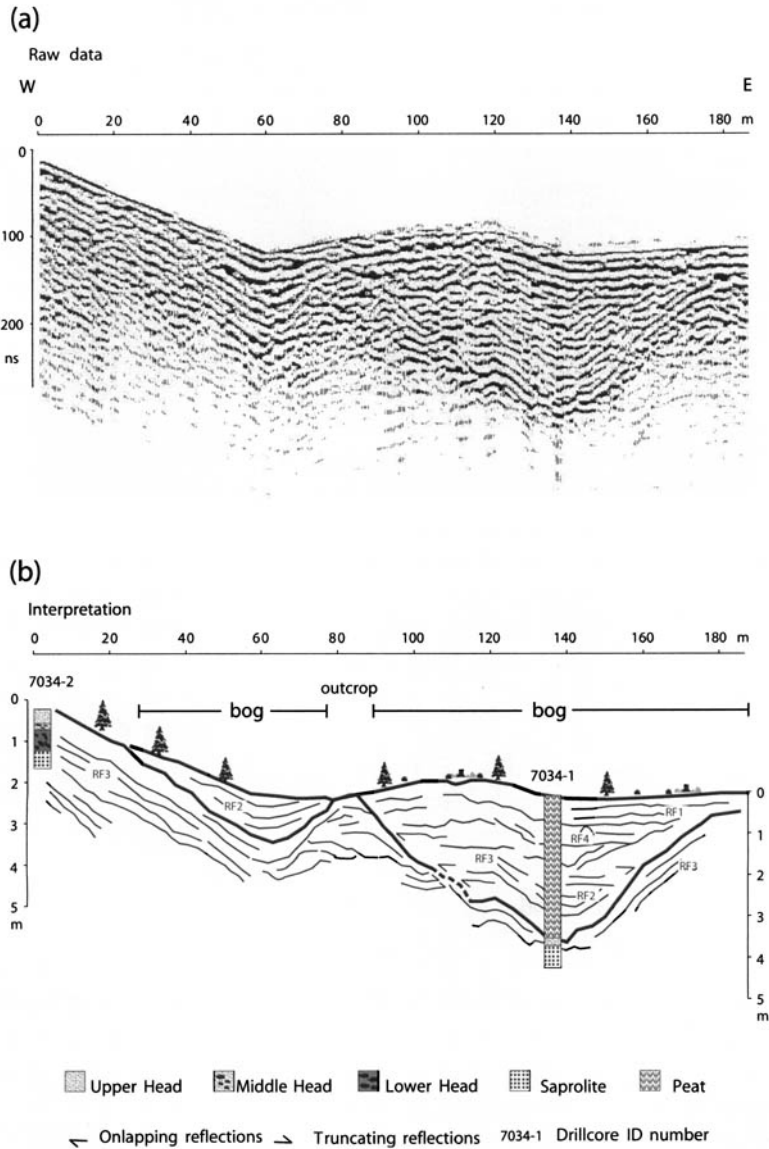
Fig. 3. GPR profiles at the edge of the Kugelstatt Moos (Bayerischer Wald); uninterpreted and interpreted profiles. RF, radar facies units.

Bedrock Granite bedrock, partly weathered to a thick saprolite, underlies the whole study area. The GPR image of saprolite is rendered transparent by the high silt and clay content of the periglacial slope deposits, which attenuate the signal.

Periglacial slope deposits Core evidence reveals that both the Upper and Lower Heads occur beneath the bog. The upper contact of the Upper Head can be correlated with the GPR reflections of radar facies 3. The contrast in dielectric constants between peat and the mineral Upper Head is so high that a reflection can be documented (e.g. Hänninen 1992). Between 70 m and 150 m the image shows up to three more reflections. Some of them may indicate the boundary between the Upper Head and Lower Head, but in most places there are no reflections along the contact zone of the Upper Head towards the Lower Head, which is probably due to signal attenuation.
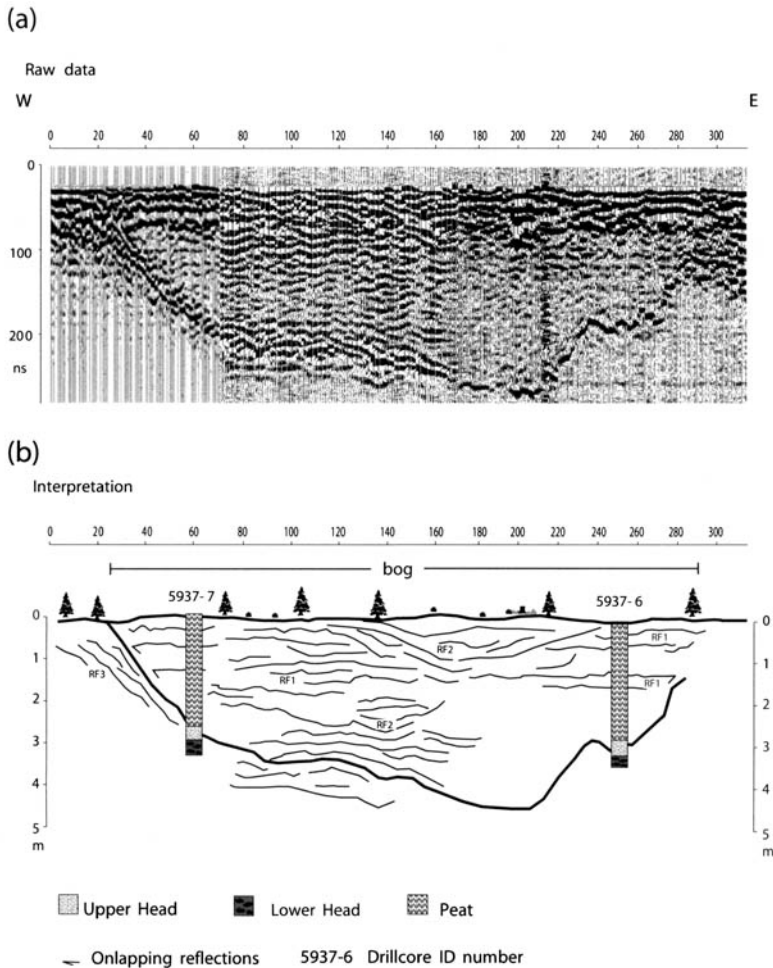
Fig. 4. GPR profiles at the edge of the Seelohe (Fichtelgebirge); uninterpreted and interpreted profiles. RF, radar facies units.

Peat The peat deposits are characterized by discontinuous reflections of radar facies 1 and 2. The peat reflections have a marked onlap relationship with the underlying Upper Head, showing how the peat filled in the basin from the bottom to the top. The horizontal reflections within the peat reflect changes in the peat composition and are characteristic of radar facies 1. Mixed mineral layers produced by aeolian processes causing these kinds of horizontal reflections (Halleux 1990) were not found in the drill cores. Neither the Upper Head nor its aeolian components have been identified in the GPR line. Furthermore there is a concave trough-shaped reflection of radar facies 2 within the peat. This could indicate changes of peat stratigraphy due to sinking processes. Cutting peat in the 1950s, with the associated drainage of the peat body, might be a reason for this phenomenon.

The Häusellohe (Fichtelgebirge)

The Häusellohe (Fig. 5) is believed to be the oldest of the bogs surveyed by GPR in this research project. Pollen stratigraphy establishes the beginning of the peat growth in Bölling time (H.-J. Beug 2001, pers. comm.), which is the earliest warm period in southern Germany after the last Glacial Maximum (LGM). New radiocarbon dates document an age of Alleröd time at the base of drill core 5839–10 (11.570–10.985 Cal BC; Hv 24391).

Bedrock The bedrock consists of thick layers of saprolite, which are imaged by reflections of radar facies 3 between 0 m and 40 m as well as between 60 m and 110 m. The silty matrix of this saprolite quickly weakens the radar signal and it disappears with depth (Annan & Cosway 1992). Drill-core
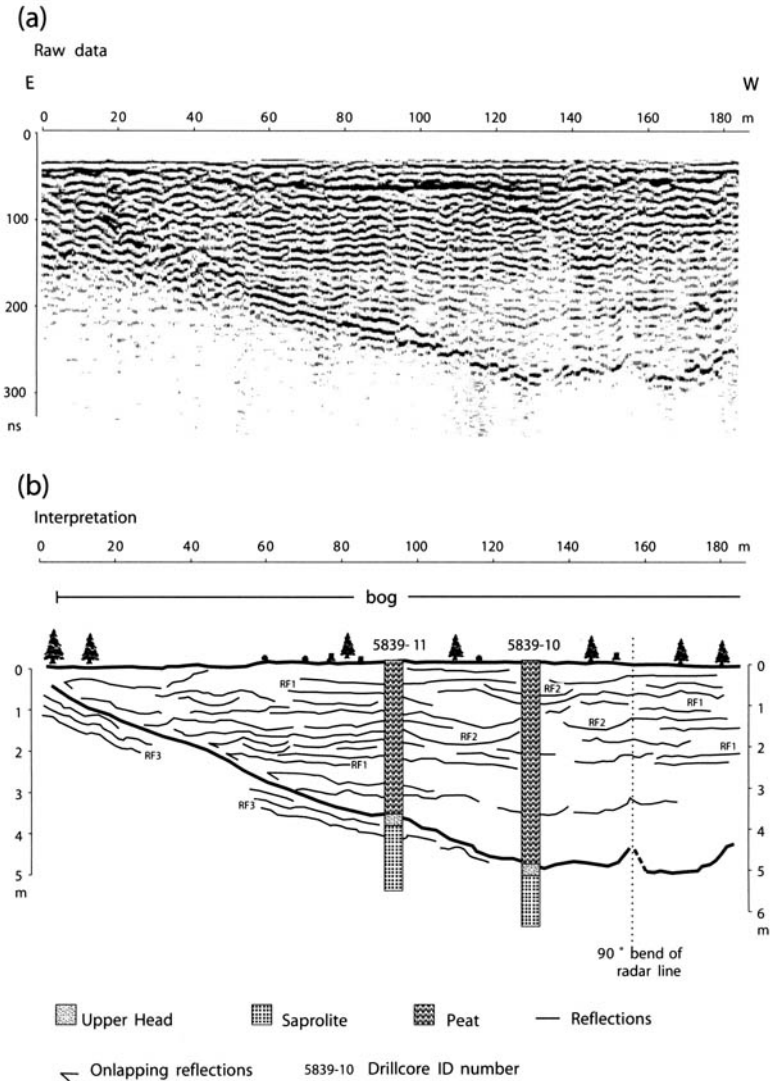
Fig. 5. GPR profiles at the edge of the Häusellohe (Fichtelgebirge); uninterpreted and interpreted profiles. RF, radar facies units.

data show that the reflection documents the existence of a thin Upper Head.

Periglacial slope deposits The lack of unweathered solid bedrock in the area surrounding Häusellohe has formed an untypical Lower Head with no stones. Continuous reflections of radar facies 3 can be documented between 50 m and 90 m and partly broken-up reflections between 100 m and the end of the line. This radar facies is also found at the eastern edge of the bog between 0 m and 20 m. Due to the low difference in the dielectric constant between the Upper Head and the saprolite at the

Häusellohe, it is not possible to separate the stratigraphy without ground-truthing the radar surveys. At 160 m between 3 m and 6 m depth the reflections are bent upward from both sides. This is the result of a 90° bend of the radar line and has no relationship to any geomorphological feature.

Peat Typical subhorizontal continuous reflections of radar facies 1 characterize the upper part of the peat and show the clear onlap relationship towards the underlying Upper Head. Several concave reflections of radar facies 2 may indicate former

waterholes which were later filled up with growing sphagnum peat.

A comparison of the radar facies between the several study sites shows that the slope deposits are characterized homogeneously by radar facies 3. Continuous clinoform reflections with different dipping angles depending on the relief can be documented at the several sites. The reflection pattern of the peat differs between the several study areas. At the Kugelstatt Moos (Fig. 3) the reflections within the peat include subhorizontal reflections (radar facies 1), concave-shaped reflections (radar facies 2), and dipping reflections (radar facies 3, indicating a complex stratigraphy. At the Seelohe (Fig. 4) and the Häusellohe (Fig. 5), the reflections within the peat are characterized by relatively continuous subhorizontal reflections (radar facies 1) with some concave trough-shaped reflections.

Conclusion

GPR can be very effective in detecting periglacial slope deposits as well as peats. Running a radar line from outside the bog and then over it makes it possible to follow the slope deposits stratigraphically. Four main radar facies allow a clear differentiation between peat complexes and periglacial slope deposits and its individual characteristics. The 100 MHz antennae had the necessary penetration in the water-saturated, organic peat complex, as well as providing sufficient details to distinguish the periglacial deposits and the bedrock. Because of the high difference in the dielectric constants of peat and a mineral loamy material, any interbedded layer with a thickness of at least 10 cm (Ziekur 2000) should be detectable even with 100 MHz antennae. All three study sites introduced here show Upper Head under the peat bog. In none of the bogs could we find the Upper Head or its correlative aeolian sediments mixed within the peat, leading to the conclusion that the head has to be older than the peat. In the Kugelstatt Moos (Bayerischer Wald) and in the Seelohe (Fichtelgebirge), the peat has an age of Younger Dryas/Alleröd, whereas, in the Häusellohe (Fichtelgebirge), the bog started to grow as early as Bölling time. For this reason the Upper Head cannot be of Younger Dryas age in the study areas; it has to be older than Younger Dryas/Alleröd and Bölling, confirming and reinforcing the results of previous work (Völkel & Mahr 1997, 2001, Völkel & Leopold 2001, Völkel et al. 2001).

References

AG BODEN, 1994. Bodenkundliche Kartieranleitung. Hannover.

ANNAN, A. P. & COSWAY, S. W. 1992. Ground penetrating radar survey design. In: pulseEKKO IV RUN: User's Guide. Sensors & Software, Inc., Mississauga, Ontario, 135 pp.

BECKER, B., KROMER, B. & TRIMBORN, P. 1991. A stable-isotope tree-ring timescale of the Late Glacial/Holocene boundary. Nature, 353, 647649.

BENDA, L. 1995. Das Quartär Deutschlands. INQUA Berlin Congress, 1995, Gebrüder Borntraeger, Berlin & Stuttgart, 408 pp.

BEUG, H. -J., HENRION, I. & SCHMÜSER, A. 1999. Landschaftsgeschichte im Hochharz. Die Entwicklung der Wälder und Moore seit dem Ende der letzten Kaltzeit. Clausthol-Zellerfeld.

BOGAARD, P. 1995. 40Ar/39Ar ages of sanidine phenocrysts from Laacher See Tephra (12.900 yr BP). Chronostratigraphic and petrological significance. Earth Planetary Science Letters, 133, 163–174.

BOGAARD, P. & SCHMINCKE, H. 1985. Laacher See Tephra: A widespread isochronous late Quaternary tephra layer in central and northern Europe. Bulletin of the Geological Society of America, 96, 1554–1571.

BRAUER, A., ENDRES, C. & NEGENDANK, J. F. W. 1999. Lateglacial calendar years chronology based on annually laminated sediments from Lake Meerfelder Maar, Germany. Quaternary International, 61, 17–25.

FRIEDRICH, M., KROMER, B., SPURK, M., HOFFMANN, J. & KAISER, K. F. 1999. Paleo-environment and radiocarbon calibration as derived from Lateglacial/Early Holocene tree-ring chronologies. Quaternary International, 61, 27–39.

GROSSE-BRAUCKMANN, G., STREITZ, B. & SCHILD, G. 1987. Einige vegetationsgeschichtliche Befunde aus der Hohen Rhön. Beiträge zur Naturkunde Osthessen, 23, 31–65.

HAHNE, J. 1992. Untersuchungen zur spät- und postglazialen Vegetationsgeschichte im nordöstlichen Bayern. Flora, 187, 169–200.

HALLEUX, L. 1990. Ground penetrating radar applied to the study of peat bogs and moors. Annales Societé Géologie Belgique, 113, 115–123.

HÄNNINEN, P. 1992. Application of Ground Penetrating Radar and Radio Wave Moisture Probe Techniques to Peatland Investigations. Geological Survey of Finland, Bulletins, 361.

JOHNSEN, S. J., CLAUSEN, H. B. ET AL. 1992. Irregular glacial interstadials recorded in a new Greenland ice core. Nature, 359, 311–313.

JUVIGNÉ, E. 1980. Vulkanische Schwerminerale in rezenten Böden Mitteleuropas. Geologische Rundschau, 69, 982–996.

MAHR, A. 1998. Lockerbraunerden und periglaziale Deckschichten im Bayerischen Wald. Untersuchungen zur Paläoumwelt und Geomorphodynamik im Spätglazial und ihrem Einfluø auf die Pedogenese. Regensburger Geographische Schriften, 30, 326 pp.

MERKT, J. & MÜLLER, H. 1999. Varve chronology and palynolgy of the Lateglacial in Northwest Germany from lacustrine sediments of Hämelsee in Lower Saxony. Quaternary International, 61, 41–59.

RAAB, T. 1999. Würmzeitliche Vergletscherung des Bayerischen Waldes im Arbergebiet. Regensburger Geographische Schriften, 32, 327 pp.

ROBERTS, M. C., VANDERBURGH, S. & JOL, H. 2000. The geomorphology and radar facies of the seepage face

of the Brookswood aquifer, BC. *In*: RICKETTS B. (ed) *Aquifer Delineation, Fraser Lowland and Delta, BC: Mapping, Geophysics and Ground Water Modelling.* Geological Survey of Canada, Bulletin **552**, 95–102.

STALLING, H. 1987. *Untersuchungen zur spät- und postglazialen Vegetationsgeschichte im Bayerischen Wald.* Dissertationes Botanicae, **105**, 201 pp.

VÖLKEL, J. 1995. *Periglaziale Deckschichten und Böden im Bayerischen Wald und seinen Randgebieten als geogene Grundlagen landschaftsökologischer Forschung im Bereich naturnaher Waldstandorte.* Zeitschrift für Geomorphologie. N.F. Supplement, **96**, 301 pp.

VÖLKEL, J. & LEOPOLD, M. 2000. *Morphodynamic Change during Late Glacial Time in Central Europe – Studies on Periglacial Slope Deposits and their Combination with Bogs.* Final Colloquium of the DFG Priority Programme 'Changes of the Geo-Biosphere during the last 15.000 years', Poster Volume, **12**.

VÖLKEL, J. & LEOPOLD, M. 2001. To the age of the youngest stage of periglacial morhodynamics on slopes in the Central European Highlands. *Zeitschrift für Geomorphologie, N.F.,* **45/3**, 273–294.

VÖLKEL, J. & MAHR, A. 1997. Neue Befunde zum Alter der periglazialen Deckschichten im Vorderen Bayerischen Wald. *Zeitschrift für Geomorphologie, N.F.,* **41**, 131–137.

VÖLKEL, J. & MAHR, A. 2001. IRSL-dating of periglacial slope deposits. Results from the Bayerischer Wald (Bavarian Forest). *Zeitschrift für Geomorphologie, N.F.,* **45/3**, 295–305.

VÖLKEL, J., LEOPOLD, M. & ROBERTS, M. C. 2001. The radar signatures and age of periglacial slope deposits, Central Highlands of Germany. *Permafrost and Periglacial Processes,* **12**, 379–387.

ZIEKUR, R. 2000. Georadar in der Bodenkunde. *Geologisches Jahrbuch,* **E52**, 9–34.

This page intentionally left blank

Soil effects on GPR detection of buried non-metallic mines

JAN M. H. HENDRICKX[1], SUNG-HO HONG[1], TIM MILLER[1], BRIAN BORCHERS[1] &
JAN B. RHEBERGEN[2]

[1]*New Mexico Tech, Socorro, New Mexico, USA (e-mail: hendrick@nmt.edu)*
[2]*TNO Physics and Electronics Laboratory, The Hague, The Netherlands*

Abstract: Landmines are a major problem in many areas of the world. In spite of the fact that many different types of landmine sensors have been developed, the detection of non-metallic landmines remains very difficult. The objective of this contribution is to synthesize our work related to the effects of soil texture and soil water content on the detection of non-metallic anti-tank landmines using ground penetrating radar (GPR). We present a model for the prediction of radar response under a wide range of soil texture and soil water content conditions. Next we present measurements from field experiments in a sand and a silt loam which validate the radar response model. The spatial variability of soil water content in field soils may strongly decrease the effectiveness of GPR for anti-tank mine detection. Uniform wetting of sand and loam soils by irrigation or rain will improve the radar signal. Radar detection in clay soils will be most effective under dry conditions.

Buried landmines are one of the most common and lethal weapons of ground conflict. Today at least 100 million landmines are scattered across more than 60 countries (Bruschini & Gros 1997). Detection and disposal of landmines is one of the most difficult and uncontrollable problems faced in ground conflict. Since mines remain lethal long after military actions have terminated, they also have become a long-term humanitarian disaster.

A wide range of new sensors have been developed, or are in development, for the detection of buried non-metallic and low-metallic landmines. Two types of landmine sensors can be distinguished: substance-analysing sensors and imaging sensors. Substance-analysing sensors are magnetometers, bio-sensors, chemical sensors, and sensors based on principles of thermal neutron activation, X-ray back-scatter and nuclear quadruple resonance. Imaging sensors are based on passive and active infrared, passive and active mm-wave radar, and ground penetrating radar (GPR). Although several of these sensors perform quite well under certain conditions, there is a general agreement that none of the present technologies can reach good enough detection while maintaining a low false-alarm rate (Bruschini & Gros 1997). One reason is the variety of landmines: there are some 2500 mine and 'fuse' combinations (Rouhi 1997). The other important reason is that the environment in which mines are placed is extremely variable owing to variable climate, vegetation, soil type, depth of groundwater table and topography. For example, the three countries that have the largest average number of mines deployed per square kilometre are Bosnia-Herzegovina in the temperate zone, Cambodia in the humid tropics and Egypt in an arid desert (Strada 1996). Variations in the environmental conditions influence sensor performance because, in general, landmine sensors exploit soil and environmental conditions to discern between mines and other objects.

Research efforts on mine detection are generally geared toward sensor development and sensor fusion. Little effort has been made on evaluating the environmental conditions that affect sensor performance. Changes in soil texture, soil bulk density, soil volumetric water content (θ) and soil salinity affect microwave radar signals (Wang & Schmugge 1980; Calvet et al. 1995; Dobson et al. 1985; Hallikainen et al. 1985; Peplinski et al. 1995). Soil volumetric water content is known to affect the thermal (van Wijk 1963) and electromagnetic (Hoekstra & Delaney 1974; Topp et al. 1980) properties of soil. The performance of sensors based on radar and infra-red imaging is expected to vary with soil and environmental conditions (Hendrickx et al. 2001; Hong et al. 2001; Šimunek et al. 2001). The objective of this contribution is to synthesize our work related to the effects of soil texture and soil

water content on the detection of non-metallic anti-tank landmines using GPR.

Model of radar response

The radar response from a buried landmine depends on the radar frequency and the electrical properties of the mine and the soil. The latter depend on the bulk density, specific density of the soil particles, texture, volumetric water content, temperature and radar frequency. We estimated soil electrical properties using the model of Peplinski *et al.* (1995). The inputs to this model consist of the volumetric water content (θ), the frequency (f), the fraction of the sand particles (S), the fraction of the clay particles (C), the density of the soil particles ρ_S (a typical value is 2.66 g/cm^3) and the bulk density of the soil (ρ_B). The application of this model in a soil context has been demonstrated by Borchers *et al.* (2000). We have prepared a MAT-LAB software package to predict the dielectric constant, velocity of the GPR signal, attenuation, and reflection coefficient from soil type and soil water content data. Using these models we can determine whether or not field conditions are suitable for the use of GPR in the detection of an anti-tank mine (Borchers *et al.* 2000). As a GPR signal travels through the soil, it is attenuated at a rate determined by the complex dielectric constant of the soil. The round-trip attenuation loss (*AL*) is given by:

$$AL = 17.3718d\alpha \qquad (1)$$

where d is the depth to the object from which the GPR signal is reflecting and α is:

$$\alpha = \frac{2\pi f}{c} \sqrt{\frac{\varepsilon_s'}{2}\left(\sqrt{1 + \left(\frac{\varepsilon_s''}{\varepsilon_s'}\right)^2} - 1\right)} \qquad (2)$$

where

$$\varepsilon_s' = 1.15\left[1 + \frac{\rho_B}{\rho_S}(\varepsilon_p^\alpha - 1) + \theta^{\beta'}\varepsilon_{fw}'^\alpha - \theta\right]^{1/\alpha} \\ - 0.68 \qquad (3)$$

and

$$\varepsilon_s'' = \lfloor\theta^{\beta''}\varepsilon_{fw}''^\alpha\rfloor^{1/\alpha} \qquad (4)$$

where ρ_B is the density of the soil particles, ρ_S is the bulk density of the soil, ε_p is the dielectric constant of soil particles, ε_s is the dielectric constant of bulk soil, θ, is the volumetric water content, f is the frequency, ε_{fw} is the dielectric constant of free water and α is a constant (0.65).

$$\beta' = 127.48 - 0.519S - 0.152C \qquad (5)$$

$$\beta'' = 1.33797 - 0.603S - 0.166C \qquad (6)$$

where S is the fraction of sand particles and C is the fraction of the clay particles.

$$\varepsilon_{fw}' = \varepsilon_{w\infty} + \frac{\varepsilon_{w0} - \varepsilon_{w\infty}}{1 + (2\pi f\tau_w)^2} \qquad (7)$$

$$\varepsilon_{fw}'' = \frac{2\pi f\tau_w(\varepsilon_{w0} - \varepsilon_{w\infty})}{1 + (2\pi f\tau_w)^2} + \frac{\sigma_{eff}}{2\pi\varepsilon_0 f}\frac{(\rho_S - \rho_B)}{\rho_S\theta} \qquad (8)$$

where ε_0 is the dielectric permittivity of free space, ε_{w0} is the static dielectric constant of water, $\varepsilon_{w\infty}$ is the high-frequency limit of ε_{fw}', and τ_w is the relaxation time of water.

A second factor that determines the performance of the GPR for landmine detection is the strength of signal reflection when it reflects back from the landmine. The reflection loss (*RL*) is given by:

$$RL = -10\log|r|^2 \qquad (9)$$

where

$$r = \frac{\sqrt{\varepsilon_s} - \sqrt{\varepsilon_m}}{\sqrt{\varepsilon_s} + \sqrt{\varepsilon_m}} \qquad (10)$$

where ε_s is the dielectric constant for the bulk soil and ε_m is the dielectric constant of the mine. Notice that the reflection coefficient depends on the difference between dielectric constants of the mine and the soil. As these constants approach each other, the strength of the reflected wave goes to zero and the mine becomes invisible.

The mathematical models described here have been integrated into a MATLAB package that can be used to predict the performance of GPR systems under field conditions. The necessary input data consists of the soil texture (in the form of sand and clay fractions), the bulk soil density and the volumetric soil water content.

Methods and materials

Two study sites were selected in the Sevilleta National Wildlife Refuge approximately 25 km north of Socorro, New Mexico: one site with a dune sand, another with a silt-loam soil. The texture of the sand is 95% sand and 5% clay; the texture of the silt loam is 10% sand, 75% silt and 15% clay. At each site we selected an area of 2 × 1 m, over which we placed a wooden frame. The frame is used to house the target mine (Figs 1 & 2) and provide a reference for the GPR system (Fig. 3). The frame has removable wooden cross-beams that are used to guide the movement of the GPR. A centimetre scale on one of the beams provided accuracy for the GPR step size. We buried an anti-tank mine 60 cm from the end and 50 cm from the
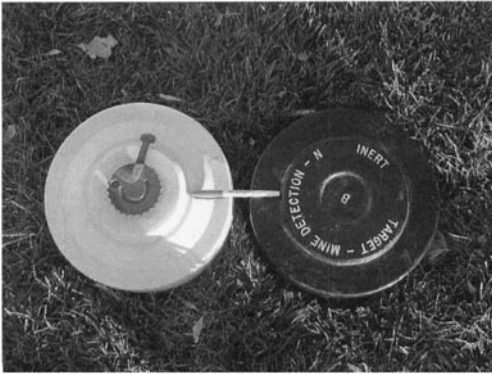
Fig. 1. Inert non-metallic anti-tank landmines.

Fig. 2. Wooden frame and buried anti-tank mine.

side of the frame, with its top surface 11 cm below the soil surface (Fig. 2). A second anti-tank mine was buried outside the wooden frame for monitoring of soil water content changes during and after

Fig. 3. GPR on wooden cross-beams inside the frame.

watering the soil. Water content was monitored with steel probes placed above and below the mine using time domain reflectometry (TDR), a common method for measuring soil water contents (e.g., Hendrickx 1990). We installed four TDR probes at 3 cm, 8 cm, 23 cm and 28 cm below the surface to monitor soil water content above and below the anti-tank mine.

GPR measurements were taken before and after application of 33 cm of water to both sites. We used a GPR pulseEKKO 1000 system, manufactured by Sensors and Software, Inc., Canada. We used the 900 MHz antennae with an antenna separation of 17 cm. For data collection we used a step size of 2.5 cm, reflection mode survey type, and 64 stacks at each point, which provided enough spatial resolution to locate the mines. During processing the data, we set our gains to automatic gain control (AGC), did not use any time or spatial filters, and set our trace correction to the dewow setting.
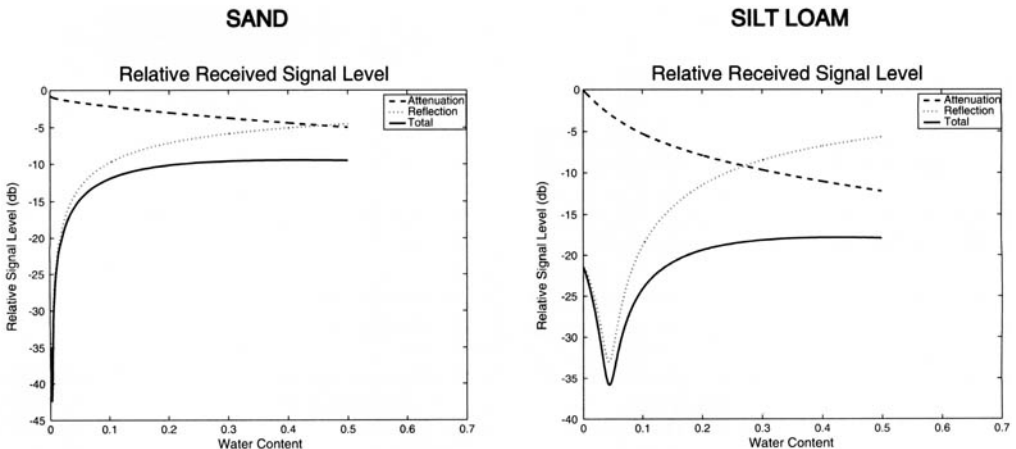
Fig. 4. Attenuation, reflection and total losses predicted with the radar response model in a sand and a silt loam at water contents from 0 *V%* to 50 *V%*.

Results and discussion

Modelling radar response in sand and silt-loam soils

We used the model to evaluate the effect of soil texture and soil water content on the radar reflection from a non-metallic buried anti-tank landmine. Figure 4 shows the attenuation and reflection losses in a sand and a silt loam as a function of soil water content. Soil texture has a large impact on the losses, which are smallest in the sand and larger in the silt loam. Zero water-content conditions yield acceptable radar results in all soils. Unfortunately, even a small increase of water content to 3 $V\%$ (volume %) or 10 $V\%$ in the sand and the silt loam, respectively, will immediately result in a loss of signal strength to its lowest level. The losses will decrease if the soil is wetted to a water content exceeding 15–30 $V\%$ in the sand and the silt loam, respectively. The losses remain quite constant in both soils at water contents exceeding 30 $V\%$. It appears that watering of minefields or waiting for the rainy season is the best strategy for detection of non-metallic mines in sand and silt-loam soils.

Field measurements

Figures 5 and 6 present, respectively, the radar images obtained in the sand and the silt loam under dry and wet conditions. Unfortunately, a winter storm wetted the normally dry sand soil to a volumetric water content of 7 $V\%$. Nevertheless, there is a clear trend which demonstrates that the radar response improves with increasing water content from 7 $V\%$ to 29 $V\%$ in the sand and from 6 $V\%$ to 40 $V\%$ in the silt loam. Thus, our field measurements confirm our model results for non-metallic mines in sand and silt-loam soils.

Spatial variability of soil water content

The application of the radar response model in sand and in silt loam (Fig. 4) assumed homogeneous soils throughout, i.e. the variability of soil water content is caused only by temporal variability of weather parameters, such as precipitation and evaporation, or by the effect of the mine on water distribution. However, many field observations have shown that soil water content has its own intrinsic spatial variability due to small differences in hydraulic properties, surface unevenness, vegetation, unstable wetting and macropore flow (e.g. Nielsen *et al.* 1973; Peck 1983; Hendrickx *et al.* 1990; Hendrickx & Walker 1997; Hendrickx & Flury 2001). Therefore, Hendrickx *et al.* (2001) have evaluated the manner in which soil water con-
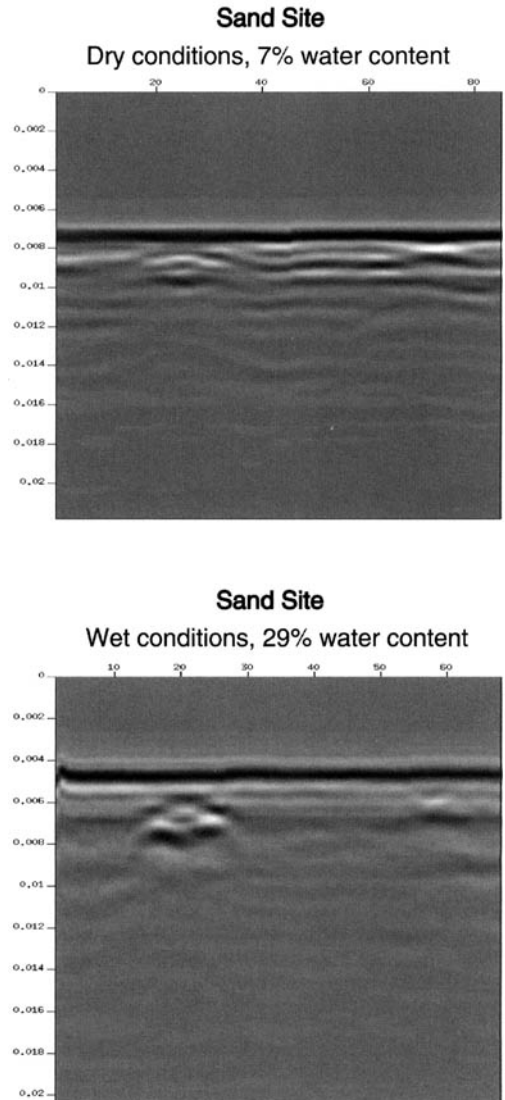
Fig. 5. Radar images in a dry and wet sand soil with non-metallic anti-tank landmine.

tent variability affects the variability of dielectric soil properties and the performance of GPR for mine detection.

Since the relationship between soil water content and dielectric constant is linear over a wide range of water contents (Topp *et al.* 1980), the water content variability is linearly related to the variability of the dielectric constant. However, the relationships between soil water content variability and variability in the strength of the GPR reflections and attenuation losses are non-linear. Hendrickx *et al.* (2001) have used a Monte Carlo analysis to

Silt Site
Dry conditions, 6% water content

Silt Site
Wet conditions, 40% water content
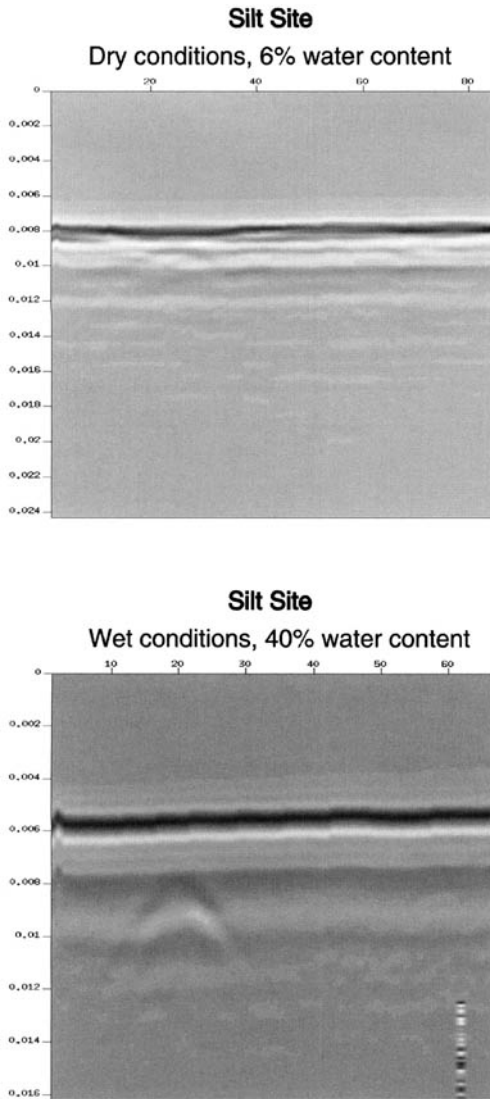
Fig. 6. Radar images in a dry and wet silt-loam soil with non-metallic anti-tank landmine.

evaluate the manner in which the variability of field soil water contents affects the variability of GPR reflections and attenuation losses. They conducted this analysis for a water-repellent sand soil in The Netherlands and a clay soil in Panama. Figure 7 shows that, in the Dutch sand soil, for a coefficient of variability (c.v.) of 10%, the radar-response model gives a good indication of the expected radar images but at 40% the radar response is greatly affected by the spatial variability of soil water content. At a soil water content of 10 V% at c.v. 10%, the losses may vary from -20 dB to -18 dB while

at c.v. 40% the losses may vary from -45 dB to -17 dB. Figure 8 shows similar results in a Panamanian clay soil. In addition to the possible increase in losses as the c.v. increases, we also observe that, in clay soils, wetting is not leading to an improved radar response. It is best to use the GPR for non-metallic mine detection in clay soil under dry conditions only. Since a soil water content c.v. of 40% is quite common in field soils (Hendrickx *et al.* 2001), the reliability of GPR in field soils is much lower than expected on the basis of the theoretical radar-response model.

Conclusions

- Soil texture and soil water content strongly affect the performance of GPR for detection of non-metallic anti-tank mines. Knowledge of soil conditions is essential for the effective deployment of GPR for mine-clearing operations.
- The presented model for radar response under different soil texture and soil water content conditions has been validated by our experimental observations. It predicts correctly attenuation and reflection losses under a wide range of soil conditions.
- Spatial variability of soil water content in field soils strongly affects the effectiveness of GPR for detection of non-metallic anti-tank mines.
- In sand and loam soils, uniform soil-wetting by irrigation or rain will improve the effectiveness of GPR for detection of anti-tank mines. In clay soils, soil-wetting will hardly improve the radar response.

References

BORCHERS, B., HENDRICKX, J. M. H., DAS, B. S. & HONG, S.-H. 2000. Enhancing dielectric contrast between land mines and the soil environment by watering: modeling, design, and experimental results. *In*: DUBEY, A. C., HARVEY, J. F. BROACH, J. T. & DUGAN, R. E. (eds) *Detection and Remediation Technologies for Mines and Minelike Targets V.* Proceedings of the Society of Photo-Optical Instrumentation Engineers, **4038**, 993–1000.

BRUSCHINI, C. & GROS. B. 1997. A survey of current sensor technology research for the detection of landmines. International Workshop on Sustainable Humanitarian Demining, Zagreb, Croatia. 29 Sep. – 1 Oct.

CALVET, J., WIGNERON, J., CHANZY, A. RAJU, S. & LAG-

CV = 10%

Relative Received Signal Level

CV = 20%

Relative Received Signal Level

CV = 30%

Relative Received Signal Level

CV = 40%

Relative Received Signal Level
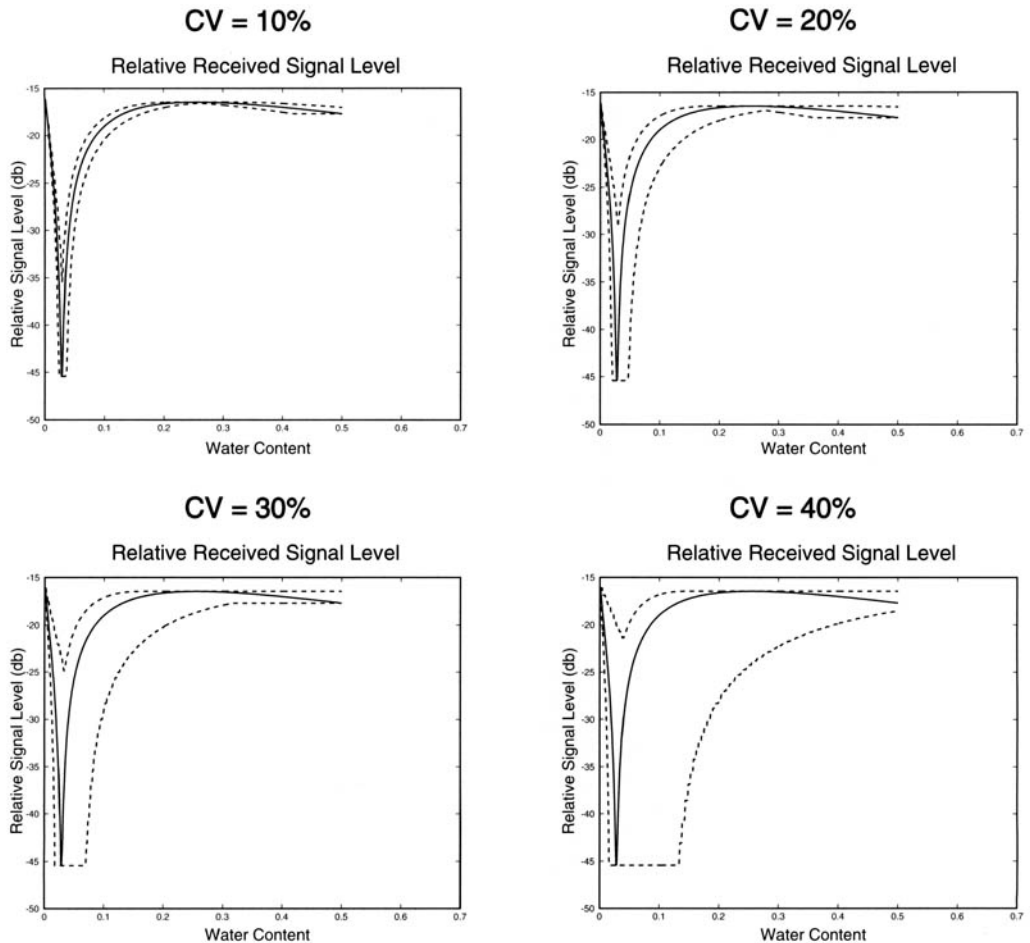
Fig. 7. Predicted losses of the GPR signal in the Dutch sand as a function of water content and the coefficient of variability of water content.

UERRE, L. 1995. Microwave dielectric properties of a silt-loam at high frequencies. *Institute of Electrical and Electronic Engineers Transactions on Geoscience and Remote Sensing,* **GE33**, 634–642.

DOBSON, M. C., ULABY, F. T., HALLIKAINEN, M. T. & EL-RAYES, M. A. 1985. Microwave dielectric behavior of wet soil. Part II: Dielectric mixing models. *Institute of Electrical and Electronic Engineers Transactions on Geoscience and Remote Sensing,* **GE23**, 35–46.

HALLIKAINEN, M. T., ULABY, F. T., DOBSON, M. C. & EL-RAYES, M. A. 1985. Microwave dielectric behavior of wet soil. Part I: Empirical models and experimental observations. *Institute of Electrical and Electronic Engineers Transactions on Geoscience and Remote Sensing,* **GE23**, 25–34.

HENDRICKX, J. M. H. 1990. Determination of hydraulic soil properties. *In:* ANDERSON, M. G. & BURT, T. P. (eds) *Process Studies in Hillslope Hydrology.* John Wiley & Sons, New York, 43–92.

HENDRICKX, J. M. H. & FLURY, M. 2001. Uniform and preferential flow mechanisms in the vadose zone. *In:* FEARY, D. A. (ed.) *Conceptual Models of Flow and Transport in the Fractured Vadose Zone.* National Research Council, National Academy Press, Washington, D.C., 149–187.

HENDRICKX, J. M. H. & WALKER, G. 1997. Recharge from precipitation. *In:* Simmers, I. (ed.) *Recharge of Phreatic Aquifers in (Semi)-Arid Areas.* Balkema, Rotterdam, 19–114.

HENDRICKX, J. M. H., WIERENGA, P. J. & NASH, M. S. 1990. Variability of soil water tension and soil water content. *Agricultural Water Management,* **18**, 135–148.

HENDRICKX, J. M. H., BORCHERS, B., WOOLSLAYER, J., DEKKER, L. W., RITSEMA, C. & PATON, S. 2001. Spatial variability of dielectric properties in field soils. *In:* DUBEY, A. C., HARVEY, J. F., BROACH, J. T. & V. GEORGE, V. (eds) *Detection and Remediation Technologies for Mines and Minelike Targets VI,* Proceedings of the Society of Photo-Optical Instrumentation Engineers, **4394**, 398–408.

CV = 10%

Relative Received Signal Level

CV = 20%

Relative Received Signal Level

CV = 30%

Relative Received Signal Level

CV = 40%

Relative Received Signal Level
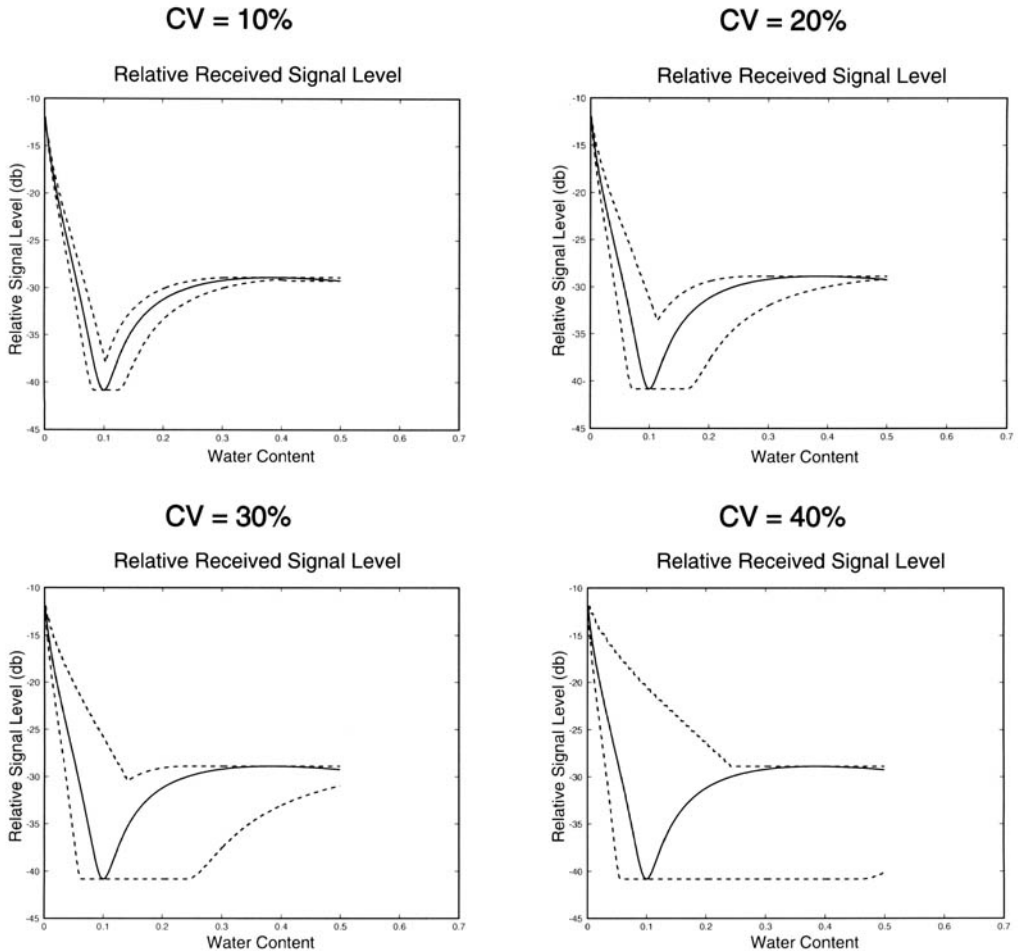
Fig. 8. Predicted losses of the GPR signal in the Panamanian clay soil as a function of water content and the coefficient of variability of water content.

HONG, S.-H., T. MILLER, T., TOBIN, H., BORCHERS, B., HENDRICKX, J. M. H., LENSEN, H., SCHWERING, P. & BAERTLEIN, B. 2001. Impact of soil water content on landmine detection using radar and thermal infrared sensors. *In*: DUBEY, A. C., HARVEY, J. F., BROACH, J. T. & GEORGE, V. (eds) *Detection and Remediation Technologies for Mines and Minelike Targets VI*. Proceedings of the Society of Photo-Optical Instrumentation Engineers, **4394**, 409–416.

HOEKSTRA, P. & DELANEY, A. 1974. Dielectric properties of soils at UHF and microwave frequencies. *Journal of Geophysical Research*, **79**, 1699–1708.

NIELSEN, D. R., BIGGAR, J. W. & EHR, K. T. 1973. Spatial variability of field-measured soil-water properties. *Hilgardia*, **42**, 215–259.

PECK, A. J. 1983. Field variability of soil physical processes. *In*: HILLEL, D. I. (ed.) *Advances in Irrigation*. Academic Press, New York, Vol. 2, 189–221.

PEPLINSKI, N. R., ULABY, R. F. T. & DOBSON. M. C.. 1995. Dielectric properties of soils in the 0.3–1.3GHz range. *Institute of Electrical and Electronic Engineers Transactions on Geoscience and Remote Sensing,* **GE33**, 803–807.

ROUHI, A. M. 1997. Land mines: horrors begging for solutions. *Chemical & Engineering News*, 10 March, **75(10)**, 14–22.

SIMUNEK, S., HENDRICKX, J. M. H. & BORCHERS, B. 2001. Modeling transient temperature distributions around landmines in homogeneous bare soils. *In*: DUBEY, A. C., HARVEY, J. F., BROACH, J. T. & GEORGE, V. (eds) *Detection and Remediation Technologies for Mines and Minelike Targets VI*. Proceedings of the Society of Photo-Optical Instrumentation Engineers, **4394**, 387–397.

STRADA, G. 1996. The horror of land mines. *Scientific American,* May, 40–45.

TOPP, G. C., DAVIS, J. L. & ANNAN, A. P. 1980. Electromagnetic determination of soil water content: measurements in coaxial transmission lines. *Water Resources Research,* **16**, 574–582.

VAN WIJK, W. R. (ed.). 1963. *Physics of Plant Environment.* North-Holland Publ., Amsterdam.

WANG, J. R. & SCHMUGGE, T. J. 1980. An empirical model for the complex dielectric permittivity of soils as a function of water content. *Institute of Electrical and Electronic Engineers Transactions on Geoscience and Remote Sensing,* **GE18**, 288–295.

Monitoring sediment infilling at the Ship Creek Reservoir, Fort Richardson, Alaska, using GPR

LEWIS E. HUNTER[1,2], MICHAEL G. FERRICK[1] & CHARLES M. COLLINS[3]

[1]*Engineer Research and Development Center, Cold Regions Research and Engineering Laboratory, 72 Lyme Road, Hanover, New Hampshire 03755, USA*

[2]*Present address: US Army Corps of Engineers, Sacramento, CA 95814, USA*

[3]*Engineer Research and Development Center, Cold Regions Research and Engineering Laboratory, Building 7040, Fort Wainwright, Alaska 99703, USA*

Abstract: The Ship Creek Reservoir serves as the municipal water supply for Fort Richardson, Elmendorf Air Force Base, and Anchorage, the largest city in Alaska. The reservoir is located at the base of a ~4.8 km-long canyon along the flanks of the Chugach Mountains, where it is fed by a 234 km^2 unglaciated drainage basin. High sediment production within the watershed results in rapid infilling of the reservoir and a need for periodic dredging. During March 2001, we conducted a ground penetrating radar (GPR) survey of the reservoir to document the current state of sedimentation and to evaluate sediment trap designs. These data are presented here as a case study in which the utility of GPR for evaluating sediment infilling in a shallow reservoir is evaluated

The survey was conducted from a 45 cm-thick ice cover in the lower reservoir that thinned to about 6 cm at a distance of 220 m above the dam. A total of 49 radar profiles were collected from the ice cover and an additional 10 profiles were collected on a gravel bar in the upper parts of the reservoir. Water depth near the dam was about 6 m and sediment in that reach forms a blanket deposit. More hummocky and asymmetric bed topography was found away from the dam, apparently controlled by palaeochannel geometry and bedrock sills. GPR profiles collected on the gravel bar document a sedimentary wedge that thickens downvalley and toward the southern edge of the reservoir, apparently the palaeothalweg of Ship Creek. Transverse profiles across the bar indicate that an average of about 2 m of sediment can be removed across this reach, with 3 m or more being available adjacent to the active channel. This survey indicates that infilling of the entire reservoir had reached a level approaching that of the pre-1995 dredging. Analysis of sediment-yield data and basin geometry showed that a weir built across the reservoir approximately 215 m from the dam would produce a trap capable of storing 60% to 70% of that currently held in the reservoir. Sediment trapped within this portion can be excavated using standard machinery, providing a more cost-effective alternative to periodic dredging.

Ship Creek is one of the most economically important streams in Alaska because of its use by three power plants and the Anchorage and Fort Richardson water-treatment plants, and because it is the principal source of recharge to the Ship Creek aquifer (Updike *et al.* 1984). The upper creek flows northwestward and then westward through Chugach State Park and, just prior to leaving the mountains, it flows through a steep and narrow canyon for 4.8 km. Ship Creek Dam and Reservoir are located near the foot of this canyon where the drainage area is 234 km^2 (Fig. 1). Relatively steep gradients in the Ship Creek basin and channel, combined with easily eroded metasediments of the Chugach terrain (Plafker *et al.* 1994) and periodic high flows produce and effectively transport large sediment volumes.

The US Army Cold Regions Research and Engineering Laboratory (CRREL) conducted a study to assess the quantities of sediment being transported by Ship Creek and to develop cost-effective methods for alleviating problems caused by deposition of these sediments in the reservoir. Sediment build-up progressively reduces the water-storage capacity of the reservoir. This sedimentation has required periodic dredging in order to maintain the water-supply function of the reservoir. As part of this study, we conducted a ground penetrating radar (GPR) study of the reservoir in March 2001. The goal of this investigation was to document the current state of sediment infilling, to conduct an evaluation to select a site for weir construction for trapping sediment in the shallow upper reach of the reservoir, and to evaluate the
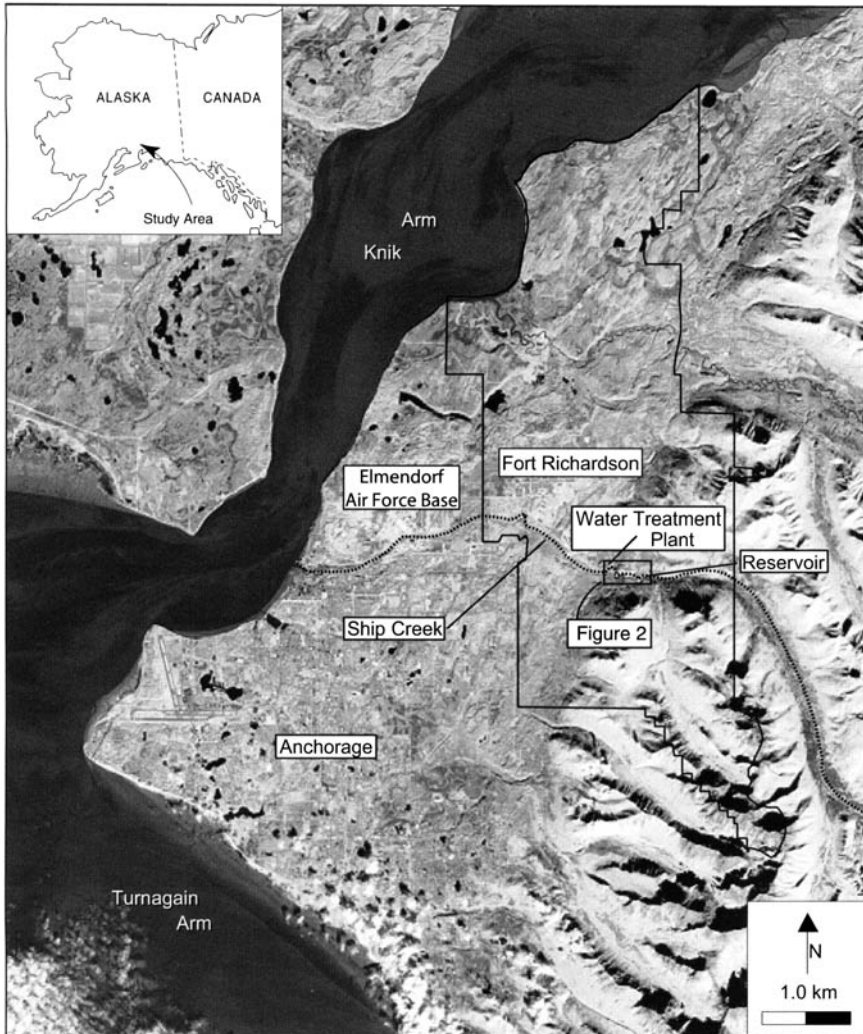
Fig. 1. Ship Creek location map showing Anchorage, Fort Richardson and Ship Creek Dam and Reservoir. Inset shows location of study area (see Fig. 2).

thickness of gravel bars in the upper reach in order to determine sediment storage and dredging capacity. The GPR investigations and their relevance are described in this paper.

Study area

Ship Creek drains an unglaciated basin of about 234 km² with forests accounting for 13%; lakes and ponds cover another 1% (Jones & Fahl 1994). The Ship Creek Dam and Reservoir are near the base of the Chugach Mountains (Figs 1 & 2). The main channel is 31 km long with an average slope of 0.0225, and the mean basin elevation is 945 m (Jones & Fahl 1994). A single US Geological Sur-

vey (USGS) gauging station is located on Ship Creek about 244 m downstream of Ship Creek Dam. The station record begins in 1947 and covers more than 50 years. The mean minimum January temperature in the basin is −14°C, cold enough for significant river-ice growth during the winter. Broad high-flow periods are typical in the spring of most years, while narrow and well-defined peaks associated with rainfall events can occur at any time from June through September. Sharp flow recessions are typical of the fall transition back to winter low-flow conditions. The highest recorded daily mean discharge at the station was 51.3 m³/s on 27 August 1989, with a maximum instantaneous discharge of 52.7 m³/s on 21 June 1949. Hydrolog-
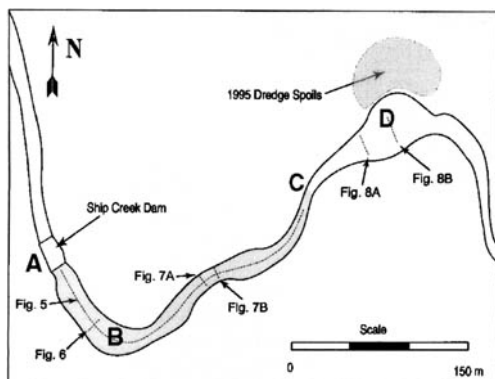
Fig. 2. Detailed map of Ship Creek Dam, Reservoir, access road, and vicinity. Letters A–D indicate locations where photographs shown in Figure 3 were taken.

ical data indicate that sediment transport in Ship Creek increases significantly at flows above 20 m³/s, causing a variable supply in different years that is related to flow.

The Ship Creek Dam is a 15.2 m-high concrete structure built in 1952 by the US Army Corps of Engineers (Figs 1 & 3). Water depths are generally shallow (<8 m) in this narrow valley, where widths range from 15 m to ~30 m. The reservoir extends for nearly 500 m upstream of the dam.

Methods

A GPR survey was conducted using a pulseEKKO 100A radar system mounted on a sled with an odometer wheel (Fig. 4). Test surveys conducted by A. J. Delaney (unpublished data) demonstrated that water in the reservoir was sufficiently shallow to allow a successful GPR survey using 100 MHz antennae. Radar performance was evaluated using the radar range equation of Annan and Davis (1977) and Davis and Annan (1989). Attenuation (α) was calculated by:

$$\alpha = 1.64\sigma/K^{1/2}$$

where conductivity is 8.13 + 0.6 mS/m, based on the average of ten field measurements and K is the dielectric constant (80 for fresh water; Davis & Annan 1989). This calculation yielded an attenuation rate of 1.5 dB/m. The radar-range equation assumes a system performance of about 150 dB, with about 36 dB being lost within the electronics, leaving an effective dynamic range of 114 dB (Sensors and Software 1996). In the ice-covered lacustrine environment, we can expect reflection coefficient losses of 15 dB at the sediment–water interface, assuming a dielectric constant of 36 (Davis & Annan 1989) and 3.5 dB for each time the radar wave penetrated the ice–water interface (Annan 2000). Using these numbers, the GPR should be able to detect the reservoir floor in water
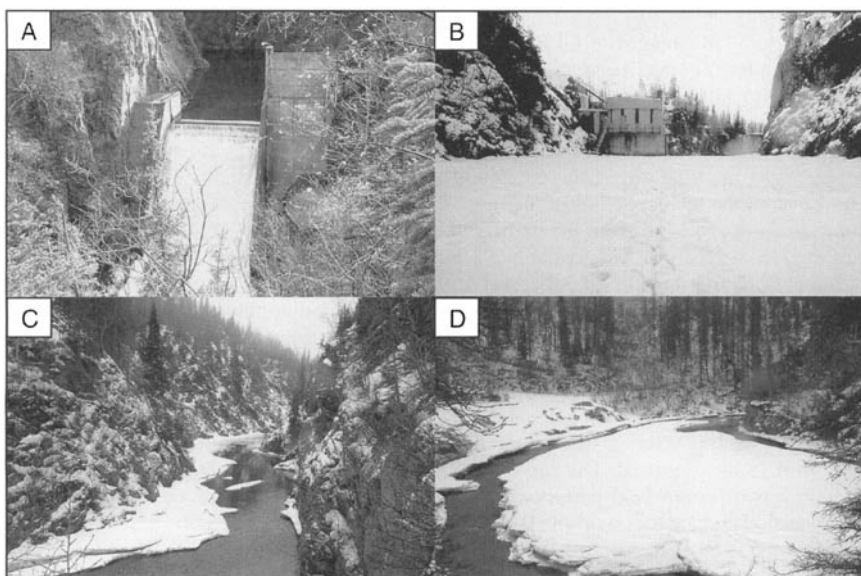
Fig. 3. Ship Creek Reservoir: 15.2 m-high concrete gravity dam (**a**); dam building with observation deck from ice-covered reservoir (**b**); southwestern view of upper reach of reservoir showing narrow, bedrock valley (**c**); and northeastern view of upper reach of reservoir showing sediment storage in large gravel bar (**d**).
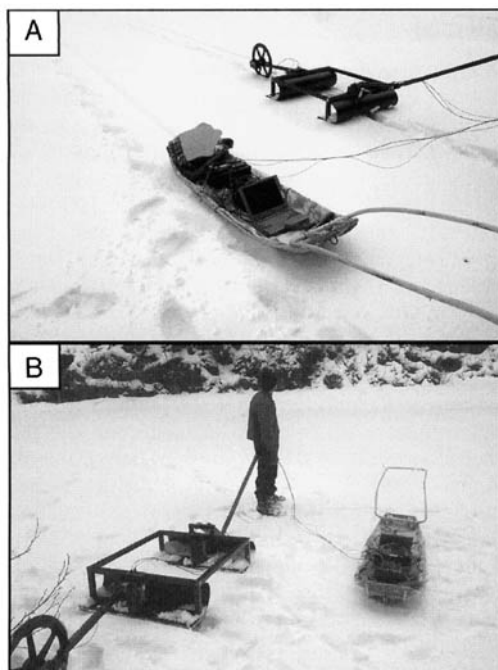
Fig. 4. Sleds with the pulseEKKO 100A digital GPR (**a**) and antennae with odometer wheel (**b**).

up to 7 m or 8 m deep. Other studies have shown that GPR is capable of profiling in fresh water to depths in excess of 20 m in less conductive water of about 1–5 mS/m (Sellmann *et al.* 1992; Moorman & Michel 1997).

One of the primary advantages of GPR surveys over acoustic sounding, as has been done on the reservoir previously, is that it can be carried out efficiently over ice. The ice forms a stable reference platform on which straight transects can be run and repeated. At the time of our survey, nearly 45 cm of ice covered the lower reaches of the reservoir, thinning to 6 cm at 214 m from the dam. The elevation of the ice surface was 162.8 m above sea level, measured from the floor of the observation deck on the dam building. This is the same reference point used by previous bathymetric surveys.

Radar profiles were collected using both 50 MHz and 100 MHz antennae. The 50 MHz profiles were collected with a 2 m spacing between antennae and a 0.5 m step size. At 100 MHz, a spacing of 1 m and step size of 0.25 m were used. The survey was conducted with a two-person field party, one pulling the antennae sled and another working the electronics on a second sled. The control unit, computer and 12 V battery were mounted in a sled and dragged across the ice. A total of 34 transverse profiles, spaced every 8 m, were run with 100 MHz antennae and another 14 transverse profiles were

run at 16 m spacing with the 50 MHz antennas. Two longitudinal profiles, one at each frequency, were run from the edge of open water 224 m away from the dam to within 15 m of the dam. These data were gained using SEC gain with a maximum of 10, an attenuation of 1 and a start gain value of 1. No other processing was required.

Results

Longitudinal profiles run along the centre axis of the reservoir extended for 209 m from the edge of the ice to 15 m from the dam. Data collected using the 100 MHz and 50 MHz antennae are shown in Figure 5. Comparison of these profiles shows that both frequencies perform well at the depths encountered in the reservoir. The 100 MHz profile shows finer detail, indicating higher resolution, but at depths below 3.5 m the bottom reflection begins to fade. The 50 MHz profile is characterized by high-amplitude reflections at all depths. Davis and Annan (1989) show that such behaviour is a function of two factors: (1) as the frequency increases, the attenuation also increases; and (2) at 50 MHz the antenna surface area is twice that of the 100 MHz antennae, resulting in an increased system performance of a factor of two.

Maximum water depth occurs adjacent to the dam, being around 6 m at 15 m from the dam and increasing rapidly toward the dam. The increased water depth probably indicates dredging around one of the intakes, conducted as part of a dam evaluation in the late 1990s. Transverse profiles collected more than 24 m from the dam but within the first bend of the reservoir indicate a smooth sediment cover on the reservoir floor (Fig. 6*b*). About 90 m upstream of the dam, the reservoir floor becomes hummocky and asymmetric. Figure 5 shows a bathymetric high between 175 m and 195 m above the dam. Transverse profiles across this high show the deepest part of the valley is to the east, apparently representing the original channel incised into bedrock (Fig. 7).

An additional 400 m of GPR lines were run on the large longitudinal gravel bar that fills the channel, located between 366 m and 396 m above the dam (Fig. 8). Sediment in the bar thickens in the downstream direction. Four transverse profiles collected on the bar indicate an average thickness of 1.7–2.3 m and a maximum thickness of 3.1 m. These data indicate that the depth of the sediment is greater than that of the last dredging in 1995 (Fig. 9). This result indicates that more sediment is stored in the upper basin than has been accessed by recent dredging operations.

Since 1976, bathymetric surveys have been conducted in the reservoir before and after dredging operations (Fig. 9). The GPR survey conducted in
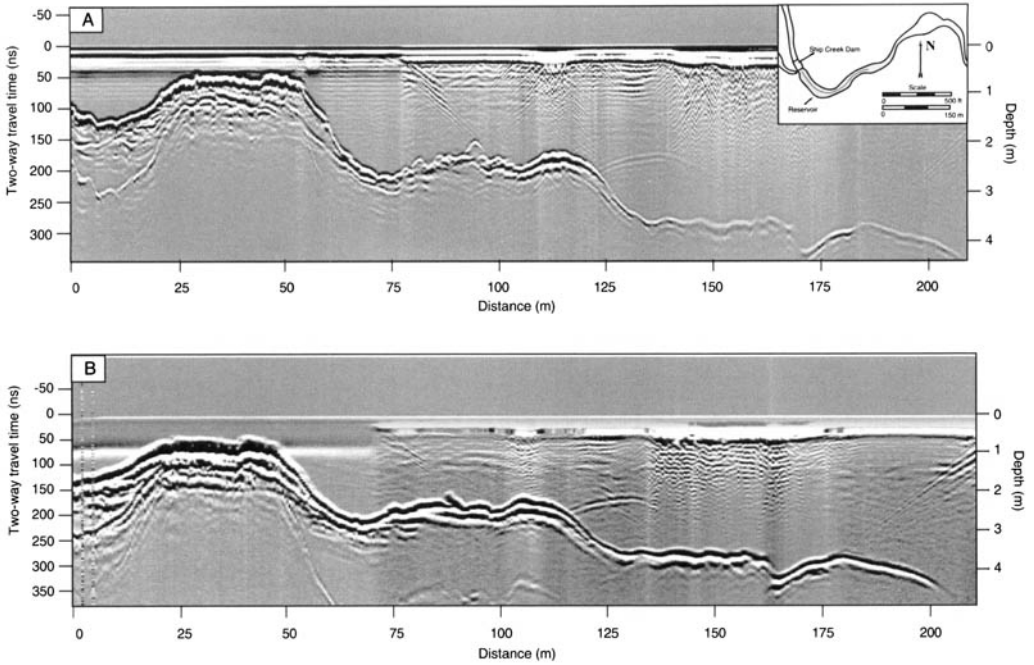
Fig. 5. Longitudinal profiles of Ship Creek Reservoir from east to west ending 15 m upstream of dam: 100 MHz (A) and 50 MHz (B). Inset map shows location of transect line in the reservoir (see also Fig. 2).
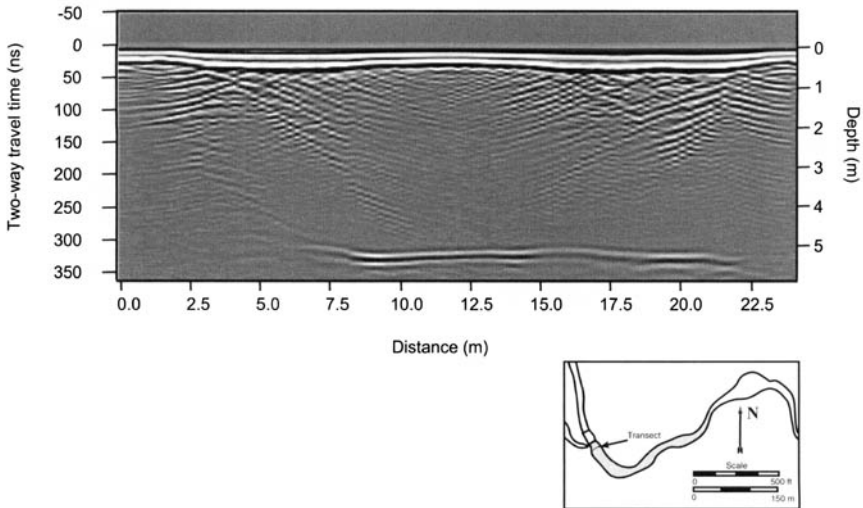
Fig. 6. 100 MHz transverse profile of Ship Creek Reservoir collected 60 m upstream of dam showing smooth, flat floor. Inset map shows location of transect line in the reservoir (see also Fig. 2).

March 2001 repeated 34 of the transect lines in the lower reaches of the reservoir so that current depths could be compared against historic profiles. Average depths for each profile were calculated to define the reservoir-floor profile and for use as quantitative comparisons. These profiles show that infilling has reached or exceeded that of previous pre-dredging levels. Using the width of the reservoir at each transect and the spacing between each transect, we estimated sediment accumulation rates

Fig. 7. 100 MHz transverse profiles across sill: 175 m upstream of dam (A), and 195 m upstream (B). Both profiles show strong reflections representing the reservoir floor. Deeper reflection (~1 m depth below reservoir floor) probably indicates bedrock surface below veneer of sediment. For locations of transect lines see 7A and 7B in Figure 2.
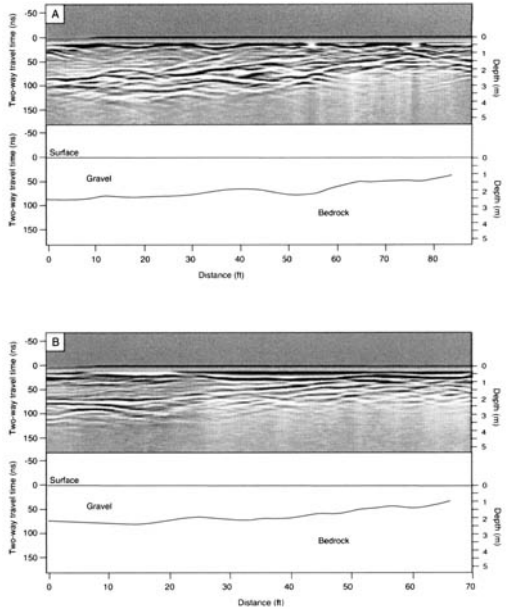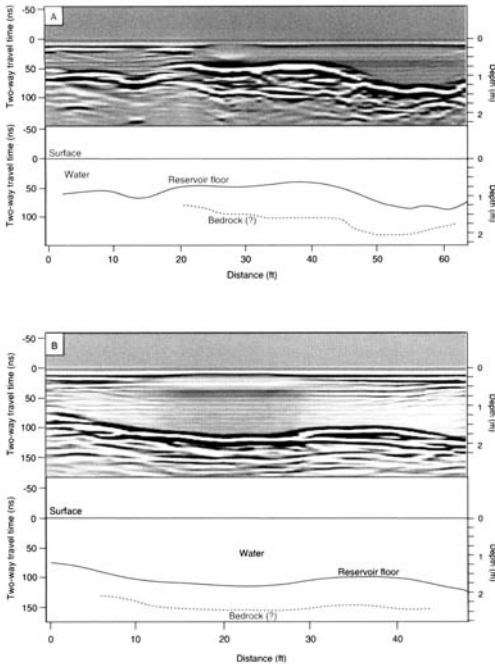
Fig. 8. 100 MHz transverse profiles across gravel bar at 366 m (A) and 396 m (B) upstream of dam. For locations of transect lines see 8A and 8B in Figure 2.

and dredging volumes from pre-dredge and post-dredge survey pairs (Tables 1 & 2). Normalized data indicate that annual accumulation ranges from 61 m³/a/m to 139 m³/a/m. Maximum annual accumulation reached 59 000 m³/a over a 6 a period from 1989 to 1995. The variability shown in these data are caused by river-flow events recorded at the USGS gauging station below the dam, and also the length of coverage of each survey.

Table 2 presents the mean annual accumulation rates and corresponding accumulation rates per unit length in the intervals between dredging. The large quantity of sediment deposited in the upper part of the reservoir since 1995 would balance the total accumulation in Table 2 with the total dredged volume in Table 1. Both the annual accumulation and the annual unit accumulation rates are comparable over all the measurement periods that consider only the lower part of the reservoir (≤260 m from the dam). The mean annual sedimentation rate in this lower reach over 22 a⁻¹ is 50 200 m³/a, corresponding to an annual accumulation per unit length of 70.2 m³/a/m. These values are significantly smaller than those indicated by the 7 a⁻¹ of sedi-

ment accumulation data for the entire 427 m reservoir length. The mean annual accumulation in the entire reservoir over this period is 27 000 m³/a, a mean unit accumulation rate of 85 m³/a/m. The agreement of the 1989–95 period with other measurement periods for the short lower reach confirms the general validity of this long-reach estimate. A sedimentation-rate estimate can also be obtained from the dredge-volume estimates by making the assumption that bed elevations in the reservoir were comparable following the 1976 and 1995 dredging operations. Data are not available to verify this assumption, but the long-term accumulation rate obtained (48 000 m³/a) is comparable to that from the sedimentation rates. Taken together, these data indicate an annual average of about 56 000 m³ of sediment from the upper watershed to the reservoir. Nearly all of this sediment is deposited between late spring and early autumn.

These data indicate that a broad-crested weir could be built in the upper reaches of the reservoir and could trap essentially all bedload and larger-sized fractions of the suspended load. The width-averaged bottom profiles shown in Figure 9 identify two locations for potential weir construction. Site A is located 275 m upstream from the dam and site B is 214 m upstream. We estimate that 64% of the available sediment storage is located upstream of site A and 75% is located upstream of site B. Time intervals between sediment-removal oper-
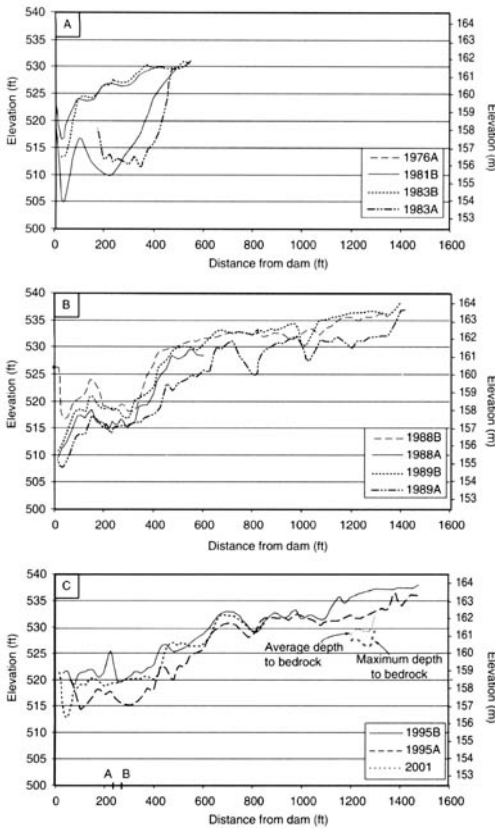
Fig. 9. Average bed elevation along centre line of reservoir with increasing distance above the dam in 1976, 1981 and 1983 (**a**); 1988 and 1989 (**b**); and 1995 and 2001 (**c**). Letters after dates refer to observation periods after (A) or before (B) dredging. The GPR survey is plotted and the 2001 data in (c).

Table 1. *Ship Creek Reservoir dredge volume estimates*

Year	Dredging length (m)	Volume (m³)	Unit volume (m³/m)
1983	183	123093	672
1988	183	61164	336
1989	427	437323	1026
1995	427	287471	675
Total, average	—	144500	677

ations from the trap will be comparable to those of current dredging and will depend on design decisions.

Conclusions

Our study shows that GPR bathymetric surveys can be used to assess the sediment infilling of reservoirs such as that on Ship Creek. Such surveys could be integrated into the annual maintenance of the reservoir in order to document infilling and to monitor basin sediment yield. The survey data presented in this case study were collected over a 3-day period, which included system set-up, testing and breakdown. This study demonstrates that GPR can be a quick and cost-effective method for mapping bathymetry when ice is present on the reservoir. Snow and ice cover simplifies field logistics by providing a smooth and stable surface from which to survey. Maintaining and repeating straight-line transects is also simplified on the ice cover.

Our survey indicates that infilling of the Ship Creek Reservoir has reached a critical level and

Table 2. *Ship Creek Reservoir sedimentation rate estimates*

Period	Years	Survey length (m)	Total accumulation (m³)	Mean annual accumulation (m³/a)	Annual unit accumulation (m³/a/m)
1976–81	5	183	56577	11315	62
1983–88	5	183	73397	14679	80
1988–89	1	427	35934	35934	84
1989–95	6	427	354753	59125	139
1989–95*	6	259	122328	20388	79
1995–01	6	251	91746	15291	61
Total	23	—	611640	26593	—

*Data for lower reach of reservoir.

dredging is required to maintain the water-supply function of the dam. The upper watershed delivers an average sediment supply of about $56\,000\text{m}^3/\text{a}$ to the Ship Creek Reservoir, with greater amounts in high-flow years. Our analyses show that a weir could be built in the upper reaches of the reservoir to produce a trap that would account for 64–75% of the current available storage. The benefit of such a structure would be more cost-effective maintenance of the reservoir by trapping sediment in the upper reaches where road access exists and wheeled vehicles could periodically excavate the trap.

References

ANNAN, A. P. 2000. *Ground Penetrating Radar Workshop Notes*. Sensors and Software, Inc., Mississauga, Ontario.

ANNAN, A. P. & DAVIS, J. L. 1977. Radar range analysis for geological materials. Geological Survey of Canada, Report of Activities Part B, Papers, **77-1B**, 117–124.

DAVIS, J. L. & ANNAN, A. P. 1989. Ground penetrating radar for high-resolution mapping of soil and rock stratigraphy, *Geophysical Prospecting*, **37**, 531–551.

JONES, S. J. & FAHL, C. B. 1994. *Magnitude and Frequency of Floods in Alaska and Conterminous Basins of Canada*. US Geological Survey, Anchorage, Alaska, Water-Resources Investigations Reports, **93–4179**.

MOORMAN, B. J. & MICHEL, F. A. 1997. Bathymetric mapping and sub-bottom profiling through lake ice with ground penetrating radar. *Journal of Palaeolimnology*, **18**, 61–73.

PLAFKER, G., MOORE, J. C. & WINKLER, G. R. 1994. Geology of the southern Alaska margin. *In:* PLAFKER, G. & BERG, H. (eds) *The Geology of Alaska*. Geological Society of America, Boulder, Colorado, The Geology of North America, **G-1**, 389–449.

SENSORS AND SOFTWARE. 1996. *pulseEKKO Radar Range: User's Guide, Version 4.2*. Sensors and Software, Inc., Mississauga, Ontario.

SELLMANN, P. V., DELANEY, A. J. & ARCONE, S. A. 1992. *Sub-bottom surveying in lakes with ground penetrating radar*. US Army Cold Regions Research and Engineering Laboratory, Hanover, New Hampshire, CRREL Report, **92–8**.

UPDIKE, R. G., DEARBORN, L. L., ULERY, C. A. & WEIR, J. L. 1984. *Guide to the Engineering Geology of the Anchorage Area*. Alaska Geological Society, Anchorage, Alaska.

The recognition of barrage and paludal tufa systems by GPR: case studies in the geometry and correlation of Quaternary freshwater carbonates

MARTYN PEDLEY[1,2] & IAN HILL[2]

[1]Department of Geography, University of Hull, Cottingham Road, Hull, HU6 7RX, UK
(e-mail: h.m.pedley@hull.ac.uk)
[2]Department of Geology, University of Leicester, University Road, Leicester, LE1 7RH, UK
(e-mail:iah@Leicester.ac.uk)

Abstract: Tufas provide virtually the only sedimentary and proxy-environmental records within karstic terrains. However, they are difficult to access. Shallow geophysical prospecting techniques, such as resistivity and shallow seismic reflection, fail to define the often complex internal bedform details in tufa deposits and many deposits appear too well lithified to auger-sample. Nevertheless, the application of ground penetrating radar (GPR) permits the recognition of up to five distinct types of radar reflectors that can be directly related to distinct lithologies commonly seen in tufa cores: (1) well-lithified phytoherms produce sharp, sinuous and often complexly truncated bright signals; (2) soft lime muds produce subhorizontal, laterally continuous lower contrast (dull) laminar bedform signals; (3) organic-rich deposits (sapropels and peats) produce poorly focused dull responses, often with internal 'noise'; (4) the tops of bladed and coarse-grained deposits, such as flint gravel, give a strong bright signal; and (5) the associated presence of clay-grade lime silts and muds within the top of gravel beds produces the same top-bed signal as 4, but internal details of the deposit are masked and a remarkably homogeneous dull signal response is typical throughout the lower parts of the deposit.

From these GPR responses it is possible to make meaningful three-dimensional comparisons of the internal geometries of Holocene tufa deposits. Problematic tufa deposits in the valleys of the Derbyshire Wye and the Hampshire Test, UK, are presented to illustrate the universal value of GPR surveying for fresh-water carbonate recognition and for providing key information on valley-bottom resurgence locations.

Tufas are the principal deposits in karstic regions throughout the world. Widespread British examples occur, mainly in valley-bottom sites, in northern Derbyshire, North Yorkshire, Oxfordshire, Hampshire and North Wales (Pentecost 1995; Ford & Pedley 1996).

The term 'tufa' is here used to encompass all ambient temperature fresh-water carbonates (Pedley 1990; Ford & Pedley 1996), regardless of crystallinity, which contain the abundant remains of macrophytes and microphytes (cf. terminology of Pentecost & Viles 1994). The commonly used alternative term 'travertine' is considered inappropriate and we reserve it for microbial and physico-chemical precipitates associated with waters of thermogenic origin (cf. Pentecost & Viles 1994; Pentecost 1995).

Most studied European tufa deposits are Quaternary in age (Griffiths & Pedley 1995; Pentecost 1995), although there does appear to be a 'Late Holocene tufa decline' in development (Goudie et al. 1993). In northerly latitudes, tufa developments appear to be climatically controlled (Pedley et al. 1996) and are associated with interglacial episodes. However, deposition over increasingly longer time spans is common in southern Europe.

Many pre-Holocene deposits are now very fragmentary as the result of continued valley incision and the selective removal of the poorly lithified parts. By contrast, Holocene deposits are frequently intact but remain inadequately described. This is because of the general absence of natural exposures in their valley-bottom sites. Nevertheless, augering tied to geophysical resistivity tech-

niques can yield important data for the softer deposits (Pedley 1993).

Phytoherm constructions, however, are frequently lithified or otherwise altered diagenetically (Golubic 1969). Much of the cement is early-formed physico-chemical and biomediated fringe cement but speleothems are also common (Pedley 1990). All of these render the deposits inaccessible to anything other than rotary drilling. Consequently, very little three-dimensional (3-D) internal detail has been resolved in tufa deposits.

Nevertheless, tufa sites are becoming increasingly important to the non-sedimentologist. This is partly because tufa deposits are virtually the only places to find intercalated organic-rich materials within karst regions. For example, barrage tufa deposits have been shown to contain continuous Holocene pollen records (Vadour 1994; Taylor et al. 1994, 1998; Gedda, et al. 1999). Faunal records (e.g. ostracods and molluscs) are also frequently well preserved and provide good alternative proxy-environmental information (Preece & Robinson 1982; Preece 1991; Preece & Day 1994; Griffiths et al. 1996). Andrews et al. (1993, 1997, 2000) have shown that carefully selected microbial carbonates also preserve important stable isotopic records of environmental change within tufa successions. Finally, the distribution of ancient tufa deposits provides useful clues about palaeo-hydrological parameters, such as water-table elevations and palaeoflow regimes within river systems (e.g. Garcia del Cura et al. 1997).

The stumbling block to accessing these proxy-data repositories, however, is the present lack of knowledge concerning depositional geometries and internal bedforms and how these relate to deposit-base slope angles and resurgence points. Consequently, core-sampling programmes have been difficult to design and the selection of specific augering sites will continue to be speculative until clearly defined depositional models are in place.

Pedley (1992) has proposed a working classification continuum of tufa facies, based on active and extinct European sites. These are embodied into four models (fluvial, lacustrine, perched spring line and paludal). Related but less ambitious schemes are also presented by Pentecost and Viles (1994). The fluvial barrage model (Pedley 1992) is currently the best-defined model, being typically developed in actively flowing river-gorge sites in Europe and North America (Pedley 1992; Ford & Pedley 1996). In this model, downstream, arcuate, transverse barrages or dams of well-cemented, plant-constructed tufa (phytoherms) impound the river and create chains of small pools to large lakes. Unlithified lime muds and fine-grained microdetrital tufas are developed in the standing water bodies and are often associated with organic-rich deposits (sapropels) in pool depocentres. Many pool-bottom deposits are subhorizontally laminated, whereas bedding in the barrage deposits is complex, more typically undulose, sometimes with a downstream-facing buttress zone of inclined tufa sheets.

In contrast, the paludal model (Pedley 1992) is at present the least constrained model. Development generally appears to be restricted to valley-bottom sites where fine granular tufa is precipitated into shallow water bodies (generally less than 10 cm deep). Resedimented tufas also contribute where erosion has washed detritus from other hillside tufa deposits. Paludal tufas commonly show the development of microherms (small cushion-shaped mounds of microbial origin) and phytoherm cushions (generally a grass or mossy tussock). The supply of calcium-enriched waters to paludal deposits is generally considered to be from line-sourced springs (often erosion-truncated aquifers, and faults).

In order significantly to improve the resolution of the models presented in Pedley (1992), a number of sites have been investigated in the past 6 years by means of ground penetrating radar (GPR) (e.g. Pedley et al. 2000). GPR is non-invasive and the only method available to rapidly obtain 3-D data on bed associations, geometries and interface depths within these highly variable and sometimes strongly lithified deposits.

Tufa deposits from the valley of the River Wye in northern Derbyshire (Fig. 1) and the valley of the River Test in Hampshire (Fig. 2) have been selected in this study to show the value of GPR to the outcrop scale-modelling of fresh-water carbonates. Furthermore, this GPR study has highlighted a new and potentially widespread variation of the paludal model defined in Pedley (1992) that could account for the development of lenticular paludal tufas in other paludal successions (e.g. Tanagro Valley, Italy, Buccino et al. 1978).

Methods

All radar data were recorded using a pulseEKKO 100 radar system owned by the Natural Environment Research Council (NERC) equipment pool. Emphasis was placed on minimizing system noise and coherent noise from the direct-transmission pulse. For this reason, the antennae were always clamped in a frame, which held them a constant distance apart (typically 2 m). The frame was then towed along the survey lines. The antennae were moved step-wise (typically 0.5 m), stopping at each measuring station while multiple (typically 32 or 64) signal pulses were stacked. Positional information was collected with a differential global positioning system (DGPS).
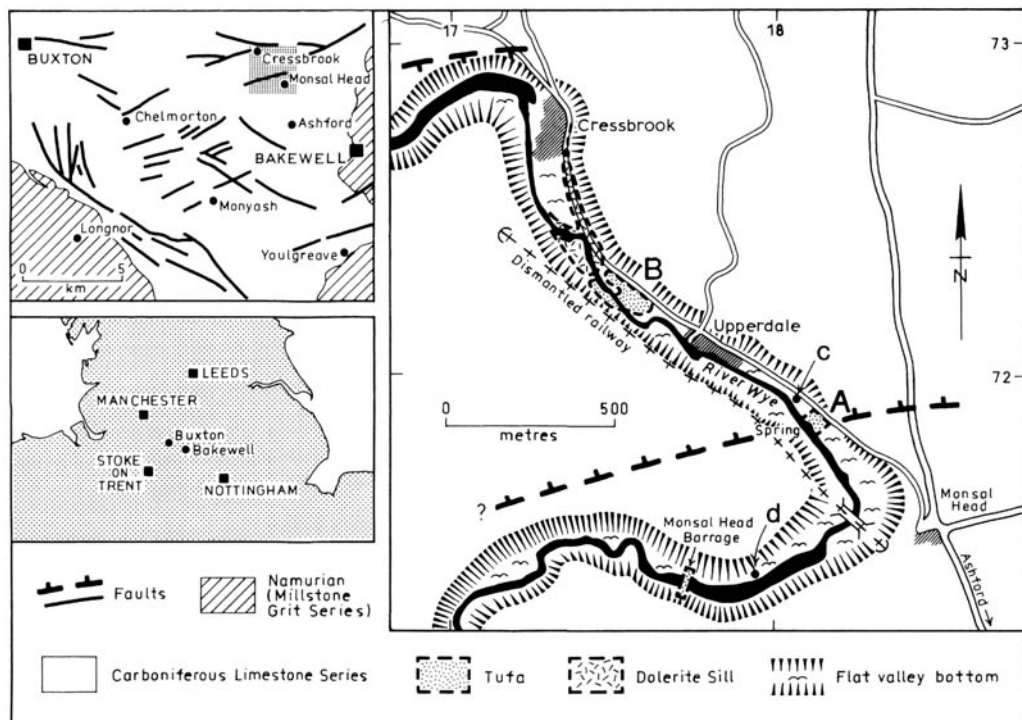
Fig. 1. Locations of sample sites in the gorge valley of the River Wye. The right-hand map shows the surface geology around the Netherdale (A), and Upperdale (B) sites. The Netherdale 1 (c) and Monsal Head (d) auger holes are shown for reference. Note the presence of a major fault which lies immediately underneath 'A' (the Netherdale tufa), and a dolerite sill aquiclude just upstream of 'B' (the Upperdale tufa barrage).

The radar traces were copied to the Leicester Promax seismic data-processing system and re-formatted as pseudo-seismic traces. The detailed processing flow within the Promax system is outlined in Table 1. Stages 1–3 compile the input data traces and the positional information recorded in trace-headers and in observers' logs. Stages 4–6 provide initial signal conditioning. Typically traces from the pulseEKKO system have direct current (DC) shifts larger than the reflected radar pulses. The DC shift of the whole trace was estimated from the average of the trace amplitudes, then subtracted. A relatively broad band-pass filter was then applied and, if necessary, the trace length was truncated or padded before further processing.

The pulseEKKO system relates the trace-sample timing to a prominent point on the direct-transmission pulse as sensed in the receiver antenna, the 'time zero'. In practice, this may vary along the recorded line, so that some traces are misplaced in time. Where present, this effect was corrected using the 'horizon flattening' processor in the Promax system. The transmission pulse dominates the recorded traces. By averaging about 200 adjacent traces, assuming the subsurface contains no near-

parallel surface-tracking horizons, the average of the traces is a good estimate of the transmission pulse alone. This value was then subtracted from each individual trace. The output traces have very reduced amplitudes, but the energy present is free of most transmission-pulse contamination.

Processes 10 and 11 use the Promax facility for correcting for the spherical spreading of the wavefront and for estimating systematic absorption of energy. Gain corrections of this type were performed with care and only as smoothly varying functions, so that variations in trace amplitudes due to subsurface conditions were preserved.

The radar-wave velocity of the subsurface was measured using common mid-point (CMP) surveys at selected points within each small survey area. Typically these were chosen at line intersections. Using the surveyed surface heights and the radar velocity, the traces were static-shifted to place the trace zero times at correct vertical positions relative to the surface topography. This is an important correction where the total depth of the survey section may be less than the topographic variation along the line.

Before final display there was a final filtering
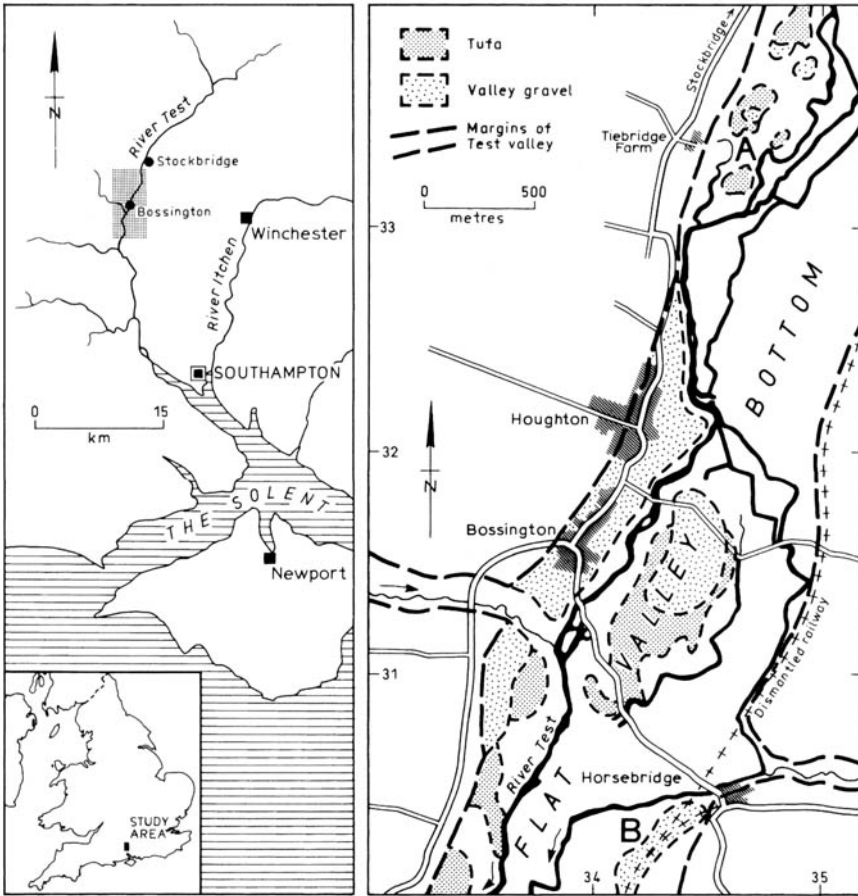
Fig. 2. Locations of the sample sites in the valley of the River Test. The right-hand map shows the surface geology around the Tiebridge Farm (A), and Bossington field (B) sites. Note the presence of valley (flint) gravels in close proximity to the tufa developments. The remaining areas of the flat valley bottom are occupied by sapropel and peat. The surrounding rock (land east and west of the 'flat valley bottom') is Cretaceous Chalk.

effort to further suppress random noise. A good test of the suitability of this processing sequence was provided by the repeated survey of the same lines at different times with different frequency radar antennae. The repeat sections clearly showed that features on the radar sections were repeatable and were features of the subsurface structure rather than artefacts. In many cases we have chosen to repeat survey lines with different radar frequencies, using the trade-off between resolution and depth of penetration to gain maximum resolution at shallow depths, while achieving high penetration using the lowest suitable frequencies (50 MHz).

The processing has revealed one peculiarity that remains unexplained. Numerous CMP measurements have shown the velocity variation with depth at each survey site. If all the velocity values for the tufa deposits are taken, they produce a robust

average velocity of about 70 m μs^{-1}. This radar data has very good borehole control along most lines. It has been found that using the average velocity value for all velocity corrections for all lines produced better ties to the boreholes than using the individual velocity variations for each CMP. This may indicate either that the velocity variation along lines was so rapid that the point-sampling of CMP values was not appropriate for much greater distances than that CMP, or that the errors in determining velocity from CMP measurements were larger than would be expected from numerical analysis of the data. The implications for field-data acquisition are clear. Many CMP measurements are necessary so that either real spatial variations can be identified or a robust average value can be determined.

Information on unlithified sediment lithologies

Table 1. *Processing operations for the GPR data*

Stage	Operation
1	Read in data
2	Input geometry
3	Header load
4	DC removal
5	Band-pass filter
6	Trace length
7	Horizon flattening
8	Static shift
9	Trace mixing
10	Gain analysis
11	True amplitude recovery
12	Apply elevation static
13	Time-depth conversion
14	Migration
15	Coherency filter/trace mix
16	Gain adjustment
17	Frequency filter
18	Plot

was provided on the Wye Valley sites by augering, using a Pionjar percussion auger. Although of limited use in well-cemented sections (e.g. phytoherm barrages), this method successfully penetrated 8 m of 'pool' deposits at the Netherdale site. Hand-augering, using a Dutch auger, provided lithological information in the Test Valley sites. Here, carbonate cementation was not a problem and deposits never exceeded 3 m in thickness.

The tufa deposits

Tufa deposits in the study sites are varied, and include microbial and detrital lime muds, peloids, oncoids, bioconstructed framestones and reworked sand-to-cobble-grade components from any of these. They may occur as single laminae or beds intercalated in organic-rich deposits, typically fibrous peats and sapropels. However, paludal tufas are often developed as massive units with fine, microbially dominated granular textures.

These deposits may be categorized into: (1) autochthonous, and (2) detrital deposits (Ford & Pedley 1996). In order to understand more fully the GPR responses of the deposits, the following additional details are presented:

Autochthonous deposits

The autochthonous deposits are much better cemented than the detrital facies. Consequently, ridges define the aerial extent of the former, whereas the latter may be partially removed by recent fluvial erosion or, at best, are defined by relatively low-lying featureless ground. Neverthe-

less, it is probable that the positive topographic relief of the autochthonous deposits may partly result from shrinkage of the intercalated and lateral organic-rich beds under present-day better-drained regimes (see Pedley *et al.* 2000).

Phytoherm framestones These are *in situ* bioconstructed tufas which are moderately to well lithified, but still preserve macroporosity (for details see Buccino *et al.* 1978; Pedley 1990; Violante *et al.* 1994). They are the commonest lithofacies in fluvial-barrage tufa deposits and generally resist weathering and erosion. In areas of moderate flow (e.g. in fluvial barrages), mosses, liverworts and even semi-aquatic higher plants and bushes can form the primary vegetation framework. This is invariably reinforced by cyclic fringe cements (see details in Pedley 1994), composed of alternations of micrite and sparite (c.f. isopachous fringe cements found in tropical marine reefs, Pedley 1992). The cements progressively build up millimetre–centimetre-thick coats on the vegetation frameworks, the latter decaying within weeks to months. The end-products are very porous, but rigid, cement frameworks, which provide support for further colonization by vegetation and are capable of diverting water flow or even damming entire river courses. These bioconstructions are hereafter referred to as 'phytoherms' (Buccino *et al.* 1978).

Microherms Cyanobacteria and heterotrophic bacteria and diatoms play an important role in the precipitation of microbial (stromatolite) tufa. The term 'microherm' is used in this paper to identify small cushion-shaped examples. They can develop from stabilized oncoids, on tufa intraclasts or even on bare rock outcrops to reach decimetres in diameter. In this study they are generally only extensively developed within fluvial channels with active flow.

Lime mud Lime mud, frequently finely peloidal in thin section, occurs at many of the sites. Much has been generated within microbial biofilms. Some has probably been formed within shallow pool areas by picoplankton microbial biomediation processes, with precipitation either directly onto the pool margins or within the water column (see Thompson 2000 for details of the biomediation process).

Oncoids In the sites examined, oncoids consist of concentrically to imperfectly laminated spheroids, generally less than 10 mm diameter. Where water flow is too slow for overturning, as in the study sites, the oncoids may be free-form in shape. Typically these are poorly laminated and micrite-dominated, with characteristic thrombolitic fabrics.

Where carbonate precipitates have developed around woody objects, and the stems of the fresh-water algae *Chara*, cylindrical oncoids develop. These generally contain a central hollow canal, created by decay of the original plant stem.

Thin tufa bands may also be present in organic-rich deposits. These may take the form of thin wisps of granular and oncoidal particles within an organic-rich fabric. Often thin surficial tufa crusts, developed originally on submerged leaves, are also present.

Detrital deposits

Lime silts and muds This material has the appearance of pale grey, gritty clay, but is readily identifiable as allochthonous carbonate material on account of the presence of reworked allochems (e.g. foraminiferans, mollusc fragments), broken oncoids, tufa intraclasts, flint, chert or limestone debris. These have been generated by local erosion and attrition of parent rocks, whether tufa, Carboniferous limestone or chalk.

Breccias and conglomerates Lithoclastic materials may also be associated with tufas. At the study sites these are either flint or limestone dominated, with individual clasts ranging from 10 mm to cobble-sized. The deposits are often well washed where they occur in the pre-Holocene successions in the basal parts of valley fills.

Organic-rich deposits Gittya to granular fabrics, and even microfelted blackish sapropels, are common in all study sites. Moreover, there appears to be a constant relationship between tufas and black sapropels. Wherever both occur in contact, the sapropels invariably underlie the tufas, both in the River Test sites and in several of the Wye and Lathkill sites (Pedley 1993).

The study sites

Upperdale field

This barrage tufa site was chosen for initial consideration as it is similar in morphology to, but more degraded than, the Raper Lodge barrage described by Pedley (1993). The site is located 200 m upstream of Upperdale hamlet (site 'B' in Fig. 1). The exposed tufa consists of a phytoherm framestone ridge about 2 m high and about 50 m wide (parallel to the valley axis). This is developed immediately downstream of a subhorizontal dolerite sill aquiclude, exposed in a 2 m-high riverside cliff. The tufas are no longer actively precipitating and subrecent channel meandering has cut through the barrage and removed a good deal of the original

structure (see Fig. 3). Surface exposures of the barrage are mainly limited to the riverbank adjacent to line 3. There are no exposures of back-barrier pool deposits.

GPR signatures Three subparallel GPR lines have been run. For lines 1 and 2, the 50 MHz antennae were used, whereas the 200 MHz antennae were employed for line 3 in order to test for finer internal details. Line 1 (Fig. 4) is most instructive as details are least affected by post-depositional fluvial incision and the 50 MHz antennae signals were capable of deeper penetration than the 200 MHz antennae. In the GPR plot, some signal details are partly obscured by hyperbolae from adjacent trees along the northeastern margins of the gorge. Nevertheless, in the 6 m depth available for interpretation, there is a clear distinction between two signal types. Between 110 m and 190 m along the section line are strong, sinuous and high-contrast (bright) returns. Between 180 m and 200 m the trace of the signal consists of low-sinuosity, broader and low-contrast (dull) bands. These also figure at depth between 0 m and 140 m along the section line.

Interpretation The sinuous (bright) signals are proved to be phytoherm tufa in the Upperdale 1 percussion-auger hole and in the hand-auger hole at 170 m along the section line. The sinuous signal appears to be caused by the well-cemented laminar nature of underlying phytoherm facies. Significantly, a major change in build-up style can be recognized at a depth of 3 m at 120 m along line 1. Here, an earlier, vertically aggrading transverse phytoherm barrage, centred at 150 m along the line, changes dramatically in build-up style to a dominantly prograding barrage which oversteps pool deposits formerly lying downstream of the tufa dam.

The dull, low-sinuosity signal responses from pool areas upstream of the barrage tufas are typical of unlithified, fine-grained, lime-mud dominated and clayey tufa materials (see Pedley *et al.* 2000). This is confirmed for the sediments directly underlying the prograding tufa in the Upperdale 1 hand-auger hole, which recorded plastic clays and silts in the lower half of the hole.

Finally, the change in bed inclination and truncations of several prominent markers toward the downstream (SE) end of the profile (between 50 m and 70 m) is caused by later fluvial incision. The resulting channel appears to be infilled by laterally prograding point bar deposits.

Line 2 (Fig. 3c) is not illustrated because very little tufa deposit remains due to post-depositional fluvial erosion. Line 3 (also not illustrated) is mainly within the prograding phytoherm frame-
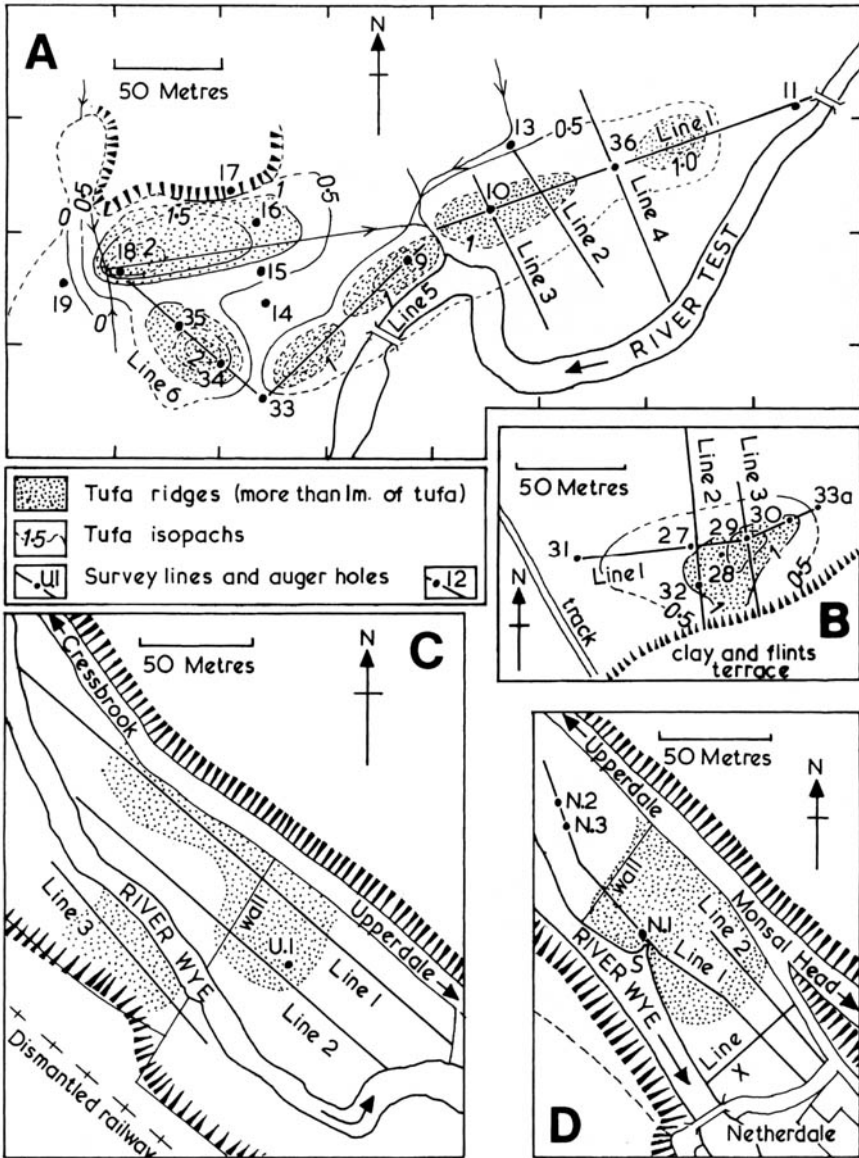
Fig. 3. Details of the study sites to show the position of GPR survey lines and auger holes. (**a**) Tiebridge Farm site with isopachs of tufa thickness indicated. (**b**) Bossington site. (**c**) Upperdale tufa site. (**d**) The Netherdale site. All areas where tufa exceeds 1 m in thickness are marked by a stipple symbol. Logged hand-auger holes are numbered in 3a and b. Logged percussion-auger holes are labelled with 'U' and 'N' numbers in Figures 3c and d. GPR lines are marked in black. Sharp slope changes are marked by lines of black arrowheads pointing in the direction of inclination.

stone facies. Here the barrage core is only 40 m wide, parallel to flow, with a characteristic low-sinuosity dull signal defining thick pool deposits (lime muds or clay-rich detrital sediments) on the upstream (NW) side of the 4.5 m-thick barrage.

In all respects the deposit conforms to the fluvial-barrage model developed from sites at

Caerwys, North Wales, and at Lathkill Valley, Derbyshire, by Pedley (1987, 1993).

Netherdale Farm

This second tufa site is selected to show how GPR can be used to discriminate between tufa models

(a)

(b)
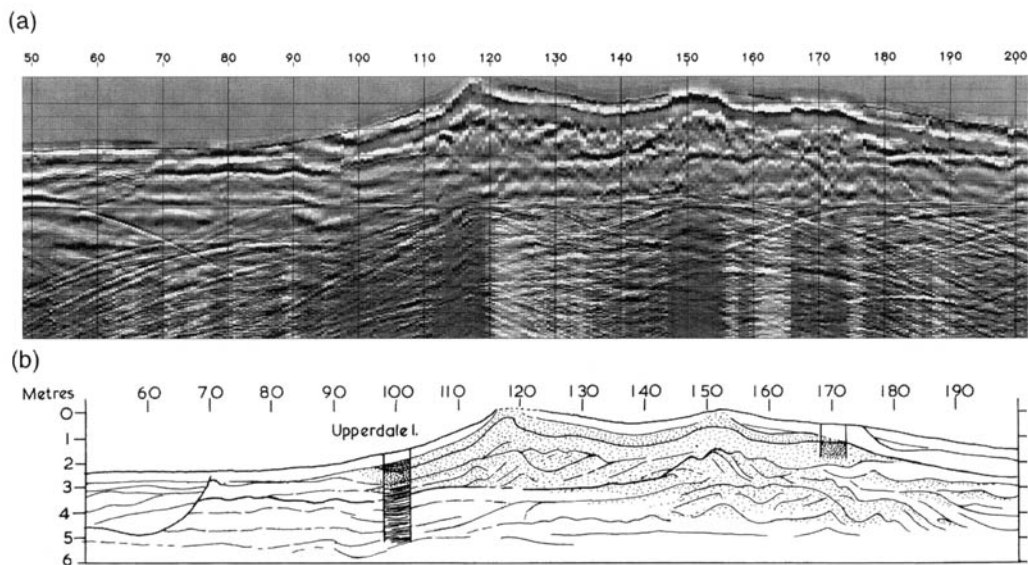
Fig. 4. Top: 50 MHz GPR profile of line 1 at the Upperdale site on the River Wye (distances starts in the southeast). Bottom: The line interpretation. The lithified phytoherm tufas present a strong, bright, sinuous signal in contrast to the more planar signal from the associated unlithified pool sediments. The prograding buttress area of the tufa barrage is well defined by the GPR signals, with evidence of a major change in regime (base marked by a heavier black line) at ~3 m depth at 120 m along the profile. Note also the subrecent fluvial channel at 60 m along the profile line. Fine stipple indicates tufa; areas without ornamentation are pool deposits.

where the topographic expression of the deposit is not diagnostic (The Netherdale site lacks the principal barrage core ridge of the Upperdale site and other barrage tufas examined by GPR in the nearby Lathkill Valley, Pedley *et al.* 2000). It lies in the upper Wye Valley, 600 m downstream of the first site (see Figs 1 and 3), and consists of a broad tufa area with multiple ridges. The tufas are well exposed in several small (10 m diameter) quarried mounds, each up to 1 m higher than the surrounding deposits.

GPR signatures Figures 3*d* and 5 illustrate the rather dog-leg line 1 which attempts to avoid the deeper quarried depressions. All lines were run using the 50 MHz antennae. However, line 2 effectively repeated the details seen in the downstream part of line 1, whereas line X confirmed a strong correlation of the signals within lines 1 and 2.

The GPR traces beneath the elevated areas give bright, moderately sinuous signals. In contrast, the right half of the trace (right-hand margin to the blank signal zone, which marks the position of a stone wall) consists of broad, planar and diffuse (dull) signals very similar to the upstream part of the Upperdale profile. At least one channel feature is present (at 153–183 m along the section); otherwise the signal style is laterally persistent until the

wall, where it changes very suddenly into the undulose, bright signal beneath the exposed tufa areas.

Interpretation At least 9 m of clean tufa is present on site (the base of the Carboniferous limestone was not reached by the GPR pulse). However, the interpretation is aided by percussion-auger hole logs labelled N.1, N.2 and N.3 on Figure 3*d*. Netherdale 1 is sited at an active resurgent point and much of the core consists of cavernous, granular tufas rather than phytoherm framestone. Netherdale 2 shows that some of the tops to the brighter banding are caused by strong responses from siliciclastic sands and angular limestone clasts up to 4 cm diameter. These alternate with *Chara* and oncoid-rich muds, which decrease in organic content toward the top of the profile.

The succession is dominated by agradational bedforms of siliciclastic-free tufa carbonate, despite being adjacent, both upvalley and downvalley, to penecontemporaneous deposits dominated by mud to coarse sand-grade siliciclastics, and organic-rich sediments (the Netherdale 2 core is remarkably similar to the Monsal Head core [Taylor *et al.* 1994] located at 'd' in Fig. 1).

Overall, the tufas beneath the elevated ground do not fit well with the fluvial-barrage model (see Pedley 1990). The internal bedform geometry of
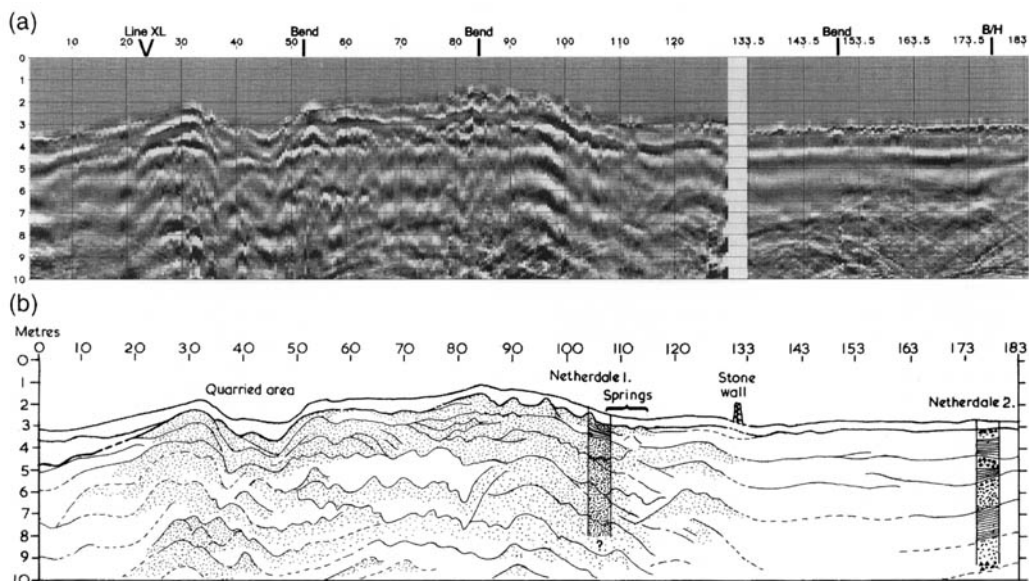
Fig. 5. Top: 50 MHz GPR profile of line 1 at the Netherdale site on the River Wye (distances commence at the southeastern end of the line). Bottom: In the line interpretation the lithified tufas are clearly recognizable from their characteristic high-contrast (bright) signal, which shows that the build-up has been predominantly agradational. The right-hand (NW) end of the profile shows broad signal bands with poor contrast, typical of pool deposits. The Netherdale 2 borehole shows this material to be uncemented tufas and lime muds, with intercalated siliciclastics. Fine stipple indicates tufa; areas without ornamentation indicate pool deposits.

the deposit is too regular and agradational. GPR bands, although bright (well lithified and clearly layered), contain little or no evidence of progradation. Nor is there much phytoherm material exposed in the quarried areas or developed within the cores.

A distinct alternative to the fluvial-barrage model is the paludal model (Pedley 1990). Paludal tufas develop typically under sluggish groundwater flow regimes associated with very low gradients, which fail to deliver a sufficient volume of carbonate-rich water for active phytoherm development. The dominance of siliciclastic muds and sands in the Netherdale 2 percussion-auger hole infers that the only carbonate-rich water supply was via underlying springs (e.g. the active, but currently non-precipitating, present-day springs near the Netherdale 1 borehole. Significantly, a normal fault crosses the valley immediately beneath the Netherdale tufa deposit (see Fig. 1). Consequently, Holocene spring waters could have been sourced from this structure.

In conclusion, we consider that the Netherdale tufa represents a spring-sourced multi-mound build-up. The deposit provides valuable details that subsequently will aid in the interpretation of the Test Valley deposits.

Bossington field

The Bossington field site (Test Valley, Fig 3b) was selected in order to increase further our understanding of the paludal tufa-mound phenomenon and the likely controls on tufa-mound development within a flat valley-bottom site located in a different catchment system to the Netherdale site. The target is a 50 m-diameter hummock lying adjacent to the northern margin of a clay- and flint-dominated terrace at point 'B' in Figure 2. The terrace is situated on the eastern side of a large permanent 'water meadow' some 500 m WSW of Horsebridge. The water meadow contains several other small (50–150 m-diameter) hummocks, each standing up to 1 m above the general land level. These are scattered apparently randomly in the area east of the eastern Test distributary and are referred to in the British Geological Survey of Southampton (sheet 315) by Edwards and Freshney (1987).

GPR signatures (line 1) The Bossington field surveys were carried out initially using the 100 MHz antenna. Subsequently, the 200 MHz antenna was used exclusively as it proved to give more detailed signals. The mound was surveyed along three lines

(Fig. 3b), all amply provided with lithostratigraphic control via hand-augering.

The 200 MHz survey is presented and interpreted in Figure 6. The characteristic bright and highly sinuous tufa signal is the easiest to recognize. GPR signals beneath the tufa are irregular and 'fuzzy' and generally indicate a transitional contact with the base of the tufas. Some internal irregular banding is recognizable in this subtufa layer. The clearest bright response from the subsurface came directly from a bright reflector lying at about 2 m depth. Below this, further broad dull signals appear to be subparallel but are clearly inclined gently westward (towards the line start).

Interpretation Figure 6 clearly shows lateral accretionary development of tufa (stipple symbol) from the thickest (2 m) central point within the mound (hole 29). Also, the considerable detail seen within the subtufa unit with the dull signal was confirmed by augering to conform to a sapropel
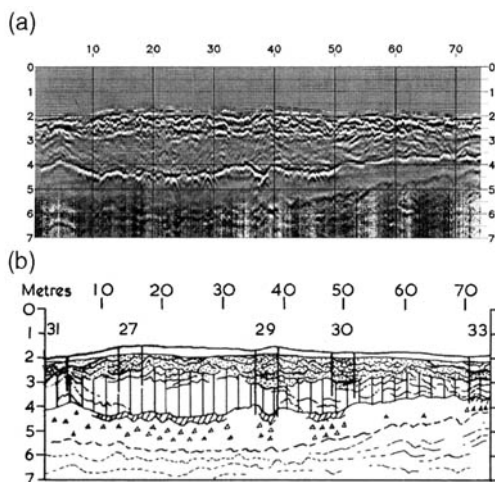
Fig. 6. Top: 200 MHz GPR profile of line 1 (distances start at the western end of the line), which follows the crest of a tufa ridge at the Bossington field site (cf. Fig. 4). The strong reflector at the basal contact of the sapropel is associated with flint gravel in a lime-mud matrix. The basal contact of the tufas is less easy to define, although tufas usually show a sinuous and higher-contrast signal than do the organic-rich deposits. Bottom: GPR reflectors within the tufas indicate that the mounds agrade and accrete laterally from discrete centres located near holes 27 and 29. The absence of a sharp basal contact to the tufas is consistent with their progressive lateral progradation into surrounding sapropel areas. Open triangle, flint gravel; diagonal hachure, detrital lime mud and lime sand; vertical bar, black sapropel; underlying unit without symbol, brown fibrous peat; fine stipple, tufa; area without symbol at base of GPR profile but with bedforms indicated by dashed lines, considered to be bedrock (chalk).

layer containing tufa laminae in the upper parts. An important piece of additional information from the auger holes shows that the single bright reflector at about 2 m deep correlates with the detrital lime-mud impregnated top (diagonal hachure symbol) of thick flint gravels (triangle symbol). The signal response is not continuous throughout the profile. In particular, there are a number of hyperbolae developed from this surface between 20 m and 50 m along the section, which strongly suggests the presence of large, rounded gravel clasts here exposed at the top of the bed. Significantly, there are no internal details from the flint gravels. This may be partly because the detrital lime muds are absorbing much of the GPR signal.

Although not encountered in cores, the westward-inclined dull signals at the base of the profile are interpreted as being caused by the valley-bottom chalk bedrock.

GPR signatures (lines 2 and 3) Figure 7 shows the GPR section for lines 2 and 3 at this site. The sediment responses are identical to those in line 1. Nevertheless, it is clear that there are further sinuous bright signals within the sapropel layer at 2.5 m depth, centred on the 50 m point. This coincides with a loss of signal for the gravel top both here and between 10 m and 18 m in both traces.

Interpretation Line 3 (Fig. 3b) clearly confirms that the essentially horizontally based tufa mound contains elements of lateral progradation from its central area of development near hole 29 (Fig. 6). The improved detail at the base of the tufas also confirms the interdigitating nature of the tufa/sapropel contact. It is concluded that the tufas appear to have been point-sourced from a valley-bottom resurgence in the vicinity of hole 29.

The variable nature of the signal signature defining the top of the flint gravel is noteworthy. Although characteristically strong between 18 m and 4 m along lines 2 and 3, it appears to be totally absent in the rest of the lines. A clue to the cause of the signal absences between 45 m and 60 m in lines 2 and 3 is linked with their coincidental occurrence at the point of greatest projected sapropel thickness. Here, a number of contorted brighter signals are recorded that are atypical of the rather weak internal details generally present within the sapropel. The data argue strongly for the presence of an erosional channel cutting into the flint gravel. We interpret the channel to be filled with particulate material at 2.5–4.5 m depth (perhaps detrital tufa, oncoids or siliciclastics) but covered by sapropel at shallower depths.

The loss of signal at 0–15 m along the section is probably also caused by channel incision into the flint gravels, which removed their clay-
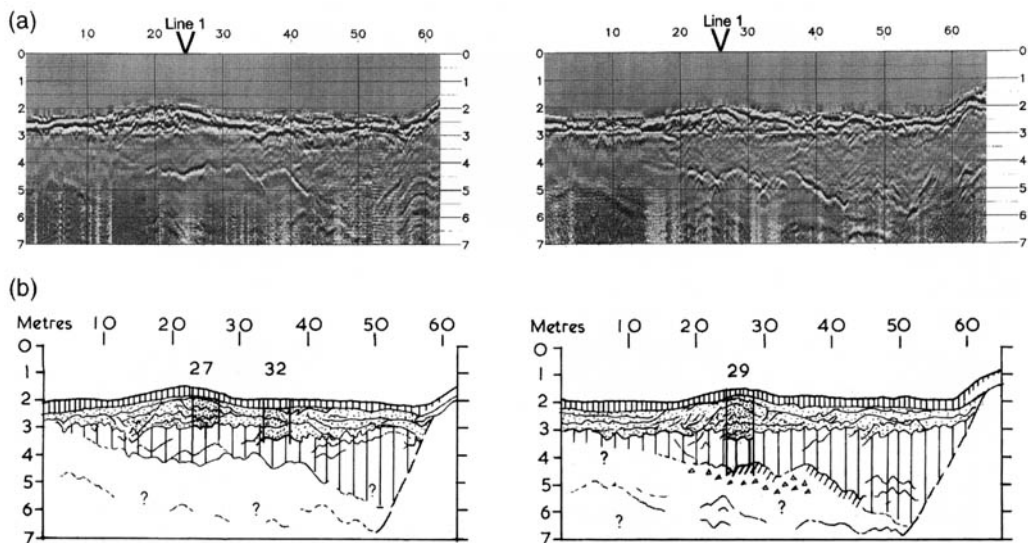
Fig. 7. Left, 200 MHz GPR profile of line 2 at the Bossington field site (distances start at the northern end of the line). Right, 200 MHz GPR profile of line 3 at the Bossington field site (distances start at the northern end of the line). The line interpretations of these subparallel transverse runs provide details of tufa and sapropel distribution adjacent to the 'flint and clay terrace' (rising ground at the southern end of the line, see Fig. 3b). These two lines confirm the laterally accreted, mound build-up of the tufas (mound centre seen where line 1 crosses line 3). Symbols as for Figure 6; in addition, close vertical bars at top of profile are dark brown peaty soil.

impregnated top. Finally, the base of each channel is ill-defined but appears to lie at the projected flint gravel/chalk contact.

The rising ground at the right end of the profile is a clay-and-flints terrace margin. The strong, steeply inclined linear signal between 5 m and 60 m in the profiles is considered to be an indication of the boundary between terrace and Holocene valley-fill succession.

Tiebridge Farm

This larger Test Valley site is located 500 m east of Tiebridge Farm ('A' in Fig. 2). The site was selected in order to resolve the uncertain relationship between resurgence points and tufa-mound developments seen at the Bossington site. It is not directly connected with any clay-with-flints terrace and is centrally positioned within the Test Valley floodplain. It consists of a group of five elongate ridges (each 40–100 m long) standing up to 1 m above the general floodplain. Ridge orientations are generally ENE–WSW and up to 2 m of tufa is developed in each structure (see isopachs in Fig. 3a). 200 MHz GPR lines cover all but the NW deposit. This is the only tufa accumulation without topographic expression and lies adjacent to a clay-and-flints ridge. Hand-auger data is available for all structures (fully logged cores are marked by superimposed columns in the figures, whereas later

spot-test sites are marked by arrows above the profiles).

GPR signatures The signals within line 1 (see Figs 3a & 8) are remarkably similar to the Bossington field site and indicate the presence of identical lithologies. The characteristic bright and undulose tufa signal is well seen in the upper part of the GPR profiles of lines 3 and 6 (Fig. 9a & b). Again, the lower contact of the tufa with sapropel is essentially horizontal. Significantly, however, a bright horizontal band (1.6 m depth at the 30 m point in Figs 8 and 9a) representing the vadose/phreatic contact complicates details.

The Tiebridge Farm site shows greater complexity within the organic-rich bed, including a prominent low-sinuosity band lying between black sapropel and brown deposits. The band is recorded in several auger holes (e.g. hole 36 in Fig. 8) and can be recognized clearly on line 1 as a zigzag trace, 2 m deep at the 80 m point along the section.

The top of the flint gravels (confirmed in auger hole 36) is again clearly defined by a strong horizontal signal. This extends from the 55 m point on line 1, where it is at 2.5 m depth, to the 112 m point, where it lies at about 2 m depth. It is again picked up on the eastern and western ends of the GPR line, being identified in auger holes 10 and 11.
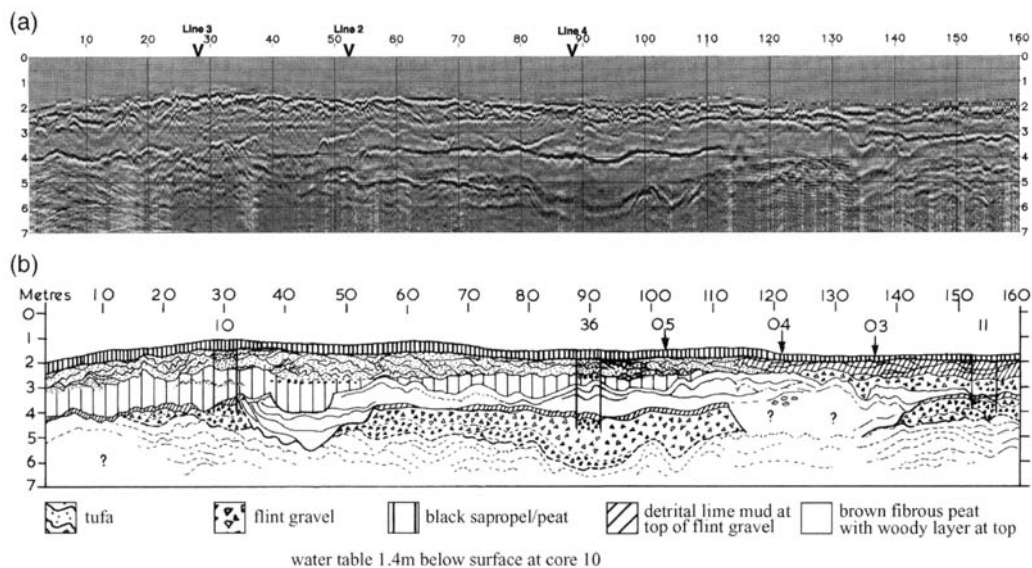
Fig. 8. Top: 200 MHz GPR profile of line 1 at the Tiebridge Farm site (distances start at the western end of the line). Bottom: line interpretation showing the same GPR characteristics as seen in the Bossington field site (Figs 6 & 7). A basal division between black sapropel above and brown fibrous *Sphagnum* peat deposits is marked by a wood layer. Added complexity in the interpretation is provided by two shallow buried fluvial channels which cut out the detrital lime muds and cut down into the flint gravels, possibly as deeply as the chalk bedrock. Note the lateral progradation (westward and eastward) of the tufa mound centred on hole 10. Symbols as for Figures 6 and 7; in addition, diagonal hachures, (inclined towards the right) river alluvium; small arrows with numbers above the profile, shallow auger holes.

Interpretation In general the deposits are thickest in the vicinity of the mound centres and the internal bedforms provide strong confirmation that successive tufa laminae are built out laterally from the mound centres, as in the Bossington site. Also, there is a similar relatively flat base to the tufas. This rules out any possibility that the mound topographies are artefacts produced by post-depositional cambering caused by shrinkage of the underlying organic-rich deposits.

The 'zigzag' bright band is shown in core 36 to be a prominent band of small woody branches. Beneath the woody layer, the organic-rich deposits consist of fibrous, pale to dark brown (?*Sphagnum*) peat.

The absence of the characteristic flint gravels signal centred on 45 m and 125 m along the section is interpreted to be the result of channelling (see Figs 8 & 9).

Line 3 (Fig. 9a) crosses line 1 and confirms that the channel seen at 40 m along line 1 (again seen at 30 m along line 3) has a north–south orientation. Further channels are present at 58 m and at 70 m in line 3 (Fig. 9a). In all cases the channels can be grouped into two sets. The earliest group cuts down to the chalk surface and probably developed early in the Holocene, but after the detrital silts and lime-muds deposition, which ubiquitously caps the basal

flint gravels. The later channels apparently were developed immediately prior to deposition of the black sapropel bed.

The flanks of the tufa mounds appear to interfinger laterally with peaty loam and silt (with gravels at their base) belonging to the present Test River system in the case of line 1 (Fig. 8) between 115 m and 160 m, and line 3 (Fig 9a) between 4 m and 70 m.

Discussion

Barrage model

Upperdale deposit The barrage deposits of the Upperdale site (Fig. 4) conform closely to the existing barrage tufa model. In particular, the GPR profile shows clear downstream progradation, with the development of a well-defined buttress zone (cf. Pedley 1987) forming the downstream side of the phytoherm barrage. Several hiatuses, defined by truncation surfaces within the GPR signature, appear to be similarly placed to those encountered in the nearby Lathkill Valley survey (Hill *et al.* 1998; Pedley *et al.* 2000). They were probably caused by seasonal variations in fluvial discharge and may record short-term environmental change.
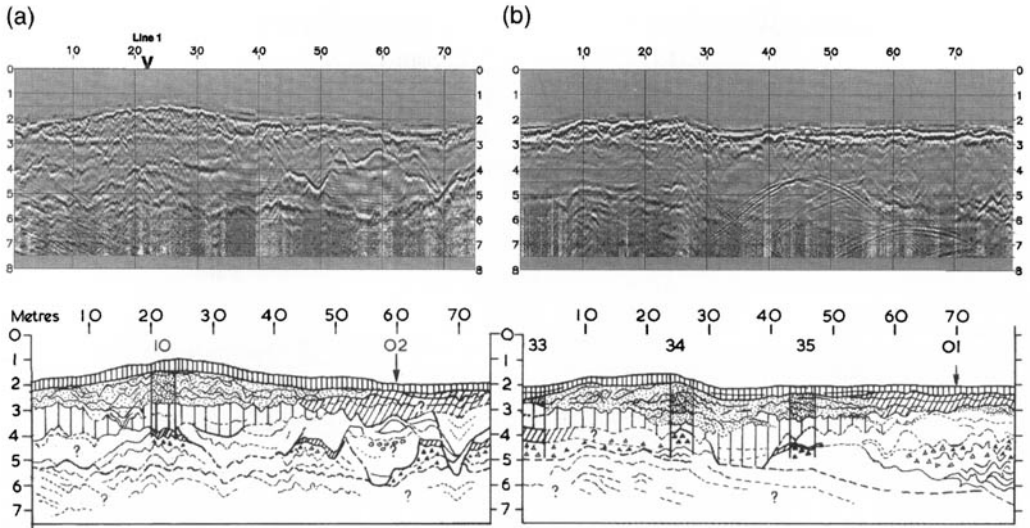
Fig. 9. (a) 200 MHz transverse GPR profile of line 3 at the Tiebridge Farm site (distances start at the northern end of the line). **(b)** 200 MHz transverse GPR profile of line 6 at the Tiebridge Farm site (distances start at the southeastern end of the line). In the interpretations beneath the GPR profiles, both lines are greatly complicated by fluvial channelling which developed before the organic-rich episode. N.B. the lateral progradation of mound fabrics north and south of hole 10 (line 3) confirms details seen in line 1 (Fig. 8) and demonstrates that the tufa mounds are focused about discrete points on the valley floor. The crests of the mounds (near holes 10 and 34) in lines 3 and 6 are closely underlain by flint gravel ridges above chalk. The resurgence points are considered to originate from these. Symbols as for Figures 6, 7 and 8.

Although the pool deposits upstream of the barrage are barely covered by the GPR profile there is ample evidence of further pool deposits downstream of the prograding barrage. These were probably generated immediately upstream of the Monsal Head barrage (see Fig. 1; Taylor *et al.* 1996).

In the case of the Upperdale barrage site, the stimulus for tufa growth was a former, relatively high-volume, line-sourced discharge of carbonate-saturated spring waters issuing from the top of the dolerite sill aquiclude (Fig. 1) that lies immediately upstream of the site.

Freshwater-spring mound tufa model

Netherdale deposit The Netherdale tufa-mound morphology is incompatible with proven barrage tufa dominated valley-bottom sites (see Pedley 1987, 1993; Pedley *et al.* 2000). Phytoherm framestone construction generally is poorly developed, whereas there is a multi-mound complex of laterally linked, vertically agrading microherms. This build-up of very pure calcium carbonate is all the more impressive on account of the dominantly siliciclastic and clay-rich nature of the surrounding 'pool' sediments. (see lithologies in Fig. 10). The Netherdale tufa is also unlike a barrage in terms of its broad spread and absence of downstream-prograding bed geometries (cf. Fig. 4).

The source of the carbonate-enriched waters is almost certainly connected with immediately underlying point-sourced resurgences lying along a fault-line marked on British Geological Survey Sheet 111 (Aitkenhead *et al.* 1985) and shown in Figure 1 at 'A'. Although not currently precipitating calcite, springs continue to issue through the tufas between 110 m and 120 m along line 1 (see Fig. 5). Furthermore, the underlying deposits in the vicinity of the Netherdale 1 borehole (Fig. 10) are honeycombed with small cavities and conduits up to 5 cm diameter. Organic nutrients, for biofilm development, could have been derived from the surrounding shallow-pool or paludal-ponded environment now represented by the flat-lying deposits upstream of the tufa.

Mounds make inefficient dams until they coalesce and, in the Netherdale context, it appears that they never developed beyond a collection of pool-floor irregularities

The general context and construction of the mounds fits well with examples of spring mounds from the Ries Crater, Germany (Arp 1995). The Netherdale example, however, appears to be the first description of a mound tufa developed under ambient temperature, fresh-water conditions (cf. saline tufa mounds in Benson 1994; Arp *et al.* 1998). At Netherdale, water depths were in the order of 1–2 m and the absence of aquatic-moss
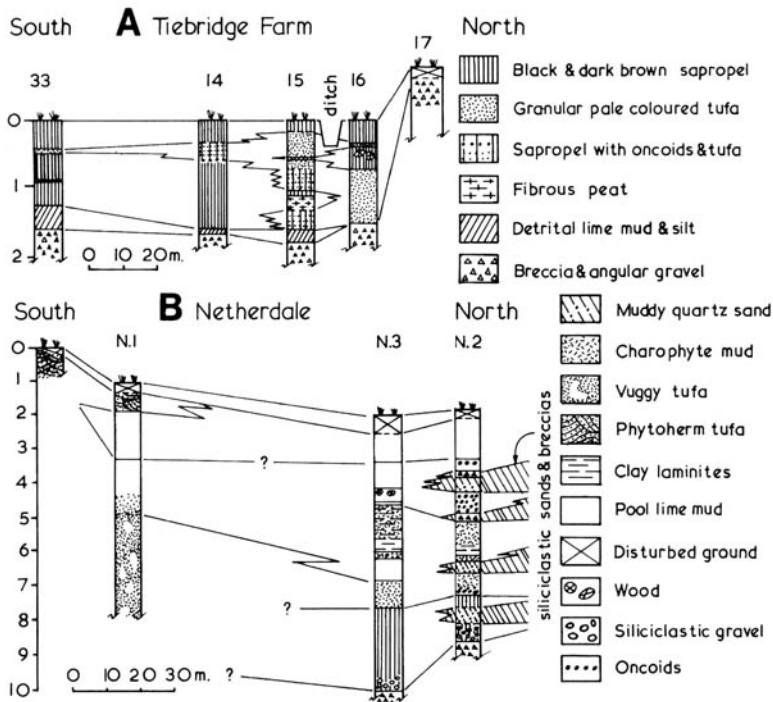
Fig. 10. (**a**) (Upper profile at Tiebridge Farm site). Hand-auger holes showing details of the lithostratigraphy along a north–south line ending in a flint-gravel ridge (black arrowheads on Fig. 3a). Note the complex interfingering of tufas and sapropel. The gravel ridge is the probable line source for lime-rich waters associated with tufa development. The gravel ridge (possibly a relict channel bar) is seen rising gently between 60 m and 80 m in Figure 9b. (**b**) Percussion-auger holes at the Netherdale site (Fig. 3d) showing the lithostratigraphic contrasts between the tufa ridge and areas at the northern end of the profile. It is probably the coarser siliciclastic bands within the northern area that produced the broad subhorizontal banding seen in the GPR trace. By contrast, the lithified phytoherm tufas are impossible to penetrate by percussion auger, except where highly cavernous tufa occurs in association with active spring development at the Netherdale 1 (N.1) borehole.

colonization but abundance of microbial carbonate suggests that water flow was weak. It is unclear why there is an absence of semi-aquatic plants.

The Netherdale site, therefore, is a good example of a previously undescribed fresh-water spring mound tufa, but one possibly developed within a shallow ponded area, well upstream of any phytoherm barrage.

The Test Valley spring mounds The Bossington field and Tiebridge Farm tufa mounds help to refine further the depositional context of newly defined fresh-water spring mound deposits (an important variant of the paludal model, Pedley 1992). There is no indication, from either contained mollusc or ostracod faunas in this part of the Test Valley, that anything other than an open vegetation cover in a groundwater-fed marsh setting existed immediately prior to and during tufa-mound development (Davies 1992, Davies pers comm. 2001; Griffiths pers. comm. 2001). The paludal environments

probably consisted of interconnecting shallow pools partly filled with decomposing organic detritus interspersed with semi-aquatic macrophyte stands of sedge and rushes and reeds. The absence of siliciclastic-filled fluvial channels in the upper parts of the Bossington and Tiebridge GPR lines shows that the tufa mounds were hosted in these shallow pools and developed far from the active fluvial watercourses. Resedimented organic detritus, possibly remobilized during early forest clearances, may have greatly added to the organic pool deposits (Davies 1992: Davies pers. comm. 2001). From the elevation of the mounds we envisage up to 60 cm of standing water in order for development to be maintained in a submerged state.

In this valley-wide, organic-rich paludal scenario the only possible source of calcium carbonate-saturated water for development of the mound tufas was via valley-bottom resurgences. We identified no present-day active lime-precipitating springs

within any of the mounds studied, although non-precipitating springs were active at two nearby mound sites. Cavities similar to those encountered in association with the springs in the Netherdale site were found at hole 10 in the Tiebridge site (Fig. 8). Comparisons between the somewhat disrupted 200 MHz GPR signal signatures at 110–115 m along Netherdale line 1 (the active spring site on the Wye) and areas near the tufa-mound centres in the River Test sites (e.g. Fig. 8, at 30 m on line 1 at Tiebridge) suggest that other spring conduits might be recognizable if higher-resolution GPR traces were to be run.

Equally important in the Test Valley sites is the geographic location of the mound centres. At only one survey site (Fig. 8, between 30 m and 50 m along line 1) does a mound centre lie directly above a fluvial channel complex. Therefore the source of the saturated carbonate-rich waters is unlikely to be from buried channel controlled flow. More significant in the positioning of mound tufas is the proximity of permeable black sapropels and underlying flint gravels close to the base of the tufa mound centres (see Figs 7a, b & 9a, b). Support for the flint gravels being the principal spring aquifer is seen in Figure 10 (top profile). Here, a line of auger holes (for positions see Fig. 3a) running out from a permeable flint gravel ridge shows the local development of paludal tufas. Tufa thicknesses are greatest adjacent to the ridge (probable the source of calcium carbonate-rich water supply) but decrease rapidly southward. A similar scenario is seen downstream of a gravel ridge 500 m east of Bossington village in Figure 2.

Although the tufa mounds could be an important mechanism for initiating tufa barrages they probably never develop into true barrages because the volume of carbonate-saturated waters being delivered via the resurgence points is never sufficient. Indeed, the microherm microbial community undoubtedly developed best under sluggish flow to static water paludal conditions.

Fluvial barrages by contrast appear to develop best where line-sourced carbonate-rich waters are abundantly supplied to an active fluvial system, as in the Upperdale site; River Lathkill sites (Pedley 1993), and the Ruidera pools, Spain (Ordonez et al. 1986; Pedley et al. 1996).

Sediment evolution and age of tufa developments

In both Test and Wye Valleys, a Late Glacial active braided stream is overlain with sharp contact by a meandering fluvial regime. The Test Valley basal flint gravels, according to Edwards and Freshney (1987), are of periglacial origin and developed from large volumes of disintegrated chalk and associated flints which were carried down the Late Glacial Test Valley. They are older than 9010 RCYBP (radiocarbon years before present) (for radiocarbon dates see Neumann & Harris 1995).

Organics close above basal gravels in the Wye Valley, Monsal Head core yielded an uncalibrated radiocarbon date of 9220 RCYBP (Taylor et al. 1994). By implication, therefore, both Test Valley and Wye Valley tufas are Holocene in age.

The initiation of paludal tufa-mound development in the Test Valley appears to have been relatively sudden and developed simultaneously over a wide area. Clearly mound development was triggered by major new spring activity issuing into the organic-rich paludal setting. An uncalibrated radiocarbon date of 6050 ($\pm$90) RCYBP (Neumann & Harris 1995) for the top of the underlying 'oxidized peat' shows that development of the paludal tufa mounds was relatively recent and commenced after the earliest human colonization of the area.

Spring activity (and tufa-mound development) was not necessarily associated with any perceptible shift in the flow regime of the River Test because organic-rich paludal conditions continued in surrounding valley-bottom sites. None of the tufa mounds in either the Wye or the Test Valleys are currently active and tufa-forming activity is now restricted to small stretches of the River Test (e.g. at Bossington Bridge), where surficial microbial microherm encrustation and oncoid developments are visible. The cause of disappearance of active mound-tufa development remains problematic.

Conclusions

This study demonstrates the value of GPR applications to valley-bottom tufa interpretations, although considerable control in the form of auger-hole data is required for precise interpretation. Five lithofacies can be recognized from their distinct radar facies signatures. (1) Tufa signals from moderately well-lithified sites (phytoherm framestones and microbial mound deposits) consist of nested sets of high contrast (bright) sinuous bands, often with intraunit truncations. These clearly display the layered nature of the deposits whether the tufas are paludal or barrage types. (2) In contrast, unlithified lime muds yield poorly contrasting (dull) subhorizontal signals which are easily confused with siliciclastic silts and clays. (3) Oncoidal tufas generally are associated with fluvial channels and were therefore uncommon in this study. Where present they give bright signal responses even if restricted to relatively thin bed developments. (4) Bladed flint gravels give a strong signal from their upper surface, especially where impregnated with lime silts; however, internal fabrics generally are masked. (5) Peats and sapropels provide an irregu-

lar dull signal with considerable local 'noise'. Signal heterogeneities are mainly related to internal woody bands and whole logs.

This GPR study has facilitated a clearer distinction between fluvial-barrage tufas and the newly described valley-bottom (paludal) spring mound tufas. Furthermore, the study has permitted a redefinition of paludal tufas into two distinct types:

1. Line-sourced tufa sheet deposits in which the paludal site is subjected to the seepage of relatively large volumes of carbonate-enriched waters escaping uniformly from aquifers exposed in long sections of valley-margin areas. The tufa sheets resulting from line-sourced seepage may be many metres thick (Pedley *et al.* in press) and are often finely laminated and tabular bedded (e.g. Tanagro Valley, Italy, Buccino *et al.* 1978; El Jardin, Spain, Taylor *et al.* 1998). Typically they contain abundant phytoherm cushions (often grasses, mosses but sometimes reeds, sedges or other semi-aquatics). Ephemeral ponds and palaeosols may also frequently figure in the deposits and organic-rich deposits are invariably associated with line-sourced tufa sheets.

2. Point-sourced mound tufa deposits, a previously undescribed paludal type, develop from slow-flowing, isolated individual springs, sourced from underlying strata in valley-bottom situations. The mounds are discrete, low-amplitude structures and typically consist of flat-bottomed lenses of pure, biomediated calcium carbonate developments. The Test Valley sites clearly indicate that these mounds can develop as lenses of microbially biomediated calcium carbonate in valley sites which otherwise exhibit chemical conditions too hostile for carbonate precipitation. The closest analogy to these are the much large tufa towers in Pyramid Lake, Nevada (Benson *et al.* 1994) and the spring mounds in the Badain Jaran Sand Sea, China (Arp *et al.* 1998). Both examples, however, have developed from carbonate-rich fresh-water springs issuing into hypersaline lakes rather than into fresh-water sapropel-rich swamps.

References

AITKENHEAD, N., CHISHOLM, J. N. & STEVENSON, I. P. 1985. *Geology of the Country around Buxton, Leek and Bakewell*. British Geological Survey Memoirs, Sheet 111, HMSO, London, 168 pp.

ANDREWS, J. E., PEDLEY, H. M. & DENNIS, P. 2000. Palaeoenvironmental records in Holocene Spanish tufas: stable isotope approach in search of reliable climatic archives. *Sedimentology*, **47**, 961–978.

ANDREWS, J. E., RIDING, R. & DENNIS, P. 1993. Stable isotope compositions of Recent freshwater cyanobacterial carbonates from the British Isles: local and regional environmental controls. *Sedimentology*, **40**, 303–314.

ANDREWS, J. E., RIDING, R. & DENNIS, P. 1997. The stable isotope record of environmental and climatic signals in modern terrestrial microbial carbonates from Europe. *Palaeogeography, Palaeoclimatology, Palaeoecology*, **129**, 171–189.

ARP, G. 1995. Lacustrine bioherms, spring mounds, and marginal carbonates of the Ries-Impact-Crater (Miocene, southern Germany). *Facies*, **33**, 35–90.

ARP. G, HOFMANN, J. & REITNER, J. 1998. Microbial fabric formation in spring mounds ('microbialites') of alkaline salt lakes in the Badain Jaran sand sea, PR China. *Palaios*, **13**, 581–592.

BENTON, L. 1994. Carbonate deposition, Pyramid Lake subbasin, Nevada. 1. Sequence of formation and elevational distribution of carbonate deposits (tufas). *Palaeogeography, Palaeoclimatology, Palaeoecology*, **109**, 55–87.

BUCCINO, G., D'ARGENIO, B., FERRERI, V., BRANCACCIO, L., PANICHI, C. & STANZIONE, D. 1978. I travertini della bassa Valle del Tanagrio (Campania): studio geomorphologico, sedimentologico e geochimico. *Bollitino Societa Geologica Italia*, **97**, 617–646.

DAVIES, P. 1992. *Subfossil Mollusca from Holocene Overbank Alluvium and Other Wet Ground Contexts in Wessex*. Ph.D. thesis, Department of History and Archaeology, University of Cardiff.

EDWARDS, R. A. & FRESHNEY, C. 1987. *Geology of the Country around Southampton*. British Geological Survey Memoirs, Sheet 315, HMSO, London, 111 pp.

FORD, T. D. & PEDLEY, H. M. 1996. A review of tufa and travertine deposits of the World. *Earth Science Reviews*, **41**, 117–175.

GARCIA DEL CURA, M., GONZALES-MARTIN, J. A., ORDONEZ, S, & PEDLEY, H. M. 1997. Las Lagunas de Ruidera. *In*: GARCIA REYEGO, J. L. & GONZALES CARDENAS, E. (eds) *Elimentos del Medio Natural en la Provincia de Cuidad Real*. Asociacion de Geographos Espanoles/Universidad de Castille-La Mancha, Cuenca, 253 pp.

GEDDA, B., LEMDAHL, G. & GAILLARD, M. J. 1999. Late-

glacial and Early Holocene environments inferred from a tufa deposit at Fyledalen, Sweden. *Geologiska Foreningen i Stockholm Forhandlingar,* **121**, 33–41.

GLOUBIC, S. 1969. Cyclic and noncyclic mechanisms in the formation of travertine. *Verhandlungen der Internationalen Vereinigung fuer Theoretische und Angewandte Limnologie,* **17**, 956–961.

GOUDIE, A. S., VILES, H. A., & PENTECOST, A. 1993. The Late Holocene tufa decline in Europe. *The Holocene,* **3**, 181–186.

GRIFFITHS, H. I. & PEDLEY, H. M. 1995. Did changes in late last glacial and early Holocene atmospheric CO_2 control rates of tufa precipitation? *The Holocene,* **5**, 283–242.

GRIFFITHS, H. I., PILLIDGE, K. E., HILL, C. J., EVANS, J. G. & LEARNER, M. A. 1996. Ostracod gradients in a calcareous stream: implications for the palaeoecological interpretation of tufas and travertines. *Limnologica,* **26**, 49–61.

HILL, I., PEDLEY, H. M. & DENTON, P. 1998. GPR, GPS and Promax, applied to detailed sedimentary architecture of tufa deposits. *Proceedings Environmental Engineering and Geophysics Society, September.1998, Barcelona,* 433–437.

NEUMANN, H. & HARRIS, C. 1995. The role of carbonate precipitation in the Early Holocene palaeohydrology of a chalkland river valley, southern England. *In:* FRENZEL, B. & VANDENBERGHE, J. (eds) *European River Activity and Climatic Change During the Late Glacial and Early Holocene.* G. Fischer, Stuttgart, 37–50.

ORDONEZ, S., GONZALEZ-MARTIN, J.-A. & GARCIA DEL CURA, M. A. 1986. Sedimentacion carbonatica actual y paraactual en las Lagunas de Ruidera. *Revista de Materiales y Procesos Geologicos,* **4**, 229–255.

PEDLEY, H. M. 1987. The Flandrian (Quaternary) Caerwys tufa, North Wales: An ancient barrage tufa deposit. *Proceedings of the Yorkshire Geological Society,* **46**, 141–152.

PEDLEY, H. M. 1990. Classification and environmental models of cool freshwater tufas. *Sedimentary Geology,* **68**, 143–154.

PEDLEY, H. M. 1992. Freshwater (phytoherm) reefs: the role of biofilms and their bearing on marine reef cementation. *Sedimentary Geology,* **79**, 255–274.

PEDLEY, H. M. 1993. Sedimentology of the late Quaternary barrage tufas in the Wye and Lathkill valleys, north Derbyshire. *Proceedings of the Yorkshire Geological Society,* **49**, 197–206.

PEDLEY, H. M., HILL, I. & DENTON, P. 2000. Three dimensional modelling of a Holocene tufa system in the Lathkill valley, north Derbyshire, using ground penetrating radar. *Sedimentology,* **47**, 721–735.

PEDLEY, H. M. 1994. Prokaryote-microphyte biofilms and tufas: a sedimentological perspective. *Kaupia, Darmstadter Beitrage zur Naturgeschichte,* **4**, 45–60.

PEDLEY, H. M., GONZALEZ-MARTIN, J.-A. ORDONEZ, S. & GARCIA DEL CURA, M. A. (In press) The sedimentology of perched springline and paludal tufas: criteria for recognition, with examples from Guadalajara Province, Spain. *Sedimentology.*

PEDLEY, H. M., ORDONEZ, S., GONZALEZ-MARTIN, .J-A. & GARCIA DEL CURA, M. A. 1996. Does climate control the morphological fabric of freshwater carbonates? A comparative study of Holocene barrage tufas from Spain and Britain. *Palaeogeography, Palaeoclimatology Palaeoecology,* **121**, 239–257.

PENTECOST, A. 1995. The Quaternary travertine deposits of Europe and Asia Minor. *Quaternary Science Reviews,* **14**, 1005–1028.

PENTECOST, A. & VILES, H. A. 1994. A review and reassessment of travertine classification. *Geographie Physique et Quaternaire,* **48**, 305–314.

PREECE, R. C. 1991. Radiocarbon-dated molluscan successions from the Holocene of central Spain. *Journal of Biogeography,* **18**, 409–426.

PREECE, R. C. & DAY, S. P. 1994. Comparison of postglacial molluscan and vegetational successions from a radiocarbon-dated tufa sequence in Oxfordshire. *Journal of Biogeography,* **21**, 463–478.

PREECE R. C. & ROBINSON, J. E. 1982. Molluscan and ostracod faunas from post-glacial tufaceous deposits in County Offaly. *Proceedings of the Royal Irish Academy,* **82B**, 115–131.

TAYLOR. D. M., GRIFFITHS, H. I., PEDLEY, H. M. & PRINCE, I. 1994. Radiocarbon dated Holocene pollen and ostracod sequences from barrage tufa-dammed fluvial systems in the White Peak, Derbyshire. *The Holocene,* **4**, 356–364.

TAYLOR. D. M., PEDLEY, H. M., DAVIES, P. & WRIGHT, M. W. 1998. Pollen and mollusc records for environmental change in central Spain during the Mid- and Late Holocene. *The Holocene,* **8**, 605–612.

THOMPSON, J. B. 2000. Microbial whitings. *In:* RIDING, R. E. & AWRAMIK, S. M. (eds) *Microbial Sediments.* Springer-Verlag, Berlin, Heidelberg, New York, 250–260.

VADOUR, J. 1994. Evolution Holocene des vallée dans le Midi Mediteranée Francais. *Geographie Physique et Quaternaire,* **48**, 315–326.

VIOLANTE, C., FERRIEWR, V., D'ARGENIO, B. & GOLUBIC, S. 1994. Quaternary travertines at Rochetta a Volturno (Isernia, central Italy). Facies analysis and sedimentary model of an organogenic carbonate system. *15th International Association of Sedimentologists Regional Meeting, April 1994, Ischia, Italy, Excursion* **A1**, 2–23.

This page intentionally left blank

The use of vertical radar profiling (VRP) in GPR surveys of ancient sedimentary strata

J. K. PRINGLE, A. R. WESTERMAN, J. D. CLARK, J. A. GUEST, R. J. FERGUSON & A. R. GARDINER

Institute of Petroleum Engineering, Heriot-Watt University, Edinburgh, EH14 4AS, UK (e-mail: jamie.pringle@pet.hw.ac.uk)

Abstract: Vertical radar profiling (VRP) is an application of ground penetrating radar (GPR) technologies that can extract important subsurface information from suitable outcrops. Using standard GPR equipment, a site-specific time-depth calibration can be obtained, along with correlation of observed sedimentological horizons exposed on cliff-faces. These horizons may then be correlated with subsurface reflection events imaged on fixed-offset profiles. Summaries of six GPR study sites, where the VRP technique was used, are detailed. Where possible, CMP and VRP velocities have been compared, and show good correlations. Geochemical analysis of selected sedimentary rocks shows that increasing grain size and quartz mineral percentages generally lead to increased GPR velocities. Reflection events tend to be associated with sandstone/shale boundaries.

Our research has focused on obtaining ground penetrating radar (GPR) datasets on sedimentary analogues of petroleum reservoirs. GPR can provide the three-dimensional (3-D) volumetric information needed to build more realistic reservoir models (Pringle *et al.* 2000, 2003). To achieve this, multiple closely spaced 2-D or, rarely, 3-D fixed-offset GPR profiles are acquired behind well-exposed outcrop cliff sections. GPR information is used to map observed sedimentological features from the outcrop face into the subsurface (Pringle *et al.* 2000, 2003; Corbeanu *et al.* 2001; Szerbiak *et al.* 2001). Digital photogrammetry, surveying information, sedimentary analysis and interpretation provide a control framework within which the GPR dataset is integrated.

In most GPR studies (e.g. Fisher *et al.* 1992), a common-mid-point (CMP) survey is carried out in order to determine an average site velocity and thus allow conversion of 2-D GPR profiles from time to depth. However, vertical radar profiling (VRP) can both measure a direct velocity and correlate observed lithological boundaries in an outcrop cliff-face to subsurface reflection events imaged on GPR profiles and CMPs behind the cliff-face. VRP velocity measurements use direct waves rather than the reflected waves of the normal move-out (NMO) technique described by Fisher *et al.* (1992). Much deeper sedimentary units can therefore be imaged by VRP than by fixed-offset profiling or CMP techniques, because the direct waves are less attenuated than reflected waves. VRP up-going and down-going wavefields are also separable, as in vertical seismic profiling (VSP). Analysing the separated wavefields allows multiple events to be clearly identified and attributed to their generating reflection events (Gal'perin pers. comm. 1987).

Site investigations have been undertaken on sedimentary sequences deposited in fluvial and proximal and distal turbidite environments (see Table 1 for site summaries). Site-specific aims have included mapping shale interbeds in sand-rich turbidite sandstones (Scottish Borders), tracing sinuous turbidite channels (Ireland, see Pringle *et al.* 2003), and mapping intrachannel fill in ancient fluvial channels (Spain). Reflection events have been recognized at depths ranging from less than 1 m to 75 m. Multiple vertical radar profiles (VRPs) were sometimes acquired at the same site, using different dominant-frequency antennae, depending on the fixed-offset profile survey. Results from these investigations are detailed in the results section.

VRP theory

The Russian geophysicist Gal'perin realized that a borehole geophone array would produce a seismic record from which the up-going and down-going seismic wavefields could be easily separated (Fig. 1a) (Westerman pers. comm. 1987). This became known as vertical seismic profiling (VSP). VSP has the benefit of greatly increasing penetration depths

Table 1. *Summary of vertical radar profiling (VRP) study sites*

Study site	Date	Location	Age (Ma)	Location	Lithological units	Study aim
Cow Peel Bridge	May 99	UK NT31443114	Llandovery (Ord.) 432 Ma*	Cow Peel Bridge, Scottish Borders	Buckholm Fm.	Locate shale interbeds within turbidite sandstones
Alport Castles	Nov. 99	UK SK143914	Namurian (Carb.) 315–318 Ma	Alport Castles, Derbyshire	Shale Grit Fm.	Trace turbidite channel, observable 30 m down cliff-face exposure
Torkeal	Aug. 00	EIRE Q759513	L. Namurian (Carb.) 325–320 Ma	Torkeal, Co. Clare, Eire	Ross Fm.	Trace turbidite channel 20 m down cliff-face exposure
Bridges of Ross	Aug. 00	EIRE Q736506	L. Namurian (Carb.) 325–320 Ma	Bridges of Ross, Co. Clare, Eire	Ross Fm.	Trace turbidite channel & intrachannel fill across study site
Castissent	May 01	0°44′25″ E 42°09′11″ N	U. Ypresian (Eoc.) 49–50 Ma	Castissent, Pyrenees, northern Spain	Castissent Sandstone Fm.	Map multistorey, fluvial sandstones across site
Caspe	May 01	0°07′58″ W 41°15′15″ N	Chattian (Oligo.) 23.3–29.3 Ma	Caspe, central Spain	Caspe Fm.	Map intrachannel fill across fluvial meander loop

*Cow Peel Bridge has been dated by Floyd (2000)
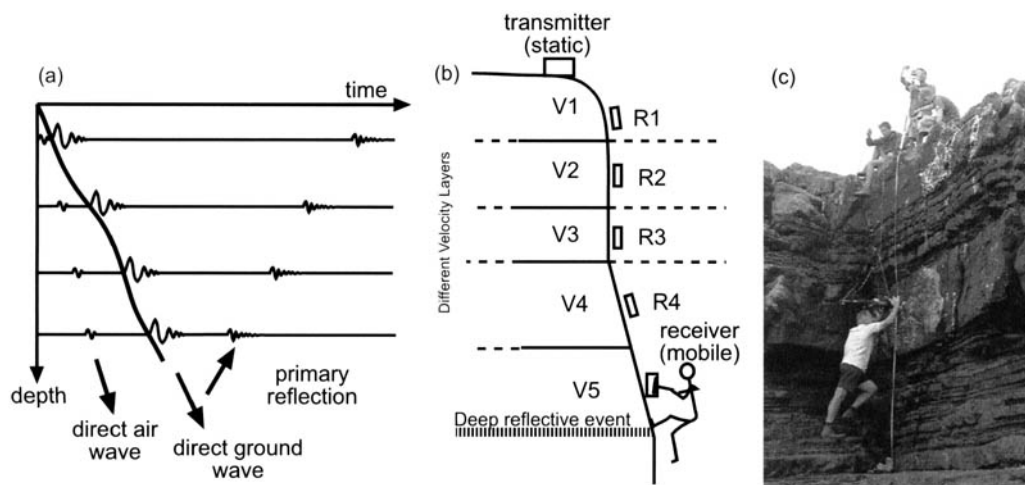
Fig. 1. (**a**) Vertical seismic profile (VSP) theory as first realized by Gal'Perin (pers. comm. 1987). By picking the first breaks, a direct measurement of velocity can be determined. This is obtained by raising a receiver progressively towards a seismic source up a well-bore. (**b**) VSP technique with GPR, adapted for outcrops, to create vertical radar profiles (VRPs). R, receiver antennae positions, situated progressively further from transmitter antennae; V, velocity layers progressively further away from transmitter antennae. (**c**) VRP acquisition at Bridges of Ross outcrop, western Ireland, using 450 MHz dominant-frequency antennae. The antennae pair were progressively separated at a constant trace sample interval down the vertical cliff-face.

and resolving thinner units thinner than those presently definable on standard seismic profiles.

Researchers such as Stewart (pers. comm. 1999) and Zhow and Sato (2000) have used the GPR technique to create VRPs. Zhow and Sato (2000) constructed a down-borehole, broad-band, stepped frequency (0.1–500 MHz) polarimetric radar system for slim boreholes to calibrate their 2-D profiles. Cross-borehole radar tomography has also been investigated (e.g. Cai & McMechan 1999; Wänstedt *et al.* 2000), whereby a receiver-antennae array was placed down a borehole at a set spacing, recording the electromagnetic wave produced from the transmitter antenna placed in another borehole. Both first-arrival travel times and amplitudes were calculated for each source/receiver pair. The interval between the boreholes was then divided into segments and populated with approximate values gained from the multiple ray paths. This technique, termed 'tomographic inversion', produced velocity tomographs (Wänstedt *et al.* 2000).

Another approach is that followed by Corbeanu *et al.* (2001) and Szerbiak *et al.* (2001), who constructed synthetic profiles from borehole log interpretations drilled behind outcrop faces. These synthetic profiles were then used to build a 3-D velocity model to convert radar profiles from time to depth. However, drilling boreholes in indurated sediments can be expensive and specialized radar equipment is required (see Waard 2001).

Instead of drilling boreholes, we have acquired

VRPs down cliff-faces of outcropping sedimentary rocks using only standard GPR equipment (Fig. 1*b*). One GPR antenna (usually the transmitter) is placed on the cliff-top, while the other antenna is moved progressively down the cliff-face at a constant trace sample interval (Fig. 1*c*).

VRP acquisition and parameters

VRPs are best acquired on vertical cliff-faces of ancient sedimentary strata. Stratigraphy containing thick (>1 m) shale units above target horizons should be avoided because such units rapidly attenuate the radar signal. Sites with significant faulting should also be avoided (unless faults are targets) because these may interfere with reflection events. Ideally, targets should be stratigraphic boundaries, showing high reflection coefficient (RC) values (see Alport Castles, equation 1, below). Targets with low RC values have been found to be imaged only by using GPR frequency antennae of 450 MHz and above. A non-vegetated cliff and top surface are preferred to enable easy access of the equipment for VRP and subsequent fixed-offset profile acquisition.

Where possible, VRPs should be located at one end of a fixed-offset profile in order to allow direct correlation of reflection events from the VRP to the profile. The transmitter antenna, power source and recording equipment should be positioned a few metres from the cliff-edge, to avoid air-wave inter-

ference, but below any potential attenuation layers, e.g. shale. The receiver antenna rather than the transmitter is generally moved down the cliff-face because not having to trigger the radar pulse simplifies the abseiler's tasks. The receiver antenna should be accurately moved at a specified interval down the cliff-face, antenna orientation being horizontal (we generally use co-pole orientation), parallel with sedimentary bedding and at right-angles to the cliff itself. VRPs are relatively unaffected by receiver coupling, since ray paths pass close to the cliff-face only as they approach the receiver, but good coupling should still be attempted. The major limitation on the length of the VRP record is the length of the cable from the receiver antenna to the recording equipment. The longest possible cables are essential on higher cliff-faces.

As the study sites summarized in Table 1 produced widely varying GPR responses, presurvey testing was critical to gaining the best possible data acquisition. Each site had a number of repeat testlines, using a variety of dominant-frequency antennae. Fixed-offset profiles, CMPs and VRPs were all used to test for optimal antenna frequency. VRPs and CMPs were acquired, the preset trace-sample interval being decided in the field from study of the raw test-profile results. Acquisition parameters were also varied on repeat sections (Table 2). The number of stacks was varied from 128-fold to 1024-fold in order to assess the cost/benefit of acquisition time v. signal : noise ratio. After field acquisition, radar processing was undertaken using the VISTA seismic processing software package. An outline processing workflow is shown in Figure 2. The processing steps for GPR reflection profiles, VRPs and CMPs are detailed in Tables 3, 4 and 5 respectively.

We describe VRP results from six sites and three different geological ages. Four of the study sites represent turbidite depositional environments and two are from fluvial examples. The surface-reflection GPR surveys, which were also carried out at each study site, are not discussed. Fixed-offset profiles from one of the Scottish Border sites are shown in Pringle et al. (1999) and results from one of the Irish study sites are detailed in Pringle et al. (see 2003).

Study sites

Cow Peel Bridge, Scottish Borders, UK

Outcrops of Ordovician (Llandovery) turbidite deposits at Cow Peel Bridge (UK grid reference: NT31443114) were the target lithology in the Scottish Borders. During the Ordovician, sand-rich successions up to 2 km thick were deposited in high-gradient, deep-sea fans (Kemp 1987; Floyd

1996). The resulting deposits typically comprise 0.5–5 m-thick, amalgamated, non-graded turbidite sandstones, interbedded with thin-bedded sandstones and shales generally less than 0.5 m thick. Bedding is subvertical, and observed bedding contacts have been offset by minor strike-slip and reverse faults (Fig. 3). Outcrop faces generally are planar, which assisted GPR data acquisition. The aim of this pilot study was to see whether GPR could successfully image 5–8 cm shale interbeds and faults as discontinuous reflection events and, if so, to establish which velocity contrasts were imaged. A series of closely spaced fixed-offset, 2-D profiles was also acquired. Profiles are presented in Pringle et al. (1999), illustrating the shale unit being investigated, as well as imaging the minor fault offsetting the interbedded sandstone and shale units.

A VRP was acquired using 900 MHz dominant-frequency antennae (Fig. 4). Smooth outcrop faces meant that the VRP did not need to be adjusted to account for any surface rugosity. The slope of the first-arrival event shows a clear relationship between time and depth through the sediments, with several clear reflection events also depicted (arrowed in Fig. 4). An average velocity (0.14 m ns^{-1}) can be determined from the overall slope profile. This value was used to convert the local radar-reflection profiles from time to depth. A five-fold decrease in amplitude was also observed where the direct arrival wave crossed a sandstone/shale boundary.

First-arrival peak picks (Fig. 5a) show three clear changes in average velocity slope angle (Fig. 5). However, only one velocity break can be definitively correlated with observed lithology (marked in Fig. 5b): the 8 cm-thick shale horizon observed at the outcrop surface (shown in Fig. 3b & c). Indeed, plotting unit 2 (Fig. 5a) (velocity values obtained in the thin shale horizon) shows a distinctly different slope from the rest of the outcrop (see values in Fig. 5). Thus plotting average velocity values can locate thin (8 cm in this case) horizons that are not resolvable using the fixed-offset profiling technique. The M2 and M3 velocity breaks shown in Figure 5a could not be correlated with observed sedimentary boundaries. Subunits 3 and 4 in Figure 5a can be further subdivided (denoted as f1–f5), a breakdown not observed on the outcrop surface. The f1 events (~0.5 m spacing) may reflect subtle grain-size changes in the sandstone beds, which may mark individual turbidite deposition events. Unfortunately, the 900 MHz fixed-offset profiles acquired at this site (positions marked in Fig. 3b) only penetrated to 2 m depth; therefore the M2 and M3 events could not be traced over the outcrop.

Table 2. *Summary of VRP parameters and overall constant velocities of the ground- and air-waves where measured*

Study site	Sensors & software system	Cable type	Ant. freq. (MHz)	VRP ground wave velocity (m ns^{-1})	No. of first arrival picks sampled	Correlation coefficient (R^2)	Air wave velocity (m ns^{-1})	No. of first arrival picks sampled	Correlation coefficient (R^2)	Sample rate (ps)	Sample rate (m)	Sed. profile length (m)	VRP length (m)	Details
CPB, UK	PE1000	Metallic	900	0.14	199	0.99				100	0.01		4.14	
Alport, UK	PE100	Fibre-optic	50	0.25	283	1.00				1600	0.10	40.00	24.00	
Torkeal, Eire	PE100	Metallic	100	0.23	17	0.99				800	0.20	12.00	11.20	
Torkeal, Eire	PE100	Metallic	50	0.28	69	0.99				1600	0.20	12.60	13.60	Repeat VRP
B of R, Eire	PE1000	Fibre-optic	225	0.23	94	0.99				400	0.02	1.92	1.86	C1 location
Castissent, Spain	PE1000	Metallic	450	0.17	62	1.00				200	0.01	1.00	0.80	Site 1
Castissent, Spain	PE1000	Metallic	450	0.10	50	0.99	0.38	39	0.98	200	0.05	2.60	2.50	Site 2 – air vel. too high
Castissent, Spain	PE1000	Metallic	225	0.11	19	0.98	0.30	37	0.99	400	0.10		4.30	Site 2
Castissent, Spain	PE1000	Metallic	110	0.28	26	0.99				700	0.25	6.00	6.25	Site 2
Caspe, Spain	PE1000	Metallic	225	0.13	28	0.99	0.28	32	0.98	400	0.10	8.50	8.50	
Alport, UK	PE100	Fibre-optic	50	0.13	18	0.83				1600	0.05	0.1	1.70	Opp. side of site to p2
Alport, UK	PE100	Fibre-optic	50	0.08	8	0.9				1600	0.05	0.1	0.70	Peat near VRP loc.

CPB, Cow Peel Bridge
B of R, Bridges of Ross
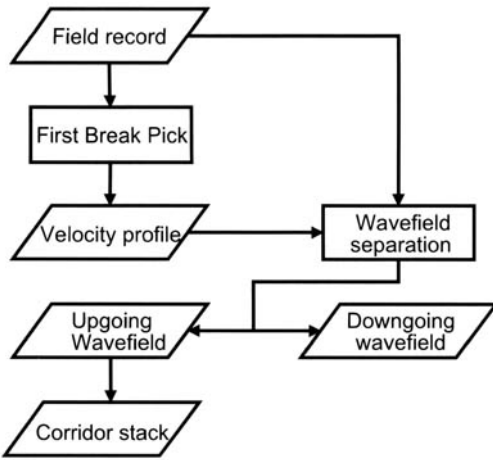
Fig. 2. Seismic data-processing workflow for VSPs, adapted to GPR vertical radar profiles (see Table 4 for more detail).

Table 3. *GPR data processing workflow for reflection profiles acquired on the fluvial Caspe study site, central Spain*

1	Output dewowed GPR file as SEG-Y data from pulseEKKO acquisition software
2	Input SEG-Y file into VISTA seismic processing software (Field sample rate 300 ps translates to processing sample rate 300 s)
3	Resample from 300 s to 100 s for more accurate first-break picks
4	Debias, flatten on first break picks, window and ramp end of trace
5	Time-variant balance to recover reflection events at relative amplitude
6	Band-pass filter to remove DC shift amplified by balance
7	Time-variant spectral balance to condition frequency spectrum and improve resolution while preserving relative amplitude
8a	FK filter to remove multiple events parallel to the acquisition surface if needed, but undertaken in second pass only after consultation with interpreters. This was used for the Caspe data, where reflection events are weak to surface multiples imaged at a high angle. FK was not used on the other six, turbidite datasets, where the reflection events are usually very strong.
9a	Elevation statistics using GPS survey results and VRP average velocity

Table 4. *GPR VRP data-processing workflow*

1	Output GPR file as a SEG-Y data from pulseEKKO acquisition software
2	Input SEG-Y file into VISTA seismic processing software (Field sample rate 300 ps translates to processing sample rate 300 s)
3	Resample from 300 s to 100 s for more accurate first-break picks
4	Debias, flatten on first break picks, window and ramp end of trace
5	Time-variant balance to recover reflection events at relative amplitude
6	Band-pass filter to remove DC shift amplified by balance
7	Time-variant spectral balance to condition frequency spectrum and improve resolution while preserving relative amplitude
8b	Median filter to parallel first breaks (now all at $t = 0$ to enhance down-going wavefield)
9b	Subtract down-going wavefield from fill record (at step 7) to produce new up-going wavefield
10	Add double first-break time, up-going wavefield creates a record in two-way time versus offset
11	Median velocity filter parallel to reflection events (now parallel $t = 0$) to enhance up-going wavefields
12	Corridor stack (see text for description) constructed to compare with first-break (time, depth) log and stratigraphic log

Table 5. *GPR CMP data-processing workflow*

1	Output GPR file as SEG-Y data from pulseEKKO acquisiton software
2	Input SEG-Y file into VISTA seismic processing software (Field sample rate 300 ps translates to processing sample rate 300 s)
3	Resample from 300 s to 100 s for more accurate first-break picks
4	Debias, flatten on first-break picks, window and ramp end of trace
5	Time-variant balance to recover reflection events at relative amplitude
6	Band-pass filter to remove DC shift amplified by balance
7	Generate: Semblance and Constant Velocity Stack sections
8	Velocity analysis (velans) based upon Normal Move-Out (NMO) assumptions
9	Output RMS and interval velocity profiles
10	Convert (Two-Way Time, Interval Velocity) profile to (Time, Depth) profile for reflection events

Alport Castles, Derbyshire, UK

Carboniferous (Namurian) proximal turbidites were investigated at Alport Castles, Derbyshire (UK grid reference: SK143914) (Walker 1966). The ~50 m-high cliff-face exposes complex chan-nel fills and sheet-like sandstones with varying sand/shale proportions. The top surface behind the cliff section is blanketed by up to 2 m of peat. The cliff section is the slip surface of a rotational slope
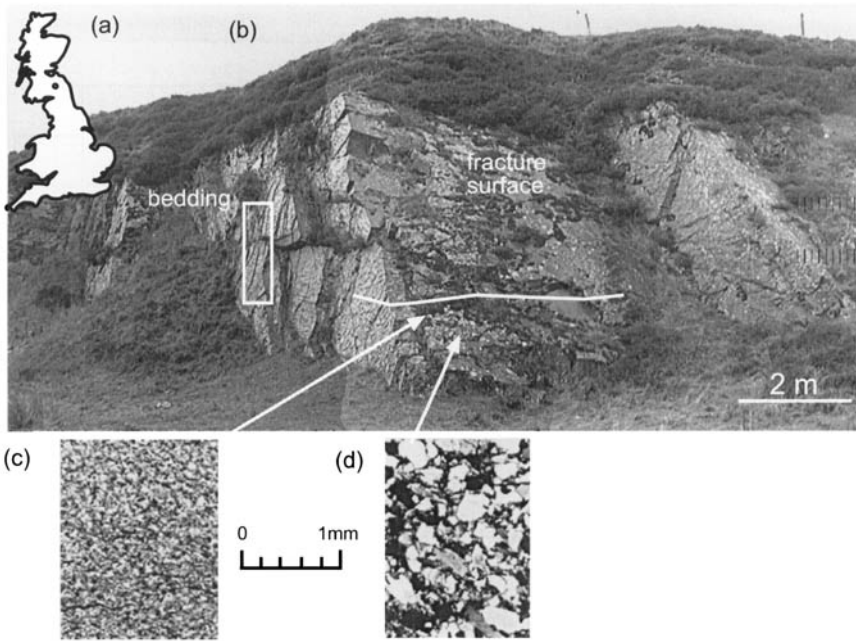
Fig. 3. (a) Location map, and (b) photomosaic of vertically dipping Ordovician, sand-rich turbidites at Cow Peel Bridge, near Innerleithen, Scottish Borders. Indurated sediments have undergone low-grade metamorphism and multiple faulting events, the latter controlling the exposed smooth faces. Rectangular outline indicates where fixed-offset GPR profiles were acquired. White line, location of VRP, oriented perpendicular to bedding. (c) and (d) Thin section photomicrographs taken from shale and sandstone units respectively.
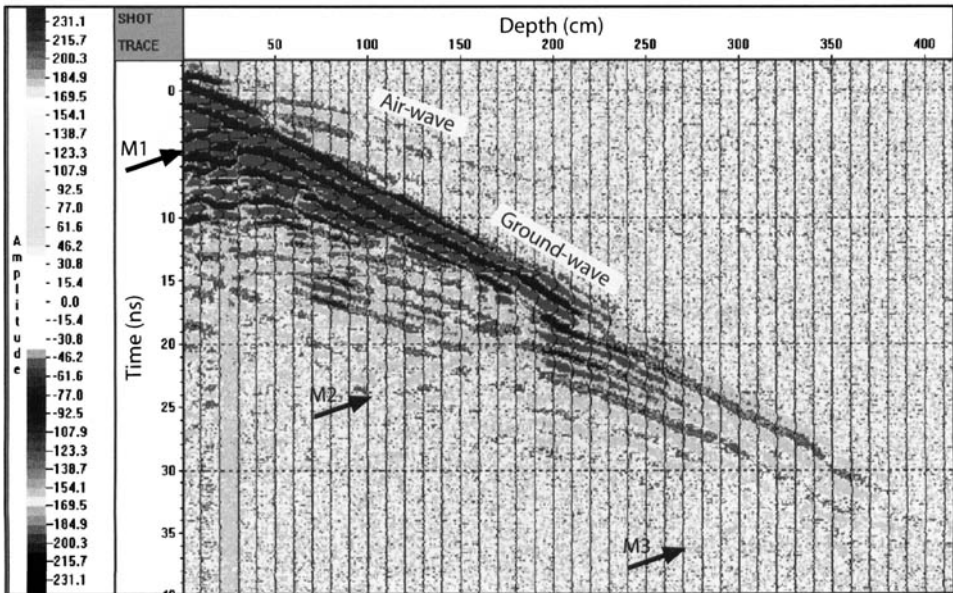
Fig. 4. VRP acquired at the Cow Peel Bridge study site. The direct ground-wave (labelled) is defined by the obvious arrivals from top left to bottom right (in conventional VSP format). The direct air-wave is also labelled. An obvious reflection event (M1) is marked around 50 cm depth, with an inclined reflection event (M2) and a weak reflection (M3) deeper in the section. The amplitude palette is shown on the left.
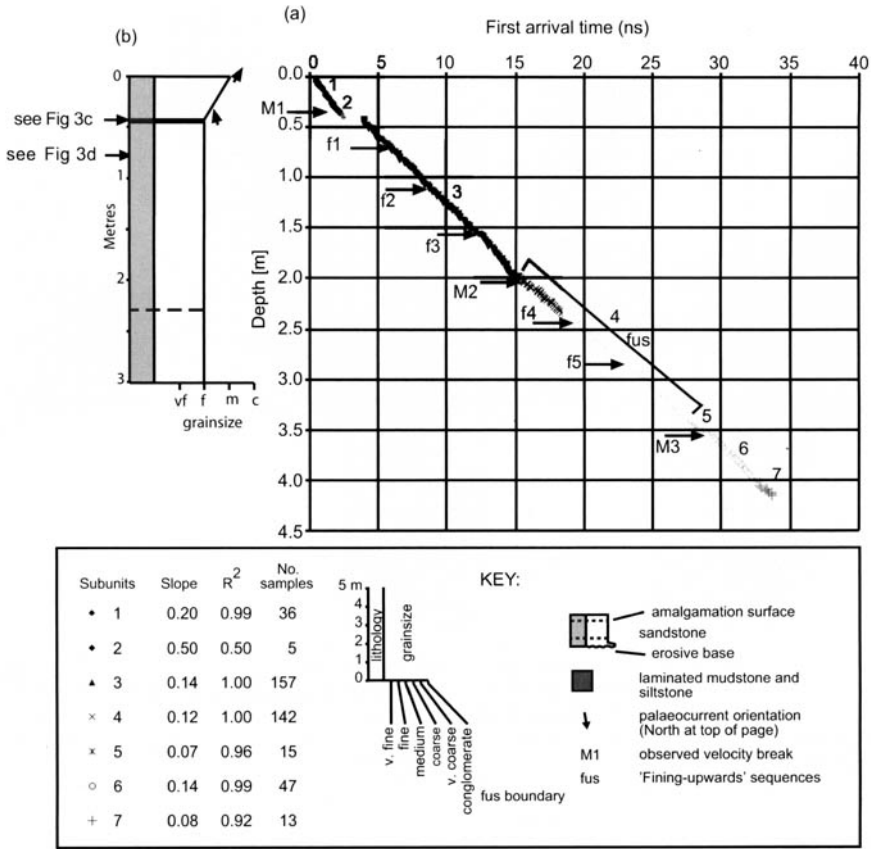
Fig. 5. (a) First-arrival break picks from the vertical radar profile shown in Figure 4 correlated with (b) the sedimentary log. Arrows in (b) relate to palaeocurrent indicators measured in the field. Arrival break at 0.42 m (M1) corresponds to 8 cm-thick shale horizon. Lithological changes responsible for (M2) and (M3) events could not be observed at outcrop. Velocity discontinuities (f1-f5) may be subtle 'fining-upward sequences' ('fus'). These also were not observed during outcrop examination. First-arrival picks have been subdivided (1–7) and analysed, with results tabulated (see text).

failure, so many of the blocks immediately behind the cliff-face are slightly rotated. A radar grid covering 1 km by 100 m was acquired using 100 MHz dominant-frequency antennae behind the cliff-face. Figure 6 shows an example of one fixed-offset profile obtained. The aim at this site was to trace small-scale turbidite channels exposed in the cliff-face across the near-surface behind the cliff-face. Initial interpretation of GPR reflection profiles allowed reflections to be traced over this area (see Pringle *et al.* 2000) but significant attenuation, presumably caused by a saturated overlying peat layer, limited maximum depth of reflection events to ~ 30 m (see Fig. 6).

A 50 MHz VRP was acquired down the outcrop face, with the transmitter sited ~5 m behind the outcrop face but below the peat layer, thereby avoiding potential peat attenuation effects. This was

also the start of the profile shown in Figure 6. VRP acquisition was a challenge, not least of which was having to abseil down the 60 m cliff-face with the 2 m-wide receiver antenna. The irregular cliff surface was also a problem, requiring the abseiler to keep the transmitter well coupled with the strata (ideally at right-angles to the cliff-face) and parallel to bedding. The velocity derived was 0.25 m ns^{-1}.

Impressive penetration depths were obtained, with reflection events observable at 53 m, 62 m, 64 m and 74 m depth (Fig. 7). The deeper events are interpreted to be stratigraphic boundaries. These are taken to be the base Shale Grit unconformity, base of the Mam Tor Beds and base of the Edale Shales respectively. The strong reflection events imaged at ~400–500 ns are interpreted to be from the Edale Shales, reflecting an abrupt lithological change from sand-rich to shalier deposits
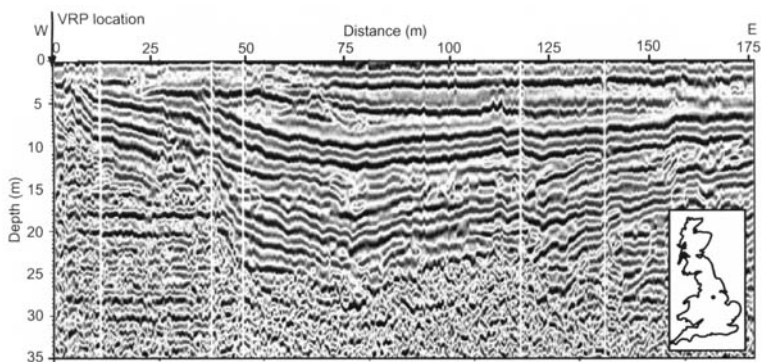
Fig. 6. Fixed-offset profile obtained at Alport Castles, Derbyshire, UK, using 50 MHz-frequency antennae, with location map (inset). The in-line is 178 m long with a trace-sample spacing of 0.5 m. The western end is also the site of the VRP.
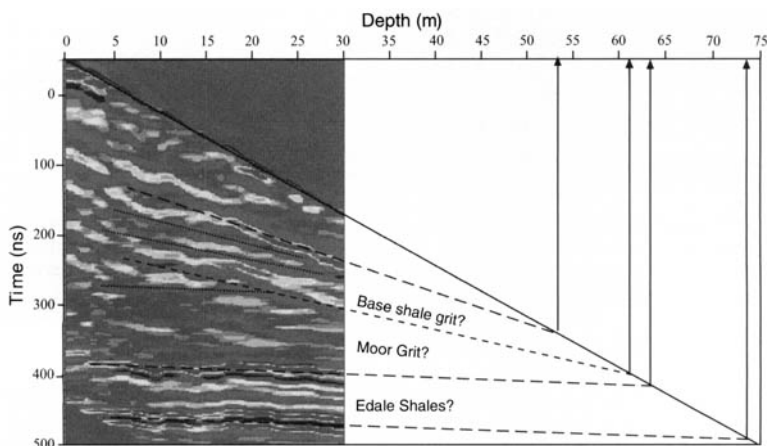
Fig. 7. VRP obtained from the Alport Castles site with a trace sample interval of 0.1 m. Reflection events and the air-/ground-wave interface have both been projected to convert reflections from time to depth. The deeper events are inferred stratigraphic boundaries. Close-dotted lines indicate onlapping relationships.

observed at appropriate depths at nearby localities (by Walker 1966).

The apparent stratigraphic dips of significant boundaries represented by strong reflection events (shown in Fig. 5) can be calculated from VRP wavefield measurements. The apparent dips for these events, interpreted to be the base Shale Grit, base Mam Tor beds and base of Edale Shales, were calculated as ~2°, ~12° and ~12° respectively. Observed outcrop dips for the base Shale Grit proximal to the study site (~3°S–E) are consistent with these calculations.

Ideally, more VRPs would have been obtained along the cliff-face, for further confirmation of the local dips, but, being in the Peak District National Park, we were only allowed one abseil site. The reflections in the upper 30 m could be correlated

with reflection events from the fixed-offset profile survey, thus correlating observed sedimentary surfaces on the cliff-faces with subsurface reflection events on the profiles. However, deeper reflection events imaged on the VRP were not exposed at the cliff-face; inferred stratigraphic boundaries (marked in Fig. 7) are exposed elsewhere in the study area. The average velocity profile is also more uniform below 15 m, but this does not correlate with more uniform sedimentary strata (see also Discussion).

The Alport Castles VRP traces were summed at a constant two-way time across a narrow mute window, parallel to the first break picks curve, to produce a corridor stack (Fig. 8). The corridor stack is the equivalent of synthetic seismic sections used to correlate lithology logs and reflection sections.
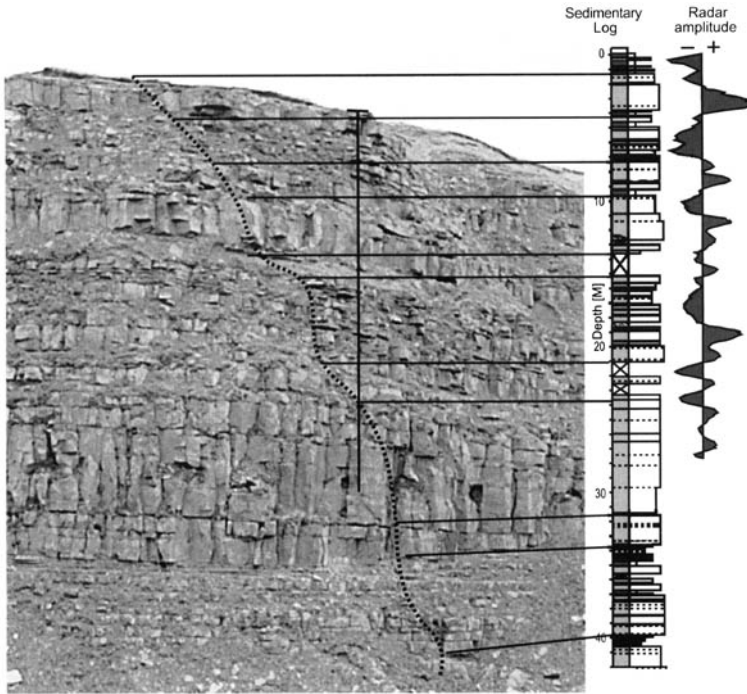
Fig. 8. Outcrop photograph at Alport Castles site, with dotted lines showing VRP and sedimentary log paths. The sedimentary log (see Fig. 5 for key) and VRP radar amplitude (see text for more information) have been placed in their correct position. A reasonable correlation may be between the positive peaks and sandy intervals in the corridor stack; negative peaks may correspond to more shalier intervals.

Successions of closely spaced reflection events overlap and stack up to produce large, composite reflection events, with either positive or negative amplitudes. The stack was then converted from time to depth and compared with observed geology and the sedimentary log (Fig. 9). Comparisons of the corridor stack with the sedimentary log show thin-bedded intervals of sandstone and shale generally corresponding with negative amplitude peaks. Positive amplitude peaks appear to correlate with more uniform, sandy intervals. This reflects a higher complex permittivity in sandstone compared with shale. Equation 1 shows that the reflection coefficient (RC) is positive if the complex permittivity of the upper bed (K_1) is greater than that of the lower bed (K_2). A positive peak amplitude reflection event will thus be produced.

$$\text{Reflection coefficient } (RC) = \frac{(K_1^{1/2} - K_2^{1/2})}{(K_1^{1/2} + K_2^{1/2})} \qquad (1)$$

where K_1 and K_2 are the complex permittivity of the upper and lower units respectively in this case.

Ross Formation: Torkeal Bay and Bridges of Ross, County Clare, Ireland

The Carboniferous Ross Formation is well exposed on coastal outcrops on the Loop Head Peninsula in County Clare, western Ireland. Two study sites were investigated: one at Torkeal Bay (Eire grid reference: Q759513) and the other at the Bridges of Ross (Eire grid reference: Q736506). The latter is described in Pringle et al. (2003). Dominantly sand-rich, sheet sandstones are observed. Interbedded within these units are small-scale channels, typically 100–500 m wide and 5–15 m deep. The turbidite channels have been interpreted to be deposited from laterally shifting sediment sources from deltaic and submarine slopes (Elliott 2000a). Estimating channel sinuosity, as well as individual bedding-unit connectivity and continuity, were the main goals of the GPR investigations at these localities.

The 50 m-high cliff at the Torkeal Bay site displayed an infilled turbidite channel 20 m down the cliff-face (Fig. 9). A profile survey was undertaken
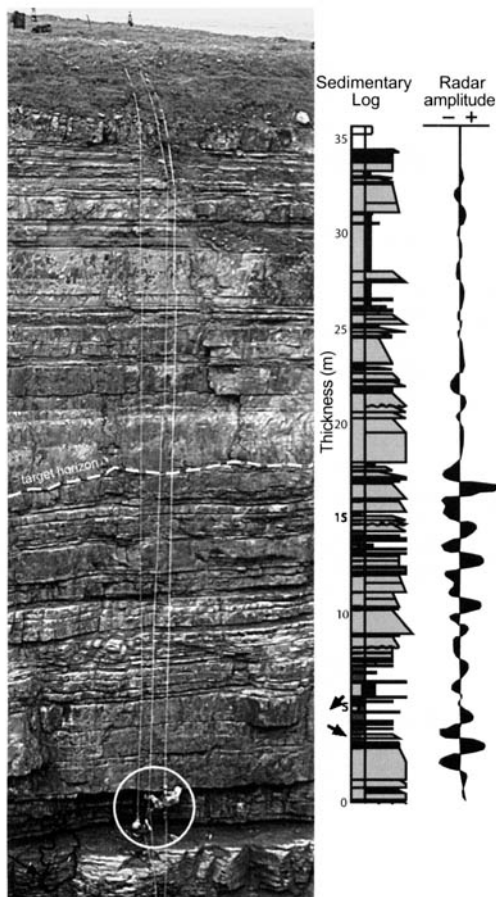
Fig. 9. Photomontage of the east-facing (~60 m-high) cliff at Torkeal Bay, western Ireland. The abseiled sedimentary log is in its approximate position (see Fig. 5 for key, abseilers for scale). Target channel surface marked as a dotted white line. A-C show sample locations mentioned in Table 9. Corridor stack produced from VRP is scaled to match the sedimentary log. The sedimentary log and VRP stack are not in complete accordance with the photograph, due to lens distortion. GPR equipment can be observed behind the cliff-top, where a series of 2-D GPR profiles were acquired.

over the top of this channel fill, with a detailed sedimentary log and two VRPs (using 50 MHz and 100 MHz dominant-frequency antennae) at the same locality obtained down the vertical cliff-face. However, attempts to image reflection events were unsuccessful on both fixed-offset profiles and VRPs, with attenuation of the signal being due to a thick peat layer on the outcrop top and/or a 1 m-thick shale layer, 3 m below the cliff-top. Radar-signal penetration depth was down to 50 m, comparable to the 73 m obtained at Alport Castles, using the same frequency (50 MHz) antennae. The average velocity was calculated to be 0.26 m ns^{-1}. Variable first-arrival pick velocities could be correlated with more heterogeneous intervals. A corridor stack was also derived from the VRP using the same methodology as at the Alport study site. However, at this site, the amplitudes could not be correlated with lithologies.

The Bridges of Ross study site (Fig. 1c) was investigated in detail, tracing a turbidite channel margin and its intrachannel fill across a surface between two vertical cliff sections by acquiring fixed-offset reflection profile grids, using 110 MHz, 225 MHz and 450 MHz frequency antennae (Pringle *et al.* 2003). Acquisition could be undertaken directly on the rock as there was no overburden present. A VRP was also acquired to calibrate the fixed-offset profiles and an average velocity of 0.23 m ns^{-1} was derived. Reflection events imaged on the VRP were correlated with subsurface reflection events imaged on the fixed-offset profiles.

Fluvial study sites

Castissent, Spanish Pyrenees The Castissent Sandstone Formation is an Eocene fluvial deposit occurring within the Tremp-Graus Sub-basin (Marzo *et al.* 1988), one of a series of Tertiary foreland basins south of the Pyrenees (Table 1). It is composed of multistorey sandstone bodies and is up to 40 m thick in the eastern part of the basin. The Castissent Sandstone Formation was interpreted by Nijman and Puigdefabregas (1978) as a coarse-grained meander-belt deposit. At the study site on the Puente de Montañana – Tremp road (at the 5 km marker point), the sequence is between 15 and 20 m thick. A top surface some 100 × 40 m occurs behind an approximately 20 m-high cliff-face. Medium-grained sandstones predominate, in trough cross-bedded sets up to 1 m thick and up to several metres long. A fixed-offset profile grid 90 × 40 m, using 110 MHz and 225 MHz dominant-frequency antennae, was obtained at the study site in an attempt to image major bounding surfaces and sedimentary structures within the deposit. Profiles generally showed few continuous reflection events, variable reflectors being observed between profiles less than 1 m apart. It was suggested that we return to the study site and use higher frequency antennae because the frequencies used (110 MHz and 225 MHz) could not resolve the sandstone/sandstone boundaries. Rainstorms soaked the study site during fieldwork, so outcrop conditions varied from dry to wet, depending on the field day. This may have contributed to the variable profile results.

Four VRPs were acquired at two locations, with one location reprofiled using 110 MHz, 225 MHz

and 450 MHz antennae. Average velocity values (Table 2) varied between 0.10 m ns^{-1} and 0.28 m ns^{-1} at the same locality, using 450 MHz and 225 MHz frequency antennae respectively. A possible reason for the average velocity variations could be that the 225 MHz frequency VRP was twice as long as the 450 MHz profile, which may have picked up more moisture-rich layers deeper in the section (Kruse pers. comm.). (See Discussion for further comments on the repeat VRP average velocity variations at the same locality.) Note that the 450 MHz VRP air-wave average velocity measurement is impossible, as it suggests a velocity faster than the speed of light!

Caspe, Aragon Province, Spain Oligocene fluvial sediments in the Ebro Basin in northeastern Spain are spectacularly exposed near the town of Caspe (Mohrig *et al.* 2000; Table 1). Stacked sandy channel-belt deposits are preserved as sinuous raised ridges up to 10 m higher than interchannel or floodplain areas, as the softer mudstones of the floodplain areas have preferentially eroded away. Individual channel-belt deposits are up to 3 m thick and 2–40 m wide. Up to five channels, stacked obliquely and vertically, form each channel belt (Fig. 10a). Within the belt, the individual channel deposits generally connect vertically with one another, but they can also be separated by shales and fine sands deposited during phases of channel abandonment. A new road-cutting has created 8 m-high exposures through channel-belt deposits, perpendicular to palaeoflow direction. Multiple 2-D GPR profiles were acquired along a channel-belt top, using 225 MHz dominant-frequency antennae. There was little to no overburden on the channel top. Small bushes posed a minor problem by interfering with good antennae coupling with rock strata. 225 MHz CMP was also acquired, oriented parallel to the channel trend (Fig. 10c), with a velocity of 0.12 m ns^{-1} being calculated. This was the best CMP profile acquired at any of the study sites described here; both shallow and deep reflection events were imaged down to 10 m. Unfortunately, the subsequent 14 fixed-offset profiles acquired did not image these deep reflection events. Only the top 1–2 m of the channel deposits exposed on the road-cut face could be interpreted on the profiles.

A 225 MHz frequency VRP was acquired at the road-face, directly below the CMP position (VRP acquisition shown in Fig. 10a). An average VRP velocity of 0.13 m ns^{-1} was determined. The CMP from the site has strong primary and multiple reflection events (Fig. 10c), but the VRP obtained (Fig. 10b) shows weaker reflection events than were imaged in the VRPs discussed in the rest of this paper. The VRP also shows a very unusual set of direct ground-waves (Fig. 10b). This could be

due to a nearby fault interfering with direct arrivals or, though less likely, to the initial ground-wave being converted to an air-wave part-way down the profile. The constant-offset GPR profiles were also of variable quality, locally as good as the CMP, but more commonly showing the weak reflection events of the VRP. The outcrop face (Fig. 10a) shows that reflection events are caused by boundaries with the medium- and granular-grained lithologies, which have lower permittivity contrasts than those present in turbidite depositional environments (Fig. 1c). The 225 MHz antennae did not produce strong reflection events from these grain-size contrasts. Higher frequency, shorter wavelength antennae may yield more usable results at this site.

Discussion

A number of factors and trends have emerged that are common to all study sites and these are discussed, factor by factor, below.

Air-wave velocities

A. P. Annan (pers. comm. 2001) suggests that the VRP methodology described in the theory section is not well established and that air-wave effects are very different in radar than from those observed in VSPs. Radar air-waves can travel many paths down a rough surface, especially at the air/ground interface. We have shown in the Alport VRP that good data can be obtained from rugose cliff sections, although this may have been a factor in the unusual Caspe VRP results.

The direct air-wave velocity was measured at four of the study sites (Table 2). The speed of radar-waves in air is given as 0.30 m ns^{-1}, depending on humidity, pressure and temperature (Fogiel 1980). However, our values ranged from 0.24 m ns^{-1} to 0.29 m ns^{-1} (discounting the impossible 0.38 m ns^{-1} value obtained from the 450 MHz frequency VRP gained at the Castissent site). Air-wave readings were obtained using 900 MHz, 450 MHz and 225 MHz dominant-frequency antennae, showing a 0.06 m ns^{-1} velocity range at the same site.

Air-wave velocity variations may be influenced by a number of factors, the most obvious being inconsistent first-arrival picking and sample interval inaccuracies (although averaging the whole profile should minimize the latter). Inconsistent first break arrival picking has been ruled out, as nearly all of the GPR data collected is of constant phase. Peak events do not seem to be affected by phase roll, as they keep a regular shape across the record. Varying environmental conditions, such as
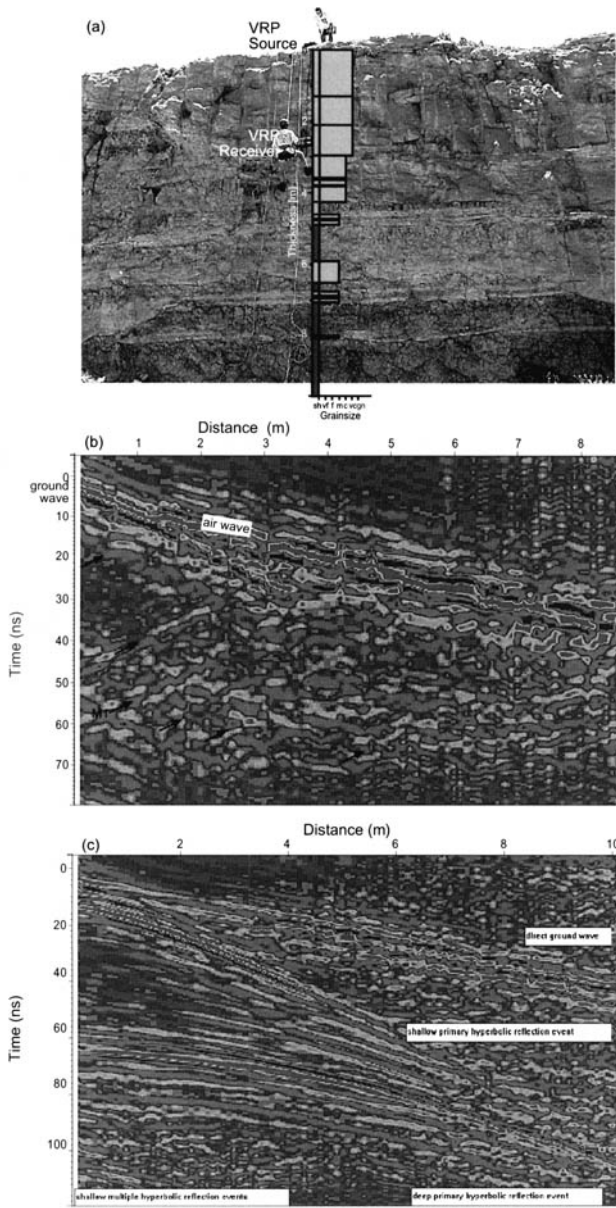
Fig. 10. (a) VRP acquisition at Caspe study site, Aragon Province, Spain. A road section has cut through Oligocene fluvial channel belts, each belt composed of up to five obliquely stacked channel deposits. Sedimentary log is shown beside the VRP location. Grain-size scale is: sh, shale; vf, very fine; f, fine; m, medium; c, coarse; vc, very coarse, gn, granular sandstones. (b) VRP acquired using 225 MHz frequency antennae, showing the direct air-wave interfering with the direct ground-wave reflection. Observed weak reflection events are arrowed, one (M1) unexpectedly appearing at the first arrival line. (c) 225 MHz frequency CMP acquired at right-angles to VRP location shown in (a). This CMP shows greater detail of shallow and deep reflection events than those from any of the six study sites.

groundwater-moisture content and air temperature and humidity are potential major variables, as the study sites vary from wet Scottish highlands to semi-arid Spanish plains.

Additionally, a range of radar equipment with different frequency antennae, and both metallic and fibre-optical cabling to connect the power source to the antennae, were used during the course of these studies (Table 2). Metallic cabling may interfere with wavefields or, indeed, provide the travel path of waves. Varying degrees of coupled direct ground-wave/air-wave interactions could be occurring, perhaps controlled by cliff-face rugosity. Sangster (pers. comm.) suggests that, if a quartz-crystal oscillator-based timing device were to be developed for GPR, this would remove variable timing readings. An alternative strategy, with current instrumentation, would be always to record an air-wave. This could be undertaken by overlapping the antennae across the cliff-edge, or holding the antennae in the air and recording the air-wave directly. Then, a statics adjustment could be made on the air-wave, which has a known velocity. This assumes, of course, that it is a direct air-wave and not a coupled ground-wave/air-wave as previously discussed. Parameters such as the distance from antenna to the cliff-edge should also be tested in order to check whether this is a significant variable.

Ground-wave velocity variations

Average ground-wave velocities were obtained from all study sites (Table 2). Values were found to be site-specific, varying from comparatively low values (~0.1 m ns^{-1}) in the Scottish Borders to ~0.25 m ns^{-1} in Derbyshire and Ireland and ~0.1–0.28 m ns^{-1} in Spain. Due to the small population of values derived, no correlation between lithology age and velocity can be ascertained (for discussion on potential variables affecting air-wave values see Air-wave velocities, above).

VRP average velocities compared to CMP gather velocities

CMP reflection data were acquired from Derbyshire, Ireland and the Spanish study sites. Analysis using the standard NMO method (see Fisher *et al.* 1992) was undertaken, which derived air- and ground-wave average velocities where they were identified (Table 6). CMP velocity analyses for reflection events were also undertaken for the Alport, Bridges of Ross and Caspe study sites, Figure 11 showing the Caspe CMP (Fig. 10c) velocity interval (V$_{int}$) analysis graphically. Reflection events were picked on the semblance plots. Some of the CMP data obtained using different frequency antennae at the Bridges of Ross outcrop was corrupt and no CMPs were conducted at the Scottish Borders sites. Nevertheless, available velocity values from CMPs can be compared with VRP average velocities obtained at the same study site, using the same frequency antennae (Table 7).

Figure 12 shows the Caspe CMP interval velocities plotted with the VRP ground- and air-waves. It is clear that the CMP and VRP values are very similar (both 0.13 m ns^{-1}). The discrepancies between the Alport Castles CMP and VRP values (~0.07 m ns^{-1} and 0.25 m ns^{-1} respectively) are due to the overlying peat layer(see below). The Caspe site results give us some confidence in suggesting VRP as an additional velocity analysis technique to CMP gathers. Also clear from Figure 12 is the closer-spaced sample interval of VRP values obtained compared to the few reflection events that were able to be calculated from the CMP.

At Caspe, the VRPs and CMPs have similar depths of penetration whereas, at the Torkeal Bay and Alport Castles study sites, the VRPs have much greater depths of penetration than the CMPs (Table 7). This greater depth of penetration achieved with VRPs is due to the lower attenuation suffered by the direct wave compared to attenuation of the reflected (two-way) time recorded by the CMP method. Table 7 compares the maximum depths of reflection events at four study sites.

At the Alport Castles study site, a major concern when conducting the fixed-offset profiling survey was the presence of a peat layer thickening behind the cliff-face. There were doubts about whether profiles were imaging stratigraphy or simply peat multiples (see Fig. 6 for fixed-offset profile example). Two VRPs were obtained of the peat layer (Table 2), one near the VRP section itself and the other at the far side of the grid. The average velocities for the peat were low: 0.13 m ns^{-1} and 0.08 m ns^{-1} at the two locations. Average rock velocities are significantly higher (0.23 m ns^{-1}), so the peat reflectors could be filtered out during processing if profiles were obtained using the CMP method for all traces. Unfortunately, using present GPR equipment, this would be too time-consuming to acquire.

VRPs are relatively unaffected by receiver coupling conditions since, in this case, the ray path passes close to the cliff-face only as it approaches the receiver. It is expected, therefore, that VRP data would have both deeper penetration and obtain more reflection events than a CMP acquired at the same site. This is observed at the Torkeal Bay and Alport Castles study sites (Table 7), where VRPs provide both deeper and more reflection events than the CMPs obtained (Table 8).

Table 6. *Summary of CMP parameters and overall constant velocities of the ground- and air-waves where measured*

Study site	CMP name	Sensors & software system	Cable type	Ant. freq. (MHz)	CMP ground wave velocity (m ns^{-1})	No. of first arrival picks sampled	Correlation coefficient (R^2)	CMP air wave velocity (m ns^{-1})	No. of first arrival picks sampled	Correlation coefficient (R^2)	Sample rate (ps)	Antenna spacing (m)	Trace spacing (m)	CMP length (m)	More GPR information
Alport, UK	AL1	PE100	Fibre-optic	50	0.07	43	0.99	0.30	67	0.99	1600	0.25	0.5	33.00	Middle of grid
Alport, UK	AL2	PE100	Fibre-optic	50	0.08	34	0.99	0.32	73	0.99	1600	0.25	0.5	36.00	100 m North of Peat2/VRP
Alport, UK	AL3	PE100	Fibre-optic	50	0.04	6	0.98	0.32	65	0.99	1600	0.25	0.5	34.50	Near peat2 VRP
Alport, UK	AL1000	PE100	Fibre-optic	50	0.07	43	0.99	0.31	77	0.99	1600	0.25	0.5	38.00	Repeat of AL1, 256 stacks
Torkeal, Eire	TK4	PE100	Metallic	50	0.11	31	0.97	0.24	31	0.99	1000	0.05	0.1	3.00	No overburden, 1024 stacks
B of R, Eire	I1-225	PE100	Fibre-optic	225	0.21	22	0.98				800	0.02	0.04	0.84	I1 in-line, 512 stacks
B of R, Eire	I1b-225	PE100	Fibre-optic	225				0.29	49	0.99	800	0.02	0.04	1.92	Repeat line
B of R, Eire	I1-110	PE1000	Fibre-optic	110				0.24	36	0.98	800	0.05	0.1	3.50	Repeat line
Castissent, Spain	CT-110	PE1000	Metallic	110				0.31	48	0.99	700	0.125	0.25	12.00	MP at 8 m on test line
Castissent, Spain	CT-225	PE1000	Metallic	225				0.31	31	0.99	300	0.05	0.1	3.00	Repeat line
Castissent, Spain	CT-450	PE1000	Metallic	450				0.35	21	0.97	100	0.025	0.05	2.00	Repeat line
Caspe, Spain	CP1	PE1000	Metallic	225	0.12	49	0.99	0.30	101	0.99	300	0.05	0.1	10.00	Along channel axis

B of R, Bridges of Roses
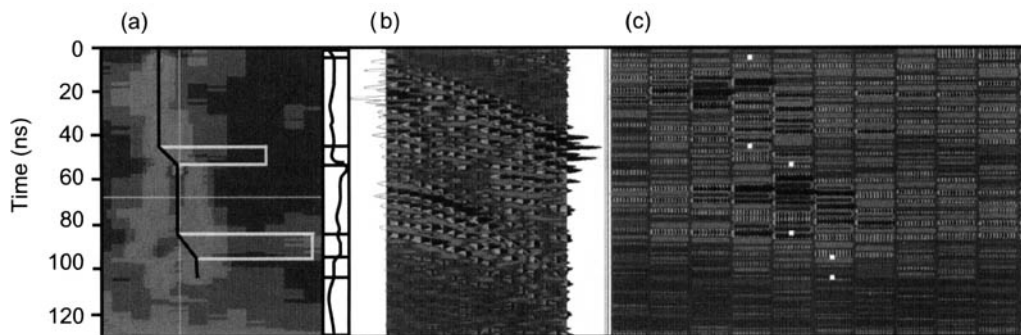
Fig. 11. Velocity analysis of Caspe CMP gather. (a) Semblance plot from 80 m ns^{-1} to 195 m ns^{-1}, showing the root-mean-square velocity profile in black (near vertical line) and the interval velocity plot (white stepped line). The track to the right shows the maximum semblance for each time level in the section. (b) CMP gather showing linear move-out from top left to upper right of the direct ground-wave, and mid-way down the section the hyperbolic move-out of a reflection event. (c) Constant velocity stacks from 80–195 m ns^{-1}, with RMS velocity picks marked as white squares.
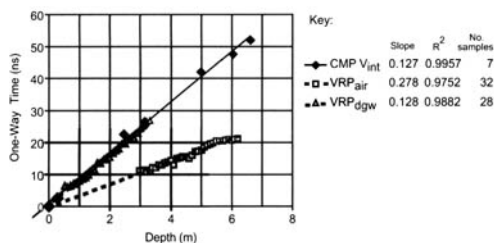
Fig. 12. Comparison of the Caspe site VRP and CMP velocity values. The VRP air-wave (VRP$_{air}$) and ground-wave (V$_{dgw}$) average velocities and CMP reflection events (V$_{int}$) are plotted. Reflection events on the CMP were analysed, average velocity intervals being calculated (see Fig. 11c). CMP events plot on a very similar slope to VRP ground-wave velocities. Note the much closer-spaced VRP average velocity picks.

Lithological analysis

Two lithological samples were taken from known positions on the sedimentary log at all sites except at Alport Castles, then thin-sectioned and polished (see Fig. 3c & d). Grain size seems to provide the best correlation with average velocity values; as grain size increases, so does the average velocity value (Fig. 13b). This is indicated by the permittivity contrast between sandy intervals and shalier units providing reflection events observed in the GPR profiles. Velocities taken from the VRPs for each sampled bed were plotted against lithological parameters (Fig. 13). Correlation coefficients were generally low for the full dataset but, for each locality, velocity values tend to increase as either grain size or quartz percentage increases. The thin sections were also analysed for element percentages (Table 8), using the energy dispersive X-ray analysis technique, on an environmental scanning

electron microscope (ESEM). Iron was expected to show a good correlation with radar velocity (as documented by van Dam & Schlager 2000), but the resulting cross-plot was scattered. An increase in velocity was also expected to correspond with a decrease in clay mineral percentage, but again the scatter was too high to show any credible trend. However, it is proposed that cement type may be affecting velocities. The Spanish study sites gave low velocities and had high percentages of calcium carbonate cement, as opposed to higher velocities at the other sites, which had quartz or chlorite cement.

In a further attempt to link mineralogy to radar reflectivity, the VRP obtained at the Alport Castles study site (Fig. 6) was examined in detail. First-arrival picks from the VRP were grouped into definable slope subunits (similar to subunits 1–7, Fig. 5), plotted separately, then compared with the sedimentary log obtained at the same location (Fig. 14). A clear correlation between shale and sandstone layers was not possible. Some of the high velocities correspond to sand-rich intervals, shown by the marked arrows in Figure 14. More heterogeneous intervals may result in larger velocity variations, whereas homogenous, massive sandstone units generally may have more uniform average velocities. Note that the values above the speed of light in air (0.29 m ns^{-1}, being to right of dotted line) are a function of the small number of picks in each subunit; we are not stating that these are 'true' average velocities. Further work could compare the observed VRP response with a synthetic VRP based upon the sedimentary log.

Further sample collection and analysis is needed before mineralogy can be definitively linked to radar reflectivity. Laboratory studies have gone some way to defining the pore-space velocity

Table 7. *Comparison of CMP with VRP direct ground- and air-wave velocities where measured*

Study site	CMP name	Sensors & software system	Cable type	Antennae frequency (MHz)	CMP ground wave velocity (m ns^{-1})	VRP ground wave velocity (m ns^{-1})	CMP air wave velocity (m ns^{-1})	VRP air wave velocity (m ns^{-1})	CMP length (m)	VRP length (m)	More GRP information
Alport, UK	AL1	PE100	Fibre-optic	50	0.07	0.25	0.30		33.00	28.20	
Alport, UK	AL2	PE100	Fibre-optic	50	0.08	0.25	0.32		36.00	28.20	Near Peat2/VRP
Alport, UK	AL3	PE100	Fibre-optic	50	0.04	0.25	0.32		34.50	28.20	
Alport, UK	AL1000	PE000	Fibre-optic	50	0.07	0.25	0.31		38.00	28.20	
Torkeal, Eire	TK4	P1000	Metallic	50	0.11	0.28	0.24		3.00	12.60	
B of R, Eire	I1-225	PE100	Fibre-optic	225	0.21	0.23			0.84	1.86	At same location
B of R, Eire	I1b-225	PE100	Fibre-optic	225		0.23	0.29		1.92	1.86	At same location
Castissent, Spain	CT-110	PE1000	Metallic	110		0.28	0.31		12.00	6.25	
Castissent, Spain	CT-225	PE1000	Metallic	225		0.11	0.31	0.3	3.00	4.30	
Castissent, Spain	CT-450	PE1000	Metallic	450		0.1	0.35	0.38	2.00	2.50	
Caspe, Spain	CP1	PE1000	Metallic	225	0.12	0.13	0.30	0.28	10.00	8.50	At same location

B of R, Bridges of Ross

Table 8. *Comparison of maximum depths of reflection events on CMPs and VRPs where measured*

Study site	CMP name	Antennae frequency (MHz)	CMP TWT (ns)	CMP VRMS	CMP velocity for interval (Vint)	CMP int. depth (m)	CMP true depth (m)	VRP max. depth (m)	CMP length (m)	VRP length (m)	More GPR information
Alport, UK	AL3	50	263	75	96	2.08	9.58	73	34.50	24.00	Near peat2 VRP
Torkeal, Eire	TK4	50	249	110	143	3.52	12.13	70	3.00	12.60	No overburden, 1024 stacks
B of R, Eire	I1-110	110	172	80	80	0.96	6.65	4	3.50	1.86	I1 in-line
B of R, Eire	I1b-225	225	135	75	75	0.34	4.83	4	1.92	1.86	Repeat line
Caspe, Spain	CP1	225	104	130	130	0.59	6.62	6.25	10.00	8.50	Along channel axis

B of R, Bridges of Ross

Table 9. *Results of ESEM analysis of samples taken from vertical radar profiling sites*

Location	Lithology	Sample	Global element: percentages of samples derived from ESEM										
			O	Mg	Al	Si	Fe	K	Na	C	Ca	Ti	S
CPB, UK*	Mudstone	Cow2	38.16	3.21	15.20	29.42	6.82	5.18	1.25			0.75	
CPB, UK*	Fine Sst.	CP8	38.80	2.03	7.86	42.59	4.49	2.13	2.11				
Alport, UK	Medium Sst.	Alport A	41.61		5.52	50.57	1.01	1.30					
Torkeal, Eire	Mudstone	TORK A	39.68	1.09	7.22	45.04	5.18	1.62	0.16				
Torkeal, Eire	Fine Sst.	TORK B	40.35	0.75	6.61	45.99	4.13	1.30	0.87				
Torkeal, Eire	Fine Sst.	TORK C	39.64	0.70	6.23	47.01	3.70	1.15	1.57				
B of R, Eire	Fine Sst.	ECPBA	41.16	0.58	4.47	48.68	3.04	0.81	0.63			0.62	
B of R, Eire	Mudstone	ECPBB	38.51	1.24	12.12	34.63	4.74	3.40	0.80	3.99		0.56	
Caspe, Spain	Medium Sst.	CP1	38.28	2.18	5.84	13.88	1.57	1.55		16.27	20.44		
Caspe, Spain	Medium Sst.	CP2	39.51	4.20	7.63	12.67	2.57	2.07		13.36	17.70	0.29	
Castissent, Spain	Fine Sst.	CT1	37.87	0.49	4.46	16.75	1.05	1.02		17.66	20.71		
Castissent, Spain	Mudstone	CT2	35.30	1.30	3.53	19.16	2.01	1.28		24.20	13.22		
		Max. range	41.61	4.20	15.20	50.57	6.82	5.18	2.11	24.20	20.71	0.75	0.00
		Min. range	35.30	0.49	3.53	12.67	1.01	0.81	0.16	3.99	13.22	0.29	0.00

ESEM, environmental scanning electron microscope
CPB, Cow Peel Bridge
B of R, Bridges of Ross
Sst, sandstone
*The two CPB samples are shown in Figure 3
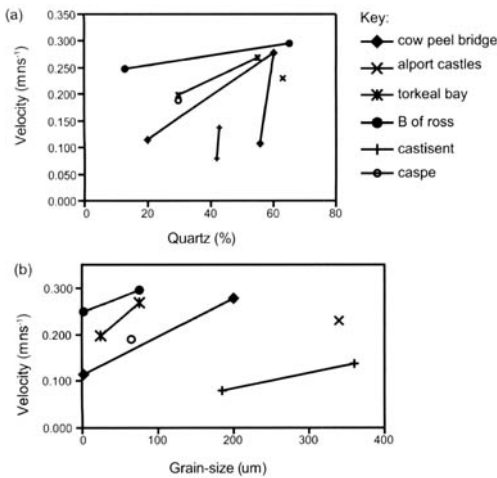
Fig. 13. Local velocity values plotted against: **(a)** quartz percentage and **(b)** grain size for samples taken from VRPs. In both cases, increasing velocity values reflect grain size and quartz percentages increases. The better correlation is seen between velocity and grain size.

relationship (Davis & Annan 1989), which shows unconsolidated sediment permittivities. However, these studies on indurated sedimentary strata show that some of the petrophysical parameters are quite difficult to differentiate. Relationships between rock type and radar-wave propagation are still relatively poorly known, especially with varying degrees of clay mineral content, pore-space content, degree of compaction, cementation etc. No definitive links could be made from our investigations. Gawthorpe *et al.* (1993) noted that radar velocities are affected by so many variables that relationships between velocity, porosity and the degree of saturation must be defined on a site-by-site basis.

Conclusions

VRP can be a valuable geophysical technique if site conditions permit, being both a direct wave and reflected-wave time-depth log. Separable wavefields allow much deeper reflection events to be imaged than those obtained using equivalent CMP or fixed-offset profiling techniques. VRP provides a direct measurement of site-specific average velocity (rather than the CMP estimation method), which can be used to calibrate subsequent fixed-offset profiles acquired behind cliff-faces. Reflection events imaged on the VRP can be correlated with observed sedimentary surfaces on cliff-faces, and subsequently with subsurface reflection events imaged on fixed-offset profiles. The depth and local dips of deep reflection events can also be

measured. The VRP technique can also identify thin sedimentary events frequently not observable on fixed-offset profiles.

When high-frequency antennae are utilized, the VRP can show small velocity changes in the first-arrival picks, which may be responding to grain-size variations that may be overlooked in a visual outcrop study. First break picks from the VRP can give a detailed velocity log. Summing these values at a constant time can create a corridor stack (equivalent to synthetic sections), on which positive amplitudes can be correlated with sandier intervals and negative amplitudes with thin-bedded intervals. First-arrival picks can be 'blocked', which shows some correlation with lithology. Sample analysis shows general trends of velocity increasing with quartz percentage and grain size.

Subvertical cliff-faces, ideally with no overburden, are the ideal sample sites. This allows VRP acquisition, as well as the correlation of reflection events to observed sedimentary surfaces. Fixed offset lines can then be obtained back from, and parallel to, the cliff-face. We recommend acquiring several VRPs and CMPs at different dominant frequencies at each study site, before choosing the parameters for a surface reflection survey.

Further studies are necessary to eliminate some of the variables that caused variable results between study sites. Considerably more research into the mineralogical composition and rock fabric of study sites is necessary before they can be definitively linked to radar reflectivity in indurated sediments.

Fig. 14. (a) Stratigraphic section measured at the Alport Castles site (see Fig. 6) plotted against (b) blocked first break velocities from 50 MHz frequency VRP (see Fig. 5). Erosive surfaces in the sedimentary log are defined by scour and/or mud-flake breccia facies. Sandy intervals typically have constant velocities, whereas heterogeneous intervals have more variable velocities (marked by black arrows).

Appendix

The Alport Castles VRP is the only one of those we have gathered in which the reflection events seem to be clearly dipping. The two deep reflection

events at Alport are the strongest in the up-going wavefield, even though they are well below the lowest level of the cliff section profiled. The down-going wavefield does not contain strong evidence for multiple events, although multiples could still be present in up-going wavefield trace segments below the base of the cliff. However, there are no obvious generators for the two strong deep events, which are therefore almost certainly primary reflections.

In VSPs, the reflection point always moves up-dip and therefore, subject to the constant velocity assumption below, the deep reflection events appear to dip toward the cliff face. The Alport Castles cliff-ace is the back-scarp of a large rotational slip and landslide. The Edale Shales formation is at approximately the correct depth to generate the deep reflection events and the grit/shale interface would provide a strong reflection coefficient. It is therefore consistent to suggest that both the modern valley and the subparallel Lower Carboniferous turbidite channels were structurally controlled.

The method used for measuring reflector dip from VSP profiles (Fig. 15) is from Peter Conn (pers. comm.). It assumes a constant interval velocity, which may be unwarranted for a VRP behind a cliff-face. In the diagram, the vertical line represents the cliff-face (or borehole in VSP) through: source (s); receiver stations (g) and (e); and the reflector/profile intersection (r). The horizontal line represents the cliff-top land surface from the source

(s) to the projected reflector outcrop (c). The reflection points for receivers (e), (g) and (s) are (f), (h) and (z) respectively. The image point (i) of the source (s) is on straight lines (efi), (ghi) and (szi).

Triangle (sir) is equilateral with the reflector, line (cr), as median. Conn's method hinges on this. Because (sh) = (hi) and (sf) = (fi), the straight lines (ghi) and (efi) are equivalent to the reflection travel paths from the source (s) to the receivers at (h) and (e) respectively. Then, by applying the law of cosines to triangles (sig) and (sie):

$$si = \sqrt{\frac{sg \cdot (se^2 - ie^2) + se \cdot (ig^2 - sg^2))}{(se - sg)}} \quad \text{(A1)}$$

The angle of dip, (scr) = (isr) = (sir), is next calculated by:

$$\angle isr = \cos^{-1}\left[\frac{se^2 + si^2 - ie^2}{(2 \cdot se \cdot si)}\right] \quad \text{(A2)}$$

One can continue to derive formulae for the coordinates of the reflection points (f) and (h) by applying the law of sines to triangle (sie) and (sig), then finding the distances (rf) and (rh) by the difference of tangents to angles (scr) and (zsf). However, we need to calculate the dips of the two strong deep reflection events. A brief investigation showed that the computed dips are very sensitive to the value used for average velocity.

References

CAI, J. & MCMECHAN, G. A. 1999. 2-D ray-based tomography for velocity, layer shape and attenuation from GPR data. *Geophysics,* **64**, 1579–1593.

CORBEANU, R. M., SOEGAARD, K. ET AL. 2001. Detailed internal architecture of a fluvial channel sandstone determined from outcrop, cores, and 3-D ground-penetrating radar: example from the middle Cretaceous Ferron Sandstone, east-central Utah. *Bulletin of the American Association of Petroleum Geologists,* **85**, 1583–1608.

DAVIS, J. L. & ANNAN, A. P. 1989. Ground-penetrating radar for high-resolution mapping of soil and rock stratigraphy. *Geophysical Prospecting,* **37**, 531–551.

ELLIOTT, T. 2000. Depositional architecture of a sand-rich, channelised turbidite system: the Upper Carboniferous Ross Sandstone Formation, Western Ireland. *Gulf Coast section of the Society of Economic Paleontologists and Mineralogists Foundation 20th Annual Conference of Deep-Water Reservoirs of the World Proceedings, 3–6 December, Houston, USA,* 342–373.

FISHER, E., MCMECHAN, G. A. & ANNAN, P. A. 1992. Acquisition and processing of wide-aperture ground-penetrating radar data. *Geophysics,* **57**, 495–504.

FLOYD, J. D. 1996. Lithostratigraphy of the Ordovician rocks in the Southern Uplands: Crawford Group, Moffat Shale Group, Leadhills Supergroup. *Transactions of the Royal Society of Edinburgh, Earth Sciences,* **86**, 153–165.
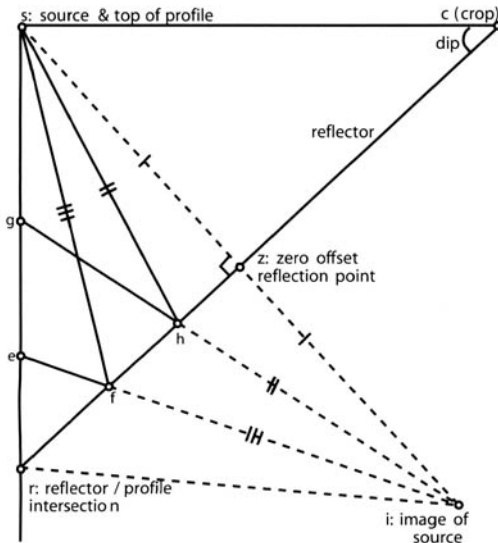
Fig. 15. Ray-trace diagram for calculating the dip and depth of a deep reflection event from VSP (or VRP) travel times. (After P. Conn pers. comm.)

FLOYD, J. D. 2000. The Southern Uplands Terrane: a stratigraphical review. *Transactions of the Royal Society of Edinburgh, Earth Sciences,* **91**, 349–362.

FOGIEL, M. 1980. *Handbook of Mathematical, Scientific, and Engineering Formulas, Tables, Functions, Graphs and Transforms.* Research and Education Association, New York.

GAWTHORPE, R. L., COLLIER, R. E., ALEXANDER, J., BRIDGE, J. S. & LEEDER, M. R. 1993. Ground penetrating radar: application to sandbody geometry and heterogeneity studies. *In*: NORTH, C. P. & PROSSER, D. J. (eds) *Characterization of Fluvial and Aeolian Reservoirs,* Geological Society, London, Special Publications, **73**, 421–432.

KEMP, A. E. S. 1987. Evolution of Silurian depositional systems in the Southern Uplands, Scotland. *In*: LEGGETT, J. K. & ZUFFA, G. G. (eds) *Marine Clastic Sedimentology,* Graham and Trotman, London, 124–155.

MARZO, M., NIJMAN, W. & PUIGDEFABREGAS, C. 1988. Architecture of the Castissent fluvial sheet sandstones, Eocene, South Pyrenees, Spain. *Sedimentology,* **35**, 719–738.

MOHRIG, D., HELLER, P. L., PAOLA, C. & LYONS, W. J. 2000. Interpreting avulsion process from ancient alluvial sequences: Guadalupe-Matarranya system (northern Spain) and Wasatch Formation (western Colorado). *Bulletin of the Geological Society of America,* **112**, 1787–1803.

NIJMAN, W. & PUIGDEFABREGAS, C. 1978. Coarse-grained point bar structure in a mollase-type fluvial system, Eocene Castissent Formation, South Pyrenean basin. *In*: MIALL, A. D. (ed.) *Fluvial Sedimentology,* Canadian Society of Petroleum Geologists Memoirs, **5**, 487–510.

PRINGLE, J. K., CLARK, J. D., WESTERMAN, A. R. & GARDINER, A. R. 2003. The use of GPR to image three-dimensional (3-D) turbidite channel architecture in the Carboniferous Ross Formation, County Clare, western Ireland. *In*: BRISTOW, C. S. & JOL, H. (eds) *Ground Penetrating Radar in Sediments.* Geological Society, London, Special Publications, **211**, 315–326.

PRINGLE, J. K., CLARK, J. D., WESTERMAN, A. R., BROWN, A. & FLOYD, J. D. 1999. A new application for digital photogrammetry: combining digital terrain models and ground penetrating radar imagery to characterise turbidite shale distribution in 3D. *Conference Proceedings of the International Association of Mathematical Geologists (IAMG), Trondheim, Norway, 6–11 August,* **2**, 653–658.

PRINGLE, J. K., WESTERMAN, A. R., CLARK, J. D., GARDINER, A. R. & CORBETT, P. W. M. 2000. 3-D GPR surveying with Vertical Radar Profiling (VRP) of petroleum reservoir outcrop analogues. *Proceedings of the 62nd European Association of Geophysicists and Engineers Conference & Technical Exhibition, Glasgow, 29 May–2 June,* **D-09**.

SZERBIAK, R. B., MCMECHAN, G. A., CORBEANU, R., FORSTER, C. & SNELGROVE, S. H. 2001. 3-D characterization of a clastic reservoir analog: from 3-D GPR data to a 3-D fluid permeability model. *Geophysics,* **66**, 1026–1037.

VAN DAM, R. L. & SCHLAGER, W. 2000. Identifying causes of ground-penetrating radar reflections using time-domain reflectometry and sedimentological analyses. *Sedimentology,* **47**, 435–449.

WAARD, R. 2001. 3D borehole radar technology development aims to transform drilling applications. News Feature, *First Break,* **19.9**, 491–493.

WÄNSTEDT, S., CARLSTEN, S. & TIRÉN, S. 2000. Borehole radar measurements aid structure geological interpretations. *Journal of Applied Geophysics,* **43**, 227–237.

WALKER, R. G. 1966. Shale Grit and Grindslow Shales: transition from turbidite to shallow water sediments in the Upper Carboniferous of Northern England. *Journal of Sedimentary Petrology,* **36**, 90–114.

ZHOU, H. & SATO, M. 2000. Application of vertical radar profiling technique to Sendai Castle. *Geophysics,* **65**, 533–539.

Visualization and characterization of active normal faults and associated sediments by high-resolution GPR

STEFAN REISS, KLAUS R. REICHERTER & CLAUS-DIETER REUTHER

Geological and Palaeontological Institute, University of Hamburg, Bundesstrasse 55, D-20146 Hamburg, Germany (e-mail: reiss@geowiss.uni-hamburg.de; reicherter@geowiss.uni-hamburg.de)

Abstract: Ground penetrating radar (GPR) is applied here to visualize sedimentary structures related to recent deformation. Several 200 MHz GPR profiles perpendicular to active normal faults in Spain and Italy were analysed. The El Camp normal fault with associated sedimentary and tectonic patterns in northeastern Spain serves as test site. Faulted alluvial and colluvial sediments of the Pleistocene were studied in a trench for direct comparison with GPR profiles. GPR investigations across buried faults from several localities are compared to these observations in a case study. The hanging walls of these faults form half-grabens or grabens, which are generally characterized by internal asymmetric, concave, displaced reflectors or wedge-like features comparable to sedimentary features in adjacent outcrops. The examples demonstrate that high-resolution GPR profiling provides not only the possibility to trace and map active normal faults but also to visualize the associated sedimentary hanging-wall patterns in the subsurface, such as heterogeneous graben and half-graben structures, including coarse-grained clastic wedges. Quantitative and qualitative GPR evaluation of those wedges yields a certain possibility of estimation of palaeomagnitudes and slip rates on active normal faults. We regard high-resolution GPR as an additional tool in pretrenching palaeoseismological investigations.

GPR in tectonic studies

Ground penetrating radar (GPR) has often been employed for detecting buried faults and underground tectonic structures. Meschede *et al.* (1997) observed tectonic surfaces and roll-over structures associated with faults in Middle Triassic limestones of southwestern Germany. Recent faults in alluvial fans in the Negev Desert (Basson *et al.* 1994) and fault-related displacement of medieval building walls at the Dead Sea transform (Marco *et al.* 1997), as well as active faults in the San Francisco Bay region (Cai *et al.* 1996), were mapped and studied with GPR imaging. However, high-resolution characterization and interpretation of the hanging wall of active faults by GPR are lacking until now, although antenna frequencies of 200 MHz and higher are able to resolve cm-sized objects (approx. 20 cm resolution with 200 MHz), discontinuities, folds or faults.

Preliminary subsurface examinations at palaeoseismological trench sites are common site-survey applications of GPR in order to locate the most promising place for costly excavations across the faulted area (Reicherter 2001; Vanneste *et al.* 2001). Other geophysical methods, e.g. resistivity surveying and/or reflection seismics, do not achieve the resolution of GPR. Electrical tomography studies in combination with GPR were carried out at the active Roer Graben in Belgium to find the position of the buried fault plane and associated fault scarp (Vanneste *et al.* 2001).

In this study, we use high-resolution GPR besides fault mapping and detection especially to characterize and interpret associated sedimentary structures in the hanging wall of normal faults, which often form grabens or half-grabens filled with post-faulting sediments. GPR investigations complement our palaeoseismological investigations along active faults and earthquake-related ruptures in southern Spain (Fig. 1, Reicherter 2001) and Sicily (Fig. 2).

Equipment, processing and methodology

The SIR 10B GPR system by Geophysical Survey Systems Inc. (GSSI) with antenna models 5103 (400 MHz) and 5106 (200 MHz) with survey
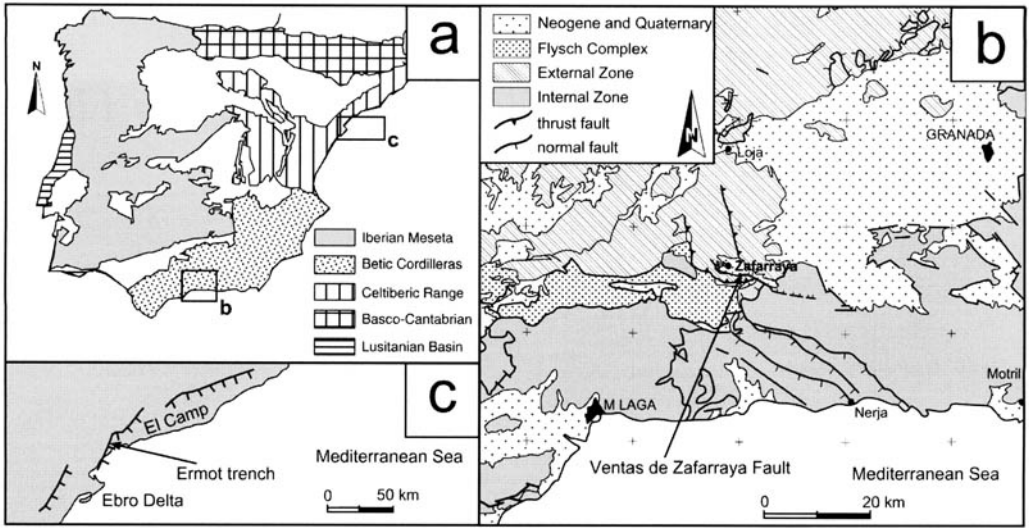
Fig. 1. (a) Simplified geological overview sketch of the Iberian peninsula, with indication of the working areas. (b) Geological map of the central Betic Cordillera. Arrow, studied section at Ventas de Zafarraya Fault north of Malaga. (c) Structural map of the El Camp/Ermot trench area south of Barcelona (Consejo de Seguridad Nuclear 1999).
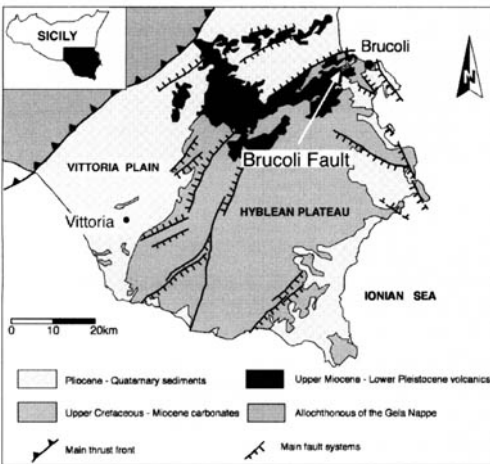
Fig. 2. Simplified structural map of southeastern Sicily. Arrow, studied section at the Brucoli Fault.

wheel is used to study subsurface tectonic structures and related features. The transmitter and receiver antennae are in one box, which is drawn over the ground during the continuous measuring process (512 shots/s). Cable length of 30 m reduces the data acquisition to a maximum section length of ~50–55 m in the field. Careful transportation of the radar computer in a car allows collection of longer sections. Data are stored directly on hard disk or Jaz-drive and can be directly displayed in the field for a preliminary evaluation. Different

parameters can be adjusted depending on soil, rock and groundwater conditions in the subsurface in order to optimize the electromagnetic signal. The applied antennae frequencies allow resolution of objects, discontinuities or strata in a dm/cm range (200 MHz ~20 cm; 400 MHz ~10 cm, respectively). Penetration depth varies depending on the antennae frequencies and the physical properties of the soil, rocks or position of groundwater table in the underground. Maximum interpretable penetration with 200 MHz antennae sets obtained in Quaternary sediments is ~5–6 m in the present study; however, in dry carbonate rocks or coarse-grained clastics up to 20 m can be achieved (Beres *et al.* 1995; Smith & Jol 1995). Applied as a geophysical pre-trenching tool, our GPR yields sufficient depth resolution and penetration for later excavations.

Normally, after good parametric field settings, the raw data do not even require reprocessing. We use the Reflex software (Sandmeier 2000) to optimize imaging. High groundwater levels and/or clay-rich palaeosols reduce penetration depths and make reprocessing necessary. A variety of filter tools can usually be applied during processing with Reflex: background removal, Butterworth band-pass, energy decay and FK filters as well as migration based on diffraction stack. If necessary, the relief of the section can be modelled later with the three-dimensional (3-D) topography correction.

The GPR studies prior to trenching are usually located at exposed active faults or historically reported surface ruptures (Reicherter 2001; Reich-

erter & Reiss 2001). The buried faults studied were often indicated by geomorphological steps, photo-lineaments and/or a significant change in the colour of the recent soil. During fieldwork GPR profiling is normally carried out perpendicular to the suspected fault trace or rupture. We generally acquire an entire section of the hanging wall of the active normal fault in order to look for secondary fault splays that may have developed at some distance from the main fault. To map the prolongation of the faults, perpendicular radar sections or rectangular grids have to be achieved in order to trace the fault length and to search for possible branches or en echelon-like fault arrays (Reicherter & Reiss 2001). Data obtained are usually in 2-D; gridding allows 3-D modelling. Additionally, a detailed structural analysis of the faulted area is necessary to interpret complex radar patterns.

Tectonic and geological setting of the studied active normal faults

Typical landform expressions of active normal faults are scarps that leave one side of the fault plane standing higher than the other side (Peacock et al. 2000). Fault-line scarps are linear features which border a steep slope or cliff, and hence point to active extension accompanied with basin formation, recent subsidence and deposition of Cenozoic sediments. Fault scarps form either by fault movement during earthquakes, by creep along a fault plane or by erosion (e.g. Mayer 1984; McCalpin 1996;Yeats et al. 1997). Surface ruptures or dislocation of the ground surface at faults require earthquakes with magnitudes of more than 5.5 (e.g. McCalpin 1996).

The asymmetric area of subsidence above a single, basin-bounding fault is called a half-graben (Peacock et al. 2000). Typically for co-seismic generation, a half-graben contains a sedimentary wedge that thickens towards the fault. Older beds generally have steeper dips than younger beds. Stratigraphic relationships along active faults often reveal successive offsets of the strata and deposition of colluvial and/or alluvial sediments as well as palaeosols (Wallace 1986). These permit the reconstruction of the faulting history, including the number and relative size of faulting events and the determination of recurrence intervals (e.g. McCalpin 1996). The initial height of the scarp in non-lithified sediments can be estimated from the dimension of the colluvial wedge (Mayer 1984; McCalpin 1996); the magnitude of the palaeoearthquake may be estimated by rupture length, rupture area or scarp–height relationships (Wells & Coppersmith 1994). Liquefaction, such as sand blows, clastic dykes and deformed beds, may reveal evidence for strong ground-shaking and provide

further support of earthquake activity. Repeated colluvial wedges along the bases of fault scarps and their stratigraphic relation with wash-off sediments and palaeosols preserved within the half-graben confirm palaeoseismological evidence for earthquake-related faulting.

Faults and associated sedimentary structures on high-resolution radar images

Case study

The El Camp Fault cuts the Catalunian coastal range in eastern Spain (Fig. 1, Province of Tarragona). Palaeoseismologic investigations have been carried out along a NE–SW trending, SE-dipping segment of the El Camp Fault which is considered to be active (Consejo de Seguridad Nuclear 1999). The southern segment is 14 km long and marked by a prominent morphological scarp that displaces Quaternary alluvial fan sediments. A number of trenches across the scarp have been excavated for palaeoseismological studies (Masana 1996; Consejo de Seguridad Nuclear 1999: Masana et al. 2000). For comparison of the radar results with the structures exposed on the trench wall, we chose Trench 4 near Ermot to perform a detailed radar survey parallel to the northern wall of the trench and perpendicular to the strike of the fault. The fault exposed in the trench forms an extensional structure with several secondary faults (Consejo de Seguridad Nuclear 1999). The hanging wall is characterized by a thick colluvial wedge which is, on the other hand, cut by a younger event (Fig. 3). Preserved in the trench are significant concave patterns above three earthquake-induced event horizons during the last 125 ka, pointing to palaeomagnitudes of >6 (Masana et al. 2000). The scarp height is ~6.5 m, resulting in a mean slip rate of 0.05 mm/a. The GPR profile runs parallel to the trench at a distance of 5 m from the northern trench wall and displays interpretable subsurface information up to 5 m depth. We interpret reflector endings as cut by vertical and subvertical faults or gashes, whereas bending of reflectors which are more or less parallel to the surface delineate sedimentary layers and/or structures. The two main strands of the El Camp Fault, associated secondary faults, and filled or open joints and gashes are partly characterized by sigmoidal patterns or 'horses', which can be clearly identified on the radar images (Fig. 3). The colluvial and alluvial sediments in the hanging wall are characterized by planar and concave reflectors, which mark the colluvial wedge and overlying younger sediments. From trenching studies, colluv-
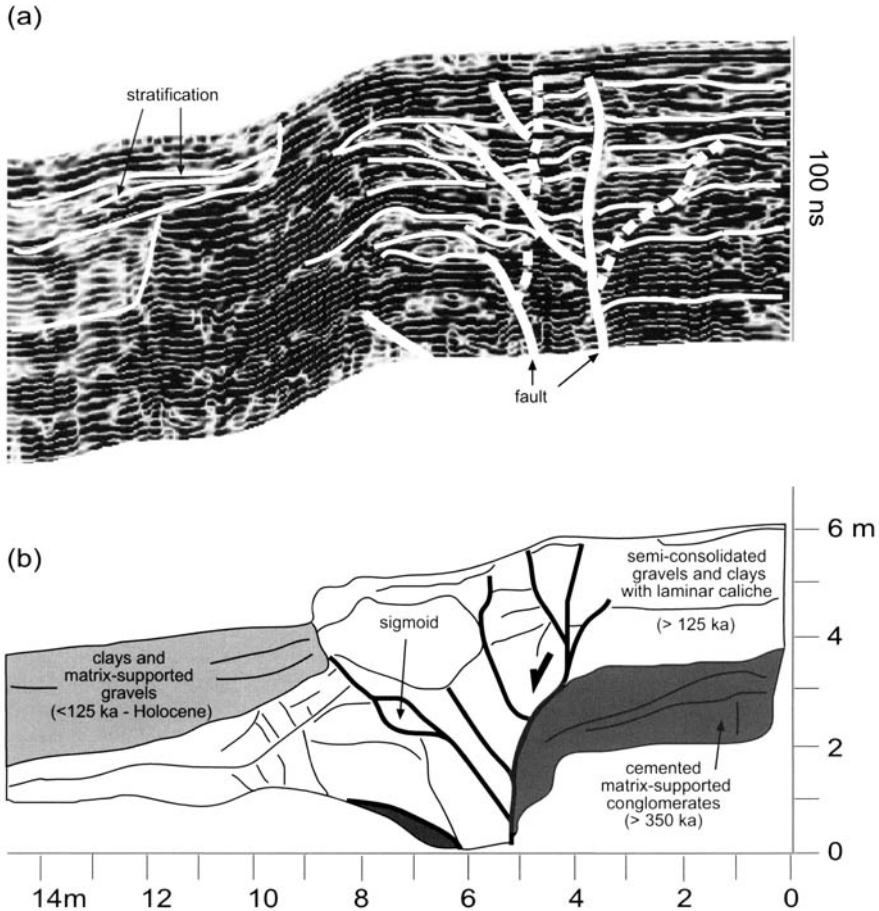
Fig. 3. (a) Interpreted high-resolution GPR profile across trench 4 (northern wall) at Ermot/El Camp Fault (northeastern Spain) and (b) geological trench log (after Consejo de Seguridad Nuclear 1999).

ial wedges are generally characterized by taper-like shapes and an internal fining-up sequence of coarse-grained material (McCalpin 1996; Masana 1996; Reicherter 2001). In contrast to well-bedded wash-off sediments and palaeosols, which produce parallel reflection patterns, colluvial wedges are characterized by diffuse GPR patterns. The diffuse patterns originate from the coarse-grained sediments (parabolas of individual boulders) and higher porosity of the colluvial wedges (weak intensity pattern in GPR images). The interpretation of GPR profiles across active faults at the El Camp site provides an insight into the internal structure of the associated half-graben and fault traces. Furthermore, the thickness of individual colluvial wedges can be deduced, which supplies a method for the estimation of the displacement and magnitude of distinct palaeo-earthquake events. Resolution of the 200 MHz antennae allows the

detection of secondary faults and small-scale sedimentary geometry.

Examples of fault-scarp associated sedimentary structures

All examples are from active tectonic regions in southern and northeastern Spain (Fig. 1) and Sicily/Italy (Fig. 2). Active normal faults are usually associated with distinct sedimentary features preserved in the hanging wall (tapering wedges, fining-up sequences). The majority of the presented profiles have been shot with the 200 MHz antenna and have been cut to 15 m length. The profiles run perpendicular to the main fault. Penetration depth depicted is 100 ns TWT (~5 m; ns, nanoseconds; TWT, two-way travel time).

The Ventas de Zafarraya Fault (VZF) in southern Spain forms a prominent east–west-trending

lineament in the Betic Cordilleras and has a multiple earthquake history (Reicherter *et al.* 2000). The last major earthquake (M7) occurred on 25 December 1884 and is associated with surface ruptures, landslides and liquefaction (Reicherter 2001) as well as a co-seismic slip of ~1 m. The northward-dipping major fault scarp of the VZF in Jurassic limestones is related with a recent sediment prism accumulated above a roll-over anticline in the hanging wall (Fig. 4) and also several smaller secondary faults. GPR has been applied to survey subsurface structures across the normal fault scarp, from karstified Jurassic limestone to Quaternary clays, sands and conglomerates with intercalated palaeosols within the hanging wall. Three colluvial wedges have been identified in an outcrop section, pointing to three palaeoearthquakes with magnitudes of >6.5 in the last 9 ka (Reicherter 2001). A GPR section was obtained across the major scarp of the VZF (GPS 36°57,500'N, 04°07,500'W), where both footwall and hanging wall consist of Jurassic limestones (Fig. 5a). The main fault in the central part can be traced in terms of distance and projected to the studied outcrop section (Fig. 4). Reflectors are interrupted and displaced by the fault along a steep lineament. Within the upper part of the hanging wall, continuous reflectors show a significant change into concave patterns, which are interpreted as deformed fault-related half-graben sediments of Holocene age. In detailed view, high-resolution GPR reveals internal structures within the half-graben sediments (Fig. 6a). The Quaternary sediments are stratified and faulted internally, as indicated by small vertical offsets. Pinching-out structures are interpreted as forming coarse-grained colluvial wedges. The concave patterns disappear at a distance of ~10 m to the fault.

A second GPR profile was shot at ~80 m north from the major scarp within the hanging wall (Fig. 5b), parallel to the above-described. The interpretation of radar pattern revealed significant evidence for an adjacent synthetic, minor normal fault within the hanging wall: the reflectors are interrupted and an apparent change in dip is observable. Some reflectors are warped. Again, a concave filling is related to the fault. A more detailed view of internal structures of the half-graben reveals further evidence for smaller offsets and earthquake-related sedimentation (Fig. 6b).

To image the internal structure of the half-graben fillings in detail, a higher resolution was obtained applying the 400 MHz antennae across the same section line of Fig. 5a. Penetration depth is drastically reduced to 50 ns TWT, equivalent to 2.2 m. The major fault plane is clearly trackable. Furthermore, we are able to portray the shapes and internal structures of the upper and middle colluvial wedges (Fig. 7). Both are characterized by low-intensity reflections, typically observed in coarse-grained sediments. The wedges mainly consist of blocky Jurassic limestone clasts and are clast-supported. The thickness of both wedges is ~35 cm and ~50 cm, respectively. The outcropping third and lowermost colluvial wedge (Reicherter 2001) was not imaged with the 400 MHz antennae. The intercalated wash-off sediments and palaeosols drape the tapered wedges (Fig. 7). On the radar images the well-stratified sediments, representing a period of seismic quiescence, form parallel reflectors. These observations, obtained by GPR, match exactly what has been found in the outcrop scale (Reicherter 2001) and can be used for the estimation of slip rates and palaeomagnitudes (see below). In conclusion, the VZF branches into sev-

Fig. 4. The main fault scarp of Ventas de Zafarraya (centre). White line, position of radar section; F, footwall; H, hanging wall.
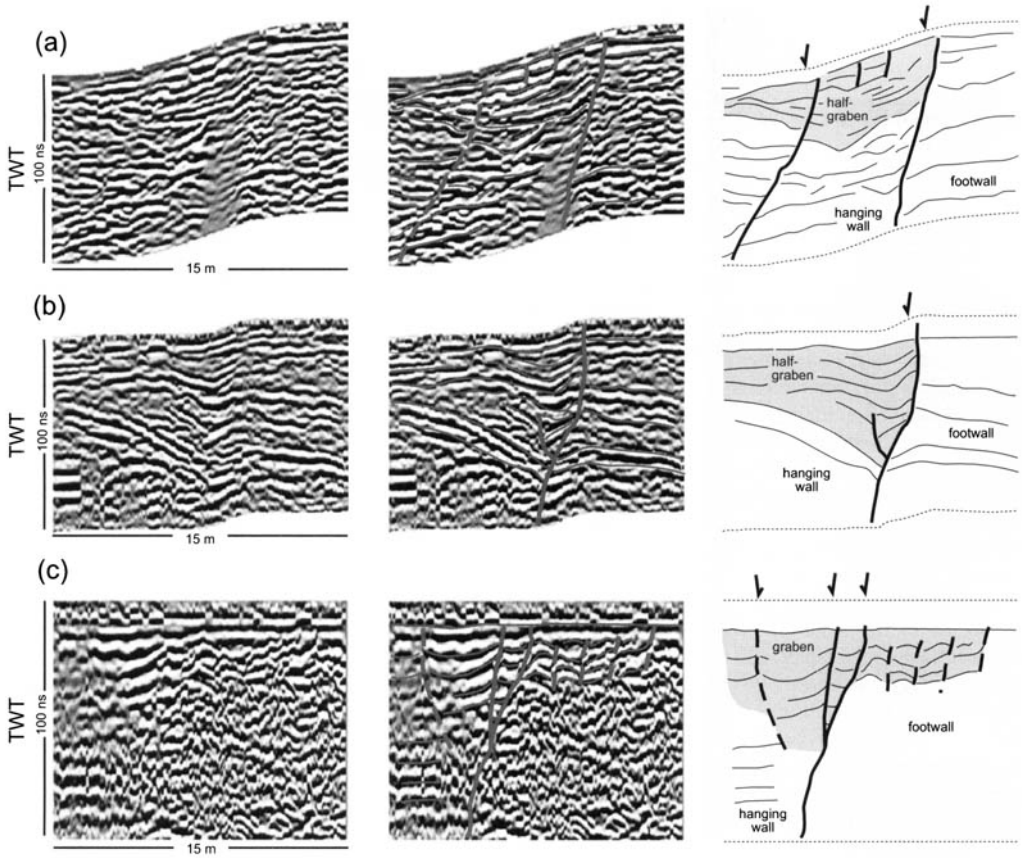
Fig. 5. High-resolution GPR images of active normal faults using the 200 MHz antennae. Profile length is 15 m, TWT is 100 ns in all examples. Hanging wall is generally located on the left, the main fault in the centre and the footwall on the right. TWT, two-way travel time; ns, nanoseconds, 20 ns are ~1 m. (**a**) Main fault strand of the Ventas de Zafarraya Fault (Betic Cordilleras, southern Spain). (**b**) Secondary fault strand of the Ventas de Zafarraya Fault (Betic Cordilleras, southern Spain). (**c**) Main fault strand of the Brucoli Fault (Hyblea Plateau, southeastern Sicily, Italy). In each: processed GPR image (left), central: interpreted GPR image (centre), line drawing of significant features (right).

eral secondary faults which also show GPR evidence for ground failure, liquefaction and compaction due to Holocene seismicity. The high-resolution GPR allows us to interpret and unravel the sedimentary filling history of the associated half-graben.

The Brucoli site is located near the small village of Brucoli at the northern margin of the Hyblean Plateau in southeastern Sicily/Italy (GPS 37°17,346′N, 15°08,204′E). The normal Brucoli Fault is associated with the complex fault system of the active Malta escarpment (Adam *et al.* 2000) and parallels the prominent Lentini Graben system. The NW-dipping normal fault displaces Miocene limestones against Holocene soils with caliche and Pleistocene calcarenites, proving recent activity. Along a roadside outcrop, the fault zone and the associated half-graben were studied. Our high-res-

olution GPR section image across the Brucoli Fault revealed a variety of radar patterns attributable to distinct lithologies (Fig. 5c). The major fault is associated with a minor normal fault. In the hanging wall an antithetic normal fault is detectable, forming a small graben within the hanging wall (Fig. 6c). The hanging-wall pattern shows concave reflectors which are obviously well-bedded, dragged younger sediments. The faults and the complex half-graben are covered and sealed by well-stratified planar patterns of the recent soil. A close-up of the hanging wall reveals internal faults which cut and displace reflectors (Fig. 6c).

Discussion

Faults can easily be identified on radar images if: (1) they juxtapose different lithologies, producing
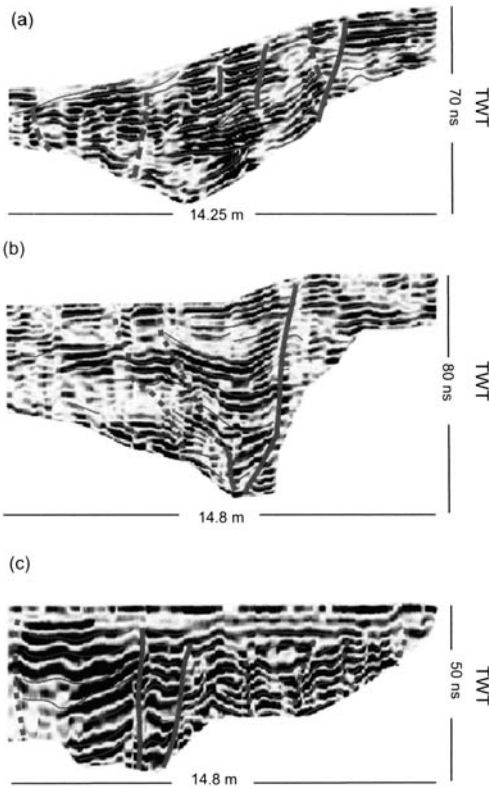
Fig. 6. Detailed images of earthquake-related sediment fillings within associated half-grabens or grabens. (For localities of A–C, see Fig. 5).

Fig. 7. (a) High-resolution GPR image of the active normal fault and (b) related colluvial wedges of the Ventas de Zafarraya Fault (400 MHz antennae). North is to the left Profile length is 38 m, maximum TWT is 50 ns. Thick white line, major normal fault; thin white line, colluvial wedges and well-stratified covering sediments. Note the different GPR patterns of the colluvial wedges with low intensity in contrast to the well-stratified palaeosols and wash-off sediments. Thicknesses of the middle wedge and upper wedge are ~50 cm and 35 cm, respectively (see time–depth conversion on the vertical bar [right]).

distinct radar patterns within footwall and hanging wall, caused by, e.g., different intensities, bed thickness, clay contents; (2) they juxtapose strata with varying dips, warp or drag reflectors, and hence produce significant changes in pattern geometries; (3) some continuous reflector bundles are interrupted and significantly displaced along vertical or subvertical linear structures (reflector offsets). Usually, the mapping and field investigations allow projection of tectonic lineaments towards natural or artificial outcrops, which structures may support later radar interpretation. Parallel GPR sections at the sites generally show that faults and related structures are traceable in distance and depth. Active normal faults may also be recognized and characterized by imaging the sedimentary structures in the hanging wall.

Characteristic hanging-wall patterns

Colluvial and alluvial sediment fillings in half-grabens formed within the hanging wall of faults are expressed on radar images as asymmetric con-

cave patterns. Generally, the half-grabens are internally well stratified. Typically, the examples of half-grabens contain wedge-like structures that thicken towards the presumed major fault plane. Reflectors recognized deeper in the half-graben, and hence in older beds, have generally steeper dips than overlying younger beds, which are characterized by flat-lying reflectors. Geometric relationships from radar patterns in hanging walls along active faults often suggest successive offsets or dragging of the reflectors. These characteristic features observed in high-resolution GPR images help to distinguish fault-related sedimentary hanging-wall patterns from fluvial channel fills or anthropogenic filling, which may produce similar concave patterns.

In particular, the characteristic patterns and the relation of colluvial wedges, covering wash-off sediments and palaeosols, allow palaeoseimic estimations. The GPR facies of low-intensity colluvium and the high intensity of stratified soily sediments delineate individual event horizons. The hanging-wall patterns of the VZF yield GPR evidence for two co-seismic surface ruptures and post-seismic sedimentation (Fig. 7). The geological record of the two youngest palaeoearthquakes of

1884 and *c.*2315 a BP (Reicherter 2001), with ~0.7 m and ~1 m displacement, respectively, was imaged with GPR. The co-seismic displacement is equivalent to a palaeomagnitude larger than 6.5, according to empirical studies of Wells and Coppersmith (1994). The thickness of the individual wedges also resembles half of the initial scarp height, as already outlined from outcrops studies by Reicherter (2001).

Conclusions

High-resolution radar profiles across several active normal faults reveal typical concave patterns within the hanging wall, which are interpreted as fault-related half-graben fillings. At the El Camp site in northeastern Spain, GPR imaging has been compared to trench-logging results in a case study. Based on this, buried faults and associated structures have been imaged by GPR, revealing comparable sedimentary patterns along various active faults in southern Spain and Sicily. Faults, displacements and sedimentary structures can be visualized by high-resolution GPR with 200 MHz and 400 MHz antennae up to 5 m penetration depth in unconsolidated, fine-grained Quaternary sediments. Internal structures, such as stratification and younger, smaller tectonic offsets within the sediment fillings, can also be imaged with GPR. The footwalls of the faults as well as the individual fault planes can be visualized in GPR images. Thus, high-resolution GPR investigations may help not only to locate faults but also to recognize fault-related sedimentary structures as needed in palaeoseismological investigations. If characteristic colluvial wedges and draping well-stratified sediments are developed in the hanging wall, high-resolution GPR imaging serves to resolve single palaeoseismic events and allows a preliminary estimation of the palaeomagnitude and slip rates.

References

ADAM, J., REUTHER, C.-D., GRASSO, M. & TORELLI, L. 2000. Active fault kinematics and crustal stresses along the Ionian margin of southeastern Sicily. *Tectonophysics*, **326**, 217–239.

BASSON, U., ENZEL, Y., AMIT, R. & BEN-AVRAHAM, Z. 1994. Detecting and mapping recent faults with a ground penetrating radar in the alluvial fans of the Arava Valley, Israel. *Proceedings of the 5th Conference on Ground Water Penetrating Radar, Waterloo Center for Groundwater Research, Kitchener, Ontario, Canada*, 777–788.

BERES, M., GREEN, A., HUGGENBERGER, P. & HORSTMEYER, H. 1995. Mapping the architecture of glaciofluvial sediments with three-dimensional georadar. *Geology*, **23**, 1087–1090.

CAI, J., McMECHAN, G. A. & FISHER, M. A. 1996. Application of ground-penetrating radar to investigation of near-surface fault properties in the San Francisco Bay region. *Bulletin of the Seismological Society of America*, **86**, 1459–1470.

CONSEJO DE SEGURIDAD NUCLEAR 1999. *Proyecto Dataci ón – Informe Fina.* CSN and ENRESA, Madrid, 159 pp.

MARCO, S., AGNON, A., ELLENBLUM, R., EIDELMAN, A., BASSON, U. & BOAS, A. 1997. 817-year-old walls offset sinistrally 2.1 m by the Dead Sea transform, Israel. *Journal of Geodynamics*, **24**, 11–20.

MASANA, E. 1996. Evidence for past earthquakes in an area of low historical seismicity: the Catalan coastal ranges, NE Spain. *Annali di Geofisica*, **39**, 689–704.

MASANA, E., VILLAMARIN, J. A., SANCHEZ CABAÑERO, J., PLAZA, J. & SANTANACH, P. 2000. Seismological behavior of a fault with no historical seismicity: El Camp fault (northeastern Iberian peninsula). *In:* CAMELBEECK, T. (ed.) *PALEOSIS – Evaluation of the Potential for Large Earthquakes in Regions of Present Day Low Seismic Activity in Europe.* Han, Belgium, 129–131.

McCALPIN, J. 1996. *Paleoseismology.* International Geophysics Series, **62**, 588 pp.

MAYER, L. 1984. Dating Quaternary fault scarps formed in alluvium using morphologic dating. *Quaternary Research*, **22**, 300–313.

MESCHEDE, M., ASPRION, U. & REICHERTER, K. 1997. Visualization of tectonic structures in shallow-depth high-resolution ground-penetrating radar (GPR) profiles. *Terra Nova*, **9**, 167–170.

PEACOCK, D. C. P., KNIPE, R. J. & SANDERSON, D. J. 2000. Glossary of normal faults. *Journal of Structural Geology*, **22**, 291–305.

REICHERTER, K. 2001. Paleoseismologic advances in the Granada Basin (Betic Cordilleras, southern Spain). *In:* MASANA, E. & SANTANACH, P. (eds) *Paleoseismology of Spain.* Acta Geologica Hispanica, Barcelona, Special Volumes, **36**, 267–281.

REICHERTER, K. & REISS, S. 2001. The Carboneras Fault Zone (southeastern Spain) revisited with ground penetrating radar – Quaternary structural styles from high-resolution images. *Netherlands Journal of Earth Sciences/Geologie en Mijnbouw*, **80**, 129–138.

REICHERTER, K., JABALOY, A., GALINDO-ZALDIVAR, J., RUANO, P., MICHEL, G. W. & BECKER-HEIDMANN, P. 2000. Paleoseismic studies in the Granada basin (southern Spain) – Evidence for large prehistoric earthquakes? *In:* Camelbeeck, T. (ed.) *PALEOSIS – Evaluation of the Potential for Large Earthquakes in Regions of Present Day Low Seismic Activity in Europe.* Han, Belgium, 129–131.

SANDMEIER, K. J. 2000. *ReflexW Version 2.1.2, User Manual.* Karlsruhe, Germany.

SMITH, D. G. & JOL, H. M. 1995. Ground penetrating radar: antenna frequencies and maximum probable depths of penetration in Quaternary sediments. *Journal of Applied Geophysics,* **33**, 93–100.

VANNESTE, K., VERBEECK, K. ET AL. 2001. Surface-rupturing history of the Bree fault scarp, Roer Valley graben: Evidence for six events since the late Pleistocene. *Journal of Seismology,* **5**, 329–359.

WALLACE, R. E. 1986 (ed.) *Active Tectonics. Studies in Geophysics, Overview and Recommendations.* National Academy of Sciences, Washington D.C., 3–20.

WELLS, D. L. & COPPERSMITH, K. L. 1994. New empirical relationships among magnitude, rupture length, rupture width, rupture area, and surface displacement. *Bulletin of the Seismological Society of America,* **84**, 974–1002.

YEATS, R. S., SIEH, K. & ALLEN, C. R. 1997. *The Geology of Earthquakes.* Oxford University Press, New York, 568 pp.

This page intentionally left blank

Radar reflections from sedimentary structures in the vadose zone

REMKE L. VAN DAM[1,2], ELMER H. VAN DEN BERG[1], MARCEL G. SCHAAP[3], LUCAS H. BROEKEMA[4,5] & WOLFGANG SCHLAGER[1]

[1]*Faculty of Earth and Life Sciences (FALW), Vrije Universiteit, De Boelelaan 1085, 1081 HV Amsterdam, The Netherlands*
[2]*Present address: New Mexico Tech, Department of Earth and Environmental Science, 801 Leroy Place, Socorro, New Mexico, USA (e-mail: rvd@nmt.edu)*
[3]*George E. Brown Jr, Salinity Laboratory, 450 Big Springs Road, Riverside, California 92507–4617, USA*
[4]*ESRI Nederland, Stationsplein 45, 3001 GA Rotterdam, The Netherlands*
[5]*Present address: National Aerospace Laboratory (NLR), P.O. Box 153, 8300 AD Emmeloord, The Netherlands*

Abstract: Ground penetrating radar (GPR) is a suitable technique for imaging sedimentary structures in the vadose zone because small texture-related capillary-pressure variations lead to changes in water content and electromagnetic properties. To study exactly how GPR reflections are generated by sedimentary structures, GPR profiles of an aeolian sedimentary succession are combined with measurements of textural, electromagnetic and water-retention characteristics from a trench. Time domain reflectometry indicates that small variations in texture in the high-angle dune sediment are associated with changes in water content. Synthetic modelling shows that these changes cause clear GPR reflections. In an experimental approach to estimate the radar response of structures below the wave resolution, i.e. features smaller than $\lambda/4$, variations in grain-size distribution and porosity in a thin section were used to reconstruct water-retention curves and impedance models of the thinly layered sediment. Synthetic radar records calculated from the impedance models show that reflections from the studied subcentimetre-scale structures are composites of interfering signals. Although these low-amplitude interfering signals will commonly be overprinted by more prominent reflections, they may cause reflection patterns that change with frequency and do not represent primary bedding.

Ground penetrating radar (GPR) has become a popular geophysical technique that is frequently used to image sedimentary structures and sedimentary architecture. GPR measures changes in electromagnetic (EM) properties of subsurface features that cause reflection of transmitted EM waves. It is generally understood that textural changes in unsaturated (vadose-zone) sediment cause variations of water content (e.g. Mishra *et al.* 1989; Hänninen 1992). Because water has EM properties that are highly contrasting with those of air and most types of sediment grains (e.g. Friedman 1998), the water content of vadose-zone sediment governs the behaviour of GPR waves. As textural characteristics vary most prominently perpendicular to depositional layering, and because radar signals reflect from boundaries between layers with different EM properties, GPR can be used to image sedimentary structures (e.g., Huggenberger *et al.* 1994; Kowalsky *et al.* 2001).

Studies that try to quantify the relationship between textural properties, water content and EM wave propagation usually consider a large range of grain and pore sizes (e.g. Hubbard *et al.* 1997; Endres 2000). Frequently used regression functions (Gupta & Larson 1979; Saxton *et al.* 1986) and the more sophisticated physico-empirical model of Arya and Paris (1981) relate water content to bulk density and to percentages of sand, silt, clay and organic matter. Knoll & Knight (1994) presented a dielectric mixing model that includes clay-volume fraction. Dobson *et al.* (1985) presented semi-empirical and theoretical four-component mixing models, including the bound water fraction, and demonstrated that this fraction varies strongly with the quantity of clay minerals in the sediment. Sutinen (1992) quantified relations between grain size, water content and dielectric properties. He found that the percentage of clay and silt had a large

effect on the dielectric properties but observed no correlation between dielectric properties and the grain size of sand and gravel.

Aeolian sediment, discussed in the present study, commonly has a very narrow range of grain sizes and usually contains only grains in the sand fraction. Nevertheless, aeolian deposits produce clear GPR reflections (e.g. Bristow *et al.* 2000; Neal & Roberts 2001). For these rather uniform sedimentary facies, important questions about reflection of radar signals remain unsolved. With respect to GPR, it is not known in great detail which textural characteristics (e.g. grain size, sorting, packing, grain shape, porosity) control the actual reflection. In addition to this, the minimum variation in these textural characteristics required to generate a reflection is unclear. Furthermore, little is known about the effect of reflection and signal interference from layering smaller than the vertical resolution limit, commonly assumed to be a quarter wavelength, $\lambda/4$ (e.g. Huggenberger 1993). Typical values for $\lambda/4$ in moist sand ($v = 0.12\ \text{m}\ \text{ns}^{-1}$) range from 0.3 m to 0.033 m for 100 MHz to 900 MHz frequencies, respectively.

Interference of radar reflections from small-scale EM-property variation in geological material and sediment is very common (e.g. Clement *et al.* 1997) but has never been studied in detail. Few modelling studies on this issue have been performed. Wave interference has gained much more attention in the interpreting and modelling of seismic reflection data. Gochioco (1992) shows that layers as thin as one-fortieth the width of the dominant wavelength can be detected. However, thin sediment layers are commonly not isolated and are often more narrowly spaced than the maximum vertical resolution (e.g. Kallweit & Wood 1982; Roksandic 1995). Consequently, recorded reflections are composites of several interfering signals (e.g. Mayer 1980; Knapp 1990; Bracco Gartner 2000). As a result, the seismic response from thinly layered sediment may not represent distinct geological horizons (Mayer 1979).

To address the above questions with respect to GPR reflections, a study area was selected in aeolian dune deposits near the Dutch coast, south of Katwijk aan Zee (Fig. 1). The deposits consist of units with clean, windblown quartz sand, separated by soils (Van Dam *et al.* 2002*b*). The upper unit, characterized by high-angle cross-stratification, was used for this study. The site was surveyed using a grid of two-dimensional (2-D) GPR lines. Following the GPR survey, trenches that allowed us to study the sediment were dug along two sides of the grid. Lacquer peels were collected for macroscopic study of sedimentary structures. Samples for grain-size analyses were taken from vertical transects in the trenches. Time domain

reflectometry (TDR) was used to obtain direct and detailed information on the EM properties of the sedimentary structures. Furthermore, undisturbed core plugs were collected for laboratory determination of the water-retention characteristics of the sediment. Finally, box cores were collected for microscopic thin-section analysis of the sedimentary structures. The small-scale textural information from the digitized thin sections was used to estimate water retention and dielectric properties perpendicular to the sedimentary bedding. The TDR measurements and thin sections were used to construct models of EM-wave impedance and to calculate synthetic radar traces. The TDR-based synthetic radar traces were used to study signal interference. The thin-section-based model serves as a more theoretical approach to improve understanding of propagation and reflection of GPR waves within and across sedimentary structures.

Water retention

The primary reason that GPR can image structures in relatively uniform unsaturated materials is that the water content is a function of the sediment properties. Porous media in natural unsaturated conditions retain some water, which indicates that certain forces prevent part of the interstitial moisture from draining. These so-called 'matric' forces can be subdivided into adsorption and capillary forces (De Marsily 1986). Adsorption is the strong molecular attraction between water and solids that creates a thin water film around sediment particles. The amount of adsorbed water depends on the specific surface area of the solid phase (e.g. Friedman 1998). Because adsorbed water has a low relative permittivity (Roth *et al.* 1990; Saarenketo 1998), and because the specific surface area of sand is small (Dobson *et al.* 1985; Sutinen 1992), its influence on the EM properties of the total sediment volume is limited. Capillary forces result from pressure differences between the water and air phases in the pores and control the amount of free water in the pore space. The capillary pressure is inversely proportional to the pore radius (r). Matric forces thus exert suction on the pore water, usually expressed by the pressure head (h) or suction potential (pF), where $pF = \log|h|$. The term 'field capacity' is defined as the specific suction potential at which gravity-driven drainage has ceased. In this paper, a *pF* of 2 refers to the natural unsaturated field-capacity conditions.

The relation between suction potential and volumetric water content (θ) is a fundamental soil hydrological property (Arya & Paris 1981) that is related to the size distribution and connectivity of the pores (Vogel & Roth 1998; Fens 2000). Pore bodies with wide entry channels (pore throats) will
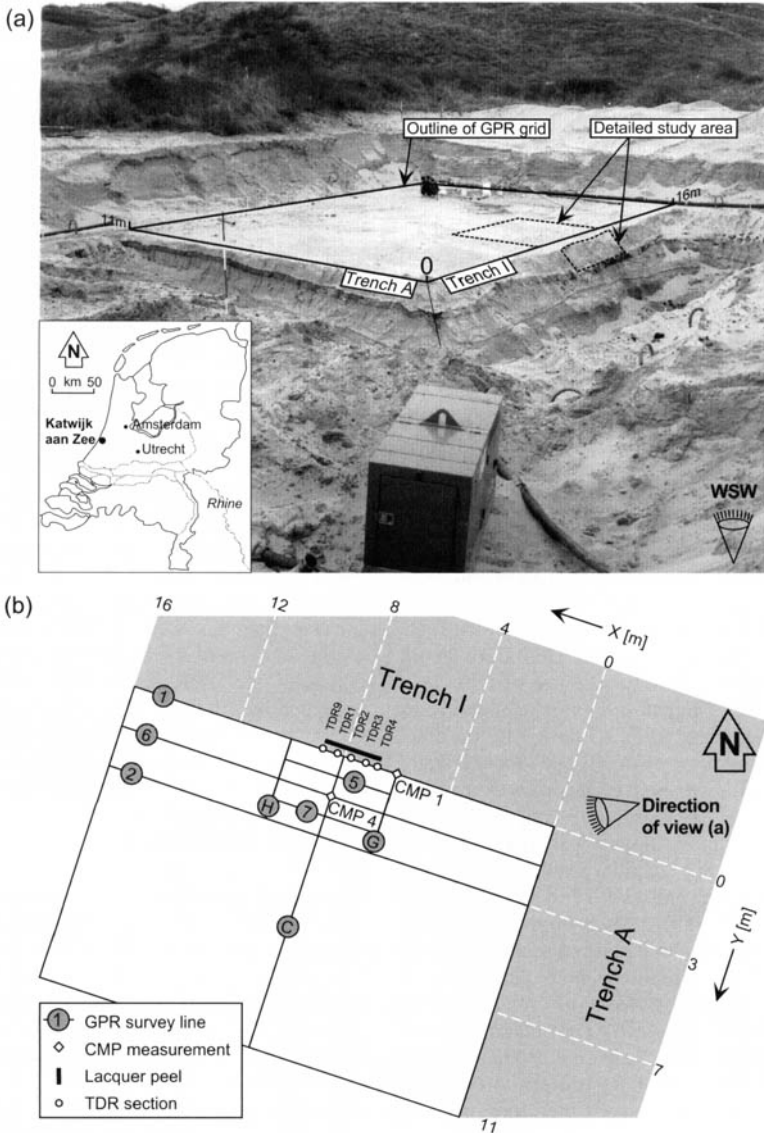
Fig. 1. (a) Study site with trenches. The inset shows the location of the study area at Katwijk aan Zee in The Netherlands. The dashed lines on the photograph mark the detailed survey area, imaged with both 450 MHz and 900 MHz antennae. (b) Measurement grid showing locations of GPR survey lines, common mid-point measurements, lacquer peels and TDR measurements.

drain at low suction, whereas those with narrow channels drain at higher suction (Bouma 1977). It is generally accepted that, at field-capacity conditions and for equal porosity values, fine-grained sediment with small pores has a higher θ than coarse-grained sediment. The same holds for poorly sorted sediment relative to well-sorted sediment. Simple laboratory experiments allow measurement of the θ-pF relation. In these experi-

ments, the initially saturated sediment cores are drained and water content is measured at specific suction potentials. Water-retention curves can be modelled by fitting the measured θ-pF pairs with the Van Genuchten (1980) function:

$$\theta = \theta_r + \frac{\theta_s - \theta_r}{(1 + (\alpha_{vg}|h|^n)^{m_{vg}}}. \tag{1}$$

Here, θ_r and θ_s represent the residual and saturated

water contents, respectively, α_{vg} [cm^{-1}] and n are parameters for a characteristic pore size and for the pore size uniformity, respectively (Wösten & Van Genuchten 1988), and $m_{vg} = 1 - n^{-1}$. This experimental method is time-consuming and cannot account for small-scale texture variations related to the sedimentary structures present in the sample volumes.

In addition to the experimental laboratory method, the θ-pF relation can also be calculated using modelling approaches that describe the relation between capillary forces and physical characteristics of the sediment. Methods like network modelling (Vogel 2000) and percolation theory are based on estimates of pore structure and pore-size distribution. However, the actual pore-size distribution of sediment is difficult to measure. Consequently, these methods are based on simplified assumptions. Mishra *et al.* (1989) argue that the grain-size distribution (GSD) of sediment can be used as a proxy for its pore-size distribution and, thus, for the water retention in non-saturated sediment. Factor analysis of the aeolian sediment at the test site shows a good correlation between the GSD and pore-size distribution (Van Den Berg *et al.* 2003). This would allow for the use of GSD as a proxy for the water-retention in non-saturated sediment. However, in addition to the GSD, the total porosity (η) is a factor of importance for the water retention in sediment as it is generally a measure for the packing. Assuming sediment with equal grain-size distribution, tighter packing results in smaller pores that hold capillary water with greater ease. Therefore, the omission of η in the method by Mishra *et al.* (1989) leads to simplified results. Both η and GSD can be measured relatively easily and a method that combines both parameters is preferable in estimating the θ-pF relation when using a modelling approach. The neural network model introduced by Schaap and Bouten (1996) uses η and GSD as input parameters to calculate water-retention curves and is therefore used in this study.

Test site

Experimental procedure

The 11 × 16 m test site was surveyed with a grid of 2-D GPR lines (Fig. 1), using a pulseEKKO radar system with 25 MHz, 100 MHz, 225 MHz, 450 MHz and 900 MHz antennae. 450 MHz and 900 MHz antennae were used to image a small, 3 × 4 m area along the long axis of the grid in greater detail (Table 1). Subsequent to the GPR measurements, two trenches (A and I), each 3 m deep, were dug for detailed study and sampling of the sediment. Lacquer peels were made for the macroscopic study of the textural characteristics. Nineteen core plugs were collected for laboratory measurements of water retention. The core plugs, with a volume of 45 cm^3, were sampled by pushing a metal ring into the sediment. The metal rings have walls of minimum thickness, so as to reduce sediment disturbance. Along vertical sections in the wall of trench I, TDR was used to obtain detailed information on the dielectric properties of the subsurface. Samples were collected for the macroscopic analysis of the textural properties (Table 2). Although the TDR and GPR measurements are separated by a 1-week time interval, no large ambiguities are expected as the wind-dried surface of the trench was removed before measuring TDR data.

To obtain detailed information on the variation in textural characteristics and EM properties normal to the high-angle sedimentary bedding, three sites, A, B and C, were selected in the detailed study area in trench I (Fig. 2b). Both A and B were set at the location of known fine-grained foreset tops; C was set at a position where foresets were absent. To measure variation in EM wave velocity perpendicular to the bedding, four detailed TDR sections with a 0.02 m spacing were measured at these locations (Fig. 2b).

In an experimental approach to measure small-scale variations in textural characteristics and EM

Table 1. *Acquisition and processing details of GPR section 1 and common mid-point (CMP) measurements*

Name*	Acquisition parameters				Processing parameters		
	Frequency (MHz)	X, Y(start) (m)	Length (m)	Step size (m)	Stacking	Dewow	Time-zero correction (ns)
Line 1	450	0.0, 0.0	15.75	0.050	16	Yes	70
Line 1	900	6.0, 0.0	10.00	0.025	16	Yes	70
CMP 1	450	6.0, 0.0	–	0.050	16	Yes	–
CMP 4	900	8.0, 1.5	–	0.020	16	Yes	–

*See Figure 1 for locations

Table 2. *Textural characteristics of the samples from unit 7 in trench I*

	N	Grain size (μm) Mean	SD	Clay* content (%)	SD	Silt† content (%)	SD	Organic matter (%)	SD
Vertical transect	15	280.13	25.73	0.43	0.05	0.61	0.11	0.46	0.21
Core plugs‡	19	268.79	12.08	0.57	0.05	1.07	0.13	0.1	0.16

N, number of samples
SD, standard deviation
*Clay is defined as the weight fraction smaller than 2 μm
†Silt is defined as the weight fraction between 2 μm and 62 μm
‡The two core plugs corresponding to the box cores and associated TDR transects are shown in Figure 2
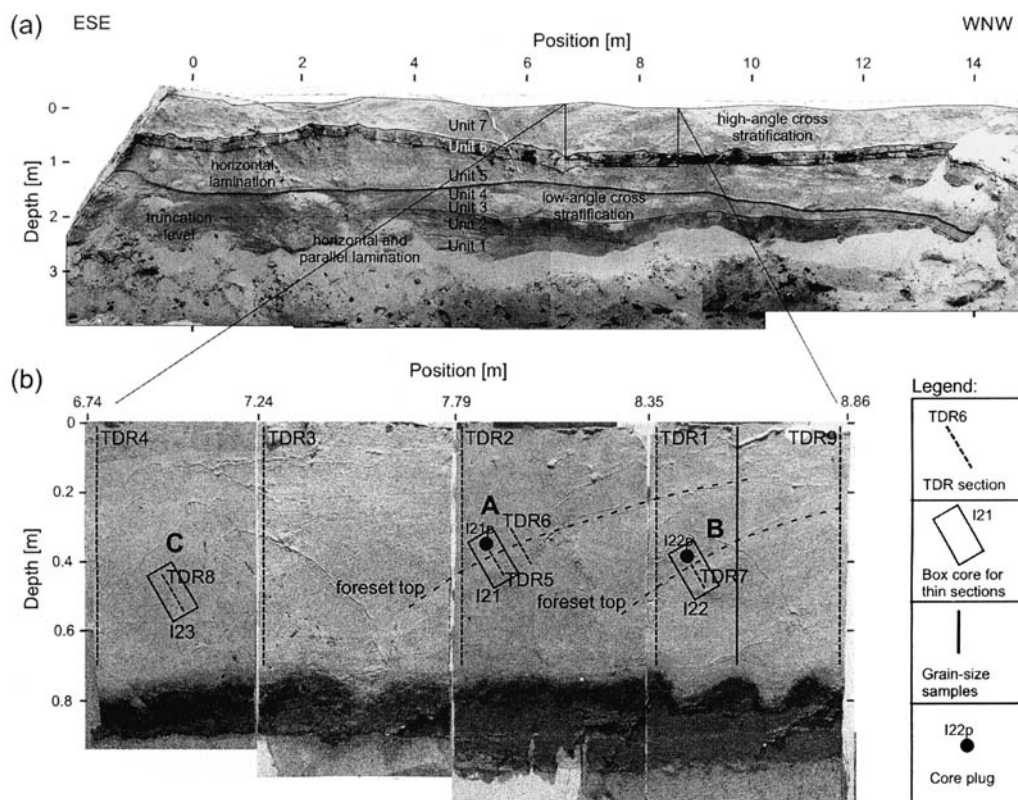
Fig. 2. (a) Trench wall panorama showing sedimentary units and (b) lacquer peels of the trench. The lacquer peels show faint foreset lamination, indicated by thin dashed lines, and the locations of grain-size samples (vertical spacing 0.05 m), TDR measurements, box cores and core plugs. Sites A and B were set at the location of known foreset tops; site C was set at a position where foresets were absent.

properties, we collected three 0.05 × 0.08 × 0.15 m (height × width × length) undisturbed box cores, I21, I22 and I23 (Fig. 2b), from sites A, B and C, respectively. The box cores have thin metal walls so as to reduce sediment disturbance. About one-third of the box cores was used to sample core plugs for laboratory measurement of water reten-

tion (Fig. 2b). The remainder of the sediment in the box cores was impregnated with a blue epoxy-resin dye and thin sections were prepared in an orientation perpendicular to the sedimentary bedding in order to reveal the maximum textural variation. Image analysis of the thin sections was used to measure sediment characteristics. Subsequent

neural network modelling was used to estimate water-retention curves for the sediment in the thin sections. Direct correlation between the box-core results and TDR measurements is difficult because the box cores were collected a few centimetres deeper into the quarry wall to avoid sediment disturbance caused by the TDR pins.

Sedimentology and stratigraphy

The sediment at the test site is subdivided into seven units. Units 1, 3, 5 and 7 consist of clean windblown sands, whereas units 2, 4 and 6 are soils (Fig. 2a). The radiocarbon ages of sampled organic material show that unit 6 was formed between AD 1260 and 1425 (Van Dam 2001). The ages were calibrated using Stuiver et al. (1998). The sediments in units 1, 3 and 5 were deposited as the so-called 'Older Dunes'. These relatively low dunes formed on top of a prograding coastal barrier system (Jelgersma et al. 1970; Cleveringa 2001). Unit 7 is part of the so-called 'Younger Dunes', which were deposited from approximately AD 1200 onwards. A period of coastal erosion led to an increased sediment supply and to the development of dunes that were up to 35 m high.

Unit 7 in trench I, on which the present study focuses, is characterized by high-angle cross-stratification, dipping at a maximum angle of 40° towards the southeast. The absence of a sharp crest can be attributed to a relatively rapid filling of the depression in which unit 6 was formed. The lacquer peels show two 0.2–0.3 m-thick convex-upward foresets in unit 7 (Fig. 2b). They are characterized by a top layer (approximately 5 cm thick) with slightly finer grain size than the bulk sediment. Subcentimetre-scale lamination is present within the high-angle foresets. The photographs of the lacquer peels do not have enough detail or contrast to show this lamination. The average grain size of the studied sediment in unit 7 is approximately 280 μm (medium sand). The average silt and clay contents are 0.6% and 0.4%, respectively (Table 2).

GPR measurements

The fundamental properties that control the behaviour of GPR signals are the dielectric permittivity (ϵ), electrical conductivity (σ), and magnetic permeability (μ), which together define the EM wave impedance (Z). Impedance contrasts in the subsurface cause part of the propagating EM energy to be reflected. The amount of reflected energy is proportional to the magnitude of change in Z. Although iron-rich sands can have distinct magnetic properties (e.g. Olhoeft 1998), for most natural sediments and iron oxide precipitates, variations in μ are insignificant (e.g. Daniels et al. 1988; Van Dam et al. 2002a). In low-loss material, such as clean, dry sand, the influence of σ on the EM signal is negligible at GPR frequencies (Davis & Annan 1989). In contrast, ϵ plays an important role in both the propagation and reflection of EM waves. If one defines the relative permittivity as $\epsilon_r = \epsilon/\epsilon_0$, where ϵ_0 is the permittivity of free space, ϵ_r of water is around 80, whereas air and quartz have values of 1 and ~4, respectively. Therefore, water content governs the relative permittivity and EM wave impedance of sediment. The EM wave velocity (v) is found by $v = c_0/\sqrt{\epsilon_r}$, where c_0 is the velocity in vacuum (3 10^8 m s^{-1}). Radar-wave reflectivity can be found from the difference in EM wave impedance at layer transitions and can, for a normal-incidence wave, be simplified with $RC = (\sqrt{\epsilon_{r2}} - \sqrt{\epsilon_{r1}})/(\sqrt{\epsilon_{r2}} + \sqrt{\epsilon_{r1}})$, where ϵ_{r1} and ϵ_{r2} are the relative permittivity above and below the transition, respectively. The quality and sharpness of the reflection depends on the transition-zone width (W, vertical range over which ϵ_r changes), relative to the predominant wavelength (W/λ). A well-defined transition in ϵ_r with depth gives a sharp reflection. In contrast, a gradual change in ϵ_r causes pulse widening. Annan et al. (1991) estimate that $W/\lambda < 0.3$ gives a sharp reflection. Under natural unsaturated conditions the transition-zone width depends on the total difference in water content above and below the contrast as well as on the water-retention characteristics of the sediment above the contrast (Young & Sun 1999).

Using common mid-point (CMP) measurements (see Fig. 1) the velocity for unit 7 was estimated to be around 0.12 m ns^{-1}, which allowed for an appropriate time-depth conversion. The 450 MHz GPR profile shows several continuous subhorizontal reflections (① and ②, Fig. 3a), which are interpreted as the soil horizons (Fig. 2). Between the horizontal positions 6 m and 15 m, dipping reflections are visible in the upper 0.75 m. These reflections are interpreted as resulting from the high-angle cross-stratified dunes in unit 7 (Fig. 2). The 900 MHz GPR profile images the high-angle foresets in greater detail (③ and ④, Fig. 3b). In addition to the reflections of the high-angle dune stratification, the 900 MHz image shows some short subhorizontal reflections (right of ③ in Fig. 3b). However, in the raw data, these reflections are of low amplitude and they cannot be linked to any sedimentary structures in the lacquer peels. These reflections probably are the result of a surface reflection from an object that was positioned at approximately metre 6.6 on the survey line. The reflection from the top of the soil horizon below unit 7 is poorly defined. This is caused by the non-lateral nature of the interface as well as by the large
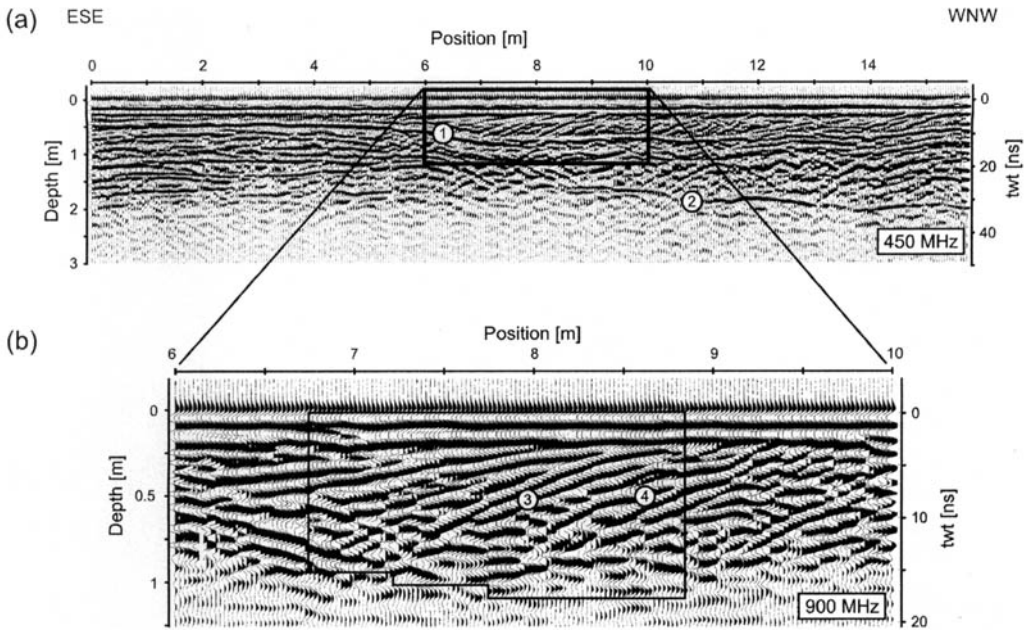
Fig. 3. GPR sections from line 1 that allow correlations to be made with the trench-wall panoramas and lacquer peels in Figure 2. (a) The 450 MHz image has the same horizontal and vertical scale as Figure 2a. (b) In the 900 MHz image, which has a horizontal and vertical scale half that of Figure 2b, the frame shows the outline of the lacquer peels in Figure 2b. The circled numbers in the radar sections refer to the text and are interpreted as: ①, reflection from the top of unit 6; ②, reflection from unit 2; ③, reflection from foreset associated with sample I21 in Figure 2b; ④, reflection from foreset associated with sample I22 in Figure 2b. Both radar sections are plotted with an automatic gain control (AGC) gain of 50.

width of the transition zone, W. For a transition zone of 0.1 m, as observed at the boundary between units 7 and 6 (Van Dam *et al.* 2002b), and a velocity of 0.12 m ns^{-1}, W/λ is 0.75 for the 900 MHz signal. Consequently, the signal would be expected to experience significant pulse widening and a decrease in reflection amplitude.

TDR measurements

TDR was developed to characterize the conductivity and water content of soils through measurement of their EM properties. The method is based on the time-domain analysis of a propagating EM signal that travels along a three-rod probe inserted into the sediment (e.g. Heimovaara & Bouten 1990). TDR can be used to measure temporal changes in water content as well as to construct vertical profiles of EM properties (Topp & Davis 1985; Van Dam & Schlager 2000). The relative permittivity (ϵ_r) can be calculated from the travel time of the EM signal in the sediment. The volumetric water content (θ) can be found by substitution of ϵ_r in empirical equations (e.g. Topp *et al.* 1980).

The vertical TDR sections show that ϵ_r in unit

7 varies between 3.75 and 4.75 (Fig. 4a & b), which is consistent with the typical value of 4 for dry sand. The results are statistically significant as the degree of error in the measurements is well below the measured variation in unit 7 (Van Dam 2001). The grain size is relatively small at the top and bottom of the measured section (approximately 250 μm), and larger (approximately 325 μm) in the middle part (Fig. 4c). Smaller grain sizes lead to a higher amount of capillary water to be present in the sediment. The two finer-grained foreset tops that are present in the lacquer peels can be identified on the TDR sections by a local increase in ϵ_r and are labelled '③' and '④' (Fig. 4a & b). They are consistent with the positions of the numbered clinoforms in Figure 3 and foreset tops in Figure 2. Events ③ and ④ are two of several similar, but unexplained permittivity changes in the TDR sections (Fig. 4) that may be related to the subcentimetre-scale lamination observed in the lacquer peels.

To obtain detailed information on the variation in EM properties in a direction perpendicular to the foresets, which allow synthetic modelling of GPR reflections, TDR measurements with a 0.02 m spacing were conducted at the three sites A, B and C, where box cores I21, I22 and I23 were collected
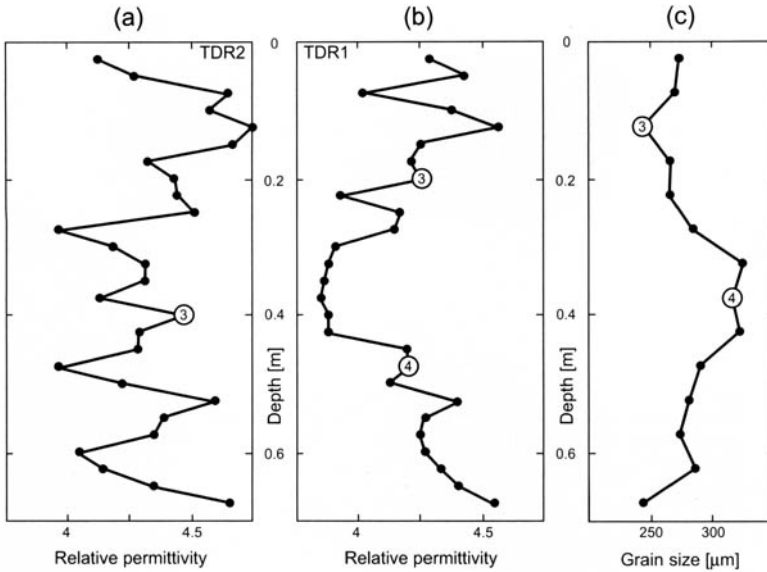
Fig. 4. Variation in relative permittivity (ϵ_r) for TDR sections (**a**) TDR2 and (**b**) TDR1 with depth, and (**c**) variation in grain size with depth for unit 7 (see Fig. 2 for locations). The circled numbers 3 and 4 relate to the clinoforms indicated in Figure 3. In the grain-size section, the fine grain sizes associated with the foreset tops in Figure 2 are superimposed on the large-scale trend in grain size.

(Fig. 2*b*). Three of the detailed sections, TDR5, TDR6 and TDR7, were set at locations of known foreset tops; the fourth section, TDR8, was taken at a position where foresets were absent. The TDR measurements at the foreset locations show a small but distinct increase in ϵ_r from around 3.75 to values between 4.25 and 4.75 (Fig. 5). This

Fig. 5. Four TDR profiles illustrating the influence of sedimentary structures on relative permittivity. Sections TDR5, TDR6 and TDR7 were measured at locations of known foreset tops; section TDR8 was taken at a position where foresets were absent. See Figure 2 for the locations. The circled numbers 3 and 4 correspond to those foreset tops identified in Figures 3 and 4.

increase marks the transition from relatively coarse-grained material to the fine-grained foreset top. The increase in ϵ_r in the foreset tops can be attributed to an increase in capillary water, which is present in the finer-grained sediment. The lower end of the 5 cm-thick foreset tops is marked by a gradual decrease in ϵ_r. The transition-zone widths (*W*) of both increase and decrease in ϵ_r is approximately 0.04 m. *W*/λ for a 900 MHz GPR wave would be around 0.3, which would be at the transition between a sharp radar reflection and significant alteration of signal width (Annan *et al.* 1991). The TDR measurements in Figure 5 were used to construct models of EM wave impedance perpendicular to the foresets. The results of the synthetic modelling of GPR reflections will be discussed later, along with the impedance models that are based on the thin sections.

Analysis of thin sections

Image analysis

The primary objective of image analysis of thin sections in this study is to estimate variations in water content and EM properties that are related to changes in textural characteristics that are too small-scale for TDR to measure. Here, the thin section that was constructed from box core I21 is described (Fig. 2*b*). Four high-resolution (176 ×

176 pixels/mm^2) digital photographs were taken with an overlapping zone (covering a total area of approximately 65×15 mm) in a transect along the long axis of the thin section. Small spectral inhomogeneities between photographs were corrected for using a histogram matching process contained in the image-processing software ERDAS IMAGINE (ERDAS 1999). The same software was used for a maximum-likelihood classification to obtain binary images of solid grains and pores. To obtain unbiased measures for textural parameters from the binary images, touching grains were separated using a cutting procedure developed by Van Den Berg et al. (2002). To prevent edge effects on the margins, the images were cropped. These processing steps were performed on the thin-section photographs before combining the different panels to produce the final image that was used for the measurements of the textural characteristics (Fig. 6).

The final image (Fig. 6) was analysed for a series of textural characteristics, including grain-size distribution (GSD) and porosity (η), using the method described in Van Den Berg et al. (2003). With the dominant textural variation being present in the direction perpendicular to the sedimentary layering, a rectangular measurement window was used to estimate the textural characteristics in the thin section (Fig. 6). Textural variation parallel to the bedding (the long axis of the measurement window) was assumed to be constant. The measurement window had a height of 1.5 mm and was moved with increments half the height of the window to obtain 85 samples (Fig. 6).

The measured 2-D grain size was converted to three dimensions by applying a multiplication factor of $4/\pi$, which, strictly speaking, is only valid for uniform-sized spheres. Because of the strongly limiting assumptions on the size and shape distributions of grains and on the grain orientation in the thin section, which are made in other available 2-D to 3-D conversions, this simplified form of the complex reality is preferred (Van Den Berg et al. 2003). The mean grain size shows a variation between 200 μm and 325 μm (Fig. 7a), which is comparable to the variation found using laser particle-size measurements (Fig. 4c). The variation in
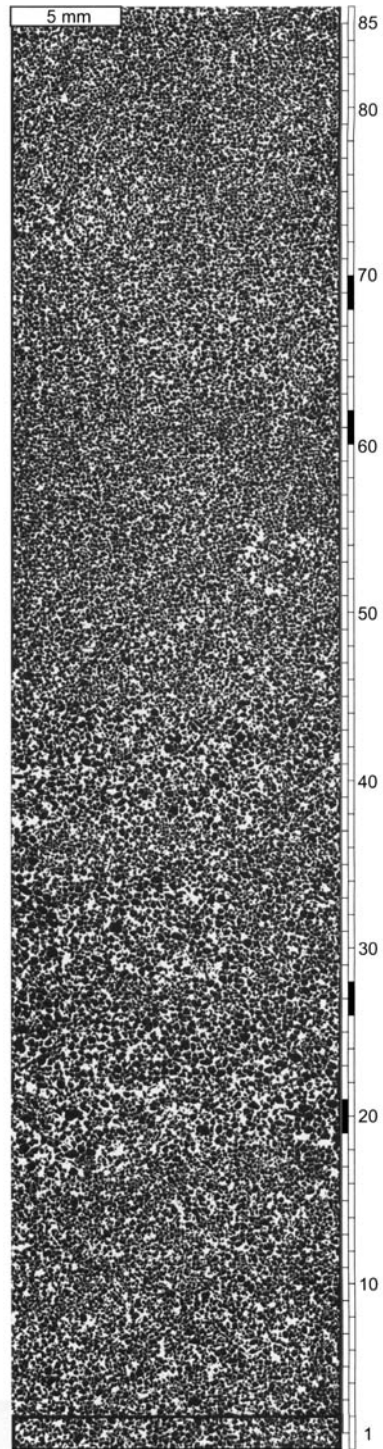
Fig. 6. Digitized thin section of box core I21. The image is based on four high-resolution (176–176 pixels/mm^2), overlapping photographs that were taken perpendicular to the sedimentary structures (Fig. 2b). The image is tilted so that the sedimentary layering appears to be approximately horizontal. The ruler to the right of the image illustrates the positions of the 85 sample windows. For sample 1, the measurement window is shown. Marked samples 20, 27, 61, and 69 have characteristic textures (Fig. 7a & b) and are analysed in Figure 9.
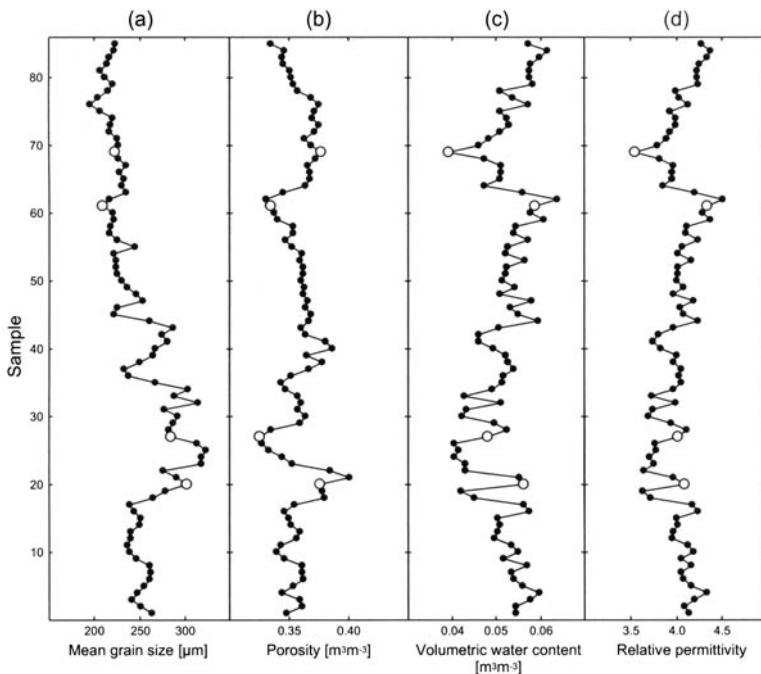
Fig. 7. Vertical transects of (**a**) mean grain size and (**b**) porosity along the long axis of thin section I21. (**c**) The water content at pF 2 along this transect was calculated using a neural network model that estimates the θ-pF relationship based on cumulative grain-size distribution and porosity. (**d**) The relative permittivity was calculated using a dielectric mixing model (Equation 3). Open circles indicate specific samples 20, 27, 61 and 69, analysed in Figure 9.

mean grain size shows a coarsening-downward trend from sample 85 to 20, with a sudden drop in mean grain size below sample 20. The porosity (η) is easily found from the binary image and varies between 0.32 and 0.4 (Fig. 7*b*). Around sample 63 there is a distinct step in η, whereas the mean grain size varies little. Another large step in porosity is found between samples 20 and 25. The zone between samples 20 and 45 shows a large range in porosity values and coincides with a large variation in mean grain size. Nevertheless, there appears to be no correlation between mean grain size and porosity (Fig. 8) for the dataset of 85 samples. The transitions in grain size and porosity (Fig. 7*a* & *b*) are not always as sharp as they appear in the thin-section image (Fig. 6). This is probably the result of the moving average window and the fact that orientation of the transition interfaces may not be perfectly perpendicular to the long axis of the image.

Estimated small-scale water-retention characteristics

To calculate the water-retention characteristics of the 85 samples in the thin section from their textu-
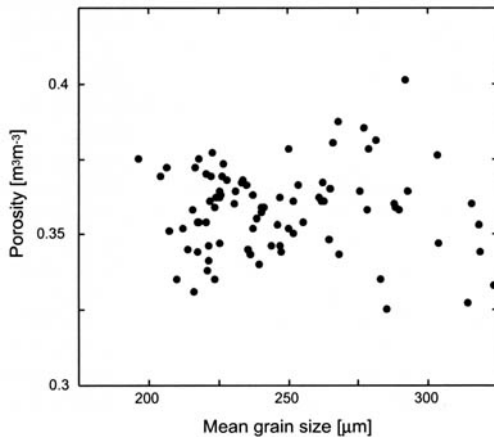
Fig. 8. Scatter plot of porosity versus mean grain size for the 85 samples in thin section I21.

ral characteristics, a neural network model was used. This model was developed for similar sediment as in the present study and required initial input of cumulative grain-size distribution and porosity (Schaap & Bouten 1996). A neural network is a black box capable of finding and quan-

tifying relationships between variables, without the existence of an initial model concept (Schaap 1996). This iterative process allows for unravelling datasets that lack physical understanding of all relationships.

First, the 85 GSDs that were measured from the thin section were fitted with the Haverkamp and Parlange equation (1986) to find specific input parameters (d_{gsd} and n_{gsd}) for the neural network:

$$GSD(d) = \frac{1}{(1 + (d_{gsd}d^{-1})^{n_{gsd}})^p}. \qquad (2)$$

Here, $GSD(d)$ is the cumulative weight fraction calculated from the thin section data, d is grain size, d_{gsd} and n_{gsd} are measures of the average grain size and grain-size uniformity, respectively, and $p = 1 - n_{gsd}^{-1}$. The average root-mean-square error of the measured and fitted cumulative grain-size distributions was 0.019. For four specific measurements with contrasting mean grain size and porosity (Fig. 7a & b), the fitted grain-size distributions illustrate the variation in grain size and sorting (Fig. 9a). Samples 61 and 69 are fine-grained and have a narrow GSD (well sorted). Samples 20 and 27 are coarser-grained, with sample 27 being relatively well sorted and sample 20 poorly sorted (Table 3). In addition to the variation in GSD, the samples show a difference in porosity (Fig. 7b). Samples 27 and 61 have a low porosity whereas 20 and 69 have a high porosity (Table 3). Although the porosity is somewhat underestimated (Table 3) the fitted GSDs agree well with the measured GSD of core plug I21p (Fig. 9a).

Next, the neural network model M6 of Schaap & Bouten (1996) was used to construct water-retention curves for each of the 85 measurements. Given input values for d_{gsd}, n_{gsd}, gravel percentage (0), organic-matter percentage (0), and porosity (Table 3), the neural network generated output values for the Van Genuchten (1980) parameters α_{vg} and n in Equation 1 (Table 4). Curves for the four specific measurements illustrate the interaction between porosity and grain-size distribution in the control of water retention (Fig. 9b). The porosity determines the saturated water content at zero suction, whereas the grain-size distribution and porosity together determine the position of the inflection point and the steepness and height of the plateau in the curve. This can be illustrated with two examples. The samples 61 and 69 have similar grain-size distributions (Fig. 9a) but differ in porosity (Fig. 7b). The higher porosity of sample 69, which is due to looser packing (higher porosity at a similar grain size), causes a higher saturated water content (Fig. 9b). However, the larger mean pore size of sample 69 causes it to drain quicker than sample 61, which has a similar grain-size dis-
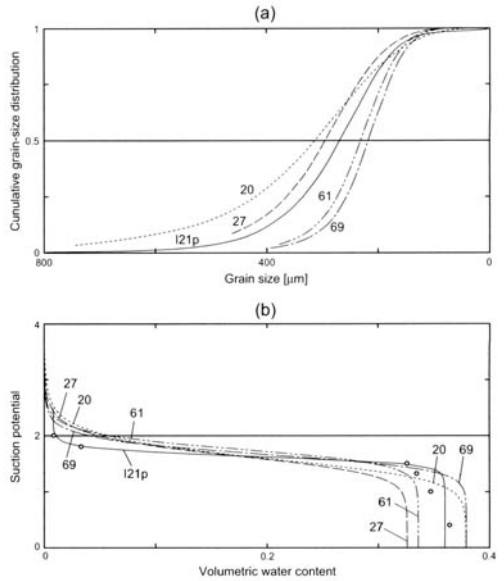
Fig. 9. Plots of (a) cumulative grain-size distribution (GSD) and (b) water-retention characteristics for samples 20, 27, 61 and 69 in thin section I21 and for core plug I21p. The four specific samples in thin section I21 are characteristic in their combination of mean grain size (Fig. 7a) and porosity (Fig. 7b). The positions are shown in Figure 6. In (a), the cumulative GSDs from the thin section were calculated using the method of Van Den Berg *et al.* (2003) and fitted with Equation 2. The grain sizes from the core-plug sediment (location in Fig. 2a) were measured with a laser-particle sizer. In (b), the θ-pF relation was calculated using a neural network model (Schaap & Bouten 1996) for the thin-section samples and standard laboratory measurement techniques for the core plug. The open circles represent the lab measurements for I21p; the solid line is the fit of these measurements with Equation 1.

tribution but a different porosity. Therefore, the water-retention curve of sample 69 has a steeper plateau and an inflection point at a lower suction potential than sample 61 (Fig. 9b). Furthermore, the curve for sample 69 crosses that of sample 61. The samples 20 and 27 have a comparable mean grain size (Fig. 7a) but differ in their grain-size distributions. The sediment of sample 20 is poorly sorted and has a wider distribution of grain sizes than sample 27 (Fig. 9a). This poor sorting of sample 20 leads to a water-retention curve that is gentler than the other curves (Fig. 9b). As a result of the relatively large grains and pores present, the sediment of sample 20 starts to drain at the lowest suction values (between pF 0.5 and 1). However, the large variety of pore sizes present in sample 20, which is due to the poor sorting, causes it to drain at a slower rate than sample 27 (see value for n in Table 4).

Table 3. *Textural properties for 4 specific measurement samples in thin section I21, for the average of all 85 samples, and for the sediment in core plug I21p (italics)*

Sample	N	Grain size (μm) Mean	SD	η (m^3 m^{-3})
20*	321	303.325	144.373	0.376
27*	387	285.545	104.758	0.325
61*	615	209.996	64.805	0.335
69*	553	223.066	69.790	0.377
Average for 1–85*	492	245.852	89.752	0.358
I21p†	–	*293.209*	*85.879*	*0.446*

N, number of grains
η, porosity
SD, standard deviation
*For the thin-section samples the textural characteristics were found by image analysis
†For the core plug the mean grain size was measured with a laser particle sizer

Comparison of the four specific measurements with the core plug shows that, although the plateaux do not exactly match, the overall pattern is very similar (Fig. 9b). At *pF* 2, which is around field-capacity conditions (Van Dam *et al.* 2002b), the results for the core plug I21p and the neural network results differ by a factor 3. The difference may be caused by the neural network modelling (the original dataset in Schaap & Bouten [1996] contains more silt) or by macroporosity in the core plug. However, in modelling GPR reflections, relative contrasts in water content and dielectric properties are more important than the absolute values. Therefore, the difference between measured

and calculated values is considered an acceptable error. For a *pF* of 2, Figure 7c shows the variation in θ across the thin section, and ranges from approximately 0.04 to 0.06 (Table 5).

Dielectric properties

Under the reasonable assumption that the influence of adsorbed water can be ignored, a simple three-phase dielectric mixing model was used to obtain

Table 5. *Volumetric water content (θ) and relative permittivity (ϵ_r) at pF 2, for four specific samples in thin section I21, the average of all 85 samples and core plug I21p*

Sample	θ (m^3 m^{-3})*	ϵ_r†
20	0.056	4.09
27	0.048	4.02
61	0.059	4.33
69	0.039	3.56
Average for 1–85	0.052	4.03
I21p‡	*0.010*	*2.53*

*For the thin section samples, θ was estimated using the neural network model (Table 4). For the core plug, the water-retention characteristics were measured in the laboratory and fitted with Equation 1 to find θ at pF 2
†Relative permittivity was calculated from Equation 3
‡The θ and ϵ_r values for the core plug I21p are low compared to the values for the thin-section samples. The difference is partly due to the sensitivity of θ for the position of the plateau in the water-retention curves. A small error in the parameter α_{vg} (Table 4) may have a large effect on θ

Table 4. *Neural network input and output for the four specific samples in thin section I21 and the average of all 85 samples*

Sample	Model input			Model output		
	d_{gsd} (μm)	n_{gsd}	ρ_b (g cm^{-3})	α_{vg} (cm^{-1})	n	θ_s (m^3 m^{-3})
20	346.856	4.080	1.654	0.032	2.614	0.379
27	311.210	5.533	1.789	0.027	2.871	0.326
61	224.326	6.841	1.762	0.019	3.512	0.336
69	238.855	6.819	1.651	0.024	3.576	0.379
Average for 1–85	266.531	5.529	1.700	0.025	3.153	0.360
*I21p**	–	–	*1.467*	*0.024*	*6.99*	*0.446*

d_{gsd}, measure for average grain size
n_{gsd}, GSD uniformity
α_{vg} and n, output parameters defining the position of the inflection point and the amount of curvature in the θ-pF relationship (Equation 1), respectively
ρ_b, dry bulk density was calculated through $\rho_b = 2.65(1 - \eta)$
θ_s, saturated water content. The marginal difference between porosity (Table 3) and modelled saturated water content output is within error bounds and can be neglected
*Laboratory measurement results for core plug I21p are given for comparison

relative permittivity, ϵ_r, from θ, using the Bohl and Roth (1994) equation:

$$\epsilon_r = (\theta\epsilon_w^{\alpha_m} + (1-\eta)\epsilon_s^{\alpha_m} + (\eta-\theta)\epsilon_a^{\alpha_m})^{1/\alpha_m}. \qquad (3)$$

Here, η is porosity, ϵ_w is relative permittivity of water, ϵ_s is relative permittivity of solid material (3.7; Van Dam et al. 2002a), ϵ_a is relative permittivity of air, and α_m is a constant. α_m is 0.5 for isotropic and homogeneous material (Roth et al. 1990). The results for the four specific samples are given in Table 5. Figure 7d shows that the ϵ_r values for the 85 samples across the thin section lie between 3.6 and 4.5. Both absolute values and observed range are comparable to those found with the TDR measurements (Fig. 4a & b). The most distinct step in permittivity lies between samples 60 and 70 and is associated with a strong variation in porosity. The major step in grain size at sample 20 (Fig. 7a) did not result in a prominent permittivity change.

GPR synthetic modelling

Using the average of the detailed TDR measurements TDR5 and TDR6 (Fig. 5) and the ϵ_r results for the thin section (Fig. 7d), two models of EM wave impedance were constructed. Figure 10 shows the reflection coefficient (RC) based on these impedance models v. depth. The TDR-based model has 0.02 m measurement increments whereas the detailed thin-section model has 0.75 mm measurement intervals. PulseEKKO software (Sensors & Software 1996) was used to construct synthetic 1-D GPR traces from the impedance models. The software transforms the impedance model from a depth scale into a time scale, and then computes the impulse response for the layered model. This is followed by the calculation of all generated reflections, including multiples and interlayer reflections. The ground response is then obtained by convolution of a standard theoretical pulseEKKO wavelet (both 450 MHZ and 900 MHz) with the impulse response. One of the assumptions inherent in the modelling software is that the wave is normal incidence, which was accepted as a reasonable simplification. Losses from spherical-waveform spreading were ignored because of the limited thickness of the model. The attenuation was set at a value of 0.01 dB m^{-1} because of the perceived low value of σ. This value was held constant because of the limited variation in dielectric properties.

In the reflectivity model for the TDR data (Fig. 10a), the first two events, at 0.22 m and 0.24 m depth, are associated with the increase in ϵ_r due to the transition to the fine-grained foreset top (Fig. 5). The next two negative events, at 0.26 m and 0.28 m depth, are due to the subsequent increase
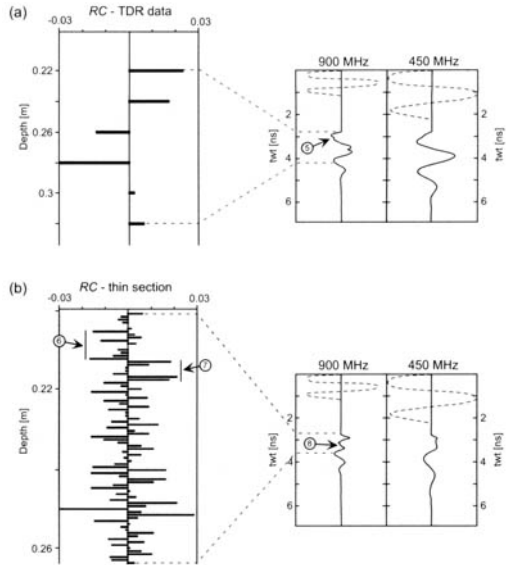
Fig. 10. Radar reflectivity and synthetic radar traces constructed from (a) an average of the TDR measurements from TDR5 and TDR6 in Figure 5 and (b) the image analysis results in Figure 7d. The impedance models used for the synthetic modelling assume a 0.2 m-thick homogeneous layer before the first event. The impedance and RC models have a depth scale whereas the synthetic traces have a time scale. Since the wave velocity is different for each layer, the relative (velocity-related) thickness of the layers changes. The synthetic radar traces have the same horizontal scale. The dashed wiggle shows the wavelet used to convolve with the impulse response model. The numbered arrows 5 to 8 are referred to in the text.

in grain size and decrease in ϵ_r at the bottom of the approximately 5 cm-thick foreset top. Figure 11 shows the individual contribution of each RC event to the composite reflection (stack). In the 900 MHz synthetic trace the first two RC events cause clearly visible negative inflections (Fig. 11a). This is an illustration of pulse widening (indicated by label ⑤ in Fig. 10a), and is due to the gradual transition in ϵ_r. The next two events cause reflections with an opposite polarity and partly overlap the two previous reflections (Fig. 11a). Here, the interference among the signals cause a large width of the positive inflection in the composite signal between 0.55 ns and 1.2 ns, relative to the negative inflection between 0 ns and 0.55 ns. The final two events are too small to be recognized in the stacked signal. In the 450 MHz synthetic trace the resolution is too low to distinguish any of the events separately in detail. This image is a stack of six different, overlapping waveforms, producing one composite reflection. Figure 11b clearly illustrates that the 450 MHz wavelength is too long to discern both
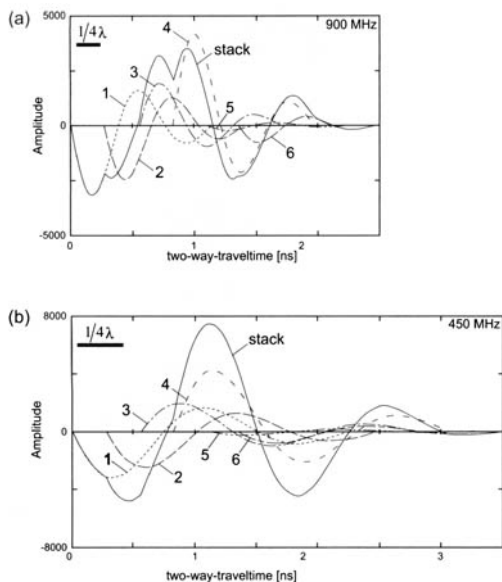
Fig. 11. Diagrams showing the stack of six interfering reflections from the TDR-based impedance model at (**a**) 900 MHz, and (**b**) 450 MHz. Numbers 1 to 6 refer to the events in the TDR reflectivity model (Fig. 10*a*). The composite trace is dominated by destructive and constructive interference. Multiples and interlayer reflections were considered to contribute little to the total reflection and were therefore ignored.

the top and bottom of the approximately 5 cm-thick foreset top ($\lambda/4$ ~7.5 cm). Between approximately 0.8 ns and 1.5 ns two-way travel time, the first inflections caused by *RC* events 3 and, especially, 4 coincide with the second inflections of events 1 and 2, and cause a composite reflection dominated by constructive interference.

In the detailed thin-section model (Fig. 10*b*) data points are 0.75 mm apart, which is only a small fraction of the wavelength. Consequently, the vertical resolution of the GPR signal is far too low to resolve the thin lamination. Moreover, radar antennae transmit their energy in a complex 3-D pattern (e.g. Van Der Kruk 2001), which complicates the attempt to study the radar response of thin lamination using 1-D synthetic models. Nevertheless, it is important to understand the behaviour of individual wave trains a few steps ahead of maximum resolution (e.g. Mayer 1979; Bracco Gartner 2000). As is seen in the 900 MHz synthetic trace, individual reflections cannot be distinguished, but groups of events can. The negative *RC*s between 0.205 m and 0.215 m (indicated by arrow ⑥ in Fig. 10*b*) together cause the first inflection to the right in the 900 MHz trace. The group of positive *RC*s between 0.21 m and 0.22 m (indicated by arrow ⑦ in Fig. 10*b*) cause the

stepped pattern in the synthetic trace (indicated by arrow ⑧ in Fig. 10*b*). Below this, interference from numerous overlapping waveforms makes it impossible to distinguish *RC* events in the synthetic image. The most important indication that the reflected signal is a composite of interfering signals is illustrated by the difference in reflected signal for two different frequencies. The 450 MHz synthetic trace is totally different from the 900 MHz trace. Also, it becomes apparent from the synthetic models that the reflection pattern in the thin-section synthetics (Fig. 10*b*) has a lower mean amplitude than the reflection pattern from the TDR model (Fig. 10*a*). This illustrates that interference from the thinly layered sediment reduces the mean amplitude of radar reflections. Furthermore, a wavefront propagating in three dimensions will cause a further increase in interference and thus a decrease in the reflection amplitude of thinly layered sediment.

Accurate comparison of the TDR and thin-section models with the original GPR images is difficult because of the assumptions in the synthetic modelling, which ignore many of the complex factors that affect the real signal response. First, the modelled and original data differ in their angle of wave incidence. Furthermore, it is difficult to accurately model losses by attenuation and by spherical-waveform spreading. In real GPR measurements with a 3-D propagating wavefront, reflections from laterally continuous, large permittivity contrasts will overprint the 1-D modelled low-amplitude interfering reflections (Kruse & Jol 2003). Nevertheless, reflections from subcentimetre-scale layering may cause energy loss. Furthermore, especially in the case of constructive interference and sediment with little along-bedding variation, it may explain reflections that do not represent original bedding.

Discussion and conclusions

This study began with the premise that, although GPR has proven a useful technique for the imaging of sediments, detailed and quantitative knowledge about radar-wave reflection from sedimentary structures is lacking. As a result, it is not known in great detail which textural characteristics control water retention and, thus, reflections. Furthermore, the minimum magnitude of change for a reflection is unclear and little is known about the contribution of structures smaller than $\lambda/4$ to the total reflection.

It has been shown that water content, and therefore the reflection of GPR waves in unsaturated sediment, is controlled by the size distribution and connectivity of the pore network. However, the exact characteristics of the pore network are diffi-

cult to estimate. Instead, grain-size distribution and total porosity, which are relatively easy-to-measure sediment properties, can be used to estimate the water-retention characteristics in sediment. Although other texture parameters, such as grain orientation, may have an influence on water retention as well, the possible effects are considered to be of minor importance. GPR is commonly used at field-capacity conditions (around pF 2), when the sediment is a mixture of solid grains, water and air. At these conditions, fine-grained and tightly packed sediment retains more water than coarse and loosely packed material. The minimum required textural variation necessary to produce GPR reflections of sedimentary structures is small. Even the smallest change in water content will cause a contrast in dielectric properties and, thus, reflection of EM energy.

Figure 4c shows a maximum textural variation of ~80 μm for unit 7. TDR measurements in this unit show that high-angle GPR reflections of fine-grained foreset tops are caused by ϵ_r variations between approximately 3.75 and 4.75. Impedance models based on the TDR measurements across one of the foreset tops (~5 cm thick) allowed modelling of GPR reflections using 450 MHz and 900 MHz synthetic wavelets. The results show that the reflected signal experiences pulse widening due to the gradual transition in dielectric properties. Moreover, the thickness of the foreset top is larger than the maximum resolution ($\lambda/4$) of the 450 MHz GPR wave and, consequently, reflections from the top and bottom of the foreset top interfere with each other.

In an experimental attempt to model the radar response across subcentimetre-scale sedimentary layering, a digitized thin-section image rendered detailed information about texture variation along a 6 cm-long transect normal to the sedimentary bedding. A neural network and dielectric mixing model estimated ϵ_r at field-capacity conditions to vary between 3.6 and 4.5, which agrees well with the values measured with TDR. Models of EM wave impedance and reflectivity constructed from this 6 cm-long transect allowed synthetic modelling of the GPR response. The GPR synthetics show that the interference of the reflected signals leads to reflection patterns that change with frequency. Unfortunately, the model is of too small a scale, with respect to both vertical and horizontal resolution of the GPR signal, to compare the results with the actual GPR reflections of the thinly bedded sediment. Moreover, the 1-D modelling simplified many complex factors that affect the real signal response. Nevertheless, it is important to stress that the interfering reflections from laterally continuous thin bedding may produce reflection patterns that do not represent the primary bedding. In order to improve the understanding of thin-layer GPR reflections further, future studies will be necessary.

References

ANNAN, A. P., COSWAY, S. W. & REDMAN, J. D. 1991. Water table detection with ground penetrating radar. Society of Exploration Geophysicists Annual Meeting, Houston, Technical Abstracts, 494–496.

ARYA, L. M. & PARIS, J. F. 1981. A physioempirical model to predict the soil moisture characteristic from particle-size distribution and bulk density data. *Soil Science Society of America Journal*, **45**, 1023–1030.

BOHL, H. & ROTH, K. 1994. Evaluation of dielectric mixing models to describe the $\theta(\epsilon)$-relation. *In*: O'CONNOR, K. M., DOWDING, C. H. & JONES, C. C. (eds). *Time Domain Reflectometry in Environmental, Infrastructure and Mining Applications*. Bureau of Mines Special Publications, **19**, 309–319.

BOUMA, J. 1977. *Soil Survey and the Study of Water in the Unsaturated Soil – Simplified Theory and Some Case Studies*. Netherlands Soil Survey Institute, Wageningen.

BRACCO GARTNER, G. L. 2000. *High Resolution Impedance Models of Outcrops and Their Applications in Seismic Interpretation*. Ph.D. thesis, Vrije Universiteit, Amsterdam.

BRISTOW, C. S., BAILEY, S. D. & LANCASTER, N. 2000. The sedimentary structure of linear sand dunes. *Nature*, **406**, 56–59.

CLEMENT, W. P., CARDIMONA, S. J., ENDRES, A. L. & KADINSKY-CADE, K. 1997. Site characterization at the Groundwater Remediation Field Laboratory. *Leading Edge*, **16**, 1617–1621.

CLEVERINGA, J. 2000. *Reconstruction and Modelling of Holocene Coastal Evolution of the Western Netherlands*. Ph.D. thesis, Utrecht University.

DANIELS, D. J., GUNTON, D. J. & SCOTT, H. E. 1988. Introduction to subsurface radar. *Institution of Electrical Engineers Proceedings*, **135**, 278–320.

DAVIS, J. L. & ANNAN, A. P. 1989. Ground-penetrating radar for high resolution mapping of soil and rock stratigraphy. *Geophysical Prospecting*, **37**, 531–551.

DE MARSILY, G. 1986. *Quantitative Hydrogeology*. Academic Press, London.

DOBSON, M. C., ULABY, F. T., HALLIKAINEN, M. T. & EL-RAYES, M. A. 1985. Microwave dielectric behavior of wet soil - part II: dielectric mixing models. *Institute of Electrical and Electronics Engineers Transactions on Geoscience and Remote Sensing*, **GE-23**, 35–46.

ENDRES, A. L. 2000. Size scale considerations in modelling the electrical conductivity of porous rocks and soils. *Exploration Geophysics*, **31**, 418–423.

ERDAS 1999. *ERDAS Field Guide*, 5th edition. ERDAS Inc., Atlanta.

FENS, T. W. 2000. *Petrophysical Properties from Small Rock Samples Using Image Analysis Techniques*. Ph.D. thesis, Delft University of Technology.

FRIEDMAN, S. P. 1998. A saturation degree-dependent composite spheres model for describing the effective dielectric constant of unsaturated porous media. *Water Resources Research*, **34**, 2949–2961.

GOCHIOCO, L. M. 1992. Modeling studies of interference reflections in thin-layered media bounded by coal seams. *Geophysics*, **57**, 1209–1216.

GUPTA, S. C. & LARSON, W. E. 1979. Estimating soil water retention characteristics from particle size distribution, organic matter content, and bulk density. *Water Resources Research*, **15**, 1633–1635.

HÄNNINEN, P. 1992. Application of ground penetrating radar and radio wave moisture probe techniques to peatland investigations. *Bulletin of the Geological Survey of Finland*, **361**, 1–71.

HAVERKAMP, R. & PARLANGE, J. Y. 1986. Predicting the water-retention curve from particle-size distribution, 1, sandy soils without organic matter. *Soil Science*, **142**, 325–339.

HEIMOVAARA, T. J. & BOUTEN, W. 1990. A computer-controlled 36-channel time domain reflectometry system for monitoring soil water contents. *Water Resources Research*, **26**, 2311–2316.

HUBBARD, S. S., RUBIN, Y. & MAJER, E. 1997. Ground-penetrating-radar-assisted saturation and permeability estimation in bimodal systems. *Water Resources Research*, **33**, 971–990.

HUGGENBERGER, P. 1993. Radar facies: recognition of facies patterns and heterogeneities within Pleistocene Rhine gravels, NE Switzerland. *In*: BEST, J. L. & BRISTOW, C. S. (eds) *Braided Rivers*. Geological Society, London, Special Publications, **75**, 163–176.

HUGGENBERGER, P., MEIER, E. & PUGIN, A. 1994. Ground-probing radar as a tool for heterogeneity estimation in gravel deposits: advances in data-processing and facies analysis. *Journal of Applied Geophysics*, **31**, 171–184.

JELGERSMA, S., DE JONG, J., ZAGWIJN, W. H. & VAN REGTEREN ALTENA, J. F. 1970. The coastal dunes of the western Netherlands; geology, vegetational history and archeology. *Mededelingen Rijks Geologische Dienst*, **NS-21**, 93–167.

KALLWEIT, R. S. & WOOD, L. C. 1982. The limits of resolution of zero-phase wavelets. *Geophysics*, **47**, 1035–1046.

KNAPP, R. W. 1990. Vertical resolution of thick beds, thin beds, and thin-bed cyclothems. *Geophysics*, **55**, 1183–1190.

KNOLL, M. D. & KNIGHT, R. 1994. Relationships

between dielectric and hydrogeologic properties of sand-clay mixtures. *Proceedings of the 5th International Conference on Ground Penetrating Radar, 12–16 June 1994, Kitchener, Ontario*, 45–61.

KOWALSKY, M. B., DIETRICH, P., TEUTSCH, G. & RUBIN, Y. 2001. Forward modeling of ground-penetrating radar data using digitized outcrop images and multiple scenarios of water saturation. *Water Resources Research*, **37**, 1615–1625.

KRUSE, S. E. & JOL, H. M. 2003. Amplitude analysis of repetitive GPR reflections on a Lake Bonneville delta, Utah. *In*: BRISTOW, C. S. & JOL, H. M. (eds) *Ground Penetrating Radar in Sediments*. Geological Society, London, Special Publications, **211**, 287–298.

MAYER, L. A. 1979. Deep sea carbonates: acoustic, physical and stratigraphic properties. *Journal of Sedimentary Petrology*, **49**, 819–836.

MAYER, L. A. 1980. Deep-sea carbonates: physical property relationships and the origin of high-frequency acoustic reflectors. *Marine Geology*, **38**, 165–183.

MISHRA, S., PARKER, J. C. & SINGHAL, N. 1989. Estimation of soil hydraulic properties and their uncertainty from particle size distribution data. *Journal of Hydrology*, **108**, 1–18.

NEAL, A. & ROBERTS, C. L. 2001. Internal structure of a trough blowout, determined from migrated ground-penetrating radar profiles. *Sedimentology*, **48**, 791–810.

OLHOEFT, G. R. 1998. Electrical, magnetic and geometric properties that determine ground penetrating radar performance. *Proceedings of the 7th International Conference on Ground Penetrating Radar, 27–30 May 1998, University of Kansas, Lawrence, Kansas, USA*, 177–182.

ROKSANDIC, M. M. 1995. Discussion on: Hardage, B. A., Levy, R. A., Pendleton, V., Simmons, J. & R. EDSEN, R. A 3-D seismic case history evaluating fluvially deposited thin-bed reservoirs in a gas-producing property, with reply by the authors. *Geophysics*, **60**, 1585–1592.

ROTH, K., SCHULIN, R., FLHLER, H. & ATTINGER, W. 1990. Calibration of time domain reflectometry for water content measurement using a composite dielectric approach. *Water Resources Research*, **26**, 2267–2273.

SAARENKETO, T. 1998. Electrical properties of water in clay and silty soils. *Journal of Applied Geophysics*, **40**, 73–88.

SAXTON, K. E., RAWLS, W. J., ROMBERGER, J. S. & PAPENDICK, R. I. 1986. Estimating generalized soil water characteristics from texture. *Soil Science Society of America Journal*, **50**, 1031–1036.

SCHAAP, M. G. 1996. *The Role of Soil Organic Matter in the Hydrology Of Forests on Dry Sandy Soils*. Ph.D. thesis, University of Amsterdam.

SCHAAP, M. G. & BOUTEN, W. 1996. Modeling water retention curves of sandy soils using neural networks. *Water Resources Research*, **32**, 3033–3040.

SENSORS AND SOFTWARE. 1996. *pulseEKKO Synthetic Radargram User's Guide*. Sensors and Software, Mississauga, Ontario.

STUIVER, M., REIMER, P. J. *ET AL.* 1998. INTCAL98 radiocarbon age calibration, 24,000–0 cal BP. *Radiocarbon*, **40**, 1041–1083.

SUTINEN, R. 1992. Glacial deposits, their electrical

properties and surveying by image interpretation and ground penetrating radar. *Bulletin of the Geological Survey of Finland,* **359**, 1–123.

TOPP, G. C. & DAVIS, J. L. 1985. Measurement of soil water content using time-domain reflectometry (TDR): a field evaluation. *Soil Science Society of America Journal,* **49**, 19–24.

TOPP, G. C., DAVIS, J. L. & ANNAN, A. P. 1980. Electromagnetic determination of soil water content: measurements in coaxial transmission lines. *Water Resources Research,* **16**, 574–582.

VAN DAM, R. L. 2001. *Causes of Ground-Penetrating Radar Reflections in Sediment.* Ph.D. thesis, Vrije Universiteit, Amsterdam.

VAN DAM, R. L. & SCHLAGER, W. 2000. Identifying causes of ground-penetrating radar reflections using time-domain reflectometry and sedimentological analyses. *Sedimentology,* **47**, 435–449.

VAN DAM, R. L., SCHLAGER, W., DEKKERS, M. J. & HUISMAN, J. A. 2002a. Iron oxides as a cause of GPR reflections. *Geophysics,* **67**, 536–545.

VAN DAM, R. L., VAN DEN BERG, E. H., VAN HETEREN, S., KASSE, C., KENTER, J. A. M. & GROEN, K. 2002b. Influence of organic matter in soils on radar-wave reflection: sedimentological implications. *Journal of Sedimentary Research,* **72**, 341–352.

VAN DEN BERG, E. H., BENSE, V. F. & SCHLAGER, W. 2003. Assessing textural variation in laminated sands using digital image analysis of thin sections. *Journal of Sedimentary Research,* **73**, 133–143.

VAN DEN BERG, E. H., MEESTERS, A. G. C. A., KENTER, J. A. M. & SCHLAGER, W. 2002. Automated separation of touching grain sections in digital images of thin sections. *Computers and Geosciences,* **28**, 179–190.

VAN DER KRUK, J. 2001. *Three-Dimensional Imaging of Multi-Component Ground Penetrating Radar Data.* Ph.D. thesis, Delft University of Technology.

VAN GENUCHTEN, M. T. 1980. A closed-form equation for predicting the hydraulic conductivity of unsaturated soils. *Soil Science Society of America Journal,* **44**, 892–898.

VOGEL, H. J. 2000. A numerical experiment on pore size, pore connectivity, water retention, permeability and solute transport using network models. *European Journal of Soil Science,* **51**, 99–105.

VOGEL, H. J. & ROTH, K. 1998. A new approach for determining effective soil hydraulic functions. *European Journal of Soil Science,* **49**, 547–556.

WÖSTEN, J. M. H. & VAN GENUCHTEN, M. T. 1988. Using texture and other soil properties to predict the unsaturated soil hydraulic functions. *Soil Science Society of America Journal,* **52**, 1762–1770.

YOUNG, R. A. & SUN, J. 1999. Revealing stratigraphy in ground-penetrating radar data using domain filtering. *Geophysics,* **64**, 435–442.

This page intentionally left blank

Downhole GPR for high-resolution analysis of material properties near Fairbanks, Alaska

LEWIS E. HUNTER[1,5], ALLAN J. DELANEY[2], DANIEL E. LAWSON[3] & LES DAVIS[4]

[1]*Engineer Research and Development Center, Cold Regions Research and Engineering Laboratory, 72 Lyme Road, Hanover, New Hampshire 03755, USA*
[2]*Engineer Research and Development Center, Cold Regions Research and Engineering Laboratory, Building 7040, Fort Wainwright, Alaska 99703, USA*
[3]*Engineer Research and Development Center, Cold Regions Research and Engineering Laboratory, Building 724, Fort Richardson, Alaska 99505, USA*
[4]*TERAD, 3509 Mississauga Road, Mississauga, Ontario, Canada L5L 2R9*
[5]*Present address: US Army Corps of Engineers, Sacramento, CA 95814, USA*

Abstract: In August 2000, we used cross-borehole ground penetrating radar (GPR) measurements to investigate sites on Fort Wainwright, Alaska, and east of the Cold Regions Research and Engineering Laboratory (CRREL) permafrost tunnel near Fox, Alaska. The sites are characterized by perennially frozen soils characteristic of much of interior Alaska. The purpose of this investigation was to define variations in GPR signal velocity and attenuation that may be indicative of hydrocarbon contamination and to determine if downhole GPR methods could detect petroleum contaminants. To acquire background information for comparison, we conducted detailed investigations in non-contaminated areas to define general conditions before we profiled at the Fort Wainwright Tank Farm where extensive contamination has been documented.

Results showed that cross-borehole GPR is a useful tool for detecting changes in electrical characteristics in permafrost and contaminated environments. Bulk electrical properties (velocity and attenuation) were observed to vary systematically between frozen and unfrozen materials, and produced distinct signal responses to frozen/unfrozen sediments, bedrock and massive ground ice. There is considerable overlap in both velocity and attenuation for soils and rock. Fine-grained silts exhibit higher attenuation (9–10 dB m^{-1}) than coarser sand and gravel (1.5–2 dB m^{-1}). Bedrock values are intermediate (2–7 dB m^{-1}). Unfrozen sediment and rock exhibit velocities between 0.05 m ns^{-1} and 0.1 m ns^{-1} and attenuation ranges from 4 dB m^{-1} to 11 dB m^{-1} at 100 MHz while frozen materials are between the velocities of 0.1 m ns^{-1} and 0.18 m ns^{-1} and 1.5 dB m^{-1} and 10 dB m^{-1} at -0.3 °C. The general trend is for frozen materials to have higher velocities than their unsaturated or saturated counterparts. Preliminary results where petroleum contamination was pervasive show that the attenuation decreases from 6 dB m^{-1} to 7 dB m^{-1} in uncontaminated schist to 4 dB m^{-1} in the hydrocarbon-contaminated schist. Additional measurements are required to determine that the observed decrease in attenuation is primarily related to petroleum contamination.

Local geological conditions can limit radio-wave transmission through the ground and, therefore, the ability of ground penetrating radar (GPR) to define subsurface material properties. However, numerous monitoring wells exist at most environmental remediation sites that provide access to the near-surface materials. Under such conditions, problems due to surficial fine-grained soils, the proximity to metallic objects and communication transmissions, which can cause reduced GPR system performance for surface GPR, may be avoided by lowering antennae below the ground surface.

In this study, we use downhole GPR to investigate material properties of several soil types characteristic of the Fairbanks area. These included several wells in the Birch Hill Tank Farm on Fort Wainwright, where residues of petroleum, fuel additives and derivative by-products measurably change soil properties. The purpose of this investigation is to measure bulk properties and define variations in GPR pulse velocity and attenuation that may be indicative of hydrocarbon contamination and to determine if downhole GPR methods can detect petroleum contaminants. Studies by the Waterloo Center for Groundwater Research
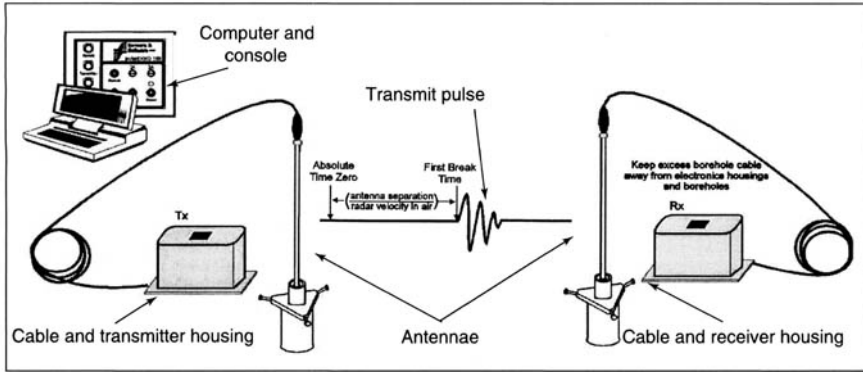
Fig. 1. Layout of borehole radar system. The system is controlled using a laptop computer connected to a radar console. Fibre-optic cables transmit optical signals between the console and electronics in the transmitter and receiver housings. 30 m-long insulated cables connect the electronics to the antennae and are used to lower these antennae down the monitoring wells (after Sensors and Software 1997).
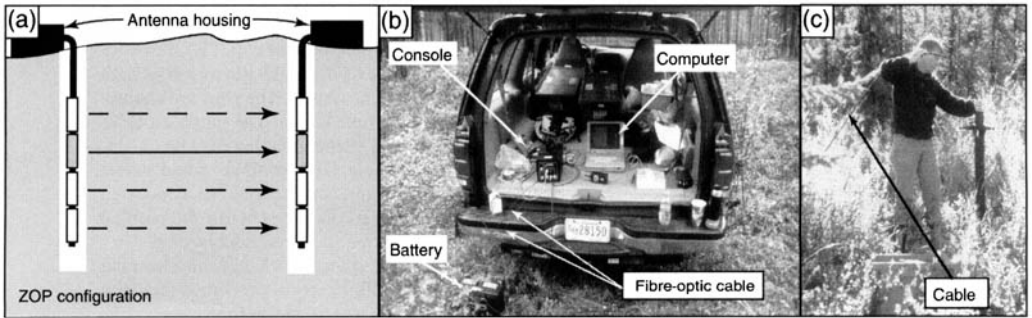
Fig. 2. Borehole radar data collection set-up. (a) Zero-offset profile (ZOP) configuration (after Sensors and Software 1997). (b) Radar is controlled using a laptop computer connected to the console with a serial cable. (c) Antennae are lowered down the borehole using 30 m-long insulated cables.
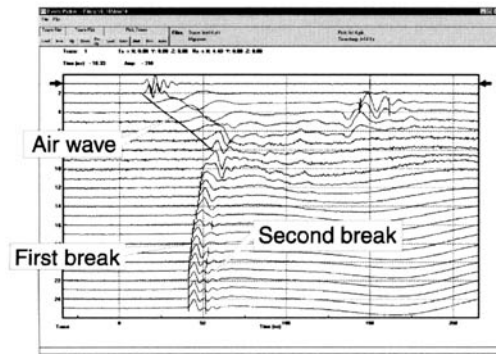
Fig. 3. Screen from borehole radar analysis software showing typical radar profile. Early returns in the upper part of the record represent air-waves that did not travel through ground and often mask the true pulse. The initial break is picked as the 'first break', which represents the arrival of the radar pulse. The 'second break' is selected 1.5 cycles after the first break.
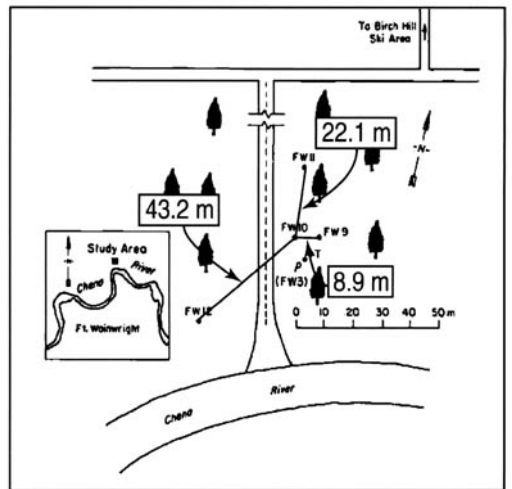
Fig. 4. Geophysical well array located on Fort Wainwright near the Chena River (modified from Arcone & Delaney 1989).
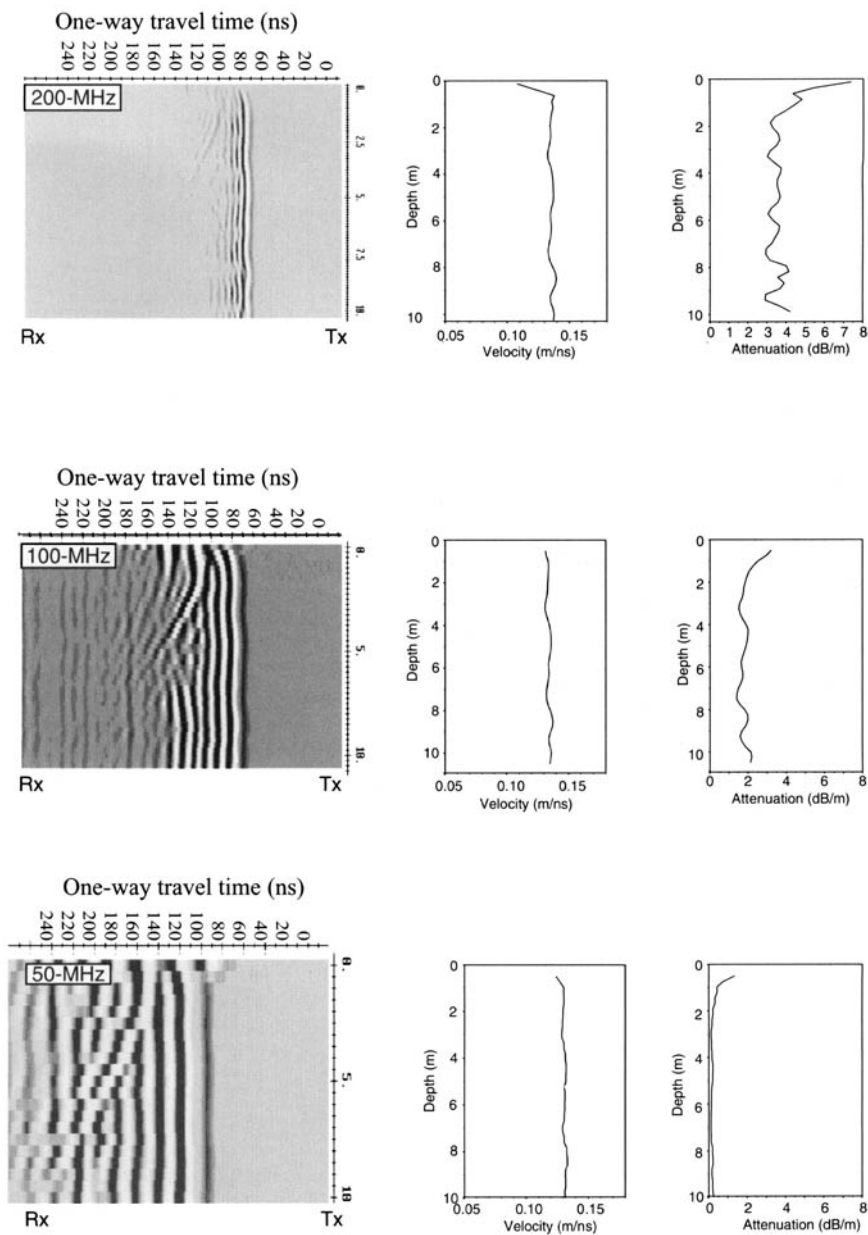
Fig. 5. Multiple-frequency transmission test between wells FW9 and FW10 at a well spacing of 8.9 m in frozen alluvium. Transmission path is shown in Figure 4.

(Annan *et al.* 1991; Redman, 1992; Brewster *et al.* 1995) have shown that GPR can be used to map changes in the dielectric properties associated with dense non-aqueous phase liquid (DNAPL) spills as they migrate downward in the ground. However, lighter petroleum products that displace soil moisture can remain as residual contamination and be far more difficult to detect. To acquire background information on *in situ* characteristics, we conducted detailed investigations in non-contaminated areas of Fort Wainwright and at the Cold Regions Research and Engineering Laboratory (CRREL) permafrost tunnel near Fox, Alaska.
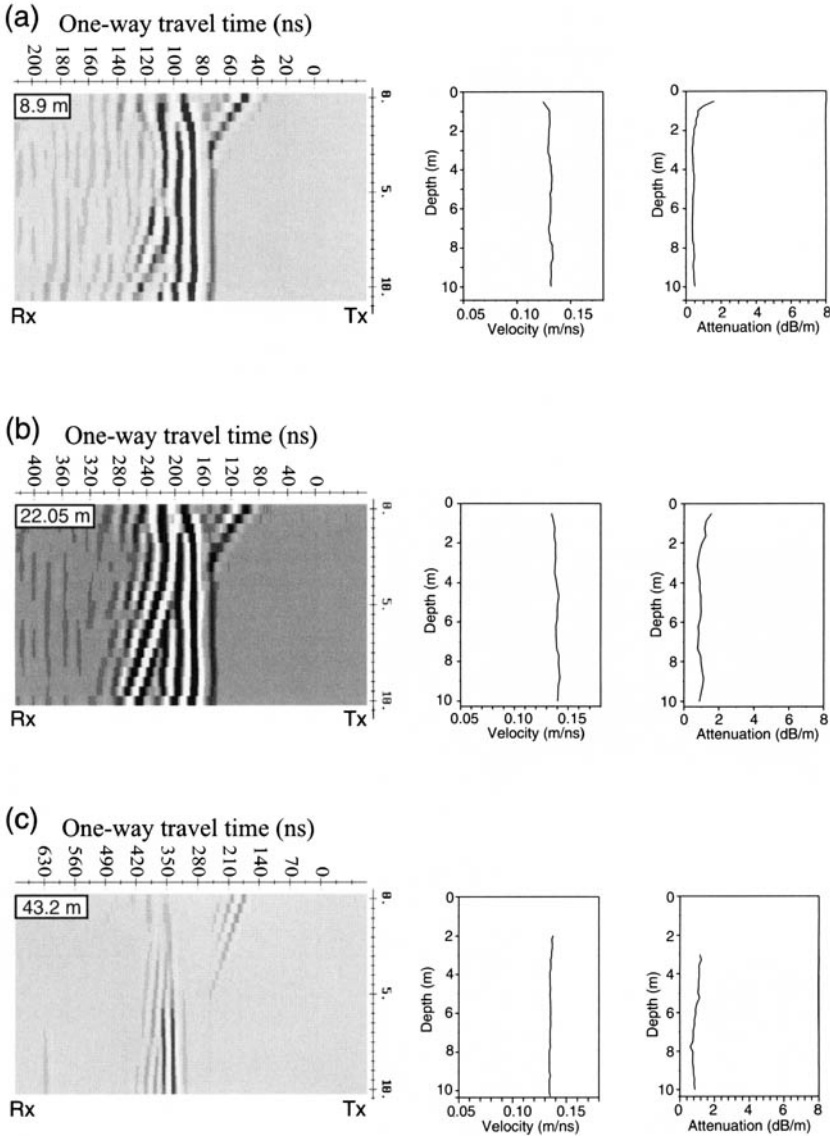
Fig. 6. Transmission test at 50 MHz and multiple well spacings in frozen alluvium: (**a**) 8.9 m between wells FW9 and FW10, (**b**) 22 m between wells FW10 and FW11, and (**c**) 43.2 m between wells FW10 and FW12. Transmission path is shown in Figure 4.

Methodology

We used multiple system configurations to evaluate lateral pulse propagation and to discriminate material properties. Profiling was accomplished using a Sensors and Software, Inc. pulseEKKO 100A digital GPR system (Fig. 1) with three borehole antenna pairs (50 MHz, 100 MHz and 200 MHz). These antennae are waterproof, slimline (<3.0 cm outer diameter) and easily deployed

in standard PVC-lined monitoring wells common to most US Army-Alaska environmental sites. These antennae are connected to the transmitter and receiver with 30 m-long cables marked at 0.25 m increments. The receiver electronics digitize received pulses. Fibre-optic cables are used on the surface to transmit digital data between the transmitter, receiver and the radar control unit (Figs 1 & 2c). Use of fibre optics minimizes electrical interference in the GPR system.
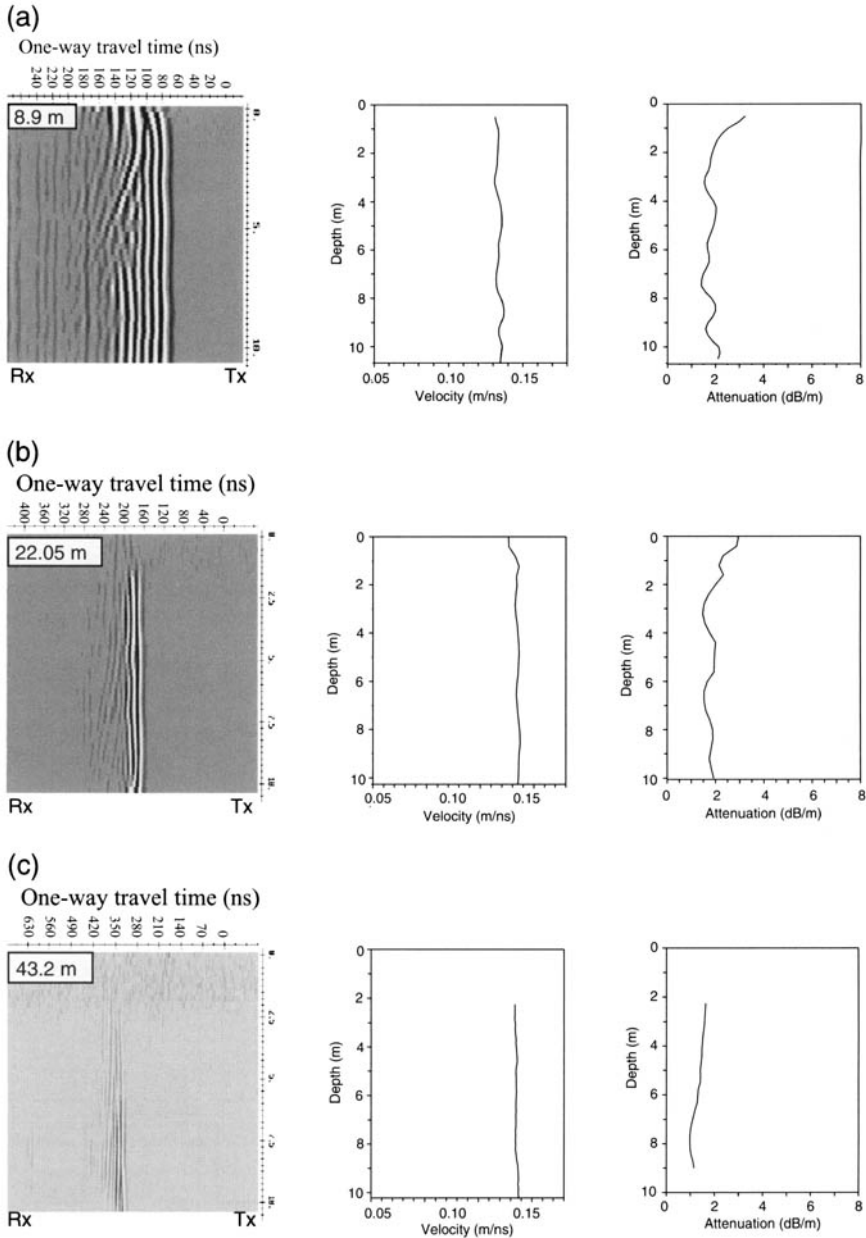
Fig. 7. Transmission test at 100 MHz and multiple well spacings in frozen alluvium: (**a**) 8.9 m between wells FW9 and FW10, (**b**) 22.05 m between wells FW10 and FW11, and (**c**) 43.2 m between wells FW10 and FW12. Transmission path is shown in Figure 4.

Borehole (or cross-hole) surveys are conducted by lowering transmitter and receiver antennae down two adjacent holes (Fig. 2). A pulse radiated at the transmitter antenna then travels through the soil to the receiver antenna in an adjacent borehole. The one-way travel time is recorded as the transmit time of the pulse through the soil (Fig. 1). This is calibrated using a measurement collected at the surface where a pulse travels through the air between the same wells. This calibration is used to determine the reference time-zero for all subsequent data processing at that well combination.
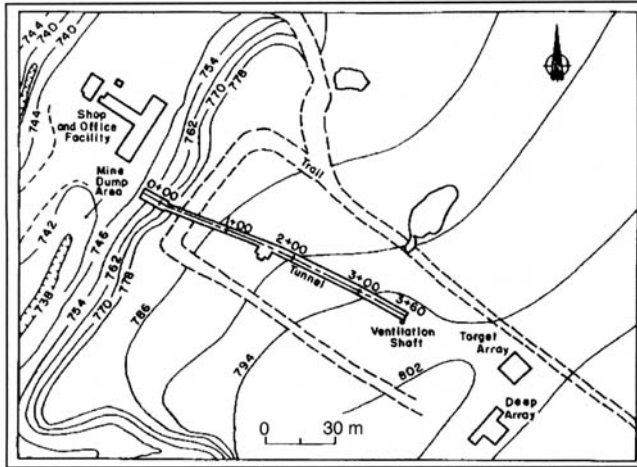
Fig. 8. Location of deep and target arrays relative to the Fox permafrost tunnel, Fox, Alaska (from Arcone & Delaney 1989).

We conducted standard cross-hole surveys using the zero-offset profile (ZOP) method (Sensors and Software 1997; Fig. 2a). The ZOPs are run as a reconnaissance-type survey where transmitter and receiver antennae are simultaneously lowered down adjacent boreholes at equal step sizes. Typical step sizes are 0.125 m, 0.25 m and 0.5 m for the 200 MH, 100 MH and 50 MHz antennae, respectively. In total, 65 ZOP files were collected, with many representing repeat investigations of the same wells at each of the three antenna frequencies, thereby providing a basis for comparing material properties and signal response among the various sites. This type of survey is relatively quick and produces a profile of vertical variations with depth in travel times for horizontal straight ray-paths between the wells. Variations in material properties determine the travel time and the amplitude of the radar pulse (Fig. 3). Measuring the signal travel time over a known distance gives the signal velocity between the antennae. The signal amplitude of the pulse varies depending on the electrical conductivity of the material between the boreholes (Davis & Annan, 1989).

Observations in frozen ground

Chena River permafrost wells

We used an existing CRREL geophysical installation consisting of dry boreholes, a temperature-
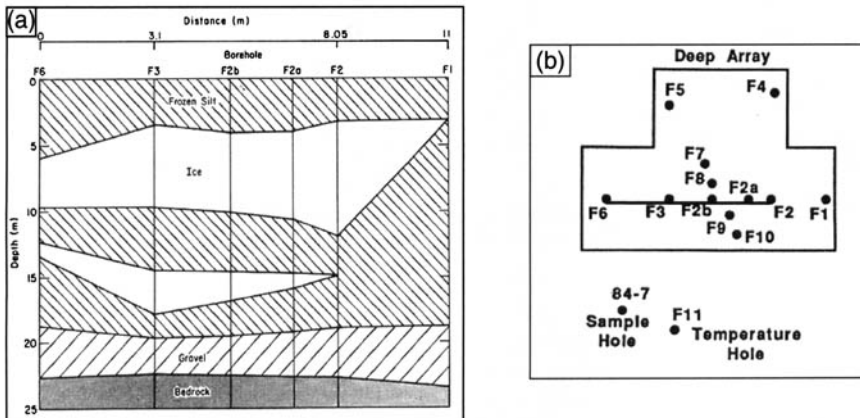
Fig. 9. Stratigraphy of the deep array: (a) cross-section based on well transect F6 to F1, and (b) location of wells (from Delaney 1987).

profiling well and a geophysical well for resistivity profiling (Fig. 4). The site was selected to provide system calibration and baseline measurements in a contaminant-free location on Fort Wainwright. The soils consist of silty sand, grading to sandy silt by 7 m depth and overlaying sandy gravel. Measurements by Arcone and Delaney (1989) indicated soil moisture of about 20% in the silt and sand and 10% in the lower sandy gravel. Sediments in the area are perennially frozen to a depth of at least 30 m at about −0.3 °C. We chose borehole combinations that provided signal propagation path lengths of approximately 9 m, 22 m and 43 m. The results show little variation in velocity for the three antenna frequencies as a function of depth, whereas attenuation increased with frequency (Figs 5–7). Transmission vs. distance tests (Figs 6 & 7) showed little variation in velocity or attenuation as a function of distance between the boreholes. The variability observed is probably due to changes in the stratigraphy between the boreholes. Both the 50 MH and 100 MHz antennae were capable of profiling to 43 m radial distance from the borehole centre. Previous 100 MHz borehole studies at the site (Arcone & Delaney, 1989) measured attenuations of 0.5–1.5 dB m^{-1} in these frozen materials (Table 1). Over the three propagation paths, we measured average attenuation rates of 0.4 dB m^{-1}, 1.7 dB m^{-1} and 3.4 dB m^{-1} at 50 MHz, 100 MHz and 200 MHz, respectively, showing that attenuation increases with frequency as expected (cf. Hoekstra & Delaney, 1974; Davis & Annan, 1989).

Fox permafrost tunnel

The Fox site consists of two-borehole arrays in silty permafrost drilled by CRREL during the 1980s (Delaney, 1987; Arcone & Delaney, 1989;

Table 1. *Velocity and attenuation of materials at 100 MHz*

Material	Velocity (m ns^{-1})	Attenuation (dB m^{-1})
Silt (active layer)	0.05–0.06	10–11
Schist (saturated/ contaminated)	~0.1	~4
Schist	0.08–0.1	~7
Meta-siltstone	0.11–0.13	2.5–3.5
Sand	0.10–0.11	2–3
Sand (saturated)	0.07–0.09	4–6
Ice wedge (clean)	0.17–0.18	6–7
Frozen silt	0.11–0.13	9–10
Frozen sand and gravel	0.13–0.14	1.5–2
Frozen schist	0.13–0.14	6–7

Fig. 8). These arrays consist of: (1) 12 boreholes drilled to 25 m depth used to investigate and describe electrical properties down to bedrock (Fig. 9); and (2) several shallow (~5 m depth) boreholes drilled around buried targets (Delaney, 1987). These are referred to as the 'deep' and 'target' arrays, respectively. Data described in this report were collected at the deep array with the intent of characterizing all of the soil types down to the local bedrock. The stratigraphy of the site is characterized by ~20 m of frozen silt that interfingers with massive and silt-rich ice lenses (Fig. 9). There are 2–3 m of frozen gravel lying between the frozen silt and high-grade metamorphic bedrock (i.e. schist). Data presented in Figure 9 represent a cross-hole survey performed between wells F6 and F2, a distance of about 8 m.

Results from the deep array show that velocity ranged from ~0.05 m ns^{-1} to 0.18 m ns^{-1} and attenuation between 6 dB m^{-1} and 13 dB m^{-1} (Fig. 10; Table 1). The slow zone (velocities ~0.05 m ns^{-1}) corresponds to the thawed active layer, which was ~1 m thick at the time of the survey, as measured using a steel probe and surface GPR. Velocity in massive ice was ~0.18 m ns^{-1} and attenuation was ~7 dB m^{-1} at 100 MHz. Frozen silt is characterized by velocities of ~0.11–0.13 m ns^{-1} and attenuation ~6–7 dB m^{-1}.

Observations in contaminated ground

Fort Wainwright

Fort Wainwright is the site of several on-going environmental studies as part of the installation characterization and clean-up. Past and on-going investigations have resulted in the drilling of more than 5000 boreholes and monitoring wells, which both provide considerable ground-truth and ready access to the subsurface for downhole GPR profiling. Previous studies by CRREL at some of these sites include lithological logging, surface GPR profiling and direct current (DC) resistivity sounding and profiling (Lawson *et al.* 1996). These background data provide critical information to aid in evaluating system performance and interpreting the radar data.

To investigate the effects of hydrocarbon contaminants on radar-pulse propagation, we profiled several wells in the Birch Hill Tank Farm. Site maps show the extent of the free-phase and benzene plumes (Fig. 11). Data from borehole AP-7526 are shown in Figure 12 where residual benzene, gas-range organics (GRO) and diesel-range organics (DRO) are found at the groundwater surface. 200 MHz antennae were used with a well spacing of <2 m to collect these ZOP data. Litho-

logical and contaminant data are shown for bore-hole AP-7526. Velocity in the upper weathered schist is 0.10–0.12 m ns^{-1} and ~0.10 m ns^{-1} in the metasiltstone. Velocity decreased to ~0.09 m ns^{-1} in the lower schist.

Figure 13 shows two logs for wells near the base of Birch Hill that are located in the centre of the benzene plume. AP-7529 contains low levels of benzene, GRO and DRO, while the corresponding contaminant levels are much higher at AP-7530. Boreholes bracketing AP-7529 and AP-7539, with a spacing of ~10 m, were profiled using 100 MHz antennae. The GPR profiles show higher attenuation above the water table. The high attenuation between 5 m and 11 m depth in AP-7529 and 2 m and 9 m depth in AP-7530 corresponds to the occurrence of the Birch Hill schist in the vadose zone. A decrease from 7 dB m^{-1} to 4 dB m^{-1} in attenuation below 9 m depth in AP-7530 corresponds with the highest levels of contamination in any of the wells observed: 58 550 mg kg^{-1} GRO and 13 900 mg kg^{-1} DRO. A pronounced difference in the radar pulse at the water table is observed between AP-7529 and AP-7530. We suggest the higher amplitude observed at AP-7530 probably reflects a decrease in electrical conductivity caused by hydrocarbons near the groundwater surface; however, further investigation is required to better define these responses and evaluate their cause (e.g., Brewster *et al.* 1995; Daniels *et al.* 1995; Bermejo, 1997).

Summary of velocity and attenuation results

Table 1 summarizes attenuation and velocity measurements for the 100 MHz data in the various material types tested during our study. As expected, there is overlap in both velocity and attenuation values for soil and rock. However, the trends are consistent; fine-grained silts result in more attenuation than coarser sand and gravel. Dirty wedge ice (between 12 m and 15 m depth in Fig. 10) provides the widest range of both attenuation and velocity because of the variable silt content and the ice wedge is not of constant thickness between wells F6 and F2 (Fig. 9).

Saturated and unsaturated schist exhibited velocities of ~0.10 m ns^{-1} and 0.08–0.1 m ns^{-1}, respectively (Table 1). The velocity in frozen schist increased from 0.13 m ns^{-1} to over 0.14 m ns^{-1}. Temperature profiles by Arcone and Delaney (1989) indicate that the equilibrium temperature below 6 m in the permafrost is about -0.3°C to 0.4 °C. Attenuation in the schist at 100 MHz is ~7 dB m^{-1}. Metasiltstone was observed to have a velocity of ~0.11–0.13 m ns^{-1} and an attenuation of ~3 dB m^{-1}. Silt in the active layer exhibits the lowest velocity (0.05–0.06 m ns^{-1}) and highest attenuation (10–11 dB m^{-1}). Frozen silt ranges from 0.11 m ns^{-1} to ~0.13 m ns^{-1} and 9 dB m^{-1} to 10 dB m^{-1}. Sand and gravel exhibits a wide range in velocity (0.11 m ns^{-1}, 0.08 m ns^{-1} and 0.13 m ns^{-1}) and attenuation (4–7 dB m^{-1}, 1–4 dB m^{-1} and ~1.7 dB m^{-1}) when unsaturated, saturated and frozen, respectively. Some of the ranges observed in these data can be explained by lack of control on the stratigraphy between the boreholes where layers are of variable thickness and lenses locally pinch out. The massive ice wedge observed at the permafrost tunnel location is characterized by velocities of ~0.17–0.18 m ns^{-1} and an attenuation of ~6 dB m^{-1} at about -0.3 °C. In general, the cleaner, massive ice exhibits higher velocities and lower attenuation rates than ice with dispersed debris.
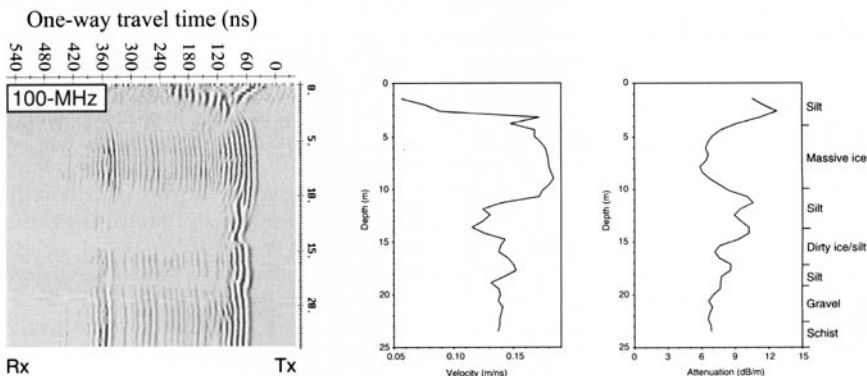
Fig. 10. 100 MHz cross-hole GPR survey with tomographic plot for velocity and attenuation between wells F6 and F2. Transmission path is shown in Figure 9.
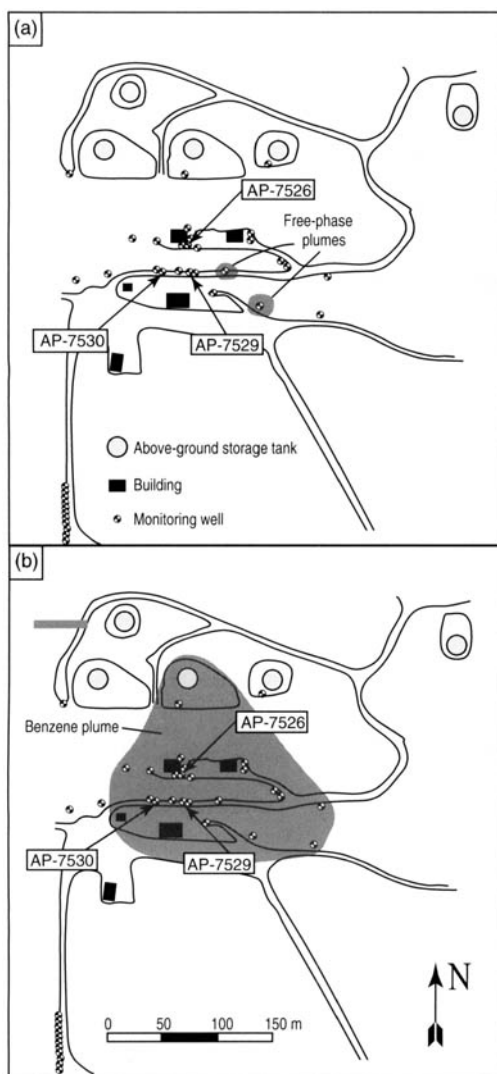
Fig. 11. Plume extent maps for Birch Hill Tank Farm: (a) free-phase plume, and (b) benzene.

Conclusions

The use of cross-borehole GPR can yield information on the electrical characteristics of both frozen and unfrozen materials; including electromagnetic propagation velocity and attenuation. Our recent measurements in interior Alaska demonstrate distinct signal responses to frozen/unfrozen sediments, bedrock and massive ground ice. Unfrozen sediment and rock exhibited velocities between 0.05 m ns^{-1} and 0.14 m ns^{-1} and attenuation ranges from 1 dB m^{-1} to 11 dB m^{-1} while frozen materials are between 0.11 m ns^{-1} and

0.18 m ns^{-1} and 2 dB m^{-1} and 11 dB m^{-1}. The general trend is for frozen materials to have higher velocities than their unsaturated or saturated counterparts (e.g., Hoekstra & Delaney, 1974). Signal attenuation in frozen sand and gravel has a narrower range and is generally lower (2–3 dB m^{-1}) than in unsaturated or saturated sand and gravel. Schist exhibits attenuation values around 7 dB m^{-1}. Massive ice is characterized by high velocities (0.17–0.18 m ns^{-1}) and attenuation rates (7 dB m^{-1}). The measurements recorded at a hillside bedrock site within the confines of the Fort Wainwright Birch Hill Tank Farm, where petroleum contamination is pervasive, show marked decrease in signal attenuation of 7–4 dB m^{-1} near the bottom of several holes and attenuation variations within the bedrock above. These data are insufficient for a conclusive evaluation of the effects that hydrocarbons have on the electrical properties; the pronounced change in attenuation warrants additional measurements. Changes in the stratigraphy between individual boreholes complicated the interpretations. Despite this drawback, data collected in this study provide useful background information on the electrical characteristics of geological material properties in the Fairbanks area and demonstrates the application of cross-borehole GPR for defining vertical changes in electrical characteristics.

References

ANNAN, A. P., BAUMAN, P., GREENHOUSE, J. P. & REDMAN, J. D. 1991. Geophysics and DNAPLS. *Proceedings of the Fifth National Outdoor Action Conference on Aquifer Restoration, Ground Water Monitoring, and Geophysical Methods, May 13–16, Las Vegas, Nevada,* 963–977.

ARCONE, S. A. & DELANEY, A. J. 1989. *Investigations of Dielectric Properties of Some Frozen Materials Using Cross-Borehole Radiowave Pulse Transmissions.* Cold Regions Research and Engineering Laboratory, Hanover, New Hampshire, CRREL Report, **89–4**.

BERMEJO, J. L., SAUCK, W. A. & ATEKWANA, E. A. 1997. Geophysical discovery of a new LNAPL plume at the former Wurtsmith AFB, Oscoda, Michigan. *Ground Water Monitoring and Remediation,* **17**, 131–137.

BREWSTER, M. L., ANNAN, A. P., GREENHOUSE, J. P., KUEPER, B. H., OLHOEFT, G. R., REDMAN, J. D. & SANDER, K. A. 1995. Observed migration of a controlled DNAPL release by geophysical methods. *Ground Water,* **33**, 977–987.

DANIELS, J. J., ROBERTS, R. & VENDL, M. 1995. Ground penetrating radar for the detection of liquid contaminants. *Journal of Applied Geophysics,* **33**, 195–207.

DAVIS, J. L. & ANNAN, P. 1989. Ground-penetrating radar for high resolution mapping of soil and rock stratigraphy. *Geophysical Prospecting,* **37**, 531–552.

DELANEY, A. J. 1987. *Preparation and Description of a*
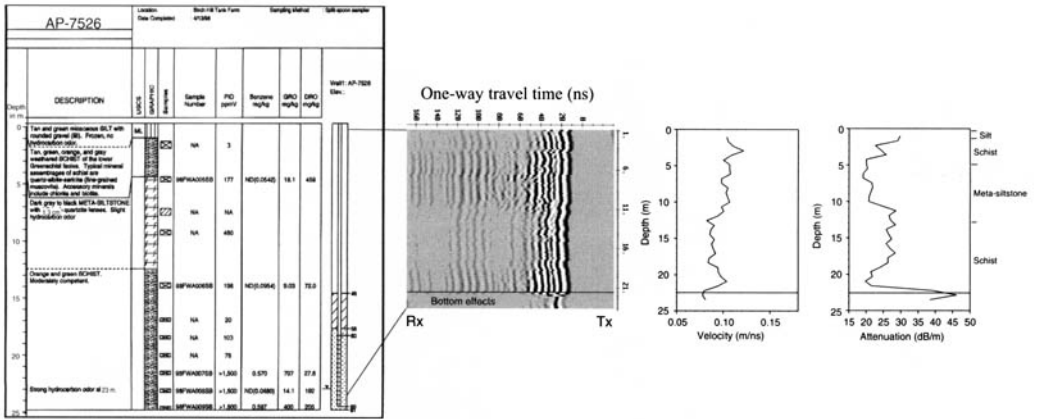
Fig. 12. Cross-hole GPR surveys crossing AP-7526 with tomographic plots for velocity.
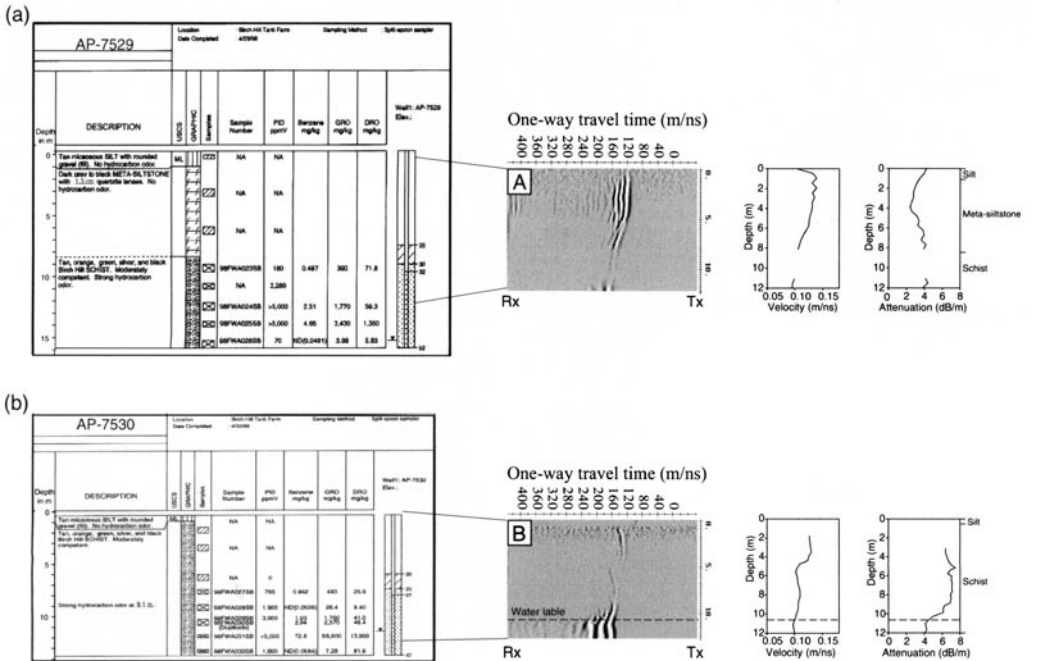
Fig. 13. Cross-hole GPR surveys crossing AP-7529 and AP-7530 with tomographic plots for velocity and attenuation. (a) Top profile shows low attenuation (2–5.5 dB m^{-1}) through the section with velocity decreasing from 0.15 m ns^{-1} to 0.1 m ns^{-1} with increasing depth. Strong signal transmission is visible through the section. (b) Profile crossing AP-7530 indicates strong attenuation (6–8 dB m^{-1}) above the groundwater table (~12 m).

Research Geophysical Borehole Site Containing Massive Ground Ice Near Fairbanks, Alaska. Cold Regions Research and Engineering Laboratory, Hanover, New Hampshire, Special Report, **87–7**.

HOEKSTRA, P. & DELANEY, A. J. 1974. Dielectric properties of soils at UHF and microwave frequencies. *Journal of Geophysical Research*, **79**, 1699–1708.

LAWSON, D. E., STRASSER, J. C., STRASSER, J. D., ARCONE, S. A., DELANEY, A. J. & WILLIAMS, C. 1996. *Geological and Geophysical Investigations of the Hydrogeology of Fort Wainwright, Alaska, Part I: Canol Road Area.* Cold Regions Research and Engineering Laboratory, Hanover, New Hampshire, Special Report, **96–4**.

REDMAN, J. D. 1992. Geophysics and the solvent-in-groundwater program. *Proceedings of the Symposium on the Application of Geophysics to Engineering and Environmental Problems, 26–29 April 1992, Chicago, Illinois,* 375–382.

SENSORS AND SOFTWARE. 1997. *pulseEKKO Crosshole Data Acquisition: User's Guide, Version 1.0.* Sensors and Software, Inc., Mississauga, Ontario, 87 pp.

This page intentionally left blank

Amplitude analysis of repetitive GPR reflections on a Lake Bonneville delta, Utah

SARAH E. KRUSE[1] & HARRY M. JOL[2]

[1]*Department of Geology, University of South Florida, 4202 East Fowler Avenue, Tampa, Florida, 33620, USA (e-mail: skruse@chuma1.cas.usf.edu)*
[2]*Department of Geography, University of Wisconsin-Eau Claire, Eau Claire, WI 54702–4004, USA*

Abstract: Several recent theoretical studies have documented the sensitivities of the amplitude and waveform of a ground penetrating radar (GPR) reflection to the contrast in electromagnetic properties across the reflecting contact. Here we show that, in a setting with repetitive layering, it is possible to place constraints on conductivity and variations in permittivity within layers and across layer boundaries. The data set consists of 50 MHz, 100 MHz and 200 MHz profiles that image subparallel dipping bedding planes in a gravelly deltaic foreset facies on a Lake Bonneville delta, Utah, USA. Strongly reflecting horizons with 1–2 m spacings bound packages with finer internal layering. From finite-difference time-domain (FDTD) simulations of radar-wave propagation through such strata, constraints are placed on the variations in permittivity across larger-scale and finer-scale layering. Modelling the relative amplitudes of reflections demonstrates that the finer-scale permittivity contrasts are ~0.4–0.8 times that of the 1–2 m layering. Amplitude v. offset (AVO) analysis yields an upper bound of ~3.5 for the contrast in permittivity at the larger-scale layer boundaries. Overall signal attenuation requires the average conductivity to be in the range of 0.7–0.8 mS/m.

Ground penetrating radar (GPR) has been widely and successfully used to image the spatial patterns of reflecting horizons in sedimentary environments. Radar stratigraphy offers unparalleled access to the three-dimensional (3-D) structures of clastic and carbonate strata (e.g. McMechan *et al.* 1997; van Overmeeren 1998; Bristow *et al.* 2000). In such studies, radar velocities within layers are generally estimated from common mid-point surveys (CMP). In practice it is difficult with this method to determine interval velocities for thin layers. More typically, average velocities are estimated for packages on the order of a metre or more in thickness.

For a variety of reasons, however, it might be useful to extract more information about velocity variations and the electromagnetic properties of the strata that determine the radar-wave velocity. The media properties controlling the radar response – relative dielectric permittivity (dielectric constant) (ϵ_r), relative magnetic permeability (μ_r), and conductivity (σ) – in turn depend on lithological and hydrogeological parameters that are of interest to sedimentologists and hydrogeologists. Among these parameters are porosity, water content, iron content, clay content, and pore-fluid conductivity. Variations in such parameters, particularly per-meability, are of interest to hydrogeologists and petroleum geologists seeking to quantify aquifer or reservoir properties on all scales (e.g. Hornung and Aigner 1999; Huggenberger and Aigner 1999). Thus GPR images may offer a window into these properties on centimetre-to-decimetre scales. Two steps are required: (1) to extract the electromagnetic properties over a range of wavelengths, and (2) to establish relationships between the electromagnetic and the sedimentological/hydrogeological properties. Because the electromagnetic behaviours of sediment-plus-porewater systems are complex (e.g. Knoll & Knight 1994; Peplinski *et al.* 1995; Saarenketo 1998; Chan & Knight 1999), the relationships of step (2) must still be assessed on a site-to-site basis (Chanzy *et al.* 1996). Nevertheless, where sufficient data are available, step (2) may indeed be feasible, as recent studies demonstrate (e.g. van Overmeeren *et al.* 1997; Olhoeft 2000; van Dam & Schlager 2000) .

This paper focuses on step (1) and demonstrates that modelling of radar records can help constrain the variability and scaling in electromagnetic properties. Figure 1 shows an example from an outcrop sedimentological study by Hornung and Aigner (1999), aimed at understanding heterogen-
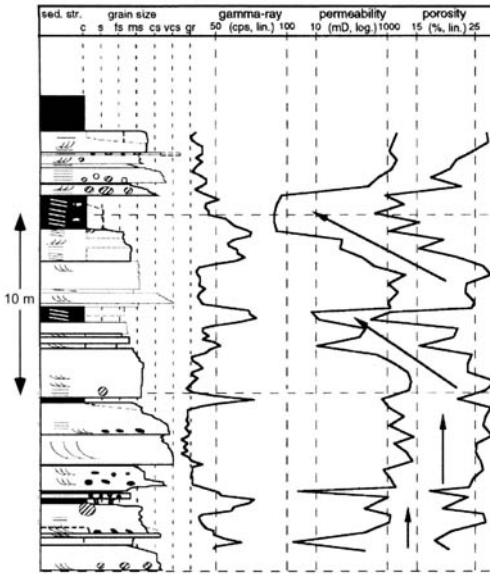
Fig. 1. Example of coarser-scale (with arrows) and finer-scale (no arrows) variability in sedimentological and hydrogeological parameters in an alluvial plain system. Arrows highlight coarser-scale variability in porosity and permeability. (Modified from Hornung and Aigner 1999, fig. 21).

eities in hydrogeological properties. The arrows (Fig. 1) emphasize larger-scale (~5 m) trends in porosity and permeability. Superimposed on these larger-scale trends are secondary, smaller-scale (<~ m) variations. In theory one might extract similar information on relative permittivity (or conductivity or magnetic permeability) from a GPR record. Because the relative dielectric permittivities of air (1) or water (80) differ so significantly from that of rock or soil matrix (~4), permittivity commonly correlates strongly with porosity and water content. Thus, for example, the sharp increase in porosity at the upper boundary of the sequences labelled with diagonal arrows in Figure 1 would be expected to produce larger-amplitude reflections than the porosity variations within the units in saturated or dry media (independent of changes in lithology). The discussion below shows that constraints on such relative contrasts within the target media can indeed be derived from radar reflections, within a given lithology.

Analysis of internal variability requires interpretation of reflection amplitudes in addition to the standard estimation of velocities from CMP surveys or comparison with outcrop or well data. The theoretical framework for understanding reflection amplitudes comes from basic electromagnetic theory (Stratton 1941; Wait 1970). The groundwork for radar applications has been laid by Zeng

et al. (2000). Such amplitude and waveform analysis has been applied to engineering studies, notably by Olhoeft (2000). For example, in Olhoeft (2000), the amplitude of a reflection off a steel pipe is used to determine overlying soil conductivity.

Amplitude modelling in geological applications is considerably more difficult, however, because the properties of media on both sides of a contact are unknown (in the engineering application the properties of steel are well known). In addition, in both geological and engineering applications the amplitude of the outgoing pulse is uncertain. While most time-domain GPRs produce a tri-lobed pulse similar to a Ricker wavelet, this source wavelet is dependent on the antenna as well as the antenna-ground impedance match, which is influenced by near-surface conductivity, surface roughness and antenna-to-ground contact. In extreme cases, such as the antenna ring-down effect (Radzevicius et al., 2000), deviation from the Ricker wavelet form can be quite significant.

The uncertainties associated with lack of knowledge of media properties and outgoing pulse amplitude can be reduced at sites where the media can be locally 'ground-truthed' with well logs or outcrop measurements or where a repetitive sequence of similar reflecting horizons exists. In the latter scenario, the sequential effects of numerous reflections can be simulated and compared with observations. This paper details simulations of a set of radar profiles collected over gravelly bedding planes, described by Smith and Jol (1992, 1995).

Geological setting and GPR surveys

Smith and Jol (1992) selected a Brigham City, Utah, USA, gravel pit as a site beautifully suited to test the capabilities of GPR because the gravels have a high quartz content (presumably low silt and clay content, and thus lower signal attenuation) and because stratigraphy is clearly visible in pit-wall exposures (Fig. 2). Strata are interpreted as bedding planes of deltaic foreset facies of a Late Pleistocene Provo-level Lake Bonneville delta (Smith & Jol 1992). The most striking features exposed in quarry walls are strata with the highest resistance to weathering, spaced ~1–2 m apart and dipping ~22°. These finer-grained strata appear as the darker bands in Figure 2a and as the lines drawn in the schematic in Figure 2b. Finer-scale layering, with thicknesses of tens of centimetres, is also apparent between the prominent resistant strata. 3-D surveys at this site show that beds are locally planar in form (Jol et al. 1996). The water table lies below depths imaged by GPR.

We refer to the 1–2 m packages bounded by the resistant units as large-scale layers, and the layering within these packages as fine-scale layering.
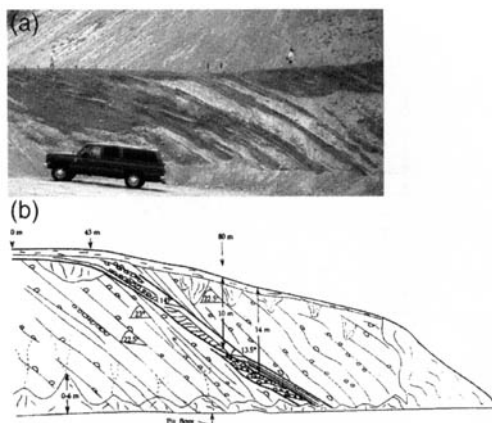
Fig. 2. (a) Quarry wall exposure, Brigham Sand and Gravel Company pit. In central part of photo resistant units with ~1–2 m spacing appear clearly as darker bands. (b) Schematic diagram of another exposure in same pit, from Smith and Jol (1992). 3× vertical exaggeration. Sandy unit discordant to 22°-dipping strata was clearly imaged in radar records reported in Smith and Jol (1992), confirming that primary arrivals are imaged to ~300 ns travel time in 50 MHz and 100 MHz records. All sites (Fig. 2a & 2b, results reported in Smith & Jol 1992 and data in this paper) share common features of 22°-dipping resistant units with 1–2 m spacing and parallel finer-scale layering.

Figures 3, 4 and 5 show data collected at 50 MHz, 100 MHz and 200 MHz antennae, respectively, with 0.5 m spacing over a 20 m transect along a level terrace within the quarry. The dipping strata are clearly visible at all frequencies. Depth of penetration is excellent – on the order of 20 m for 100 MHz antennae. Late-arriving pulses are principally primary reflections and not multiple reflections off shallower contacts, as documented by the imaging of a discordant sandy unit to 20 m depth (Fig. 2) (Smith & Jol 1992) and verified by modelling described below.

The average velocity throughout the records, determined from fitting hyperbolae of reflection events on CMP surveys, is ~0.15 m ns^{-1} (Smith & Jol 1992). As the true dip of beds is known to be ~20–25° from quarry-wall observations, the velocity determined from the CMP analysis, assuming that reflecting horizons are horizontal, overestimates the true average velocity by ~6–10%. After correcting for the known dips, average velocity is estimated at ~0.14 m ns^{-1}. Given this velocity, the timing of the 50 MHz returns and the prominent high-amplitude returns in the 100 MHz and 200 MHz transects correspond to those expected for reflections from the large-scale layering (bounded by resistant horizons) seen in the quarry walls. This correspondence is also clear in GPR transects run over exposed highwalls shown in Smith and Jol (1992) and Jol et al. (1996).

Fig. 3. 50 MHz transect across a lower terrace within the Brigham Sand and Gravel Company pit. (a) Full record shown with AGC gain, AGC window = 2 pulse widths, gain max. 200. (b) Central section of record, exponential gain with gain max. 50, gain attenuation 0.12 dB/m.

The bedding patterns are caused by the progradational nature of a fan-foreset delta, with finer-grained layers deposited during lower water flow (probably autumn/winter) and coarser-grained layers deposited by spring melts with greater water flow.

The 100 MHz and 200 MHz profiles (Figs 4 and 5) show additional coherent reflections that arrive between the times of the large-scale layer reflections. These lower-amplitude events parallel the strong reflections, so we infer that they represent energy reflected from both the fine-scale layering
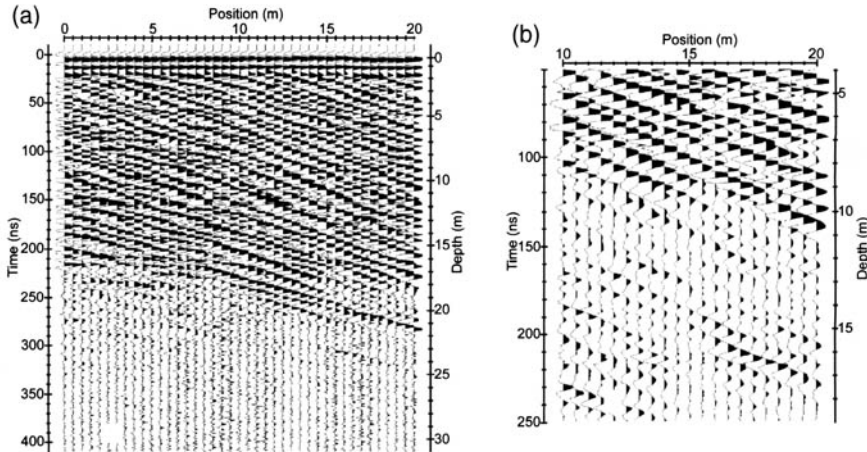
Fig. 4. 100 MHz transect at same location as 50 MHz (Fig. 3). (**a**) Full record shown with AGC gain, AGC window = 2 pulse widths, gain max. 200. (**b**) Central section of record, exponential gain with gain max. 50, gain attenuation 0.12 dB/m.
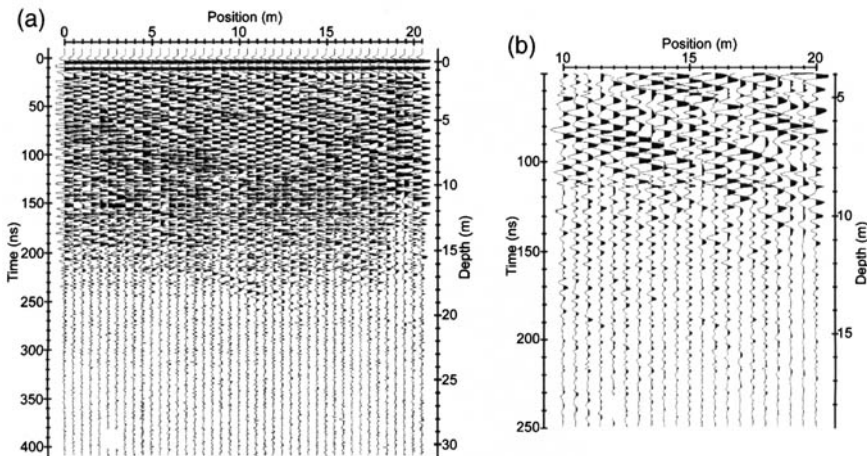
Fig. 5. 200 MHz transect at same location as 50 MHz (Fig. 3). (**a**) Full record shown with AGC gain, AGC window = 2 pulse widths, gain max. 200. (**b**) Central section of record, exponential gain with gain max. 50, gain attenuation 0.12 dB/m.

and multiply reflected ray paths. Figures 3*b*, 4*b* and 5*b* display a subset of the data with an exponential gain that increases smoothly over the 50–250 ns time window shown. This gain was subjectively chosen to maximize uniformity in amplitude of the 'strong' reflections throughout the 130–250 ns time window on the 50 MHz and 100 MHz records and the 130–200 ns time window on the 200 MHz records. Following application of this gain, the amplitudes of intermediate reflections were compared with those of neighbouring high-amplitude reflections. Most intermediate reflections have amplitudes ranging from ~0.25 to 0.7 times that of neighbouring high-amplitude reflections. Thus the

contrasts in electromagnetic properties associated with the fine-scale layering appear smaller than that of the contrasts associated with the large-scale layers. This pattern of GPR amplitudes suggests an internal structure similar to that shown in Figure 1 (measured by Hornung & Aigner [1999] within an alluvial plain). We use the observed relative amplitudes (large-scale layers v. fine-scale layers) to constrain the relative magnitudes of the permittivity contrasts associated with each type of layering.

Modelling GPR wave propagation

We use 1-D, 2-D and 3-D FDTD models to simulate radar-wave propagation through media of specified conductivity, relative dielectric permittivity and relative magnetic permeability. Figure 6 shows 'snapshots' from a sample 2-D run with transverse electric polarization. Computations are based on the second-order staggered grid difference scheme of Yee (1966). This formulation applies finitedifference approximations to Maxwell's equations and has been used by numerous researchers to simulate GPR transmissions (e.g. Wang & Tripp 1994). The codes have been verified against analytical solutions and published test cases (Kunz & Luebbers 1993). Second-order Mur absorbing boundary conditions (Mur 1981) are applied at the margins of the computational grid. The source pulse characteristics are designed to emulate those of the pulseEKKO 100 system manufactured by Sensors and Software, Inc. The pulse is tri-lobed and consists of a decaying exponential superimposed on a Ricker wavelet. A suite of models, run to test the dependence of the conclusions drawn in this paper on the source wavelet, shows that the results presented below are independent of minor variations in the form of the simulated pulse.

Simulation output includes the electric and magnetic fields at any point on the grid, so the radar response can be simulated at arbitrary receiver locations. To avoid computational expense 1-D and 2-D models with plane or line sources, respectively, were used when the amplitudes (after correction for geometric effects) differed insignificantly from those of 3-D models.

The FDTD code can incorporate dispersivity in the form of a series of Debye relaxation mechanisms (Kunz & Luebbers 1993). However, for the unsaturated quartz-rich gravels of the Brigham City site, and for the antenna frequencies used, the dielectric losses associated with matrix and water relaxation should be negligible. We thus assume that attenuation is dominated by conductivity and characterize attenuation in terms of a constant conductivity. Permittivity is assumed to vary across the boundaries of both the large-scale and fine-scale layers. It is unlikely that these gravels contain a significant heavy mineral content, so the relative magnetic permeability is set to a uniform value of 1 throughout the section. The unusually good radar penetration at this site further indicates that ground conductivities are quite low. If conductivities are low, then the contribution of conductivity variations to the reflection coefficients at layer boundaries will be small relative to the effect of permittivity variations. Thus it is reasonable to ignore conductivity contrasts at layer boundaries and our models assume a uniform media conductivity.
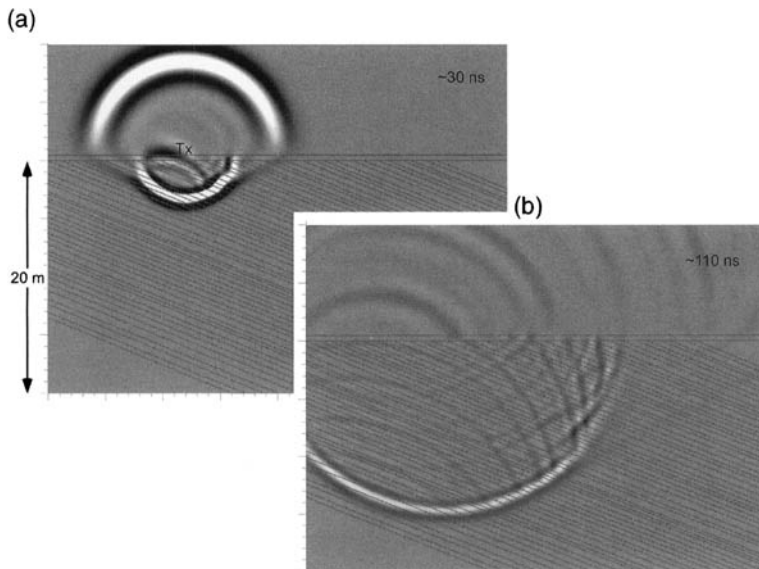
Fig. 6. Vertical slice snapshots of 2-D FDTD models as used in this study. (a) ~30 ns after simulated pulse transmission at location marked with Tx. (b) After ~110 ns of travel time. Uppermost layer represents air with $\epsilon_r = 1$, $\mu_r = 1$, $\sigma = 0$. Air underlain by uniform 'road fill' layer 0.5 m thick at surface with $\epsilon_r = 4$, $\mu_r = 1$, $\sigma = 0.07$ mS/m. Lower dipping layers as described in text. Shading represents amplitude of out-of-plane (TE) component of E-field.

1-D models assume plane waves and zero transmitter–receiver offset; the 2-D models shown mimic the 1 m antenna separation used in the 100 MHz gravel-pit surveys.

Constraints on the form and relative amplitudes of permittivity contrasts

Large-scale layers

Repetitive stratigraphic packages with different overall forms – e.g. gradual versus sharp changes in permittivity with depth – produce different radar reflection patterns. Figure 7 shows several simple models designed for comparison with the radar response to the large-scale (1–2 m) layering in the gravel quarry. These initial 1-D models ignore fine-scale internal layering, geometrical and conductive attenuation, and angle of incidence dependence in reflection coefficients – factors considered further below. The models assume that layer thicknesses vary with a Gaussian distribution about a mean value of 1.6 m, to avoid resonance effects associated with perfectly uniform layer thicknesses. The contrast in permittivity is set to a uniform value and form across each layer boundary. This uniformity is, of course, not realistic, but testing a range of such models serves the goals of capturing upper and lower bounds on the permittivity contrasts as well as the overall structure of permittivity variations.

Models 1 and 3 (Fig, 7) show gradational 1–2 m-thick packages, with a sharp contrast at their upper boundaries. On these 'sawtooth' models only the sharp contrasts produce distinct reflections. Contrasts that separate an overlying low-permittivity zone from underlying high permittivity, such as in model 1 of Figure 7, produce reflections with the opposite polarity of the down-going wave. Reflections from top of low-permittivity zones, as in model 3, show no polarity change. (Note the opposite polarities in the GPR traces from models 1 and 3 on Fig. 7.) The polarities of the air-wave, the direct ground-wave, and strong reflections from larger-scale boundaries at different separations on the CMP records collected at the Brigham City quarry (Smith & Jol 1995) were compared with a 3-D model with conductivity 0.7 mS/m (see Discussion below) and a 22°-dipping contact with sharp permittivity contrast. The data are better fit by the sharp boundaries between 1–2 m larger-scale layers separate underlying high ϵ_r (presumably low porosity in this dry environment) zones from lower ϵ_r (higher porosity) zones, as in model 1. Apparently, internally within the 1–2 m units porosity decreases from bottom to top.

The pattern of the ϵ_r increase from bottom to top within each larger-scale layer is more difficult to resolve. In contrast to the sawtooth of model 1, model 2 in Figure 7 incorporates a thin high-ϵ_r layer at the top of each large-scale layer. The form of the reflected pulse from the model 2 thin layers (predominantly a peak-trough pair) differs from the tri-lobed form of the reflections from the top of the model 1 sawteeth. In practice the overall continuity of reflections makes it difficult to distinguish
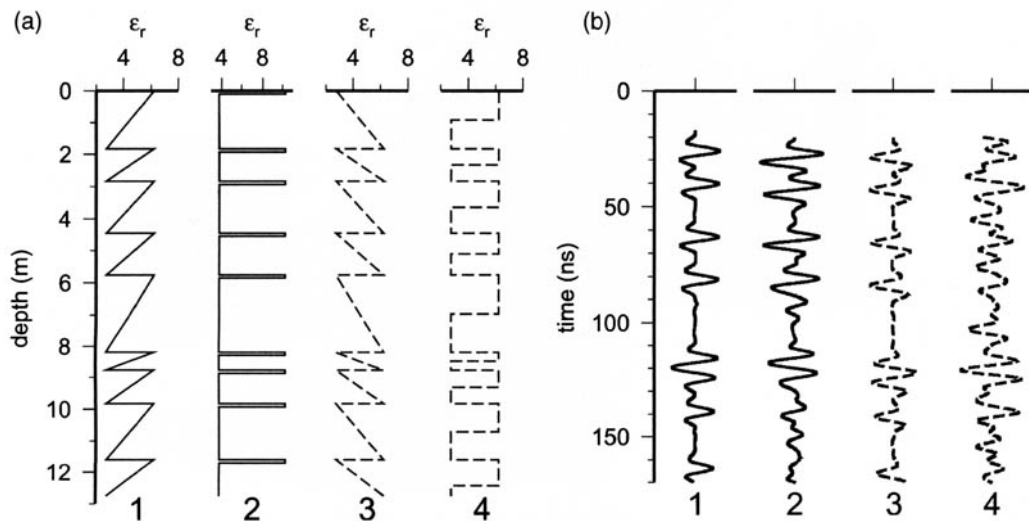
Fig. 7. Models for large-scale permittivity structure. (a) Schematic of permittivity as a function of depth. (B) Simulated GPR response to permittivity structure shown at left, from 1-D models of 100 MHz pulse. Solid lines (models 1 and 2) show successful models that predict observed features in radar traces. See text for discussion.

whether the large-scale reflections in the data more closely resemble model 1 or model 2 forms. (This is true at all three antenna frequencies.) Thus, from the radar record alone, we cannot tell whether the packages are internally gradational (such as a fining-upward sequence and model 1) or bounded by a thin ($<\sim30$ cm) distinct low-porosity layer (as in model 2). We can exclude from consideration, however, models with a significant sharp lower boundary to a high-ϵ_r layer more than about 30 cm thick, such as model 4 in Figure 7. Model 4 (and others with distinct high-ϵ_r layers $>\sim30$ cm thick) show clear reflections associated with the lower boundary of the high permittivity layer in 100 MHz and 200 MHz simulations. Such lower-boundary reflections are not compatible with the observed overall pattern of 20–30 ns between strong reflections. Essentially the observed GPR patterns preclude models in which the high-ϵ_r layers have a sharp lower boundary, unless the layers are less than about 30 m thick.

Fine-scale layers

Simultaneous modelling of the 50 MHz, 100 MHz and 200 MHz data sheds light on the finer-scale layering within the 1–2 m packages. The relevant observations are: the 50 MHz reflections (20–30 ns spacing) are quite strong; equivalently spaced high-amplitude reflections appear in the 100 MHz and 200 MHz data; the 100 MHz and 200 MHz traces also show returns between the high-amplitude reflections; when plotted with an exponential gain that renders the amplitudes of the high-amplitude returns roughly uniform through the 130–250 ns time interval, the amplitudes of these intermediate returns are ~0.25–0.7 times those of the preceding or subsequent high-amplitude reflections. The lower amplitudes of the intermediate returns demonstrate that the fine-scale permittivity variations cannot be as sharp or as pronounced as those at the boundaries of the larger-scale layers. To place bounds on the relative amplitudes of the fine-scale and large-scale permittivity variations, we add fine-scale layering to the successful models (models 1 and 2) of Figure 7.

Figure 8 shows suites of 1-D models for both sawtooth and uniform layer permittivity patterns, with four internal layers superimposed on the larger-scale 1–2 m layering. These 1-D models assume a plane wave and neglect geometrical spreading and non-zero angle of incidence, with the conductivity set to zero. As a result the amplitudes of the high-amplitude returns are relatively uniform throughout the trace, facilitating comparison with the exponential gain records in Figures 3b, 4b and 5b. After geometric corrections, errors associated with the 1-D (rather than 3-D with a

dipole source) modelling for the purpose of comparing the relative amplitudes of intermediate returns with preceding or following high-amplitude returns are less than 10% for the time range (130–250 ns) considered here. As a result it was considered reasonable to compare the relative amplitudes of neighbouring returns from the 1-D models with those from the exponential gain records. If the finer-scale permittivity contrasts are as large as those associated with the larger-scale layering (left column on Fig. 8), the 1–2 m wavelength in the structure is lost and the 50 MHz signal is weak (its long wavelengths are relatively insensitive to the wavelength of the finer-scale variations). A weak 50 MHz signal contradicts the observations – in fact a coherent 50 MHz return is observed from depths to 25 m (Smith & Jol 1992).

Models also conflict with observations if we assume that fine-scale permittivity contrasts are much smaller ($<\sim40\%$) than those bounding the 1–2 m-thick layers. The right-hand column in Figure 7 shows models with internal permittivity contrasts 0.2 times those at the larger-scale boundaries. These models with low-amplitude fine-scale variability predict the relative amplitude of 100 MHz and 200 MHz reflected energy arriving between the times of the package boundary reflections to be consistently less than about half that of the strong boundary events. The data show more variability in the amplitudes of the intermediate arrivals on the 100 MHz and 200 MHz records (Figs 4 & 5).

Overall, models with fine-scale permittivity contrasts between 0.4 and 0.8 times the contrasts at the large-scale boundaries best share the amplitude characteristics seen in the data. The central column in Figure 8 shows results for models with fine-scale permittivity contrasts that are 0.5 times the larger-scale contrasts.

Constraints on conductivity

The observed overall attenuation in the amplitude of GPR returns as a function of travel time is caused by: (1) the spreading of the wave energy over a spherical shell of increasing radius, (2) dissipative losses in a conductive ground (higher conductivity = stronger attenuation), and (3) energy partitioning at reflecting boundaries, including multiple reflections. At the Brigham City quarry the observed attenuation for arrivals between ~30 ns and 330 ns two-way travel time can be fitted with the simple expressions:

$$A(r) = (A_0/r)e^{-\alpha r} \text{ and } r = vt$$

where t is the travel time, r is the distance the wave has traveled at time t, A is the amplitude, and α is the attenuation coefficient. α and the constant A_0 are determined from the fitting this expression to
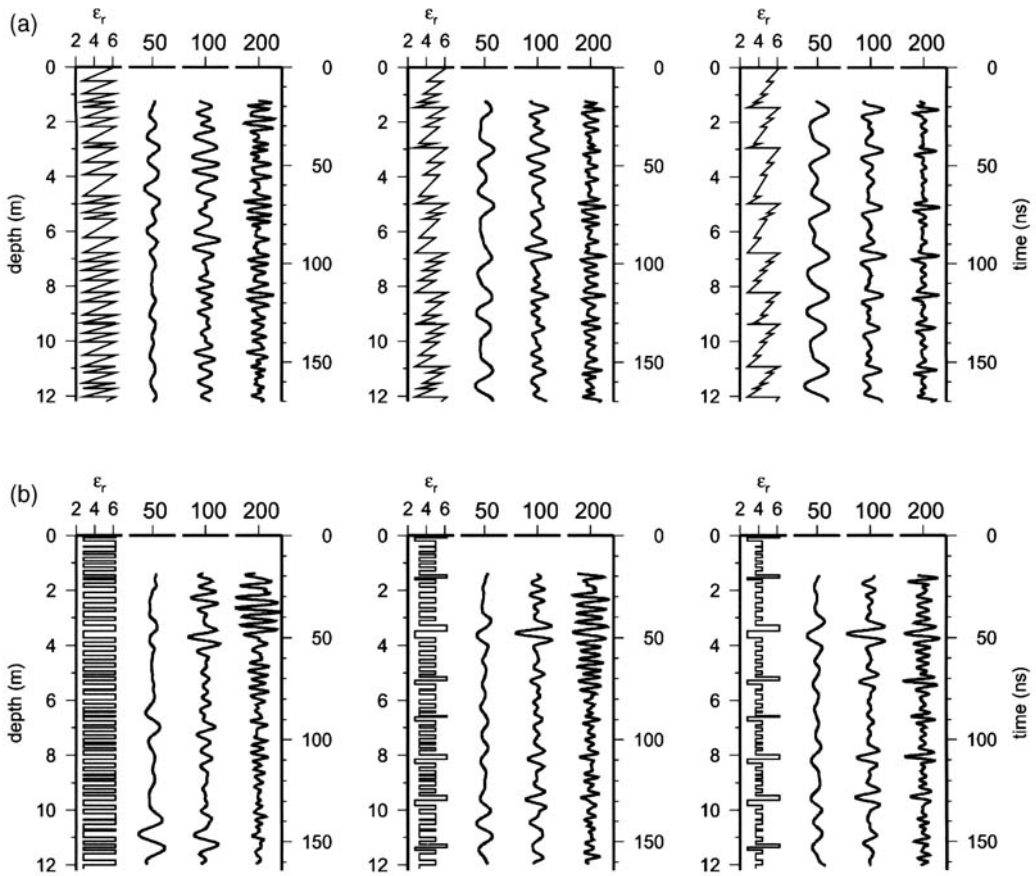
Fig. 8. Models for large- and small-scale permittivity structure. Each of the six diagrams shows permittivity structure at the left, with 1-D simulated GPR response at 50 MHz, 100 MHz and 200 MHz, in traces immediately to the right. (a) Sawtooth structures. (b) Uniform layer structures. Left-hand column: fine-scale $\Delta\epsilon_r$ = large-scale $\Delta\epsilon_r$. Middle column: fine-scale $\Delta\epsilon_r$ = 0.5 times large-scale $\Delta\epsilon_r$. Right-hand column: fine-scale $\Delta\epsilon_r$ = 0.2 times large-scale $\Delta\epsilon_r$.

the data. v is the average velocity ($= 0.15$ m ns^{-1}). The term in brackets describes geometrical spreading (process (1) above), while the exponential decay is used to represent the combined effects of conductivity and both primary and internal multiple reflections (processes (2) and (3)). (This expression fails at shorter travel times because the air-wave and direct-wave dominate the signal, and fails at longer travel times because the amplitude of the noise exceeds that of the signal.) We do not explicitly include a directivity function in this simplified expression for amplitude. Jiao *et al.* (2000) showed that TE mode radiation from a 450 MHz antenna at the air/ground interface has a maximum amplitude close to the critical angle $\theta_c = \sin^{-1}(\epsilon_r^{-1/2})$, as predicted from theoretical expressions for far field radiation from a horizontal half-wave dipole antenna. (θ is the angle between the radiation direction and the vertical axis.) At the

Lake Bonneville delta site $\theta_c \sim 30°$. The radiation direction for energy in primary reflections from 22.5°-dipping reflectors that arrives in the 30–330 ns time window ranges from ~ 34–12°. Thus, from the directivity function alone, higher amplitudes are expected at the earlier (smaller r, larger θ) arrivals. By fitting the observed average attenuation to the form above, the directivity function is in effect incorporated into the combined $r^{-1}e^{-\alpha r}$ term.

The best-fitting attenuation coefficient α for the 100 MHz data is 0.086 m^{-1} (0.75 dB/m) (Fig. 9). Attenuation modelling in this discussion is restricted to the 100 MHz data. Ground conductivity is typically frequency-dependent, but exploration of this frequency dependence is beyond the scope of this paper.

Because α is a function of both the ground conductivity and the reflection coefficients at layer
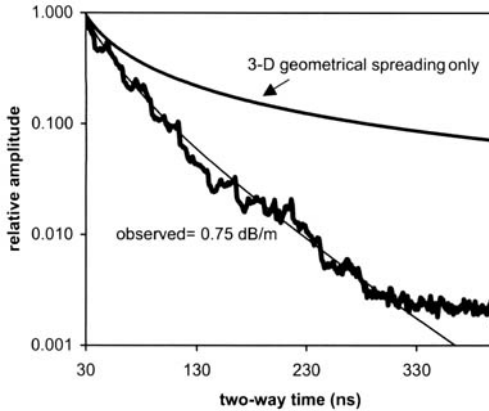
Fig. 9. Attenuation. Thick line, observed average amplitude as a function of travel time for all 100 MHz traces; medium line, attenuation expected from geometrical spreading only; thin line, best-fitting attenuation following expression in text, with attenuation coefficient $\alpha = 0.86$ m^{-1} or 0.75 dB/m.

boundaries, the two properties cannot be constrained independently. Furthermore, reflection coefficients are, in theory, a function of both permittivity and conductivity contrasts (as well as magnetic permeability contrasts, which can be neglected here). However, models that fit the observed attenuation for geologically plausible values of reflection coefficients require very low average conductivities, $<\sim 1.2$ mS/m, as is documented below. For such low conductivities the contribution of conductivity contrasts to reflection coefficients is likely to be negligible. (For example, for a plane wave incident on a planar boundary [Stratton 1941], for an angle of incidence of 10° and a change in ϵ_r of 3.5 [about a mean ϵ_r value of 4] across the contact, the reflection coefficient is 0.210. Adding a contrast in conductivity of 1 mS/m changes the reflection coefficient by less than 1%.) The fortunate consequence is that contrasts in conductivity at layer boundaries can reasonably be neglected, and model conductivities can be simplified to a uniform average value throughout the section.

Table 1 lists the best-fitting attenuation coefficients determined from amplitudes on simulations of TE mode waves in 2-D sawtooth models with line sources and 1 m transmitter–receiver separation, corrected to 3-D geometrical spreading, with layer permittivity contrasts and uniform conductivities of varying amplitudes. The attenuation coefficients (with geometrical spreading correction) derived from these 2-D models differed by less than ~5% from the attenuation coefficients from comparable 3-D TE mode dipole source models; it was thus deemed reasonable to conduct the

Table 1. *Observed and model 100 MHz attenuation*

	$\Delta\epsilon_r$	$\Delta\nu$ (m ns^{-1})	σ (mS/m)	Attenuation α (1/m)	dB/m	Q
Observed				0.086	0.75	12
Models						
	9.1	0.12	0	0.027	0.23	80
	9.1	0.12	1.2	0.086	0.75	24
	3.5	0.06	0	0.047	0.40	44
	3.5	0.06	0.8	0.086	0.75	24
	1.3	0.012	0	0.053	0.46	40
	1.3	0.012	0.7	0.086	0.75	24
	0.64	0.006	0	0.053	0.46	40
	0.64	0.006	0.7	0.086	0.75	24

$\Delta\epsilon_r$ = contrast in relative dielectric permitivities across package boundaries
$\Delta\nu$ = corresponding velocity contrast across package boundaries
σ = conductivity
In all models average $\epsilon_r = 4$ (average velocity = 0.15 m ns^{-1}). Models assume 'sawtooth' permittivity pattern as in Figure 8 with permittivity contrasts of finer-scale layering = 0.5 times those at package boundaries. Attenuation is expressed as the attenuation coefficient α, in dB/m, and as the quality factor $Q = \omega/2\nu\alpha$, where $\omega = 2\pi f$, $f = 100$ MHz, and $\nu = 1.5 \times 10^8$ m/s. Attenuation coefficients calculated for amplitudes between 30 ns and 330 ns.

suite of simulations with 2-D models. The attenuation coefficients α thus describe the combined effects of transmission losses, primary and internal multiple reflections, and the directivity function. Models listed in Table 1 incorporate fine-scale permittivity contrasts 0.5 times those at boundaries of the larger-scale layers (as in the centre column of Fig. 8). The pattern of permittivity contrasts is the same for all models, but the absolute magnitude of permittivity contrasts differs. Models listed have either zero conductivity or the value that best fits the observed attenuation.

Figure 10 summarizes the parameters of the best-fitting sawtooth models. To fit the observed attenuation, models with higher permittivity contrasts (more energy returned to surface) require higher conductivities. With lower permittivity contrasts attenuation is driven predominantly by conductive losses. Where conductive losses dominate, the best-fitting conductivity is 0.7 mS/m. A conservative upper bound on the plausible change in ϵ_r across a contact is ~9, given the mean velocity of 0.15 m ns^{-1} and a lower bound on relative permittivity of ~2 for unsaturated gravel. For this upper bound permittivity contrast, the average ground conductivity must be ~1.2 mS/m. To sum-
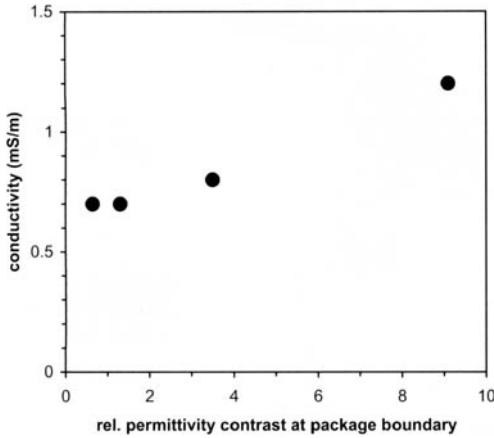
Fig. 10. Parameters of models that fit observed attenuation. Results shown for sawtooth models with fine-scale $\Delta\epsilon_r = 0.5$ large-scale $\Delta\epsilon_r$. Horizontal axis shows magnitude of $\Delta\epsilon_r$ at boundaries of large-scale layers.

Fig. 11. Observed and model AVO. Thick lines with symbols, two observed distinct reflection events with arrivals between 110 ns and 140 ns. Lines without symbols, model AVO curves for sawtooth models with fine-scale $\Delta\epsilon_r = 0.5$ large-scale $\Delta\epsilon_r$, with varying absolute magnitudes of $\Delta\epsilon_r$. Numbers in legend, $\Delta\epsilon_r$ across large-scale boundaries. All AVO curves are scaled to align relative amplitudes at 5 m offset.

marize, plausible models that fit the observed attenuation require average conductivities in the range of 0.7–1.2 mS/m.

Constraints on permittivities from AVO modelling

Seismologists have long recognized that information about a reflecting boundary could be derived from the relative amplitudes of acoustic or elastic wave reflections recorded with different source-receiver offsets (e.g. Castagna & Backus 1993). Baker (1998) and Zeng et al. (2000) have demonstrated that parallels can be drawn for GPR surveys. Significantly for this study, Zeng et al. (2000) showed that, for reflecting boundaries with large permittivity contrasts, amplitudes decay rapidly with increasing offset at large offsets.

Figure 11 shows observed AVO curves for individual 100 MHz reflection events identified from the CMP survey and for the sawtooth models with fine-scale permittivity contrasts 0.5 times those of the larger-scale. The reflections picked arrive between ~110 ns and 140 ns, and represent reflections from large-scale boundaries as their amplitude clearly exceeded those of neighbouring pulses in the GPR traces. The 110–140 ns time window was chosen because reflections are strong and easily identifiable, yet are late enough that the amplitude determinations are independent of the choice of dewow or other filter for removing the low-frequency early energy. Observed AVO curves show a peak at ~5 m offset; such a central peak is expected in GPR surveys at the offset where the angle of incidence on the ground/air boundary is

the critical angle for refraction [e.g. Zeng et al. (2000)]. The model AVO curves tend to flatten at smaller offsets, but do not show a central peak. The origin of the discrepancy between model and observed AVO curves at small offsets is unclear. Hence we restrict comparison of model results and data to the decay in amplitudes at larger offsets. Figure 11 shows that models with large-scale ϵ_r contrasts less than ~3.5 fit the observed slope of the AVO curve, while those with greater ϵ_r contrasts do not. Thus, in this setting the AVO analysis proves useful for establishing an upper bound, but not a lower bound, on the magnitudes of ϵ_r contrasts.

With an upper bound of 3.5 on the ϵ_r contrasts across the large-scale contacts, Figure 10 shows that the conductivity is constrained to ~0.7–0.8 mS/m.

Direct ground-wave amplitudes

Because the units at the quarry site dip ~22°, the direct-wave travelling between transmitter and receiver at large offsets on a CMP survey should travel through multiple layers. Thus we can check whether the amplitudes of direct-wave arrivals on the 100 MHz CMP survey are compatible with the best-fitting conductivities and permittivities derived from the analysis of the reflected arrivals. The models assume 22°-dipping beds overlain by a 0.5 m-thick horizontal layer, where 0.5 m is a rough estimate of the thickness of 'road fill' along the terrace on which the survey was collected. Fig-

ure 12 shows the observed relative amplitudes of the direct wave arrivals between 5 m and 7.5 m. The direct ground-wave amplitude can be reliably identified (free from interference with air-wave or reflections) only in this offset window. The observed direct-wave attenuation appears greater than that of the best-fitting models (Fig. 12). One possible explanation for the discrepancy between models and data is that the observed amplitude at 5 m offset is anomalously high because of constructive interference between the out-going direct-wave and reflected energy. Models with permittivity contrasts as low as 3.5 show noticeable 'zig-zags' in the direct-wave amplitude v. offset curve, due to reflections occurring at the dipping beds. As direct-wave amplitudes are quite sensitive to the properties of the surficial layer, it is also possible that the models neglect significant complexities in fill at the terrace surface, or that there is higher attenuation in the fill at the surface. Overall there are no misfits between model and observed direct-wave amplitudes that require us to reject our best-fitting models.

Conclusions

This study demonstrates that bounds on permittivity structure and conductivity can be derived from modeling of GPR records in a setting with repetitive strata. FDTD modelling of the Brigham City, Utah, gravel quarry surveys shows the following:

1. The upper boundary of large-scale layers (1–2 m in thickness) marks a contact between overlying lower permittivity (probably higher porosity) and underlying higher permittivity (lower porosity).
2. No independently distinguishable sharp contrasts marking higher permittivity over lower permittivity strata are apparent, implying that, within the large-scale layers, either the high permittivity layer is thin (less than ~30 cm) or that permittivity increases gradually upward through the layers.
3. Permittivity contrasts associated with finer-scale layering within the 1–2 m-thick layers are 0.4–0.8 times those at the larger-scale layer boundaries.
4. AVO analysis provides an upper bound of ~3.5 on relative permittivity contrasts at the larger-scale boundaries.
5. Given these bounds on the permittivity structure, signal attenuation requires average conductivities in the range of ~0.7–0.8 mS/m (for the bandwidths in the 100 MHz signal).

At the site chosen for this study we specifically exploit the repetitive nature of the layering, and these conclusions could be derived in the absence of direct measurements of the electromagnetic properties. This method holds promise for broader applicability, namely for detailed resolution of electromagnetic properties at more complex sites, if local 'ground-truthing' of electromagnetic properties can be established at wells or outcrops. If the relationships between the electromagnetic and hydrogeological properties can be locally established as well, then GPR clearly offers promise as a tool to extrapolate from wells or outcrops, and to aid in statistical characterization of aquifer heterogeneities.

Fig. 12. Observed and model direct-wave amplitudes. Diamonds, observed amplitudes from 100 MHz CMP; dashed lines, predicted AVO for sawtooth models with fine-scale $\Delta\epsilon_r = 0.5$ large-scale $\Delta\epsilon_r$, with varying absolute magnitudes of $\Delta\epsilon_r$. See text for discussion.

References

BAKER, G. S. 1998. Applying AVO analysis to GPR data. *Geophysical Research Letters*, **25**, 397–400.

BRISTOW, C. S., BAILEY, S. D. & LANCASTER, N. 2000. The sedimentary structure of linear sand dunes. *Nature*, **406**, 56–59.

CASTAGNA, J. P. & BACKUS, M. M. (eds). 1993. *Offset-Dependent Reflectivity – Theory and Practice of AVO Analysis*. Investigations in Geophysics Series, Society of Exploration Geophysicists, Tulsa, **8**, 348 pp.

CHAN, C. Y. & KNIGHT, R. J. 1999. Determining water content and saturation from dielectric measurements in layered materials. *Water Resources Research*, **35**, 85–93.

CHANZY, A., TARUSSOV, A., JUDGE, A. & BONN, F. 1996. Soil water content determination using a digital ground-penetrating radar. *Soil Science Society of America Journal*, **60**, 1318–1326.

HORNUNG, J. & AIGNER, T. 1999. Reservoir and aquifer characterization of fluvial architectural elements: Stubensandstein, Upper Triassic, southwest Germany. *Sedimentary Geology*, **129**, 215–280.

HUGGENBERGER, P. & AIGNER, T. 1999. Introduction to the special issue on aquifer-sedimentology: problems, perspectives and modern approaches. *Sedimentary Geology*, **129**, 179–186.

JIAO, Y., MCMECHAN, G. A., AND PETTINELLI, E. 2000. In situ 2-D and 3-D measurements of radiation patterns of half-wave dipole GPR antennas. *Journal of Applied Geophysics*, **43**, 69–89.

JOL, H. M., SMITH, D. G. & MEYERS, R. A. 1996. Three dimensional GPR imaging: of a fan-foreset delta: an example from Brigham City, Utah, U.S.A. *Proceedings of the Sixth International Conference on Ground Penetrating Radar (GPR '96), 30 September – 3 October, Sendai, Japan*, 33–37.

KNOLL, M. D. & KNIGHT, R. 1994. Relationships between dielectric and hydrogeologic properties of sand-clay mixtures. *Proceedings of the Fifth International Conference on Ground Penetrating Radar, 12–16 June 1994, Waterloo Center for Groundwater Research, Kitchener, Ontario, Canada*, 45–61.

KUNZ, K. S. & LUEBBERS, R. J. 1993. *The Finite Difference Time Domain Method for Electromagnetics*. CRC Press, Boca Raton, 448 pp.

MCMECHAN, G. A., GAYNOR, G. C. & SZERBIAK, R. B. 1997. Use of ground-penetrating radar for 3-D sedimentological characterization of clastic reservoir analogs. *Geophysics*, **62**, 786–796.

MUR, G. 1981. Absorbing boundary conditions for finite-difference approximation of the time-domain electromagnetic-field equations. *Institute of Electrical and Electronics Engineers Transactions on Electromagnetic Compatibility*, **23**, 1073–1077.

OLHOEFT, G. R. 2000. Maximizing the information return from ground penetrating radar. *Journal of Applied Geophysics*, **43**, 175–187.

PEPLINSKI, N. R., ULABY, F. T. & DOBSON, M. C. 1995. Dielectric properties of soils in the 0.3–1.3 GHz range. *Institute of Electrical and Electronics Engineers Transactions on Geoscience and Remote Sensing*, **33**, 803–807.

RADZEVICIUS, S. J., GUY, E. D., & DANIELS, J. J. 2000.

Pitfalls in GPR data interpretation: Differentiating stratigraphy and buried objects from periodic antenna and target effects. *Geophysical Research Letters*, **27**, 3393–3396.

SAARENKETO, T. 1998. Electrical properties of water in clay and silty soils. *Journal of Applied Geophysics*, **40**, 73–88.

SMITH, D. G. & JOL, H. M. 1992. Ground-penetrating radar investigation of a Lake Bonneville delta, Provo level, Brigham City, Utah. *Geology*, **20**, 1083–1086.

SMITH, D. G. & JOL, H. M. 1995. Ground penetrating radar: antenna frequencies and maximum probable depths of penetration in Quaternary sediments. *Journal of Applied Geophysics*, **33**, 93–100.

STRATTON, J. A. 1941. *Electromagnetic Theory*. McGraw-Hill Book Company, Inc., New York, 615 pp.

VAN DAM, R. L. & SCHLAGER, W. 2000. Identifying causes of ground-penetrating radar reflections using time-domain reflectometry and sedimentological analyses. *Sedimentology*, **47**, 435–449.

VAN OVERMEEREN, R. A., SARIOWAN, S. V. & GEHRELS, J. C. 1997. Ground penetrating radar for determining volumetric soil water content; results of comparative measurements at two test sites., *Journal of Hydrology*, **197**, 316–338.

VAN OVERMEEREN, R. A. 1998. Radar facies of unconsolidated sediments in The Netherlands: A radar stratigraphy interpretation method for hydrogeology. *Journal of Applied Geophysics*, **40**, 1–18.

WAIT, J. R. 1970. *Electromagnetic Waves in Stratified Media*. Pergamon Press, Oxford, 608 pp.

WANG, T. & TRIPP, A. C. 1994. Simulation of electromagnetic wave propagation in three-dimensional media by an FDTD method. *Proceedings of the Fifth International Conference on Ground Penetrating Radar, 12–16 June 1994, Waterloo Center for Groundwater Research, Kitchener, Ontario, Canada*, 247–267.

YEE, K. S. 1966. Numerical solution of initial boundary problems involving Maxwell's equations in isotropic media. *Institute of Electrical and Electronics Engineers Transactions on Antennas and Propagation*, **AP-14**, 302–309.

ZENG, X., MCMECHAN, G. A., & XU, T. 2000. Synthesis of amplitude-versus-offset variations in ground-penetrating radar data. *Geophysics*, **65**, 113–125.

Influence of antenna configurations for GPR survey: information from polarization and amplitude versus offset measurements

P. LUTZ[1], S. GARAMBOIS[2] & H. PERROUD[1]

[1]Laboratoire d'Imagerie Géophysique, IPRA, CNRS UMR 5831, Université de Pau et des Pays de l'Adour, BP 1155, 64013 Pau Cedex, France (e-mail: Pascale.Lutz@univ-pau.fr; Herve.Perroud@univ-pau.fr)

[2]LIRIGM, Maison des Géosciences, Université Joseph Fourier, BP 53X, 38041 Grenoble Cedex 9, France, (e-mail: Stephane.Garambois@ujf-grenoble.fr)

Abstract: Ground penetrating radar (GPR) images depend strongly on the relative geometry between the transmitter, the receiver and the subsurface reflectors. This dependence results from the directional properties of the antennae and from the sensitivity of the reflector to the polarization of the incident electromagnetic wave. In the present study, GPR data sets have been recorded using several 100 MHz antennae configurations, including transverse electric (TE) or transverse magnetic (TM) modes that have been used both parallel and perpendicular to the recording line. The images obtained show a high complementarity that provides more detailed information of the studied geological reflectors compared to the image derived from a single conventional acquisition configuration. Consequently, we compute pseudoprofiles that gather information derived from all acquisition modes, thus improving the GPR images. These pseudoprofiles are characterized by either a low directional degree of the antennae or a neutral acquisition mode. In addition, we have conducted a polarization analysis by surveying the studied profile twice with parallel and perpendicular antennae, in both modes (TE and TM). The comparison of these data sets provided three-dimensional (3-D) information on reflectors, particularly their depolarization properties. These studies clearly emphasize how multiconfiguration antennae surveys have the potential to improve GPR imaging and interpretation. Furthermore, polarimetric surveys have been carried out in order to explore further whether depolarization phenomena could explain observations of phase inversion and amplitude decrease on TE common mid-point gathers that would induce perturbations of the GPR images in the stacking procedure for multioffset surveys.

Ground penetrating radar (GPR) surveys are usually conducted for civil engineering purposes, with emitting and receiving dipoles parallel to each other, in a broadside configuration, both perpendicular to the recording line. This operating mode is based on scattering polarization studies as presented in Balanis (1989), Roberts and Daniels (1996) and Radzevicius and Daniels (2000). These authors have studied the polarization state of the scattered electromagnetic field for simple reflectors, such as planar interfaces and cylinders of different geometry and composition. These studies were conducted considering an incident wave which was polarized toward the perpendicular component (transverse electric [TE] mode) as well as toward the parallel component (transverse magnetic [TM] mode) compared to the plane of propa-

gation. More precisely, the comparison of scattering polarization parameters relative to the two components allows determination of the component which is preferentially scattered by the target. These results, combined with studies of dipole radiation patterns (Annan et al. 1975; Engheta & Papas 1982), allow the choice of the best antennae configuration depending on the target.

The usual operating mode is therefore explained by the following reasons, assuming the search for pipes perpendicular to the recording line.

- The incident field component parallel to the axis of a small-diameter metallic cylinder is preferentially scattered.
- The TE component is not affected by depolarization when reflected by a planar interface.

- The field radiated by a dipole is polarized towards the antenna axis.

However, for geological purposes, the complexity of the geometry, orientation and location of the targets require multiconfiguration surveys, which should improve GPR images and provide more information on geological reflectors (3-D location – depolarization properties) compared with the usual operating mode. For example, Jol *et al.* (1994) obtained a greater depth of penetration using antennae parallel to the recording line, in the dip direction of coastal barrier reflectors. Moreover, Lehmann *et al.* (2000) showed the benefit of recording data using two antennae orientations and thus proposed to built pseudoprofiles characterized by a low dependence on the antennae orientation. Using multicomponent measurements (recordings with the antennae both parallel and perpendicular to each other), these authors correctly located a quarry wall. This reflector was out of the recording line plane and could have been misinterpreted using a unique antennae configuration. The other advantages of using crossed dipoles are the detection of rough reflectors (Luzitano & Ulrych 1994, 1996) and improvement of the GPR images due to the decrease of the antenna coupling (Radzevicius *et al.* 2000a, b). Note that Van Gestel and Stoffa (2001) applied the Alford rotation (Alford 1986) to four multiconfiguration data to extract the amplitude reflected from a target versus the dipole orientation angle. The comparison of these experimental curves with modelling allows the orientation of simple subsurface targets (metallic dipping layers and cylinders, vertical fractures) to be determined. Finally, the use of the antennae in an end-fire configuration for common mid-point (CMP) measurements should help to identify air cavities as well as to determine the velocity of the medium below the deepest reflector (Helm & Yaramanci 1998; Reppert *et al.* 2000). This is a consequence of the amplitude decrease and phase inversion of the TM component reflection coefficient occurring at a certain incident angle.

The aim of this paper is to present, in a theoretical and experimental way, how surveys conducted using antennae multiconfigurations can improve GPR images by providing additional details on the geological reflectors (3-D location and scattering polarization properties), thus allowing image interpretation with greater confidence than classical single recordings. Considering the recent development of multichannel GPR recording systems, we finally propose the use of four dipole configurations when imaging geological reflectors.

Theoretical considerations

In this section we present the main theoretical considerations needed for the understanding of the dipole configuration influences on GPR images (directional properties of dipoles and polarization scattering by simple reflectors).

Directional properties of dipoles

Dipole antennae for GPR purposes radiate and receive electromagnetic waves with high directional dependence. The radiation patterns usually considered to model these directional properties are described in Annan *et al.* (1975) and Engheta and Papas (1982), who determined analytically far-field radiation patterns of an infinitesimal steady-state dipole at an interface. The main features are presented in Figure 1, where φ is the azimuth relative to the dipole axis and θ is the deviation from the vertical:

- In the $\varphi = 90°$ plane of the transmitter, only the TE waves are radiated. The radiation pattern presents the largest amplitude at the critical angle $\theta_c = sin^{-1} \left(\frac{\epsilon_{ground}}{\epsilon_{air}} \right)$ where ϵ_{ground} and ϵ_{air} are the dielectric permittivity of the ground and of the air respectively.
- In the $\varphi = 0°$ plane, only the TM waves are radiated. The radiation pattern consists of three lobes: one vertical and two on the sides. At the critical angle, the amplitude is equal to zero.
- In the planes $0° < \varphi < 90°$, both components are generated and have radiation patterns similar to those described before.

Polarization scattering by planar interfaces

The reflection coefficients at a planar interface (Fig. 2) are described by the Fresnel equations (Strattom 1941). Figure 3 shows the reflection coefficients versus the incident angle for both TE and TM components obtained with various contrasts of permittivity and conductivity in a stratified medium. The main features are as follows:

- The reflection coefficient of the TE component is always greater than the TM component, whatever the incident angle (when different to zero) and the medium.
- Considering the TM component, an angle, called 'the Brewster angle' ($\theta_b = Arctan \sqrt{\frac{\epsilon_1}{\epsilon_2}}$ with ϵ_1 and ϵ_2 the permittivity of the upper and lower medium respectively), corresponds to a significant loss of amplitude and a phase shift of 180°.

(a) Coordonate diagram

P: observed point
θ: deviation from the vertical
φ: azimuth relative to the dipole axis

(b) Radiation patterns

Amplitude patterns

Phase patterns

ε_{air}: dielectric permittivity of the air
ε_{ground}: dielectric permittivity of the ground
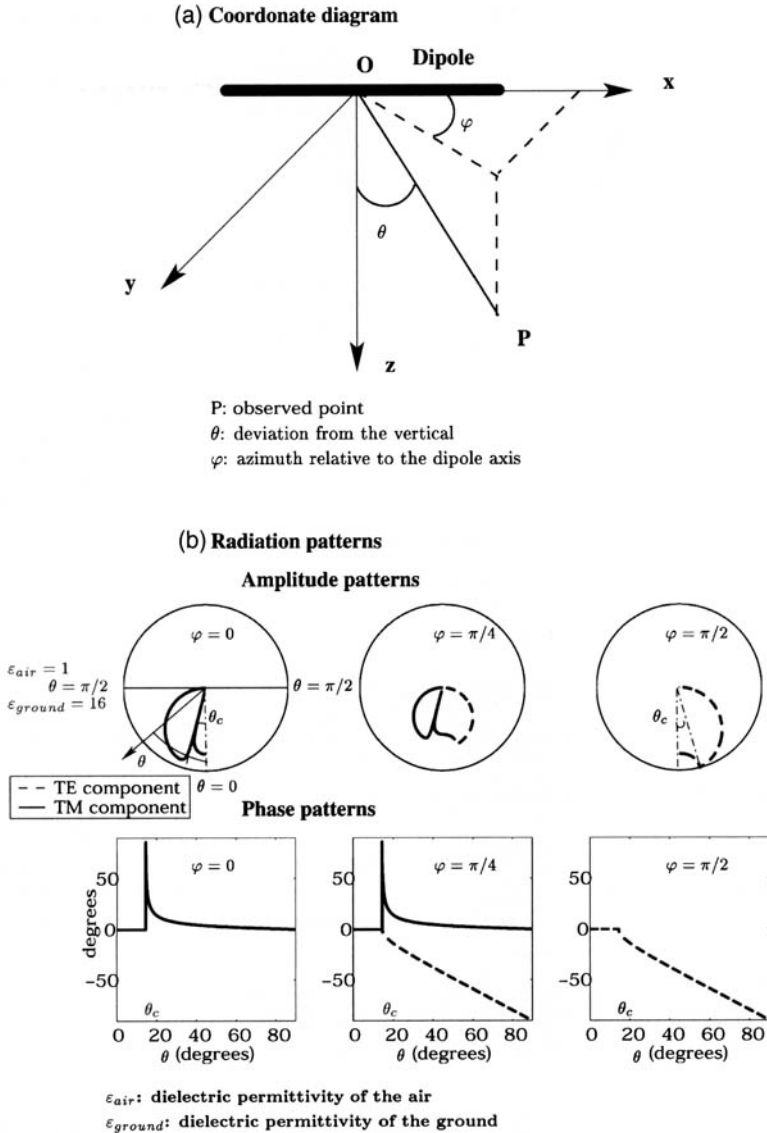
Fig. 1. Amplitude and phase radiation patterns of an infinitesimal steady-state dipole at an air/ground interface (from Annan *et al.*, 1975). (**a**) Coordinate diagram. (**b**) Radiation patterns.

The parameter used to describe the polarization state of the field scattered by a planar interface is the scattering polarization loss factor (SPLF) (Roberts & Daniels 1996):

$$SPLF = (\vec{e}^{\,i}.\vec{e}^{\,r})^2 = \qquad (1)$$

$$\frac{(R_{TE}cos^2\theta_p + R_{TM}cos^2\theta_i sin^2\theta_p - R_{TM}sin^2\theta_i sin^2\theta_p)^2}{R_{TE}^2cos^2\theta_p + R_{TM}^2sin^2\theta_p}$$

where $\vec{e}^{\,i}$ and $\vec{e}^{\,r}$ are the incident and scattered

wave polarization respectively; θ_p is the angle between $\vec{e}^{\,i}$ and $\vec{e}^{\,i}_{TE}$; and θ_i is the incident angle.

If $\vec{e}^{\,i} = \vec{e}^{\,i}_{TE}$ ($\theta_p = 0°$), then $SPLF_{TE} = 1$: the scattered wave is polarized toward the TE component only.

If $\vec{e}^{\,i} = \vec{e}^{\,i}_{TM}$ ($\theta_p = 90°$), then $SPLF_{TM} = (1 - 2sin^2\theta_i)^2$: the scattered wave is polarized towards both TE and TM components for all $\theta_i \neq 0°$.

Because of its depolarization properties, the TM
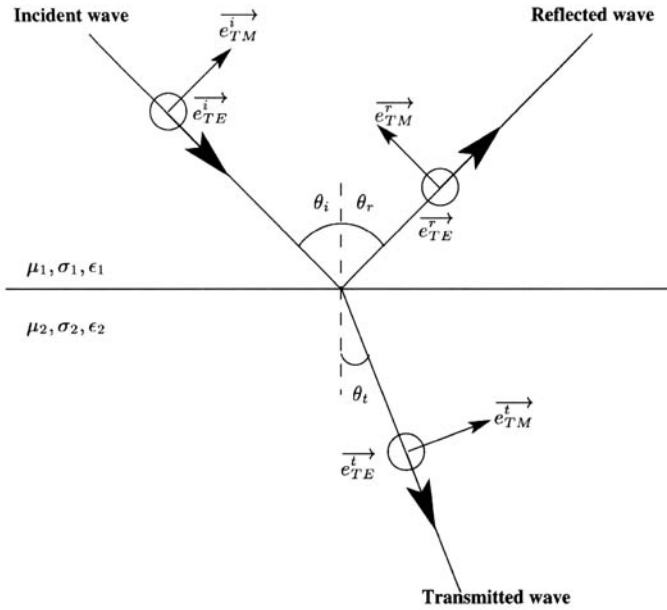
$\overrightarrow{e^i_{TE}}, \overrightarrow{e^r_{TE}}, \overrightarrow{e^t_{TE}}$:
Transverse Electric components of the incident, reflected and transmitted waves
$\overrightarrow{e^i_{TM}}, \overrightarrow{e^r_{TM}}, \overrightarrow{e^t_{TM}}$:
Transverse Magnetic components of the incident, reflected and transmitted waves
$\theta_i, \theta_r, \theta_t$:
Angles of the incident, reflected and transmitted waves
$(\mu_1, \sigma_1, \varepsilon_1)$; $(\mu_2, \sigma_2, \varepsilon_2)$:
Dielectric parameters of the upper and lower medium respectively

Fig. 2. Illustration of an incident wave, which is polarized toward both TE and TM components, and is reflected and refracted at a planar interface.

mode is used only for experimental tests in the case of soil studies (Tillard 1991; Reppert *et al.* 2000). Nevertheless, the TM mode is commonly used for glacier studies for practical reasons (Arcone *et al.* 2000).

Polarization scattering by circular cylinders

The polarization scattering properties of a cylinder (Fig. 4) can be described by the scattering width (SW) (Roberts & Daniels 1996), which is defined as:

$$SW = \lim_{r \to \infty} 2\pi r \cdot \left(\frac{E^s}{E^i}\right)^2, \qquad (2)$$

where E^i and E^s are the incident and scattered field amplitude respectively and r is the distance between the target and the observed point.

When the transmitter and the receiver are at the same location, the scattering width is usually referred to as 'back-scattering width'.

The comparison of the back-scattering width for the parallel and perpendicular incident field components relative to the cylinder axis allows the best orientation of the transmitter antenna to be determined, according to the cylinder dimension and composition, i.e. dipole parallel to the axis for small-diameter metallic and low-velocity cylinders and dipole perpendicular to the axis for large, high-velocity cylinders.

These theoretical results have been experimentally confirmed by Radzevicius and Daniels (2000) with data recorded over cylinders of different geometry and composition for several dipole orientations (every 15°). It is noticeable that small-diameter metallic cylinders were not imaged using dipoles with an orientation from 45° to 90° relative to the cylinder axis.

Depolarizing reflectors

The synthesis of these theoretical considerations allows the conditions under which planar interfaces
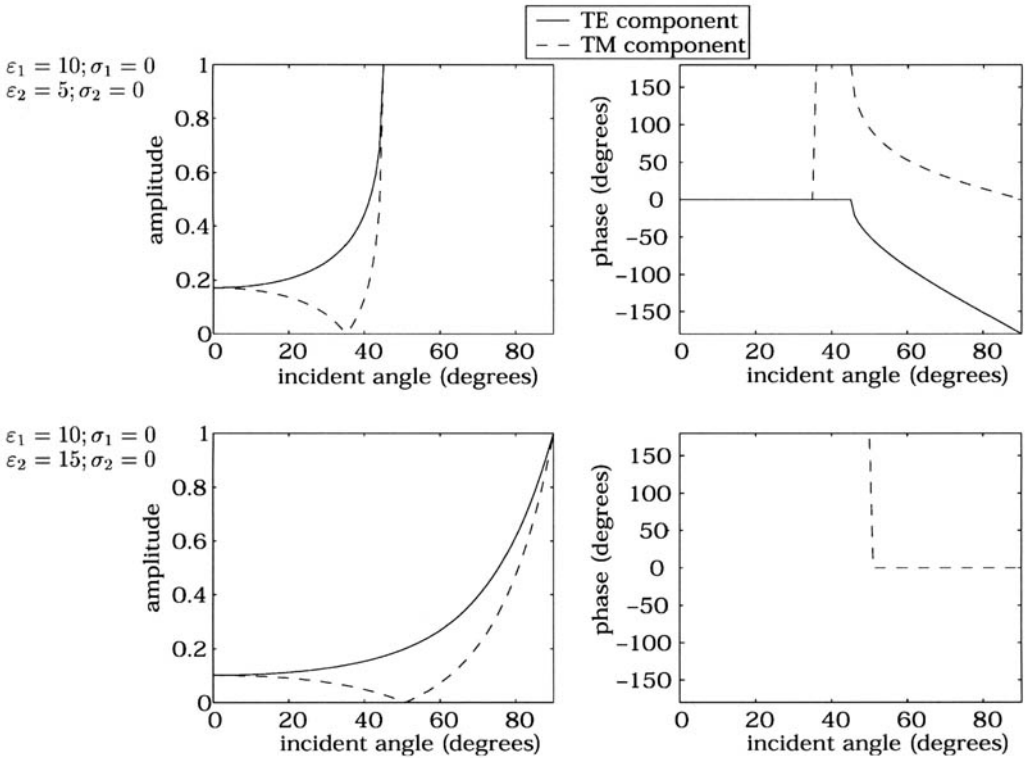
ε_1 and ε_2: **permittivity of the upper and the lower medium respectively**
σ_1 and σ_2: **conductivity of the upper and the lower medium respectively**

Fig. 3. Reflection coefficients at a planar interface relative to the TE and TM components versus incident angle (amplitude and phase).

and cylinders become depolarizing reflectors to be determined.

Planar interfaces have depolarizing properties in the case $\theta_i \neq 0$ and when the TM component of the incident wave exists in the following two different cases: (1) if the incident wave TE component is nil, the scattered wave is polarized toward both TE and TM components (Eq. 1); (2) if the incident wave TE component is not nil, the TE and TM component reflection coefficients are not equal and, thus, the polarization of the scattered wave differs from the incident wave polarization.

In the same way, cylinders that lead to different parallel and perpendicular component back-scattering widths are targets which can induce changes to the incident wave polarization. In fact, if the incident wave is composed of both parallel and perpendicular components relative to the cylinder axis, the polarization of the scattered wave will be different to the incident wave polarization. The main cases are: (1) small diameter metallic cylin-

ders, (2) small diameter low-velocity cylinders, (3) large high-velocity cylinders.

According to these theoretical considerations, non-nil GPR signals obtained from crossed-dipole surveys can be due to different phenomena.

1. Depolarizing medium. Hargreaves (1977) determined from polarimetric measurement an elliptical polarization due to the depolarization properties of the ice; Tillard (1991) revealed a polarization modification due to the propagating medium in a shale quarry.

2. Depolarizing interfaces. Luzitano and Ulrych (1994, 1996) identified amplitude anomalies in parallel component profiles due to the altering of the wavelet polarization. According to these authors, the most significant mechanism involved in this depolarization phenomenon is the scattering from rough targets (features within the ice layer above a frozen lake and objects just above the lake
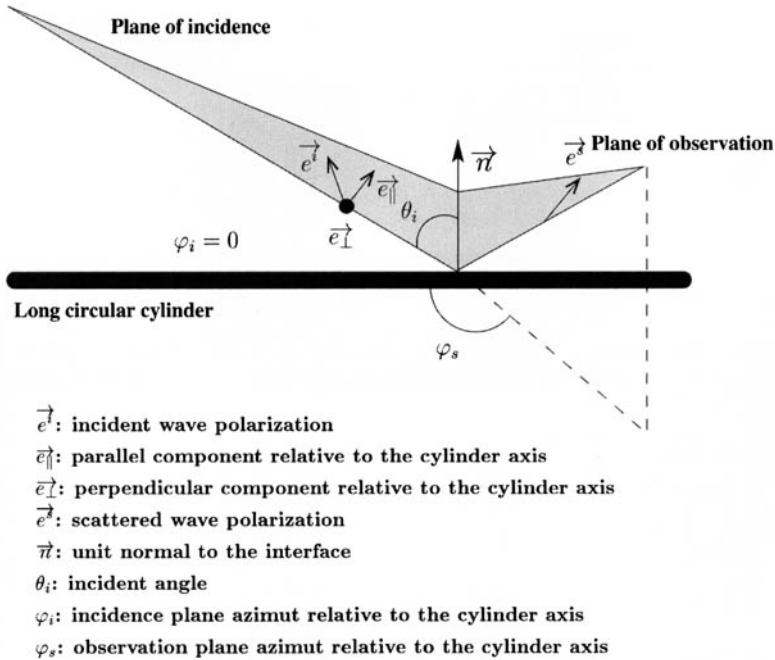
Fig. 4. Illustration of the scattering of an incident wave by a cylinder. The incident wave is polarized towards both parallel and perpendicular components relative to the cylinder axis.

bottom) at points where wavefronts interfered. In the same way, Radzevicius *et al.* (2000*a*, *b*) experimentally showed that crossed dipoles can produce cleaner images than parallel dipoles, depending on the targets of interest (linear targets and small or rough targets which scatter cross-polarized components). The decrease of cross-coupling noise for crossed dipoles can explain the increase of the quality of images.

3. Reflectors located out of the recording line plane. The incident wave polarization is composed of both TE and TM components and consequently both parallel and cross-polarized components at the receiver location are not nil. Roberts and Daniels (1996) have experimentally underlined the effects on cross-polarized component profiles when the recording line is 45° relative to a pipe, or when the line is shifted horizontally in relation to a sphere. In this case, Lehmann *et al.* (2000) correctly located a quarry wall that was located out of the recording-line plane using multicomponent profiles. These studies indicate that an electromagnetic reflection, which is visible on the four profiles relative to the TE parallel, TE cross-polarized, TM parallel and TM cross-polarized components, can be interpreted with great confidence as being due to an out-of-plane reflector.

Multi-configuration surveys

100 MHz GPR data sets have been recorded on a test site mainly composed of alluvial deposits located in the valley of the Gave de Pau River near Pau in southwestern France. This area has been previously investigated by combined geophysical methods (GPR, seismic and electric) to assess hydrological parameters (Garambois *et al.* 2002). For information, Figure 5 displays a pedological log based on sample analysis. In the present study, recordings have been acquired using several configurations in order to estimate the influences of the antennae orientation relative to the reflectors, of the acquisition mode (TE or TM component recording) and of the recorded component (parallel or cross) (Fig. 6). The antennae step size was 20 cm over a distance of 80 m, with an antennae separation (offset) of 2 m. The data were filtered with a zero-phase pass-band frequency filter (20–200 MHz), then muted to remove the direct wave in the air, and finally normalized using a division of each trace by the average envelope amplitude trace of the whole profile. The resulting multiconfiguration profiles are presented in Figures 7 and 8.
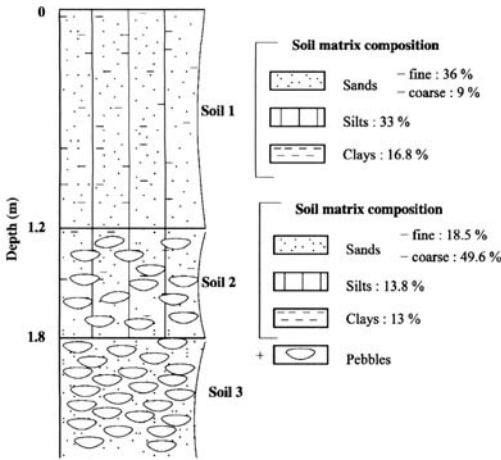
Fig. 5. Pedological log based on sample analysis of a trench located 600 m from the test site.

The influence of the antennae orientation and acquisition mode

T: transmitter – R: receiver

1) T and R parallel to the recording line – TE mode

2) T and R perpendicular to the recording line – TE mode

3) T and R parallel to the recording line – TM mode

4) T and R perpendicular to the recording line – TM mode

The influence of the recorded component

5) TE mode – Parallel component

6) TE mode – Cross component

7) TM mode – Parallel component

8) TM mode – Cross component

Fig. 6. Antennae configurations used for the 100 MHz constant offset profiles. They have been chosen in order to reveal the influences of the antennae orientation, of the acquisition mode, and of the recorded component.

Information on GPR reflectors

The GPR images presented in Figure 7 allows detailed comparison of reflections in relationship with the incident wave polarization. Figure 8 also gives information on the 3-D location and on the depolarizing properties of the reflecting structures. It is noticeable that, in the following discussion, the simplifications $TE^{\perp}$ and $TM^{\perp}$ (respectively $TE^{\parallel}$ and $TM^{\parallel}$) represent the TE and TM components perpendicular to the recording line (respectively parallel to the line). The main properties of the principal reflectors deduced from the principal reflections are now summarized.

- The reflector A scatters all components, presents a greater sensitivity to the TE component whatever its orientation and is a non-depolarizing in-plane reflector.
- The reflectors B and C preferentially scatter the $TE^{\parallel}$ component and are non-depolarizing in-plane reflectors.
- The reflector D presents a greater sensitivity to the $TM^{\parallel}$ component and has an equal sensitivity to the $TE^{\parallel}$, $TE^{\perp}$ and $TM^{\perp}$ components. It is an in-plane reflector which depolarizes the $TE^{\perp}$ component.
- The reflector E is sensitive to all components and preferentially scatters the $TE^{\perp}$ and $TM^{\parallel}$ components. It is an in-plane reflector weakly depolarizing the $TE^{\perp}$ component.
- The reflector F equally scatters the $TE^{\parallel}$, $TE^{\perp}$ and $TM^{\parallel}$ components and presents a low sensitivity to the $TM^{\perp}$ component. It is a non-depolarizing in-plane reflector.
- The reflector G (respectively H) preferentially scatters the $TE^{\parallel}$ and $TE^{\perp}$ components

(respectively the $TE^{\parallel}$ and $TM^{\parallel}$ components). It is a non-depolarizing in-plane reflector.
- The reflector I scatters all components with a greater sensitivity to the $TE^{\perp}$ component. It is an out-of-plane and/or $TE^{\perp}$ and $TM^{\parallel}$ component depolarizing reflector.
- The reflector J scatters the $TE^{\parallel}$ and $TM^{\parallel}$ components only and is a non-depolarizing in-plane reflector.
- The reflector K is an in-plane reflector, which
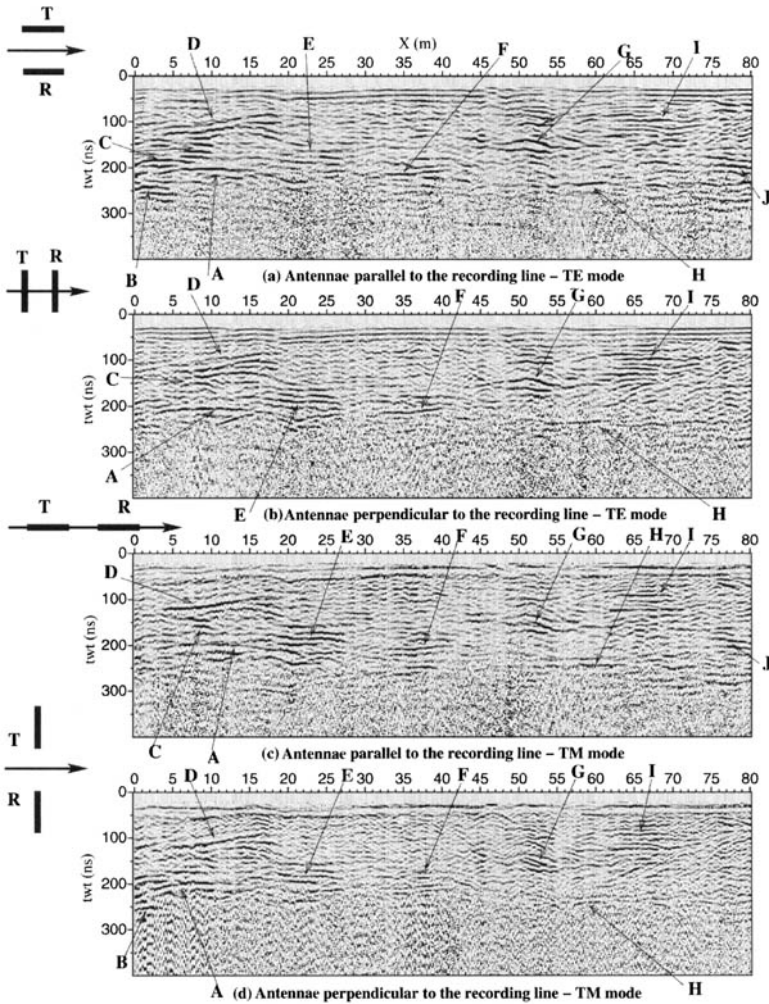
Fig. 7. 100 MHz constant offset profiles after processing. The configurations used reveal the influence of the antennae orientations and of the acquisition mode. Arrows indicate the main GPR reflected signals associated with the principal reflectors.

depolarizes the TE$^\perp$ component of 90° but does not scatter the TM$^\parallel$, as well as the TE$^\parallel$ and TM$^\perp$ components except with a 90° depolarization.

- The reflector L is an in-plane reflector, which depolarizes the TE$^\perp$ component of 90° and the TM$^\parallel$ component. It does not scatter the TE$^\parallel$ and the TM$^\perp$ components except with a 90° depolarization.

Figure 9 presents the comparison of individual traces, relative to reflections K and L, when recorded using the receiver dipole parallel or perpendicular to the transmitter dipole in the TE mode. It shows the high amplitudes associated with the cross component.

Averaged spectra and envelopes

Averaged spectra and envelopes of each profile have been plotted in order to reveal the influences of the antennae orientations, of the acquisition mode and of the recorded component on these quantities. According to Figure 10*a*, these quantities depend mainly on the acquisition mode and to a lesser extent on the antennae orientation in relation to the recording line. In particular, the peak frequency of the TE-mode profiles appears around 82 MHz whereas it decreases to 52 MHz for the TM-mode profiles. Moreover, until 75 ns, envelopes of the TE-mode profiles have higher amplitudes than that of the TM-mode profiles. Note that
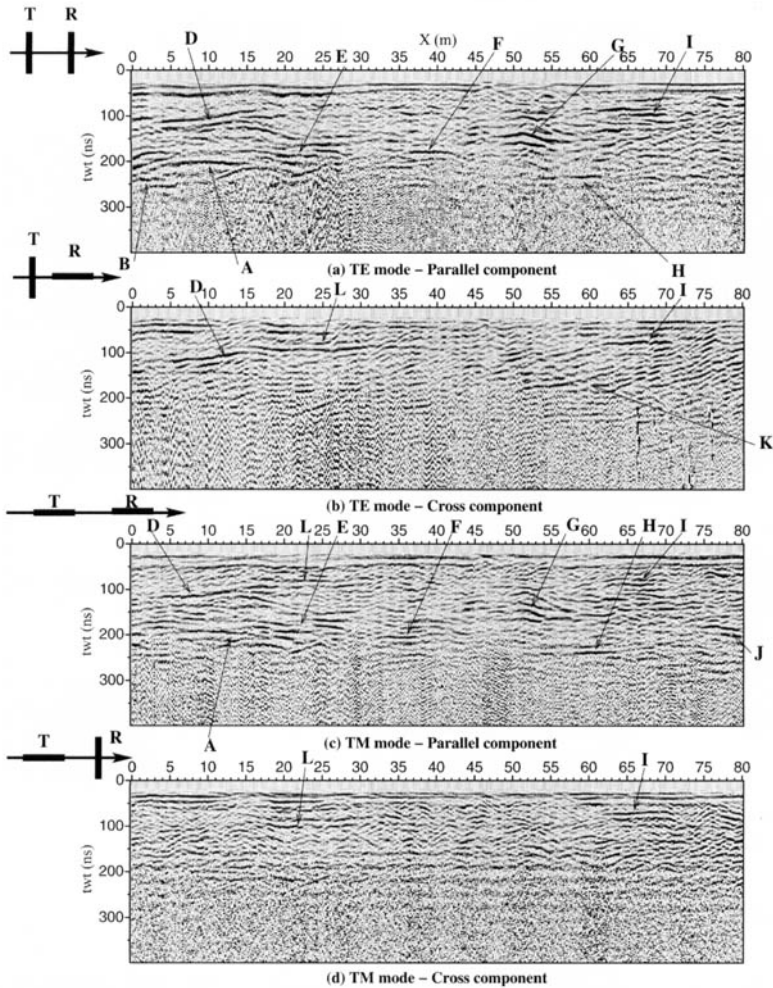
Fig. 8. 100 MHz constant offset profiles after processing. The configurations used reveal the influence of the recorded component. The main structural features are shown by arrows.
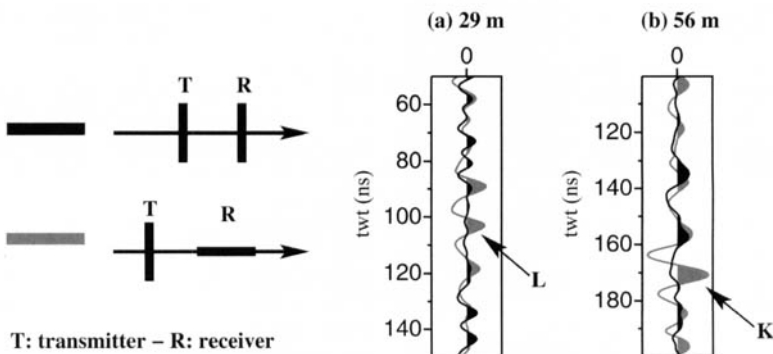
Fig. 9. Comparison of traces recorded using the receiver dipole parallel or perpendicular to the transmitter dipole at a distance of (**a**) 29 m, and (**b**) 56 m. They display high amplitudes for reflections L and K when the dipoles are perpendicular.
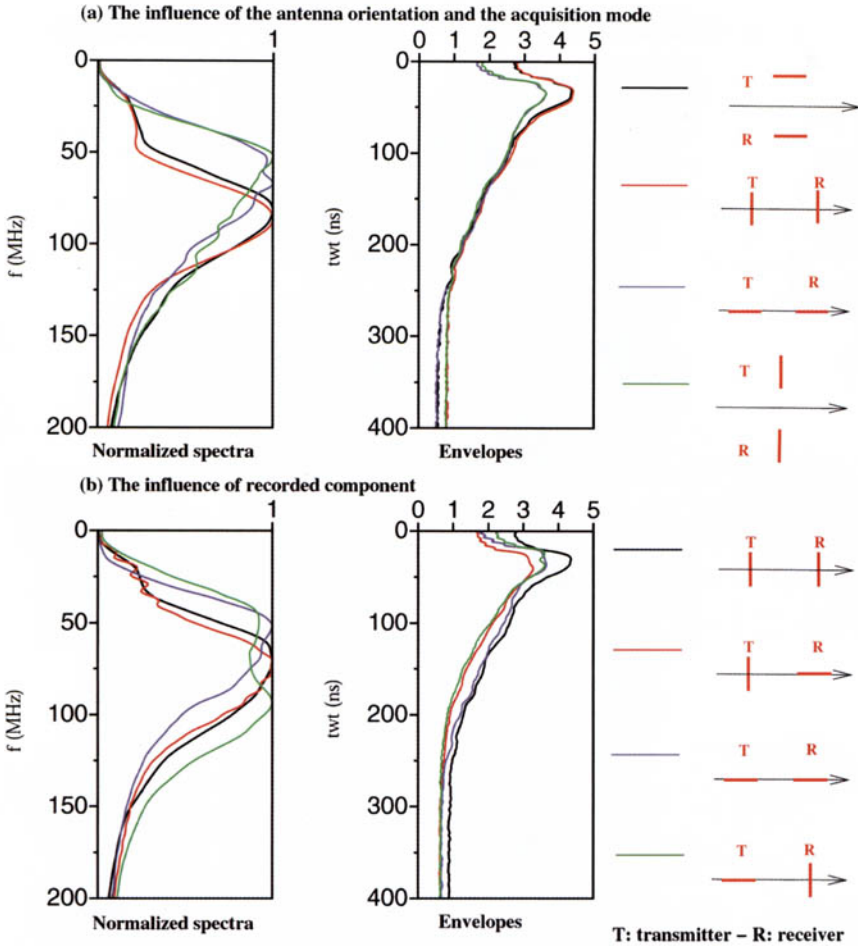
Fig. 10. Averaged spectra and envelopes of the 100 MHz constant offset profiles using the different antennae configurations. The comparison of the curves reveal the influence of (**a**) the antennae orientations and the acquisition mode and (**b**) the influence of the recorded component on these quantities.

the noise level is slightly greater when using the antennae perpendicular to the recording line. On the other hand, Figure 10*b* reveals that the envelope relative of the TE parallel-polarized component profile has a greater amplitude compared to that of the TE cross-polarized component profile, although the spectra are similar. Lastly, concerning the TM component, the bandwidth spectra of the cross-polarized component profile is the largest, but the envelope amplitude is significantly reduced, except below the time 60 ns, which corresponds to the direct ground wave.

Pseudoprofiles

Lehmann *et al.* (2000) proposed to built pseudo-profiles little influenced by the antennae orientation

by simply summing, before any processing, the two profiles recorded with the antennae parallel and perpendicular to the line in each acquisition mode (Fig. 11). These pseudoprofiles allowed us to gather information from the different profiles and to improve the subsurface image quality. Most reflections appear stronger on the TE pseudo-profile, certainly because of the greater TE component reflection coefficient amplitude, when considering the same incident angle and the same medium properties.

To go further, we built additional pseudoprofiles, which are characterized by a low dependence on the acquisition mode, by summing, firstly, the two profiles relative to the TE$^\parallel$ and TM$^\perp$ components and, secondly, the two profiles relative to the TE$^\perp$ and TM$^\parallel$ components (Fig. 12). These pseudo-
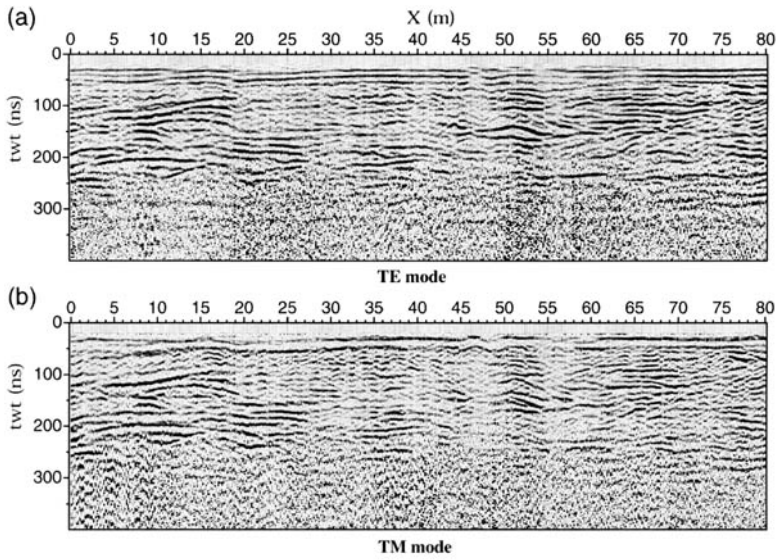
Fig. 11. (a) TE and (b) TM mode pseudoprofiles, corresponding to the sum of the profiles recorded using the dipoles parallel and perpendicular to the recording line in each acquisition mode.
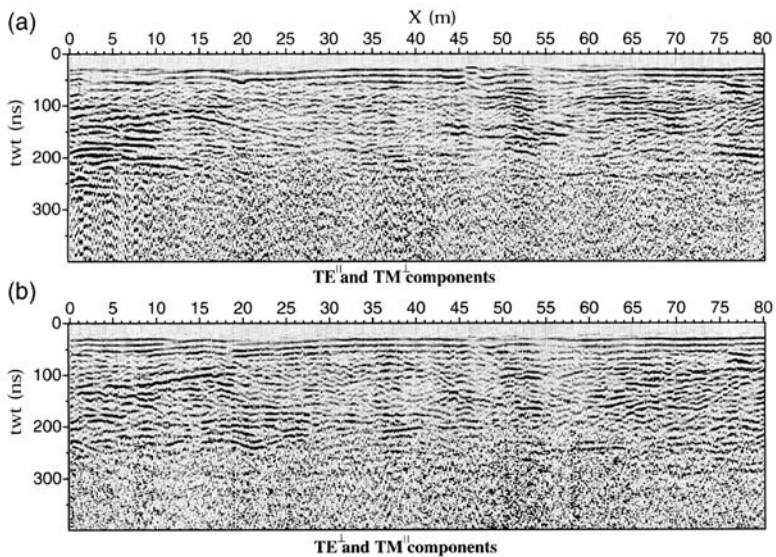
Fig. 12. Pseudoprofiles corresponding to the sum of the profiles relative to (a) the TE$^{\parallel}$ and TM$^{\perp}$ components, and (b) the TE$^{\perp}$ and TM$^{\parallel}$ components.

profiles reveal differences due to the propagation path (preferentially perpendicular and parallel to the recording line respectively), thus suggesting the presence of significant 3-D effects on GPR images.

Maps of the polarization match factor

The polarization match factor p is defined as $p = |\vec{P}_r.\vec{P}_w|^2 = (sin(atan(\frac{A_p}{A_q})))^2$, where $\vec{P}_r$ and $\vec{P}_w$ are

the receiver antenna polarization unit vector and the incident wave polarization unit vector respectively. A_p and A_q are the envelope amplitudes of the recorded signal when the receiver antenna is respectively parallel and perpendicular to the transmitter antenna. When p is close to 1, most of the energy is recorded with the receiver antenna parallel to the transmitter antenna, while when p is close to 0 there is a loss of information when the antennae are parallel to each other.

Figure 13 displays maps of the polarization match factor. It shows that, for the TE mode, the direct wave in the ground corresponds to p values close to 1, thus revealing few polarization modifications due to the superficial medium. Most reflections, well marked on the parallel profile, correspond to high p values. It can be verified that reflections seen on the cross-component profile only (reflector L for example) correspond to low p values on the polarization match-factor map. In TM mode, p values corresponding to the direct wave in the ground vary a lot, thus revealing modifications of the wave polarization due to the superficial medium at some places. Most reflections, well marked on the TM parallel component profile, correspond to high p values, except reflection 1, marked on both profiles.

Polarimetric measurement

Additional surveys have been carried out in order to have the polarization unmatched phenomena

with a better precision. This polarimetric measurement is made by rotating the receiver antenna every 10°, while the transmitter dipole is kept parallel or perpendicular to the recording line (Fig. 14). After a 180° rotation, both antennae are displaced by 10 cm, so that the mid-point remains at the point corresponding to the position 20 m along the acquisition line. These experiments have been conducted for offsets ranging from 1 m to 6 m. Figure 15a presents the evolution of the traces when the receiver is rotated, while the transmitter dipole is perpendicular to the recording line, for an offset of 3 m. The amplitude versus rotation angle relative to the reflection at 75 ns is presented on Figure 15b, for offsets ranging from 1 m to 6 m. It appears that the minimum amplitude does not appear uniquely at 90°, neither the maximum at 0° or 180°, as expected normally when considering a $TE^\perp$ polarized component. We therefore deduce an important modification of that TE component polarization. This depolarization phenomenon can
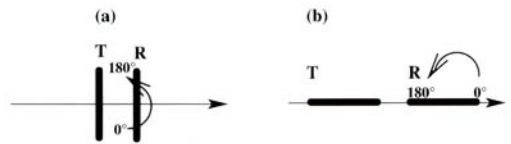
Fig. 14. Antennae configurations used for the 100 MHz polarimetric measurement at the distance X = 20 m.
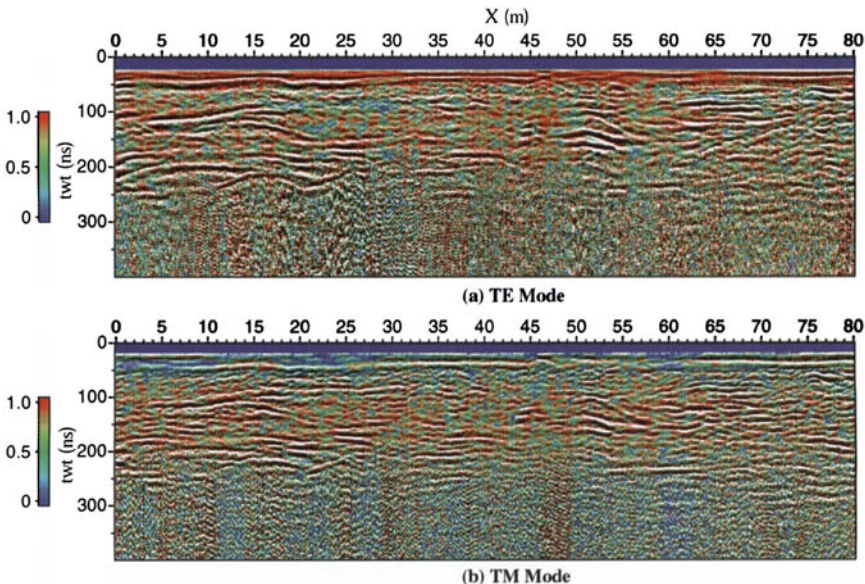
Fig. 13. Maps of the polarization match factor relative to both (**a**) TE, and (**b**) TM acquisition modes. Superimposition with the parallel component profiles.
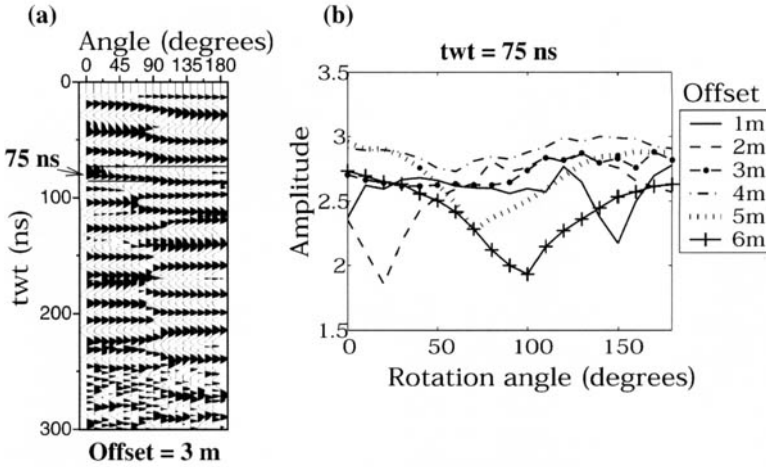
Fig. 15. (a) Evolution of the traces when the receiver dipole is rotated for an offset of 3 m. The transmitter remains perpendicular to the recording line. (b) Amplitude versus rotation angle of the receiver dipole relative to the reflection at 75 ns for different offsets.

explain the unusual observation of phase inversion and amplitude decrease on the corresponding TE CMP gathers (Fig. 16). In fact, according to the theory of the reflection coefficient, such obser-

Fig. 16. Phase inversion and amplitude decrease on TE mode common mid point gather due to field depolarization phenomenon.

vations should appear on TM CMP gathers only, at the Brewster angle. Such phase inversion and amplitude decrease would induce disturbances during usual velocity analysis from CMP gathers, and above all, during the stacking procedures after normal move-out corrections, and thus produce imaging artifacts.

Conclusion

This preliminary field study, built on theoretical considerations relative to dipole radiation patterns and polarization scattering properties of simple reflectors, reveals the potential of multiconfiguration recordings. Firstly, measurements with two antennae orientations in both modes provide supplementary information about the reflector sensitivity to the incident wave polarization. Secondly, measurements of both parallel and cross components provide useful information upon the depolarization properties of the reflectors, and/or on their 3-D out-of-plane location. Finally, according to our amplitude versus receiver angle measurements, depolarization phenomena can be of great importance in some cases and can explain unusual observations, such as decrease in amplitude and phase inversion on TE CMP gathers, that could induce high disturbances during velocity analysis. To sum up, appropriate multi-antennae configuration recordings provide more information about reflectors than single-mode recording and can also be interpreted with greater confidence. As multichannel GPR control units are now widely available, we suggest that, for geological purposes, GPR profiles should systematically be conducted using a quadri-
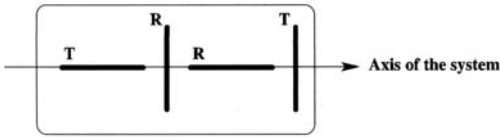
T: transmitter – R: receiver

Fig. 17. System composed of four antennae (two transmitters and two receivers) that could be used to conduct surveys using antennae multiconfigurations.

pole configuration (two transmitters, two receivers) disposed in both parallel and perpendicular configurations (Fig. 17). The use of this system of four antennae oriented with its axis parallel and then perpendicular to the recording line, would allow all of the required data for the proposed antennae multi-configuration methodology (building of pseudo-profiles and polarization analysis) to be obtained. Furthermore, multi-offset surveys should also be conducted in both parallel and cross-polarized configurations, to avoid the artifacts previously described when building stack profiles.

Additional theoretical and experimental work is required to deduce quantitative intrinsic properties of a geological reflector that explain its sensitivity to the incident wave polarization and to its depolarization properties. The theoretical study might be based on 3-D electromagnetic wave propagation modelling for reflectors of different intrinsic properties of a geological reflector that explains its sensitivity to the incident wave polarization and its depolarization properties. The experimental work should consist of multiconfiguration measurement over a test site where different underground reflectors and heterogeneities are known.

References

ALFORD, R. M. 1986. Shear data in the presence of azimutal anisotropy. *56th Annual International Meeting of the Society of Exploration in Geophysical, Expanded Abstracts*, 476–479.

ANNAN, A. P., WALLER, W. M., STRANGWAY, D. W., ROSSITER, J. R., REDMAN, J. D. & WATTS, R. D. 1975. The electromagnetic response of a low-loss, 2 layer, dielectric earth for horizontal dipole excitation. *Geophysics*, **40**, 285–298.

ARCONE, S. A., LAWSON, D. E., DELANEY, A. J. & MORAN, M. 2000. 12–100 MHz depth and stratigraphic profiles of temperate glaciers. *Proceedings of the 8th*

International Conference on GPR, 23–26 May, Gold Coast, Australia, 377–382.

BALANIS, C. A. 1989. *Advanced Engineering Electromagnetics*. J. Wiley, New York, USA.

ENGHETA, N. & PAPAS, C. H. 1982. Radiation patterns of interfacial dipole antennae. *Radio Science*, **17**, 1557–1566.

GARAMBOIS, S., SÉNÉCHAL, P. & PERROUD, H. 2002. On the use of combined geophysical methods to assess water content and water conductivity of near-surface formations. *Journal of Hydrology*, **259**, 32–48.

HARGREAVES, N. D. 1977. The polarization of radio signals in the echo sounding of ice. *Journal of Physics, D: Applied Physics*, **10**, 1285–1304.

HELM, A. & YARAMANCI, U. 1998. Cavity identification with GPR using variable offset and antenna orientation. Proceedings of the 60th European Association of Geophysicists and Engineers Conference and Technical Exhibition, 8–12 June, Leibzig, Germany, 5–14.

JOL, H. M., MEYERS, R. A., LAWTON, D. C. & SMITH, D. G. 1994. A detailed ground penetrating radar investigation of a coastal barrier spit, Long Beach, Washington, U.S.A. *Proceedings of the Symposium on the Application of Geophysics to Engineering and Environmental Problems, 27–31 March, Boston, Massachusetts, 107–127.*

LEHMANN, F., BOERNER, D. E., HOLLIGER, K. & GREEN, A. G. 2000. Multicomponent georadar data: Some important implications for data acquisition and processing. *Geophysics*, **65**, 1542–1552.

LUZITANO, R. D. & ULRYCH, T. J. 1994. Instantaneous polarization match: identifies amplitude changes due to anomalous polarization in GPR data. *Proceedings of the 5th International Conference on GPR, 12–16 June, Kitchener, Ontario, Canada*, 101–115.

LUZITANO, R. D. & ULRYCH, T. J. 1996. The value of two-component GPR data: identifying the polarization contribution in amplitude anomalies. *Proceedings of the Symposium on the Application of Geophysics to Engineering and Environmental Problems, 2 May, Keystone, Colorado*, 1179–1187.

RADZEVICIUS, S. J., & DANIELS, J. J. 2000. Ground penetrating radar polarization and scattering from cylinders. *Journal of Applied Geophysics*, **45**, 111–125.

RADZEVICIUS, S. J., GUY, E. D. & DANIELS, J. J. 2000a. Pitfalls in GPR data interpretation: differentiating stratigraphy and buried objects from periodic antenna and target effects. *Geophysical Research Letters*, **27**, 3393–3396.

RADZEVICIUS, S. J., DANIELS, J. J., GUY, E. D. & VENDL, M. A. 2000b. Significance of crossed-dipole antennae for high noise environments. *Proceedings of the Symposium on the Application of Geophysics to Engineering and Environmental Problems, 20–24 February, Arlington, VA*, 407–413.

REPPERT, P. M., MORGAN, F. D. & TOKSÖZ, M. N. 2000. Dielectric constant determination using ground penetrating radar reflection coefficients. *Journal of Applied Geophysics*, **43**, 189–197.

ROBERTS, R. L. & DANIELS, J. J. 1996. Analysis of GPR polarization phenomena. *Journal of Environmental and Engineering Geophysics*, **1**, 139–157.

STRATTOM, J. A. 1941. *Electromagnetic Theory.* McGraw-Hill, New York, 615 pp.

TILLARD, S. 1991. *Evaluation des performances de la technique radar en prospection géophysique.* Ph.D. thesis, Strasbourg I, France.

VAN GESTEL, J.-P. & STOFFA, P. L. 2001. Application of Alford rotation to ground-penetrating radar data. *Geophysics,* **66**, 1781–1792.

This page intentionally left blank

The use of GPR to image three-dimensional (3-D) turbidite channel architecture in the Carboniferous Ross Formation, County Clare, western Ireland

J. K. PRINGLE, J. D. CLARK, A. R. WESTERMAN & A. R. GARDINER

Institute of Petroleum Engineering, Heriot-Watt University, Edinburgh EH14 4AS, UK (e-mail: jamie.pringle@pet.hw.ac.uk)

Abstract: Petroleum reservoir models are currently built from two-dimensional (2-D) information. An understanding of both the large-scale and internal three-dimensional (3-D) architecture of turbidite channel deposits is important for both hydrocarbon exploration and production. A ground penetrating radar (GPR) survey was undertaken on a study site exposing Upper Carboniferous Ross Formation deposits in western Ireland. Both channel margins and intrachannel fill were imaged in 3-D. Constant-offset, 2-D reflection sections were calibrated by vertical radar profiles. GPR data were integrated with sedimentary and survey data to produce a 3-D model of the study site.

In petroleum reservoirs, highly detailed, down-borehole information constrains near-well geology, but only a very small amount of the reservoir is sampled. Where spacing between wells is relatively large (typical values in the North Sea being ~1000 m, Henson pers. comm.), the inter-well volume is poorly understood. Conventional seismic datasets over reservoirs can identify large-scale sedimentary features, such as 15–25 m-thick sand bodies observed on moderate-quality two-dimensional (2-D) seismic lines (Weber 1993). Kolla *et al.* (2001) detailed how high-resolution, closely spaced three-dimensional (3-D) seismic surveys of Tertiary deposits offshore of Angola could resolve sinuous turbidite channels in 3-D. However, while seismic datasets usually cover the whole reservoir, their low resolution has been a limiting factor in interpreting internal architectures, which can prove barriers to reservoir flow, especially laterally (Arnot *et al.* 1997).

Studies of outcrops of analogous reservoir rocks can provide quantitative data on the inter-well volumes, which can then be used to populate reservoir models (e.g. Stephens *et al.* 2001). Outcrop analogue studies generally involve detailed analysis of well-exposed 2-D, planar-like cliff-faces (methodology summarized in Arnot & Lewis, 1997). Subsequent measurements obtained have to be manipulated to account for the problem of estimating 'partial' geometries of architectures bigger than the outcrop itself, a major drawback when using outcrops. Geehan (1993) and Geehan and Underwood (1993) presented a mathematical solution by measuring 'complete' bed lengths, observable in outcrops, and mathematically calculating the most probable 'partial' bed lengths. Visser and Chessa (2000) produce a refinement of this method, removing outcrop length as a factor, based on conditional probability theory.

While typical outcrop exposures allow detailed characterization of 2-D vertical sections through channel-fill deposits, they rarely provide data on the detailed planform architecture. The representivity of a single outcrop is difficult to judge; therefore current models are built either using appropriate subsets of a representative outcrop analogue, or using several analogues to assess sensitivity of the model to the input data (e.g. Beauboeuf *et al.* 2000). A major problem is the uncertainty in characterizing 3-D volume. 2-D outcrop exposures have been used to generate geostatistics for modelling, but shale-horizon lengths exposed in planar outcrops, for example, do not fully reflect shale distributions, since they may be influenced by the outcrop shape and orientation (Weber 1986). Even if exposures are exceptional and palaeocurrent direction can be inferred (Fig. 1*a*), the 3-D distributions cannot be known with any certainty (Fig. 1*b* & *c*).
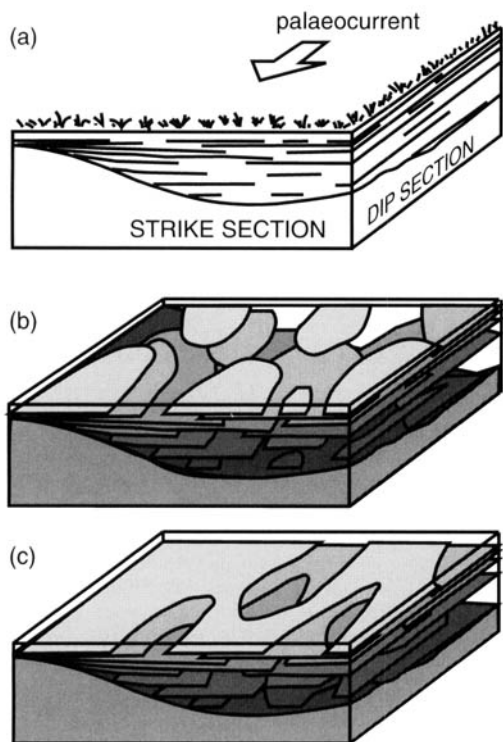
Fig. 1. The schematic diagram illustrates the difficulty in creating 3-D models from 2-D outcrop data, in this case of a turbidite channel fill. Both (**b**) showing elliptical shale units and (**c**) showing elliptical amalgamation surfaces, cutting through continuous shale horizons, honour the observed shale lengths exposed on the strike- and dip-sections of the outcrop shown in (**a**). (From Stephen *et al.* 2001).

Research has been undertaken by other researchers (Bryant *et al.* 2000; Xu *et al.* 2000) to create 3-D digital models of outcrops. Recent research at Heriot-Watt University has obtained 3-D geometries from outcrop analogue sites (Pringle *et al.* 2000). Our technique combines detailed sedimentary field logs with GPR data and digital photogrammetry products. Datasets are integrated to form a digital 3-D outcrop model.

Digital outcrop model techniques were developed in studies on Ordovician turbidites in the Scottish Borders and on Carboniferous turbidites in Derbyshire, UK. This paper introduces a study of the Carboniferous Ross Formation, County Clare, Ireland, an internationally recognized turbidite outcrop analogue site. The aims of this research are two-fold: (1) to create digital 3-D volumetric models of the study site, and (2) to image intrachannel stratal patterns in 3-D. Resulting models can then be analysed to provide 3-D quantitative data for

reservoir modellers and used as reference for reservoirs with similar depositional units.

Carboniferous Ross Formation

The Carboniferous (Namurian) Ross Formation represents a thick accumulation of sandstones and shales forming the early fill of the Western Irish Namurian Basin (Collinson 1991). The basin shows a systematic progradational fill from basinal shales (Clare Shales) to deep-water shales and turbidites (Ross Formation), to chaotic slope deposits (Gull Island Formation) and shallow-water upward-coarsening deltaic sequences (Central Clare Group). Figure 2 shows the stratigraphic column.

The deep-water facies of the Ross Formation are interpreted as having been deposited in front of a major delta system, similar in size and character to the delta system that deposited the overlying Central Clare Group (Collinson 1991). The Ross Formation is very well exposed in coastal sections around the Loop Head peninsula (Fig. 3). Here, the formation is 380 m thick and consists of 75% sandstone, but rapidly thins to the north and south. North of the Loop Head peninsula, near the Cliffs of Moher, the Ross Formation forms only part of a 12 m succession of black shales. Within these shales, and within discrete shale horizons of the turbidite sequence, Goniatites of H to R1 age have been identified, which can be used to correlate outcrops across the basin (Hodson 1954). Palaeocurrents in the Ross Formation show that sediment was largely sourced from the southwest.

The sandstone depositional units consist predominantly of sheet-like turbidites formed within laterally extensive, layered or amalgamated sand-rich units. Interbedded within these sheet sandstones are erosional, small-scale channels, typically 100–500 m wide and 5–15 m deep. These channels have been interpreted as being deposited from laterally shifting sediment sources from deltaic and submarine slopes (Elliott 2000*a*). Other features of interest include extensive slides with large slump folds, spectacular, large, flute-shaped scours, sand volcanoes and small-scale sandstone dykes. Elliott (2000*b*) has suggested that the 'megaflutes' occur in specific distributions and may be the site of turbidite channel initiation.

Bridges of Ross study site

Several turbidite channels with inclined beds comprising alternations of mud-clast conglomerate and sandstones have been identified above the Ross Slide in the Bridges of Ross outcrop (Eire grid reference: Q736506). The study site, east of the Bridges of Ross car park, was chosen because the
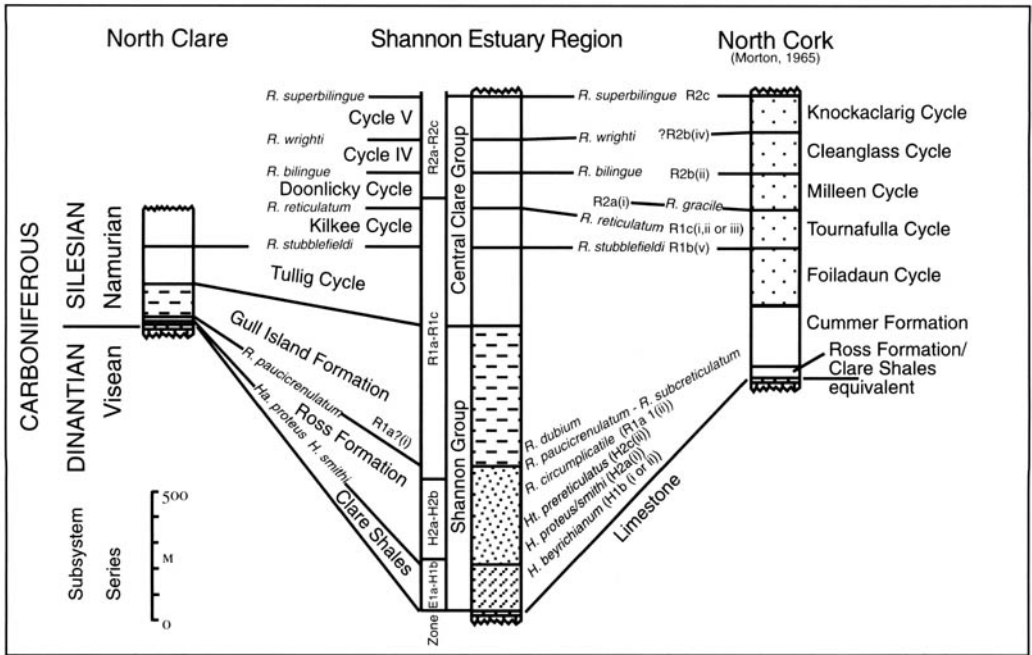
Fig. 2. Stratigraphy of the fill of the Namurian Western Irish Basin, showing the thickening of the Ross Formation in the Shannon Estuary area. (After Collinson *et al.* 1991)

cliff-faces show a turbidite channel exposing both margins and intrachannel fill (Fig. 4), with no overburden and almost planar top surfaces (Fig. 5). This made GPR data acquisition relatively straightforward. The fill of this channel was described and interpreted (Fig. 4*b*); it consists of medium and thick-bedded sandstones, thin discontinuous shales and mud-clast conglomerates deposited along inclined bedding surfaces.

Extensive surveying using standard theodolite equipment allowed the reconstruction of the study site surface. A 3-D surface model of the outcrop was generated in Roxar RMS software (Fig. 6). Survey data from the terrace edges were used to generate synthetic 'faults', which 'offset' the topographic surface, in order to avoid smoothing in the generation of the surface grid. The surface top was subdivided into ten terraces(T^{1-10}) for easier identification (marked on Fig. 6). Note that T^1 includes more than one surface, but this area is not part of the GPR survey site.

The west cliff-face shown in Figure 4 was also extensively surveyed. Three sedimentary logs, acquired at locations VRP1 and VRP2 and one location on the eastern cliff-face, were converted into pseudo-well logs, which have been incorporated into the models (represented by the subvertical columns in Fig. 6).

GPR acquisition and testing

An intensive week of GPR acquisition was undertaken at the Bridges of Ross study site in September 2000. A series of in-lines and cross-lines (Fig. 7) were acquired using the fixed-offset profiling technique across the top surface of the study site, using pulseEKKO 1000 GPR equipment. Survey lines were often reprofiled using a variety of antenna frequencies (Table 1 lists the parameters used for profiling). Profiles were also surveyed, for later static corrections to be applied during processing, to account for surface rugosity.

Extensive testing was undertaken before the main survey in order to choose the optimal dominant frequency antennae to image the turbidite channel base, channel margin and the intrachannel fill. Figure 8 shows fixed-offset profiles acquired on the same line (I6) using: (1) 225 MHz, and (2) 450 MHz dominant frequency antennae. Note that statics adjustments have not been applied on these sections (the obvious distortions at ~5.5 m occur as a result of crossing a terrace edge). Figure 8*b* shows the 450 MHz frequency antennae profile, which images the shallow subsurface (0–25 ns) much better than the same area profiled by the 225 MHz frequency antennae. The 110 MHz dominant frequency antennae profile, not shown here,
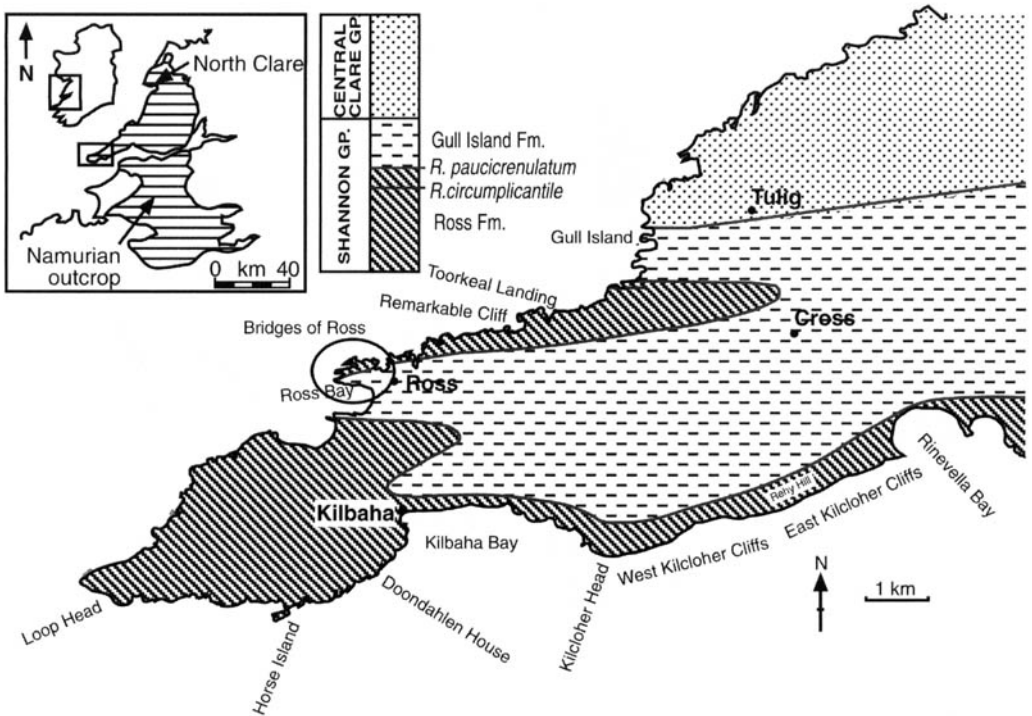
Fig. 3. Location map of the study area (circled), with (inset) location of the Loop Head peninsula and the outcropping of the Shannon Group and overlying Central Clare Group. The outcrop pattern reflects the ENE–WSW-oriented Variscan structures. The extent of the *R. circumplicantile* marine band (used for dating purposes) is uncertain.

successfully imaged the channel base, but did not resolve reflection events in intrachannel areas. Fixed-offset profiles using 225 MHz antennae were utilized over all the profile lines shown in Figure 7. Although these profiles imaged the whole channel (see Fig. 9 for example), intrachannel-fill reflection events were not resolvable. A smaller profiling survey was then undertaken over the southwestern side of the survey area using 450 MHz dominant frequency antennae (shown as bold lines on Fig. 7).

The frequency spectra of the reflection events recorded with different frequency antennae in the test lines were also analysed (Fig. 8c). The 110 MHz and 225 MHz antennae show comparatively narrow bandwidths, although they have the greatest penetration depths. The 450 MHz antennae show by far the widest bandwidth, which should provide the best profiles. Ideally a combination of 225 MHz and 450 MHz dominant frequency profiling should give the clearest picture of the shallow subsurface. Testing all available frequencies on a study site before a full survey commences was shown here to be critical in order to gain the best possible data.

Techniques to calculate site velocities

Common mid-point (CMP) gathers

As is the usual practice when acquiring GPR data, common mid-point (CMP) gathers were acquired on a test line (I1), using 110 MHz and 225 MHz frequency antennae. During subsequent processing, interval velocities between reflection events were calculated, the average velocities derived from the two CMPs being 0.15 m ns^{-1} (eight samples with a reflection coefficient [RC] of 0.99) and 0.14 m ns^{-1} (five samples, with an R2 of 0.97) for the 110 MHz and 225 MHz frequency antennae respectively. This variation in velocities is interesting and is discussed further in Pringle *et al.* (2003).

Vertical radar profiles (VRPs)

Subsurface GPR reflection events need to be correlated with observed geology. Research at Heriot-Watt University has adapted the vertical seismic profiling (VSP) technique to acquire vertical radar profiles (VRPs) (see Pringle *et al.* 2003 for a more detailed description). The transmitter and recorder
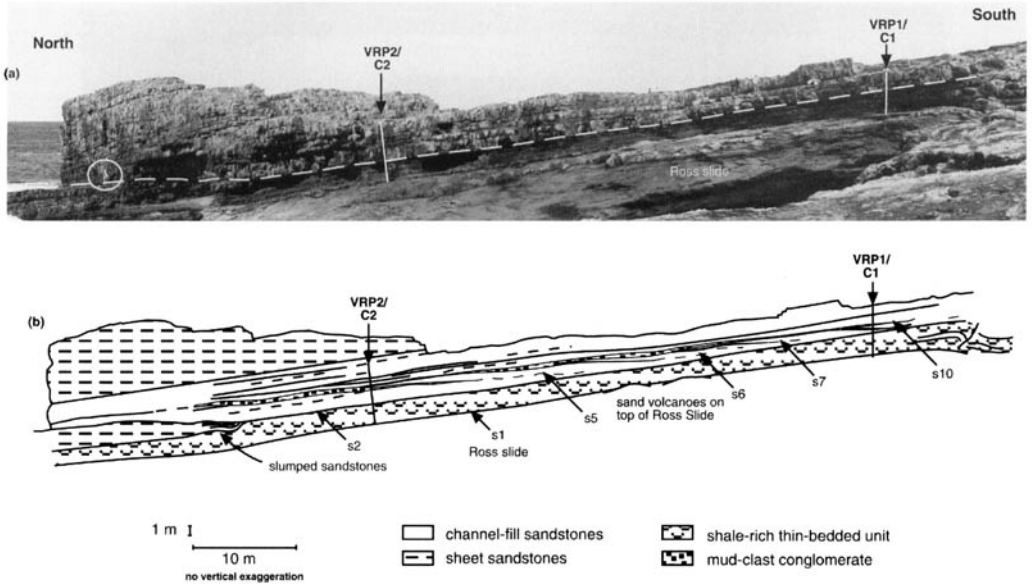
Fig. 4. (**a**) Photomosaic of the western cliff-face at the Bridges of Ross study site (circled figure for scale), showing a turbidite channel with erosive base (marked by the dashed line). VRP1 and VRP2 locations are marked, as are the end-points of cross-lines C2 and C1. (**b**) Sketch of architecture shown in (a), section oriented slightly oblique to palaeocurrent direction (northeast). Intrachannel fill of south-dipping sandstones and mud-clast conglomerates are shown. Possible correlations with GPR interpreted horizons (s1, s2, s5, s6, s7 and s10) are marked (compare GPR profiles in Figs 10–13).

Fig. 5. (**a**) View of the top surface of the Bridges of Ross study site, looking northwestward. The planar surface (although interrupted by terraces) was ideal for GPR profile acquisition. The top surface has been subdivided (T^{1-9}) for easier identification. The C2 cross-line can be seen (white tape). (**b**) Photograph of the VRP2 location on the west cliff.

are left at the cliff-top, with the receiver being moved progressively down the cliff-face at a constant sample interval. After processing, the up-going wavefield is displayed within time/distance axes. Reflection events can then be tied to observed sedimentological horizons on the cliff-face and extended into the subsurface data. Unfortunately the first VRP was corrupted, but the VRP acquired at location VRP2 (1.86 m long) shows a strong direct ground-wave, with an overall average velocity of 0.23 m ns^{-1} being calculated from the 95 first-arrival picks. Small velocity changes are
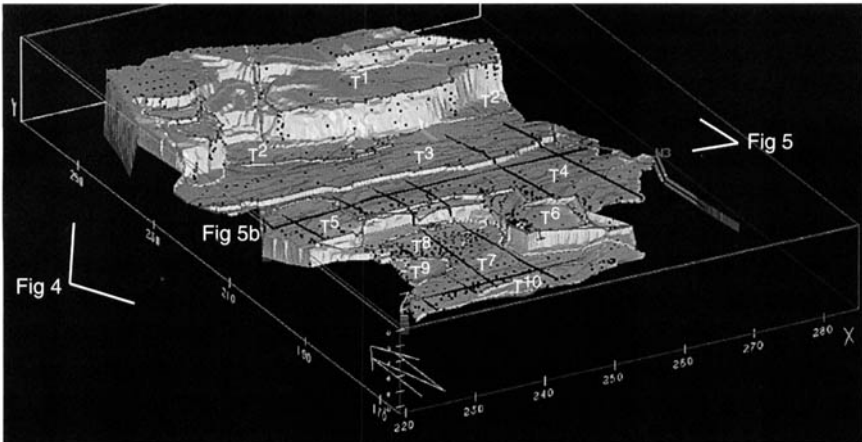
Fig. 6. Standard surveying techniques (using theodolite equipment) of the study-site outcrop surface produced a set of coordinate points (dots). These data were used to grid a 3-D surface using Roxar RMS software. The terrace edges were modelled as 'faults' to help in the surface gridding process. The terraces are numbered (T^{1-10}) for identification on profiles. 225 MHz GPR profile locations are shown (black lines). Three sedimentary logs acquired on cliff-faces were imported as pseudo-well logs (columns).
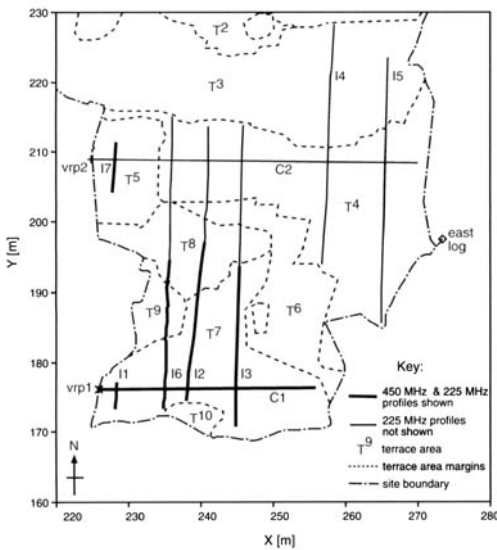
Fig. 7. Plan-view map of the study area showing the location of the GPR profiles, VRP profiles and sedimentary log locations. GPR profiles included in subsequent figures are shown as bold solid lines. Dashed lines show the terraces (T^{1-10}); compare with Figure 6. Note 450 MHz frequency data part-profiles lines I2, I3 and I6, i.e. do not extend to T^4 or T^6 areas.

observed at reflecting horizons, which may reflect lithological velocity variations (for further discussion see Pringle *et al.* 2003). The average velocity was used to correct elevation statics on subsequent fixed-offset profiles, as well as converting the 2-D profiles from time to depth.

GPR fixed-offset profile results and interpretation

Once the fixed-offset profiles had been processed using standard seismic techniques (Pringle *et al.* 2003, table 3), reflection events could be interpreted as mappable horizons. In-line I7, nearest the west cliff-face at the northern end of the study site, was only profiled using 225 MHz frequency antennae (Fig. 9a). However, the northern channel margin observed in Figure 4 could be found to correlate with reflection events on the radar in-line (Fig. 9b). The I1 in-line (used for initial frequency tests) was profiled using all frequencies, and reflection events were tied to nearby vertical cliff-edges. The 450 MHz frequency profile is shown in Figure 10a. Interpretation of this in-line (Fig. 10b) shows dipping bedforms, which can be correlated with observed sedimentary horizons (Fig. 10c). This profile gave us some confidence that the high-frequency GPR profiles were imaging subsurface reflection events which could be correlated to observed sedimentary horizons in cliff-faces.

Westward of in-lines I7 and I1 are in-lines I2, I6 and I3 (see Fig. 7 for location). These in-lines were profiled with 450 MHz frequency antennae (Figs 11–13). Figure 11 shows the statically corrected in-line I6. The mud-clast conglomerate layer exposed on terrace T^9 can be correlated with our interpreted horizon s10, which extends below both the T^7 and T^8 terraces.

Table 1. *GPR F-O, CMP and VRP profile parameters**

Instrument system	Antenna frequency (MHz)	Acquisition technique	Antennae separation (m)	Trace sample spacing (m)	Time window (ns)	Window range (m)	Stacks	Sampling interval (ps)
PE100	50	F-O profile	2	0.2	300	15	512	800
PE100	100	F-O profile	1	0.2	200	10	512	800
PE100	200	F-O profile	0.5	0.1	200	10	512	800
PE1000	225	F-O profile	0.5	0.1	20	1	512	300
PE1000	450	F-O profile	0.25	0.05	20	1	512	100
PE100	100	CMP	–	0.1	300	15	256	800
PE1000	225	CMP	–	0.05	100	5	128	300
PE1000	225	VRP	–	0.02	180	9	512	300

F-O, fixed offset
CMP, common mid-point
VRP, vertical radar profiling
*These parameters were used unless otherwise stated in the text.

From the interpreted surfaces (s1–s10) shown in Figures 11–13, it is clear that the southerly channel margin (represented by s8 surface) is migrating northward and is oriented SW–NE. This reflects the average palaeocurrent direction observed in this study and by other authors (Elliott 2000*a*). Interpreted horizons clearly show intrachannel dipping horizons (e.g. s5, s6 and s7). These interpreted surfaces have been corrected to depositional dip (flattened on T^7 surface) and correlated between inlines. Time values were converted to depth, and contour plots of surfaces s5, s6 and s7 were generated (Fig. 14). Interpreted surfaces s6 (Fig. 14*b*) and s7 (Fig. 14*c*) can be clearly seen increasing in dip and eroding the interpreted surface s5 (Fig. 14*a*). From this contour information, dip and strikes were calculated: s5 dips 1.4° toward 090°; s6 dips 3° toward 151°; and s7 dips 3.7° toward 137°. The shallow s5 surface is dipping oblique to channel orientation, whereas the steeper s6 and s7 surfaces are approximately parallel to channel orientation. Contouring the surfaces produced from correlating interpreted horizons from the GPR profiles was important because it shows the 3-D geometry of the intrachannel stratal patterns.

3-D model building

Three volumetric 3-D digital models of the study site were produced, incorporating varying degrees of detail and input data. The simplest model was created from surveyed data of the outcrop surface, sedimentary log information and surfaces digitized from the west cliff-face (Fig. 15*a*). Resulting horizons, however, were planar, as data was simply extrapolated from the 2-D cliff-face. A more detailed model was produced, incorporating surface data as well as interpreted subsurface horizons

imaged on the comparatively low-resolution 225 MHz frequency profiles (Fig. 15*b*). This was an improvement on the initial model (Fig. 15*a*) as it provides 3-D volumetric data. Interpreted horizons from the 450 MHz frequency profiles were then incorporated into a third model; the high-resolution data shows the interpreted channel margin migrating northward (Fig. 15*c*).

Further work

From these models, reservoir models can now be built, probably both deterministically and stochastically, using the surfaces to provide a framework within which 3-D geobodies are stochastically infilled, which honour observed bedding length, width and thickness variations. Fluid-flow simulations can also be undertaken on the resulting models, to see how the 3-D intrachannel-fill heterogeneities, mapped from this GPR survey, affect hydrocarbon sweep efficiency.

A further field season was planned for the summer of 2001, with the aim of acquiring many more 450MHz frequency profiles right across the study area, at a NW–SE orientation to better capture the channel margins. However, because of the foot-and-mouth outbreak in the British Isles during that time, this was prohibited. It is hoped that the site can be returned to at a future date and the fieldwork completed.

Conclusions

The 225 MHz and 450 MHz GPR profiles have imaged the erosive discordant channel base, exposed in the western vertical outcrop face at this study site. In addition, southward-dipping mud-clast conglomerate layers observed in the western
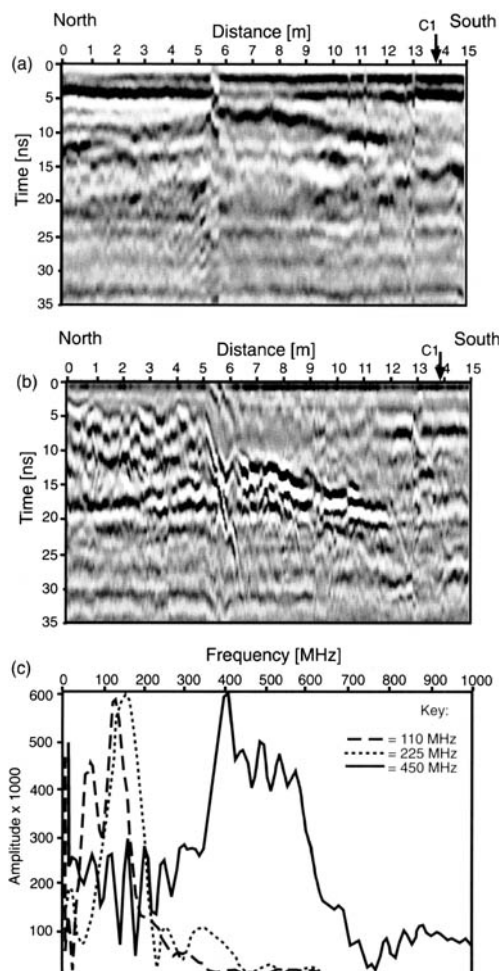
Fig. 8. Comparison of profiles acquired on I6 in-line, using (**a**) 225 MHz and (**b**) 450 MHz frequency antennae. Improved resolution in the top 15 ns can be observed in the 450 MHz section. C1 cross-line location is marked. Note statics corrections have not been applied here, and terrace-edge distortions are clearly observed (at ~5.5 m) on both sections. (**c**) Dominant GPR frequency spectra produced by 110 MHz, 225 MHz and 450 MHz antennae, derived on the same section of line I1. 110 MHz and 225 MHz results show a typically narrow band. 450 MHz antennae results are much more broadband, providing the most useful information.

Fig. 9. (**a**) Statically corrected I7 in-line profiled using 225 MHz frequency antennae, with (**b**) subsequent interpretation. Trace-sample spacing was 10 cm. The incised surface (s8) correlates with the northern channel margin, exposed in the vertical western outcrop face of the survey area, m west of this in-line (see Fig. 4*a*).

cliff-face could also be resolved using higher frequency (450 MHz) GPR antennae. The southern channel margin can be seen to be oriented NW–SE, reflecting the palaeocurrent trend, and can be shown to migrate northwards. Dip and strike measurements of inclined reflectors in intrachannel fill have been calculated from the 3-D subsurface information. If the 450 MHz GPR antennae are used to acquire a 3-D reflection survey, the turbidite channel fill will be fully characterized in 3-D. Integration of sedimentary data, surveying data, GPR profiles and interpreted horizons were used to create 3-D digital models of the study site, with varying detail, depending on the input data.

Presurvey testing of available antennae frequencies to optimize subsequent surveys was shown to be critical to gain the best subsurface data. Applying elevation statics, even on relatively planar, ancient sedimentary study sites was shown to be important in correctly interpreting GPR reflection events.

Fig. 10. (a) Statically corrected I1 in-line partly profiled using 450 MHz frequency antennae, with (b) subsequent interpretation. Trace-sample spacing was 5 cm. Interpreted horizons are numbered. Comparison with nearby outcrop cliff-face (c) shows interpreted horizon 8 may correspond to southerly dipping mud clast conglomeratic layers.
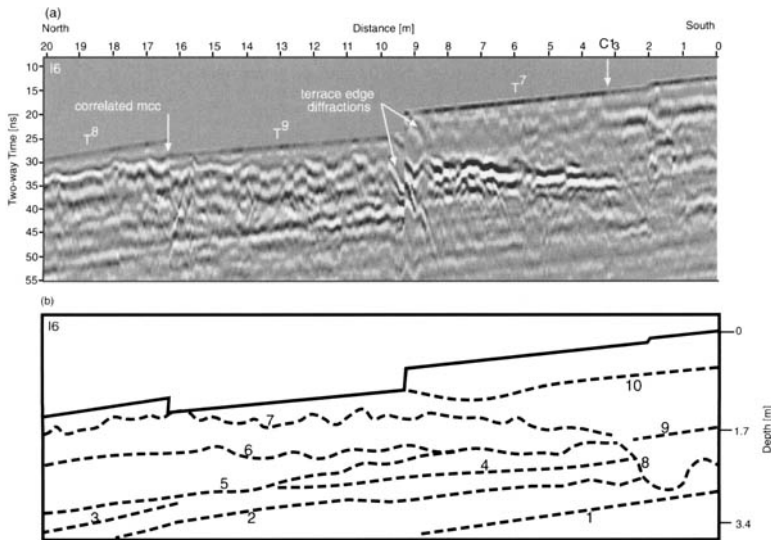
Fig. 11. (a) Statically corrected I6 in-line, partly profiled using 450 MHz frequency antennae, with (b) subsequent interpretation. Trace-sample spacing was 5 cm. Interpreted horizons are numbered. Terrace edges have caused diffractions (marked), illustrating the importance of statically correcting profiles. An exposed mud-clast conglomerate layer in T^9 can be correlated with a subsurface reflector. Comparisons with Figure 4a show the southerly channel margin is possibly imaged in this profile.

References

ARNOT, M. J., GOOD, T. & LEWIS, J. M. 1997. Photogeological and image-analysis techniques for collection of large-scale outcrop data. *Journal of Sedimentary Research*, **67**, 984–987.

BRYANT, I. D., CARR, D., CIRILLI, P., DRINKWATER, N., McCORMICK, D., TILKE, P. & THURMOND, J. 2000. Use of 3D digital analogues as templates in reservoir modelling. *Petroleum Geoscience*, **6**, 195–201.

COLLINSON, J. D., MARTINSEN, O., BAKKEN, D. & KLOSTER, A. 1991. Early fill of the western Irish Namurian Basin: a complex relationship between turbidites and deltas. *Basin Research*, **3**, 223–242.

ELLIOTT, T. 2000a. Depositional architecture of a sand-rich, channelised turbidite system: the Upper Carboniferous Ross Sandstone Formation, Western Ireland. *Proceedings of the Gulf Coast Section of the Society of Economic Palaeontologists and Mineralogists Foundation 20th Annual Conference of Deep-Water Reservoirs of the World, 3–6 December, Houston, USA*, 342–373.
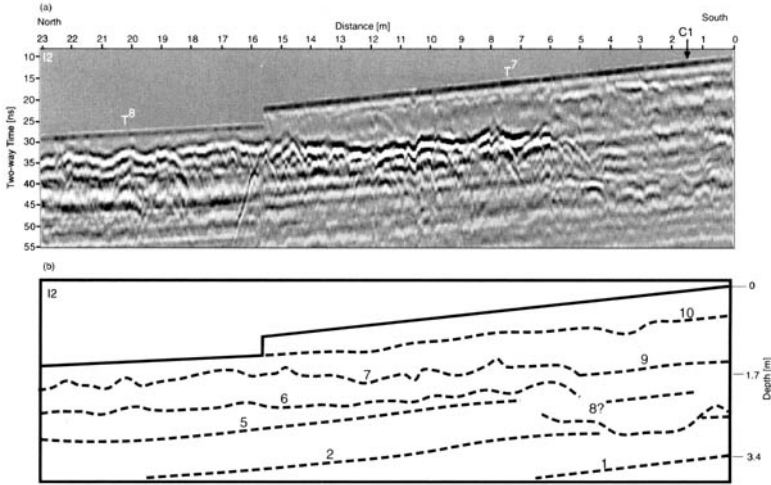
Fig. 12. (a) Statically corrected I2 in-line partly profiled using 450 MHz frequency antennae, with (b) subsequent interpretation. Trace-sample spacing was 5 cm. Interpreted horizons are numbered (cf. Fig. 11).
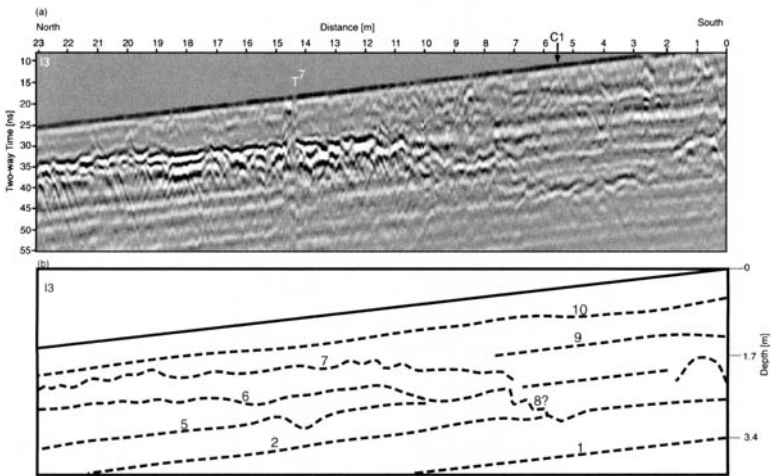
Fig. 13. (a) Statically corrected I3 in-line partly profiled using 450 MHz frequency antennae, with (b) subsequent interpretation. Trace-sample spacing was 5 cm. Interpreted horizons are numbered (cf. Fig. 12).

ELLIOTT, T. 2000*b*. Megaflute erosion surfaces and the initiation of turbidite channels. *Geology,* **28**, 119–122.

GEEHAN, G. 1993. The use of outcrop data and heterogeneity modelling in development planning. *In*: ESCHARD, R. & DOLIGEZ, B. (eds) *Subsurface Reservoir Characterization from Outcrop Observations*. Editions Technip, Paris, 3–64.

GEEHAN, G. & UNDERWOOD, J. 1993. The use of length distributions in geological modelling. *In*: FLINT, S. S. & BRYANT, I. D. (eds) *The Geological Modelling of Hydrocarbon Reservoirs and Outcrop Analogues*. International Association of Sedimentologists Special Publications, **15**, 205–212.

HODSON, F. 1954. The beds above the Carboniferous Limestone in north-west County Clare, Eire. *Quarterly Journal of the Geological Society of London,* **109**, 259–283.

JOSEPH, P., BABONNEAU, N. *ET AL.* 2000. The Annot sandstone outcrops (French Alps): architecture description as input for quantification and 3D reservoir modelling. *Proceedings of the Gulf Coast Section of the Society of Economic Palaeontologists and Mineralogists Foundation 15th Annual Research Conference on Submarine Fans and Turbidite Systems, 4–7 December,* 422–449.

KOLLA, V., BOURGES, P., URRUTY, J. & SAFA, P. 2001. Evolution of deep-water Tertiary sinuous channels offshore Angola (west Africa) and implications for reservoir architecture. *Bulletin of the American Association of Petroleum Geoscientists,* **85**, 1373–1405.
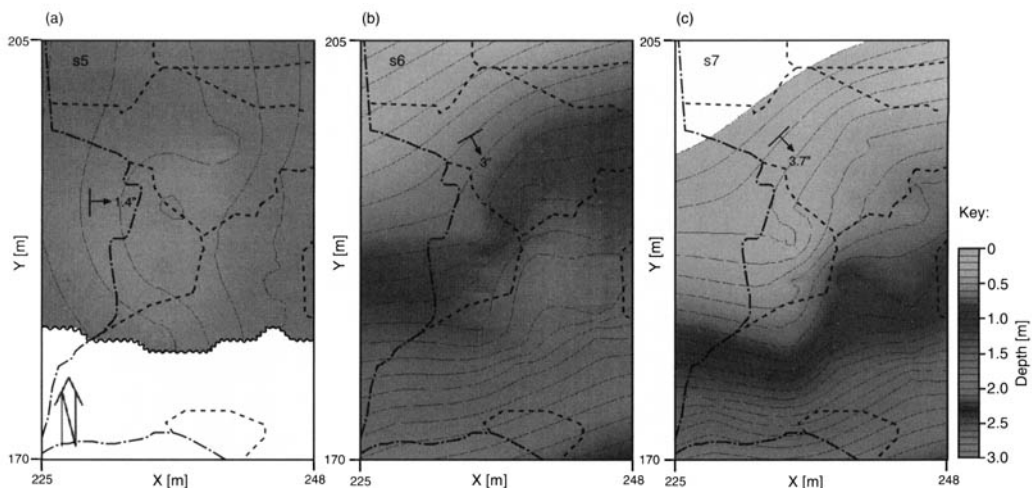
Fig. 14. Interpreted horizons (**a**) s5, (**b**) s6, and (**c**) s7 on 450 MHz profile in-lines I1, I2, I3 and I6 have been picked, correlated and the data have been rotated back to original sedimentary dip. From the picks (dots), interpreted surfaces have been generated, s5 (bottom surface), s6 (grid) and s7 (top), in Roxar RMS software. Surfaces have then been contoured, allowing strike and dips to be calculated for the three horizons.

PICKERING, K. T., COLMAN, J. M. ET AL. 1986. A high sinuosity, laterally migrating submarine fan channel-levee-overbank: results from DSDP Leg 96 on the Mississippi Fan, Gulf of Mexico. *Marine and Petroleum Geology*, 3–18.

PIPER, D. J. W., & NORMARK, W. R. 1983. Turbidite depositional patterns and flow characteristics, Navy submarine fan, California Borderland. *Sedimentology*, **30**, 681–694.

PRINGLE, J. K., WESTERMAN A. R., CLARK J. D., GUEST J. A., FERGUSON R. J. & GARDINER A.R. 2003. The use of vertical radar profiling (VRP) in GPR surveys of ancient sedimentary strata. *In*: BRISTOW, C. S. & JOL, H. (eds) *GPR in Sediments*. Geological Society, London, Special Publications, **211**, 225–246.

STEPHEN, K. D., CLARK, J. D. & GARDINER, A. R. 2001. Outcrop-based stochastic modelling of turbidite amal-gamation and its effects on hydrocarbon recovery. *Petroleum Geoscience*, **7**, 163–172.

VISSER, C. A. & CHESSA, A. G. 2000. Estimation of length distribution from outcrop datasets – application to the Upper Permian Cutler Formation, Utah. *Petroleum Geoscience*, **6**, 29–36.

WEBER, K. J., 1993. The use of 3-D seismic in reservoir geological modelling. *In*: FLINT, S. S. & BRYANT, I. D. (eds) *The Geological Modelling of Hydrocarbon Reservoirs and Outcrop Analogues*. International Association of Sedimentologists Special Publications, **15**, 181–188.

XU, X., AIKEN, C. L., BHATTACHARYA, J. P., CORBEANU, R. M., NIELSEN, K.C., McMECHAN, G. A. & ABDELSA-LAM M. G. 2000. Creating virtual 3-D outcrop. *Leading Edge*, February, 197–202.
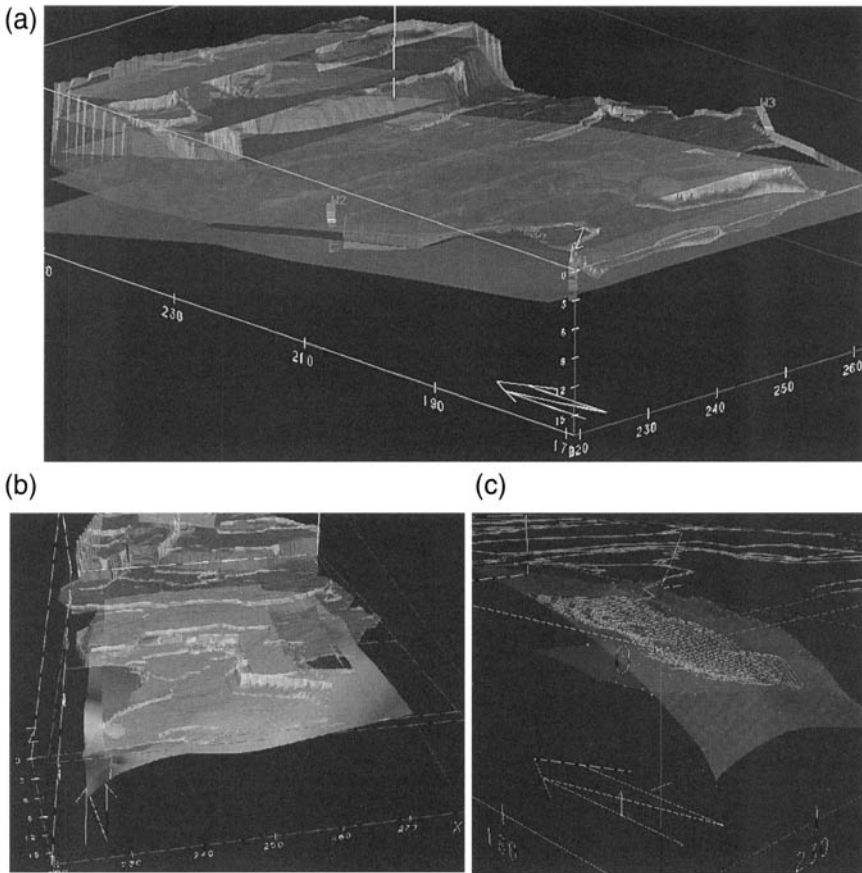
Fig. 15. 3-D digital models of the Bridges of Ross study site, produced in Roxar RMS software. (a) Surface data of the outcrop surface has been used to create this model. Sedimentary log information has been incorporated as pseudo-well logs and used to correlate sedimentary horizons. (b) Interpreted horizons from 225 MHz frequency profiles have been added to the previous model. The contoured surface is interpreted as the channel base. (c) Interpreted horizons from 450 MHz frequency profiles have been incorporated into the surface model, showing the interpreted southerly channel margin migrating northwards.

Index

Note: Page references in *italics* refer to Figures and Tables